Design Development for Steel Strongback Braced Frames to Mitigate Concentrations of Damage

by

Barbara Gwynne Simpson

A dissertation submitted in partial satisfaction of the

requirements for the degree of

Doctor of Philosophy

in

Engineering – Civil and Environmental Engineering

in the

Graduate Division

of the

University of California, Berkeley

Committee in charge:

Professor Stephen A. Mahin, Chair

Professor Filip C. Filippou

Professor Panayiotis Papadopoulos

Summer 2018

Abstract

Design Development for Steel Strongback Braced Frames to Mitigate Concentrations of Damage

by

Barbara Gwynne Simpson

Doctor of Philosophy in Engineering - Civil and Environmental Engineering

University of California, Berkeley

Professor Stephen A. Mahin, Chair

Steel braced frames are characteristically efficient seismic force-resisting systems. However, multi-story steel braced frames tend to concentrate demands in one or a few stories in response to severe ground shaking. Brace buckling and yielding results in a reduction in story strength and/or stiffness. Unless a mechanism exists to re-distribute the inelastic demands to other stories, demands tend to concentrate in the story where the inelastic response was initiated, indicative of story mechanism behavior.

Research has identified the advantages of using pivoting seismic force-resisting systems, herein termed strongback-braced frames, to mitigate story mechanism behavior. Strongback-braced frames employ an essentially elastic truss, or “strongback”, that provides an explicit mechanism of re-distributing demands to adjacent stories. Yielding and energy dissipation is provided through inelastic actions, or fuses (e.g., through brace yielding/buckling and/or beam plastic hinging). Forces and moments developed in these fuses are transferred vertically to adjacent stories by the flexural stiffness and strength of the strongback. As such, strongback-braced frames are expected to result in more uniform drift distributions, reduced peak inelastic demands, and improved design flexibility compared to conventional seismic force-resisting systems.

Despite being employed successfully in both research and practice, systematic assessment of the strongback’s behavior and practical design methods have not been developed or validated. Since the behavior of strongback systems is not characterized by the formation of story mechanisms, prior studies have found it difficult to proportion the elastic members in the strongback truss and have recognized detailing issues related to large deformation demands induced in the fuses. As such, a series of investigations were aimed at understanding the dynamic behavior and seismic performance of steel strongback-braced frames.

Archetype designs were numerically analyzed to characterize the seismic demands in the strongback elements. A four-story strongback-braced frame was used to benchmark the dynamic behavior observed during nonlinear dynamic analysis. Improved numerical models were calibrated to more realistically simulate the buckling-restrained brace response and to characterize the modeling parameters influencing brace buckling and low-cycle fatigue. The FEMA P695 methodology was used to assess potential design methods based on collapse performance. Extensive parametric studies were carried out on strongback geometries with a range of bracing configurations, ground motion characteristics, and design alternatives.

Higher mode effects were identified as the cause of substantial force amplification in the elastic strongback truss. Unlike typical yielding systems where force demands are limited by the capacity of the fuses in every mode, force demands in the strongback are characterized by a yielding first-mode "pivoting" and elastic higher-mode "bending" force demands. Since the strongback is designed to remain elastic in all modes, it can exhibit significant strength and stiffness in higher mode bending. Under the second and higher modes, the strongback truss remains elastic and continues to accumulate force demands after the fuses have yielded and as the ground shaking intensifies. These force demands in the strongback members can be significantly larger than those estimated per traditional capacity design assuming first mode-only demands.

The addition of a strongback results in improved dynamic response from typical yielding systems, including a more uniform drift profile compared to reference buckling-restrained braced frames. Based on this research, this study proposes recommendations for the design, analysis, and modeling of strongback-braced frames. Simplified static methods to estimate the dynamic demands in the strongback truss are also proposed, including modal pushover and modal enveloping analysis methods.

To the memory of Stephen Mahin.

1946-2018

ACKNOWLEDGEMENTS

First and foremost, this dissertation was the result of many years of support and guidance from my research advisor, Prof. Stephen Mahin. His brilliance, vision, and creativity continue to influence me daily.

This research would not have been possible without the insight and advice from a number of outside contributors, including numerous individuals, companies, and organizations whose time, expertise, and services were essential to the completion of this work. The analytical work reported herein was supported by a research grant titled, “Design of Strongback-braced frames”, funded by the American Institute of Steel Construction (AISC). A special thanks goes to Leigh Arber and Tom Schlafly of AISC for their support of this project.

An Advisory Committee of practicing engineers met incrementally to advise the design and development of the strongback system. Each member of the advisory committee was unhesitant about committing their time and expertise towards the success of this project. A sincere thanks goes to James Malley of Degenkolb Engineers, San Francisco; Rafael Sabelli of Walter P. Moore, San Francisco; Leo Panian of Tipping Structures, Berkeley; Tom Kuznik of Herrick Steel, Stockton; and Walterio Lopez of Rutherford and Chekene, San Francisco. Their ideas, insight, and advice were invaluable to this research.

The buckling-restrained brace data used to calibrate the numerical models was provided by Brandt Saxey of CoreBrace, UT. Thanks also to Dr. Ian Aiken and Dr. Cameron Black of Seismic Isolation Engineering, Emeryville for their input on the state-of-practice for buckling-restrained and self-centering braces. The numerical modeling used in this investigation benefited from numerous discussions with Dr. Frank McKenna and Dr. Andreas Schellenberg. Thanks also to my friends, Shanshan Wang, Benshun Shao, and Tal Feinstein, for sharing their ideas, time, and questions.

This work was assisted by many professors, including Prof. Filip Filippou and Prof. Panayiotis Papadopoulos who served on my dissertation committee, Prof. Jon Wilkening and Prof. Abolhassan Astaneh-Asl who served on my qualifying committee, and Prof. Keh-Chyuan Tsai of the National Taiwan University who hosted me as a visiting scholar. Their teaching and guidance were instrumental to the completion of this dissertation. A special thanks goes to Prof. Jack Moehle. I am deeply grateful for his mentorship during the final semester of my Ph.D.

Finally, to my parents and brother who supported me without fail throughout my academic career. As ever, my deepest gratitude goes to my partner, Connor Bybee. I couldn’t have done it without you.

The design of the experimental test that initiated this work was the result of an international collaborative project titled, “Collaborative Developments for Seismic Rehabilitation of Vulnerable Braced Frames,” funded by the National Science Foundation (Grant Number CMMI 1208002) through the George E. Brown Jr. Network for Earthquake Engineering Simulation research program. Any opinions, findings, and conclusions or recommendations expressed in this report are those of the authors and do not necessarily reflect the views of the National Science Foundation, American Institute of Steel Construction, or other participants in the overall research program.

CONTENTS

LIST OF FIGURES

LIST OF TABLES

1 Introduction

1.1 BACKGROUND

Steel braced frames are inherently stiff systems that are naturally efficient in resisting seismic demands. During earthquakes, concentrically braced frames dissipate energy through tensile yielding and compression buckling of the braces. Successful designs recognize and account for the re-distribution of forces as braces buckle in compression, yield in tension, and subsequently lose strength after buckling. But reliance on brace buckling can be less than ideal, and braced frames can exhibit a number of undesirable damage modes, such as deterioration of brace compression capacity, local buckling of the braces, and rupture of the connections and members.

To attain acceptable behavior, diagonal braces are specially detailed to exhibit a stable inelastic response. The introduction of special ductile-detailing, buckling-restrained braces, and capacity-design principles in modern building codes has resulted in improved brace deformability and protection of critical connections and elements. However, though these and other design recommendations have improved their reliability and ductility, conventional steel braced frames are still susceptible to concentrations of demand in one or a few stories [e.g., Uang and Bertero (1986), Foutch et al. (1987), Khatib et al. (1988), Sabelli (2001), Tremblay (2003), Rai and Goel (2003), Hines et al. (2009), Uriz and Mahin (2008), Chen and Mahin (2012), Lai and Mahin (2013), Simpson and Mahin (2018a), etc.], indicative of story mechanism behavior like that shown in Figure 1.1(a).

Story mechanisms in braced frames stem from the strength deterioration of the buckled braces and resulting reduction in story strength and stiffness. Though this tendency is reduced, the low post-yield stiffness in buckling-restrained braces can cause analogous behavior in buckling-restrained braced frames (BRBFs) (Tremblay, 2003; Chen & Mahin, 2012). Unless a mechanism exists to redistribute yielding to other stories, inelastic demands tend to concentrate in the story where the braces buckled or yielded first. These concentrations of demands can increase localized structural and nonstructural damage, increase $P\Delta$ effects and residual displacements, and render repairs impractical or uneconomical.

Providing an alternative vertical force path to adjacent stories can aid in distributing these inelastic demands. Studies employing the continuity of lateral or gravity columns in conventional (Ji et al., 2009; MacRae et al., 2004) or multi-tiered [e.g., Imanpour et al. (2016b)] systems have demonstrated that the re-distribution of demands to adjacent stories can be accomplished through column flexural stiffness and strength. Likewise, dual systems with back-up moment-resisting frames utilize frame action to compensate for the loss of story shear capacity due to brace buckling (Whittaker et al., 1990; Kiggins & Uang, 2006).

Though the flexural strength and stiffness of beams and columns can implicitly re-distribute demands, such methods raise issues related to the sizing of such members and detailing of the load path in the case where gravity columns are expected to provide additional flexural stiffness (Ji et al., 2009; Imanpour et al., 2016a). If the implicit mechanism is insufficient or unreliable, alternative bracing configurations, like zipper (Khatib, 1988) or tied eccentrically braced frames (Martini et al., 1990), provide an explicit mechanism to distribute yielding. Similarly, the inclusion of an essentially elastic truss, or *strongback*, provides a defined force path that can delay or prevent story mechanisms; see Figure 1.1(b).

The strongback-braced frame (SBF) is a hybrid of a conventional inelastic system and an essentially elastic steel truss. Input seismic energy is dissipated by supplemental fuses typical of a traditional system; e.g., through primary yielding and/or buckling in the bracing elements and secondary flexural yielding in the beam links. The strongback truss is then proportioned to remain essentially elastic, resulting in a relatively stiff and strong vertical spine. Axial forces and bending moments developed in the fuses are transferred vertically to adjacent stories through the strongback.

The strongback is not intended to provide supplemental lateral strength. Rather, the spine pivots about its base to maintain an imposed first-mode shape. Inelastic demands are not eliminated but distributed and averaged, resulting in smaller peak and residual drifts distributed across the frame height, increased behavior predictability, and reduced probability of yellow or red tagging following an earthquake.

The flexibility of brace location inherent to the strongback system provides the engineer with a choice of a number of arrangements to bypass potential geometric or mass irregularities; see Figure 1.2. Provided the strongback is strong enough to bridge across multiple stories, one or more of the inelastic braces could be removed to satisfy architectural constraints or to compensate for un-anticipated failures in the fuses; see Figure 1.2(c). Inelastic braces can also be dis-proportionally sized to their expected demand-to-capacity ratios, allowing the same inelastic brace sizes to be used across multiple stories. One or more strongbacks separated from the braced bay can be used to rehabilitate existing buildings (Pollino et al., 2017); see Figure 1.2(d). Depending on building height, the strongback truss could also be efficiently designed as a deep column or shear wall (Qu et al., 2012; Djojo et al., 2014).

In research, numerical analyses (Merzouq & Tremblay, 2006; Tremblay & Poncet, 2007; Lai & Mahin, 2013) and one experimental test (Simpson & Mahin, 2018b) have demonstrated that strongbacks can successfully distribute inelastic demands and mitigate concentrations of damage, even after degradation in stiffness and strength in the opposite inelastic braces. Strongback-braced frames have also been implemented and constructed in practice with comparable cost to conventional systems (Mar, 2010; Panian et al., 2015) and greater design flexibility (Osteraas et al., 2017).

However, none of these prior investigations have identified a dependable, economical, and practical design method for strongback-braced frames. Numerical studies have been preliminary, have found it difficult to identify appropriate strongback sizes, and have recognized practical detailing issues related to large deformation demands induced by the strongback truss. Limited experimental studies have been loaded quasi-statically and have not included the system's dynamic response. Trial-and-error designs developed in practice have been iterative in nature and validated through nonlinear dynamic analyses; requiring extensive data reduction, modeling expertise, and computational expense. Such methods also require expert knowledge of earthquake engineering within the context of dynamic response history analysis.

While an iterative nonlinear dynamic analysis approach would be capable of simulating transient dynamic demands, it is not a design method that would be regularly used by design engineers for most steel structures. Moreover, an iterative design approach still needs a preliminary design to initiate the iteration process. As such, this study seeks to systematically characterize the strongback's dynamic response and to develop and evaluate simple design and analysis methods for strongback-braced frames.

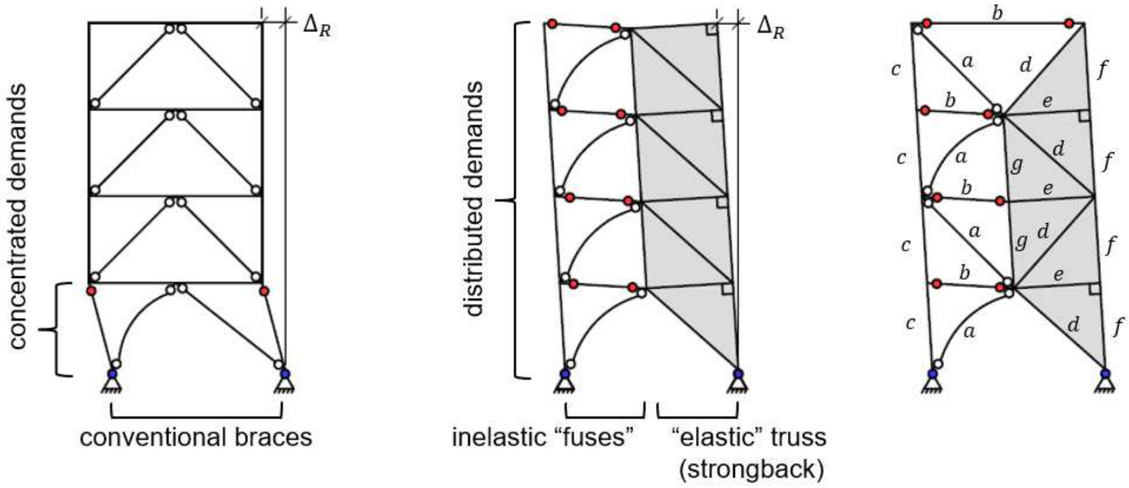

(a) (b) (c)

a – inelastic brace
b – beam link
c – inelastic column
d – essentially elastic (strongback) brace
e – beam outside link
f – strongback column
g – vertical tie strut

Figure 1.1. (a) weak story mechanism; (b) strongback mechanism; (c) member labels.

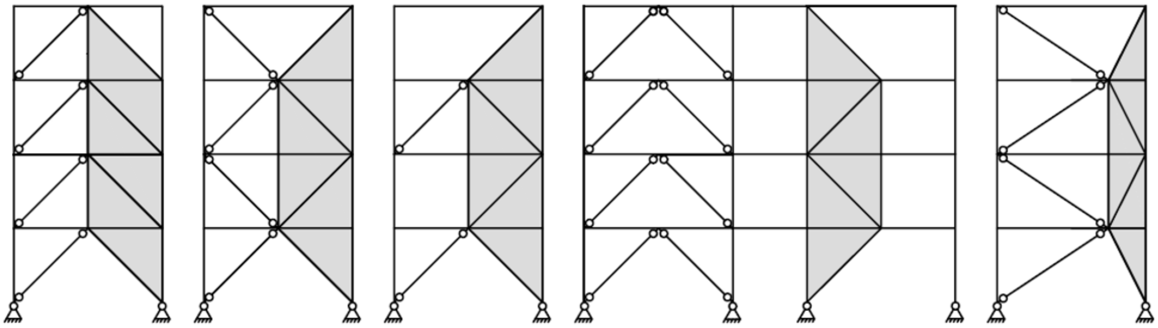

Figure 1.2. Strongback brace configurations.
(a) inverted-V or chevron, (b) double story-X, (c) intermittent chevron, (f) separated bay, (e) offset scheme.

1.2 DESIGN PHILOSOPHY

Strongback systems are characterized by an essentially elastic strongback designed to engage the designated fuses, distribute demands uniformly, and mitigate story mechanism behavior. However, though the strongback system has been employed successfully in both research and practice, its dynamic behavior has not been systematically assessed or evaluated. Just as importantly, practical code-oriented design methods have not yet been developed or validated.

To engage the opposite fuses, the strongback must be designed to have appropriate strength and stiffness. Figure 1.1(b) shows the desired plastic mechanism for an SBF. Designated *deformation-controlled actions*, or fuses, are those actions intended to dissipate energy in the strongback system and are designed with ductile detailing. The remaining actions are considered *force-controlled* – those actions that are protected and designed to remain essentially elastic. The deformation-controlled and force-controlled designated actions for strongback-braced frames utilizing BRBs are listed in Table 1.1. Member designations are labeled in Figure 1.1(c).

For the SBF systems studied herein, the strongback portion of the system should be proportioned so that [i] primary inelastic activity is accomplished through axial yielding and/or buckling in the designated inelastic braces and [ii] secondary inelastic activity is accomplished through flexural yielding in the beam links. Provided the strongback is strong and stiff enough, axial forces and bending moments induced by the inelastic braces and inelastic beam links would then be transferred vertically to adjacent stories through the strongback.

Considering these designated actions, conceptually, the following design concepts apply to inelastic and strongback elements in strongback braced frames:

1. the ductile yielding elements – e.g., buckling-restrained braces (BRBs), beam links, or other fuses – are proportioned for load combinations including seismic loads reduced by a response modification, or R, coefficient;
2. inelastic deformations, concentrated within the yielding core of the BRB and beam links, are checked against acceptable limits;

3. the remainder of the system is designed to remain essentially elastic based on the expected capacity of the yielding elements and the demands generated from the ground motion.

The required strength of inelastic braces and beam links in [1] can be determined by conventional analysis methods for reduced seismic forces as required by ASCE-7-16 (2016) or an equivalent building code. However, a supplemental analysis is needed to determine the required strength for strongback elements, connections, and force-controlled actions in the beams and columns.

This study addresses the development of the supplemental analysis needed to determine the required strength/stiffness for the strongback portion of the system. It focuses on the development of guidelines consistent with code-based design approaches and basic performance criteria. To achieve this objective, an analytical and numerical study was undertaken to: (i) characterize the strongback's behavior, (ii) optimize the strongback's required strength and stiffness; (iii) simplify estimation of the strongback-force demands, and (iv) propose simple design methods for multi-story strongbacks.

Table 1.1. Deformation- and force-controlled actions.

Action	Deformation-Controlled Action	Force-Controlled Action
Inelastic Brace	P	-
Strongback Brace	-	P
Strongback Tie	-	P
Beam	M	P, V
Column	M [a]	P
Connection	-	M, P, V

M = moment; P = axial, V = shear

[a] At column base only.

1.3 RESEARCH PROGRAM OBJECTIVES

The overarching goal of this research is to investigate and develop analysis methods for estimating demands in the strongback elements. To this end, the study:

- identifies promising design approaches and other issues of concern.
- develops optimized designs consistent with these concerns and conducts nonlinear dynamic analyses to characterize behavior and performance.
- Investigates the ability of various simple and refined analysis methods to estimate demands extracted from the nonlinear dynamic response.

The study focuses on the development of simple and robust analysis tools for design that have a physical basis in the strongback's dynamic response without relying on nonlinear dynamic analysis.

1.4 REPORT ORGANIZATION

This study is organized into 9 chapters. Following the introduction, Chapter 2 provides a literature review of the relevant research on strongback-braced frames and similar systems. Chapter 3 presents an analytical investigation of a simple, one-story strongback system. This simple frame was used to define the parameters influential to the strongback's behavior. Special attention was paid to optimization of an offset bracing configuration to reduce deformation demands caused by the kinematics of the strongback system; see Figure 1.2(e). Chapter 4 describes the numerical model used to investigate the strongback's behavior under nonlinear dynamic analyses, including development of the modeling method used for the strongback and buckling-restrained inelastic braces. Chapter 5 describes the optimization process used to design a four-story benchmark strongback-braced frame. Comparison of the benchmark's performance was made to a reference BRB system. Chapter 6 presents a parametric study investigating the sensitivity of peak dynamic response quantities to different design alternatives. The analytical investigation presented in Chapter 3 is extended to multi-story strongback systems in Chapter 7. This chapter also studies the dynamic behavior of multi-story strongbacks in terms of higher-mode effects. Chapter 8 introduces proposed design and analysis methods for strongback-braced frames. Finally, Chapter 9 summarizes the work and conclusions of this study and suggests future work. Appendix A through Appendix E provide additional plots of the work described in the body of this text.

1.5 SYMBOLS

Due to the two distinct inelastic and essentially elastic portions of the strongback, a descriptive set of labels was used to concisely represent the portion of the system that a parameter refers to. The strongback portion of the system is typically hatched in gray to illustrate which elements are part of the essentially elastic truss. The subscripts $(\cdot)_j$ and $(\cdot)_R$ represent the j^{th} story or floor level and the roof level. The subscripts, $(\cdot)_r$ and $(\cdot)_s$ represent the inelastic and elastic portions of the system, respectively. The super-script $(\cdot)^*$ is used in some figures to indicate the flexural or axial capacity of an element. For force-controlled actions, this capacity is calculated using the nominal yield strength of the material, f_y. For deformation-controlled actions, this capacity is calculated using the expected yield strength of the material (i.e., $f_y^* = R_y f_y$ in the strength equations in AISC-360-16).

2 Literature Review

2.1 INTRODUCTION

The intent of this chapter is to discuss the research on strongback-braced frames and similar systems. Due to the extent of the relevant body of research, this section only summarizes systems relevant to the development of the strongback concept. Emphasis has been placed on the expected mechanism of energy dissipation for each system. This chapter is broken into three parts: [i] conventional braced-frame mechanisms, [ii] methods of mitigating story mechanisms, and [iii] research on strongback-braced frames.

2.2 CONVENTIONAL BRACED FRAME MECHANISMS

Available literature on braced frames extends over several decades. The parallel evolution of seismic design provisions and braced frame research has led to inconsistencies between much of the research described in this section and now-typical detailing requirements. However, the fundamental observations made in these studies are often salient to the behavior of modern systems. As such, this section summarizes the design and expected inelastic response of concentrically braced frames, eccentrically braced frames, and buckling-restrained braced frames. Emphasis is placed on design considerations relevant to the design of the strongback system. The reader is referred to in-depth literature reviews for more detailed information on previous research on braced frames and their performance in past earthquakes [e.g., Lee and Bruneau (2005), Uriz and Mahin (2008), Bruneau et al. (2011), Lai and Mahin (2013), etc.].

2.2.1 Concentrically Braced Frames

Concentrically Braced Frames (CBFs) are expected to dissipate energy primarily through brace buckling and yielding. To achieve adequate hysteretic response of the braces, ductile details are required for both the braces and connections; see Table 2.1. Remaining elements, like beams and columns, are then expected to develop the unbalanced demands generated from the difference between the tension and post-buckled compression strength of the braces.

Modern building codes have implemented simplified capacity design procedures to estimate the force re-distributions resulting from brace buckling and yielding. For example, beams in inverted-V, or "chevron", configurations are required to remain essentially elastic under the bending demands developed by an unbalanced load – the vertical load resulting from the difference between the tension and post-buckled compression brace expected capacities. This results in the "strong" beam plastic mechanism favored by current building codes; see Figure 2.1(a). The strong beam aids yielding in the tension brace after buckling occurs in the compression brace.

In contrast, the inelastic response of weak beam mechanisms additionally includes beam flexural yielding; see Figure 2.1(b). Some researchers have hypothesized that beam flexural yielding may be a more stable form of energy dissipation compared to brace buckling and yielding [e.g., Khatib et al. (1988)]. This mechanism, however, leads to plastic hinge formation in the beam, resulting in potentially large vertical deflections that may cause unwanted damage in the slab and floor diaphragm. Vertical deflections may also increase axial shortening in the braces, leading to larger deformation demands in the bracing elements. The occurrence of this "weak beam" phenomenon in multistory CBFs has been well demonstrated by research [e.g., Uang et al. (1986), Foutch et al. (1987), Khatib et al. (1988), Sen et al. (2016), Bradley et al. (2017), Simpson and Mahin (2018a), etc.] and by post-earthquake reconnaissance reports [e.g., Tremblay et al. (1995), Tremblay et al. (1996)].

Table 2.1. Special CBF member ductility requirements.

Member	Action	Highly Ductile	Moderately Ductile	Adjusted Strength of Fuse
braces	deformation-controlled	X		(1.0 or 0.3)·1.14f_{cr} [a] or $R_y f_y$ [b]
beams	force-controlled		X	-
columns	force-controlled	X		-

[a] in comrpession, critical buckling stress determined per AISC-360 Chapter E using expected yield stress $R_y f_y$, in lieu of f_y.

[b] in tension.

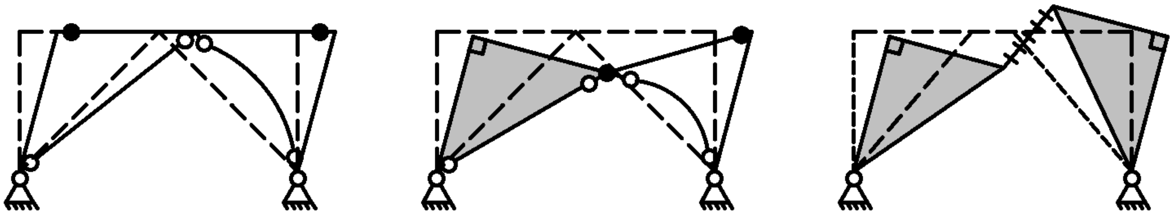

Figure 2.1. Braced frame mechanisms.

(a) CBF strong beam mechanism; (b) CBF weak beam mechanism; (c) EBF mechanism

2.2.2 Eccentrically Braced Frames

In the 1970s and 1980s, eccentrically braced frames (EBFs) were studied in both Japan [e.g., Fujimoto et al. (1972), etc.] and the United States [e.g., Roeder and Popov (1978), Engelhardt and Popov (1989), Hjelmstad and Popov (1984), Kasai and Popov (1986), Ricles and Popov (1989), etc.] as a means of combining the high elastic stiffness associated with CBFs with the greater ductility capacity associated with moment-resisting frames.

In EBFs, energy is dissipated through flexural or shear yielding in a small segment of the beam, or beam “links”. Since the braces in EBFs are not expected to buckle or yield, many of the ductility-related detailing requirements for CBFs are not needed for EBFs. Braces in EBFs are designed by capacity design principles to develop yielding in the beam link, including material overstrength and cyclic strain hardening; see the R_y and the 1.25 strain hardening adjustment factor in Table 2.2. Axial forces induced by the braces are transferred throughout the system by shear or bending in the beam link, the primary energy dissipating “fuse”.

Current design codes permit limited yielding in the beam outside of the beam link. This is recognized by a 0.88 reduction factor in calculating the beam link’s expected capacity (AISC-341-16, 2016). These recommendations caution that a larger adjustment factor should be utilized when a floor slab is not present. As it is not expected that all the beam links will yield at the same time (Whittaker et al., 1990), a similar 0.88 reduction factor is also allowed for the design of columns for frames three stories and greater. Since the braces are designed to remain essentially elastic, ordinary details are permitted for the brace connections.

Shear versus flexural hinging in the beam link is dependent on the beam link length, e. Flexural hinging is expected when the length of the link is greater than $2.6M_p^*/V_p^*$ and shear hinging is expected when the length of the link is less than $1.6M_p^*/V_p^*$; where $M_p^* =$ expected plastic moment strength of the beam and $V_p^* =$ expected shear strength of the beam; see Figure 2.2. Simultaneous shear and flexural yielding occur for intermediate beam links between these limits (Engelhardt & Popov, 1989).

Within this context, the weak beam mechanism for CBFs is similar to that of EBFs with long flexural links; see Figure 2.1(b) and (c). Piece-wise allowable link deformation limits, γ, were developed in AISC-341-16 (2016) to represent the effect of link length on deformation capacity; see Figure 2.2. Shorter link lengths are expected to develop relatively uniform shear yielding along the link length, corresponding to larger deformation capacities. Longer link lengths, on the other hand, are controlled by flange local buckling with only limited web yielding and are generally associated with less deformation capacity – and smaller deformation limits – than shorter links (Kasai & Popov, 1986).

Table 2.2. EBF member ductility requirements.

Member	Action	Highly Ductile	Moderately Ductile	Adjusted Strength of Fuse
beam links	deformation-controlled	X [a]		$1.25R_yf_y$
braces	force-controlled		X	-
beams outside links	force-controlled		X	[b]
columns	force-controlled	X		[c]

[a] Some exceptions apply.

[b] Reduction of 0.88 allowed. A larger adjusted strength factor should be used when a floor slab is not present.

[c] Reduction of 0.88 only allowed for frames of three or more stories.

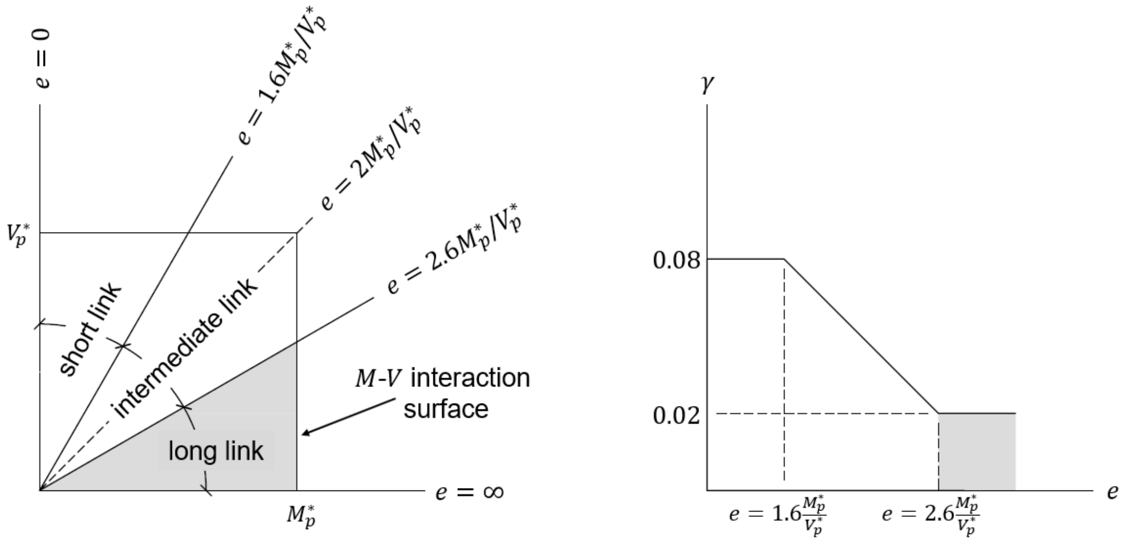

(a) (b)

Figure 2.2. (a) Classification and (b) deformation limits of EBF links.

2.2.3 Buckling-Restrained Braced Frames

Over the last two decades, buckling-restrained braces (BRBs) (Watanabe et al., 1988) have become increasingly popular as fuses in lateral force-resisting systems (Clark et al., 2000). BRBs restrain buckling of a steel core, allowing the brace to yield in both compression and tension. This results in improved hysteretic behavior and energy dissipation capacity at the component level; see Figure 2.3.

Simplified capacity design procedures are used to proportion the remaining frame (beams, column, and connections). The adjustment factors, ω, account for the significant combined isotropic and kinematic hardening that can be exhibited by the steel core. A second adjustment factor, β, accounts for the difference in BRB compression and tension strength due to Poisson expansion and friction between the BRB core and restrainer; see Table 2.3. Since BRBs are a proprietary device in the U.S., these factors are typically given to the engineer by manufacturers such as CoreBrace (www.corebrace.com), Nippon Steel (www.unbondedbrace.com), etc.

Buckling-restrained braced frames tend to be more flexible than CBFs, because the BRB core areas are selected based on yielding rather than buckling strength. In some cases, they can be governed by drift rather than strength requirements (Kersting et al., 2015). The low post-yield stiffness of BRBs can result in permanent deformations that may be larger than that of a conventional CBF [e.g., Sabelli (2001), Uriz and Mahin (2008), Kiggins and Uang (2006), Fahnestock et al. (2007), Ariyaratana and Fahnestock (2011), Chen and Mahin (2012), etc.]. Performance-based studies based on peak and residual story drifts and floor accelerations have also found that BRB frames can exhibit increased repair time and repair costs compared to other conventional systems (Terzic & Mahin, 2017).

Table 2.3. BRBF member ductility requirements.

Member	Action	Highly Ductile	Moderately Ductile	Adjusted Strength of Fuse
buckling-restrained braces	deformation-controlled	X		$\omega R_y f_y$ or $\omega\beta R_y f_y$
beams	force-controlled	X		-
columns	force-controlled	X		-

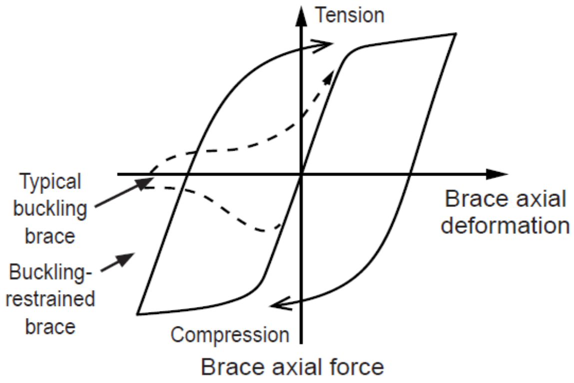

Figure 2.3. Buckling versus buckling-restrained brace hysteretic response. (Kersting et al., 2015)

2.2.4 Story mechanisms

Though capacity design principles and other design requirements have resulted in improved ductility capacity for braced frame systems, numerical studies [e.g., Khatib et al. (1988), Sabelli (2001), Tremblay (2003), Hines et al. (2009), Uriz and Mahin (2008), Chen and Mahin (2012), Lai and Mahin (2013)] and experimental tests [e.g., Uang and Bertero (1986), Foutch et al. (1987), Simpson and Mahin (2018a)] have demonstrated that braced frames tend to concentrate damage in a few "weak" stories in response to strong earthquake shaking.

An idealized diagram demonstrating story mechanism behavior in concentrically braced frames is shown in Figure 2.4. The braces are oriented in a "chevron" configuration with equal brace sizes and mass in each story. It is assumed that the majority of the story stiffness and strength comes from the braces in that story (i.e., the contribution of column shear to the story shear is small and can be neglected). If an inverted triangular load distribution is laterally applied to the frame, the first-story brace will buckle under the story shear demand, D_1. After brace buckling, the first-story will be relatively weaker than the upper stories where the braces did not buckle. Assuming the forces remain similar before and after buckling, this relative reduction in story strength, C, and stiffness, k, promotes concentrations of demands in the first-story.

Unless these demands can be re-distributed to other stories by some other force path, e.g., frame action provided by the columns and/or beams, this concentration of demands can lead to story mechanism behavior. While the extent of this phenomenon is dependent on a variety of factors (e.g., the size, slenderness, and configuration of the braces, the type of ground motion, the number of stories, etc.), story mechanisms arise because of an insufficient means of distributing demands to adjacent stories. These concentrations in demand cause localized story drift demands that could lead to irreparable residual drift or global instability due to P-Δ effects (Kersting et al., 2015).

Both vintage and modern braced frames are susceptible to story mechanism behavior. Modern designs mitigate story mechanisms by recommending near uniform demand-to-capacity ratios with building height. However, any non-uniformity or failure along the lateral load path can reduce a braced frames ability to resist seismic demands. This behavior has been recognized in post-earthquake reconnaissance studies [e.g., Rai and Goel (2003)]. Figure 2.5 shows locations observed damage in a four-story commercial building after the 1994 Northridge earthquake. This damage was concentrated in the second-story, typical of story mechanism behavior.

Though the tendency is reduced, the low post-yield stiffness of BRBs can result in concentrations of drift demands in one or a few stories, resulting in story mechanisms similar to systems with buckling braces [e.g., Tremblay (2003), Chen and Mahin (2012), etc.]. Using BRBs with large strain hardening can aid engagement of adjacent stories. However, realistic consideration of the magnitude of this strain hardening in capacity design can impact the size of columns, foundations, and other surrounding structural elements. To aid the columns in distributing demands, Canadian design provisions require columns to be designed for interaction between the axial forces developed by the BRBs and twenty-percent of the column's plastic moment strength (CSA-S16-14, 2014). "Tuning" the steel grades of the BRB cores has also been suggested as a means of providing controlled yielding with positive stiffness at larger drift demands (Atlayan & Charney, 2014).

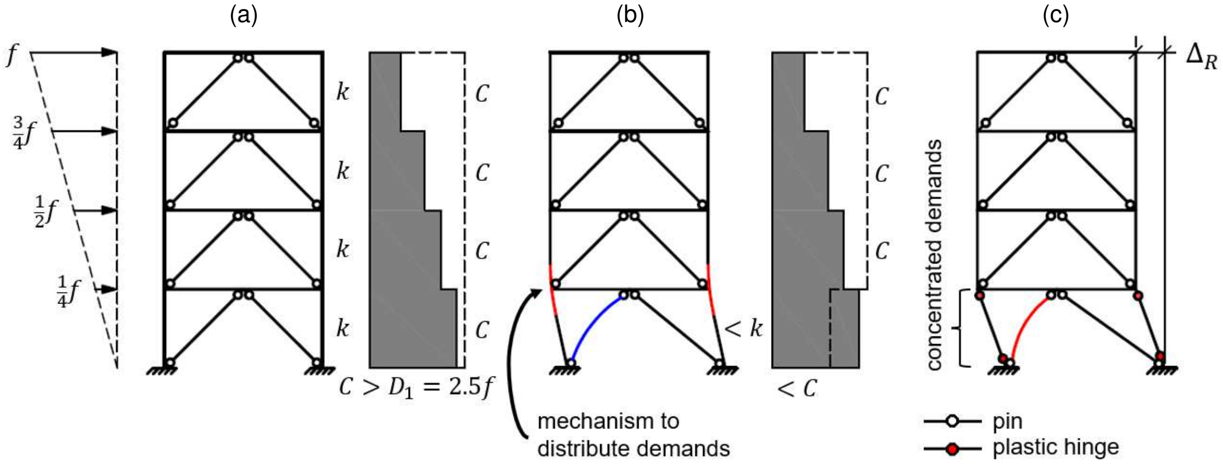

Figure 2.4. Story mechanism behavior in concentrically braced frames.
(a) prior to initial brace buckling; (b) after initial brace buckling; (c) story mechanism.

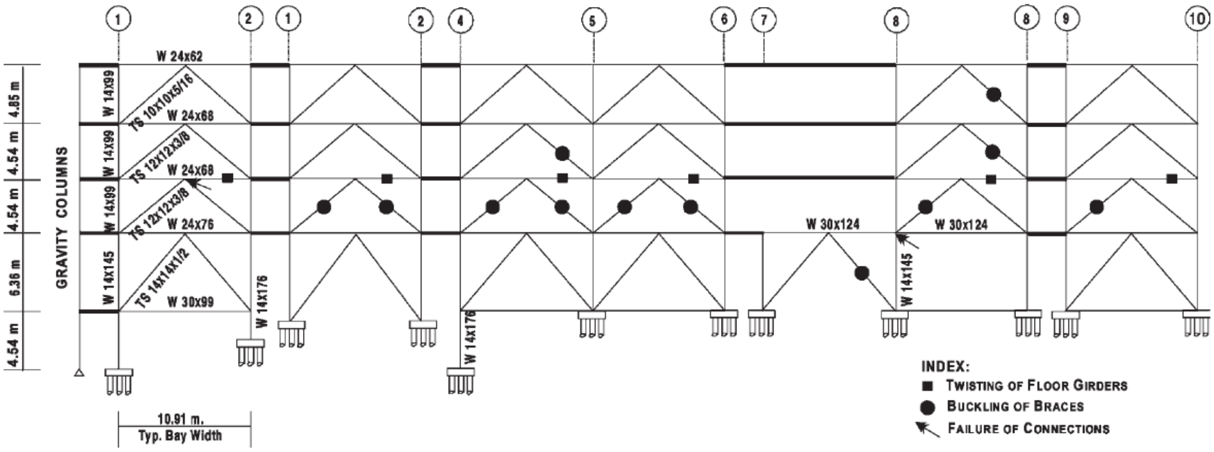

Figure 2.5. Locations of observed damage after 1994 Northridge earthquake (Rai & Goel, 2003).

2.3 MITIGATING STORY MECHANISMS

In light of the story mechanism tendency described in Section 2.2.4, researchers have investigated a number of alternative methods of mitigating story mechanism behavior. This section describes approaches used in the following systems: [i] dual systems, [ii] zipper braced frames, [iii] tied eccentrically braced frames, [iv] continuous column systems, [v] walls-type systems, and [vi] rocking and self-centering braced frames.

2.3.1 Dual systems

A dual system is comprised of at least two different, yet compatible, structural systems that in combination are intended to overcome shortcomings of the individual systems. They resist the total seismic force through a combination of conventional primary lateral-resisting frames and secondary moment-resisting "back-up" frames. The primary frames supply energy dissipation under major earthquakes while the secondary frames aid in re-distributing inelastic demands, supply an elastic self-centering restoring force (Kiggins & Uang, 2006), and improve redundancy of the combined system against structural collapse (Whittaker et al., 1990).

Though dual systems have been recognized in building codes for several decades, distributing inelastic demands solely by frame action has been recognized as an inefficient means of mitigating story mechanisms (Tremblay, 2003). Additionally, the relationships between the relative lateral stiffness, deformability, ductility, and yielding strengths of the combined primary and secondary frames is complex (Whittaker et al., 1990; Ariyaratana & Fahnestock, 2011), and the necessary strength and stiffness of the back-up system is not easily quantified in terms of achieving a desired performance goal (Khatib, 1988).

2.3.2 Zipper Braced Frames

In the late 1980s, Khatib (1988) proposed a zipper braced frame as a means of distributing inelastic demands over multiple stories. The unbalanced force induced by brace buckling and yielding pulls down or pushes up on a weak beam. The addition of a vertical tie strut to connect stories can be used to engage adjacent stories through this vertical unbalanced load; see Figure 2.6(a). The vertical movement transfers demands between stories, resulting in a more uniform distribution of inelastic response with frame height. The example commercial building in Figure 2.5 was retrofitted as zipper frame to mitigate the weak story mechanism behavior observed after the 1994 Northridge earthquake (Kelly et al., 2000).

Though effective, subsequent analyses and designs using zipper frames have found this distribution of unbalanced load to be complicated, and it can be difficult to identify appropriate member sizes to achieve the desired response (Tremblay, 2003). Large unbalanced forces must be transferred through the vertical tie strut, causing the size of the tie to approach that of an additional column. Higher-mode effects in multi-story zipper frames can be problematic, and global collapse can occur upon formation of a complete mechanism. This has been especially apparent for zipper frames subjected to near-fault effects (Tremblay & Tirca, 2003). Yang et al. (2008) proposed an essentially elastic hat truss to re-direct unbalanced forces back to the ground to avoid full-height mechanisms [see Figure 2.6(b)]. However, even though they are referenced in the design commentary in AISC-341-16 (2016), current seismic codes do not provide specific requirements for the design of zipper braced frames.

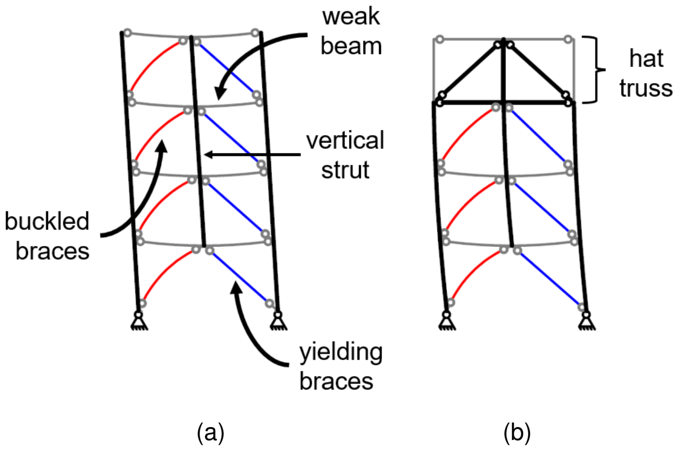

Figure 2.6. Zipper braced frame: (a) full mechanism and (b) mechanism with essentially elastic hat truss.

2.3.3 Tied Eccentrically Braced Frames

Researchers have observed that beam links in EBFs can exhibit non-uniform deformations with building height (Whittaker et al., 1990). This tendency can be reduced with proper proportioning of the beam links with respect to their height-wise distribution demands. However, as the height of the EBF increases, the contribution of higher modes to the total response tends to increase shears in the upper stories and decrease shears in the middle and lower stories. Popov et al. (1992) noted that inclusion of the second and third mode response in determining static demands was key to avoiding non-uniform link deformations with building height.

Martini et al. (1990) proposed a tied eccentrically braced frame, or “zipper EBF”, as an alternative method of inducing uniform deformations in the beam links; see Figure 2.7(a). Tied EBFs sandwich the beam links between two “super” columns. These columns are pinned at the base and engage the beam link like a coupled shear wall. To counteract the added cost of the tied EBF, the study proposed reduced strength for the beam links to complement the overstrength of the super columns. Emphasis was placed on the behavior predictability of the tied EBFs and the supplemental "back-up" story stiffness provided by the columns, braces, and ties in the super columns.

Rossi (2007) proposed a displacement-based design approach for tied EBFs. The beam links were designed per elastic response spectrum analysis. The study then noted that, unlike conventional EBFs, axial forces of the braces, ties, columns, and beam segments outside of the links were not solely a function of the shear force in the links but also a function of higher-mode effects. As such, elements outside the links were additionally designed for higher-mode effects corrected by a reduction factor to account for link yielding in the higher modes.

Tremblay et al. (2014) developed a modular approach for tall tied EBFs; see Figure 2.7(b). The super columns were divided into segmented modules to reduce the large demands that develop in the tie with increasing building height. Beam links were designed for the average story shear force in a module. This modular configuration resulted in reduced tie demands but increased drift demands at locations between modules. Supplemental energy dissipation devices - including BRBs, friction dampers, and self-centering braces - were able to reduce these drift effects; see Figure 2.7(c).

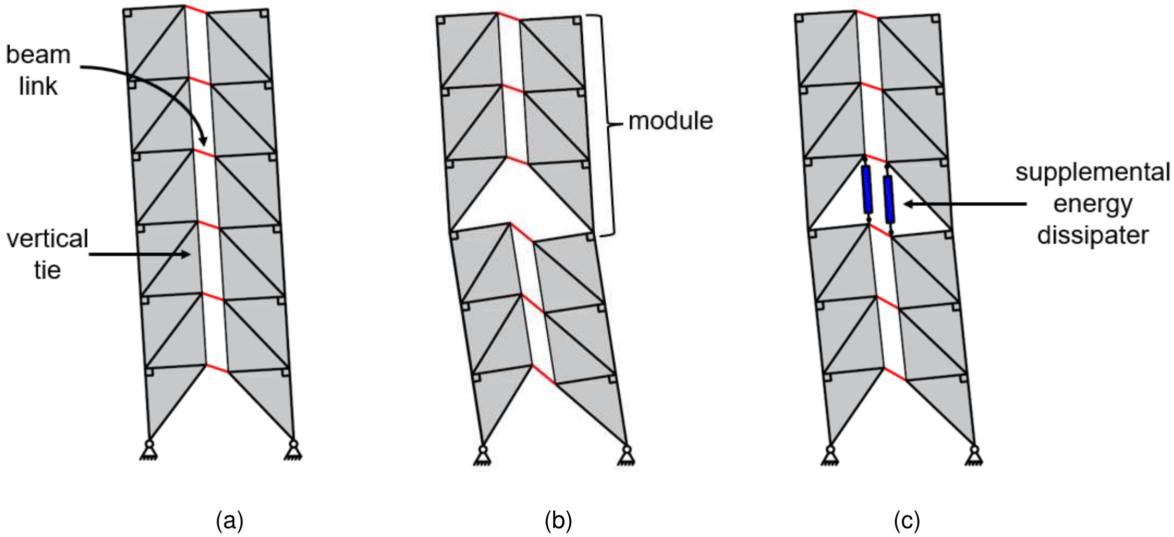

Figure 2.7. Tied EBF braced frame: (a) full mechanism; (b) and (c) with modules.

2.3.4 Continuous Column Systems

Studies employing the continuity of lateral or gravity columns in conventional (MacRae et al., 2004; Ji et al., 2009; Imanpour et al., 2016a) or multi-tiered (Imanpour et al., 2016b) systems have shown that vertical re-distribution of demands can be accomplished through column flexural stiffness and strength. If provided with sufficient in-plane flexural stiffness and strength, continuous columns in both the lateral and gravity systems can elicit inelastic response in adjacent stories; see Figure 2.4. As the combined stiffness of these columns increases, story drift concentrations are reduced and the lateral frame experiences a more uniform drift distribution.

In multi-tiered systems, suitability of a column is determined by progressive yielding in the tiers, beginning in the critical story where brace inelastic behavior is first initiated. The horizontal unbalanced force arising from the brace tension and compression capacities between tiers can be used to obtain flexural demands in the columns. For multi-tiered systems using BRBs where the difference between compression and tension adjusted brace strength is small, a notional load can be used to account for unbalanced demands due to variations in brace strains, yield core strength, and tolerances in the core (AISC-341-16, 2016). This method allows for direct relation between the applied loading, brace axial force, column internal shear, and column internal bending moments. Columns are then designed for flexural-axial interaction imposed by yielding and/or buckling of the braces.

However, analysis by progressive yielding in multi-tiered braced frames becomes increasingly complex with more stories or where the critical story is not immediately evident (Imanpour & Tremblay, 2017). Moreover, the amount of mass is small at each tier-level. As such, this method is indeterminate in multi-story buildings where inertial forces are distributed on a story-by-story basis. Sizing of continuous columns in both multi-tiered and conventional systems has been found to become cost inhibitive (Ji et al., 2009). If utilizing the collective flexural strength and stiffness of gravity columns, the distributed nature of continuous columns can also raise other issues related to detailing of the load path between the seismic and gravity load-resisting systems and is neither an efficient or dependable mechanism of distributing demands

2.3.5 Wall-type Systems

Due to their deep cross section, shear walls can be an effective means of controlling story drift and mitigating story mechanism behavior. Shear walls establish a stiff vertical element that provides continuous lateral resistance over the height of the frame, enforcing a global tilting mode [e.g., Qu et al. (2015) Grigorian and Grigorian (2016)]. This mechanism can be imposed by either a concrete or steel plate shear wall (Wiebe et al., 2007; Djojo et al., 2014) and can be designed to engage additional supplemental energy dissipation devices (Qu et al., 2012).

Shear wall designs should be provided with proportions and details that enable it to form the intended inelastic mechanism. Walls pinned at their base are not expected to contribute lateral strength or stiffness but are expected to maintain a global tilting mode through interaction with the surrounding structural elements. Comparably, fixed slender concrete walls are designed to yield in a flexural "cantilever-like" mode. To enforce these responses, the shear capacity of the wall is capacity-designed to develop the expected strength of the inelastic actions (e.g., the expected flexural overstrength of the wall base in the fixed case) plus amplification of the dynamic shear due to the wall's higher-mode response.

Amplification of dynamic shear has been well-documented in experimental tests of concrete shear walls [e.g., Aoyama (1986), Ghosh and Markevicius (1990), Eberhard and Sozen (1993), Panagiotou and Restrepo (2011), etc.]. In the case of slender concrete walls, moments at the base of the wall are well-constrained by the wall's moment strengths. However, moments and shears in essentially elastic regions of the wall are less well constrained because inertial forces are constantly changing with time.

Inertial forces can experience a sign reversal due to higher-mode effects. In some cases, this can result in a downward shift of the force resultant, producing larger base shear than that suggested by a first-mode inertial force distribution; see Figure 2.8. Flexural yielding at the base of the wall limits the contribution of the first-mode response to the total response, but shear forces in the higher modes are not similarly limited by the wall's shear capacity. Thus, these shear forces continue to increase as the earthquake shaking intensity increases (Moehle, 2014). Amplification in these shear forces can be over three times the shear calculated from a purely first-mode response (Kelly, 2009). An extensive bibliography on the effects of higher-mode effects in shears in concrete walls is provided by Rutenberg (Rutenberg, 2013).

To approximate this dynamic shear effect, researchers have proposed various design approaches (Aoyama, 1986; Ghosh & Markevicius, 1990; Eberhard & Sozen, 1993). A scalar dynamic amplification factor, ω, of 1.25 to 4.1 has been recommended to account for dynamic effects in the design base shear (NZS3101, 2006; SEAOC, 2008). Note that this factor is an amplification factor that cannot account for the height-wise distribution of lateral forces; see Figure 2.8. It has also been suggested that such behavior can be approximated by combining the modal responses using a strength adjustment factor, $R = 1$, for the higher modes (Eibl & Kreintzel, 1988). This is the method that has been adopted by Eurocode 8 (2004) for concrete shear walls. Ongoing research is still investigating appropriate approaches for the design of concrete shear walls.

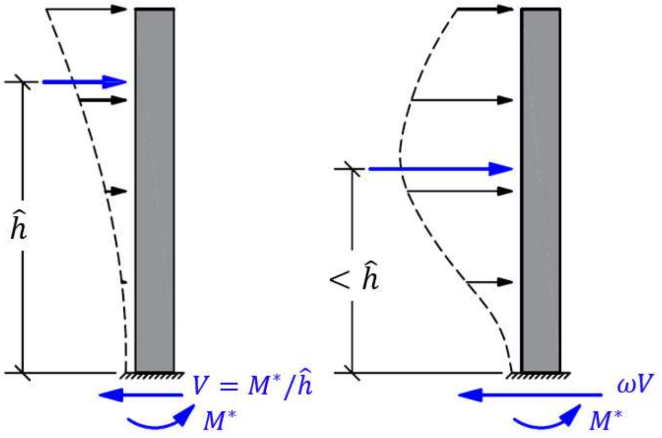

Figure 2.8. Dynamic shear effect in shear walls.

2.3.6 Rocking and Self-Centering Braced Frames

Similar to but distinct from the pivoting response characteristic of wall-type systems, rocking frames dissipate energy through uplift and impact or through supplemental devices installed in the direction of uplift; see Figure 2.9(a). The rocking frame itself is a stiff vertical truss that is designed to remain essentially elastic. Fuses outside of this truss are expected to be replaceable after yielding. Post-tensioning (Roke et al., 2006) or self-centering braces (Christopoulos et al., 2008; Miller et al., 2012) can additionally be provided to reduce permanent displacements.

The rocking frame engages the building in a uniform drift response. Some of the earliest investigations and experiments of rocking frames were conducted in the 1970s and 1980s (Clough & Huckelbridge, 1977; Yim et al., 1980). More recently, researchers have conducted quasi-static tests [Roke et al. (2006), Eatherton et al. (2014a)], shake table tests [Ma et al. (2011), Tremblay (2008), Weibe (2013a; 2013b)] and hybrid simulation [Sause et al. (2010), Eatherton and Hajjar (2014)] of rocking and self-centering systems.

Similar to wall-type systems, the elastic nature of the rocking frame amplifies higher-mode contributions to the system's total dynamic response. Though the base overturning moment is primarily dominated by a first-mode response, story shears are more heavily influenced by higher-modes effects (Roke et al., 2009; Eatherton et al., 2014b; Wiebe & Christopoulos, 2015b). Since these higher-mode effects can play a dominant role in design of the rocking frame, researchers have proposed providing multiple uplift location to mitigate these higher-mode effects (Wiebe & Christopoulos, 2009; Tremblay et al., 2014); see Figure 2.9(b).

Proposed methods to incorporate higher-mode response in the design of rocking frames are briefly summarized here and compared extensively by Steele and Wiebe (2016). Eatherton and Hajjar (2010) and Ma et al. (2011) proposed enveloping the responses from several proposed lateral-force distributions to estimate higher-mode amplification; see Figure 2.6. An inelastic modal analysis method utilizing a modified complete quadratic combination (CQC) rule to combine the modal responses was developed by Roke et al. (2009). Other simplified modal combinations have also been proposed (Wiebe et al., 2015), for example:

$$r = |r_1| + \sqrt{r_2^2 + \cdots + r_n^2 + \cdots + r_J^2} \qquad \text{Equation 2.1}$$

r = total response; r_1 = first-mode response including yielding of the fuses; r_2, …, r_n, …, r_J = higher-mode responses. This modal combination assumes that the higher modes oscillate about a dominant fundamental mode. Wiebe and Christopoulos (2015a) further extended this modal method to include an equivalent cantilever beam analogy to estimate the profile of higher-mode inertial force distributions; see Figure 2.11. A linear dynamic analysis method using a truncated response spectrum to determine higher-mode response was also developed by Steele and Wiebe (2016); see Figure 2.12(b). In this method, transient modes were estimated per eigenvalue analysis of a numerical model utilizing the inelastic tangent stiffness at locations of expected yielding, as recommended by Sullivan et al. (2008); see Figure 2.12(a).

Eatherton et al. (2014b) provides a detailed summary of possible configurations and locations of re-centering and uplifting fuses, collector details with slotted holes or pin details, and alternative slab framing details to isolate the floor from the vertical motion of the rocking frame (Eatherton & Hajjar, 2010). However, design procedures for rocking frames are still active areas of research and refinement of proposed design methods is ongoing.

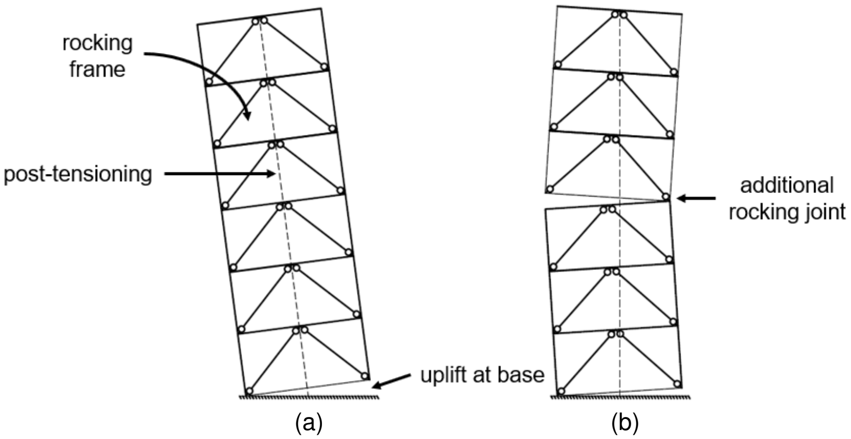

Figure 2.9. Rocking frame: (a) base uplift with re-centering post-tensioning; (b) multiple rocking joints.

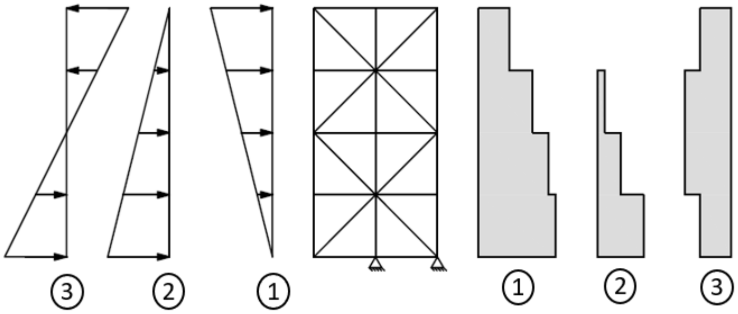

Figure 2.10. Envelope of loading cases and story shears proposed by Eatherton and Hajjar (2010).

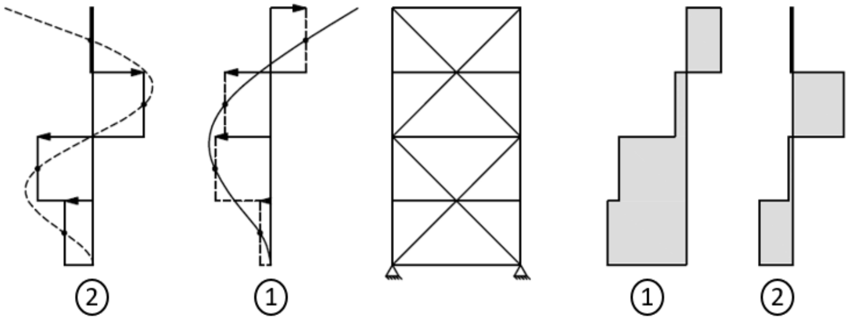

Figure 2.11. Discretization of second and third mode response with fixed base model (Wiebe & Christopoulos, 2015a).

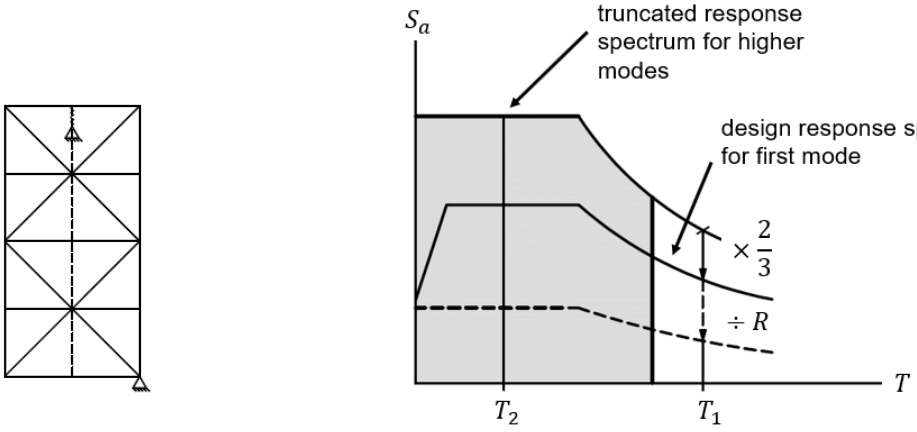

(b) (c)

Figure 2.12. Schematic of simplified modal analysis method.
(a) modified boundary conditions; (b) truncated response spectrum (Steele & Wiebe, 2016).

2.4 RESEARCH ON STRONGBACK SYSTEMS

The strongback system investigated in this study is an offshoot of the zipper frame, tied eccentrically braced frame, and continuous column concept. Like dual systems, strongback systems utilize a hybrid of two systems. Its kinematic mechanism combines the weak beam braced frame mechanism with buckling-restrained brace yielding. In embedding an essentially elastic truss within a conventional system, the strongback leverages the full energy dissipation of the fuses by distributing demands across multiple stories. The addition of the tie completes the strongback truss and mimics the vertical propagation strategy proposed for zipper and tied EBF systems. The essentially elastic nature of the strongback truss is also linked to that of pivoting wall and rocking frames. This section presents a summary of the limited numerical and experimental research on strongback systems.

2.4.1 Numerical Analysis on Strongback Systems

Several studies have examined the strongback system from an entirely numerical perspective. These studies have illustrated the ability of the SBF system to defer or eliminate weak stories. However, they have also demonstrated the difficulty in identifying appropriate sizes of the members of the essentially elastic strongback. Herein, emphasis is placed on proportioning strategies proposed by these studies.

2.4.1.1 Elastic Truss Systems

Strongback-braced frames were proposed as a dual buckling-restrained brace system by Tremblay (2003); herein termed elastic truss systems. The system was composed of two vertical steel trusses: one that dissipated energy through its inelastic response and one whose members were designed to remain essentially elastic. The study recognized the promise of the addition of a strongback to reduce potential dynamic instabilities in braced frames. However, the study did not provide specific requirements for the design of the elastic truss, and emphasized that nonlinear dynamic analysis was required to determine demands in the strongback members.

Tremblay and Poncet (2007) examined elastic truss systems with heights of 12- and 16-stories with braces oriented in an inverted-V, or “chevron”, configuration. Buckling-restrained braces were utilized for the inelastic braces in the system. Similar brace and tie sizes were used at every story of the elastic truss. The strongback brace size was selected based on two times the force developed from yielding of the first story buckling-restrained brace. The tie was designed based on the unbalanced load generated from the adjusted compression capacity of the BRBs and yield capacity of the adjacent strongback brace. Though the elastic truss system was found to result in better performance compared to conventional buckling and buckling-restrained braced frames, the study noted that the design approach used for the comparison was not optimal and that more refined design guidelines were needed.

Merzouq and Tremblay (2006) extended this study to two-bay 8-, 12-, 16, 20-, and 24-story elastic truss systems; see Figure 2.13(a) and (b). The buildings were designed for a site located in Victoria, British Columbia, Canada and were subjected to near-fault and simulated subduction ground motion suites. Braces and ties in the elastic truss were designed in groups of four successive stories. The study noted that the BRBs yielded in a sequence of batches of stories between 1/5 and 1/4 the height of the frame (Merzouq, 2006). Peak demands in the elastic braces similarly occurred in batches of 1/4 and 1/3 the height of the frame, but experienced a lag behind the that of the BRBs. The study also noted that higher-mode effects resulted in increased elastic brace demands in the upper stories of the frame.

Based on this propagation phenomena, Merzouq and Tremblay (2006) proposed empirical guidelines for the design of the elastic truss members. Elastic brace demands were calculated by empirically amplifying demands delivered by the inelastic braces by a factor varying with building height and a chosen level of probability. Tie demands were calculated based on the accumulation of unbalanced demands from the inelastic and elastic brace forces summed twice from the top and from bottom of the structure. The peak tie demands were then taken as the minimum envelope of this cumulative unbalanced demand. Empirical correction factors dependent on frame height were applied for the design of the vertical tie to account for: [i] amplification of the response in the upper stories and [ii] the variation in brace forces in consecutive stories. It was noted that tie demands were maximized when the brace demands changed sign in consecutive stories.

Comparison between the resulting elastic truss system and similarly designed BRB frames found that the elastic truss system exhibited more uniform distributions of deformations with building height and had greater reserve capacity compared to a conventional BRB frame. The study also indicated that the duration of subduction events could be critical to the performance of elastic truss systems, possibly leading to formation of a full collapse mechanism and global instability. Accelerations were observed to be uniform but higher than that of a BRB frame.

2.4.1.2 Strongback-braced frames

Lai and Mahin (2015) compared 6-story chevron and X-braced frames with buckling braces and strongback-braced frames utilizing BRBs. The study examined the use of an offset configuration where the intersection of the strongback and inelastic braces was shifted from the centerline of the bay; see Figure 2.13(c). This facilitated longer yield lengths in the BRBs and increased length of the beam, reducing strains in the BRBs and shear and plastic hinge rotations in the beam links. The study also examined the use of low-yield strength BRBs capable of increasing stiffness for the same strength, resulting in reduced period, decreased lateral displacements, and increased BRB yield-to-tensile failure capacity.

Members in the strongback were designed to remain essentially elastic under design-level seismic forces. The strongback braces were designed utilizing the system overstrength factor, $\Omega_0 = 2.0$, for BRBFs (ASCE-7-16, 2016). Stress ratios in the strongback elements were checked to be less than $\Omega_0/2 = 0.5$ under code-level forces. Vertical ties were designed based on the unbalanced forces derived from the adjusted tension and compression force induced in the BRBs and the expected yield strength of the strongback braces. It was expected that under severe ground shaking, some elements of the strongback would buckle.

The study noted that utilization of a strongback resulted in near uniform distribution of deformations with building height. However, the study also noted that the design strategy provided under-estimated demands in the upper stories of the strongback. Additional studies employing the addition of gravity columns had little effect on the strongback's behavior. A simplified cost analysis indicated that the strongback design resulted in similar costs to a double-story X-braced frame and reduced costs compared to a chevron braced frame employing buckling braces. Though the strongback system studied utilized BRBs, no comparisons in behavior and cost were made to a conventional BRB frame.

2.4.1.3 Spine Systems

Takeuchi et al. (2015) proposed a non-uplifting spine system utilizing supplemental buckling-restrained columns; see Figure 2.13(d). A back-up moment frame was provided as a partial re-centering mechanism to reduce peak and residual drift response. The system's behavior was comparable to systems utilizing self-centering post-tensioned strands and was employed in a building in Japan in 2015.

Chen et al. (2017) subsequently proposed a stiffness-based design method for the spine frame. The method simplified the spine into a single equivalent column. The spine frame's response was characterized by an inelastic-to-elastic frame stiffness ratio and a moment frame-to-spine frame stiffness ratio. As the stiffness of the spine was increased relative to fuses and moment frame, the spine frame became more effective at achieving a uniform drift demand. The study also proposed a simplified design procedure utilizing a single-degree-of-freedom model.

A more recent study by Chen et al. (2018) has since noted that higher-mode effects can dominate demands in the spine – especially in taller structures – and that estimates of spine demands using of a first mode-only response can be prone to large errors. The study proposed modal pushover and response spectrum procedures to estimate these higher-mode demands. A segmented spine frame was proposed to reduce demands in the spine elements while achieving similar drift response to a continuous spine frame; see Figure 2.13(e). Two-segmented spine frame was recommended for buildings less than 30-stories.

2.4.1.4 Implementation in Practice

Strongback-braced frames have been implemented and constructed in practice (Mar, 2010; Panian et al., 2015; Osteraas et al., 2017). Tipping structural engineers constructed a four-story laboratory building similar to the embedded strongback system proposed herein (Mar, 2010; Panian et al., 2015). The frame was iteratively designed utilizing nonlinear dynamic analysis. Supplemental checks were also conducted using elastic modal response spectrum analysis and the code-prescribed overstrength factor for BRBFs, Ω_0 (Panian et al., 2015). The constructed frame employed the offset bracing configuration scheme proposed by Lai and Mahin (2015); see Figure 2.13(c). Pins were provided at the base of the columns in the lateral frame to facilitate the desired pivoting motion.

Tipping successfully made the case that the strongback system could be designed utilizing a redundancy factor, $\rho = 1$ (ASCE-7-16, 2016). This was justified by leveraging the strongback's ability to re-distribute demands vertically to adjacent stories after consecutive removal of the inelastic braces. This allowed the building to be designed utilizing two lateral-resisting frames in both directions, resulting in significant cost savings. It is imagined that an engineer would have to demonstrate the applicability of this assumption on a case-by-case basis to local regulatory authorities using code mandated procedures [e.g., ASCE-7-16 (2016)].

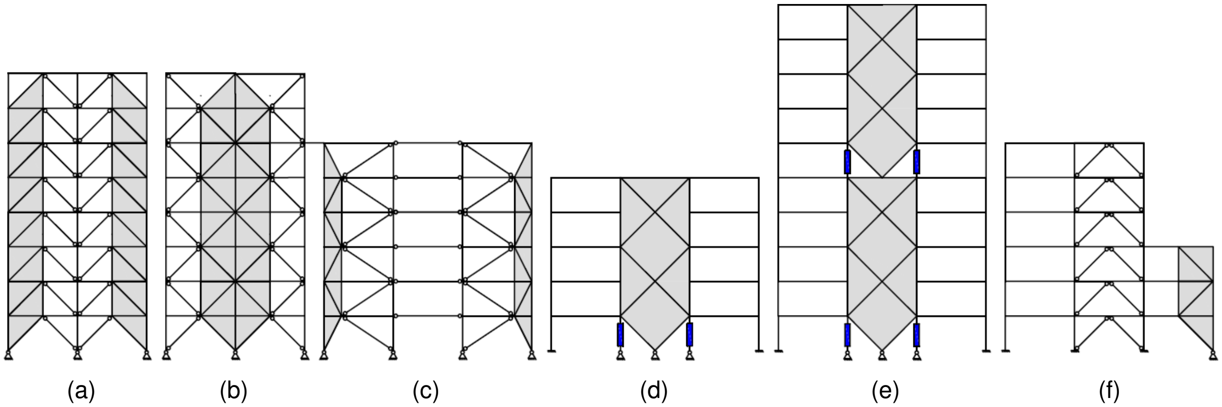

Figure 2.13. Schematic of strongback studies.
(a) and (b) two-bay elastic truss systems by Merzouq and Tremblay (2006);
(c) offset strongback scheme by Lai and Mahin (2015); (d) spine frame by Chen et al. (2017);
(e) segmented spine frame by Chen et al. (2018); (f) stiff rocking core by Slovenac et al. (2017)

2.4.2 Experimental Tests of Strongback-braced frames

Strongback-braced frames have been subjected to few experimental tests. Limited experiments on strongback systems to date have been loaded statically, and nonlinear numerical models described in Section 2.4.1 have yet to be comprehensively verified through dynamic testing.

2.4.2.1 Quasi-static Testing of Strongback-braced frames

Simpson and Mahin (2018b) carried out nearly full-scale laboratory quasi-static experiments on a strongback retrofit braced frame. The retrofit was intended as an upgrade to two previously tested vintage CBFs representative of 1970s and 1980s construction practices. Results showed that the strongback can effectively limit weak story behavior and result in uniform drift demands. Schematics of the inelastic behavior of the two vintage braced frame tests and strongback retrofit are shown in Figure 2.14.

A number of practical detailing issues were identified during the experiment. the strongback geometry and corresponding kinematic relations can induce relatively large demands on the components of the inelastic portion of the system. In a centered scheme where the strongback intersects the beam at half the bay width, these demands are approximately double the demands of a conventional braced frame where the beam does not yield and deflect vertically at midspan; see the idealized kinematic diagram in Figure 2.15(a). The undesirable failures observed in the inelastic bracing element and beam-column connections during the experiment confirmed the significance of these demands; see Figure 2.16(a) and (c). These inelastic demands can be reduced utilizing an offset bracing configuration where the intersection of the braces is offset from the centerline of the bay, like that proposed by Lai and Mahin (2015). A supplemental numerical study by Simpson and Mahin found that this scheme allowed the strongback frame to go to larger displacement amplitudes with less deformation demands than configurations without offsets.

The connections at the base of the strongback column and between the inelastic and strongback portions of the system can be complex and involve loading conditions not encountered in conventional braced frame construction. For example, the base of the strongback experiences significant plastic rotations, shears, and axial load demands. In the strongback test specimen, the strongback column was oriented in weak-axis bending to minimize strains associated plastic hinging in a fixed base column. However, it was noted that a weak axis orientation may not be possible in all cases. Though adequate, details used for the region between the inelastic and strongback portions of the system were deemed conservative.

The design of the test specimen assumed the plastic mechanism shown in Figure 2.15(a) subjected to an inverted triangular force distribution. The elastic braces were designed to be 1.1 times stronger than the forces delivered by the expected capacity of the inelastic braces and flexural yielding of the beam at incipient collapse, as shown by the moment and axial force diagrams in Figure 2.15 (b and c). However, it was noted that this design method could not reasonably be extended to a system subjected to dynamic loading conditions where the applied demand distribution generated by the ground accelerations was unknown.

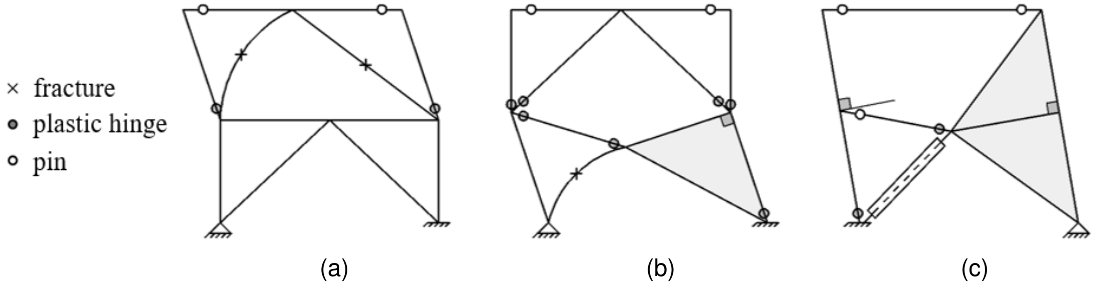

Figure 2.14. Schematic of damage in experiments conducted by Simpson and Mahin (2018b). (a) benchmark vintage braced frame; (b) concrete-filled brace upgrade; and (c) strongback retrofit.

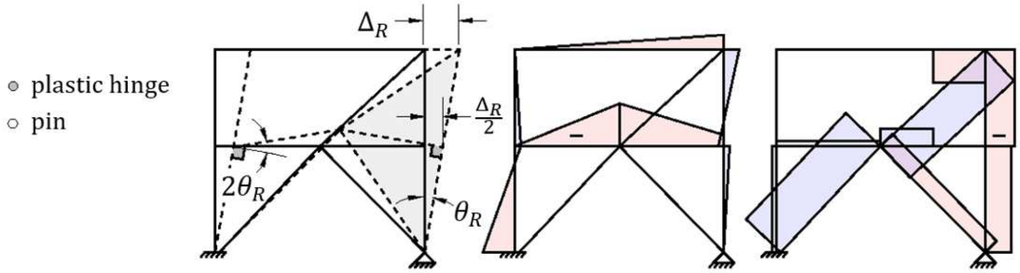

(a) (b) (c)

Figure 2.15. Idealized behavior of strongback experiment (Simpson & Mahin, 2018b). (a) kinematic; (b) moment; and (c) axial force diagrams.

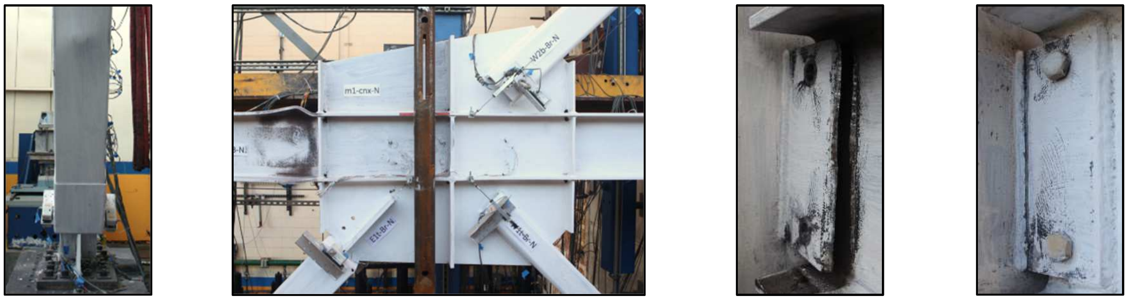

(a) (b) (c)

Figure 2.16. Observed damage in experimental test of a strongback retrofit (Simpson & Mahin, 2018b). (a) BRB; (b) center gusset; (c) beam-column connections.

2.4.2.2 Pseudo-dynamic Hybrid Testing of Stiff Rocking Cores

Researchers have investigated the addition of stiff rocking cores for the rehabilitation for existing braced frames. Slovenec et al. (2017) investigated this rehabilitation technique on two approximately 1/3-scale experimental specimens. The prototype frames were subjected to slow pseudo-dynamic hybrid testing to simulate dynamic effects in a six-story building. The lower three-stories of the building were tested experimentally and the upper three stories were simulated numerically. The stiff rocking core was separated from the braced bay and only extended over the first three stories of the prototype structure; see Figure 2.13(f). Equilibrium and compatibility in the rotational and vertical translational degrees of freedom at the boundary between the experimental specimen and numerical simulation were neglected during the test.

Peak story drift demands and their associated dispersion were reduced with the addition of a stiff rocking core. Column shears, however, exceeded the design column shear forces. A subsequent design methodology was proposed by Pollino et al. (2017) including additional higher-mode stiffness for the design of the rocking core. The study concluded that the proposed design method was conservative and inaccurately considered higher-mode forces, concluding that further research was needed.

2.5 SUMMARY

This chapter summarized the expected inelastic behavior and traditional design strategies for conventional steel braced-frame systems. As these systems are susceptible to story mechanism behavior, alternative methods of mitigating story mechanisms were also highlighted. Though these methods can be successful at distributing drift demands, essentially elastic elements in such systems can result in amplified higher-mode effects (e.g., tied EBF systems, shear wall systems, and rocking systems). Since higher-mode effects are critical to the design of essentially elastic "spine" systems, they likely also need to be considered in design methodologies for strongback-braced frames. Although the inclusion of higher-mode effects in the design procedures for rocking and wall-like systems offers insight into potential static analysis methods, the characteristics of the behavior of such systems may not be directly applicable to strongback-braced frames.

Numerical studies have illustrated the effectiveness of strongback-braced frames in delaying or preventing story mechanisms in low-, mid-, and high-rise steel braced frames. However, nonlinear dynamic analyses have been inconsistent, utilized simple models for the fuses, or were not calibrated to relevant experimental data. Proposed static design methods for strongback-braced frames have consistently under-represented upper story strongback demands. Though revealing of potential detailing issues, experimental tests have been conducted under static loading. Moreover, numerical models intended to simulate the nonlinear dynamic behavior of spine systems have not been comprehensively verified through dynamic testing. None of these prior investigations have identified dependable, economical, or practical design methods. Nor have they described simple or robust means of modeling higher-mode effects.

3 Analytical Investigation of Offset Configurations

3.1 INTRODUCTION

The strongback geometry and corresponding kinematic relations can induce relatively large demands on the fuses in strongback-braced frames; see Section 2.4.2.1. In a centered scheme where the strongback intersects the beam at half the bay width, these demands are double the demands of a conventional braced frame where the beam does not yield and deflect vertically at midspan, see Figure 3.1(a) versus (b). The undesirable failures observed in the inelastic bracing element and beam-column connections of an experimental test of a two-story SBF with a centered scheme (Simpson & Mahin, 2018b) confirm that these imposed demands can be significant.

The offset scheme introduced in two previous numerical studies (Lai & Mahin, 2015; Simpson & Mahin, 2018b) is capable of reducing these inelastic demands. The kinematics of an offset configuration, as shown in Figure 3.1(c), address the relatively high axial strains in the inelastic braces by providing longer yield lengths for the buckling-restrained braces. The offset scheme also provides longer beam lengths that reduce the in-plane rotational demands that can develop at the ends of the beam links. Because of these desirable properties, an offset configuration was used for the bracing configuration of a constructed strongback building in Berkeley, CA (Panian et al., 2015).

Like the length of a link in an eccentrically braced frame (Hjelmstad & Popov, 1984), the amount of offset determines both the elastic stiffness and strength of the lateral-resisting system under low-to-moderate shaking and the ductility demand on the inelastic braces and beam links under severe shaking. In an SBF system, the strongback components of the frame must additionally remain essentially elastic while the inelastic braces and beam links deform inelastically. Thus, the amount of offset is constrained by three objectives: [i] providing enough strength and stiffness to limit displacements in the elastic range, and [ii] reducing plastic deformations to provide enough energy dissipation in the inelastic range, and [iii] limiting the demands on the elastic "strongback" truss. Determination of the maximum offset to meet elastic requirements and the minimum offset to limit inelastic demands bound the optimal length of the offset.

The analysis of a simple one-story frame was conducted to: [1] describe the fundamental response of the strongback and characterize the parameters important to the strongback's behavior; [2] develop the premise for an analysis procedure based on perfectly plastic idealization; and [3] determine the optimal location of the offset. For this purpose, a conventional braced frame was compared to a family of strongback-braced frames with offsets varying from zero to half the bay width. A simple one-story-by-one-bay system was characterized by its behavior in terms of geometry in both the elastic and inelastic ranges; see Figure 3.2. Based on this characterization, a set of criteria were designated as critical for the successful design of an SBF. These multi-objective criteria were used to establish a "give-and-take" optimization study to determine a suitable offset location for the one-story system. The selection of this offset location was then verified through nonlinear dynamic analysis of the one-story frame.

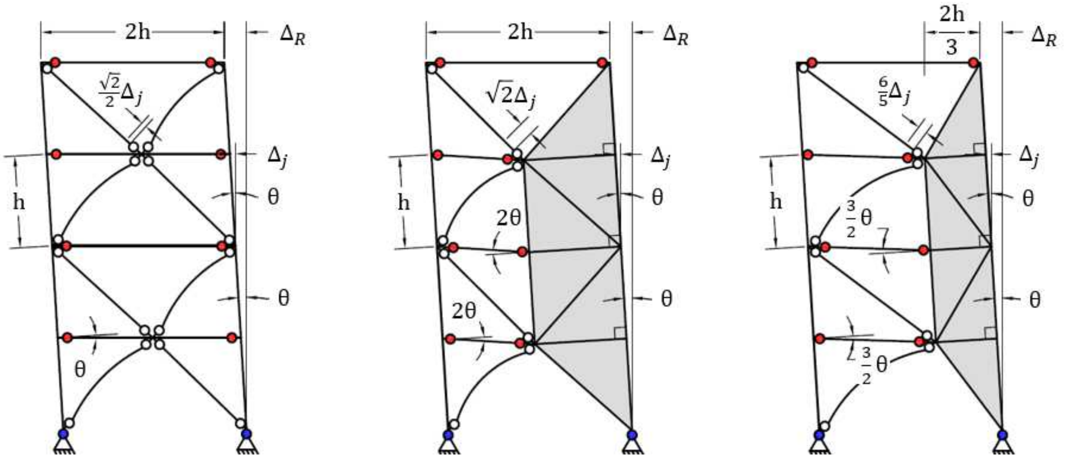

(a) (b) (c)

Figure 3.1. Example of plastic mechanism: (a) conventional braced frame scheme, (b) centered strongback scheme, and (c) offset strongback scheme.

3.2 ANALYTICAL METHOD

It is instructive to compare strongback geometries with a range of offsets in both the elastic and inelastic ranges in an analytical, closed-form sense to quantify the influence of geometry on the SBF system. For this purpose, consider the variation of the simplest SBF shown in Figure 3.2(b) as a function of the strongback lateral width, b, normalized by the total bay width, L.

In this system, $(\cdot)_r$ and $(\cdot)_s$ represent the inelastic and elastic portions of the system respectively. A continuous spectrum of offsets is available from a centered, "chevron", scheme representing the stiffest and strongest arrangement ($\frac{b}{L} = \frac{1}{2}$) to a single diagonal bracing configuration representing minimum plastic demands ($\frac{b}{L} = 0$). In this system, $l = L - b$ represents the horizontal width of the fuses; h represents the vertical height of the frame; and $r = \sqrt{l^2 + h^2}$ and $s = \sqrt{b^2 + h^2}$ represent the elastic and inelastic brace lengths. Since the horizontal component of the stiffness, strength, and ductility demands depend on the cosine angle of the braces, each of these parameters will change nonlinearly with varying offset.

The normalization of the offset scheme in Figure 3.2(b) by the centered scheme represents the range at which the parameters vary from the centered, or $(\cdot)_0$, configuration. In the following sections, parameters of interest derived from the offset scheme, c, are plotted in terms of their ratio to the same parameter derived from the centered scheme, c_0. The horizontal line, $\frac{c}{c_0} = 1$, represents the centered scheme. Any deviation from $\frac{c}{c_0} = 1$ represents the offset's influence on the chosen parameter with normalized offset, $\frac{b}{L}$.

For simplicity, the following analytical investigations were based on a perfectly plastic material assumption. As such, the inelastic braces in this study are representative of idealized BRBs with negligible strain hardening and no strength degradation behavior. Beam and column elements of the surrounding frame are assumed to be inextensible; energy dissipation occurs only in zero-length plastic hinge regions. Moments at the ends of all bracing elements are released. In this initial study, nonlinear geometry effects and flexural-axial interaction were neglected for simplicity.

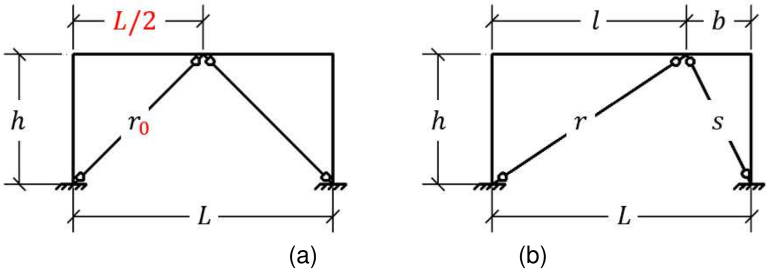

Figure 3.2. Simplified study of an offset scheme (a) centered case and (b) offset case.

3.3 ELASTIC CHARACTERISTICS OF OFFSET GEOMETRIES

Drift control is satisfied by providing the strongback with sufficient elastic stiffness. Static equilibrium under elastic analysis also dictates how much demand is imposed on the inelastic braces prior to yielding. Thus, quantifying elastic stiffness and strength as a function of the amount of offset determines both the initial strength and stiffness of the frame under low to moderate shaking.

3.3.1 Elastic lateral stiffness

Let x and y be the horizontal and vertical translational degrees of freedom respectively; see Figure 3.3(a). Neglecting nonlinear geometry effects, the total stiffness matrix, $\boldsymbol{K}$, for the translational degrees of freedom can be written as the sum of the following:

$$\boldsymbol{K} = \boldsymbol{K}_{br} + \boldsymbol{K}_{fr}$$

$\boldsymbol{K}_{fr}$ = stiffness matrix of the surrounding frame, $\boldsymbol{K}_{br}$ = stiffness matrix of the braces. Each of these matrices can be condensed to the two translational degrees-of-freedom, x and y:

$$\boldsymbol{K}_{br} = \begin{bmatrix} K_{br,xx} & K_{br,xy} \\ K_{br,xy} & K_{br,yy} \end{bmatrix} = EA_r \begin{bmatrix} \frac{l^2}{r^3} + \beta \frac{b^2}{s^3} & \frac{hl}{r^3} - \beta \frac{hb}{s^3} \\ \frac{hl}{r^3} - \beta \frac{hb}{s^3} & \frac{h^2}{r^3} + \beta \frac{h^2}{s^3} \end{bmatrix}$$

$$\boldsymbol{K}_{fr} = \begin{bmatrix} K_{fr,xx} & K_{fr,xy} \\ K_{fr,xy} & K_{fr,yy} \end{bmatrix}$$

$\beta = \frac{EA_s}{EA_r}$ = the ratio of the elastic stiffness of the strongback brace (EA_s) to the inelastic brace (EA_r). For the centered scheme (i.e., $b = L/2$), the brace lengths are equal, $r = s = r_0$, and the condensed stiffness matrix for the braces can be re-written as:

$$\boldsymbol{K}_{br,0} = EA_r \begin{bmatrix} \frac{L^2}{4r_0^3}(1+\beta) & \frac{hL}{2r_0^3}(1-\beta) \\ \frac{hL}{2r_0^3}(1-\beta) & \frac{h^2}{r_0^3}(1+\beta) \end{bmatrix}$$

Assuming equal brace area for the inelastic and strongback brace ($\beta = 1$), the horizontal and vertical component of the brace stiffness decouple for the centered scheme:

$$\boldsymbol{K}_{br,0} = EA_r \begin{bmatrix} \frac{L^2}{2r_0^3} & 0 \\ 0 & 2\frac{h^2}{r_0^3} \end{bmatrix}$$

$\boldsymbol{K}_{br,0}$ = brace contribution to the lateral stiffness in the centered scheme when $b = l$; r_0 = brace length if $b = l$. The $\boldsymbol{K}_{br}$ and $\boldsymbol{K}_{fr}$ matrices can be condensed to the lateral translation, x, by:

$$\widehat{K} = \left(K_{br,xx} + K_{fr,xx}\right) - \frac{\left(K_{br,xy} + K_{fr,xy}\right)^2}{K_{br,yy} + K_{fr,yy}}$$

$\widehat{K}$ = lateral stiffness condensed to direction x. Neglecting the stiffness contributions from the surrounding frame, the condensed lateral stiffness of the braces can be re-written as:

$$\widehat{K}_{br} = EA_s \frac{L^2}{\beta r^3 + s^3} \qquad \text{Equation 3.1}$$

$$\widehat{K}_{br,0} = EA_r \frac{L^2}{2r_0^3} \qquad \text{Equation 3.2}$$

$\widehat{K}_{br}$ = brace lateral stiffness for the offset scheme; $\widehat{K}_{br,0}$ = brace lateral stiffness for the centered scheme. The normalized stiffness of the offset scheme with respect to the centered scheme, $\widehat{K}_{br} \backslash \widehat{K}_{br,0}$, is:

$$\frac{\widehat{K}_{br}}{\widehat{K}_{br,0}} = \frac{2\beta r_0^3}{\beta r^3 + s^3} \qquad \text{Equation 3.3}$$

The ratio in Equation 3.3 is plotted in Figure 3.4(a) for different height-to-bay width ratios, $\frac{h}{L}$, and equal inelastic and elastic brace stiffness ($\beta = 1$). As $\frac{b}{L}$ approaches $\frac{1}{2}$, the frame stiffness approaches that of an inverted-V configuration, and both braces contribute equally to the lateral stiffness. As $\frac{b}{L}$ approaches 0, the frame tends towards a single diagonal, and the strongback contribution to the lateral stiffness decreases to zero. As the offset increases, the system's lateral stiffness tends to decrease.

The strongback brace is expected to be stronger, and therefore stiffer, than the inelastic brace. To incorporate this effect, the influence of the strongback stiffness relative to the inelastic brace stiffness, β, is plotted in Figure 3.4(b) with constant $\frac{h}{L}$. The stiffer the strongback brace is with respect to the inelastic brace ($\beta = \frac{EA_s}{EA_r} > 1$), the higher the lateral stiffness of the frame. However, this effect becomes less significant as the offset, b, approaches 0 and the bracing configuration becomes a single diagonal. Figure 3.5 shows similar plots in terms of an estimate of the elastic period, T.

In summary, too much offset will significantly decrease the overall stiffness of the frame. This effect is reduced by providing $\beta > 1$ so long as the offset is not too large.

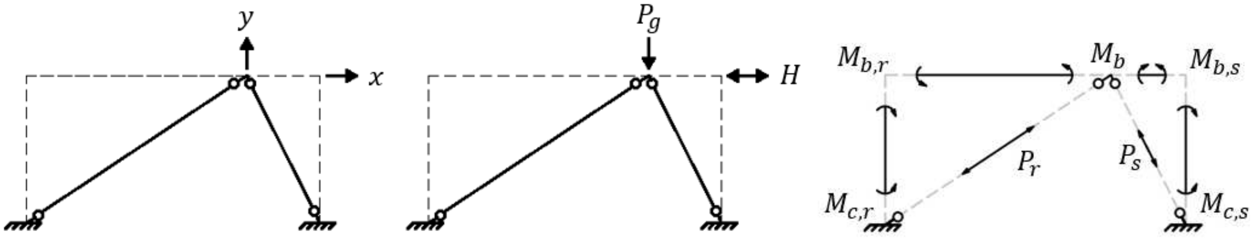

(a) (b) (c)

Figure 3.3. Schematic of (a) degrees-of-freedom; (b) applied loads; (c) internal forces.

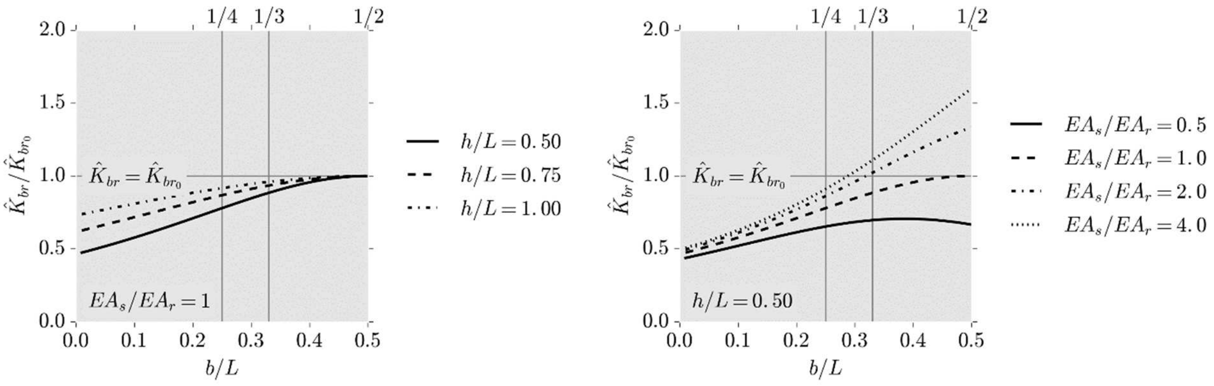

(a) (b)

Figure 3.4. Influence of offset on elastic stiffness.
(a) variations of stiffness for different aspect ratios with constant member sizes;
(b) variations of stiffness with strongback strength.

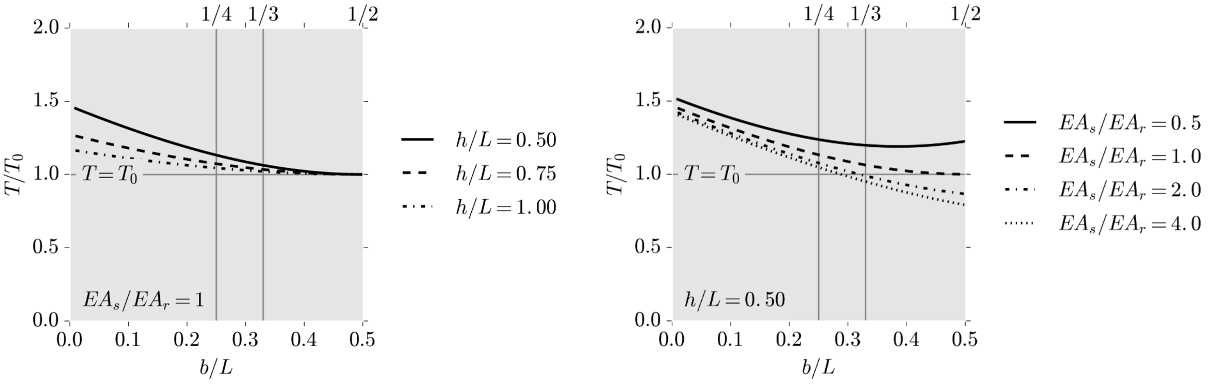

(a) (b)

Figure 3.5. Influence of offset on estimate of period.
(a) variations in estimated period for different aspect ratios with constant member sizes;
(b) variations in estimated period with strongback strength.

3.3.2 Elastic equilibrium

Let H and V represent possible applied horizontal and vertical lateral loads; see Figure 3.3(b). The equilibrium equations in the horizontal and vertical direction in the global coordinate system can be written as:

$$\pm H = \frac{M_{c,r} + M_{c,s}}{h} - \frac{M_{b,r} + M_{b,s}}{h} + \frac{l}{r} P_r - \frac{b}{s} P_s \qquad \text{Equation 3.4}$$

$$-P_g = \frac{M_b - M_{b,s}}{b} + \frac{M_{b,r} + M_b}{l} - \frac{h}{r} P_r - \frac{h}{s} P_s \qquad \text{Equation 3.5}$$

The horizontal applied load, H, can act in both the $\pm x$ direction and is representative of equivalent seismic loading while the vertical load, P_g, acts only in the $-y$ direction and is representative of typical gravity loading. Internal forces are defined in Figure 3.3(c). Equation 3.4 and Equation 3.5 assumes positive moments are counterclockwise and axial forces are positive in tension.

Since the one-story frame is statically indeterminate, the equilibrium solutions for the axial force in the braces can be separated into a particular solution describing the influence of the applied loading on the brace force, $(\cdot)^p$, and a homogeneous solution describing the influence of the internal force distributions on the brace force, $(\cdot)^h$.

3.3.2.1 Particular Brace Force Solution

The particular solution of the applied load can be written in terms of the magnitude of the brace axial force:

$$\begin{aligned} |P_r^p| &= \frac{r}{L}|H| \mp \frac{br}{hL}|P_g| \\ |P_s^p| &= \frac{s}{L}|H| \pm \frac{ls}{hL}|P_g| \end{aligned} \qquad \text{Equation 3.6}$$

The sign of P_s acts opposite the force in the inelastic brace, P_r. The gravity load, P_g, can be additive or subtractive depending on the direction of the horizontal load, H (i.e. if $+H$, the gravity load is subtractive for P_r and additive for P_s; the opposite is true for $-H$).

It is apparent from Equation 3.6 that the brace angle has a significant influence on the brace axial force. Neglecting P_g, as the offset, b, decreases, the magnitude of the axial force in the inelastic and elastic braces, P_r and P_s, tends to increase and decrease as the brace lengths, r and s, become longer and shorter respectively. In other words, the axial force in the inelastic brace will tend to increase with increasing offset and decreasing angle of inclination. In contrast, the axial force in the strongback brace will tend to decrease with increasing offset and increasing angle of inclination.

3.3.2.2 Homogeneous Brace Force Solution

The homogeneous solution including the internal forces in the surrounding beam and column elements can be written in terms of the contributing internal moments, $M_{(\cdot)}$, or shears, $V_{(\cdot)}$:

$$\begin{aligned} P_r^h &= \frac{r}{h}\frac{M_{b,r}+M_b}{l}-\frac{r}{h}\frac{M_{c,r}+M_{c,s}}{L}=\frac{br}{hL}\left(V_{b,r}-V_{b,s}\right)-\frac{r}{L}\left(V_{c,r}+V_{c,s}\right) \\ P_s^h &= \frac{s}{h}\frac{M_{b,s}-M_b}{b}-\frac{s}{h}\frac{M_{c,r}+M_{c,s}}{L}=\frac{ls}{hL}\left(V_{b,s}-V_{b,r}\right)-\frac{s}{L}\left(V_{c,r}+V_{c,s}\right) \end{aligned} \qquad \text{Equation 3.7}$$

$V_{b,r}$, $V_{b,s}$ = beam shear in the inelastic and strongback portion of the beam, $V_{c,r}$, $V_{c,s}$ = column shear in the inelastic and strongback columns.

3.3.2.3 Total Brace Force Solution

If the frame displaces to the right under $+H$, the beam moments are negative and the column moments are positive; see Figure 3.7. Substituting appropriate signs for these moments into Equation 3.7 and combining the particular and homogeneous solutions, the total solution for the magnitude of the axial force in the braces can be written as:

$$\begin{aligned} |P_r| &= \left|P_r^p\right|+\left|P_r^h\right|=\frac{r}{L}|H|\mp\frac{br}{hL}|P_g|-\frac{r}{h}\frac{|M_{b,r}|+|M_b|}{l}-\frac{r}{h}\frac{|M_{c,r}|+|M_{c,s}|}{L} \\ |P_s| &= \left|P_s^p\right|+\left|P_s^h\right|=\frac{s}{L}|H|\pm\frac{sl}{hL}|P_g|+\frac{s}{h}\frac{|M_b|-|M_{b,s}|}{b}-\frac{s}{h}\frac{|M_{c,r}|+|M_{c,s}|}{L} \end{aligned} \qquad \text{Equation 3.8}$$

These equations can be simplified if it is assumed that the beam ends and the column bases are pinned (i.e., $M_{c,r} = M_{c,s} = M_{b,r} = M_{b,s} = 0$):

$$\begin{aligned} |P_r| &= \frac{r}{L}|H|\mp\frac{br}{hL}|P_g|-\frac{r}{h}\frac{|M_b|}{l} \\ |P_s| &= \frac{s}{L}|H|\pm\frac{sl}{hL}|P_g|+\frac{s}{h}\frac{|M_b|}{b} \end{aligned} \qquad \text{Equation 3.9}$$

The algebraic signs in Equation 3.9 can be dissected to determine how the offset and corresponding particular and homogeneous solutions affect the axial force in the braces. Neglecting P_g, the particular solution of P_r tends to increase with H as the offset, b, decreases and the brace length,

r, increases. The beam shear, $\frac{M_b}{l}$, tends to reduce P_r; the magnitude of this shear force decreases as the beam link length, l, increases. In contrast, the particular solution of P_s tends to decrease with H as the offset, b, and brace length, s, decreases. However, the beam shear in the strongback half of the beam, $\frac{M_b}{s}$, tends to increase P_s; the magnitude of this shear force increases with decreasing offset, b.

In summary, though the axial force in the strongback brace tends to decrease with increasing offset, the beam shear and vertical gravity loading contributions will increase with increasing offset. More information on this effect is provided in Section 3.4.2.

3.4 INELASTIC CHARACTERISTICS OF OFFSET GEOMETRIES

The effective performance of a frame under severe seismic excitation depends on its ability to absorb and dissipate energy without loss of strength. In an SBF system, the strongback components of the frame must additionally remain essentially elastic while the inelastic braces and beam links deform inelastically. An estimate of the ductility and strongback demands can be obtained from a rigid, plastic analysis of the structure at the "limit load" – the load needed to form a mechanism at incipient collapse.

3.4.1 Ductility demand

The plastic mechanism of the simple frame under a rigid, plastic assumption is shown in Figure 3.6. The strongback "weak" beam plastic mechanism is compared to a conventional braced frame "strong" beam plastic mechanism in Figure 3.7 and Figure 3.8. Conventional braced frames are typically designed with strong beams that remain elastic under the unbalanced load induced by yielding in the braces; see Figure 3.6(b). In contrast, strongback-braced frames allow the beam to secondarily dissipate energy through flexural yielding; see Figure 3.6(a). The strong and weak beam mechanism are differentiated by the relative flexural strength of the beam to the braces. Energy dissipation in strong beam mechanisms is dominated by the hysteretic response of the braces, while a weak beam response includes beam yielding.

Plastic hinging in the beam causes the beam to displace vertically in the weak-beam mechanism. From rigid-plastic geometry, the vertical deflection, y, is:

$$y = \theta b \qquad \text{Equation 3.10}$$

Geometric considerations including this vertical deflection lead to the following deformation relations for the weak-beam (i.e., strongback) mechanism.

$$\theta L = \theta_b l \qquad \text{Equation 3.11}$$

$$\frac{\delta_r}{x} = \frac{b+l}{r} = \frac{L}{r}, \frac{\delta_s}{x} = 0 \qquad \text{Equation 3.12}$$

The deformation relations for the strong-beam (i.e., conventional braced frame) mechanism ($y = 0$) are:

$$\theta = \theta_b$$ Equation 3.13

$$\frac{\delta_r}{x} = \frac{l}{r}, \frac{\delta_s}{x} = \frac{b}{s}$$ Equation 3.14

$\theta = \frac{x}{h}$ = story drift ratio; θ_b = flexural deformation of the beam link; δ_r, δ_s = axial deformation of the inelastic and strongback brace respectively. The axial deformations can be converted to axial strains by dividing by the yield length, $\varepsilon_r = \frac{\delta_r}{r_y}$ and $\varepsilon_s = \frac{\delta_s}{s_y}$, where r_y and s_y are the yield lengths of the inelastic and strongback braces respectively.

Plastic deformations for four different cases of offset, $\frac{b}{L} = \frac{1}{2}, \frac{1}{3}, \frac{1}{4}$, and 1, for both plastic mechanisms are shown in Table 3.1. Case D with $b = 0$ represents a single diagonal geometry when the deformations of the strong and weak beam mechanisms are equal. Case A with $b = \frac{L}{2}$ represents the centered scheme when the deformations of the weak-beam mechanism are double that of the strong-beam mechanism.

The deformations, δ_r and θ_b, in the weak-beam mechanism are the ratio of $\frac{L}{l}$ times that of the strong-beam mechanism. The ratio $\frac{L}{l}$ is a measure of the amplification in deformations seen in the SBF mechanism compared to a conventional CBF mechanism. As the length, l, increases with increasing offset, $\frac{l}{L}$ increases and the strongback deformations approach that of the strong-beam mechanism.

The plastic deformations for the strongback mechanism are normalized by the centered scheme in Figure 3.9. As the offset decreases, the beam vertical deflection, beam rotations, and brace axial deformations decrease with increasing l. Beam rotations are independent of the ratio of story height to bay width, $\frac{h}{L}$.

Table 3.1. Comparison of "weak" and "strong" beam plastic mechanism.

Case	**Offset**			**SBF or weak-beam CBF**			**Strong-beam CBF**		
	$\frac{b}{L}$	$\frac{l}{L}$	$\frac{b}{l}$	$\frac{\theta_b}{\theta}$	$\frac{\delta_r r}{x}$	$\frac{\delta_s s}{x}$	$\frac{\theta_b}{\theta}$	$\frac{\delta_r r}{x}$	$\frac{\delta_s s}{x}$
A	1/2	1/2	1	2	$L/r = 2l/r = 2b/r$	0	1	$L/2r = l/r = b/r$	$L/2s = l/s = b/s$
B	1/3	2/3	1/2	3/2	$L/r = 3l/2r = 3b/r$	0	1	$2L/3r = l/r = 2b/r$	$L/3s = l/2s = b/s$
C	1/4	3/4	1/3	4/3	$L/r = 4l/3r = 4b/r$	0	1	$3L/4r = l/r = 3b/r$	$L/4s = l/3s = b/s$
D	0	1	0	1	$L/r = l/r$	0	1	$L/r = l/r$	0

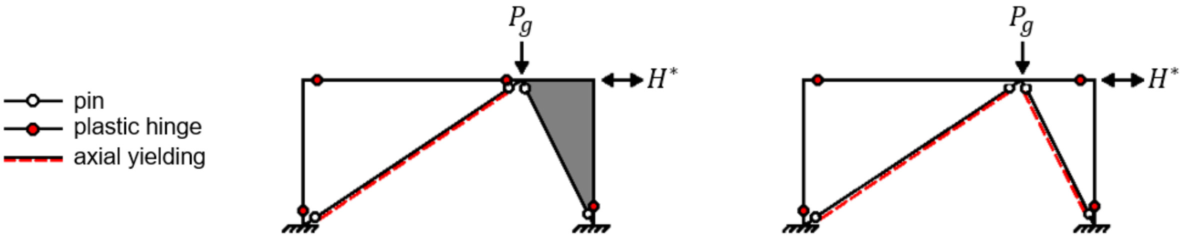

(a) (b)

Figure 3.6. Locations of yielding for the plastic mechanisms of a one-story system.
(a) weak-beam (stongback) mechanism and (b) strong-beam (conventional braced frame) mechnism.

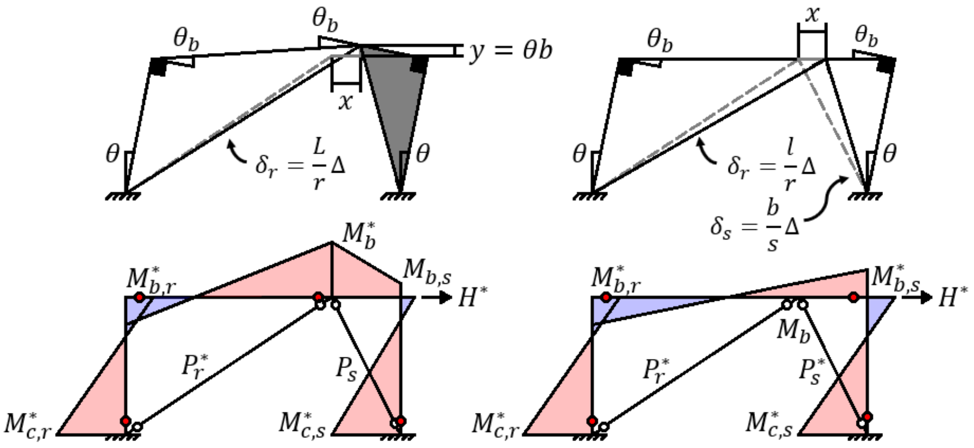

(a) (b)

Figure 3.7. Plastic mechanisms for one-story system, $+H$.
(a) weak-beam (stongback) mechanism and (b) strong-beam (conventional braced frame) mechnism.

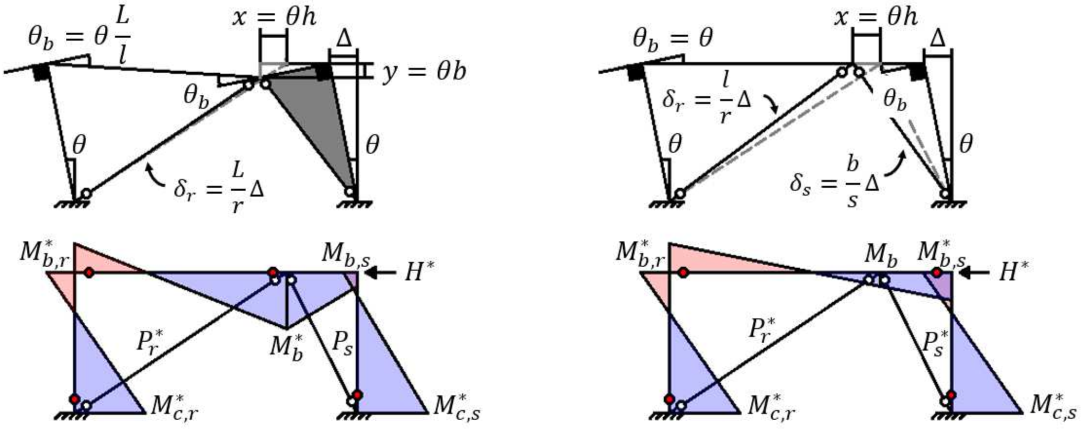

(a) (b)

Figure 3.8. Plastic mechanisms for one-story system, $-H$.
(a) weak-beam (stongback) mechanism and (b) strong-beam (conventional braced frame) mechnism.

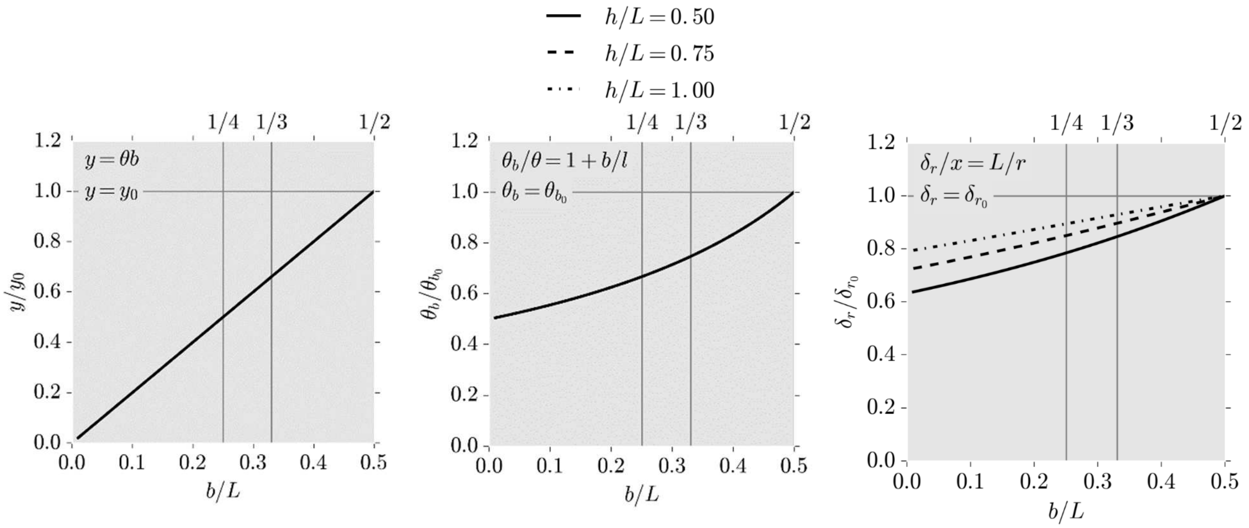

(a) (b) (c)

Figure 3.9. Variation of ductility demands.
(a) vertical translation; (b) inelastic beam rotation; (c) inelastic axial deformation

3.4.2 Limit load

The equilibrium at the limit load can be used to approximate the axial-force demands in the strongback brace. By virtual work, the magnitude of the horizontal limit load, H^*, needed to form the weak-beam mechanism can be written in terms of the plastic capacity of the yielding elements:

$$|H^*| = \frac{M^*_{c,r} + M^*_{c,s}}{h} + \frac{L}{l}\frac{M^*_{b,r} + M^*_{b}}{h} + \frac{L}{r}P^*_r \pm \frac{b}{h}|P_g| \qquad \text{Equation 3.15}$$

$(\,\cdot\,)^*$ = plastic capacity of the beam, column base, and inelastic brace elements. The definitions of the variables used in these equations are called out in the moment diagrams of Figure 3.7(a) and Figure 3.8(a). The sign of the gravity load, P_g, depends on the direction of lateral loading, H ($+P_g$ for $+H$; $-P_g$ for $-H$).

Substituting the limit load, H^*, from Equation 3.15 for H in the equilibrium equation for the strongback demand in Equation 3.8 gives the magnitude of the axial force in the strongback brace, P_s, at incipient collapse:

$$|P_s| = \frac{s}{h}\frac{L}{lb}M^*_b + \frac{s}{h}\frac{M^*_{b,r}}{l} - \frac{s}{h}\frac{|M_{b,s}|}{b} + \frac{s}{r}P^*_r \pm \frac{s}{h}|P_g| \qquad \text{Equation 3.16}$$

This equation is independent of the column capacity for the one-story frame. Equation 3.16 can be simplified by assuming the beam ends are pinned (i.e., $M^*_{b,r} = M^*_{b,s} = 0$):

$$|P_s| = \frac{s}{h}\frac{L}{lb}M^*_b + \frac{s}{r}P^*_r \pm \frac{s}{h}|P_g| \qquad \text{Equation 3.17}$$

At the limit load, the demands in the strongback brace depend directly on the gravity loading, P_g; the capacity of the beam, M_b^*; and the capacity of the opposite inelastic brace, P_r^*.

The strongback brace demand in Equation 3.17 is a convex function of the offset. Neglecting P_g, the magnitude of P_s at the limit load is plotted against the normalized offset, $\frac{b}{L}$, for $\frac{h}{L} = \frac{1}{2}$ in Figure 3.10(a). When the derivative, $\frac{dP_s}{db} = 0$, the axial force in the strongback brace is minimized. The derivative of the strongback demand for different beam capacities, M_b^*, is plotted against the amount of offset in Figure 3.10(b). Generally, strongback brace demands are minimized around $\frac{b}{L} = \frac{1}{3}$, depending on the relative strength of the beam to the inelastic brace.

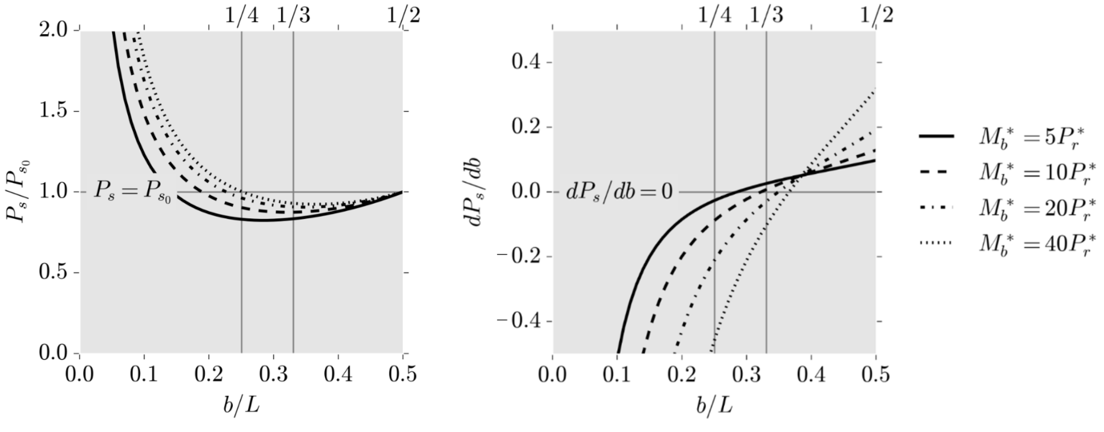

(a) (b)

Figure 3.10. Minimization of P_s at incipient collapse.
(a) function of the offset and (b) derivative with respect to the offset.

3.5 OPTIMIZATION OF THE OFFSET

The normalization of a response quantity in an offset scheme by the same response in the centered scheme illustrated how demands are influenced by the offset location. In summary of the results in Sections 3.3 and 3.4 –

1. *The lateral stiffness of the braces, $\widehat{K}_{br}$, decreases as the offset increases in the elastic range.* As the offset increases, the inclination angle of the inelastic brace decreases while the inclination angle of the strongback brace increases. This angle causes the inelastic brace to contribute more and strongback brace to contribute less to the lateral stiffness of the frame. However, the stiffness contributions of the inelastic and the strongback brace to the total lateral stiffness are not one-to-one. As the angle of the strongback brace increases, its contribution to the lateral stiffness decreases at a higher rate than the inelastic brace contribution increases. Thus, even though the inelastic brace contributes more to the lateral stiffness as its angle decreases, the total brace lateral stiffness tends to decrease as the offset increases. Use of a stiffer strongback brace relative to the inelastic brace can increase the total brace lateral stiffness but is advantageous only if the offset is not too large.

2. *The inelastic brace demand, P_r, increases as the offset increases in the elastic range.* Similar to observation [1], the inelastic brace contributes increasingly more to the lateral strength of the frame as the angle of inclination of the brace decreases. This results in larger axial-force demands in the inelastic brace, P_r, in the elastic range. In contrast, the elastic brace demand, P_s, tends to decrease with increasing offset in the elastic range. In both cases, the gravity loading can have an additive effect on the particular solution of the brace force depending on the direction of loading.

3. *The plastic deformations (y, θ_b, δ_r, and ε_r) decrease as the offset increases in the inelastic range.* The in-plane rotation of the beam link, θ_b, is inversely proportional to the inelastic width, l. Therefore, the beam plastic rotation angle, θ_b, and vertical displacement, y, tend to decrease as the offset increases. The inelastic brace deformations, δ_r and ε_r, are inversely proportional to the length of the inelastic brace in the inelastic range. Thus, as the length of the inelastic brace increases with increasing offset, the axial strain, ε_r, and the axial deformation, δ_r, decrease. These deformations are fundamentally different from the deformations of a conventional strong-beam mechanism where $y = 0$.

4. *The elastic brace demand, P_s, is a convex function of the offset in the inelastic range of response.* At the limit load, H^*, the axial-force demand in the strongback brace, P_s, depends on the limit load and the flexural and axial capacities of the beam link and inelastic brace; see Equation 3.17. Depending on the flexural capacity of the beam, the axial-force demand in the strongback brace at the limit load can be minimized for offsets between $\frac{L}{4} \leq b \leq \frac{L}{3}$.

Each of these parameters is minimized at different offset locations. Only the equation for P_s at the limit load in [4] is convex and has a minimum between $0 < b < \frac{L}{2}$; see Figure 3.10(a). Other response quantities can only be minimized at the boundaries of the beam link length (i.e., at either $b = 0$, for observations [1] and [3] or $b = \frac{L}{2}$ for observation [2]).

3.5.1 Optimization Objectives

An optimal offset location should maximize the lateral stiffness under the constraint that the member ductility demands are physically realizable. The offset is additionally constrained by limiting force demands on the strongback truss. To satisfy these constraints, the following goals are desirable for the optimization of the offset location:

- Maximization of the lateral brace stiffness, $\widehat{K}_{br}$, to achieve appropriate drift control in the elastic range.
- Minimization of the plastic deformations (y, θ_b, δ_r, and ε_r) to achieve adequate ductility in the inelastic range.

- Minimization of the axial load in the inelastic brace, P_r, to reduce design demands in the elastic range.
- Minimization of the axial load in the elastic strongback brace, P_s, to reduce demands on the strongback at the limit load.

To achieve the desired optimization goals, the ideal offset depends on a give-and-take of coupled parameters. Analysis of the strongback's behavior in the elastic and inelastic range lends itself well to multi-objective optimization. The amount of offset is also constrained by satisfying code-prescribed limits on allowable plastic deformations. The following section demonstrates a range of choices for the offset location based on: [i] a simplified multi-objective optimization study and [ii] code-prescribed minimums.

3.5.2 Multi-Objective Optimization

Several multi-objective criteria were used to evaluate the give-and-take of different parameters in the elastic and inelastic ranges of response for the following three optimization objectives:

1. The maximization of $\widehat{K}_{br}$ in the elastic range and the minimization of the plastic deformations (y, θ_b, δ_r, and ε_r) in the plastic range.
2. The minimization of P_r in the elastic range and δ_r or ε_r in the inelastic range.
3. The minimization of P_s in the inelastic range.

The goal of this multi-objective optimization scheme was to find the offset, b, that simultaneously minimized two sub-functions, c_1 and c_2, that depend on the strongback width, b. The weighted sum optimization method allows multi-objective functions to be written as a single objective function. The multi-objective function is minimized by setting its derivative with respect to b equal to zero:

$$w_1 \frac{dc_1(b)}{db} + w_2 \frac{dc_2(b)}{db} = 0, 0 \leq b \leq \frac{L}{2} \qquad \text{Equation 3.18}$$

w_i = weights representing the contribution of each of the sub-functions to the multi-objective function. Equal weights were assigned to each sub-function as each of the objectives was considered to be equally desirable.

The weighted sum method highly depends on normalization of the sub-functions, c_1 and c_2. This study utilized feature normalization – normalizing c to a number between 0 and 1 subject to the boundary constraint $0 < \frac{b}{L} \leq \frac{1}{2}$. This ensured that each goal contributed equally to Equation 3.18.

$$c_{norm} = \frac{c - c_L}{c_U - c_L}$$

c_L = lower bound (utopia point) optimal value; c_U = the upper bound (Nadir point) optimal value. If c is to be minimized, $c_L = \min c$ and $c_U = \max c$. If c is to be maximized, $c_L = \max c$ and $c_U =$

$\min c$. Feature normalization allows the weighted sum method to compare paired parameters of equal relative magnitudes.

Feature normalization for objectives [1] and [2] are shown in Figure 3.11(a) and (b). The corresponding multi-objective functions are shown in Figure 3.11(c) and (d). Objective 3 is a convex function of the offset and can be minimized by setting the derivative, $\frac{dP_s}{db} = 0$, as shown in Figure 3.10(b). The following represent the optimal offset location based on each multi-objective function:

- For a trade-off between maximizing $\widehat{K}_{br}$ and minimizing the plastic deformations, $b \cong \frac{L}{3}$; see Figure 3.11(c).
- For a trade-off between minimizing P_r and δ_r or ε_r, $b \cong \frac{L}{4}$; see Figure 3.11(d).
- For minimizing P_s at the limit load, $b \cong \frac{L}{3}$; see Figure 3.10(b).

The ideal offset range for the one-story strongback is between $\frac{L}{4} \leq b \leq \frac{L}{3}$ depending on the selected parameter criteria and associated optimization goals. Note that other optimization methods or normalization strategies may give different results, and the intention of this relatively simple optimization study was to find a range of ideal offset locations, not to find a global minimum for all possible design alternatives.

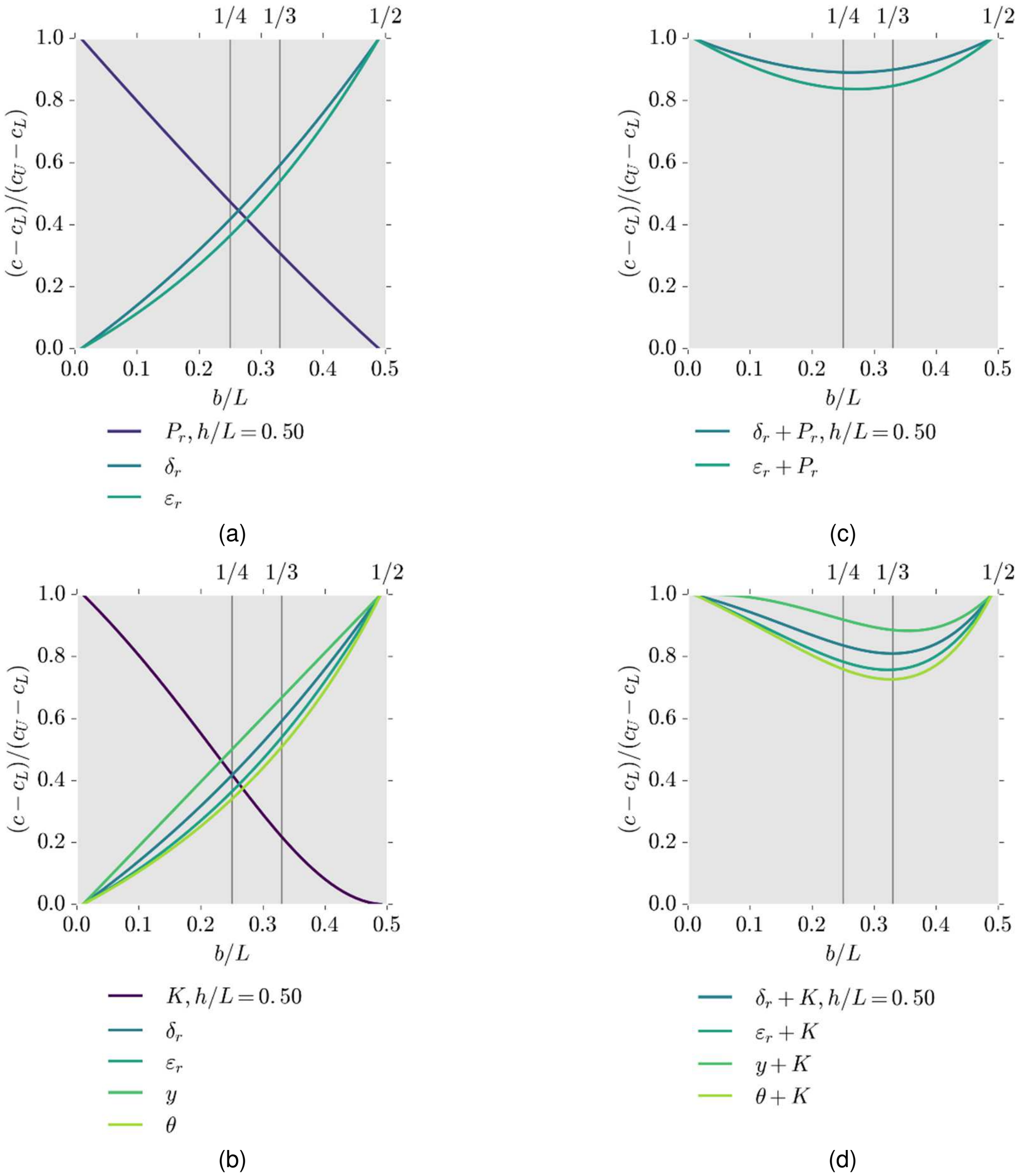

(a) (c)

(b) (d)

Figure 3.11. Results of multi-objective optimization.
(a-b) normalized parameters using feature normalization and (c-d) minimization function.

3.5.3 Code Limits

Modern seismic provisions recommend acceptable limits for deformation demands in the fuses. These deformation limits can also be utilized in choosing an offset location.

For example, the beam link in the strongback system can be regarded as a long link in an eccentrically braced frame. Based on this consideration, the maximum in-plane rotation of the beam link is limited to 0.02 radians by AISC-341-16 (2016); see Figure 2.2. Equation 3.11 for the in-plane beam rotation can be estimated in terms of this limit as:

$$\theta_b = \frac{L}{l}\theta \leq 0.02 \qquad \text{Equation 3.19}$$

Equation 3.19 can be written in terms of the offset b/L by solving for $l = L - b$:

$$\frac{b}{L} \leq 1 - \frac{\theta}{0.02} \qquad \text{Equation 3.20}$$

The offset location, b, can then be selected based on the design story drift ratio, θ.

The maximum axial strain of the inelastic brace can be limited in a similar fashion. ASCE-41-17 (2017) limits design-level axial strains in an existing BRB frame to 2.5%. Equation 3.12 for the axial deformation can be estimated in terms of the axial strain, ε_r, and this limit:

$$\varepsilon_r = \frac{\delta_r}{r_y} = \frac{L}{rr_y}x \leq 0.025 \qquad \text{Equation 3.21}$$

Assuming the yield length of the brace is some proportion of the workpoint brace length ($r_y = \alpha r$), the minimum brace length, r, can be written in terms of the design drift ratio, θ, as:

$$r^2 \geq \frac{L}{\alpha}\frac{\theta h}{0.025} \qquad \text{Equation 3.22}$$

The amount of offset can be estimated based on the appropriate brace length, $r = \sqrt{b^2 + h^2}$:

$$b^2 \geq \frac{L}{\alpha}\frac{\theta h}{0.025} - h^2 \qquad \text{Equation 3.23}$$

The amount of offset can then be selected in terms of the overall frame geometry, yield length ratio, α, and the design story drift ratio, θ.

An appropriate offset can additionally be selected based on minimum stiffness or drift requirements. This process has been omitted but follows standard structural analysis and design procedures. Between the selection of an offset based on stiffness requirements and the use of Equation 3.20 and Equation 3.23, an appropriate range of offset can be selected based on code limits for ductility demands and stiffness.

3.6 NONLINEAR DYNAMIC ANALYSIS

An archetype one-story strongback frame was subjected to nonlinear dynamic analysis to confirm the analytical results in this chapter. The ground motion suite consisted of forty-four far-field ground motions scaled to the design response spectrum at the approximate fundamental period of the building (FEMA-P695, 2009); see Section 5.3.2 for information on the ground motion suite. The design of this archetype strongback was based on the equations of equilibrium in Equation 3.9 and Equation 3.16. The intent of this section is to verify trends from the static elastic and plastic analyses. As such, the simple strongback design is used for illustrative purposes only and should not be applied to multi-story strongback frames with significant higher-mode contributions.

The columns were fixed at the base and oriented in strong-axis bending. The beams were modelled as non-composite, and all beam-column connections were modelled as fixed. Elastic material models were used for the strongback braces. The inelastic brace was modelled with a single co-rotational truss element with isotropic and kinematic hardening calibrated to the experimental test conducted by Simpson and Mahin (2018b). Distributed-plasticity elements were utilized for the beams and columns. Rigid elastic elements were representative of beam-column and brace connection regions. Applied mass was typical of a one-story office building with a mechanical penthouse on the roof. Tributary gravity loading was included on the main lateral frame, and leaning columns on either side of the frame simulated $P\Delta$ effects. Mass- and stiffness-proportional Rayleigh damping was specified as 3% at the fundamental period, T_1, and $1.5T_1$. Other numerical modelling parameters are similar to those described in Section 4.5.

To isolate the contribution of elastic stiffness to the archetype's period and dynamic deformation response, two suites of analysis were conducted: [1] holding the elastic lateral brace stiffness, $\widehat{K}_{br}$, constant while changing the inelastic brace size with offset and [2] holding the inelastic brace size constant and letting the elastic lateral brace stiffness, $\widehat{K}_{br}$, change with offset. The two analysis suites are presented side-by-side in Figure 3.12 and Figure 3.13. Beam, column, and strongback sizes are constant for both analysis suites; see Table 3.2.

Plotted response quantities were normalized by the response derived from the centered scheme. Offsets varied from $\frac{b}{L} = \frac{1}{10}$ to $\frac{1}{2}$. The story drift ratio, θ, and vertical displacement response, y, are plotted in Figure 3.12 against the elastic spectral displacement, $S_{d,el}$ at T. For both analysis suites, y tends to decrease with increasing b. The drift response was more variable. With constant lateral stiffness, drifts tend to decrease with increasing offset. For variable lateral stiffness and constant inelastic brace size, the trend is less clear but drifts tend to increase with increasing offset and decreasing lateral stiffness.

The inelastic brace axial strains and the beam link rotation are plotted against elastic spectral displacement at T in Figure 3.13. With constant lateral stiffness, the deformations tend to decrease with increasing offset and follow similar trends to those observed for the static analyses. For variable lateral stiffness and constant inelastic brace size, the inelastic deformations still tend to decrease with increasing offset, but were also influenced by the growing global displacements associated with the smaller lateral stiffness and longer period at larger offsets.

The peak axial-force demand in the strongback brace is plotted against the elastic spectral pseudo-acceleration, $S_{a,el}$, in Figure 3.14. Though these demands were similar, under constant lateral stiffness, the strongback brace demands tend to be minimized for an offset of $\frac{b}{L} = \frac{1}{3}$. For variable lateral stiffness and constant inelastic brace size, demands tend to become smaller with increasing offset. Note, however, that the axial force in the strongback seems less affected by the amount of offset than other response parameters. This may indicate that strongback demands may not be a primary parameter for the selection of the offset location.

In summary, provided the elastic lateral stiffness (and period) remains unchanged with increasing offset, trends from the nonlinear dynamic analyses are generally similar to trends observed from the static analyses. If the lateral stiffness is allowed to vary with offset, the global displacements increase and the trends from static analysis may no longer hold.

Table 3.2. Design of one-story strongback.

Offset	Element Sizes			
b/L	**Beam**	**Column**	**Strongback Brace**	**BRB**
1/2	W14 × 68	W12 × 50	HSS10 × 10 × 5/8	2.500 in^2
1/3	W14 × 68	W12 × 50	HSS10 × 10 × 5/8	3.912 in^2
1/4	W14 × 68	W12 × 50	HSS10 × 10 × 5/8	4.885 in^2
1/5	W14 × 68	W12 × 50	HSS10 × 10 × 5/8	5.567 in^2
1/6	W14 × 68	W12 × 50	HSS10 × 10 × 5/8	6.067 in^2
1/8	W14 × 68	W12 × 50	HSS10 × 10 × 5/8	6.745 in^2
1/10	W14 × 68	W12 × 50	HSS10 × 10 × 5/8	7.182 in^2

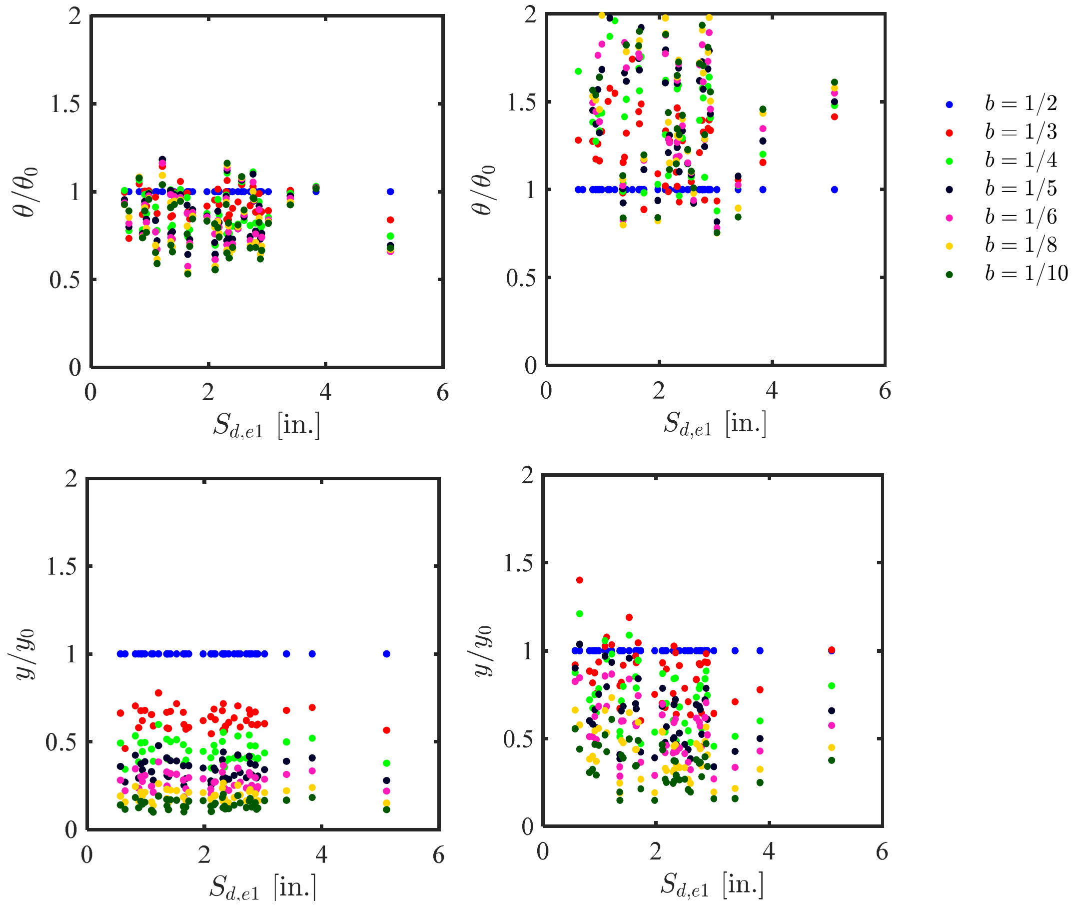

(a)

(b)

Figure 3.12. Global demands: (a) same $\widehat{K}$ with different inelastic brace sizes; (b) different $\widehat{K}$ with same inelastic brace size

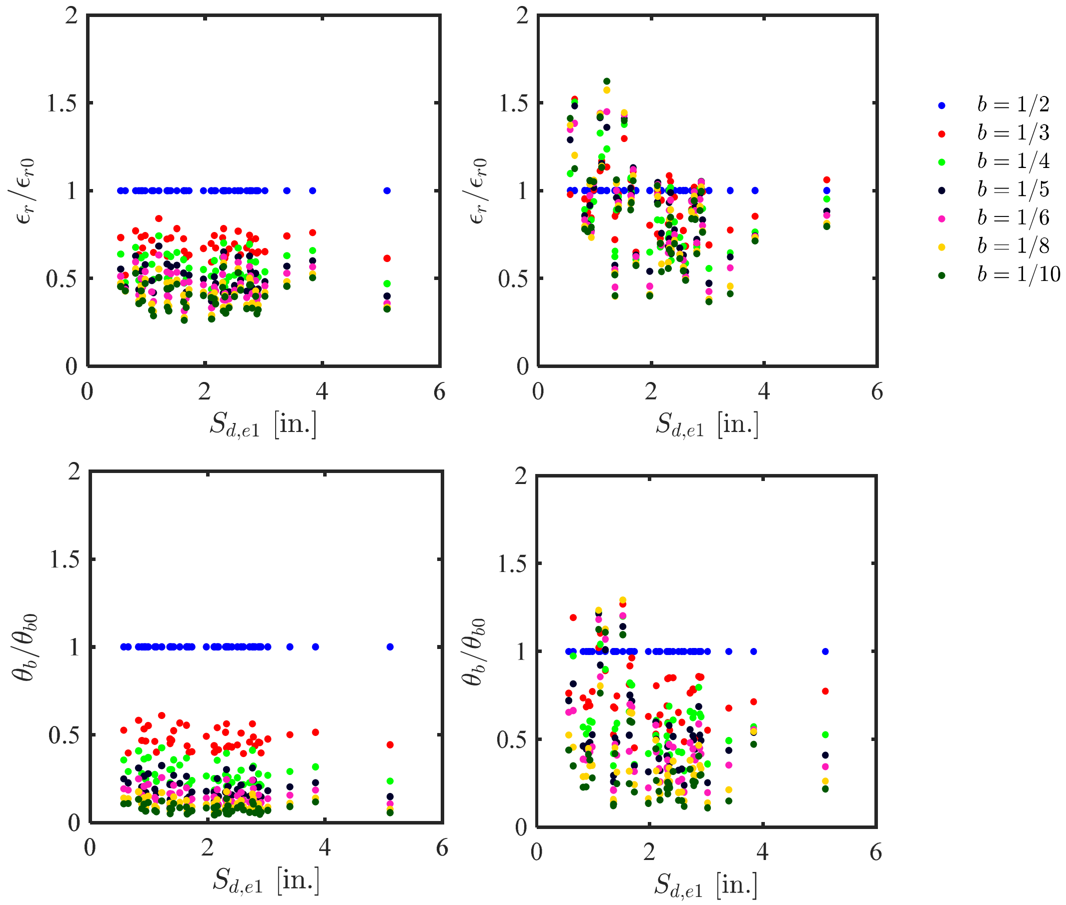

(a) (b)

Figure 3.13. Deformation demands: (a) same $\widehat{K}$ with different inelastic brace sizes; (b) different $\widehat{K}$ with same inelastic brace size

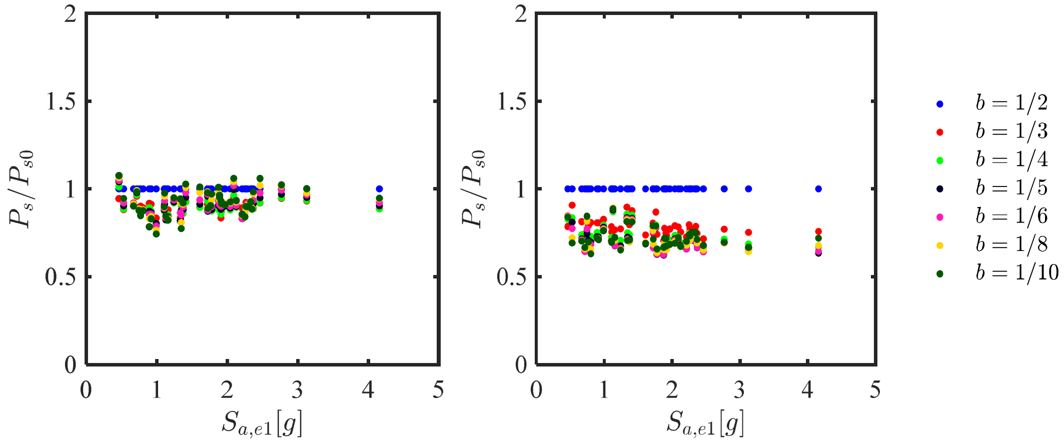

(a) (b)

Figure 3.14. Force demands: (a) same $\widehat{K}$ with different inelastic brace sizes; (b) different $\widehat{K}$ with same inelastic brace size

3.7 SUMMARY AND CONCLUSIONS

The amount of offset determines the elastic strength and stiffness of the frame under low-to-moderate shaking and the plastic deformations and imposed strongback demand under severe shaking. An analytical study of the simplest strongback system was conducted to investigate the influence of the geometric configuration, or offset, on strongback behavior. Parameters derived from an offset scheme were compared to parameters from a centered scheme. In summary –

1. Elastic lateral stiffness of the system tends to decrease with increasing offset.
2. Axial force in the inelastic brace tends to increase with increasing offset in the elastic range.
3. Plastic deformation demands tend to decrease with increasing offset.
4. Strongback demands depend on the capacity of the elements in the system and can increase or decrease relative to the centered scheme depending on the amount of offset.

The strongback "weak" beam mechanism is characterized by vertical displacement of the beam due to beam flexural yielding. This vertical deflection can significantly impact inelastic deformation demands. As such, its significance should be recognized in designs employing strongbacks embedded within the same bay as the fuses.

A multi-objective optimization scheme combined pairs of design criteria to find a range of optimal offset locations. This range fell between $\frac{L}{3} \leq b < \frac{L}{4}$. Selection of offset can also be derived based on deformation limits recommended by modern building codes. Provided the lateral stiffness of the strongback frame remained unchanged, these trends generally hold under nonlinear dynamic analysis. Inelastic deformation demands and lateral stiffness depended more on offset location than strongback brace axial force.

Extrapolations to more complex assemblages can be based on this study of a one-story SBF system. However, note that some observations may not apply to multi-story strongback systems. Demands in the strongback were derived from equilibrium of the one-story frame at the limit load, but it must be kept in mind that failure may also result from other causes, such as [i] stability, [ii] excessive deformations, or [iii] fatigue fracture. Higher-mode effects can also significantly exacerbate multi-story strongback demands; these higher-mode effects are described in more detail in Chapter 7.

4 Numerical Model Development

4.1 INTRODUCTION

Braced frame behavior primarily depends on the hysteretic response of the braces. However, the cyclic inelastic response of steel braces is notoriously difficult to represent and involves several physical phenomena, including yielding in tension, buckling compression, post-buckling strength deterioration, and low-cycle fatigue (Ikeda & Mahin, 1986). Global buckling, yielding, or fracture causes deteriorating element strength and/or stiffness and a corresponding decrease in story strength and/or stiffness, resulting in new and potentially unanticipated load paths. Such force re-distributions put greater demands on adjacent elements and connections and can result in other subsequent failure modes, especially near collapse. These failure modes and resulting force re-distributions can impact the strongback demands, peak displacements, and structural integrity of the braced frame under severe earthquake ground motions.

Accurate characterization of strongback behavior and evaluation of performance depends on adequately simulating these force re-distributions. Though many studies have recommended numerical modeling procedures for conventional braced frames, it is difficult to recognize which recommendations are suitable for investigation of strongback systems, especially since recent recommendations have primarily focused on the post-buckling response rather than the initial buckling capacity of conventional braces. While this behavior is important in simulating global displacements after the braces in the strongback buckle, it is not a critical mode of energy dissipation for the strongback system, which herein dissipates energy primarily through yielding in the buckling-restrained braces and secondarily through flexural yielding in the beam links.

In the case of strongback-braced frames, simulating [i] yielding and strain hardening in the buckling-restrained braces, [ii] potential brace buckling in the strongback braces, and [iii] potential failure in the fuses due to low-cycle fatigue is critical to the determination of the global system response and the demands in the strongback elements. As such, this chapter emphasizes the buckling-restrained brace hysteretic response and strongback brace buckling response, rather than the post-buckling response.

This chapter describes the development of a nonlinear modeling approach for strongback-braced frames. Specifically, this chapter is divided into four parts: (4.2) typical modeling methods, (4.3) nonlinear modeling of the strongback braces, (4.4) nonlinear modeling of the buckling-restrained braces, and (4.5) numerical modeling of the strongback system.

4.2 TYPICAL MODELING METHODS

To summarize, numerical modeling recommendations for steel members typically fall into three categories:

1. Phenomenological models,
2. Physical-theory models, and
3. Continuum finite-element models

Phenomenological models represent the simplest and most computationally-efficient method of modeling brace behavior. Braces are represented by a truss element with material behavior that mimics the hysteretic behavior of a bracing element (Zayas et al., 1980; Ikeda et al., 1984; Khatib, 1988). Flexurally-dominant beams are represented by a linear elastic beam-column element with inelastic springs concentrated at the element ends (Ibarra, 2005; Lignos & Krawinkler, 2011). These types of beam models are typically used for collapse assessment and are included in the modeling recommendations for beam and column elements in ASCE-41-17 (2017), the ATC-114 project (2017), and the Tall Building Initiative project (PEER, 2017). However, phenomenological models need extensive calibration to existing experimental data and can require a large number of parameters to mimic stiffness and strength hardening and softening response. Though it can be considered, these types of formulations typically lack axial-flexural interaction. Simplifications introduced during the calibration process can result in errors in stiffness, energy dissipation, and peak responses (Uriz & Mahin, 2008).

Three-dimensional continuum models represent the most sophisticated of the numerical models. Such models can simulate the local response of the material under large deformation theory and are capable of modeling localized behavior like local yielding, local buckling, and potentially fatigue (Fell et al., 2009; Huang & Mahin, 2010; Lai & Mahin, 2013). While such models are attractive, they can be computationally expensive and are not normally used to model large structures or for running a large number of analyses (e.g., for the collapse simulation involving a large number of archetype structures) in structural engineering applications.

As the name implies, physical-theory models (i.e., beam-column models) simulate some of the physical phenomena occurring in the elements, overcoming certain limitations of phenomenological models while remaining relatively simple and computationally efficient compared to three-dimensional finite-element models (Ikeda & Mahin, 1986). Physical-theory models include distributed plasticity models able to model the section response at several points along the element length or along a specified plastic hinge length. Fiber discretization of the cross-section at specified integration points along the element length can simulate the combined effect of axial and flexural demands by integration of the material model over the cross section. Though physical-theory models have a number of advantages – including less dependency on empirical parameters - physical-theory models often derive strains based on the assumption that plane-sections remain plane. As such, physical-theory models can fail to account for a number of factors – including changes in shape of the cross-section during loading, triaxial stress states, etc. – and may require empirical parameters to improve fidelity

4.3 NONLINEAR MODELING OF STRONGBACK BRACES

Numerical models incorporating brace buckling and low-cycle fatigue have been calibrated to a number of existing experiments on brace component and sub-assemblage braced frame tests [e.g., Uriz and Mahin (2008), Hsiao et al. (2012), Salawdeh and Goggins (2013), Karamanci and Lignos (2014), Tirca and Chen (2014), Sizemore et al. (2017), Simpson and Mahin (2017), etc.]. As such, a considerable amount of literature exists on the numerical simulations of braces in concentrically braced frames and detailed literature reviews on their simulation can be found elsewhere [e.g., Uriz and Mahin (2008)].

Though many of these simulations follow similar modeling techniques, modeling criteria – like number of integration points, number of elements, and number of fibers – can be variable, especially since brace hysteretic response depends on a broad range of geometric, material, and numerical parameters; see Table 4.1. The bulk of this modeling criteria has been placed on post-buckling response rather than on buckling initiation. However, representation of buckling initiation is a more critical behavior mode in strongback systems. Moreover, past parametric studies have focused on modeling tubular steel braces, but wide-flange (WF) sections are more likely to be used for the strongback elements. As such, a parametric study was undertaken to better understand the parameters influencing buckling in WF members, especially as related to simulating the critical brace buckling load. Some emphasis was also placed on the post-buckling response of the braces for collapse studies.

This section introduces modeling methods typical for brace buckling and low cycle fatigue. Emphasis has been placed on simulating the buckling response of WF sections. Numerical models were implemented in OpenSees (McKenna, 1997). A parametric study of simulation variables, like number of fibers, integration points, elements, etc., is also presented. Finally, calibration of brace buckling is optimized with respect to the nominal buckling capacity as calculated from the elastic and inelastic buckling equations in AISC-360-16 (2016).

4.3.1 Modeling Buckling

The modeling approach utilized herein was based on the fiber-based approach developed by Uriz and Mahin (2008); see Figure 4.1. In this approach, each brace is sub-divided into nonlinear sub-elements based on the force-formulation by Spacone et al. (1996). Equilibrium in the absence of second-order effects is satisfied directly under the force-formulation and errors in the response only depend on the accuracy of the numerical integration. Alternatively, a displacement-based formulation could be utilized provided a large enough number of sub-elements was used to approximate the section deformations along the brace length.

Fibers are used to discretize the cross-section at designated integration points along each element. The mechanical properties of each fiber are defined by a uniaxial stress-strain material model; herein the Menegotto-Pinto material model (Filippou et al., 1983). Interaction of axial-force and bending moment are calculated by integration of the steel material model over the cross-section of the brace. This section response is then monitored at the integration points located along the element length. To initiate out-of-plane buckling, an initial out-of-plane perturbation, Δ, is specified at the midpoint of the brace. If more than two sub-elements are utilized, nodes adjacent to this mid-point perturbation can be located in a parabolic (Uriz & Mahin, 2008), sinusoidal

(Karamanci & Lignos, 2014), or linear (Lai & Mahin, 2013) scheme. The brace simulation accounts for the large displacements associated with brace buckling through a co-rotational transformation (de Souza, 2000). As summarized in Table 4.1, a number of studies have investigated the sensitivity of cyclic response to the initial camber, number of elements, number of integration points per element, and number of fibers at each section.

4.3.2 Modeling Low-Cycle Fatigue

Low-cycle fatigue in the braces can be empirically represented by tracking the strain history in each fiber. Herein, the low-cycle fatigue wrapper developed by Uriz and Mahin (2008) was used to simulate rupture of the critical sections. Other fatigue models are also available [e.g., Lee and Goel (1987), Shaback and Brown (2001), Tremblay et al. (2003), Kanvinde and Deierlein (2007), Yoo et al. (2008), Huang and Mahin (2010), Hsiao et al. (2013), etc.].

The fatigue material model "wraps" around any OpenSEES uniaxial material that monitors strain. The algorithm uses a modified rainflow counting scheme to determine the recent strain history in each fiber. The material fatigue wrapper assumes a linear log-log relationship between fatigue life, N_f, and the equivalent strain amplitude experienced by a fiber, ε_i, as shown in the following Coffin-Manson relationship (Manson, 1965):

$$\varepsilon_i = \varepsilon_0 \left(N_f\right)^m \qquad \text{Equation 4.1}$$

$i =$ the cycle increment; $m =$ relationship between fatigue life and equivalent strain amplitude, ε_i (i.e., slope of the log-log relation); and $\varepsilon_0 =$ the strain at which fracture of the undamaged material occurs in one cycle. The parameters m and ε_0 are values calibrated to experimental data. The damage in a fiber during each cycle, D_i, is expressed by the ratio of the number of cycles at a strain amplitude, $n_i(\varepsilon_i)$, to the number of cycles to failure at that amplitude, $N_{f,i}$:

$$D_i = \frac{n_i}{N_{f,i}} = \frac{1}{10^{\frac{1}{m}\log\left(\frac{\varepsilon_i}{\varepsilon_0}\right)}} \qquad \text{Equation 4.2}$$

Damage is accumulated through Miner's rule (Miner, 1945):

$$D = \sum_i D_\mathrm{i} \qquad \text{Equation 4.3}$$

If the accumulated damage, D, in a fiber is greater than one, that fiber's fatigue life has been exceeded, the engineering stress of the wrapped material is reduced to near zero, and the fiber exhibits a computationally negligible strength and stiffness. Full rupture is determined when all fibers at a section (i.e., integration point) have reached damage measures greater than one.

Values for ε_0 and m from different calibration studies for WF braces are shown in Table 4.1. The calibrated values, ε_0 and m, are conditioned on both the experimental data and the OpenSEES model. As empirical parameters, m and ε_0 relate the geometry of the brace to the numerical parameters used in the simulation. Re-calibration is necessary for braces with different geometries or numerical parameters. In the past, m and ε_0 have been calibrated to braces sub-divided to twenty sub-elements (Uriz & Mahin, 2008). While two to four sub-elements may be enough to simulate brace buckling, ten to twenty elements have been recommended to represent the inelastic strains needed for the low-cycle fatigue model; see Equation 4.1.

Table 4.1. Modelling Recommendations for WF braces.

Year	Study	Δ	ne	NIP	nbf	ntw	b	m	ε_0
2014	Karamanci and Lignos	$L/1000$	2	5	6	2	0.001	-0.3	[a]
2013	Salawdeh and Goggins	$L/100$ to $L/1000$	2	10	$\frac{2(h+b)}{3}$	3	0.008	[b]	
2013	Lai and Mahin	$L/1000$	4	5	4	4	0.003	-0.458	0.22
2012	Hsiao et al.	$L/500$	10	4	10	2	0.01	[c]	
2008	Uriz and Mahin	$L/2000$ to $L/1000$	20 for fatigue 2 for symmetric buckling 4 for asymmetric buckling	3	5	5	0.003	-0.458 [d]	0.191 [d]

Δ = initial camber, ne = number of sub-elements, NIP = number of integration points, nbf = number of fibers across the flange depth, ntw = number of fibers across the web thickness, b = strain hardening ratio, m and ε_0 = fatigue parameters, h = section depth, b = section width.

[a] $\varepsilon_0 = 0.0391\left(\frac{kl}{r}\right)^{-0.234}\left(\frac{b_f}{2t_f}\right)^{-0.169}\left(\frac{h}{t_w}\right)^{-0.065}\left(\frac{E}{F_y}\right)^{0.351}$ for $27 \leq \frac{kl}{r} \leq 85, 4.2 \leq \frac{b_f}{2t_f} \leq 30.4, 223\text{ MPa} \leq F_y \leq 532\text{ Mpa}$

[b] calibrated for HSS braces only.

[c] used alternative fatigue model [see Hsiao et al. (2013)]

[d] calibrated to flextural tests only (Ballio & Castiglioni, 1995)

4.3.3 Numerical Parameters for Buckling Braces

The results of a parametric study of a pin-ended brace model are presented in this section to demonstrate the sensitivity of the model parameters to the simulated brace buckling response. For comparison purposes, a WF brace from a previous sub-assemblage experiment (Lai & Mahin, 2013) was used as a benchmark for the parametric study. Based on the number of fibers, number of sub-elements, and number of integration points selected from this parametric study, empirical values for the fatigue parameters, m and ε_0, and brace camber, Δ, were calibrated to that of other numerical models and the buckling equations from AISC-360-16 (2016).

4.3.3.1 Model Description

The benchmark numerical model used throughout the parametric study is shown in Figure 4.1. In particular, focus was placed on comparing the simulated buckling load, P to the nominal tensile yielding and buckling load, P^*, and the strain history, $\varepsilon(t)$.

Numerical modeling was conducted in two-dimensions with three-degrees of freedom (DOFs) per node. Fiber sections representing the WF section were oriented in weak-axis bending to simulate likely buckling about the weak axis direction of the brace. Several wide-flange sections were compared to observe the effect of different cross-sections on the model response. A $\mathrm{W8} \times 28$ section modeled from a previous experimental test (Lai & Mahin, 2013) was compared to heavier and deeper WF sections, $\mathrm{W12} \times 152$ and $\mathrm{W14} \times 257$.

The effective brace buckling length, L, was estimated as 0.9 times the workpoint-to-workpoint length of a typical brace. The bracing element in the benchmark simulation was modeled with two force-based nonlinear beam-column elements with an out-of-plane camber of $L/500$ and co-rotational transformation to initiate out-of-plane buckling. Where a greater number of sub-elements was utilized, notes were placed in a parabolic shape about the initial camber. Five integration points per the Gauss-Labotto quadrature rule were initially assigned to each sub-element. The material model is based on the Menegotto-Pinto uniaxial material (Filippou et al., 1983) with nominal yield strength of 50 ksi, Young's modulus of 29,000 ksi, and isotropic strain hardening ratio of 0.1%.

Gusset-to-brace connections were modeled as pins for simplicity, though a number of models exist for simulating the out-of-plane flexural strength and flexibility of the gusset plates [e.g., Uriz and Mahin (2008), Hsiao et al. (2012)]. Open circles in Figure 4.1 represent the locations of these pins. Rigid elastic end elements were provided outside of the pin connections to represent the regions where gusset plates would intersect with the beams and columns. Thick black lines in Figure 4.1 represent the locations of these rigid regions. Rigid elements were assigned with 10 times the area, A, and the moment inertia about the weak-axis direction, I_y, of the interior bracing element.

The numerical model was subjected to static cyclic loading. Except where noted, a constant displacement amplitude history was applied at the end of the element end. These constant amplitude cycles were similar to the displacement protocol conducted by Uriz and Mahin (2008). Strains were monitored at the outermost tension and compression fibers of the cross section and can be identified in plots by their respective sign: positive for tension and negative for compression.

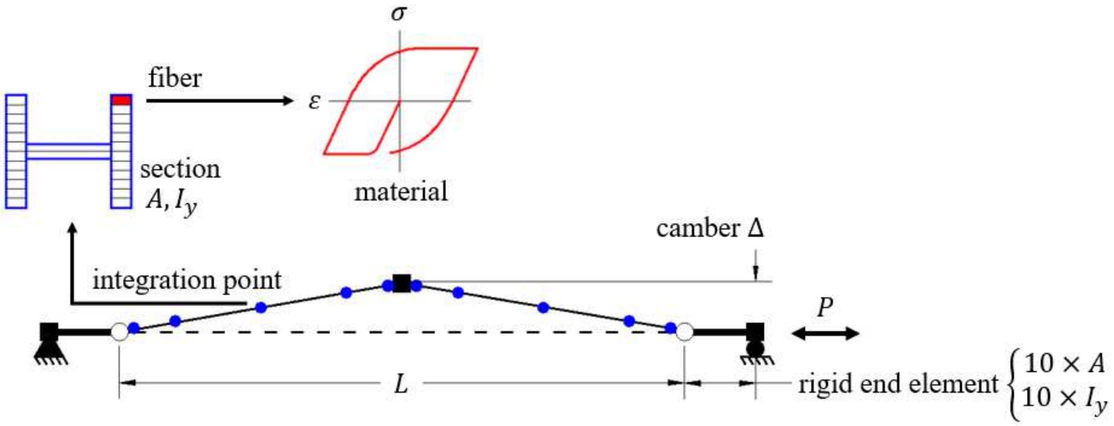

Figure 4.1. Model geometry and loading.

4.3.3.2 Number of Fibers

Fibers were oriented in one direction to reflect the two-dimensional nature of the simulation. Focus was placed on the fibers oriented along brace flanges as these were the regions of critical strain.

The number of fibers across the brace flange, nb_f, were varied from 4, 8, 12, 16, to 32 fibers. Two fibers across the web depth were kept constant. Other modeling parameters were fixed as described for the benchmark model in Section 4.3.3.1. The buckling load remained similar for each case, regardless of the cross-section and number of fibers, see Figure 4.2(a). The strain response was little changed from twelve to a greater number of fibers; see Figure 4.3. The wider the flange, the more fibers needed to simulate the response. This is consistent with the fiber discretization recommended by Kostic and Filippou (2012) of 24 to 40 fibers for WF sections oriented in weak-axis bending.

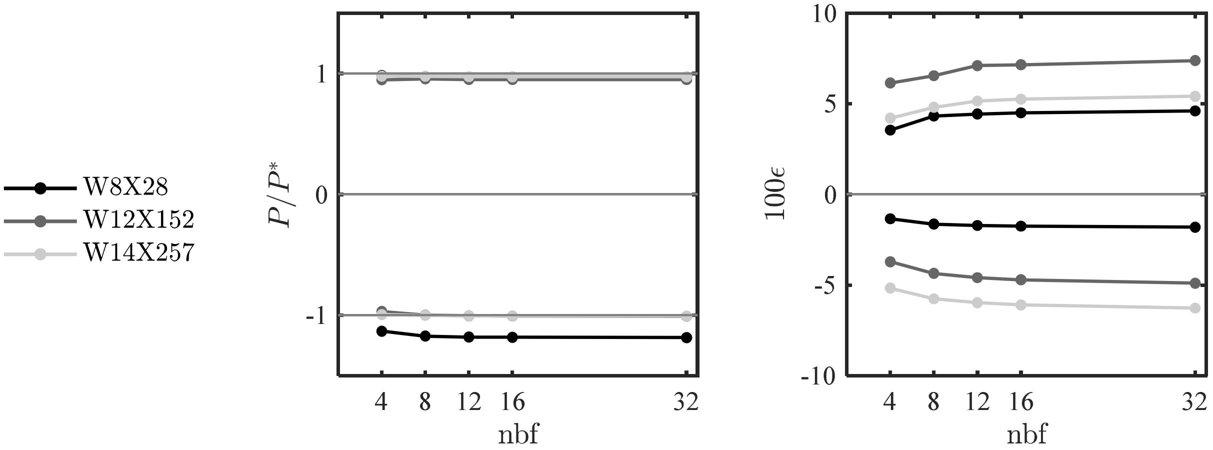

(a)

(b)

Figure 4.2. Number of fibers, nbf: (a) buckling load and (b) peak strains (with $NIP = 5$, $ne = 2$).

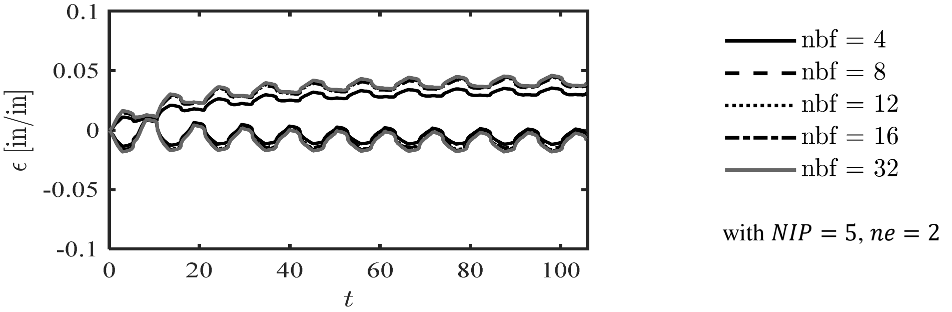

W8 × 28

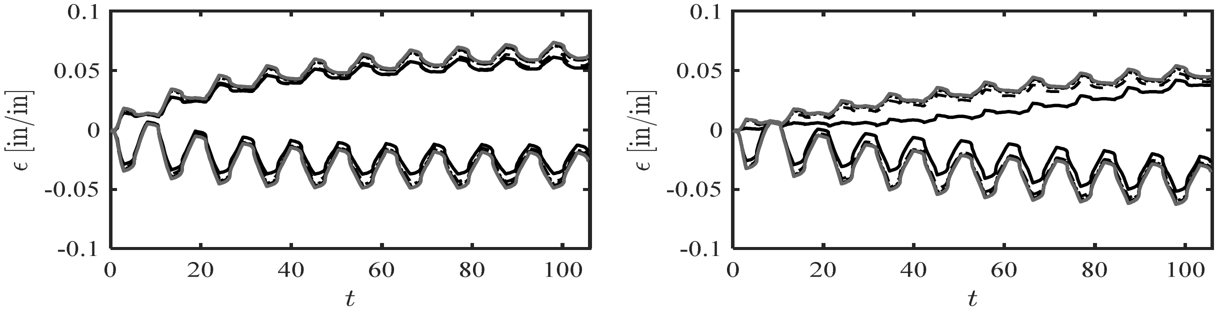

W12 × 152

W14 × 257

Figure 4.3. Number of fibers, nbf: strain pseudo-history.

4.3.3.3 Number of Elements and Integration Points

The number of sub-elements was varied from 2, 4, 10, and 20 and the integration points in each sub-element was varied from 2 to 10. The maximum number of integration points per element that can be used in OpenSees is 10. Based on the results from Section 4.3.3.2, the number of fibers across the flange was fixed to 12.

As shown in Figure 4.5(a), the brace element needs at least two sub-elements to simulate symmetric buckling. However, a finer sub-division is needed to achieve constant estimates for the strains used in the low cycle fatigue material model discussed in section 4.3.2; see Figure 4.5(b). As noted by Uriz and Mahin, an applied constant displacement history does not result in constant amplitude strains; see Figure 4.6 and Figure 4.7. This can be attributed to the co-rotational transformation used to model large deformations associated with the buckling response and localization of the inelastic response at a few integration points.

Deformations are calculated from the weighted sum of the curvatures at the integration points. The larger the number of integration points, the shorter the length associated with each integration point and the larger the curvature needed to maintain the same displacement response. To illustrate this numerical problem, the peak curvature response, κ, is plotted over half the brace length in Figure 4.8(a). As the number of integration points increases, the finite length associated with each integration point decreases, resulting in increased curvature and strains near the middle of the brace. Since strains due to buckling exhibit little strain hardening and spread of plasticity, strains extracted from a buckled brace become constrained to the end integration point and are dependent on the nearness of the end integration point to its neighbor integration point.

The use of force-based fiber elements minimizes the error in displacement-compatibility and force-equilibrium at the element level by iteratively satisfying material constitutive relations at the section-fiber level. However, as noted in the previous paragraph, the material constitutive relations non-objectively depend on the number of integration points used to obtain the deformations. In the case of a hardening material, plasticity will spread beyond the first integration point and this problem depends on providing enough integration points to model the smooth spreading of inelastic behavior (Neuenhofer & Filippou, 1997). In the case of buckling, strain hardening is small and plasticity does not spread far from the buckled location to neighboring integration points; see Figure 4.8(b). This behavior is similar to that described by Coleman and Spacone (2001) for a cantilever utilizing an elastic perfectly plastic material model; see Figure 4.9. These adjacent integration points remain elastic, confining inelastic curvature to the sub-element end where buckling was initiated. This results in large localized strains where a large number of integration points are utilized and the length associated with the end integration point is small. Any of these observations are further exacerbated by small values of material strain hardening.

Mesh refinement (i.e., use of a greater number of sub-elements) results in a converging estimate of the strains needed to model low cycle fatigue; see Figure 4.7. However, the use of 20 elements as recommended by Uriz and Mahin can result in unusual buckling modes, is computationally expensive, and belies the advantage of using force-based over displacement-based elements. Since the strain response is non-objective, the empirical damage parameters, m and ε_0, must be re-calibrated to new integration point locations (i.e., strains) when using a smaller number of sub-elements. This issue can be circumvented by the use of fiber hinge elements, like the beam with hinges element in OpenSees (Scott & Fenves, 2006), provided the plastic hinge length was chosen consistently between calibrations.

Other studies have recommended concentrations of short sub-elements near the expected plastic hinge region (Chen & Mahin, 2012; Simpson et al., 2017). This approach results in similar values of m and ε_0 so long as the integration points of the new numerical model are at the same location of the integration points used during the calibration process. A brace model with one or two concentrated sub-elements of length, $L/20$, near the plastic hinge region results in similar strains to a model utilizing 20 equally spaced sub-elements and is computationally cheaper. Alternatively, the strains observed in a brace model utilizing twenty sub-elements could be mimicked by two sub-elements with user-defined weights and manual placement of the integration points at similar locations to that of a brace model using twenty sub-elements. These approaches would allow for similar values for ε_0 and m to that calibrated for 20 sub-elements.

Herein, five integration points with two sub-elements were chosen for the final brace numerical model. Five integration points provide enough integration points for integration over the sub-element length while keeping strains relatively consistent with the applied displacements. The odd number of integration points explicitly provides an integration point at the midpoint of the sub-element and is capable of simulating symmetric curvature. Though outside the scope of this study, the fatigue model specified in Equation 4.1 could alternatively be defined in terms of element deformation rather than fiber strain to achieve an objective damage quantity.

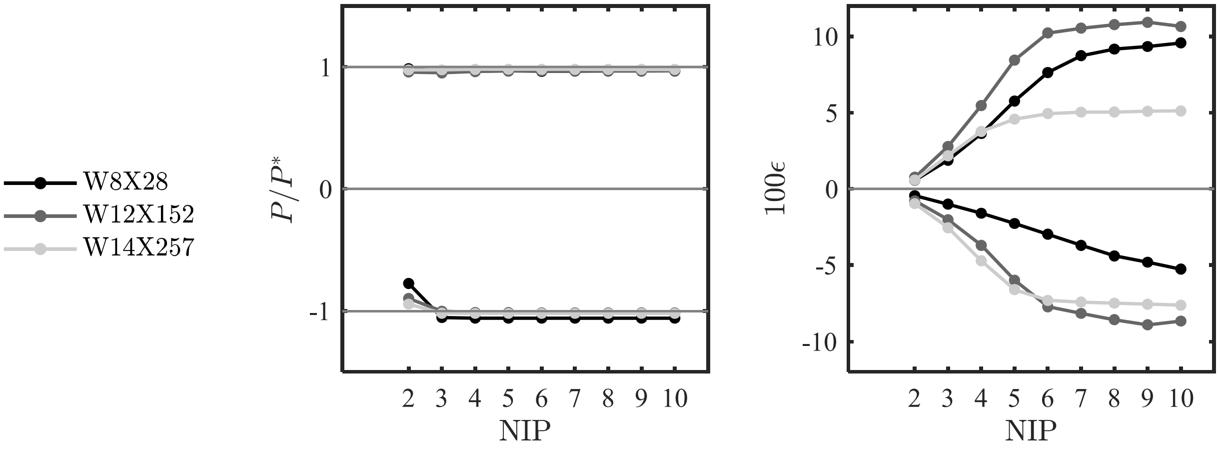

(a) (b)

Figure 4.4. Number of integration points, NIP: (a) buckling load and (b) peak strains (with with $nbf = 12$, $ne = 2$).

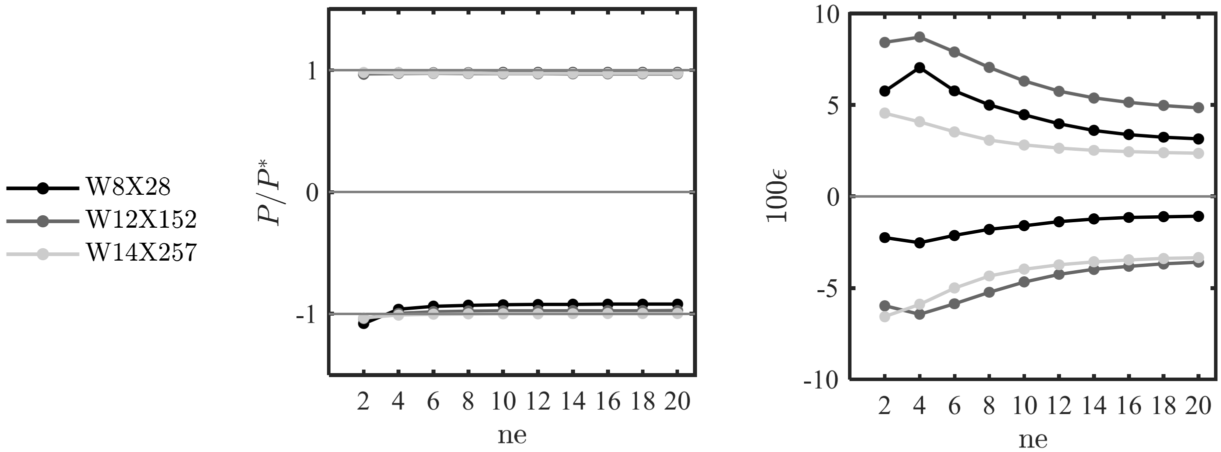

(a) (b)

Figure 4.5. Number of sub-elements, ne: (a) buckling load and (b) peak strains (with $nbf = 12$, $NIP = 5$).

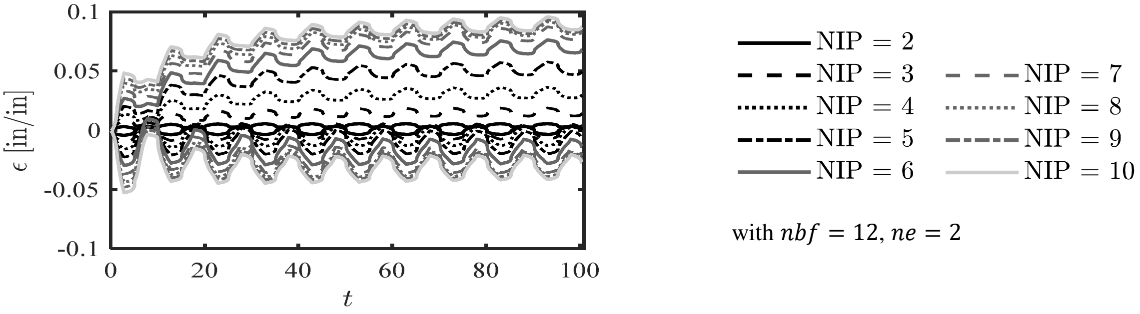

W8 × 28

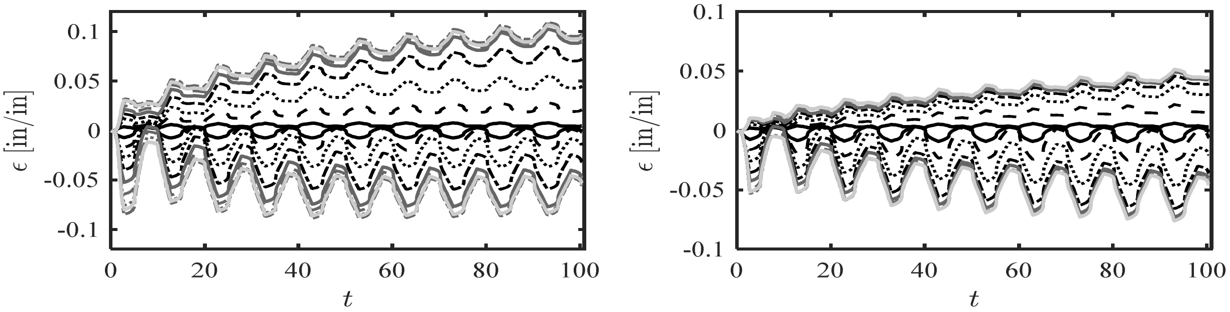

W12 × 152 W14 × 257

Figure 4.6. Number of integration points, NIP: strain pseudo-history.

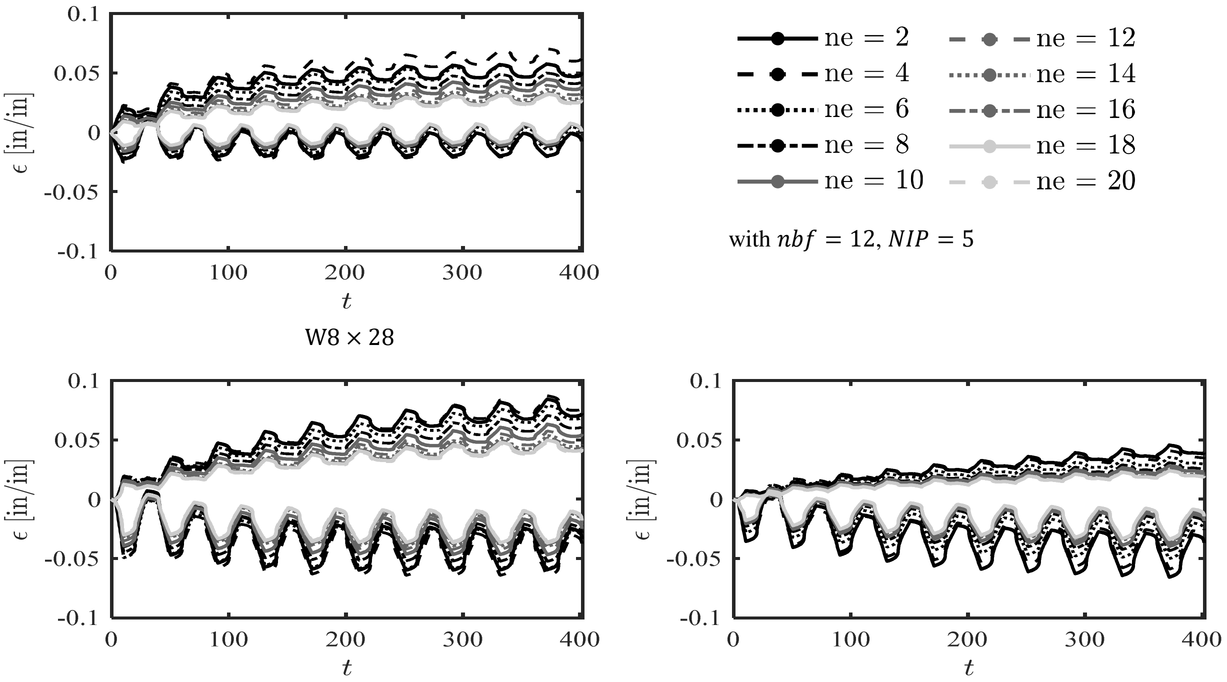

W8 × 28

W12 × 152

W14 × 257

Figure 4.7. Number of sub-elements, ne: strain pseudo-history.

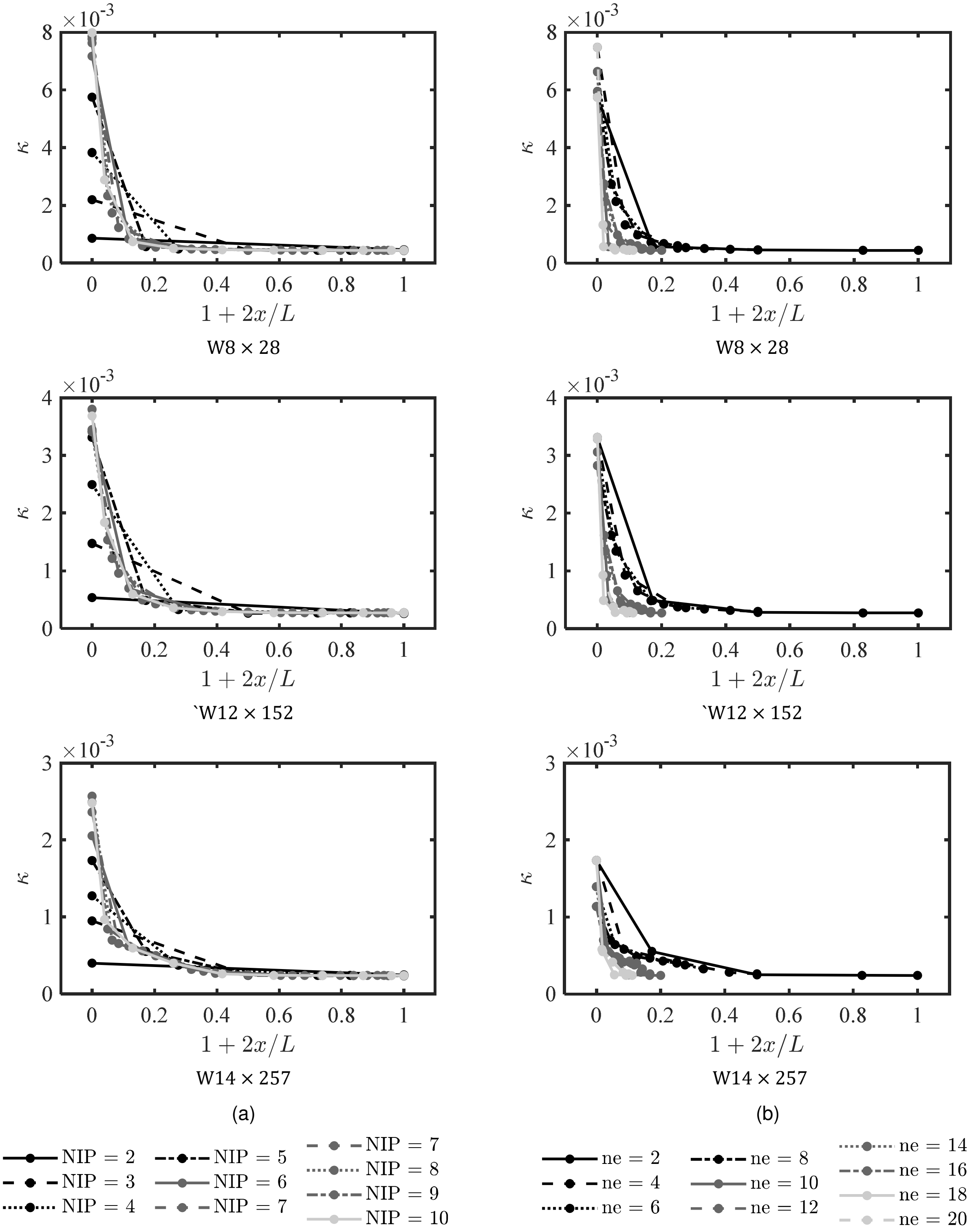

Figure 4.8. Variation of curvature with element length: (a) with NIP and with ne.

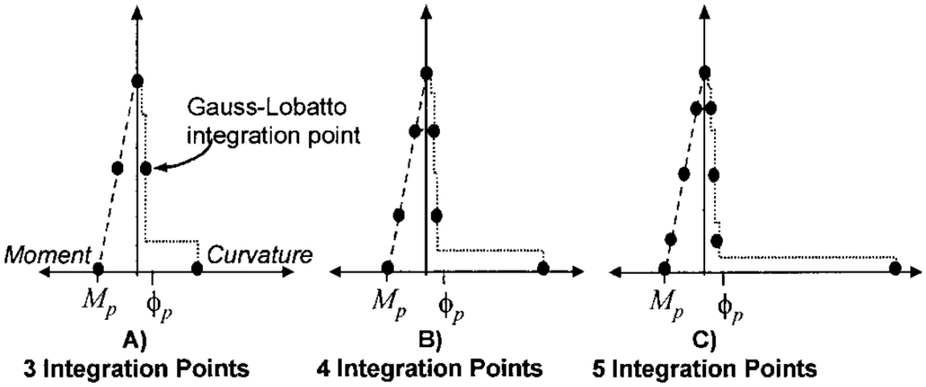

Figure 4.9. Moment and curvature profiles for an elastic perfectly plastic cantilever by Coleman and Spacone (2001).

4.3.4 Calibration of Perturbation

The previous section provided a detailed parametric study of brace numerical modeling parameters. In that parametric study, the brace out-of-plane perturbation used to initiate buckling was kept constant at $\Delta = L/500$. However, previous studies hypothesized that this perturbation could be varied with brace slenderness to better represent the initial buckling load of the member (Goggins & Salawdeh, 2013; Sizemore et al., 2017).

Initial perturbations used in the brace numerical models are substitutes for initial crookedness of the member, accidental eccentricity of load, and residual stresses that affect the buckling load. Column strength curves (i.e., average tress versus slenderness ratio curves) in column design formulas empirically account for these factors through corrections to the buckling load to account for variability in behavior exhibited by experimental tests. Since brace buckling was considered to be a critical behavior mode for the strongback braces, the out-of-plane perturbation, Δ, was fit to the nominal buckling loads provided in AISC-360-16 (2016), repeated below for convenience:

$$P^* = F_{cr} A_g$$

$$F_{cr} = \begin{cases} 0.658^{F_y/F_e} F_y & KL/r \le 4.71\sqrt{E/F_y} \\ 0.877 F_e & KL/r > 4.71\sqrt{E/F_y} \end{cases} \qquad \text{Equation 4.4}$$

$$F_e = \frac{\pi^2 E}{(KL/r_y)^2}$$

P^* = nominal buckling strength; F_{cr} = critical buckling stress; F_e = Euler elastic buckling stress; KL/r_y = effective slenderness ratio; F_y = nominal yield stress; E = Young's modulus. The piecewise nature of the column design formulas provides a transition between elastic buckling and yielding – represented by an exponential function and the Euler hyperbola – that reflect the effects of residual stresses. These equations were considered to be vetted estimates for the brace buckling capacity and representative of data from a large number of experimental tests [e.g., Hall (1981)].

An optimization study was conducted to find an empirical function for Δ to best match the nominal buckling load with the buckling strength extracted from the brace numerical models. The optimization study was performed on numerical models with 12 fibers across the depth of the flange, 2 fibers across the web width, two sub-elements, and five integration points per sub-element; brace lengths corresponding to a bay width of 30'-0"; story heights of 5', 15', 18', and 25'; and a strongback offset to 1/3 the bay width. To represent the full breadth of cross-sectional shapes considered typical for the strongback braces, all of the W8, W12, W10, and W14 sections found in AISC-360-16 (2016) were used for test data set.

The optimization scheme employed the Mesh Adaptive Algorithm (Abramson et al., 2009) available in MATLAB (Version 9.3.0.713579, 2017b). The optimization study minimized an objective function, e, representing the difference between the buckling load in the model, P^*_{model}, dependent on the perturbation, Δ, and the nominal buckling capacity, P^*, calculated per AISC-360-16:

$$e(\Delta) = P^*_{model}(\Delta) - P^* \qquad \text{Equation 4.5}$$

The model buckling load, $P^*_{model}(\Delta)$, was simulated by monotonically applying a compressive force at one end until buckling occurred about the weak-axis of the brace.

Optimized camber, Δ, is plotted against brace slenderness in Figure 4.10. Stockier braces with low KL/r_y required smaller initial perturbations while slender braces with larger KL/r_y required larger initial perturbations; see Figure 4.10(a). This trend agrees with observations made by Goggins and Salawdeh (2013) and Sizermore et al. (2017). For inelastic buckling (i.e., $KL/r_y \leq 4.71\sqrt{E/F_y}$), the data hovers about cambers of $L/500$ (0.2% of the brace length, L). As the slenderness increases beyond 200, the optimized camber approaches infinity.

A smooth piece-wise curve representing the needed perturbation for a given KL/r_y given elastic or inelastic buckling was fit to the data in Figure 4.10(b). To account for the transition between elastic and inelastic buckling, the data was fit to a third order and second order polynomial respectively:

$$\Delta = \begin{cases} -0.002(x - x_0)^3 - 0.2545(x - x_0)^2 - 7.8698(x - x_0) + 385.9262 & KL/r_y \leq x_0 \\ 0.0403(x - x_0)^2 - 7.8698(x - x_0) + 385.9262 & KL/r_y > x_0 \end{cases} \qquad \text{Equation 4.6}$$

$x_0 = 4.71\sqrt{E/F_y}$ is the point where the Euler hyperbola and exponential function become tangent to each other in Equation 4.4 for $F_y = 50ksi$. To enforce a smooth transition between the elastic and inelastic buckling curves at x_0, the parameter $\Delta(x_0)$ and the first derivative at x_0 were constrained to be equal during the curve fitting process. Because the data was fit to the piecewise line in Equation 4.4, the correlation coefficient is close to one. Use of actual test data would result in more scatter.

Equation 4.6 is valid only for $F_y = 50ksi$, and the WF sections used for the test data set. Other yield strengths, cross-sections, or simulation parameters would result in different scatter and fit of Δ. For example, the optimization and fitting study was conducted again for $F_y = 36ksi$, as shown in Figure 4.11 and below:

$$\Delta = \begin{cases} -0.0013(x - x_0)^3 - 0.2020(x - x_0)^2 - 7.1512(x - x_0) + 474.5841 & KL/r_y \leq x_0 \\ 0.0274(x - x_0)^2 - 7.1512(x - x_0) + 474.5841 & KL/r_y > x_0 \end{cases}$$

Because the parameters are fit to a piecewise line rather than scattered data, these equations could be generalized to depend on A_g, F_y, and KL/r_y (i.e., the independent variables in Equation 4.4). Though a generalized equation may be useful for future studies, an empirical equation for Δ was not pursued beyond that shown in Equation 4.6.

The piecewise curve in Equation 4.6 was fit to slenderness ratios, $KL/r_y \leq 200$, as the likelihood of using braces with higher slenderness ratios was considered small. Braces with higher slenderness ratios, noncompact sections, or different boundary conditions may not suitably fit within the described empirical equation. Other significant parameters influencing brace buckling, like reduction in capacity due to local buckling, were also not included.

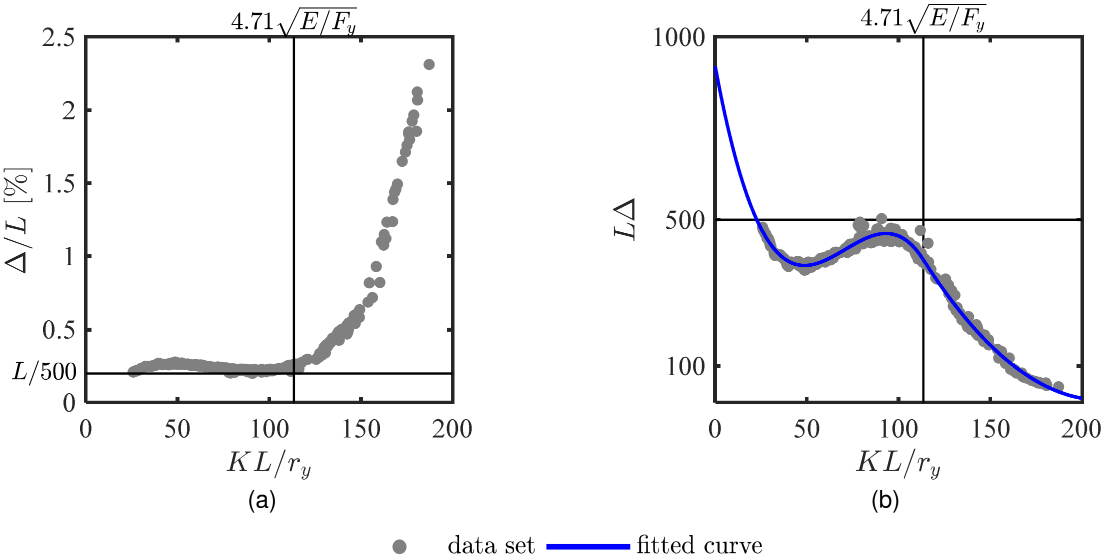

Figure 4.10. Calibrated perturbation with $f_y = 50ksi$: (a) optimized perturbation; (b) fitted perturbation

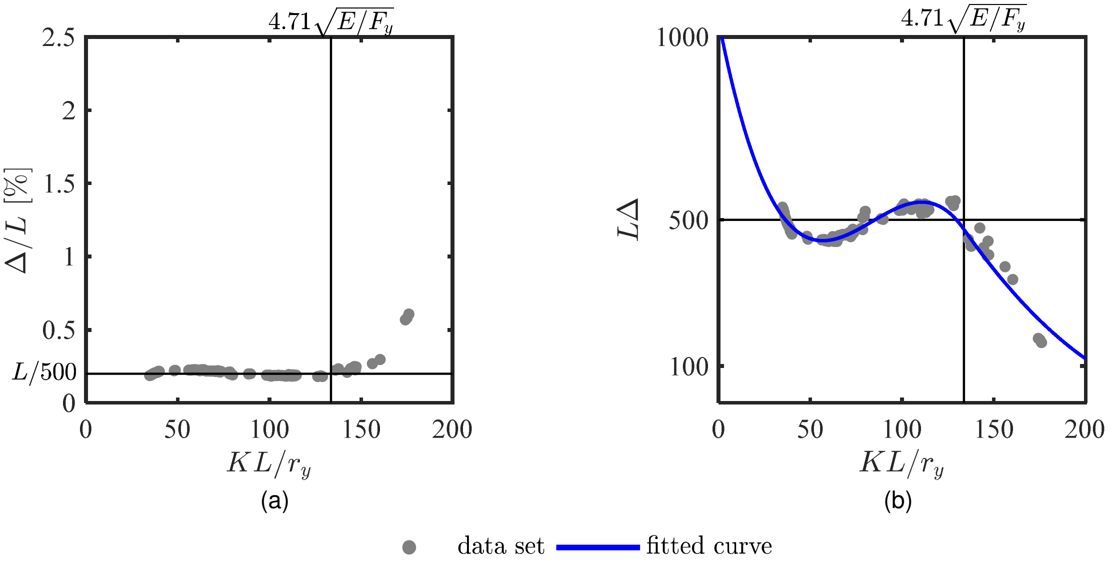

(a)

(b)

Figure 4.11. Calibrated perturbation with $f_y = 36ksi$: (a) optimized perturbation; (b) fitted perturbation

4.3.5 Validation of Buckling Model

The derived buckling model was validated against the experimental results of a W8X28 brace from a sub-assemblage experiment, TCBF-B-3, tested by Lai and Mahin (2008). The geometry was modeled to reflect the brace length including gusset regions of the first story west W8 × 28 steel brace. The applied displacement loading protocol for the simulation was extracted from wire pots located to either side of the brace to monitor brace elongation and shortening.

The buckling model proposed herein was similar to that described in Section 4.3.4. Brace perturbation was tuned to the buckling equations from Equation 4.4 using the mill-certificate yield strength of the experimental specimen ($\frac{\Delta}{L} = 436$; $F_y = 54ksi$). As discussed in Section 4.3.3.3, the strain response is non-objective, and the empirical damage parameters, m and ε_0, must be re-calibrated to the numerical parameters used in the new brace model. Calibration of the fatigue parameters to the initiation of brace fracture in the experiment resulted in $m = -0.458$ and $\varepsilon_0 = 0.22$.

Numerical modeling parameters and fatigue parameters from Uriz and Mahin (2008), Lai and Mahin (2013), and Karamanci and Lignos (2014) for WF sections were compared to interpret the impact of simulation parameters on the fatigue results; see brace sub-element layout in Figure 4.12. The study by Uriz and Mahin was additionally modified with concentrations of sub-elements with length of $L/20$ near the plastic hinge region to reflect the numerical modeling method outlined in Chen and Mahin (2012). Other modeling parameters used by these studies are shown in Table 4.1.

Global parameters were similar for all the numerical models considered, and brace axial force adequately matched results from the experimental test; see Figure 4.13(a) and (b). However, estimates for strain and damage, D, in the outermost tension fiber varied widely; see Figure 4.13(c) and (d). Fatigue life was smallest and largest for the studies by Karamanci and Lignos and Uriz and Mahin, respectively. These studies used different damage slopes of $m = -0.3$ and $m =$

-0.458. The fatigue parameters proposed by Karamanci and Lignos appear to be ill-suited to represent the experimental results for the WF section considered. As expected, the modified numerical model with concentrated elements from Chen and Mahin resulted similar damage states to that of Uriz and Mahin.

Fatigue parameters from Lai and Mahin resulted in the closest representation of the fracture initiation observed in the experiment; see proximity to the vertical red line in Figure 4.13(d). Note that the fatigue parameters from Uriz and Mahin were calibrated to the experiments conducted by Ballio and Castiglioni (1995) conducted under purely flexural loading conditions while the fatigue parameters from Lai and Mahin were calibrated directly to the sub-assemblage experiment and accounted for axial-flexural interaction due to buckling. The initiation of fatigue from the calibration study was similar to that of Lai and Mahin and closely matched the initiation of fracture observed in the experimental results.

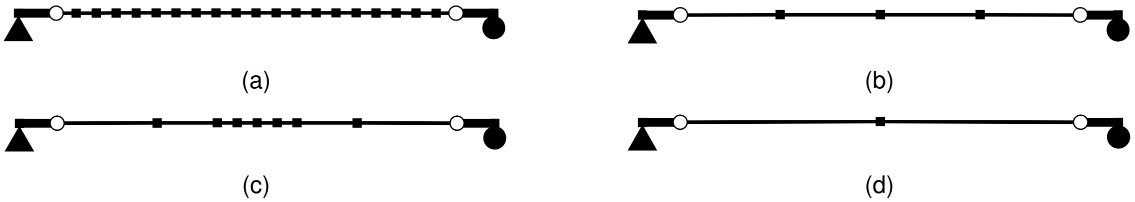

Figure 4.12. Schematic of fatigue models: (a) Uriz and Mahin (2008), (b) Lai and Mahin (2013), (c) concentrated sub-elements (Chen & Mahin, 2012), and (d) Karamanci and Lignos (2014) and the calibration study herein.

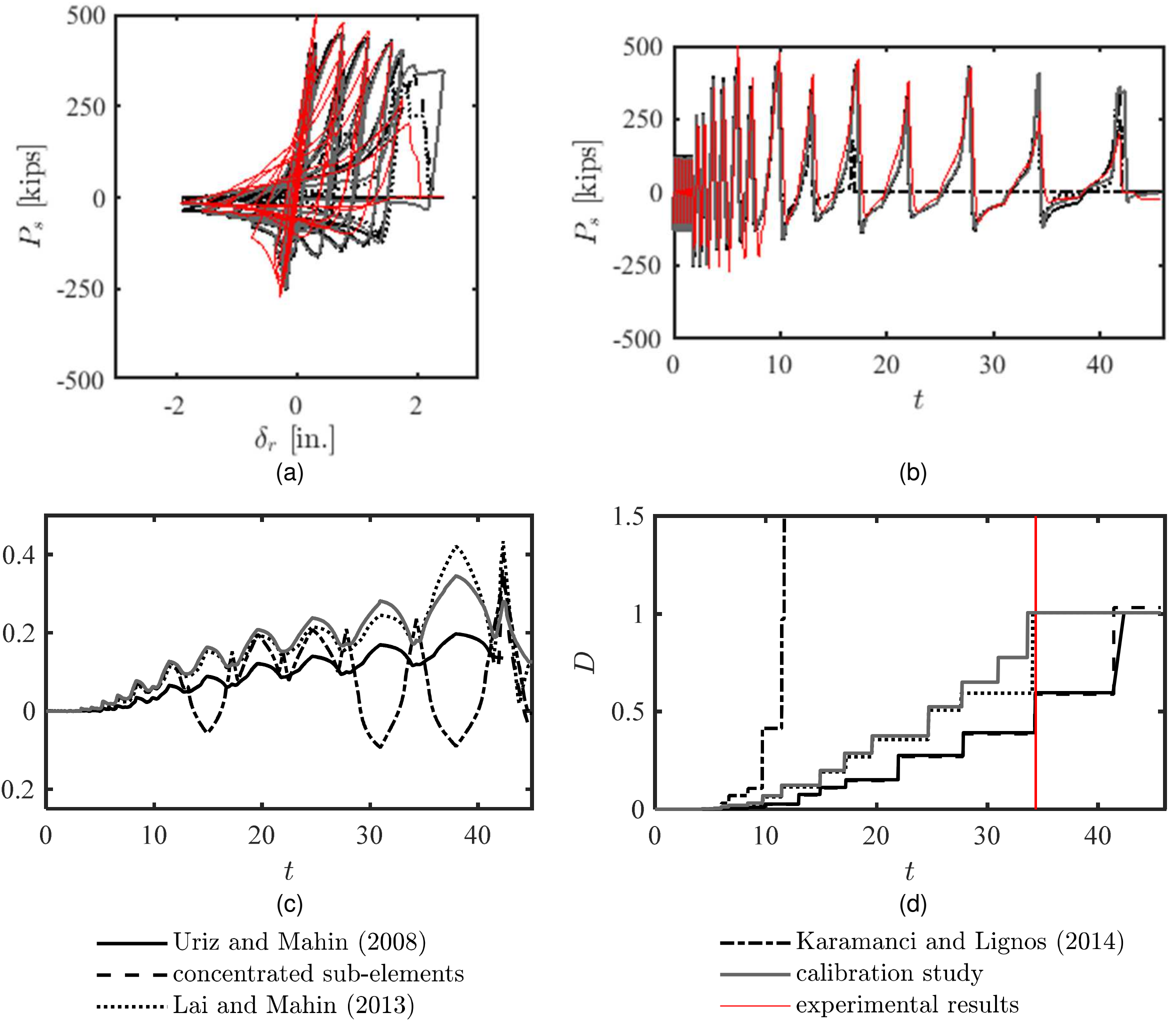

(a) (b)

(c) (d)

Figure 4.13. Calibration of fatigue parameters, m and ε_0 for $W8X28$: (a) hysteretic shape; (b) brace axial force pseudo-history; (c) strain pseudo-history; (d) damage pseudo-history

4.3.6 Summary of Buckling Brace Model

The parametric study conducted in this section focused on WF cross-sections and the use of two sub-elements to simulate brace buckling. Twelve fibers across the width of the flange, two fibers across the web thickness, and five integration points were found to acceptably simulate the brace buckling phenomenon. Calibration studies found that fatigue parameters, $m = -0.458$ and $\varepsilon_0 = 0.22$ and the initial perturbation, Δ in Equation 4.6, could be used to simulate brace buckling and fatigue response using the described numerical brace model. This buckling model was validated against results extracted from an experimental test of a braced frame sub-assemblage using WF braces.

The use of two, rather than 20, sub-elements has the advantage of computational efficiency. Upon rupture at the mid-length of the brace, numerical problems resulting from the abrupt loss of strength and stiffness in both sub-elements are easily controlled. The use of a greater number of sub-elements may require manual removal of the sub-elements of the brace (e.g., remove element command in OpenSEES) to ensure convergence. The use of fewer sub-elements also eliminates any undesirable or unusual buckling modes.

However, the use of two sub-elements ignores the possibility of buckling away from the mid-length of the brace. Strains in force-based beam-column elements non-objectively depend on the number of integration points used to integrate across the brace length. Elements with manual calibration of the location and weights of the integration points, use of an alternative integration scheme besides Gauss-Lobatto quadrature (Scott, 2011), or the use of other nonlinear beam-column elements [e.g., beamwithhinges element in OpenSEES (Scott & Fenves, 2006)] can alternatively be used to simulate brace buckling and post-buckling response.

The observations made in this study focused on highly ductile WF seismically compact sections. Local buckling response, especially for non-compact sections, is not modeled using fiber-based sub-elements and care should be taken in extending the findings of this study to brace properties other than those described herein.

4.4 BUCKLING-RESTRAINED BRACE CALIBRATION

Numerical modeling of buckling-restrained braces is relatively simple compared to modeling buckling behavior in conventional braces; see Section 4.3. Typically, buckling-restrained braces are represented by phenomenological models defined by truss element and a material model. Such models require empirical calibration of the material model to experimental test data to accurate simulation of the buckling-restrained brace response.

Accurately simulating strain hardening in the inelastic braces is critical to characterizing the demands in the strongback elements. Moreover, any capacity design principles used in the design of force-controlled actions must rely on accurate adjustment factors, β and ω, used to account for the expected strain hardening of the BRB in tension and friction that can develop between the core and the fill material of the BRB in compression; see Figure 4.14. In this sense, modeling of the buckling-restrained brace elements depends on two factors:

i. The BRB material model used in the simulation.
ii. The BRB adjustment factors, ω and β, used for capacity design.

The adjustment factors in [ii] should be consistent with the material model used in [i]. To achieve these conditions, the following calibration process was implemented in OpenSEES (McKenna, 1997):

1. Calibrate a generalized material model to available BRB experimental data.
2. Subject component BRB simulations with different core areas and yield lengths to the qualification test protocol from Section K3.2 of AISC-341-16 to determine ω and β factors consistent with the generalized material model in [1].
3. Utilize the ω and β factors from [2] for the capacity design of relevant force-controlled actions in the strongback system.

4. Characterize the behavior of the strongback system through nonlinear dynamic analyses using the design from [3] and the calibrated BRB material behavior from [1].

In following these steps, any simulations in later chapters used to characterize the strongback behavior and to develop design methods are based on adjustment factors, ω and β, that are consistent with a realistic BRB numerical model.

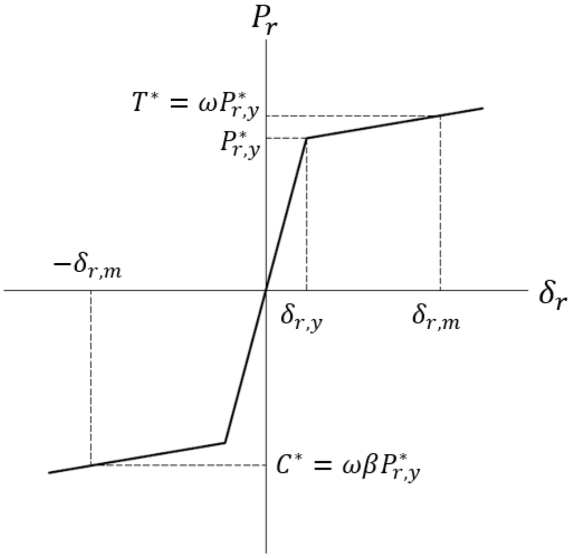

Figure 4.14. Bilinear BRB material behavior.

4.4.1 Material Model

In the past, buckling-restrained braces have been modeled with bilinear phenomenological models including expected strain hardening and adjustments for compression overstrength; see Figure 4.14. Some studies have also incorporated material models with more accurate estimates of energy dissipation by accounting for Bauschinger effects [e.g., Bouc-Wen material model (Bouc, 1971) used by Black et al. (2002)] and for kinematic and isotropic hardening [e.g., Menegotto-Pinto material model (Filippou et al., 1983) used by Uriz and Mahin (2008)].

Recently, the Menogotto-Pinto material model has been extended to include asymmetric kinematic and isotropic strain hardening that is more suitable for simulating the asymmetric response of yielding of the BRB core in tension and compression. This material model has been implemented as *steel4* in OpenSees (Zsarnoczay, 2013) and has the advantage of explicitly including distinct modeling parameters for asymmetric isotropic and kinematic hardening. For this reason, this was the material model utilized herein to simulate the buckling-restrained braces.

Though the *steel4* material model has a number of obvious advantages, it can be also be prone to marginal errors. Errors can occur in the stiffness of unloading from high strain levels in compression, continued hardened strength upon unloading to smaller amplitude cycles (i.e. no reduction in the yield surface), and inadequate simulation of the friction between the concrete casing and steel core upon large compression amplitudes. The optional ultimate stress asymptote of the *steel4* material was also not utilized herein as it tended to result in unrealistic compression behavior when the ultimate strength was reached in tension. These errors are well documented in Zsarnoczay (2013).

4.4.2 Stiffness Modification

The inelastic response in buckling-restrained braces is restricted to the portion of the BRB length contained within the restraining mechanism, termed the yield length, r_y. To estimate the brace area and stiffness outside of this yielding zone, an inelastic truss component was sandwiched between two rigid elastic elements representing the end connection regions; see Figure 4.15. As summarized in more detail below, an effective stiffness was then used to represent the larger areas associated with transition regions within the BRB core per Tsai et al. (2014).

The total inelastic brace length, r, was broken into three lengths of different stiffness: the joint connection region, r_j, the transition region, r_t, and the yielding region, r_y; see Figure 4.15. The stiffness of the truss was modified by a stiffness adjustment factor, Q, to obtain the effective stiffness of the truss, $\hat{k}$, including the transition regions. This adjustment factor was calculated from the series sum of the stiffness of transition region, $k_t = r_t/EA_t$, and yielding region, $k_y = r_y/EA_r$:

$$\hat{k} = \frac{1}{\frac{2}{k_t} + \frac{1}{k_y}} = \frac{1}{\frac{2r_t}{EA_t} + \frac{r_y}{EA_r}} = \frac{1}{\frac{2r_t/r_T}{A_t/A_r} + \frac{r_y}{r_T}} \frac{EA_r}{r} = \frac{(QE)A_r}{r} = \frac{\hat{E}A_r}{r} \qquad \text{Equation 4.7}$$

The stiffness adjustment factor can be extracted from this series model:

$$Q = \frac{1}{\frac{2r_t/r_T}{A_t/A_r} + \frac{r_y}{r_T}} \qquad \text{Equation 4.8}$$

Using this method, one element with effective material stiffness, $\hat{E} = QE$, and length, r, can be used to model the full stiffness of the BRB without explicit modeling of the transition regions. This stiffness adjustment factor excludes the end connection regions as they were explicitly modeled in the simulations; see Figure 4.15.

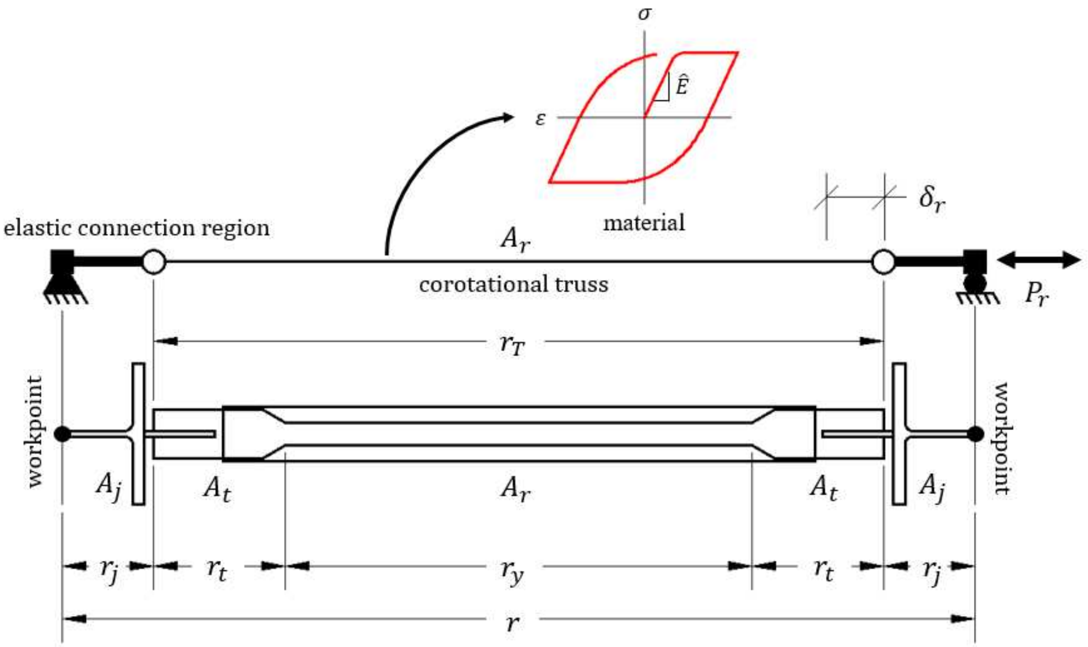

Figure 4.15. Schematic of BRB model.

4.4.3 Test Data

A considerable amount of test data is available for buckling-restrained braced frames from manufacturers, such as Nippon, StarSeismic, and CoreBrace. Test data is also available from limited research on BRBF sub-assemblies and components [e.g., Merritt et al. (2003a; 2003b; 2003c), Uriz and Mahin (2008), Fahnestock et al. (2007), Simpson and Mahin (2018b), etc.]. Herein, the OpenSees material, *steel4*, was calibrated to cyclic tests of eight pin-ended braces (Merritt et al., 2003b) and one sub-assemblage test utilizing a weld-ended buckling-restrained brace in a strongback-braced frame (Simpson & Mahin, 2018b); see Section 2.4.2.1.

4.4.4 Optimized Calibration

A minimization study was conducted to calibrate the material model described in Sections 4.4.1 and 4.4.2 to the experimental data summarized in Section 4.4.3. This was step [1] in the process outlined in the introduction of Section 4.4. The measured material yield strengths and geometric properties of each BRB experiment were used to define the geometry and known uniaxial material properties in the simulations; see Table 4.2. Rigid end zones representing the additional length of the BRB from the pin connection to the workpoints were not included in for the calibration of the CoreBrace component tests as the experimental data had been previously modified to exclude the end zone regions. End zones were considered for calibration to the BRB sub-assemblage test. Each simulated brace was subjected to the same displacement-controlled loading protocol of its corresponding experimental test.

To automate the calibration process, an optimization scheme was used to minimize the squared L_2-norm, $\|\cdot\|_2^2$, of the difference between the forces observed in the experiment, $\boldsymbol{f}$, and the forces extracted from the numerical simulation, $\hat{\boldsymbol{f}}$:

$$\|\hat{\boldsymbol{f}}_n - \boldsymbol{f}_n\|_2^2 = \left(\hat{\boldsymbol{f}}_n - \boldsymbol{f}_n\right)^T \left(\hat{\boldsymbol{f}}_n - \boldsymbol{f}_n\right) \qquad \text{Equation 4.9}$$

n = experimental test being calibrated. To avoid interpolation of the full test data at the points sampled by the numerical simulation, load-drift pairs were compared at select characteristic points in the loading protocol. These load-drift pairs, termed critical points, corresponded to points of zero displacement, three-quarters of the displacement amplitudes, zero load, and peak load amplitudes. Each cycle of the loading protocol was thus represented by 10 characteristic points. Additional fatigue loading cycles were not included as critical points. This optimization scheme was individually conducted for each of the experiments to obtain the expected range of the input parameters for the *steel4* material model. This resulted in different optimized parameters for the *steel4* material for each experimental test.

A second optimization study was then conducted to generate input parameters capable of being generalized to all the available experimental data. This second calibration study minimized the summed L_2 norm for each experiment normalized by the number of critical points, T_n, used for that experimental calibration:

$$\min \frac{1}{\sum_n w_n} \sqrt{\sum_n \frac{w_n^2 \left(\hat{\boldsymbol{f}}_n - \boldsymbol{f}_n\right)^T \left(\hat{\boldsymbol{f}}_n - \boldsymbol{f}_n\right)}{T_n^2}} \qquad \text{Equation 4.10}$$

The vectors, $\boldsymbol{f}$ and $\hat{\boldsymbol{f}}$, only contain the critical points. The weights, w_n, of the component BRB tests were set to 1.0. The sub-assemblage experiment was assigned a weight of 2.0. This was done to more highly weigh the sub-assemblage experimental test as it was the only experiment that tested the BRB under the large strain demands expected of a strongback-braced frame; see Section 2.4.2.1. These deformation demands can result in a different strain hardening profile than that of a typical BRB component test under a standard loading protocol.

Minimization employed the *fmincon* command available in MATLAB (Version 9.3.0.713579, 2017b), which minimizes a constrained nonlinear multivariable function, herein Equation 4.10. Constraints on the parameters were based on the range of results from optimization of the experiments individually. The transition parameters, R_0, r_1, r_2, R_i, and l_{yp} were held constant during this optimization process. The saturated hardening ratio, b_l, was constrained to be equal in tension and compression. Other upper and lower bounds on the material parameters can be found in Table 4.3. The resulting optimized *steel4* material parameters are shown in Table 4.4.

Comparisons of the experimental and numerical results using the generalized material model are plotted in Figure 4.17 for the sub-assemblage strongback test and in Figure 4.16 for the component tests. The fit of the generalized material model somewhat under-estimates the tension force for the sub-assemblage test and somewhat over-estimates the tension force for the component experiments. Note that this fit could be calibrated to better match the experimental hysteretic shape on an individual-by-individual basis, but the resulting generalized model represents the best fit of all of the experimental tests considered, including the large strain data from the strongback sub-assemblage experiment.

Errors in the loading history can be seen when the experimental component tests are subjected to fatigue loading cycles; see component tests PC160, PC750B, and PC1200B in Figure

4.16. This error stems from the material model, *steel4*, continuing to exhibit hardened strength upon unloading to smaller amplitude cycles (i.e. no reduction in the yield surface). More experimental data could further refine the results of this calibration study, especially as related to developing different material parameters based on different BRB manufacturers, different connection details, and different core profiles.

Table 4.2. Properties of experimental tests.

Specimen	**1**	**2**	**3**	**4**	**5**	**6**	**7**	**8**	**9**
Name	**PC160**	**PC250**	**PC350**	**PC500**	**PC750A**	**PC750B**	**PC1200A**	**PC1200B**	**NCBF-B-3SB**
f_y [ksi]	41.3	41.3	41.3	37.9	41.3	41.3	41.3	41.3	40.0
A_r [in^2]	3.8	6.0	8.3	12.7	17.9	17.9	28.5	28.6	5.0
A_t/A_r	4.0	2.8	2.2	2.0	2.1	2.7	1.9	2.2	7.7
A_j/A_r[a]	-	-	-	-	-	-	-	-	2.0
r [a] [in.]	-	-	-	-	-	-	-	-	171
r_T [in.]	252	252	252	252	252	252	252	252	138
r_y [in.]	176	179	183	185	184	179	185	181	76
r_y/r_T	0.70	0.71	0.73	0.73	0.73	0.71	0.73	0.72	0.55

[a] Connection regions not included for calibration of BRB component experiments.

Table 4.3. Optimization constraints.

Constraints	b_k	$b_{k,c}$	b_i	$b_{i,c}$	$b_l = b_{l,c}$	ρ_i	$\rho_{i,c}$
Lower bound	0.001	0.01	0.001	0.001	0.0001	1.0	0.5
Upper bound	0.01	0.05	0.01	0.01	0.001	1.5	1.0

All other material parameters were assumed constant and can be found in Table 4.4.

Table 4.4. Generalized BRB material model.

Asymmetric behavior	**Kinematic Hardening**				**Isotropic Hardening**				
	b_k	R_0	r_1	r_2	b_i	ρ_i	b_l	R_i	l_{yp}
Tension	0.003	25.0	0.9	0.15	0.0025	1.34	0.004	1.0	1.0
Compression	0.023	25.0	0.9	0.15	0.0045	0.77	0.004	1.0	-

b_k = kinematic hardening ratio, R_0, r_1, r_2 = transition from linear elastic to hardening asymptote,
b_i = initial isotropic hardening ratio, ρ_i = intersection location between intiial and saturated hardening asymptotes,
b_l = saturated hardening ratio, R_i = exponential transition from initial isotropic to saturated asymptote,
l_{yp} = length of yield plateau.

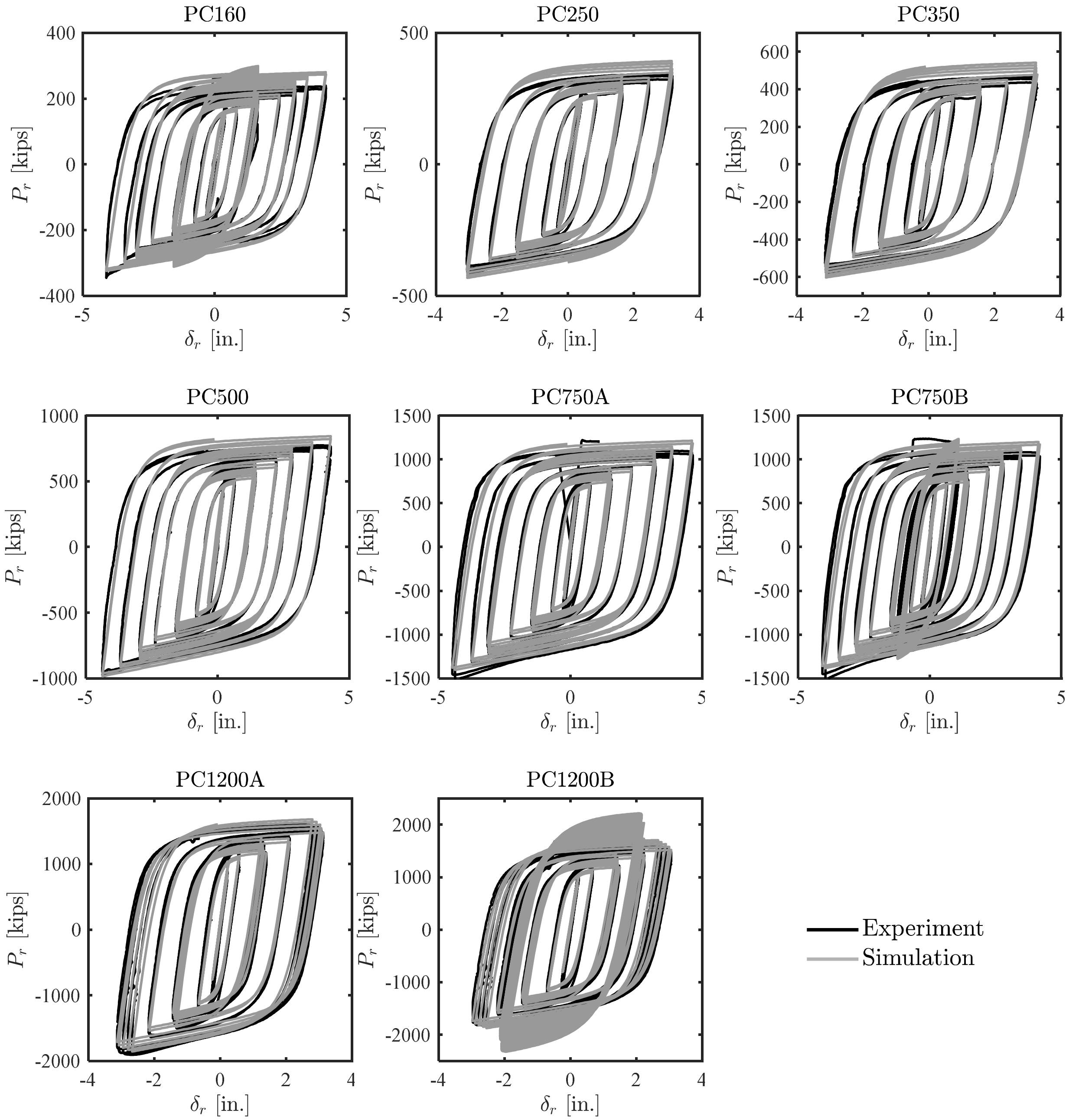

Figure 4.16. BRB calibration to CoreBrace component experiments.

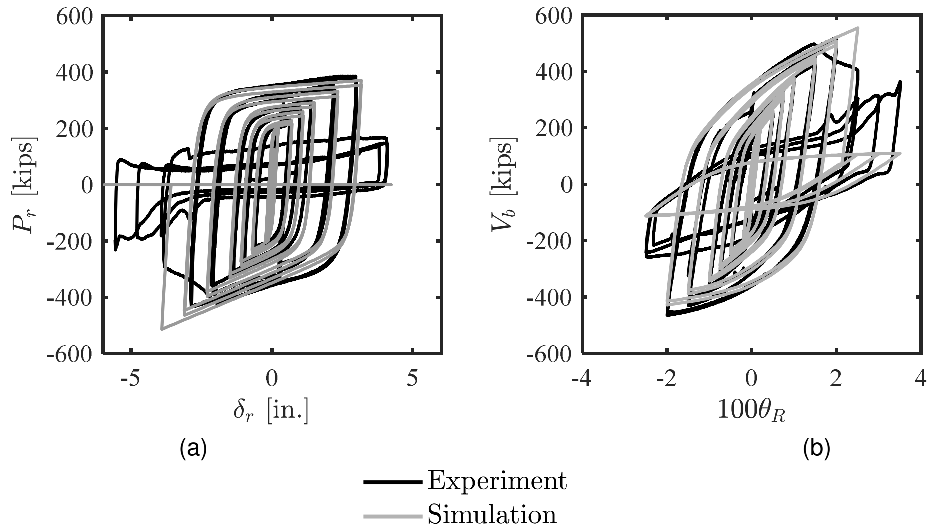

(a)

(b)

Figure 4.17. BRB calibration to stronback sub-assemblage test.
(a) estimated brace force-deforamtion relation; (b) global hysteretic response.

4.4.5 Generalized Material Model

The generalized material parameters derived in Section 4.4.5 were used to estimate the adjustment parameters, ω and β, needed for capacity design. This was step [2] in the process outlined in the introduction of Section 4.4. Conceptually, this step uses a simulated BRB – rather than an experimental BRB – to conduct the qualification testing procedure in AISC-341-16 (2016). In this way, derived factors for adjusted brace strength used during the design development phase would be consistent with the generalized material model used in the numerical simulations.

The numerical model was similar to the model used for the previous calibration study; see Figure 4.15. The length of BRBs considered was based upon a benchmark building archetype that will be outlined in more detail in Chapter 5. The strongback width, b, was fixed to $1/3$ the bay width, L, of 30 ft. The story brace workpoint-to-workpoint length, r, corresponded to story heights, h, of 18 and 15 ft, the first and typical story heights of the archetype building respectively.

The length of the BRB yielding core, r_y, and the length of the truss defining the connection regions, r_T, were set to 60% and 80% of the workpoint length, r, respectively. Connection regions were defined with area, A_j, of 7 times the area of the BRB core, A_r. Transition areas, A_t, were taken as $1/3$ the area of these connection regions. These area and length parameters were considered typical of buckling-restrained braces with a range of different lengths and core areas provided by CoreBrace. A stiffness adjustment factor, Q, of 1.4 for the total BRB length including the end connection regions was found to be representative of the effective stiffness of several BRBs (Lopez & Sabelli, 2004). Nominal brace material yield strength was $f_y = 42ksi$.

The adjusted brace strength used in capacity design is determined by the expected brace deformation. The AISC-*Seismic Provisions* (2016) require consideration of deformations at the greater of twice the design story drift ratio or 2% story drift ratio. The brace deformation at twice the design story drift, including expected inelastic action can be estimated as:

$$\delta_{r,m} = 2C_d\delta_{r,y} \qquad \text{Equation 4.11}$$

$\delta_{r,y} = \varepsilon_y r_y =$ brace yield deformation; $\varepsilon_y =$ material yield strain; $C_d = 5 =$ deflection amplification factor for BRBs per ASCE-7-16 (2016). At $\theta = 2\%$ story drift ratio, the deformation in the inelastic braces including vertical deflection of the beam, $b\theta$, assuming rigid rotation of the strongback can be estimated as:

$$\delta_{r,m} = \sqrt{(h + b\theta)^2 + (l + h\theta)^2} \qquad \text{Equation 4.12}$$

The 2% story drift ratio controlled for all of the BRBs considered. The generalized brace simulation was subjected to the cyclic loading sequence of Section K3.2 of AISC-341-16 (2016), repeated below for convenience and shown in Figure 4.18:

a. 2 cycles of loading at the deformation corresponding to $\delta_r = \delta_{r,y}$
b. 2 cycles of loading at the deformation corresponding to $\delta_r = 0.5\delta_{r,m}$
c. 2 cycles of loading at the deformation corresponding to $\delta_r = 1.0\delta_{r,m}$
d. 2 cycles of loading at the deformation corresponding to $\delta_r = 1.5\delta_{r,m}$
e. 2 cycles of loading at the deformation corresponding to $\delta_r = 2.0\delta_{r,m}$
f. Additional fatigue cycles of loading at the deformation corresponding to $\delta_r = 1.5\delta_{r,m}$ as required for the brace test specimen to achieve a cumulative inelastic axial deformation (CPD) of at least $200\delta_{r,y}$.

$\delta_r =$ imposed amplitude of deformation. A CPD of $200\delta_{r,y}$ was reached during cycles [a] through [e] without needing to apply the additional fatigue cycles in [f]. More research is needed to verify whether a higher C_d-factor would be more appropriate for SBF designs. This loading protocol was performed on core areas of 2.5:0.5:5 in^2, 5:0.5:10 in^2, and 10:1.0:20 in^2, where : (·): represents the increment between the first and last areas in a consecutive list.

The adjustment factors, β and ω, were calculated at each strain amplitude of the loading protocol and are diagrammatically shown Figure 4.19. Similar ω and β values were found upon comparison to ω- and β- backbone curves provided by CoreBrace at similar strain amplitudes, confirming the appropriateness of this calibration process. These adjustment parameters were independent of core area and varied little with story height.

The strains of BRBs in a conventional BRBF would be expected to be less than the strains of BRBs in an SBF subjected to similar story drift ratios. The simulated loading protocol was repeated to obtain appropriate β and ω factors for a BRBF system (i.e. $\delta_{r,m} = \sqrt{h^2 + (l + h\theta)^2}$ with $b\theta = 0$ in Equation 4.12). To reach a CPD of 200, fatigue cycles in [f] were additionally included in the above loading protocol. Adjustment parameters at these additional cycles can be seen in the BRBF plots in Figure 4.19. As stated in Section 4.4.4, the material model, *steel4*, exhibits errors in continued hardened strength upon unloading to the smaller amplitude fatigue cycles.

The derived adjustment parameters, ω and β, for an SBF brace and BRBF brace with brace lengths corresponding to story heights of 15 ft and 18 ft can be found in Table 4.5. Note that these parameters may be further differentiated by connection region, manufacturer, or yielding lengths given a larger database of experiments.

Table 4.5. Derived adjusment parameters, $\boldsymbol{\omega}$ and $\boldsymbol{\beta}$.

System Type	Story height [ft]	$\boldsymbol{\omega}$	$\boldsymbol{\beta}$
Strongback-braced frame	15	1.47	1.20
	18	1.48	1.20
Buckling-restrained braced frame	15	1.34	1.15
	18	1.34	1.15

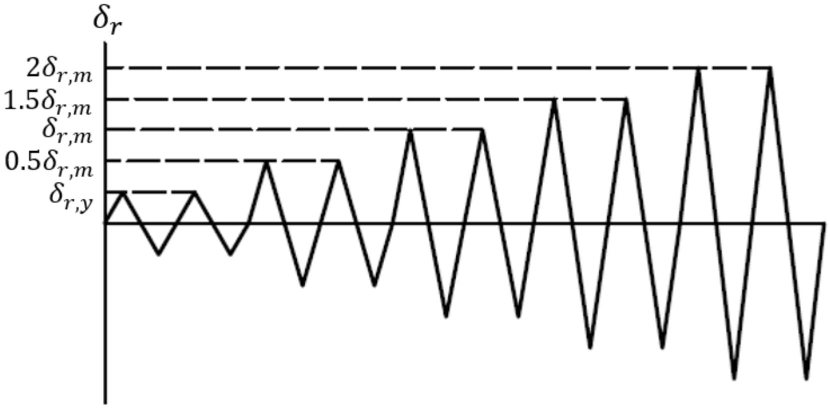

Figure 4.18. BRB cyclic loading sequence.

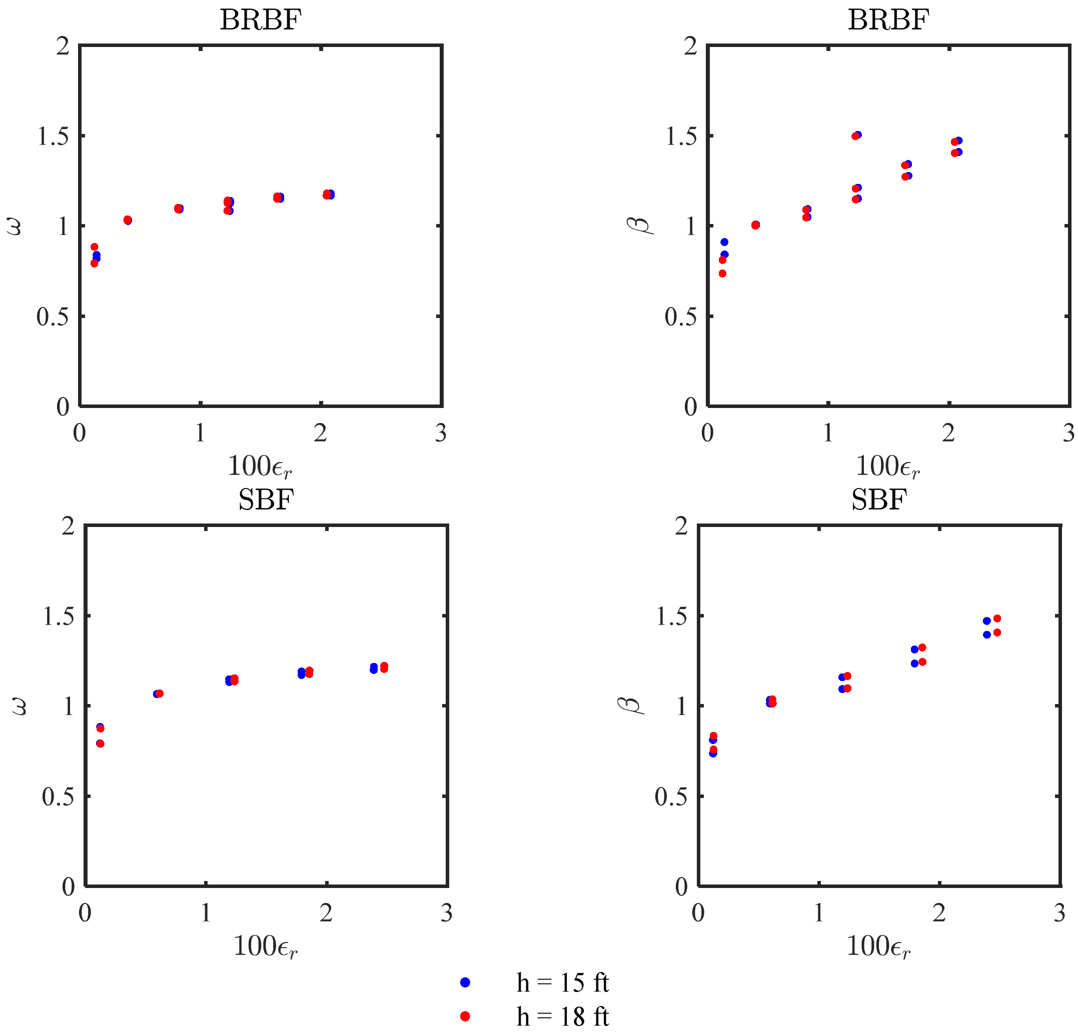

Figure 4.19. Adjustment factors.

4.4.6 Low-Cycle Fatigue

Incorporation of a realistic fatigue model for the buckling-restrained braces was important to determining the strongback's global response and in accurately characterizing demands in the strongback elements. These numerical models used the low cycle fatigue material model described in Section 4.3.2. This model determines whether fatigue has occurred based on empirical input parameters and a fiber's strain history.

The default parameters provided by Uriz and Mahin (2008) for buckling-restrained braces simulated the observed rupture of the BRB in the sub-assemblage strongback test by Simpson and Mahin (2008); see Figure 4.17. However, it was also important that the modeled fatigue life of the BRBs did not exceed the valid range of the numerical model, especially since little experimental data is available for buckling-restrained braces subjected to a few cycles of large strain amplitudes under dynamic loading conditions. As such, simulation of fatigue also considered a maximum strain limit to ensure appropriate simulation of BRB fracture. If this maximum strain limit, ε_{max}, was exceeded, the fatigue material model triggered rupture of the BRB truss element.

Maximum strain could be chosen to correspond to ductility requirements specified by code. These requirements are summarized below:

1. The strain needed to achieve $CPD = 200\delta_{r,y}$ under the loading protocol specified in Figure 4.18 per AISC-341-16.
2. The strain at a story drift ratio, $\theta = 2\%$ per the minimum deformation requirements in AISC-341-16.
3. A maximum strain of $14.3\varepsilon_y$ as provided by the acceptance criteria for collapse prevention for BRBs in ASCE-41-17. This was derived based on the CPD specified in [1].
4. A maximum design level strain of $\varepsilon = 2.5\%$ per the footnotes for the acceptance criteria of BRBs in ASCE-41-17.

Note, however, that these limits are meant to assess the performance of a BRBF which depends almost entirely on the adequacy of the BRBs. In an SBF, the strongback could bridge across the story of a ruptured BRB and still engage the remaining stories in reserve capacity. Moreover, design iterations by BRB manufacturers have resulted in greater fatigue life than that indicated by code (Haselton Baker Risk Group, 2018), and previous experimental studies have tested BRBs to cumulative plastic deformations much greater than a CPD of 200.

For these reasons, $\varepsilon_{max} = 5\%$ was determined to be an appropriate value for the maximum strain limit. This assumption was supported by observed BRB rupture at an estimated strain of 4.5% during the sub-assemblage experiment by Simpson and Mahin (2018b). The empirical fatigue values, ε_0 and m, were kept the same as that of Simpson and Mahin (2018b) and Uriz and Mahin (2008). Alternatively, m, ε_0, and ε_{max} could be calibrated to published S/N curves if these S/N include data for ultra-low cycle fatigue under a few large amplitude cycles [e.g., Nakamura et al. (2000)].

The strain parameters, ε_0 and ε_{max}, used in this fatigue model were adjusted to account for the yielding region, r_y, of the BRBs, r_y; in Section 4.4.2. These parameters were multiplied by the ratio of the truss length to the yield length, r_T/r_y, to adjust the fatigue parameters to represent the geometry of the inelastic truss used in the numerical model.

4.4.7 Summary and Limitations of the BRB Model

This section summarized the qualification testing of the simulated buckling-restrained braces. A simplified simulation utilizing a stiffness modification factor, Q, was used to model the BRB transition and yielding regions with a single truss element. The material model, *steel4*, used in conjunction with a low cycle fatigue material wrapper was capable of simulating asymmetric isotropic and kinematic strain hardening and rupture of the BRBs when properly calibrated to experimental data. Though this material model has the advantage of explicitly accounting for asymmetric hardening, some error cases were noted.

This qualification testing was performed based on the loading protocol specified in AISC-341-16 for quality assurance of new buckling-restrained braced frames. The two-step process of [i] calibration to obtain a generalized material model fit to the experimental data and [ii] subsequent calculation of adjusted strength parameters, ω and β, allowed for consistent design parameters with realistic simulation of the BRB response.

Though the generalized material model was calibrated to component buckling-restrained brace test data and one cyclic sub-assemblage test of a strongback system, these experiments have not included strongback specimens under different loading protocols, geometries, dynamic conditions, or different BRB types and manufacturers. A larger database of experimental data could allow these calibrated studies to be differentiated based on similarities and differences in the response due to the BRB connection, manufacturer, or core profile. This may be especially significant in calibration of the material model to experimental tests under the large strain demands exhibited by SBFs. Fatigue parameters could also be refined given more data on the fatigue life of the BRBs under different loading conditions.

4.5 NUMERICAL MODEL

The parametric and numerical studies of Sections 4.3 and 4.4 were used to develop a benchmark numerical model to simulate SBF and comparison BRBF systems. This benchmark numerical model was implemented in the structural analysis framework, OpenSees (McKenna, 1997); see Figure 4.20. Numerical models of conventional BRBF systems were implemented using a similar modeling approach.

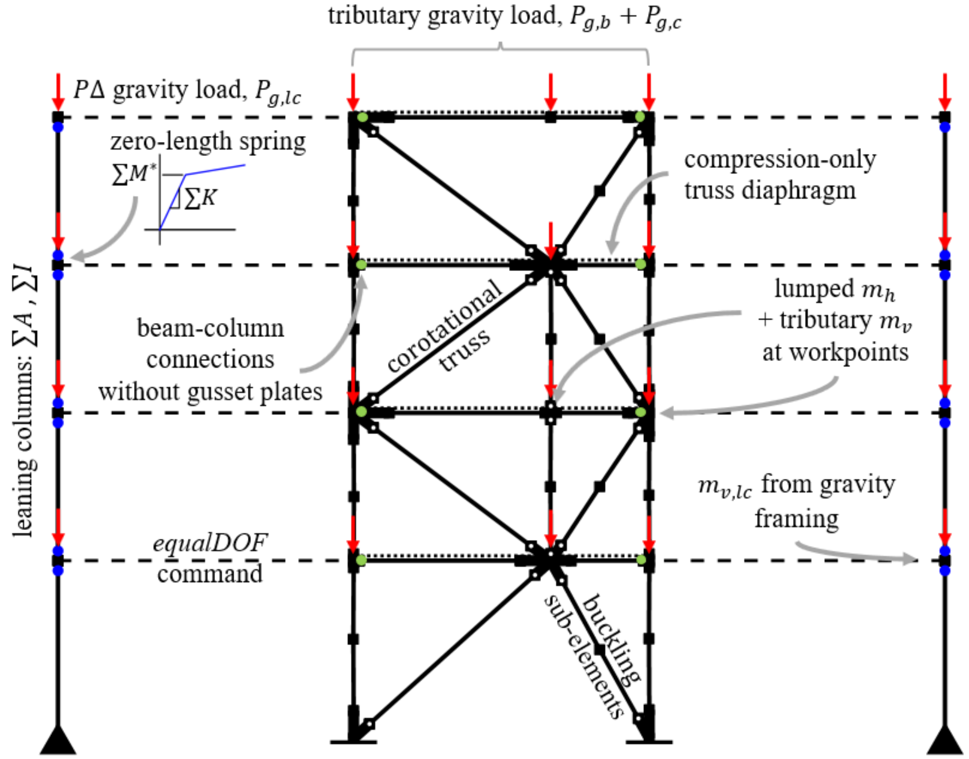

Figure 4.20. Schematic of numerical model.

4.5.1 Constraints and Boundary Conditions

Numerical models considered herein are two-dimensional with three degrees-of-freedom per node. Brace end conditions were modeled as pinned. Open circles in Figure 4.20 represent the locations of these pins.

Beam-column connection tests have indicated bare steel shear tabs and shear tabs with slabs can on average develop 20% and 30 to 45% of the plastic moment of the connecting beam (Liu & Astaneh-Asl, 2000). If supplemented by gusset plates, yield strengths range between 50 to 84% the expected plastic moment of the beam (Stoakes & Fahnestock, 2011). To consider this non-negligible reserve capacity, beam-column connections were modeled with springs per the backbone curves provided in ASCE-41-17 (2017) for partially restrained *beam-column connections without slab*. Moment capacity of beam-column connections with and without gusset plates was specified as 30% and 70% of the expected plastic moment strength of the connecting beam respectively. Strain hardening corresponded to 0.3%. Green circles in Figure 4.20 represent the locations of these beam-column springs.

Elastic elements at the beam-column connections and brace-to-framing connections were used to represent the physical size and stiffening effect of the gusset plates (Yang et al., 2009; Uriz & Mahin, 2008; Hsiao et al., 2012). The area and moment of inertia of these elements were the same as that described for the calibration studies of the braces (e.g., 10 times the moment of inertia of the connecting element for all connection regions; 10 times area of the connecting buckling brace, beam, or column; and 7 times the area of the connecting buckling-restrained brace). Thick black lines in Figure 4.20 correspond to these elastic element regions.

A semi-rigid truss element connected the beam workpoint nodes to include axial effects of a concrete slab. The material model for this slab exhibited resistance in compression-only. The truss area was equal to the effective width and depth of the concrete slab. Composite action between the beam and slab was neglected. Modeling of this diaphragm was the subject of a parametric study conducted in Section 6.2.5.

4.5.2 Material

A uniaxial Giuffre-Menegotto-Pinto steel material model (Filippou et al., 1983) with 0.3% kinematic strain hardening was used for all the beams, columns, and braces, except for the BRB which utilized the calibrated material model from Section 4.4.4.

The yield strength assigned to deformation-controlled components corresponded to the expected yield and ultimate strengths per AISC-341-16 (i.e., $f_y^* = R_y f_y$ and $f_u^* = R_t f_u$). Force-controlled components, like those elements used for the strongback, used a yield strength equal to the nominal strength of the chosen material. Buckling-restrained braces were modeled with a yield strength of $46ksi$. Note that the material model for the BRBs was calibrated using the nominal yield strength, $f_y = 42ksi$. Using an expected yield strength of $f_y^* = 46ksi$ accounts for potential overstrength of the BRB with respect to nominal values used for design.

The OpenSEES low-cycle fatigue wrapper (Uriz & Mahin, 2008) was used to model fracture of the buckling and buckling-restrained braces under axial loading (Uriz & Mahin, 2008; Lai & Mahin, 2013; Simpson et al., 2017) and the beams and column under flexural loading (Uriz

& Mahin, 2008; Simpson & Mahin, 2018b). The maximum strain of the beams and column was limited to $\varepsilon_{max} = 10\%$ to ensure strains were reasonable under large deformations. Beams and column material models used an asymptotic ultimate strength after which the material exhibited perfectly plastic behavior to limit strain hardening of the beams and columns to realistic values.

Table 4.6. Material parameters.

Element	Material Parameters				Fatigue Parameters		
	f_y [ksi]	f_u [ksi]	E [ksi]	b	m	ε_0	ε_{max}
buckling braces	50	- [a]	29,000	0.003	-0.458	0.22	- [b]
Buckling-restrained braces	46	- [a]	Q 29,000	0.003	-0.458	0.15 r_T/r_y [c]	0.05 r_T/r_y [c]
beams and columns	55	71.5	29,000	0.003	-0.458	0.191	0.10

[a] not implemented for braces.

[b] not implemented for bucklng braces.

[c] strain parameters multiplied by r_T/r_y to adjust for BRB yield length.

4.5.3 Sections

Fiber elements were used for all fuses except for the buckling-restrained braces. Fibers were oriented in one direction to reflect the two-dimensional nature of the simulations. Wide-flange sections oriented in strong-axis bending utilized four fibers across the flange thickness and four across the section depth. Wide-flange sections oriented in weak-axis bending, like the buckling braces and some select columns, utilized 12 fibers across the flange width and two fibers across the web thickness as outlined in the parametric study in Section 4.3.3.2. Note that buckling braces were oriented in weak-axis bending to preserve in-plane buckling in the two-dimensional model. The thickness of the flanges and webs were modified so that the area of the fiber section was equal to the actual area of the section including any rounded corners.

4.5.4 Elements

Force-based nonlinear beam-column elements were used for the beams, columns, and buckling braces. Buckling braces were modeled with two force-based nonlinear beam-column elements with co-rotational transformations and calibrated initial imperfections to simulate buckling; see Section 4.3.4. Directions of these imperfections were randomly assigned to each of the buckling elements in the simulation. Five integration points were used for all elements, except the buckling-restrained braces.

The modeling parameters used for the buckling-restrained braces were chosen to match those of the calibration study conducted in Section 4.4. The yielding length of the braces, r_y, was 60% of the work-point-to-work-point length, r. The total effective stiffness, Q, of the buckling-restrained braces including the rigid end conditions fluctuated around 1.4, depending on the length of the elastic elements used to model the connection regions.

4.5.5 Mass and Gravity Effects

Two leaning columns located one bay width to either side of the lateral-resisting frame (Chen & Mahin, 2012) accounted for P-delta effect from loads on the gravity system. The horizontal displacement of these leaning columns was constrained to be equal to the associated floor displacement of the subject braced bay (*equalDOF* command in OpenSees). These leaning columns were assigned the sum of the area and moment of inertia of the gravity columns included in the analysis. Potential inelasticity in the leaning columns was accounted for through bilinear moment-rotation springs with 0.1% strain hardening at the ends of each column at each floor level. The strength of these springs was assigned the sum of the plastic moment capacity of the contributing gravity columns. The axial load on a leaning column, $P_{g,lc}$ was taken as the portion of the total system gravity load that could be attributed to a braced bay, excluding the load directly tributary to the braced bay. Tributary column gravity loads were applied directly to the lateral frame by point loads at the workpoint nodes of the columns, $P_{g,c}$. Distributed loads on the beam, $w_{g,b}$, were applied through equivalent point loads at the workpoint nodes of the beams, $P_{g,b}$. The following gravity load combination was applied in the numerical model per FEMA-p695 (2009):

$$P_g = 1.05D + 0.25(0.5L) \qquad \text{Equation 4.13}$$

D = dead load; L = live load.

This gravity combination was also used to calculate the mass applied in the numerical model. Horizontal mass, m_h, was assigned to the workpoint nodes of the lateral frame considering the floor mass attributed to the brace bay. The vertical floor mass, m_v, tributary to the beam in the braced frame was modeled at the workpoints of the main lateral resisting frame. The remaining vertical mass, $m_{v,lc}$, was applied to the leaning columns. In this fashion, the gravity loading, horizontal mass, and vertical mass contributing to the braced bay were consistent in the simulation.

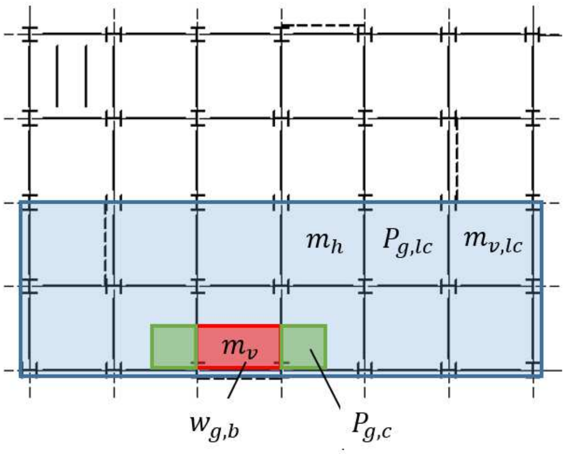

Figure 4.21. Attributed mass and gravity loading.
m_h =horizontal mass; m_v = vertical mass on braced bay; $m_{v,lc}$ = vertical mass on leaning column;
$P_{g,lc}$ = gravity loading on leaning column; $w_{g,b}$ = distributed gravity loading on beam;
$P_{g,c}$ = gravity loading on leaning column.

4.5.6 Damping

There are many different methods of incorporating damping in OpenSees, including Rayleigh damping, modal damping, and supplemental numerical damping (such as the Hilber-Hughes-Taylor integration method). The numerical models herein utilized Rayleigh damping with a target damping ratio, $\zeta_n = 2.5\%$, in $1.5T_1$ and T_3, where T_1 is the fundamental elastic period and T_3 is the third mode elastic period. This was deemed representative of steel structures exhibiting 2-3% damping (PEER, 2017; ASCE-41-17, 2017).

The first and third mode periods were selected to ensure that damping ratios were not too large or too small in the first four modes; see Table 4.7 and Figure 4.22. The multiplier of 1.5 was used to account for potential period elongation due to the inelastic response of the structure (SNZ, 2004; ASCE-41-17, 2017). Selection of these target damping ratios resulted in a minimum damping ratio of $\sqrt{a_0 a_1} = 1.6\%$ at a period of $\frac{1}{2\pi}\sqrt{a_0/a_1} = 0.5\ s$.

Use of the committed rather than initial stiffness was found to reduce spurious damping forces by a number of researchers [e.g., Charney (2008), Petrini et al. (2008), Chopra and McKenna (2016a)]. As such, damping of the high frequency modes was applied by stiffness proportional damping based on the committed stiffness, $\zeta_{n,k}$. Damping of the low frequency modes was applied by mass proportional damping, $\zeta_{n,m}$, at the primary nodes where mass was specified.

To reduce over-damping of near-rigid elastic regions with high initial stiffness (Charney, 2008), elastic elements representing the connection regions were reduced by the multiplier used to impose rigidity in those regions (e.g., a factor of 10 for buckling brace, beam, and column elements and a factor of 7 for buckling-restrained brace elements). Where concentrated plasticity zero-length elements were used, the stiffness-proportional damping of the connecting element was modified to account for the elastic stiffness of the adjacent plastic hinge regions (e.g., in the leaning columns). Zero-length elements did not include damping.

Note that other methods of damping, such as modal damping, would effectively eliminate spurious forces that can develop using Rayleigh damping (Chopra & McKenna, 2016a). However, modal damping depends on the elastic modes and cannot explicitly account for period elongation due to inelastic behavior unless modal damping is evaluated at every time step or unless the damping matrix is explicitly re-formulated to determine damping contributions at the elongated periods. Rayleigh damping was used herein to be consistent with current modeling practice and to allow explicit target damping ratios to be specified at elongated periods. The reader is referred to more detailed studies for assessment of spurious or artificial damping forces [e.g., Hall (2006), Charney (2008), Petrini et al. (2008), Chopra and McKenna (2016a), Chopra and McKenna (2016b), etc.].

Table 4.7. Rayleigh damping.

Mode	$\mathbf{1.5}\boldsymbol{T_1}$ [a]	$\boldsymbol{T_1}$ [b]	$\boldsymbol{T_2/T_1}$	$\boldsymbol{T_3/T_1}$	$\boldsymbol{T_4/T_1}$
Period, T_n	$1.4\ s$	$0.94\ s$	3	5	7
Damping ratio, ζ_n	2.5%	1.9%	1.8%	2.5%	3.3%

[a] Estimate of period elongation.

[b] Upper design period of a four-story strongback-braced frame per ASCE-7-16 (2016).

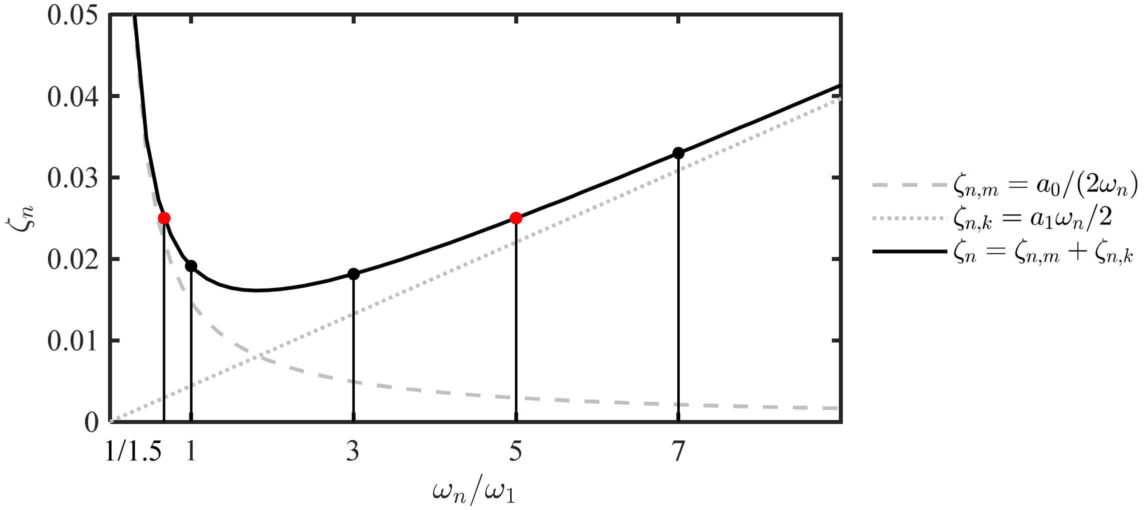

Figure 4.22. Rayleigh damping in $1.5T_1$ and $T_3 \cong 5T_1$.

4.5.7 Non-Simulated Limit States

Simulating sidesway collapse requires simulation of material or element strength degradation and softening. Concentrated plasticity models, represented by zero-length plastic springs at the end of an elastic element, are often used for collapse assessment. Such models can model post-capping negative stiffness through empirical force-deformation relationships calibrated to past experimental tests. This negative stiffness is critical for accurate simulation of collapse. However, such series models do not include axial-flexural interaction as currently implemented in OpenSEES.

Since axial demands in all elements of braced frames can be significant, distributed-plasticity elements were used herein to characterize the behavior of regions of potential inelasticity in the strongback system. Distributed plasticity models (e.g., elements utilizing fiber sections) can allow plasticity to distribute along the element length while explicitly accounting for axial-flexural interaction. Implementing a softening response in fiber-based models, however, can be onerous, especially since softening must be implemented at the material level instead of the force-deformation level.

Non-simulated limit states can be considered in lieu of direct simulation of collapse where high-fidelity modeling of the softening response is limited. To the extent possible, the numerical model includes explicit deterioration mechanisms that could lead to structural collapse, including the effects of a low-cycle fatigue material model (Uriz & Mahin, 2008). However, non-simulated failure modes that were difficult to model were accounted for indirectly using post-process limit-state checks on responses measured during the analyses. This approach evaluated non-simulated failure modes based on comparisons between the modeling criteria in ASCE-41-17 (2017) and the demands extracted from the analysis. This assumes that the first exceedance of a limit state would result in collapse of the structure, which can result in an overly conservative estimate of the median response where these limit-state checks were used to assess collapse performance.

A summary of the simulated, non-simulated, and neglected failure modes is listed in Table 4.8. Gusset plate connection failures have been neglected and were assumed to be prevented through adequate detailing. Though a node was provided in the columns to simulate in-plane buckling, the two-dimensional nature of the simulation did not allow for out-of-plane buckling in the columns. As such, geometric instability of the columns was checked through limit state checks based on the nominal buckling capacity of the columns. Generally, beam and column elements were assumed to be adequately braced to prevent out-of-plane buckling and lateral torsional buckling.

Deformation limits are shown in Table 4.9. These limits correspond to the deformation limits specified in ASCE-41-17 prior to loss of load-carrying capacity (denoted by a in ASCE-41-17) and are used to ensure the deformations do not exceed the valid range of the numerical model. Flexural limits assume that flange and web slenderness satisfy requirements for highly ductile sections. Flexural limits were reduced by the axial load taken within a time instant. The yield rotation, θ_y, was estimated based on the point of contraflexure along the length of the element depending on moments measured at the element's ends. Where the axial demand-to-capacity ratio, P/P^*, exceeded 20%, the estimated yield strength was reduced to $\hat{\theta}_y = \theta_y(1 - |P_g|/P_y^*)$ ($P_g =$ axial force due to gravity loading, $P_y^* = Af_y^* =$ the expected tensile yield strength of the element). Elastic properties of elements with $|P| \geq 0.6P_y^*$ were modified by τ_b per AISC-360, Chapter C (2016).

Table 4.8. Numerical modeling of deterioration modes.

Component	**Action**	**Modeling**		
		Explicitly Modeled	**Non-Simulated Limit State Checks**	**Neglected**
Buckling Brace	Global Buckling	X		
	Low Cycle Fatigue	X		
	Local Buckling			X
BRB	Low Cycle Fatigue	X		
	Concrete Crushing and Casing Failure			X
Beam	Global Beam Buckling		X	
	Lateral Torsional Buckling			X
	Shear Failure			X
	Flexural Deformation Limit States		X	
Column	Fracture	X		
	Splice / Baseplate Failure			X
	In-Plane Column Buckling	X		
	Out-of-Plane Column Buckling		X [a]	
	Torsional Buckling			X [a]
	Flexural Deformation Limit States		X [b]	
Connection	Beam-column connection failure	X [c]		
	Brace-to-gusset connection failure			X
	Net Section Failure			X

[a] Strength checked per the compression capacity of column about the weak-axis of bending.

[b] Limit state check based on plastic rotation angle in ASCE-41-17 for beams and columns in flexure.

[c] Spring modeled per backbone curve in ASCE-41-17 for partially-restrained *shear connection without slab*.

Table 4.9. Plastic Deformation limits.

Component or Action	**Axial Load**	**Plastic Deformation Limit, $\boldsymbol{\theta_p}$**
Beam-column in compression	$\frac{\lvert P_g \rvert}{P_y^*} \leq 0.6$ [a]	$0.8\left(1-\frac{P_g}{P_y^*}\right)^{2.2}\left(0.1\frac{l}{r_y}+0.8\frac{h}{t_w}\right)^{-1}-0.0035 \geq 0$
Beam-column in tension	$\frac{\lvert P_g \rvert}{P_y^*} < 0.2$	$9\hat{\theta}_y$
	$0.2 \leq \frac{\lvert P_g \rvert}{P_y^*} \leq 0.6$ [a]	$\left[13.5\left(1-\frac{5}{3}\frac{\lvert P_g \rvert}{P_y^*}\right)\right]\hat{\theta}_y \geq 0$
Shear connections without slab	- [b]	$0.15-0.0036d_{bg}$

$d_{bg} = d - 2k_{des}$ = estimate of the depth of the bolt group. θ_y = yield rotation.

[a] Elements with $\frac{\lvert P_g \rvert}{P_y^*} > 0.6$ or $\theta_p = 0$ are considered force-controlled in flexure.

[b] not applicable.

4.5.8 Limitations of the Numerical Model

Though the OpenSEES benchmark model incorporated many aspects critical to the response of the SBF and comparison BRBF systems, the following limitations of the benchmark numerical model should be noted:

1. The fiber elements used in this model assume that plane sections remain plane. Distortions and multi-axial stress states in the cross-section are not considered (e.g., due to local buckling).
2. The described model is two dimensional. Three-dimensional (e.g., out-of-plane or torsional) behavior is not represented by the simulation. Columns were allowed to buckle only in the plane of bending (strong-axis bending in most cases) and were checked through post-process limit state checks to ensure efficacy of the simulation.
3. Gusset plate connections were assumed to be adequately detailed. Failures in these regions were not modeled in the simulation and were considered through post-process limit state checks.
4. The low-cycle fatigue parameters used in this study were derived assuming a maximum strain capacity of 5% in the BRBs and were calibrated to experiments on smaller WF sections. More data is needed to sufficiently calibrate these parameters to real member sizes.
5. Rayleigh damping was assumed to be 2.5% at $1.5T_1$ and T_3. This means that damping will be less than the target damping ratio in the first and second modes. Other methods of damping (e.g., modal damping) may offer an alternative method of explicitly modeling damping in each mode.

5 Benchmark Strongback

5.1 INTRODUCTION

Simulations of a working strongback were needed to understand the strongback's behavior and to develop initial design methods. If the response of this preliminary, or *benchmark*, strongback under nonlinear dynamic analysis was considered an accurate representation of system's potential dynamic response, the benchmark design could be used to evaluate the demands from proposed static analysis methods.

This chapter studies the optimized design of a four-story benchmark strongback-braced frame using an iterative nonlinear dynamic design scheme, herein termed *dynamic capacity design*. This benchmark design was used to characterize the dynamic response of the strongback system and to assess the static analysis methods proposed in later chapters. In this chapter, characterization of behavior is empirical and based on observations of response quantities extracted from the numerical analysis. Acceptability of the benchmark design was determined through statistical evaluation of its response using the methodology outlined in FEMA-P695 (2009) and incremental dynamic analysis. The general methodology, ground motions, benchmark design, and a discussion of the results are outlined in the following sections. To give the results context, peak response quantities from the final benchmark-strongback design were also compared to that of a conventional BRBF system.

5.2 METHODOLOGY FRAMEWORK

A developed design method for strongback systems did not exist at the start of this study. Therefore, dynamic capacity design supplemented by the performance-based methodology provided in FEMA-P695 was used as a rational basis for preliminary design of the benchmark strongback. Dynamic capacity design was used to compare demands extracted from nonlinear dynamic analyses to the acceptable performance metrics provided in FEMA-P695. This design and assessment framework is outlined in this section.

5.2.1 Dynamic capacity design

Though traditional capacity design presented a good starting point for design for the benchmark strongback, it was unclear at the start of the design development process whether a purely capacity design approach would account for all aspects of strongback behavior while providing an appropriately conservative representation of the strongback's dynamic response. Since the behavior of a successful strongback was uncertain, study of a benchmark design was initially approached using an iterative design scheme, termed dynamic capacity design, that was able to account for uncertainty in demands in the force-controlled actions, the randomness of the ground motions, and the variability in the element's capacities and construction quality.

Like traditional capacity design, dynamic capacity design designates desirable locations of inelastic actions, termed deformation-controlled actions. Statistical metrics are then used to characterize demands in the remaining force-controlled actions. Use of nonlinear dynamic analysis during the design process explicitly simulates higher-mode effects and variations in demands over time that may be absent in a traditional capacity design approach.

Dynamic capacity design also directly incorporates uncertainty in the random behavior of the selected ground motions and variations in structural characteristics like material properties and construction quality. Force-controlled actions are designed in terms of an acceptably low probability of failure, including uncertainty in both the median demands, D, in terms of a rare enough event, γD, and the capacities, C, times a resistance factor, ϕC, where $\omega > 1$ and $\phi < 1$. In this fashion, the dynamic capacity method approaches design in terms of achieving less than $x\%$ probability of "failure" by any one of the force-controlled actions in y years. A schematic of this process is shown in Figure 5.1. Herein, demands are typically compared to the 85th percentile of peak demands extracted from nonlinear dynamic analyses. Variability in capacities are accounted for by traditional strength reduction factors, ϕ, in load and resistance factor design (AISC-360-16, 2016). Based on this approach, the steps for the dynamic capacity design methodology are as follows:

1. Designate deformation- and force-controlled actions.
2. Design deformation-controlled actions (e.g., axial force in the inelastic braces, flexural force in the beams, etc.) by traditional analysis methods, such as those provided in ASCE-7-16 (2016).
3. Estimate the stiffness and capacity of the force-controlled actions (e.g., area and moment of inertia).
4. Perform nonlinear dynamic analyses for several relevant ground motion records.
5. Calculate statistics (e.g., median and 85th percentile) for the force demands, D, designated as force-controlled actions.
6. Check that the demands accounting for dispersion, γD, are less than the associated capacities, C, of the force-controlled actions times a resistance factor, ϕC.
7. Check the deformation capacity of the deformation-controlled actions and drift requirements.
8. Iterate between steps 3-7 until the design is considered acceptable.

Dynamic capacity design incorporates dynamic characteristics that may not be represented by static plastic or pushover analysis methods or a strict capacity design approach where demands are calculated on an element- or story-wise basis. The principles embedded in traditional capacity design can still be used to establish a clear hierarchy of desirable and anticipated responses, but dynamic capacity design extends that hierarchy to also include uncertainty and time-varying dynamic behavior. If the demands from these analyses are considered close to the "true" demands, the acceptability of any proposed design method could then be measured against the statistics of the estimated benchmark response and an associated resistance factor.

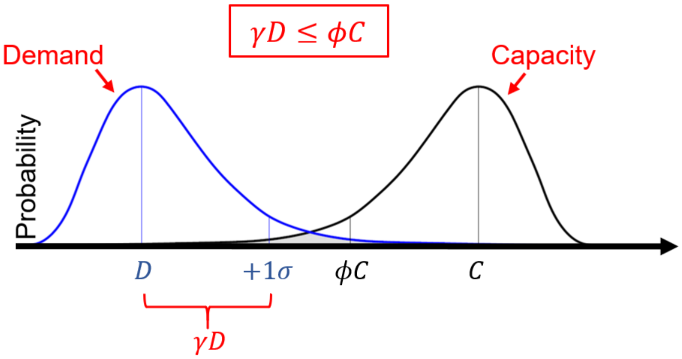

Figure 5.1. Schematic of dynamic capacity design.

5.2.2 Performance Evaluation

The nonlinear dynamic procedure from the FEMA-P695 (2009) methodology was used to evaluate acceptability of the benchmark design and to incorporate uncertainty metrics into the design process. Even though the FEMA-P695 methodology evaluates structures primarily in terms of collapse assessment, the procedure was used herein to determine the probability of "failure" in the force-controlled actions (i.e. the initiation of inelastic behavior in the designated essentially elastic portions of the strongback). In terms of the dynamic capacity design procedure outlined in Section 5.2.1, the FEMA-P695 methodology was used in steps 4 through 6.

In this methodology, the given ground motion set is scaled by increasing median intensity until half of the ground motion in the set cause "failure" in the structural model. Failure is characterized by inelastic action in the strongback elements, triggering of non-simulated limit states, or global instability. This median failure intensity level, $\hat{S}_{CT}$, is representative of the median intensity above the Maximum Considered Earthquake (MCE-level) ground motion intensity, S_{MT}, and is quantified through a collapse margin ratio, CMR:

$$CMR = \frac{\hat{S}_{CT}}{S_{MT}} \qquad \text{Equation 5.1}$$

$S_{MT} = MCE$ intensity level representative of the 5% damped, spectral acceleration at the upper limit period, T; $\hat{S}_{CT}$ = the median spectral intensity above the MCE-level at which less than one-half of the ground motions cause failure. In FEMA-P695, the upper limit period is defined as:

$$T = C_u T_a = C_u C_t h_n^x$$
$$x = 0.75, C_u = 1.4, C_t = 0.02 \qquad \text{Equation 5.2}$$

h_n = building height in feet. Parameters x, C_u, and C_t were calculated per ASCE-7-16 (2016) based on the criteria for a BRBF system.

Acceptability is achieved when the median strongback response is an acceptable ratio above the MCE response. This is an alternative way of characterizing $\gamma D \leq \phi C$ in Figure 5.1. The following sections provide more details on adjustments to the CMR, characterization of uncertainty, β, and the acceptance criteria, $ACMR_{(\cdot)\%}$. The overall method used in the dynamic capacity design process is more fully summarized in Section 5.2.3.

5.2.2.1 Adjusted Collapse Margin Ratio and Spectral Shape

The FEMA-P695 methodology adjusts the CMR to account for the frequency content, or spectral shape, of the scaled ground motion suite. The unrealistic shape of the response spectrum arises from near uniform intensities at periods longer and shorter than the fundamental period of interest. The SSF adjusts the CMR to account for the expected spectral characteristics of extreme ground (Baker, 2005; Baker & Cornell, 2006). The adjusted CMR, or $ACMR$, including the SSF modifier is:

$$ACMR = SSF(\mu, T, SDC) \cdot CMR \qquad \text{Equation 5.3}$$

T = building's upper design period; T, μ = period-based ductility; SDC = seismic design category. The values for SSF given μ, T, and SDC are tabulated in FEMA-P695. The period-based ductility is calculated based on displacement values from pushover analysis results under a first-mode force distribution.

Acceptability is measured by comparing the adjusted CMR, or $ACMR$, to values representing an acceptably low probability of failure for MCE ground motion. Note that spectral shape could also be directly accounted for by using a suite of ground motions uniquely selected for each hazard level and conditioned on multiple periods.

5.2.2.2 Uncertainty

Acceptability per FEMA-P695 considers record-to-record uncertainty, β_{RTR}; design requirement uncertainty, β_{DR}; test data uncertainty, β_{TD}; and modeling uncertainty, β_{MDL}. Acceptable values of the adjusted collapse margin ratio assume a lognormal distribution of failure-level spectral intensities with median intensity, $\hat{S}_{CT}$, and total uncertainty, β_{tot}:

$$\beta_{tot} = \sqrt{\beta_{RTR}^2 + \beta_{DR}^2 + \beta_{TD}^2 + \beta_{MDL}^2} \qquad \text{Equation 5.4}$$

Uncertainties associated with quality ratings (i.e., β_{DR}, β_{TD}, β_{MDL}) are subjective in nature and are described in more detail in FEMA-P695.

In this study, design requirements were categorized as good ($\beta_{DR} = 0.2$) as the proposed design criteria is expected to be developed similar to that of BRBF systems. While the numerical models were calibrated to a range of available component buckling-restrained brace test data and one cyclic sub-assemblage test of a strongback specimen (see Section 4.4.3), this test data did not include strongback specimens under different loading protocols, geometries, dynamic conditions, or different BRB types and manufacturers. As such, the test data was categorized as good ($\beta_{TD} =$

0.2). Numerical modeling was characterized as good ($\beta_{MDL} = 0.2$) as it simulated many, but not all, possible failure modes; see Section 4.5.

The record-to-record variability reflects the variation in response from ground motion-to-ground motion. Ideally, explicit calculation of record-to-record variability would be conducted by fitting a lognormal distribution to the data points. For simplicity, it was assumed that the constant value of record-to-record variability used in FEMA-P695 was adequate for this preliminary design phase. FEMA-P695 assumes a fixed value of $\beta_{RTR} = 0.4$ for building with $\mu \geq 3$.

The above uncertainties can be combined in Equation 5.4 for a total system uncertainty of $\beta_{tot} = 0.525$.

5.2.2.3 Acceptable probability of collapse

Acceptable values of the adjusted collapse margin ratio, or $AMCR_{(\cdot)\%}$, depend on the total uncertainty, β_{tot}, and an acceptable probability of failure, $(\cdot)\%$. If the $ACMR$ is greater than these acceptable values (e.g., $ACMR \geq ACMR_{10\%}$, $ACMR_{20\%}$, etc.), the assumptions used to design the benchmark building are considered acceptable. Re-evaluation is required if the $ACMR$ is less than these acceptable values.

$ACMR < ACMR_{(\cdot)\%} \rightarrow$ unacceptable Equation 5.5

On average, the probability of collapse due to an MCE-level ground motion is limited to 10%, or $ACMR_{10\%}$.

By default, a conventional BRBF system is expected achieve less that 10% probability of collapse at the MCE-level, because it is a typical structural system in modern building codes. As a better performing system, the strongback system would hypothetically achieve better performance. Thus, the benchmark strongback was designed for a more stringent measure of acceptability than a conventional system. In addition to achieving less that 10% probability of collapse, the benchmark strongback was required to achieve less that 10% probability of inelastic behavior in any one of the force-controlled actions at the MCE-level. As such, calculated $ACMR$ values were assessed against $ACMR_{10\%}$ values corresponding to a 10% failure probability. This ensured confidence in the strongback's behavior if ordinary details were used in the strongback portion of the system. Note that less stringent acceptance criteria would also be acceptable if the strongback portion of the system was provided with ductile detailing.

5.2.3 Framework Summary

In summary of the FEMA-P695 framework, acceptability per FEMA-P695 is determined through the following steps:

1. Scale the normalized ground motion to the target spectral acceleration, S_{MT}, at the upper limit period, $T = C_u T_a$.
2. Scale the suite of ground motion records until half of the record set result in failure. The intensity level at which this occurs is the median failure intensity, $\hat{S}_{CT}$.
3. Calculate the collapse margin ratio, $CMR = \frac{\hat{S}_{CT}}{S_{MT}}$

4. Adjust the collapse margin ratio to account for spectral shape, $ACMR = SSF \cdot CMR$.
5. Evaluate acceptability in terms of the acceptable collapse margin ratio, $ACMR > ACMR_{(\cdot)\%}$, based on the total system uncertainty, β_{tot}.

To assess the performance of an individual building using dynamic capacity design, the above process can be "reverse-engineered" to the following:

1. Define the failure level.
    a. Choose the quality rating uncertainties (i.e., $\beta_{DR}, \beta_{TD}, \beta_{MDL}$) and use the default record-to-record uncertainty, β_{RTR}, to calculate the total system uncertainty, β_{tot}. Choose a failure probability (e.g., 10%, 20%, etc.) and determine the associated acceptance criteria, $ACMR_{(\cdot)\%}$.
    b. Determine the spectral shape factor, SSF, based on the structure's period-based ductility, μ, upper limit period, T, and seismic design category, SDC.
    c. Scale the ground motion record suite to the required median failure-level intensity, $\hat{S}_{CT}$, at the upper limit period, T, back-calculated from the following:

$$CMR = \frac{\hat{S}_{CT}}{S_{MT}} = \frac{ACMR_{(\cdot)\%}}{SSF}$$ Equation 5.6

2. Iterate upon the benchmark design.
    d. Designate deformation- and force-controlled actions and design the deformation-controlled actions for code-level reduced design forces. Define appropriate limit states.
    e. Estimate the stiffness and capacity for the force-controlled actions.
    f. Perform nonlinear dynamic analyses with the scaled ground motion suite from [c] and evaluate performance.

If less than one-half of the records at the intensity level calculated in [c] cause failure, the trial design is acceptable. If one-half or more of the records cause failure, then the benchmark design needs to be re-designed and re-evaluated.

5.3 BENCHMARK ARCHETYPE DESCRIPTION

A four-story strongback archetype was chosen for the preliminary benchmark structure. The number of stories for the benchmark frame was chosen to be simple enough for hand calculations while having enough degrees-of-freedom to simulate higher-mode contributions under dynamic loading conditions.

5.3.1 Structural System Description

For the four-story benchmark building, design requirements were assumed to be given and the system design requirements for buckling-restrained braced frames (BRBF) in AISC-341-16 (2016) were used as an initial framework. All pertinent design requirements (e.g. R, C_d, etc.) of ASCE/SEI

7-16 (2016), including drift limits and minimum base shear requirements were assumed equal to that of a BRBF; see Table 5.1. The benchmark frame was assumed to be an exterior frame of a four-story building that is rectangular in plan; see Figure 5.2.

Recall that an offset scheme (Chapter 3) can reduce the significant inelastic demands that can develop in the strongback system. An offset of $1/3$ the braced bay width was utilized for the benchmark configuration. This offset provided enough stiffness to limit displacements in the elastic range and reduced plastic deformations in the inelastic range compared to a centered bracing configuration. The benchmark building and gravity framing were designed to be consistent with a typical office occupancy; see Table 5.2 and Figure 5.3. Details of the benchmark loading and general layout were the product of relevant conversations with local engineering offices. Accidental eccentricity was not considered during the design process. More information on the four-story benchmark building can be found in Figure 5.2.

The design base shear, V_b, used to design the inelastic (deformation-controlled) elements was based on spectral accelerations calculated at the upper limit period, T per FEMA-P695. The fundamental period of vibration, T_1, was calculated from an eigenvalue analysis of the numerical models and may be different from T.

Table 5.1. Design Properties.

Seismic Design Criteria	**Design Parameters**
R	8
I	1.0
C_d	5
Ω_0	2.5
T $[s]$	0.94
T_1 $[s]$	0.84 (SBF); 0.93 (BRBF)
V_b/W $[g]$	0.08
$S_{MT}(T)$ $[g]$	0.96

Table 5.2. Gravity loading.

Weights/story	**Floor Area**	**Design Seismic Weight** [a]	**Numerical Seismic Weight** [b]
Penthouse	3,600 ft^2	438 kips	352 kips
Roof	18,000 ft^2	1483 kips	1552 kips
Typical Floor	21,600 ft^2	1794 kips	1926 kips
First Floor	21,600 ft^2	1812 kips	1945 kips

[a] Used for design base shear.

[b] Used in numerical model per Equation 4.13.

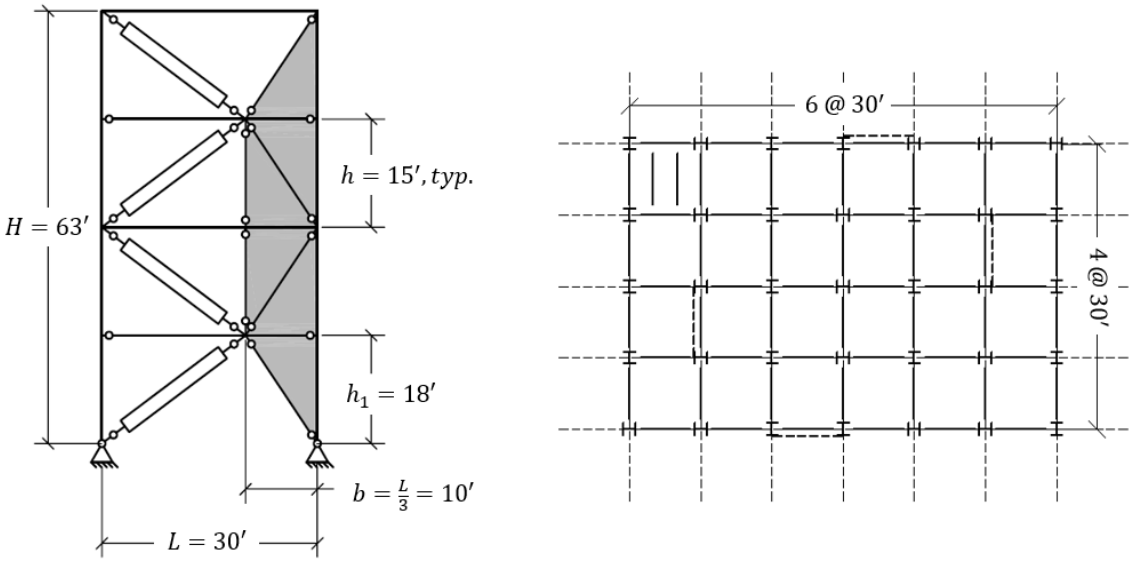

Building Description
Occupancy category: office
Generic building site per FEMA-P695
Gravity loading: perimeter framing

Building Geometry
Number of stories: 4 stories
Typical story height $h = 15'$
First story height $h_1 = 18'$
Bay width $L = 30'$
Offset, $b = L/3$

Seismic Design Parameters
Design Codes: ASCE-7-16, AISC-341-16
Analysis procedure: dynamic capacity design
Seismic Design Category (SDC): D_{max}
Risk Category II

Figure 5.2. Benchmark building floor plan and elevation.

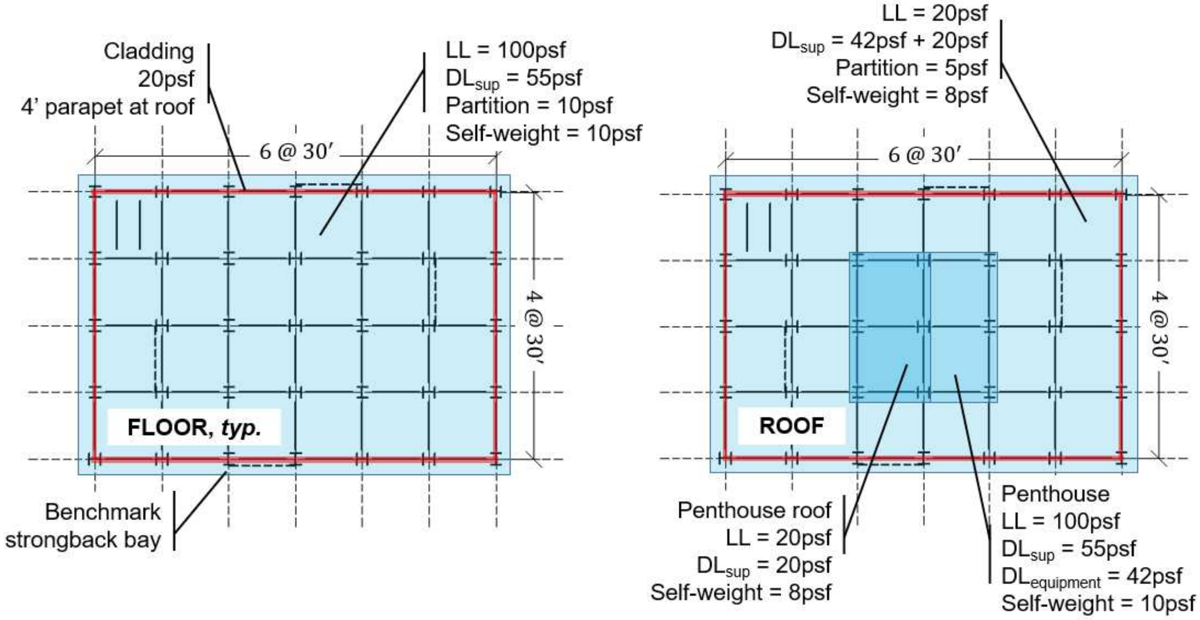

Figure 5.3. Gravity loading.

5.3.2 Ground Motion Suite

The Far-Field ground motion set provided in the FEMA-p695 methodology was used for the ground motion suite. This set includes twenty-two component pairs of horizontal ground motions from sites located greater than or equal to 10 km from fault rupture. Vertical excitation was not included since FEMA-P695 does not consider that direction to be of primary importance for performance evaluation. Future studies may wish to incorporate the vertical ground motion component as it can impact the brace buckling response (Chen & Mahin, 2012).

Each of the ground motions in the set were normalized by their peak ground motion velocities to remove unwanted variability in the record set per FEMA-P695. These normalized ground motions records were then collectively scaled so that the median spectral response, S_{MT}, matched the MCE target design spectra at the upper limit period of the building, T (Equation 5.2); see Figure 5.4. Note that this results in large pseudo-accelerations at higher-mode periods in the constant acceleration range of the design response spectrum. More information on the ground motion record set can be found in FEMA-P695.

This target spectrum is intended to represent a generic building site for $SDC = D$, per the FEMA-P695 methodology. The maximum MCE spectral values for $SDC\ D$, or D_{max}, are shown in Table 5.3. It was inferred that adequate performance for D_{max} would imply acceptability for lower seismic design categories like D_{min}.

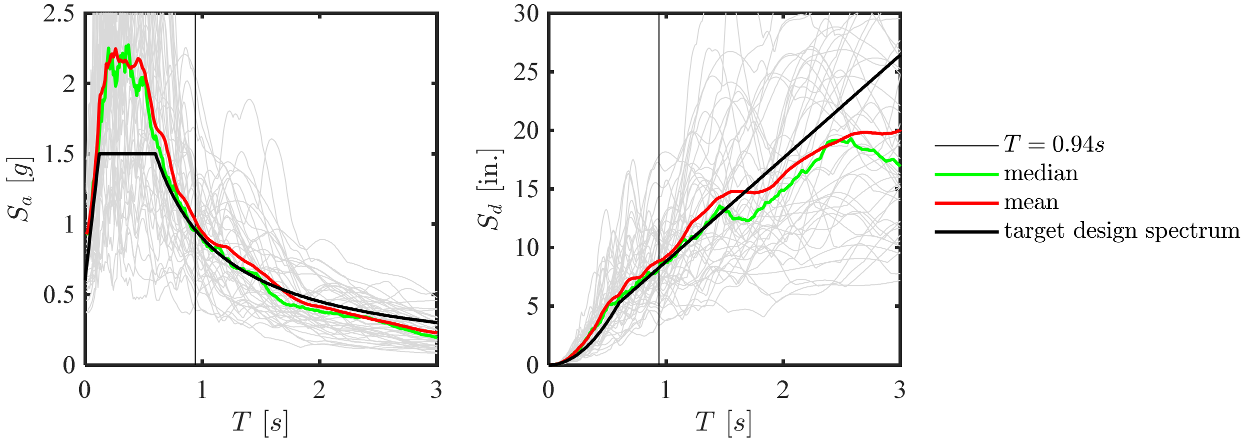

Figure 5.4. Scaled response spectra for the FEMA-P695 far-field record set.

Table 5.3. Spectral values for $SDC = D_{max}$.

Intensity	Pseudo-acceleration
S_S	1.5 g
S_1	0.6 g
S_{MS}	1.5 g
S_{M1}	0.9 g
S_{DS}	1.0 g
S_{D1}	0.6 g

5.4 DESIGN SPACE

A grid-search optimization study was conducted to explore the design space of possible reference frames. Ideally, such a preliminary design would be representative of acceptable, or benchmark, strongback behavior and would be neither over- or under-conservative. It was also expected that additional insight into the seismic behavior of strongback systems would be gained during the optimization process.

The optimization procedure was not performed in the rigorous numerical sense (i.e. in finding a global minimum solution for all possible design alternatives), but was deterministically achieved by iterating through possible W12 section sizes for the strongback braces. The beams, columns, tie, and inelastic bracing elements were fixed during this process. If the force-controlled actions of the beams, columns, and tie were not acceptable, another round of iterations for the strongback brace sizes was performed with new beam, column, and tie sizes. A design was considered "minimized" if the design was acceptable and had least-weight strongback sizes.

5.4.1 Design of Fuses and Beam-Column Elements

Inelastic braces were designed based on the design base shear calculated per the structural system description in Section 5.3.1. Typically, BRB sizes would be selected in proportion to a height-wise distribution of story shear demands to achieve a uniform demand-to-capacity ratio with building height. However, it was anticipated that some re-distribution of internal forces should be permissible with the inclusion of a strongback. To account for the plastic capacity of the strongback as an entire system, similar BRB sizes were used in every story. Thus, all four BRBs were designed with the same steel core area, A_r.

Fuses were designed in terms of the total resistance of the structure at the limit load rather than at yield. A 20% reduction factor for design base shear was used to account for increased capacity in the upper stories at the limit load due to use of the same BRB size in every story. This is similar to the 20% reduction allowed for moment re-distribution in reinforced concrete beams to account for shifts the moment diagram after yielding (Cohn, 1965; Bondy, 2003). In this sense, BRB sizes were selected based on the base shear at the ultimate capacity of the system which depends on yielding in all the fuses yielding rather than the elastic base shear capacity which depends on the strength of the first-story braces.

Since beams were deformation-controlled in flexure, flexure in the beam links was designed only for gravity loading assuming the braces below and above were not present. Shear capacity of the beam links was capacity-designed for the shear developed from plastic hinging at the beam link ends. As beam and column axial action was considered force-controlled, beam and column sizes were iteratively designed based on the compression capacity extracted from the nonlinear dynamic analyses.

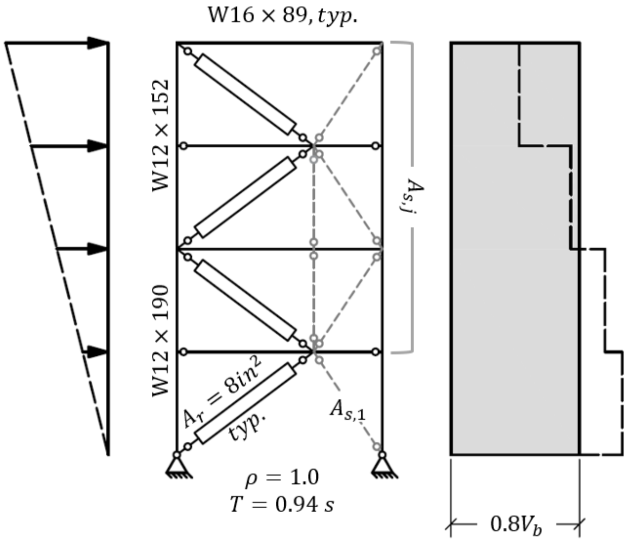

Figure 5.5. Deformation-controlled components.

5.4.2 Design of Strongback Elements

All strongback elements were iteratively designed during the optimization procedure per the dynamic capacity design procedure. A higher strongback brace-to-inelastic brace stiffness ratio would be more capable of asserting a uniform drift response. As such, the strongback brace stiffness in a story, $k_{s,j}$, was scaled with respect to the lateral stiffness of the opposite inelastic brace, k_r. This lateral stiffness was simplified to include only the lateral component of the global elastic stiffness matrix at each story:

$$k_r = \frac{QEA_r}{l_r}\left(\frac{l}{r}\right)^2 \qquad\qquad k_{s,j} = \frac{EA_{s,j}}{l_{s,j}}\left(\frac{b}{s_j}\right)^2 \qquad\qquad \text{Equation 5.7}$$

$l_r, l_s =$ yielding length of the inelastic and strongback brace, respectively. Strongback braces were also scaled by the ratio of the inelastic brace area, A_r, to the strongback brace area in a story, $A_{s,j}$. Scaling by area is similar to exploring the ratio of the strongback brace to inelastic brace stiffness, EA_s/EA_r.

The first-story strongback brace area was used as the control during the iteration process as it consistently exhibited the largest axial-force demands. To explore the distribution of the strongback brace stiffness with building height, the second-to-fourth story strongback brace areas, $A_{s,j}$, were additionally scaled with respect to the first story brace area, $\frac{A_{s,j}}{A_{s,1}}$. The same brace area was used for the strongback braces in stories two-through-four as they exhibited similar demands during the iteration process.

In summary, a grid of possible strongback brace sizes were scaled to [1] the ratio of the first-story strongback to inelastic brace lateral stiffness, $\frac{k_{s,1}}{k_r}$ and area, $\frac{A_{s,1}}{A_r}$, and [2] the distribution of the strongback brace area in the upper stories relative to the first-story strongback brace lateral stiffness, $\frac{k_{s,j}}{k_{s,1}}$, and area, $\frac{A_{s,j}}{A_{s,1}}$.

5.4.3 Objectives and Acceptance Criteria

For a strongback to meet the force-controlled objectives outlined in Table 1.1, the median probability of failure in any one of the force-controlled actions must be an acceptable ratio above the MCE intensity level. Using the procedure outlined in Section 5.2.3 and working backwards from a failure probability of 10%, a period-based ductility, $\mu \geq 8$, a spectral shape factor of $SSF = 1.45$, and an uncertainty of $\beta_{tot} = 0.525$, the numerical model must survive one-half or more of the ground motions scaled to $1.36 \times S_{MT}$ at the upper limit period, $T = 0.94\ s$. This corresponds to $CMR = 1.36$ and is similar to the suggested initial scale factor in FEMA-P695.

If the numerical model survived one-half or more of the ground motions scaled to this level, then the trial benchmark design was considered acceptable. The numerical model used during this process was described in detail in Section 4.5. Designs were considered unacceptable if any of the following occurred in the numerical model:

1. Numerical solution failed to converge,
2. Global displacements exceeded the valid range of modeling,
3. Force demands in non-simulated force-controlled actions exceeded the element capacity, or
4. Deformation demands exceeded the non-simulated deformation limits.

Axial compression in force-controlled regions were checked by limit state checks using the nominal buckling strength of the element and a resistance factor, $\phi = 0.9$. Non-simulated limit state checks of flexural deformations in beams and columns ensured modeled demands did not exceed the valid range of the numerical models; see Section 4.5.7.

5.4.4 Design Space Results

To explore the design space of possible strongback sizes, elastic brace and tie strut sizes were evaluated systematically in terms of their median peak demands for all 22 ground motion pairs scaled to the $1.3 \times MCE$-level. Median and 85th percentile results at the MCE-level were also assessed for comparison.

Global responses for the strongback system at each iteration of strongback-to-inelastic brace stiffness are shown in Figure 5.6 and Figure 5.7. Strongback axial-force demands for the resulting design space are shown in Figure 5.8 through Figure 5.13. Though other column, beam, and tie sizes were also explored, the results presented here are representative of the final round of column, beam, and tie sizes; see Figure 5.5. As trends were less apparent by the inclusion of non-simulated failure modes, results with and without non-simulated failure modes were included at the $1.3 \times MCE$ intensity level. To give these trends context with respect to a conventional system, results were additionally compared to that of a reference BRBF system.

5.4.4.1 Global Response

The peak story drift response was plotted against the strongback-to-inelastic brace stiffness (or area) ratio in Figure 5.6. Peak story drift was measured in terms of the maximum story drift ratio of all four stories, $\max \theta_j$. The peak story drift ratio decreases as the strongback brace area increases. This is representative of the strongback becoming more effective at imposing a uniform drift distribution with increasing strongback-to-inelastic brace lateral stiffness. The median drift response for the $1.3 \times MCE$-level plateaus at $\max \theta_j = 2.5\%$. This trend aligns with a plateau in the drift concentration factor. This plateau occurs when the strongback brace lateral stiffness is approximately three times larger than the inelastic brace lateral stiffness, $\frac{k_{s,1}}{k_r} = 3.3$ (or six times larger in terms of area, $\frac{A_{s,1}}{A_r} = 6.3$). This plateau was also observed in the median and 85th percentile drift response at the MCE-level. Up to this plateau, both drift measures decrease as the strongback sizes become larger with respect to the inelastic brace sizes. Drift response depends little on the ratio of the upper story strongback sizes to the first-story strongback size, $\frac{A_{s,j}}{A_{s,1}}$, unless non-simulated failure modes were included in calculations of the response.

Lateral resistance of the system was measured in terms of the ratio between the peak base shear extracted from the model, V_1, to the design base shear, V_b; see Figure 5.6. As would be expected, this quantity increased as the strongback sizes increased, indicating increasing strength and accelerations and decreasing period with increasing strongback stiffness.

Though trends were similar, non-simulated failure modes triggered flexural deformation limits in the beam links resulted in increased response quantities compared to results calculated without inclusion of the non-simulated failure modes. Lines that ended prematurely at the MCE-level of response indicate non-simulated collapse states at some 85th percentile levels.

The median peak drift profile at $1.3 \times MCE$ for the strongback design space is shown in Figure 5.7(a) for $\frac{A_{s,j}}{A_{s,1}} = 1$. For comparison, the median and 85th percentile drift profile at MCE are shown in Figure 5.7(b). With larger strongback brace area to inelastic brace area, the story drift profile becomes increasingly uniform. It is clear from these plots that a stronger and stiffer strongback, increases the system's ability to impose a uniform drift response. Note, however, that though this drift response is near uniform, it does not result in reduced drift response everywhere. Rather, the strongback results in an averaging effect that causes increased drift in the upper stories and decreased drift in the lower stories.

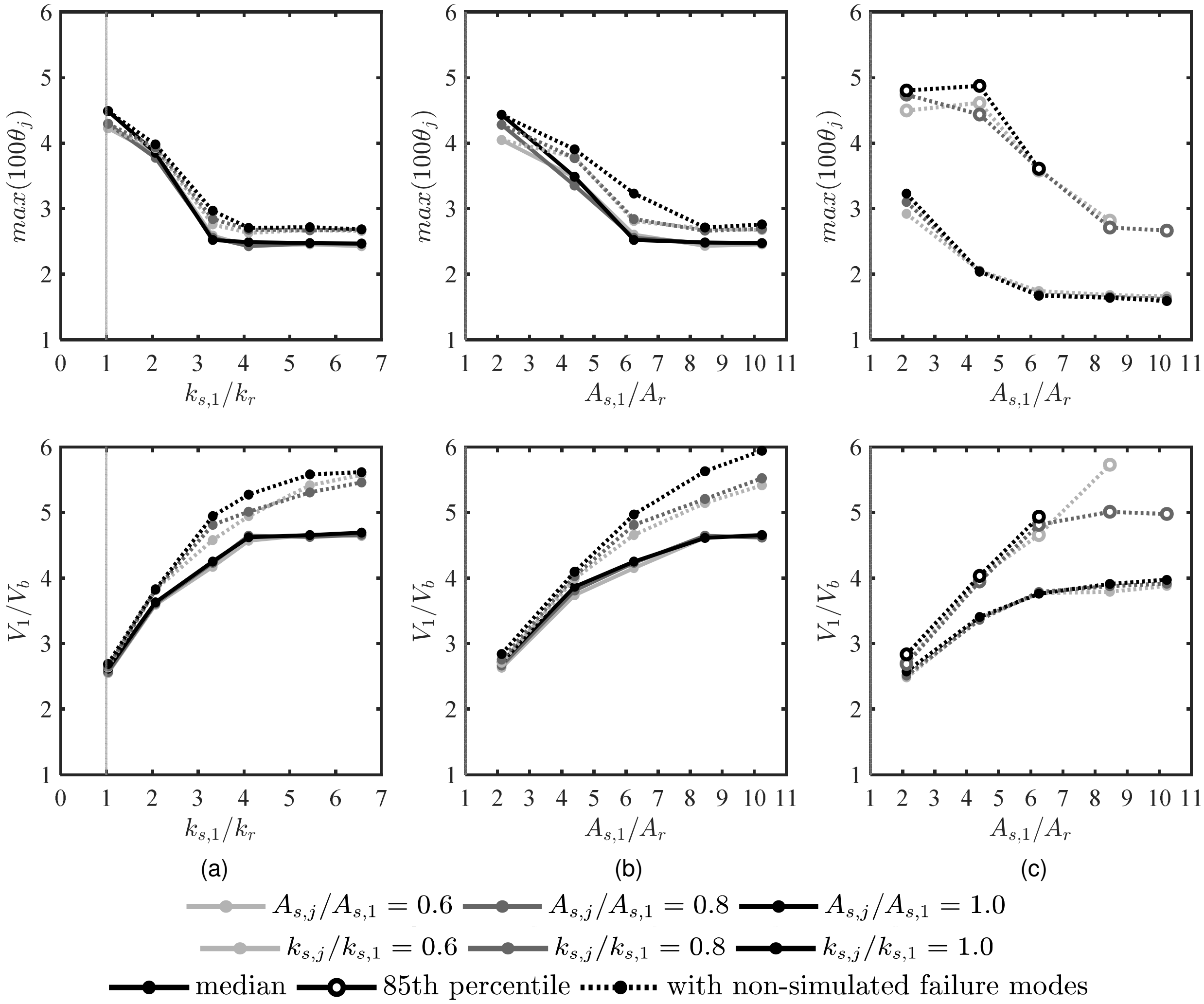

(a) (b) (c)

Figure 5.6. Global demands versus brace stiffness ratio.
(a) and (b) median global demands at 1.3 × MCE, (c) median and 85th percentile global demands at MCE.

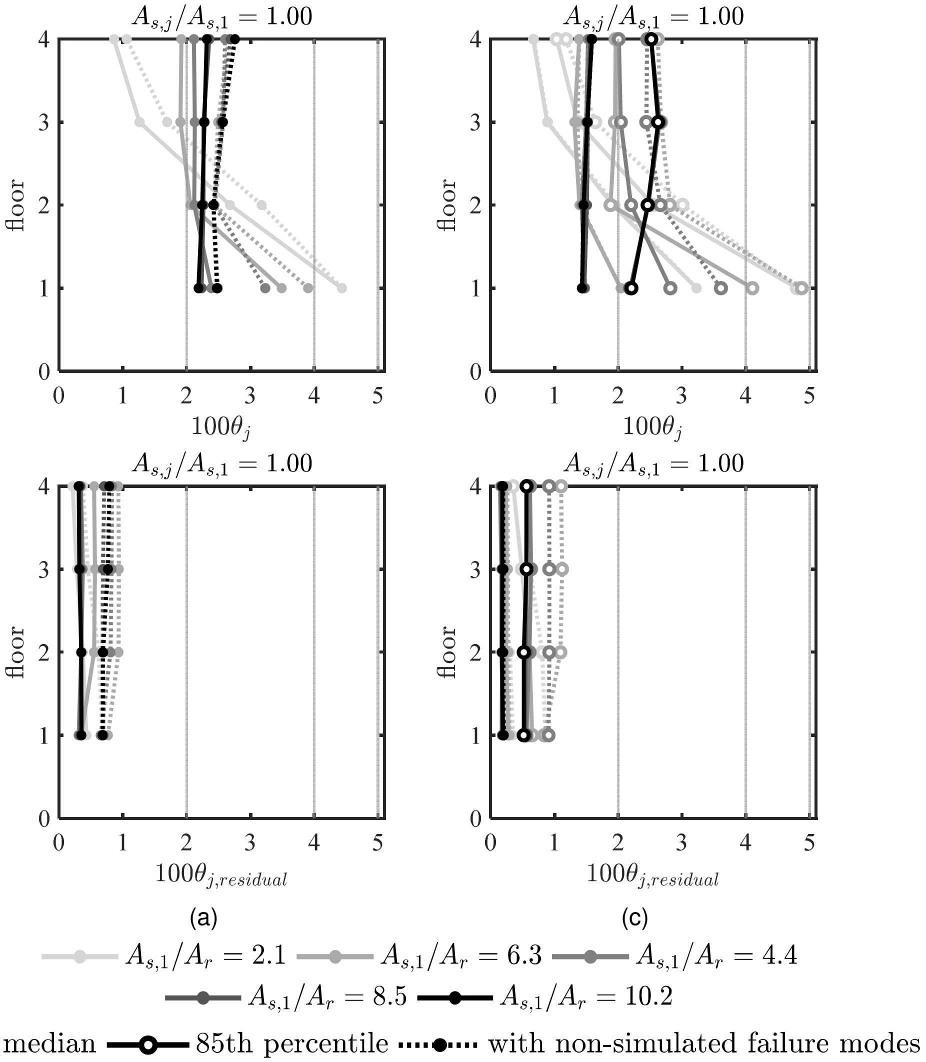

(a) (c)

Figure 5.7. Peak and residual story drift ratio profile.
(a) median global demands at 1.3 × MCE, (b) median and 85th percentile global demands at MCE.

5.4.4.2 Strongback demands

The ratio of the median strongback brace peak demand-to-capacity ratio, $P_{s,j}/P^*_{s,j}$, is shown for each story ($j = 1$ to 4) in Figure 5.8 through Figure 5.11. This demand-to-capacity ratio is plotted against both the first-story strongback-to-inelastic brace lateral stiffness and area in terms of the median response at $1.3 \times MCE$ and the 85th percentile response at MCE. Plateaus in these plots indicate that the peak strongback brace demand has reached or exceeded its buckling capacity in the numerical model. Inclusion of non-simulated collapse modes resulted in higher estimates of force demands in the strongback elements.

The compression capacity of the first-story strongback brace controlled the design of the strongback braces. An area of 8.5 times the adjacent inelastic brace area is required for the first-story brace to remain safely elastic for more than half of the ground motion pairs considered (i.e., the median $\frac{P_{s,1}}{\phi P^*_{s,1}} < 1$ for $\frac{A_{s,1}}{A_r} = 8.5$). Upper story braces can be reduced to an area of 0.8 times the first-story strongback brace area and still be acceptable (i.e., the median $\frac{P_{s,j}}{\phi P^*_{s,j}} < 1$ for $A_{s,j} = 0.6A_{s,1}$). In terms of stiffness, the strongback first-story brace lateral stiffness must be 4.1 times the inelastic brace lateral stiffness for the strongback to safely remain elastic at the $1.3 \times MCE$-level. For this $k_{s,1}/k_r$, the upper story brace stiffness can be reduced to 0.6 times the first-story strongback brace stiffness and still remain acceptable.

The demands on the tie are shown in Figure 5.12 and Figure 5.13. Tie demands tend to increase with increasing strongback brace sizes but tend to depend more on global displacements than strongback brace size. A plateau in the tie demands occurs at a similar stiffness and area ratio as the plateau observed for the story drift plots in Figure 5.6. Unlike plots of the strongback braces, these plateaus do not correspond to brace buckling.

Mitigation of drift concentration was achieved with smaller strongback brace sizes in Figure 5.6 than as indicated by the median strongback brace peak demands in Figure 5.8 through Figure 5.13. This may indicate some level of inelastic behavior in the strongback components could still result in an acceptable global response. Inclusion of non-simulated failure modes resulted in even more stringent criteria for strongback element demands with little benefit in global drift response.

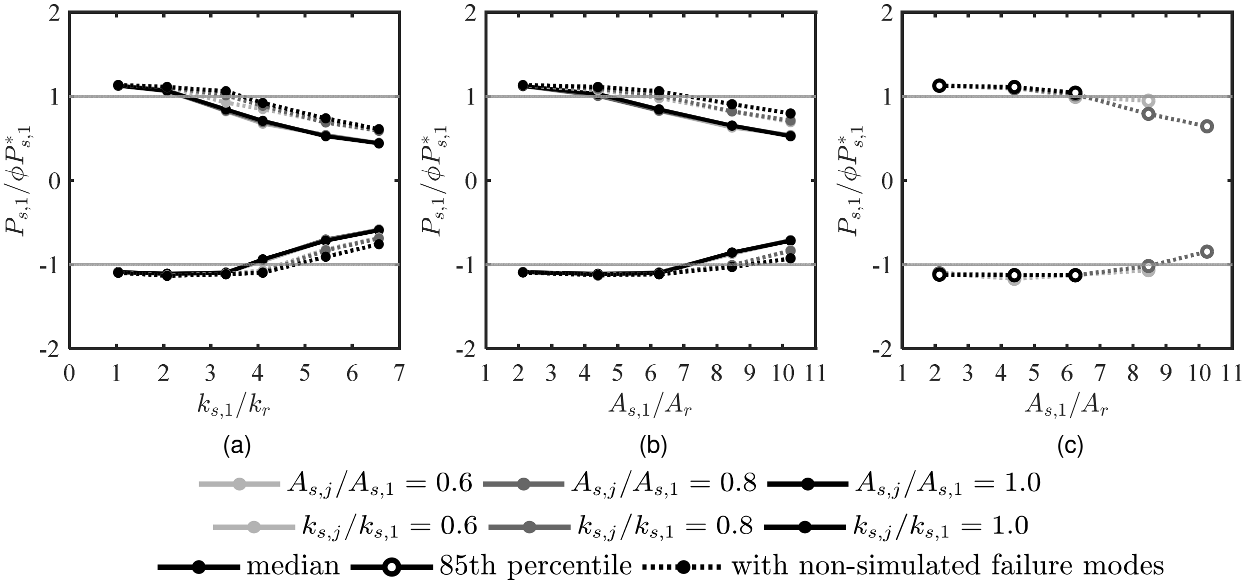

Figure 5.8. First-story strongback brace peak axial-force demands versus brace stiffness ratio. (a) and (b) median demand at $1.3 \times MCE$, (c) 85th percentile demand at MCE.

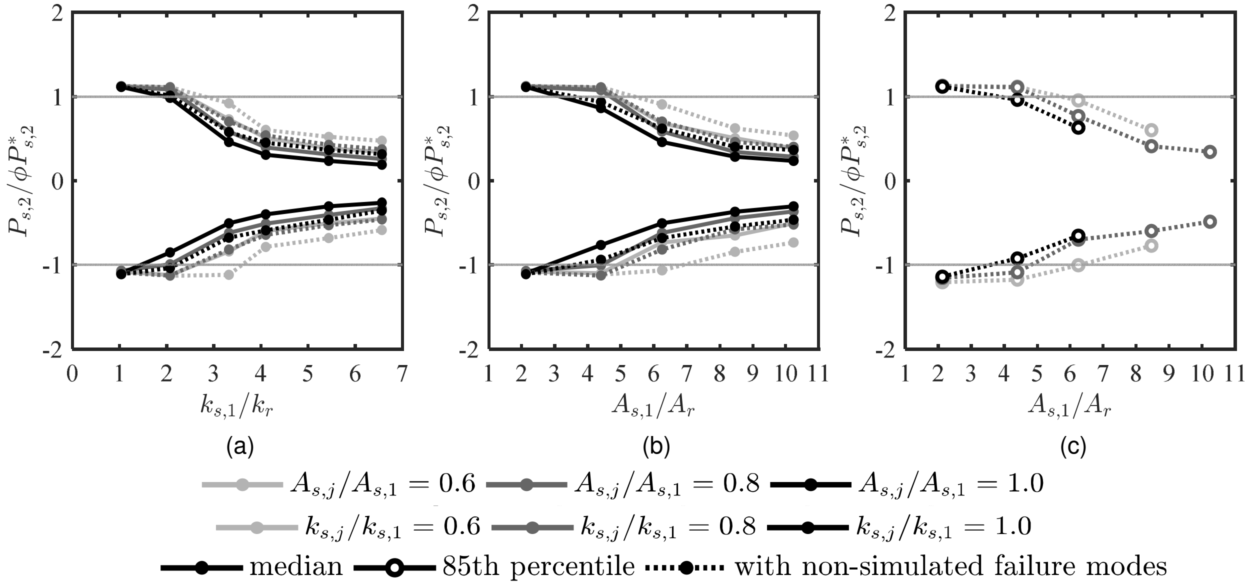

Figure 5.9. Second-story strongback brace peak axial-force demands versus brace stiffness ratio. (a) and (b) median demand at 1.3 × MCE, (c) 85th percentile demand at MCE.

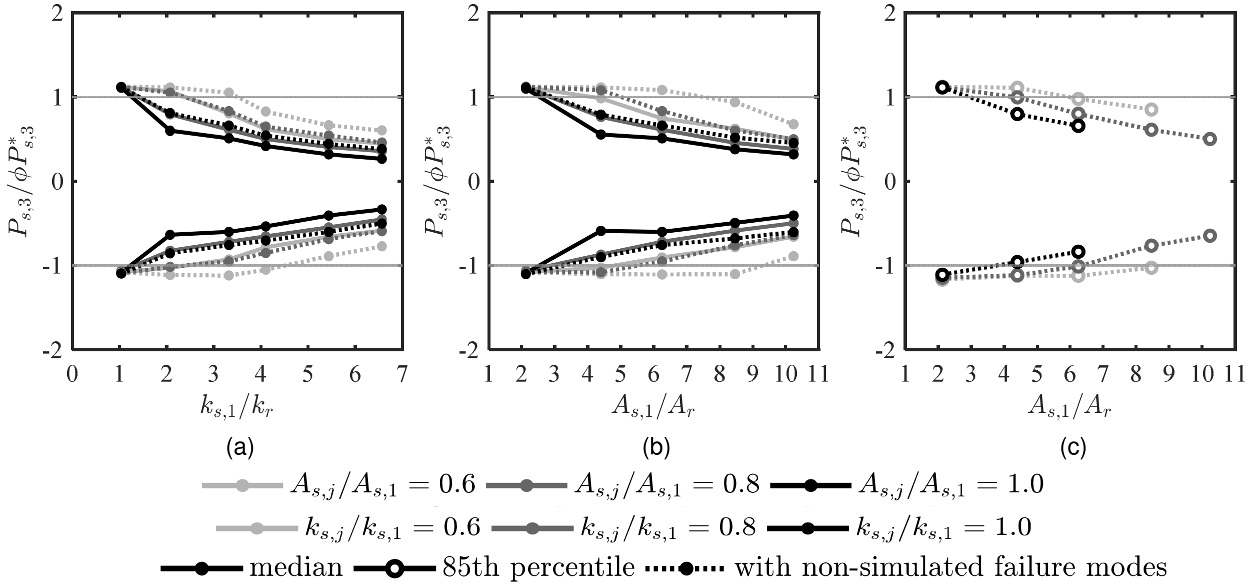

Figure 5.10. Third-story strongback brace peak axial-force demands versus brace stiffness ratio. (a) and (b) median demand at 1.3 × MCE, (c) 85th percentile demand at MCE.

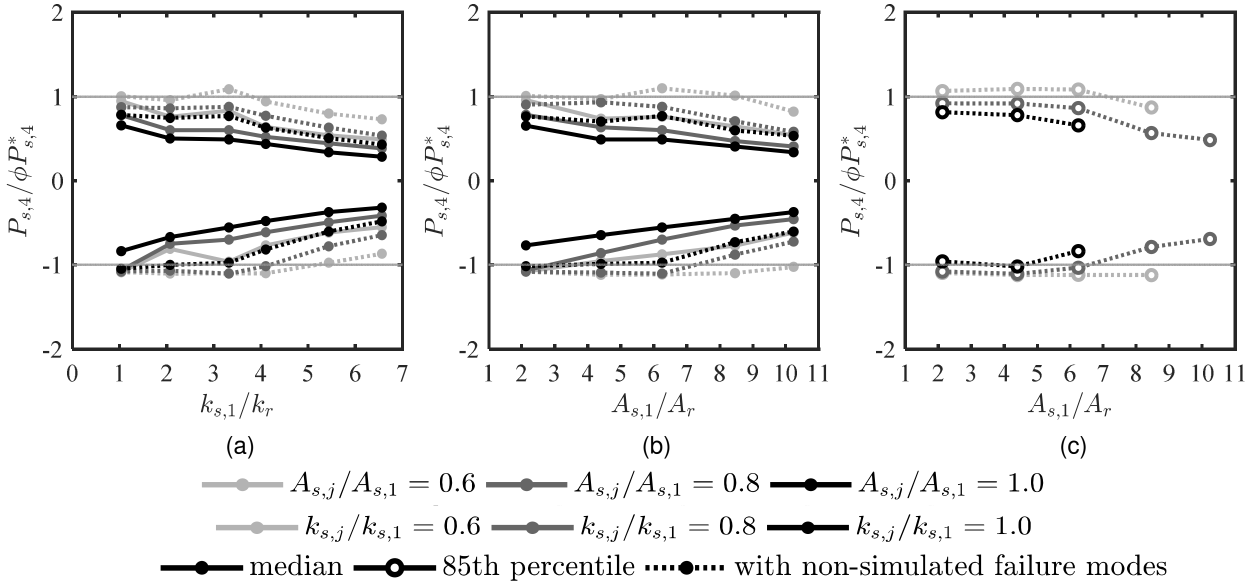

(a) (b) (c)

Figure 5.11. Fourth-story strongback brace peak axial-force demands versus brace stiffness ratio. (a) and (b) median demand at 1.3 × MCE, (c) 85th percentile demand at MCE.

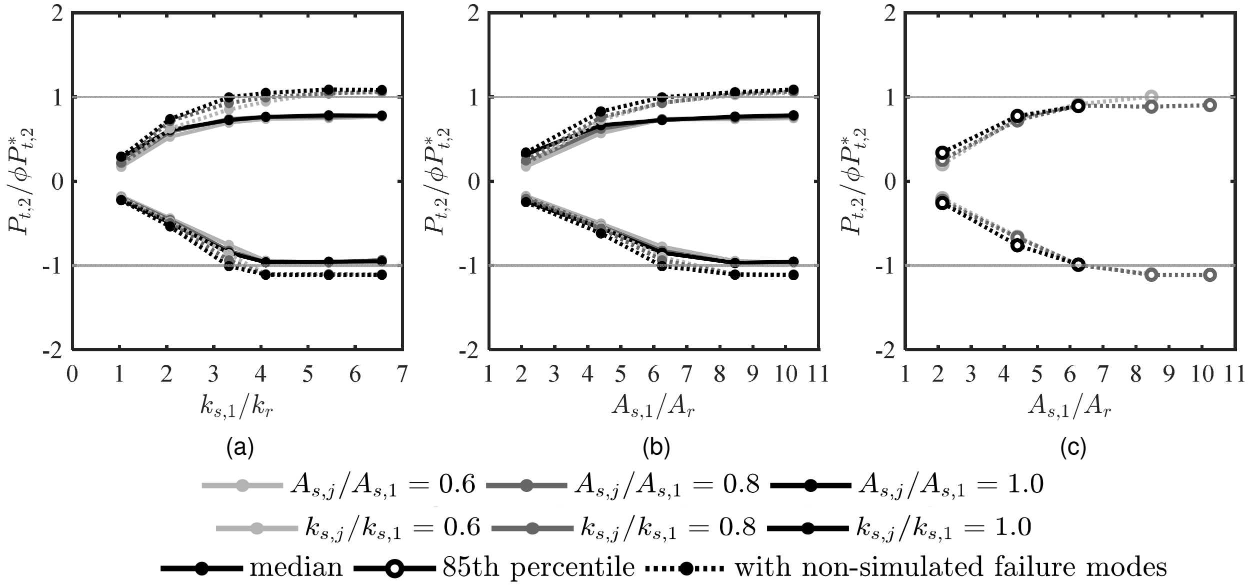

(a) (b) (c)

Figure 5.12. Second-story tie peak axial-force demands versus brace stiffness ratio. (a) and (b) median demand at 1.3 × MCE, (c) 85th percentile demand at MCE.

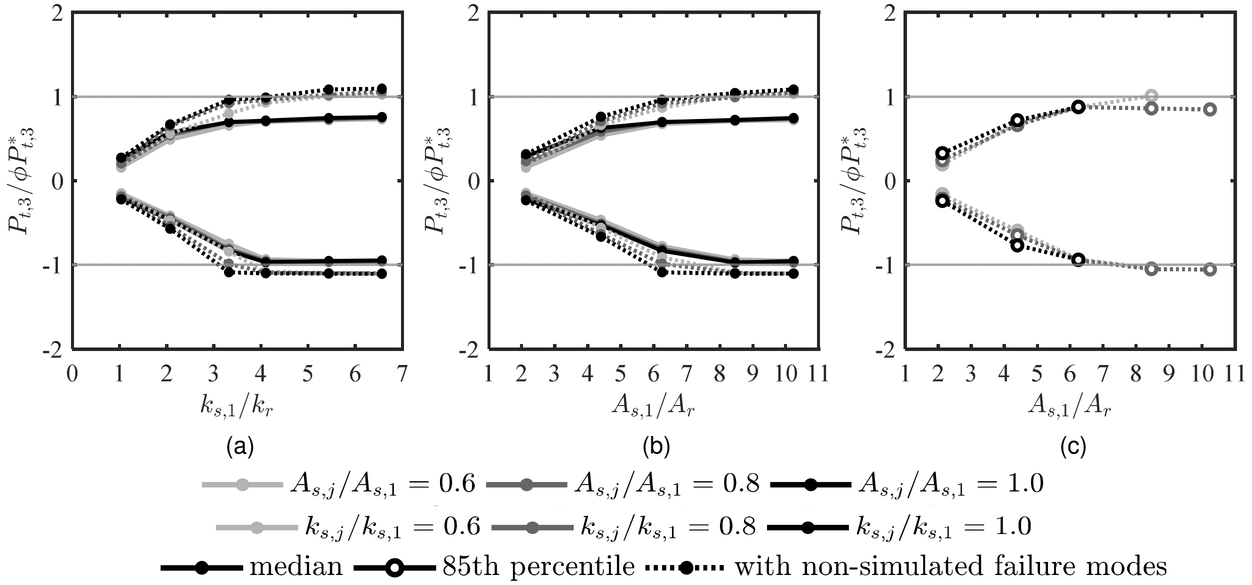

(a) (b) (c)

Figure 5.13. Third-story tie peak axial-force demands versus brace stiffness ratio. (a) and (b) median demand at 1.3 × MCE, (c) 85th percentile demand at MCE.

5.4.4.3 Comparison of SBF and BRBF response

The final minimized strongback sizes are shown in Figure 5.14(a) for the constant column, beam, and tie sizes shown in Figure 5.5. These sizes correspond roughly to $\frac{A_{s,1}}{A_r} = 7.5$ and $\frac{A_{s,j}}{A_{s,1}} = 0.6$. For the forty-four far-field ground considered, the benchmark-strongback design represents a possible design that achieves less than twenty-two instances of strongback "failure" for ground motions scaled to 1.3 × MCE intensity level. The system was additionally acceptable under the criterion of less than 10% probability of system collapse (e.g., system instability). For comparison, acceptability was also satisfied for the 85th percentile response for ground motions scaled at the MCE-level.

The plots in Figure 5.15 show the peak story drift ratio for all forty-four ground motions scaled to 1.3 × MCE (gray lines) and their median response (green line). This median was calculated including non-simulated failure modes. The median peak and residual drift responses in this plot are approximately 2.2% and 0.35%, respectively and are nearly uniform with building height.

To give the behavior of the SBF context with respect to a conventional system, a BRBF was designed and analyzed under the same suite of ground motions; see Figure 5.14(b). Note the period of vibration, T_1, for the BRBF was larger than the SBF system; see Table 5.1. Though both designs passed the collapse assessment criteria in FEMA-P695 (i.e., less than half the ground motions at 1.3 × MCE exhibited collapse), the BRBF system showed increased concentrations of drift compared to the SBF system, as exhibited by the median peak story drift ratio and drift concentration factor in the first story of Figure 5.15(b). Peak residual drifts were also larger in the first and second story in the BRBF (though they were also smaller in the third and fourth story). These results indicate increased peak drift and residual drift demands compared to that of the benchmark strongback design.

In contrast, the SBF system exhibited higher peak accelerations and story shear demands compared to the BRBF system; see Figure 5.16(a) and (b). This is especially true of the upper story envelope response, usually indicative of higher-mode contributions. The benchmark strongback exhibited a large fourth story acceleration response that is absent in the BRBF envelope. Story shears estimated from the lateral story resistance indicate entirely different height-wise distributions and are reflective of the differences in acceleration profiles for the two systems. Envelope plots including the median, 85th percentile, and 100th percentile scaled to the DE-(Design Earthquake) and MCE-levels showed similar trends; see Appendix B.

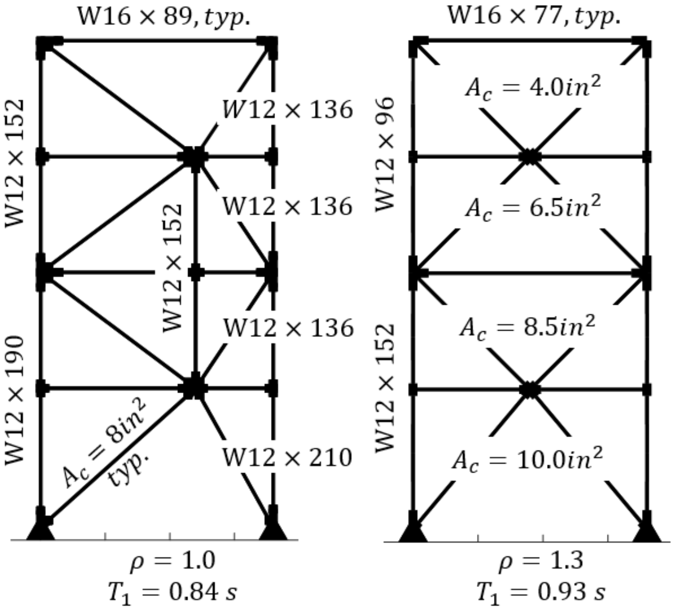

(a) (b)

Figure 5.14. (a) benchmark embedded SBF, (b) reference BRBF.

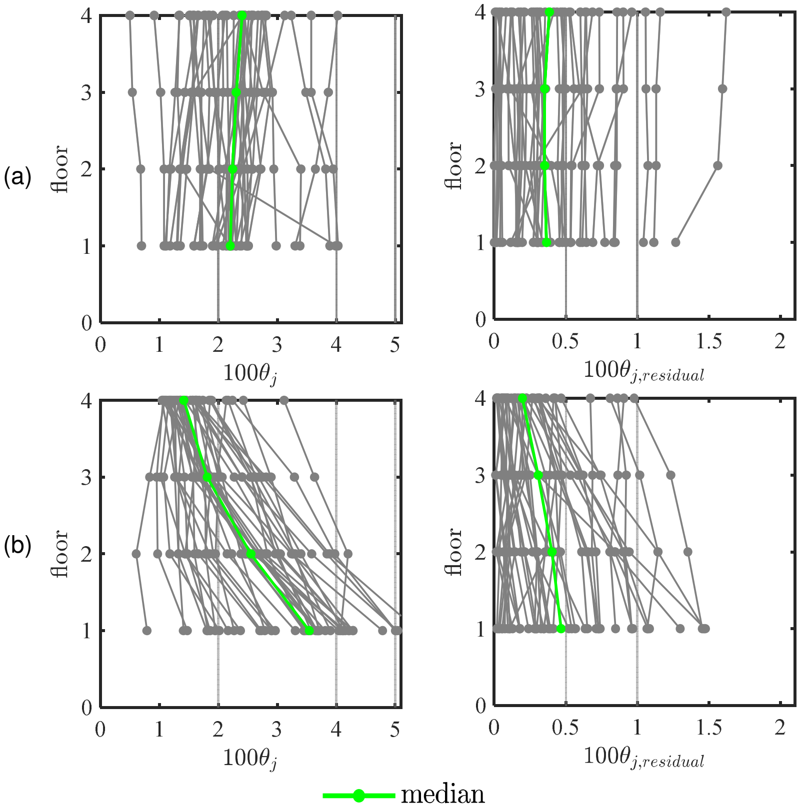

Figure 5.15. Peak drift response at 1.3 × MCE: (a) SBF and (b) BRBF

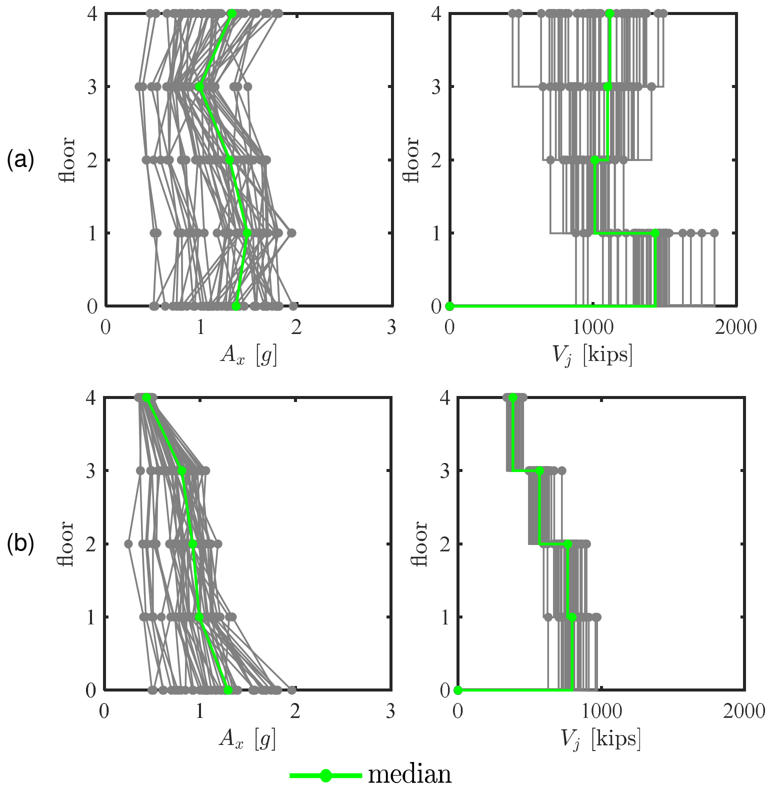

Figure 5.16. Peak acceleration, A_x and story shear, V_j, response at 1.3 × MCE: (a) SBF and (b) BRBF.

5.5 INCREMENTAL DYNAMIC ANALYSIS

The benchmark-strongback design was based on the acceptance criteria outlined in the FEMA-P695 methodology. However, this methodology was developed for collapse performance in terms of the behavior of the overall system and not the failure of individual components or elements, like those in the strongback. Though the record-to-record variability, β_{RTR}, was used to estimate the intensity level for preliminary design of the strongback, the constant β_{RTR} used in FEMA-P695 was calibrated to structural collapse and not strongback failure. Use of this methodology for strongback qualification implies that inelastic behavior in the strongback results in collapse of the system, an overly conservative assumption as this behavior mode is unlikely to result immediate collapse.

In light of these limitations, an incremental dynamic analysis (IDA) (Vamvatsikos & Cornell, 2002) was conducted to justify the assumptions used in evaluating performance of the benchmark-strongback design (e.g., assuming constant β_{RTR}). This procedure is similar to but distinct from the FEMA-P695 methodology. The IDA methodology incrementally scales a ground motion by increasing intensity until a limit state threshold is reached. The intensity associated with that threshold can be associated with demand measures extracted from the analysis. This process can be repeated for a suite of ground motions to get a distribution of intensity values that include variability in the structural response. Fragility functions can then be fit to failure data extracted from the IDA results to relate the probability of failure to a ground motion intensity.

The IDA analysis procedure was used to verify that the strongback design resulted in less than 10% probability of collapse. The IDA data was also utilized to construct fragilities for the probability of failure in any one of the strongback elements. To give these results context, comparisons were made to the collapse potential of the reference BRBF design from Section 5.4.4.3.

5.5.1 IDA Results

Results from the incremental dynamic analyses are shown in Figure 5.17. The intensity measure, S_T, represents the scaled median spectral acceleration of the normalized record set at the upper limit period. Horizontal lines in these plots represent the DBE-, MCE-, and $1.3 \times MCE$-level intensities (i.e., $\frac{S_{CT}}{S_{MT}} = \frac{2}{3}$, 1, 1.3).

Green, red, and blue lines in these plots correspond to the median, 85th percentile, and 100th percentile values at each intensity level. Dotted lines represent calculations of statistical response without non-simulated failure modes. The end of these lines represents intensities corresponding to the 50th, 85th, and 100th percentile failure-levels. If the non-simulated failure modes are neglected, the strongback system exhibited smaller peak story drifts compared to the reference BRBF at similar intensity levels, as indicated by the higher slope of the analysis lines for the SBF compared to those of the BRBF.

However, results including non-simulated failure modes indicate smaller collapse levels for the benchmark strongback compared to the reference BRBF. Black dots in these plots represent failure states triggered by non-simulated failure modes. These non-simulated limit state checks trigger failure prior to collapse simulated in the numerical model. It is apparent that the benchmark strongback exhibited numerous non-simulated failure modes that were not triggered by the reference BRBF. These were all triggered by flexural deformation limits in the beam at the tie-to-beam intersection.

Peak compression and tension demands in the strongback braces and tie are shown on the negative and positive sides of the IDA plot in Figure 5.17(c), respectively. The lower slope of the compression side of this plot indicates that compression, rather than tension, controlled demands in the strongback. Based on the intersection of the median, 85th, and 100th percentile lines with the intensity levels corresponding to DBE, MCE, and $1.3 \times MCE$, the final benchmark strongback exhibited essentially elastic behavior at each of these intensity levels.

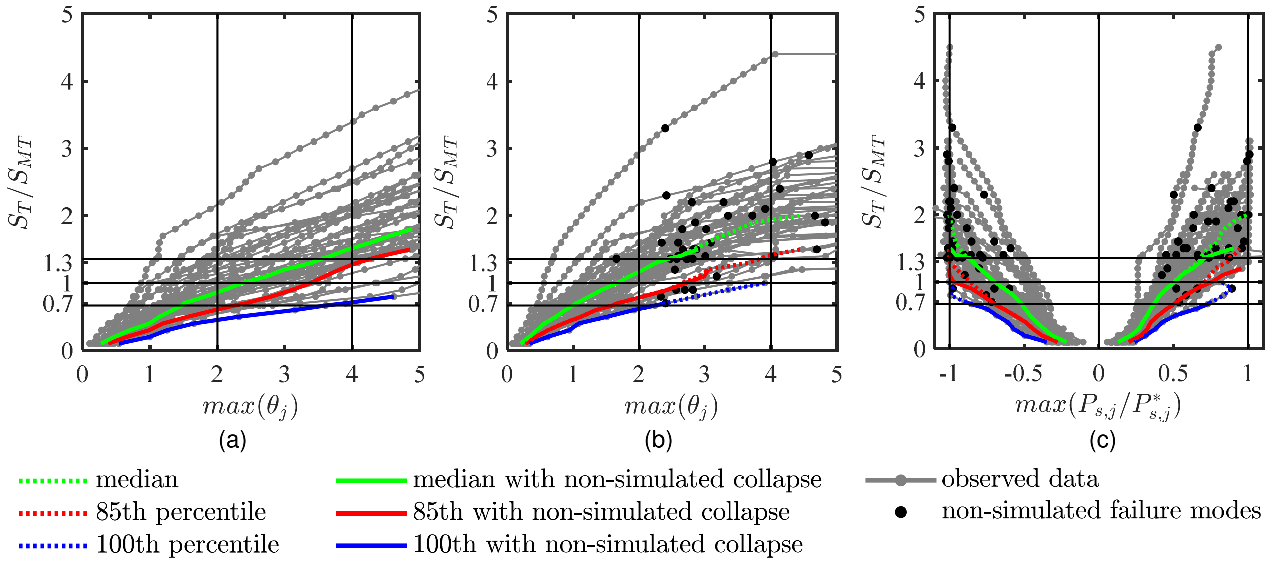

Figure 5.17. Results of incremental dynamic analyses: (a) collapse for referene BRBF, (b) collapse for benchmark SBF, and (c) failure of any one strongback element

5.5.2 Fragility curves

Fragility curves were constructed by relating increasing values of median spectral acceleration, S_{CT}, to the collapse or failure potential. Lognormal fragility functions were estimated using the methodology outlined in Baker (2014). The sample mean, $\hat{\mu}$, and lognormal standard deviation, $\hat{\beta}$, assumed a lognormal cumulative distribution function and were fit to the failure data per the maximum likelihood method.

Several fragility curves are plotted in Figure 5.18. A lognormal distribution was fit to the raw data with and without inclusion of the non-simulated failure modes. Slopes of these curves represent the record-to-record variability. Fragilities including non-simulated failure modes were adjusted to account for uncertainty due to the quality ratings per Equation 5.4. The final fragility curve was then modified by the spectral shape factor, SSF, per Section 5.2.2.1; this effectively shifted the mean of the curves to the right. Values extracted the resulting fragility curves for collapse probability and strongback failure probability are shown in Table 5.4. The estimated record-to-record variabilities were similar to the constant $\beta_{RTR} = 0.4$ used in FEMA-P695 for design of the benchmark strongback.

The red line in these plots corresponds to the failure probability at the MCE-intensity level. Both the benchmark strongback and reference BRBF exhibited less than 10% probability of collapse at the MCE-level. Without consideration of the non-simulated failure modes, the strongback benchmark showed decreased collapse potential compared to the reference BRBF. Though it was hypothesized that the addition of a strongback would result in increased collapse potential, the benchmark strongback system considered here, though still acceptable, showed increased collapse probability compared to the reference BRBF frame if the non-simulated failure modes were included in the response. The fragility curve in Figure 5.18(c) shows that the benchmark strongback successfully achieved less than 10% probability of exhibiting inelastic behavior at the MCE-level.

Note that there is a conservative bias to the collapse/failure assessment of the strongback benchmark as a number of non-simulated failure modes were not directly incorporated into the nonlinear dynamic analysis model. Alternative models including the in-cycle deterioration of the response would be better able to explicitly model collapse. Other frameworks of estimating risk, like the Conditional Scenario Spectra (CSS) methodology (Arteta & Abrahamson, 2017), could also provide more robust interpretations of strongback performance.

Table 5.4. Summary of fragility curves.

Fragility Curve	**BRBF collapse**		**SBF collapse**		**Strongback failure**	
	$\hat{\mu}$	$\hat{\beta}$	$\hat{\mu}$	$\hat{\beta}$	$\hat{\mu}$	$\hat{\beta}$
observed data	1.89	0.29	2.08	0.27	1.38	0.44
including non-simulated failure modes	1.89	0.29	1.64	0.31	1.26	0.31
including quality rated uncertainty	1.89	0.45	1.64	0.47	1.26	0.46
adjustment for spectral shape	2.73	0.45	2.38	0.47	1.82	0.46

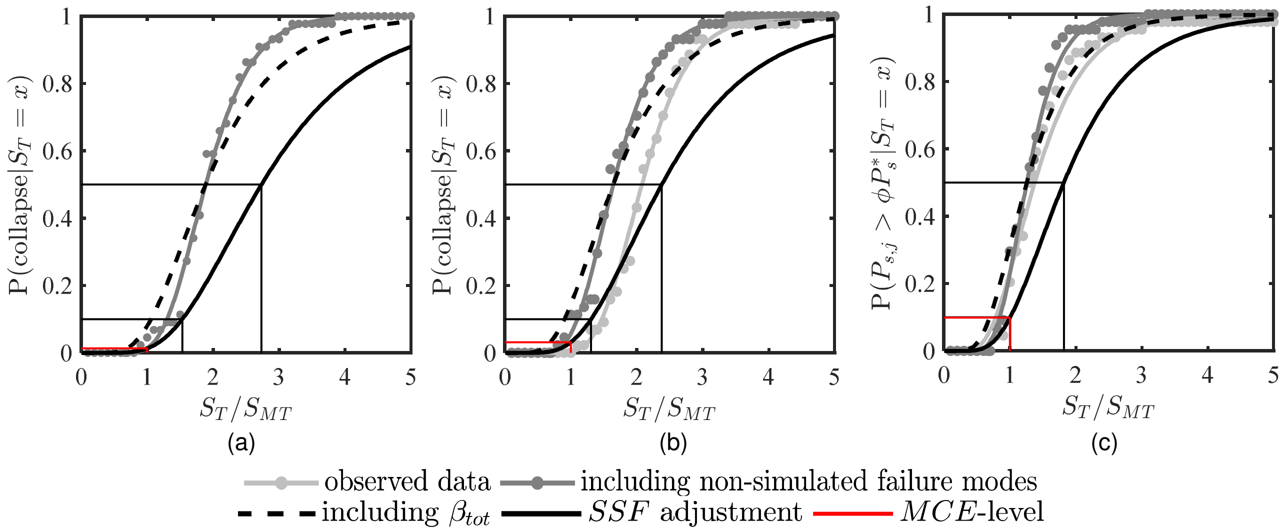

Figure 5.18. Fragility curves: (a) collapse for reference BRBF, (b) collapse for benchmark SBF, and (c) failure of any one strongback element

5.5.3 Beam Link Deformations

In light of the non-simulated limit state triggered in the beam links, the incremental dynamic analysis was repeated for the following strongback-braced frame designs:

i. The benchmark SBF but with fully pinned beam links representing connection regions with larger deformation capacity.

ii. A hybrid BRBF-SBF that separates the strongback from the inelastic brace bay; see Figure 5.19. Incremental dynamic analysis for this design was conducted using both continuous and fully pinned beam links.

Rotational demands in the pinned beam links were checked through deformation limit checks assuming shear tab details at the beam link ends. The IDA results and corresponding fragility curves are shown in Figure 5.20 and Figure 5.21. The collapse probabilities and strongback failure probabilities are tabulated for the BRBF, embedded SBF, and separated SBF configurations in Table 5.5.

With the pinned beam links, the SBF exhibits near-zero collapse probability. The probability of inelastic behavior in the strongback is also reduced. The pinned beam links delayed triggering of the non-simulated limit states to peak story drift ratios from near 2.5% to above 4%. This is primarily due to the increased rotational capacity of the beam links. Note that the pinned beam links remove some of the back-up redundancy of the secondary system and could result in potentially smaller reserve capacity if the strongback braces buckled.

Removal of the strongback bay to an adjacent bay reduced the ductility demands on the inelastic braces but did not address the rotational demands in the beam links. A modified model with pinned beam links resulted in near zero-collapse probability and reduced probability of strongback failure to 1.3% at the MCE-level. The separated SBF configuration with pinned beam links exhibited the lowest collapse potential out of the BRBF and SBF designs. Note that if the strongback braced buckle in an SBF configuration, the system reverts to a near-conventional BRBF.

Table 5.5. Failure probabilities.

Failure Probability	**BRBF**	**Benchmark SBF**		**Separated SBF**	
		continuous beams	pinned beam links	continuous beams	pinned beam links
collapse probability at MCE-level	1.3%	3.2%	0.5%	4.4%	0.3%
strongback probability at MCE-level	-	9.8%	7.0%	5.0%	1.3%

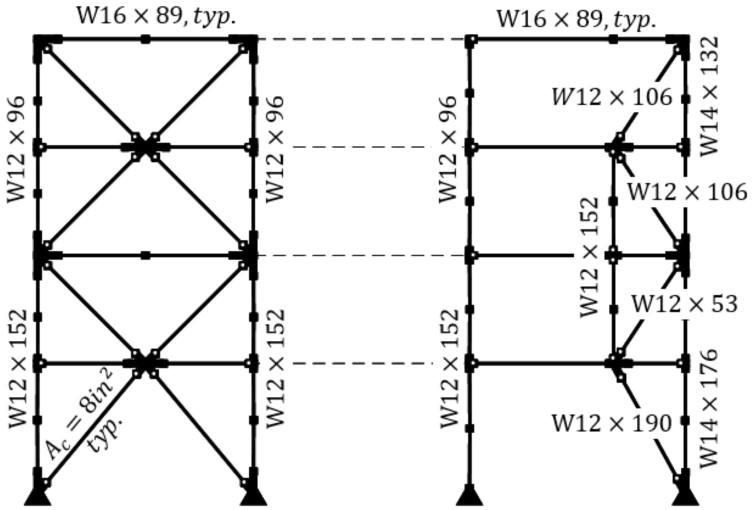

Figure 5.19. Modifed design: (a) separated SBF.

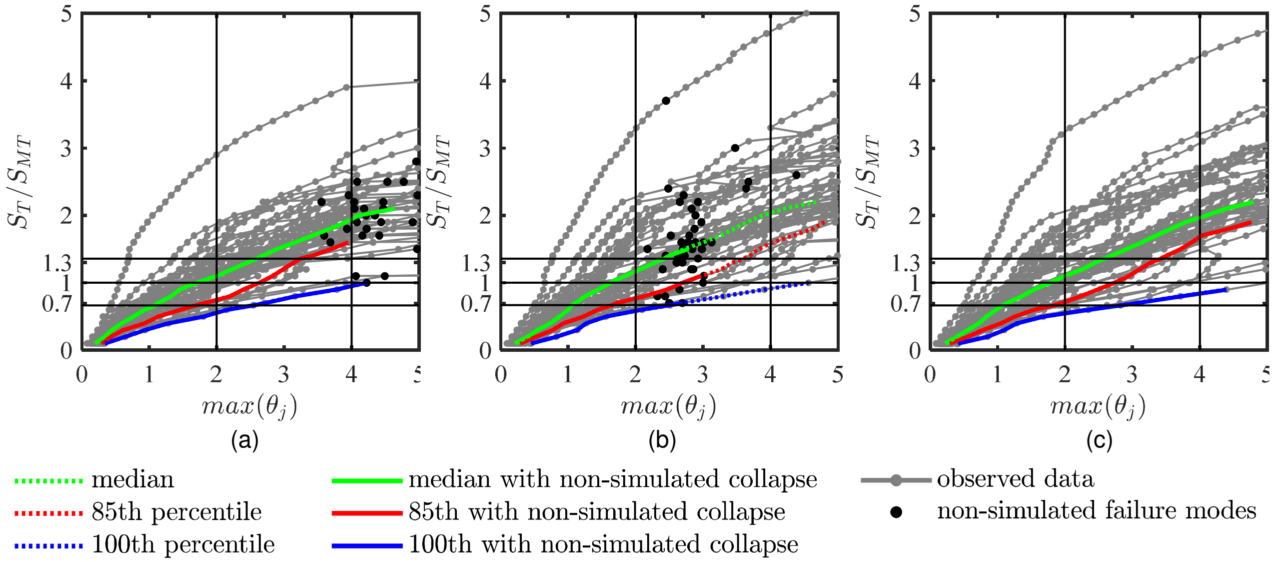

(a)

(b)

(c)

Figure 5.20. Results of incremental dynamic analyses: (a) embedded SBF with pinned beam links, (b) separated SBF, and (c) separated SBF with pinned beam links.

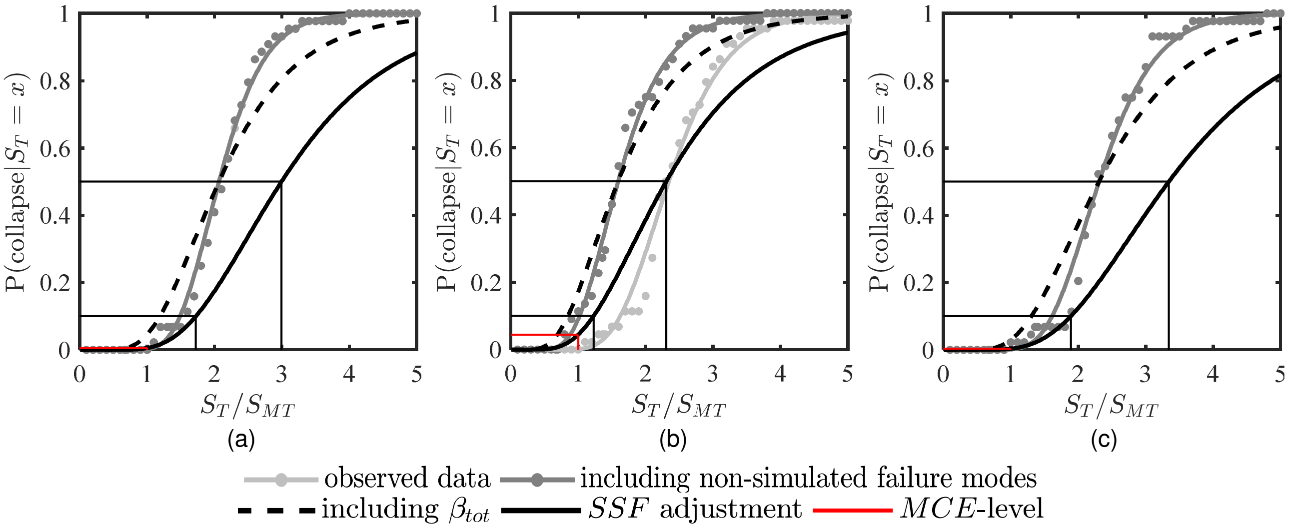
(a) (b) (c)

Figure 5.21. Fragility curves: (a) embedded SBF with pinned beam links, (b) separated SBF, and (c) separated SBF with pinned beam links.

5.5.4 Limitations of FEMA-P695

The following limitations were recognized in using FEMA-P695 to evaluate the strongback's response:

- Use of this methodology for strongback qualification implies that inelastic behavior in the strongback results in collapse of the system, an unnecessarily conservative assumption as this damage mode has energy dissipation capacity. The methodology also ignores the influence of secondary systems, like the reserve strength from gravity beam-column connections and nonstructural components and the impact of varying degrees of irregularity.
- Collapse simulation is a detailed, data-intensive process with a high degree of uncertainty. Values for uncertainty are based on judgement. As the FEMA-P695 methodology was intended to apply broadly to all buildings, it incorporates a variety of simplifying assumptions.
- The numerical model used in the nonlinear dynamic analyses was described in detail in Section 4.5. As noted in that section, the softening response of to the beam-column elements was not explicitly considered. Though these failures were accounted through non-simulated limit state checks, they resulted in a conservative bias in assessing strongback collapse performance. Models with pinned beam links circumvented this issue, but the incorporation of numerical models that include axial-flexural interaction and in-cycle softening response would provide further estimates of the SBF's collapse performance.
- Though utilized herein as the standard for the state-of-practice, FEMA-P695 is inadequate for evaluation of archetypes whose failure response is dominated by higher-mode effects, like that of the strongback system. Over-estimation of the ground motion intensity at the higher-mode periods due to ground motion scaling near the fundamental period is ignored by the methodology. Inclusion of higher-mode response may be critical for characterization of the force demands in the force-controlled actions.

- Use of the far-field record set provided by FEMA-P695 does not appropriately reflect the shape of the response spectrum. Since the higher-mode response of the strongback can be critical, a more robust ground motion selection procedure that is better able to represent the response at the higher-mode periods may be important in evaluating the strongback's collapse performance. The most direct approach to account for spectral shape would be to select a unique set of ground motions that have an appropriate shape for each site, hazard level, and structural periods of interest. Conditional mean spectra conditioned on the first three periods, for example, may be a more suitable method of selecting ground motions to characterize the strongback's dynamic response.

5.6 CONCLUSIONS

A benchmark strongback-braced frame was developed to initiate the design development process. The benchmark-strongback design was the result of an iterative dynamic capacity design procedure. The FEMA-P695 methodology was used to estimate the probability of inelastic behavior in any one of the strongback elements. Based on an acceptable 10% failure probability, a design space of possible strongback element sizes was developed and validated in terms of probability of exceedance at the MCE-level. A deterministic grid-search optimization study revealed the following:

- A stronger and stiffer strongback increases the SBF's ability to impose a uniform drift response. Note, however, that the addition of the strongback averages the drift profile, resulting in increased drifts in some stories and decreased drifts in other stories.
- Adequate drift response can still be achieved even when the strongback elements buckle, indicating that smaller strongback element sizes could still achieve an acceptable global response. For example, strongback sizes with areas of 8.5 times the inelastic brace area and 4 times the inelastic brace stiffness were needed for the strongback braces to remain elastic while strongback sizes with areas of 6.3 times the inelastic brace area and 3.3 times the inelastic brace stiffness were needed for drift control.
- For the benchmark configuration studied in this chapter, the first-story strongback brace experienced the largest strongback demands. Upper story brace sizes could be reduced to 0.6 times the first-story strongback brace stiffness and area and still be effective.
- Though all the archetype designs passed the collapse assessment criteria in FEMA-P695, a reference BRBF system showed increased concentrations of peak and residual drift compared to the SBF benchmark design. In contrast, peak accelerations were larger for the benchmark strongback than the reference BRBF.
- A reference BRBF system exhibited comparable – if somewhat lower - collapse potential to the SBF benchmark design with continuous beams. This design triggered collapse through non-simulated flexural deformation limits in the beam links. This collapse mode was not modeled in the numerical simulation, and it is unclear whether these results are biased by the inclusion of these non-simulated limit states. Triggering of this limit state emphasizes the significant ductility demands that can develop in the beam links. Designs utilizing pinned beam

links and separated strongback configurations exhibited near-zero collapse probability in increased collapse performance compared to the reference BRBF.

6 Parametric Study of Design Alternatives

6.1 INTRODUCTION

Previous numerical studies and one experimental test revealed a number of practical design concerns for strongback-braced frames (Simpson & Mahin, 2018b), especially with regards to the large deformation demands that can develop in the fuses due to the kinematic response of the strongback truss. These induced deformations were described in detail in Chapter 3 and impacted the strongback's collapse performance in Chapter 5. Appropriate design methods for strongback-braced frames depend on being aware of possible design alternatives and their impact on the strongback's behavior.

The benchmark four-story strongback-braced frame developed in Chapter 5 was used to systematically study the effects of different design alternatives on the strongback's dynamic, inelastic response. Several cases of design alternatives, including ground motion selection and detailing conditions, are considered for the parametric study. General conclusions are drawn regarding the relative impact of design alternatives on the behavior of strongback-braced frames.

6.1.1 Cases Considered

Changes in different boundary condition parameters can result in changes to the system's dynamic response. This chapter focuses on sensitivity of the response to design alternatives and ground motion selection. A case study considering one ground motion was used to characterize the following design alternatives:

1. *Case 1:* ground motion selection
2. *Case 2:* beam end connections
3. *Case 3:* column base fixity and column bending orientation
4. *Case 4:* beam composite action and diaphragm rigidity
5. *Case 5:* strongback brace and tie connection conditions

A second parametric study then investigated the median response quantities of the above cases under the far-field suite of ground motion records described in Section 5.3.2. The following additional cases were included in this second statistical study:

1. offset of the brace-to-beam intersection

2. height-wise distribution of inelastic brace size in BRBFs and SBFs

Except where indicated, cases were compared to the finalized benchmark design in Figure 5.14(a) using the numerical model described in Section 4.5.

6.1.2 Response Quantities

The response quantities used for studying behavior in this chapter include:

1. Peak inelastic brace strain and axial demand, ε_r and P_r
2. Peak strongback brace and tie axial demand, $P_{s,j}$ and $P_{t,j}$
3. Peak beam moments and axial demand, $M_{b,r}$ or $M_{b,s}$ and $P_{b,r}$ or $P_{b,s}$
4. Ratio of beam deformation to acceptability limits from Section 4.5.7, $\mu_{b,r}$ and $\mu_{b,s}$
5. Peak column moments and axial demand, $M_{c,r}$ or $M_{c,s}$ and $P_{c,r}$ or $P_{c,s}$
6. Peak story drift ratio, θ_j
7. Peak residual story drift ratio, $\theta_{j,residual}$
8. Drift concentration factor, $DCF = max(\theta_j)/\theta_R$
9. Peak absolute horizontal acceleration, A_x
10. Peak story shear, V_j
11. Deflected shape, bending moment diagram, and axial force diagram at peak story shear
12. Deflected shape, bending moment diagram, and axial force diagram at peak drift ratio

$j =$ story, $R =$ roof level, $(\cdot)_s =$ strongback element designation, $(\cdot)_r =$ fuse designation. The system's tendency for drift concentration, or drift concentration factor, is represented by the ratio of the maximum drift response in all the stories, $max(\theta_j)$, with respect to the average or peak roof drift ratio, θ_R (MacRae et al., 2004; Ji et al., 2009; Chen & Mahin, 2012):

$$DCF = \frac{max(\theta_j)}{\theta_R} \qquad \text{Equation 6.1}$$

The maximum DCF taken over all stories represents the tendency of the system to form a story mechanism. The larger the drift concentration factor, the higher the system's tendency to concentrate drift demands. A DCF of 1.0 represents a uniform drift distribution over the building height. This factor was used to determine the structure's potential for non-uniform lateral displacements and to identify the magnitude and uniformity of inelastic demands on the strongback system.

6.1.3 Response Envelopes

Peak response envelopes are plotted over building height and are overlaid to emphasize the effect of different cases on the response quantity of interest. For some design alternatives, plots show the demand-to-capacity ratio using $(\cdot)^*$ to indicate whether an element exhibited inelastic behavior. To condense information into a single plot, moment plots show $(\cdot)_r$ quantities on the negative side of the plot and $(\cdot)_s$ quantities on the positive side of the plot. The sign change indicates whether the data is from the inelastic or elastic portion of the frame and does not indicate the sign or direction of the moment demands. The designation mid-beam is a misnomer and refers to the location of brace intersection between the beam ends, which may be offset from the beam centerline; see Chapter 3. Plots of axial force show peak tensile demands on the positive side of the plot and peak compressive demands on the negative side of the plot. Note that some information is lost in comparing response envelope rather than response history plots.

"Snapshots" of the deflected shape, moment diagrams, and axial force diagrams were taken at the time instant of peak story drift and peak story shear; for example, see Figure 6.9 and Figure 6.10. Additional demand-to-capacity plots to the far right of these figures highlight those elements most engaged in lateral force-resistance during that snapshot in time. Yellow elements are above their flexural or axial strength capacity. Those elements in violet have demands less than 50% of their strength capacity. Other colors represent the gradient in color scale between violet and yellow (i.e., between > 50% to < 100% the element strength capacity). These plots are intended to visually display distributions of demands and do not include axial-flexural interaction.

6.2 CASE STUDY

Ideally, this parametric study would account for variability by considering the mean (or median) and coefficient of variation (COV) of a response quantity subjected to the entire suite of far-field ground motions. The computational time and additional amount of data required for such a parametric study, however, makes in-depth analysis and understanding of the behavioral characteristics under each ground motion difficult. Moreover, means and medians can result in smoothed response quantities, making it challenging to distinguish differences in behavior as design alternatives result in similar response quantities "on average"; see plots in Appendix D.

Thus, the response results for the four-story parametric study presented herein were initially described in terms of a case study for one of the records, gm44. This record was selected for: [i] its close spectral proximity to the target design spectrum around the fundamental period of the four-story benchmark design; [ii] its reasonable amplification of higher-mode effects compared to other ground motions in the far-field record suite; and [iii] its similarity to response quantities representing the median response calculated using the full far-field record set. Statistical evaluation of the seismic response was then conducted in Section 6.3 with more in-depth knowledge of the relation between certain design alternatives and the strongback's seismic response. Member sizes were kept constant irrespective of design alternative to isolate the impact of the chosen design alternative on the structure's response. Additional envelope plots for each case study under gm44 can be found in Appendix C.

The gm44 record was recorded at the Tolmezzo receiving station during the 1976 Friuli, Italy earthquake. This record was scaled by a factor of 3.6 to match the MCE-level target design spectra at the upper design period, T. The median and mean response spectra for the far-field record suite are shown in Figure 6.1. The response spectra for gm44 is overlaid for comparison purposes. From these figures, it can be observed that gm44 matches the elastic response spectra well at the fundamental period, T_1, but over-estimates the response in potential higher modes like at the second period, T_2. To properly account for these higher-mode effects, the design spectrum for the benchmark frame was modified to the dotted line shown in Figure 6.1 ($S_s = 2.09g$ and $S_1 = 0.63g$). Though record gm44 still exhibits spectral accelerations above this modified design spectrum, this amplification highlights the higher-mode contributions to the response quantities of interest and was considered reasonable for this parametric study. These higher-mode effects are elaborated on in more detail in Section 7.5.4.2.

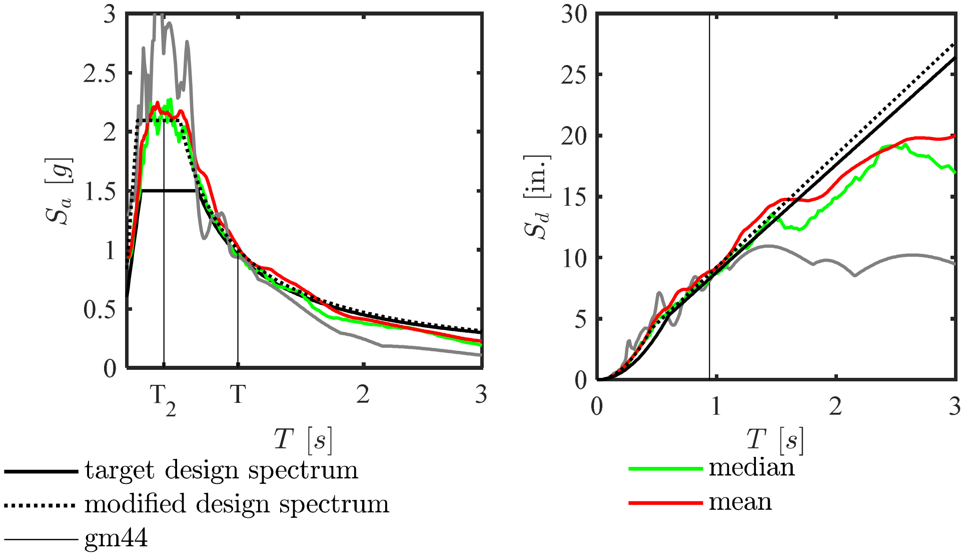

Figure 6.1. Characteristics of ground motion 44 (gm44).

6.2.1 Case 0 – Benchmark Response

To emphasize the difference between responses due to varying design alternatives and that of the benchmark design, this section will present a general description of the behavior of the benchmark frame. The response of the benchmark frame to gm44 is represented by the solid black line in Figure 6.4 through Figure 6.10.

The axial strain and axial force envelope for the inelastic braces under gm44 was nearly uniform, indicating similar peak demands for all four inelastic braces; see Figure 6.4. Axial-force demands were largest on the first and fourth story strongback braces; see Figure 6.5(a). This is indicative of higher-mode contributions, which tend to affect the forces in upper stories more than lower stories (Chopra, 2011). Axial-force demands were largest for the fourth story strongback brace and are close to the buckling load; see Figure 6.5(b). Tie demands were similar in both tension and compression demands; see Figure 6.5(c).

End-beam moments in the strongback, $M_{b,s}$, were relatively small compared to the mid-beam moments and end-beam moments of the beam link in the inelastic portion of the system, $M_{b,r}$; see Figure 6.6(a). The beam link exhibited flexural yielding at both ends. Peak moments at the ends of the roof beam tended to be smaller than beam moments at other floors, consistent with the lack of vertical motion that would have occurred had the roof beam had a brace-to-mid beam intersection. Beam axial-force demands were near or below 20% of their axial strength capacity, indicating the beams are primarily operating in flexure; see Figure 6.6(b). Beam deformation demands were in the acceptable range of the model. These demands were near zero for the strongback portion of the beams and largest for the beam links; see Figure 6.6(c).

Column bending moments tended to be largest near the top of the column where the beam column connection was modeled as partially restrained; see Figure 6.7(a). Flexural demands at the column base were negligible, consistent with the pinned column base. Axial-force demands were on average 3.8 times larger in tension and 2.2 times larger in compression in the strongback column than the inelastic column; see Figure 6.7(b) and (c). This stems from the larger demands delivered to the columns by the strongback braces compared to the inelastic braces.

Peak story drift ratios were nearly uniform, but showed some larger drift demands in the upper stories; see Figure 6.8(a). Residual drifts were approximately 0.18%, and indicated a nearly uniform distribution of drift with story height; see Figure 6.8 (b). The benchmark design tended to concentrate drifts in the fourth story during gm44, the location of the largest DCF, see Figure 6.8(c). Higher-mode contributions were apparent in the upper story shear envelopes; see Figure 6.8(e). Accelerations were to some extent uniform with building height; see Figure 6.8(d).

The benchmark frame showed complete engagement of the inelastic braces at the time of peak story shear, but only partial engagement of the upper level inelastic braces at the time of the peak story drift ratio; see the yellow color of the inelastic braces in Figure 6.9(d) and Figure 6.10(d). This and the displaced shape indicate that the upper story strongback elements may be most engaged when demands are non-uniform and the strongback exhibits "bending"; see the light blue color of the third and fourth story strongback braces in Figure 6.9(d) compared to the first through third story strongback braces in Figure 6.10(d).

In summary of the benchmark response:

1. Axial strain and axial force are similar for all four inelastic braces under gm44.
2. Strongback demands tend to be largest for the first- and fourth-story strongback braces under gm44.
3. The bending moment envelope indicates the beam link ends have yielded. Beam axial-force demands are near 20% of the beam axial strength.
4. Column moment demands tend to be large near the top of the column where the beam-column connection is partially restrained and reinforced by a gusset plate. Axial-force demands in the strongback column are significantly larger than in the inelastic column.
5. Peak and residual drift ratios are nearly uniform. Plots of the drift concentration factor illustrate a tendency for the benchmark design to form a story mechanism in the fourth story under gm44.
6. The peak story shear demands occur in the first and fourth story, illustrating higher-mode contributions to the upper story shear response. The profile of absolute accelerations is nearly uniform with a pinched response at the third-floor level.

6.2.2 Case 1 – Ground Motion Selection

It is important to identify which response quantities are sensitive to the characteristics of the ground motion. Case 1 investigated three additional ground motions. This comparison included ground motions with larger spectral pseudo-accelerations in the first mode (gm1), larger spectral pseudo-accelerations at the higher modes (gm13 and gm44), and longer duration of strong amplitude shaking (gm10).

The modified design spectrum is overlaid with the response spectra for gm1, gm10, gm13, and gm44 in Figure 6.2. The T_1 and T_2 labels represent the elastic first- and second-mode periods from an eigenvalue analysis of the benchmark design. The selected ground motions vary widely in pseudo-acceleration values at both the fundamental and higher-mode periods. The four selected ground motions also vary in amplitude, duration, and general appearance; see ground acceleration history plots and information on magnitude, fault type, site class, and the horizontal component of acceleration [e.g., fault normal (FN) or fault parallel (FP)] in Figure 6.3.

Envelopes of the peak response quantities are shown in Figure 6.4 through Figure 6.8. Axial strains in the inelastic braces were by far largest for gm10, the ground motion with the largest duration of strong amplitude shaking; see Figure 6.4(a). This corresponded to larger strain hardening in the inelastic braces compared to that of the other ground motions; see Figure 6.4(b). Ground motion 10 resulted in the largest compression demand in the first story strongback brace; see Figure 6.5(a) and (b).

In contrast, gm44 and gm13 resulted in the largest compression demand in the upper stories. These were the ground motions with the largest pseudo-accelerations at the higher-mode periods; see Figure 6.2. Compared to the other ground motions, gm1 tended towards the smallest strongback brace demands. Though compression demands in the tie were similar for all four ground motions, tension demands in the tie were more variable, indicating a tendency towards asymmetric behavior depending on whether bending in the strongback puts the tie in compression or tension; see Figure 6.5(c). Tie demands were smallest for gm1, the ground motion with the smallest pseudo-accelerations at the higher-mode periods.

In general, axial force and bending moment demands in the beams and columns were largest for gm10, were similar for gm13 and gm44, and were smallest for gm1, though this trend was not perfect in all cases; see Figure 6.6 and Figure 6.7. The axial-force demand in the inelastic column was largest for gm10, consistent with the larger axial forces observed in the inelastic braces. The demand in the strongback column was largest for gm13 and gm44, the ground motions with the largest axial force in the upper story strongback braces. Deformation demands indicate that non-simulated defamation limit states were exceeded in the beam links for gm10; see Figure 6.6(c).

Ground motion 10 resulted in the largest peak and residual drift ratios, likely due to increased strain hardening and permanent elongation or shortening of the inelastic braces; see Figure 6.8(a) and (b). The drift concentration factor was largest for the fourth story in gm13 and gm44, indicating higher-mode influence in the upper levels of the strongback; see Figure 6.8(a) and (b). In contrast, the drift concentration factor was nearly uniform for gm1 and gm10.

Higher-mode contributions to the upper story response were apparent in the story shear response for gm44 and gm13; see Figure 6.8(e) and (f). In contrast, the story shears for gm1 and gm10 indicated a more dominant first-mode story shear distribution (i.e., the story shear envelope increases incrementally from the roof level to the base level). Ground motion 10 exhibited the largest base shear (i.e., first story shear). Absolute accelerations were smallest for gm1 and similar for gm10, gm13, and gm44; see Figure 6.8(d).

Except for gm13, all four inelastic braces were at or beyond yield at the instance of peak story shear; see Figure 6.10. Ground motions 13 and 44, the ground motions with the largest higher-mode response, engaged only a portion of the inelastic braces during the instant of peak story drift ratio.

In summary:

1. Ground motions with larger pseudo-accelerations at the higher-mode periods can result in “bending” in the strongback truss. These higher-mode contributions can result in larger demands in the upper strongback braces, tie, and columns.
2. The duration of ground shaking gives time for the inelastic braces to exhibit substantial strain hardening, leading to increased peak and residual drifts and surrounding frame demands. Longer duration also gives the strongback system ample time to for a complete mechanism, potentially resulting in higher risk of collapse with longer ground motion shaking.

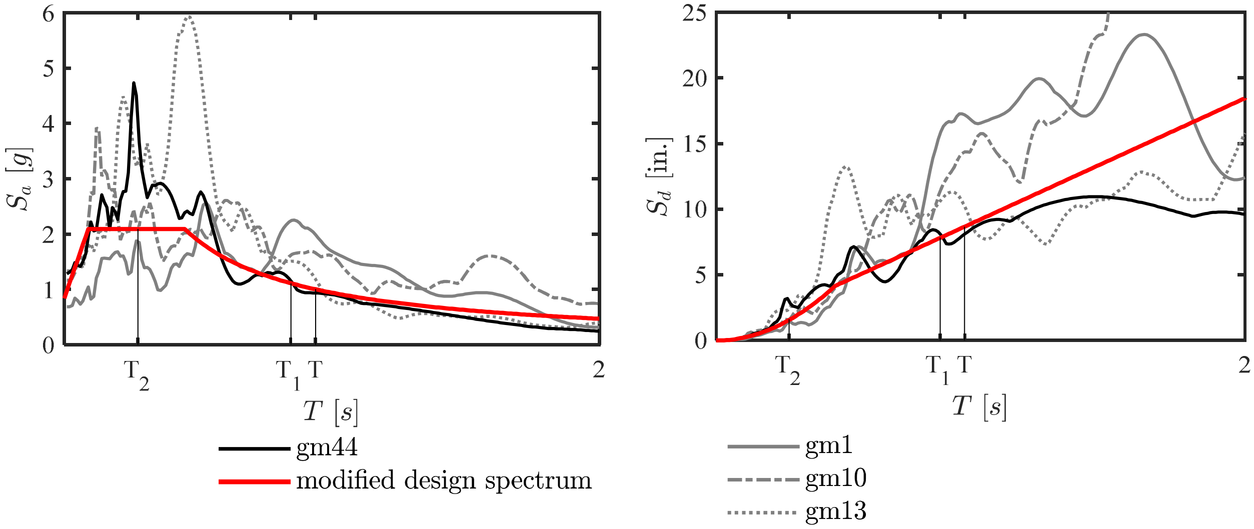

Figure 6.2. Response spectra of compared ground motions.

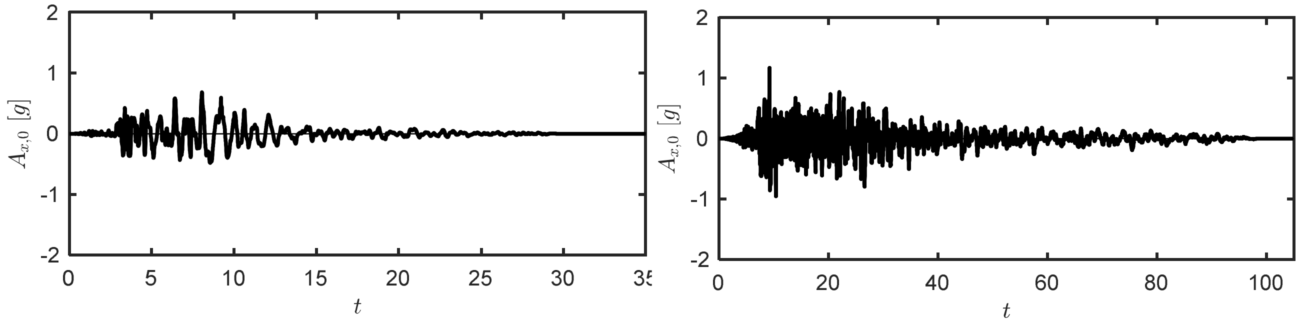

$gm1$ - $M6.7$ 1994 Northridge Beverly Hills – Mulhol
Site Class D, Fault Type – Thrust, FN component

$gm10$ - $M6.5$ 1979 Imperial Valley Delta
Site Class D, Fault Type – Strike-slip, FP component

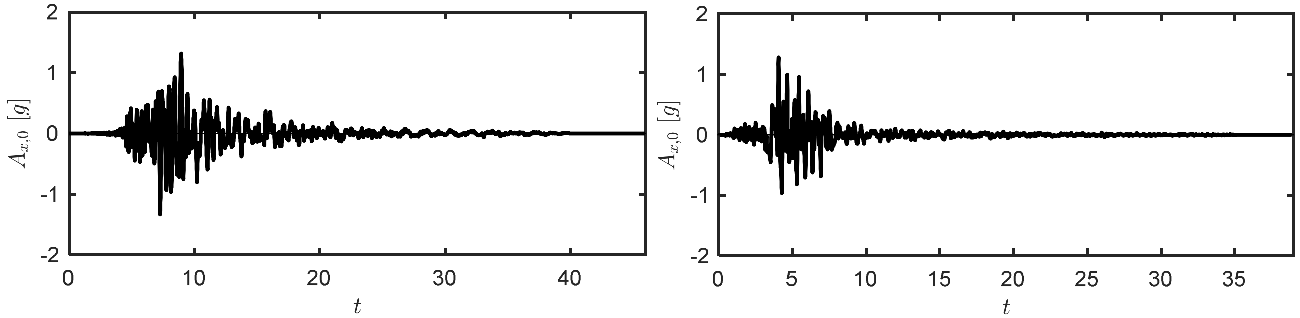

$gm13$ - $M6.9$ 1995 Kobe, Japan Nishi-Akashi
Site Class C, Fault Type – Strike-slip, FN component

$gm44$ **-** $M6.5$ 1976 Friuli, Italy Tolmezzo
Site Class C, Fault Type – Thrust, FP component

Figure 6.3. Ground acceleration histories.

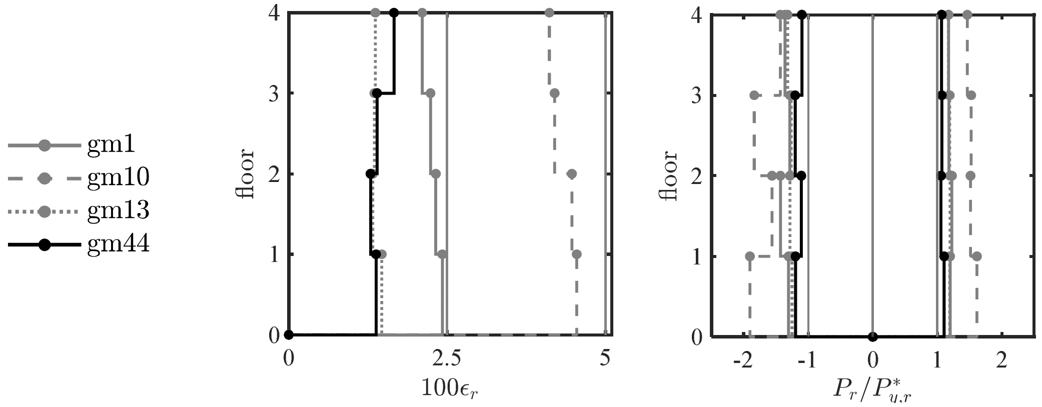

(a)

(b)

Figure 6.4. Case 1 – Inelastic brace peak response envelopes.
(a) strain demand, (b) axial demand-to-capacity ratio

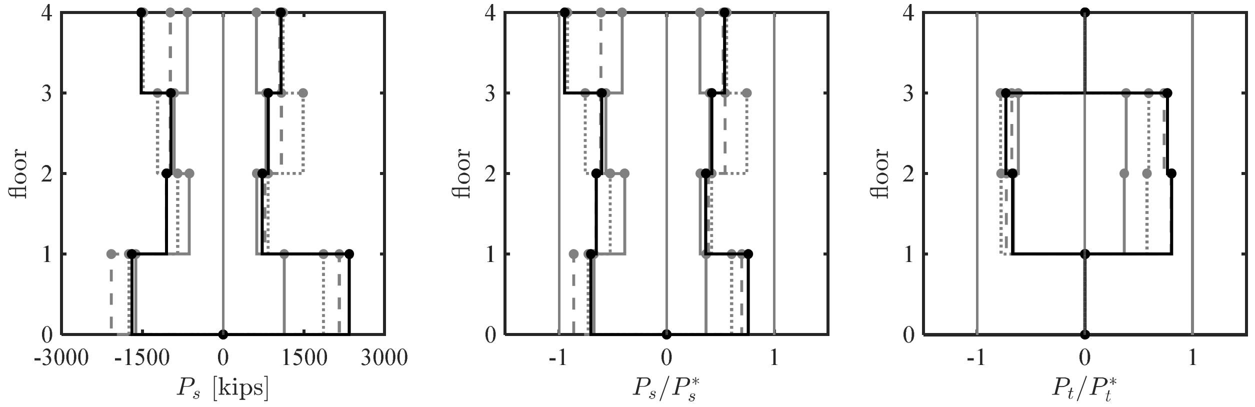

(a) (b) (c)

Figure 6.5. Case 1 – Strongback elements peak response envelopes.
(a) axial-force demand; (b) and (c) axial demand-to-capacity ratio

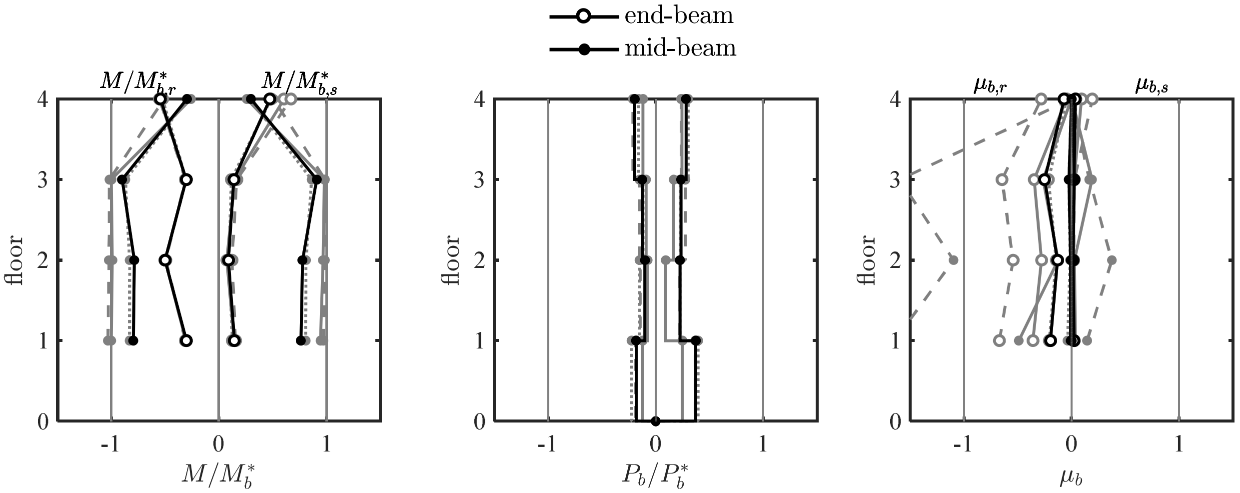

(a) (b) (c)

Figure 6.6. Case 1 – Beam peak response envelopes.
(a) moment demand, (b) axial-force demand; (c) deformation acceptability ratio

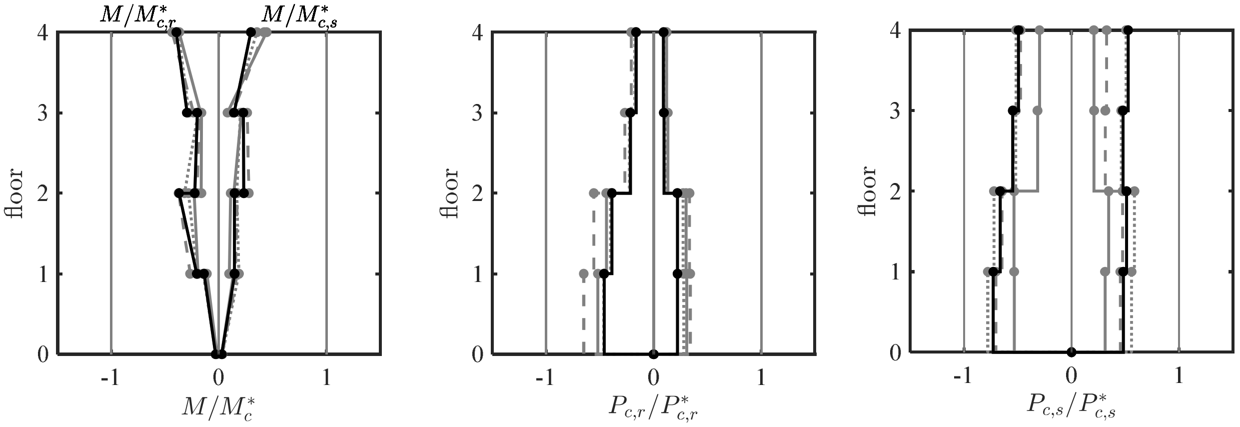

(a) (b) (c)

Figure 6.7. Case 1 – Column peak response envelopes.
(a) moment demand; (b) and (c) axial-force demand. (a) axial-force demand; (b) and (c) axial demand-to-capacity ratio

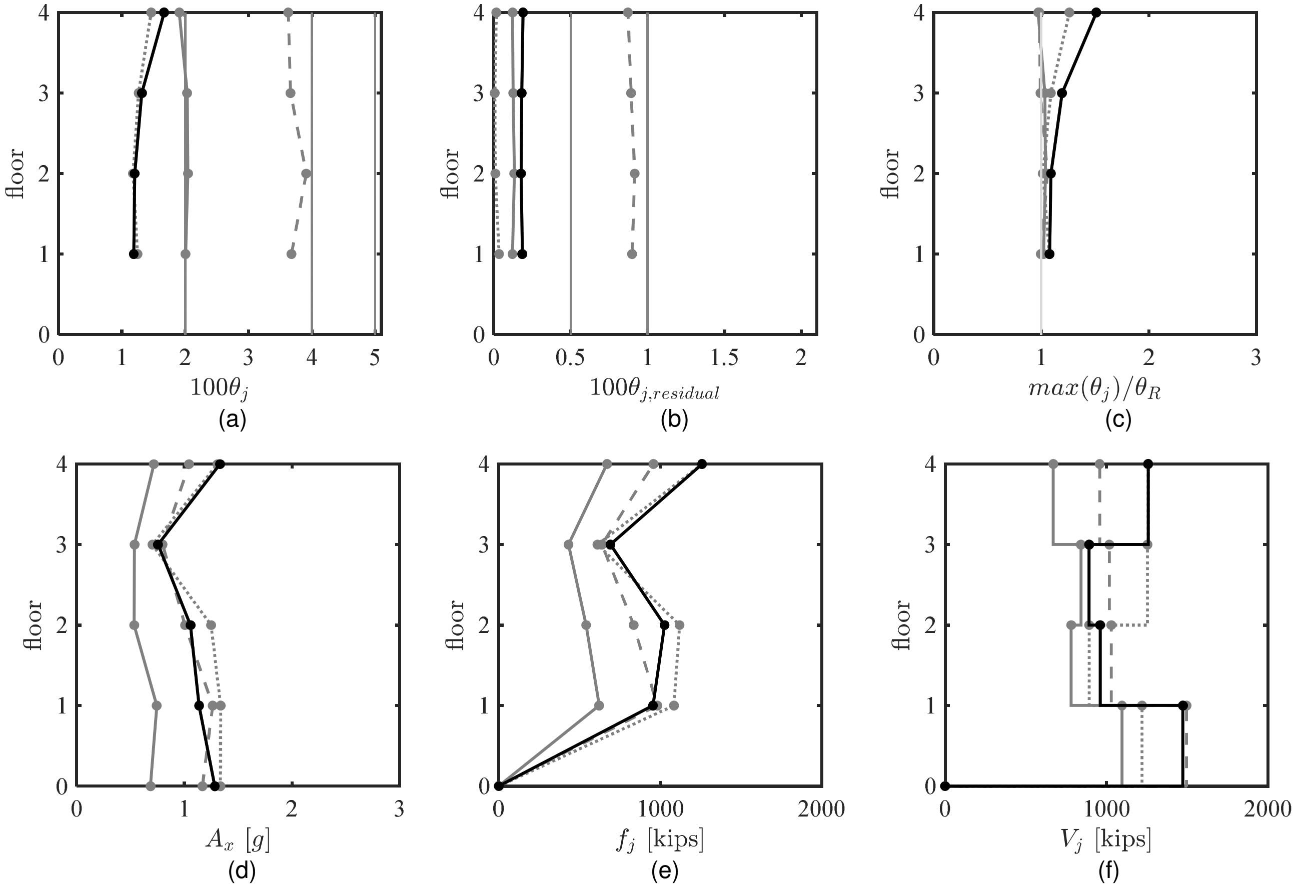

Figure 6.8. Case 1 – Global peak response envelopes.
(a) peak story drift ratio; (b) peak residual drift ratio; (c) drift concentration factor; (d) absolute acceleration; (e) estimated peak equivalent-lateral force distribution; (f) peak story shear

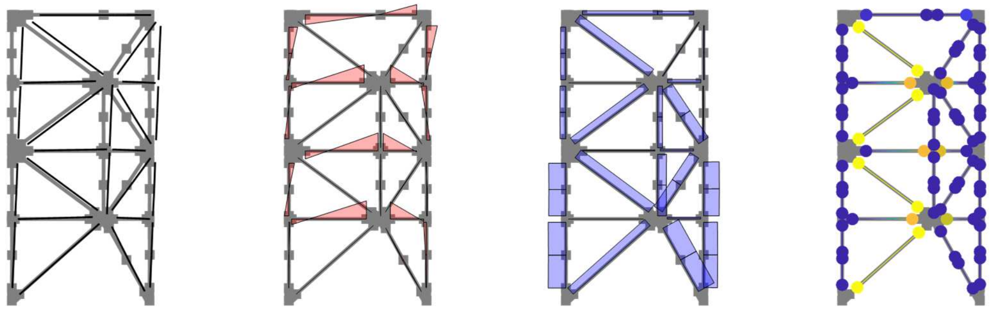

(a) gm1

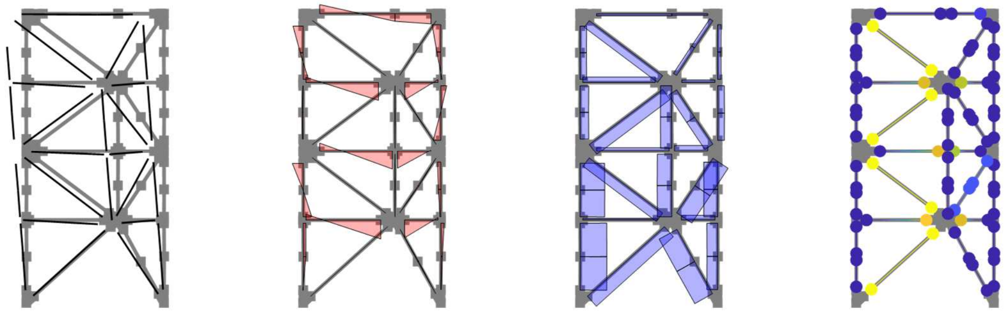

(a) gm10

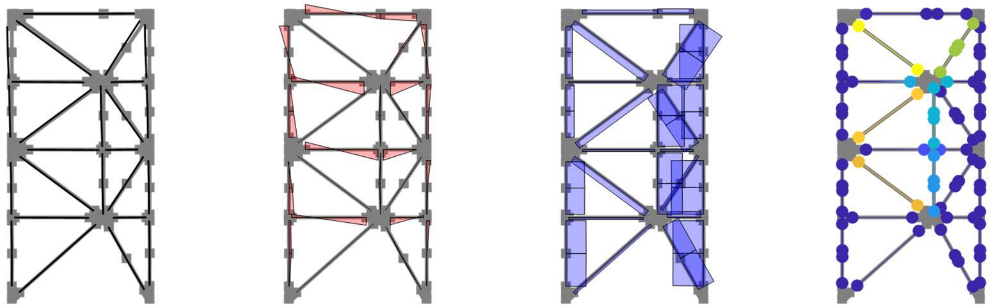

(c) gm13

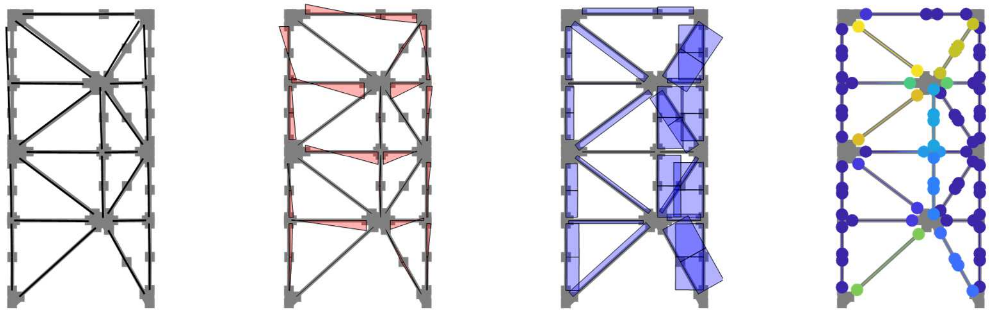

(d) gm44

Figure 6.9. Case 1 – Response diagrams at time of peak story drift ratio.

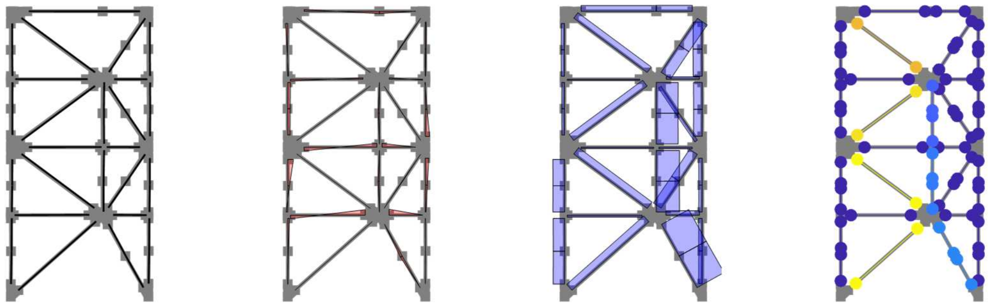

(a) gm1

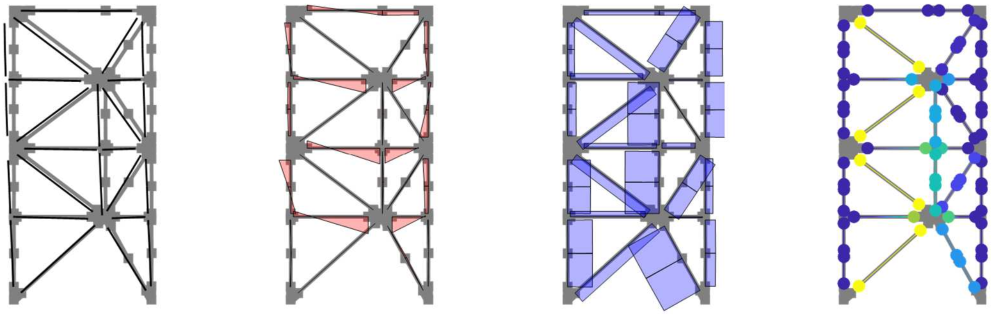

(a) gm10

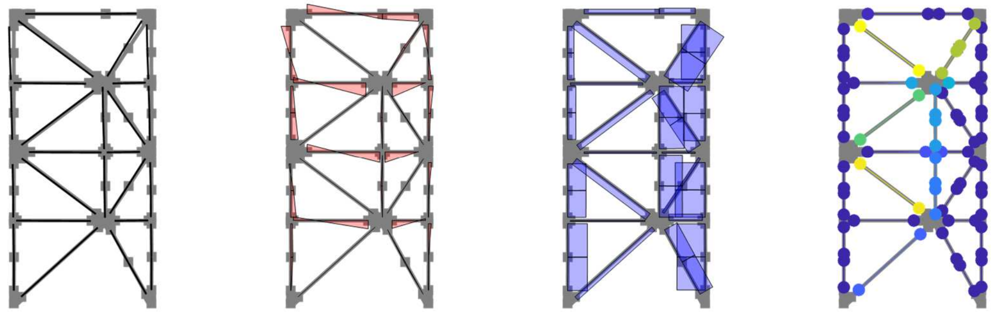

(c) gm13

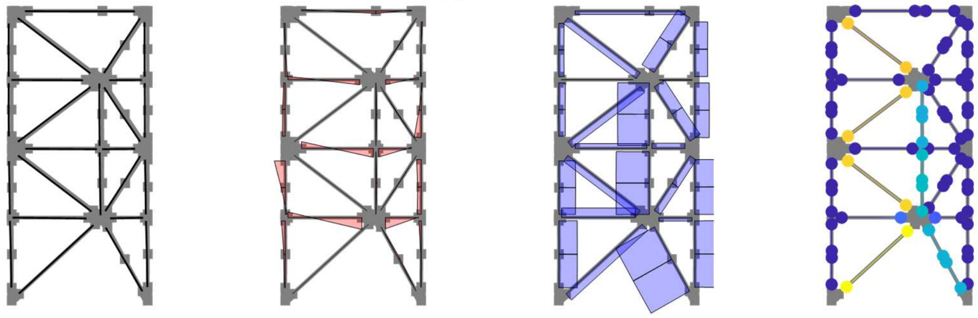

(d) gm44

Figure 6.10. Case 1 – Response diagrams at time of peak story shear.

6.2.3 Case 2 – Beam-Column Connections

Large shears can develop along the beam link upon the formation of plastic hinges at the beam link ends. These vertical shears can put additional demands on the strongback braces and tie. Pinned versus fixed connections can also affect the stiffness and residual strength of the global system. As such, Case 2 investigated the impact of the beam end condition on the surrounding structural elements.

Five cases of beam-column connections were considered. The alternating beam-column connections used pinned conditions to represent beam-column regions without gusset plates and fixed conditions to represent regions with gusset plates. Pinned beam-column connections, fixed beam-column connections, fully pinned beam links, and partially-restrained (PR) beam-column connections were also considered. The fully pinned beam links were pinned at both the beam-end and on the inelastic side of the mid-beam connection. The PR connections were modeled per Section 4.5.1.

The envelopes for each of the beam-column connection cases are overlaid in Figure C.1 through Figure C.5. The moment diagrams and demand-to-capacity ratios at the instance of peak story drift ratio and story shear for each beam end condition are shown in Figure 6.11 and Figure 6.12 for each beam end condition. The deformed shape, axial force diagrams, and response at time of peak story shear are omitted because they are relatively similar to Figure 6.9(d) and Figure 6.10(d). The beam end condition has the largest affect the moment distributions in the system. The case of the fully pinned beam link exhibits negligible moments at the time of peak story drift ratio. In contrast, almost every beam-column element exhibited double curvature with fixed beam-column conditions.

In summary of Appendix C.1:

1. The beam-column end condition has the most impact on the moments in the beams and, through equilibrium, the columns. When the moments at the beam-ends were released, the envelope of the column moment is non-zero and developed primarily from bending.
2. Residual drifts were largest for the fixed beam condition and smallest for the fully pinned beam link and pinned end conditions. The DCF in the fourth story indicates that drifts tend to concentrate more in the fourth story as more moment conditions are released. Provided the strongback can overcome this increased tendency, peak and residual drifts were smaller with pinned beam conditions for gm44. This contradicts later statistical observations about the median and 85th percentile response.

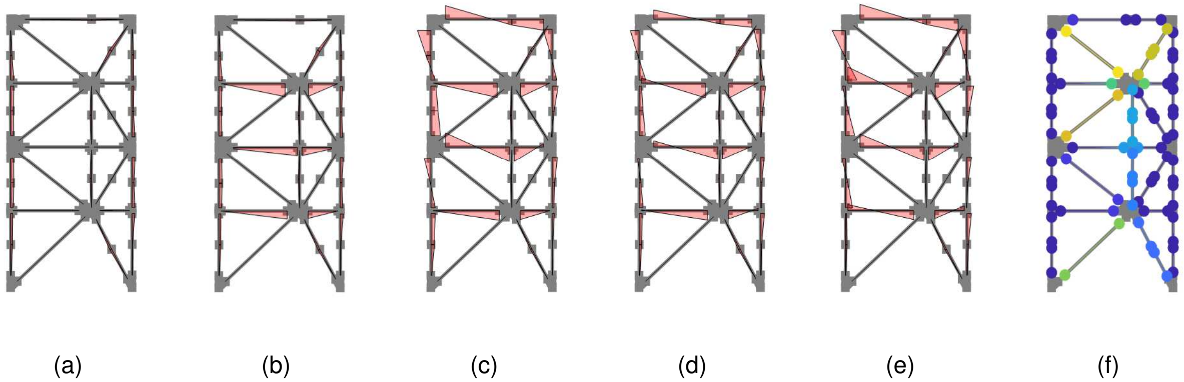

Figure 6.11. Case 2 – Response diagram at time of peak story drift ratio.
(a) fully pinned beam link; (b) pinned beam-column connection; (c) alternating beam-column connection; (d) PR beam-column connection; (e) fixed beam-column connection; (f) demand-to-capacity ratio.

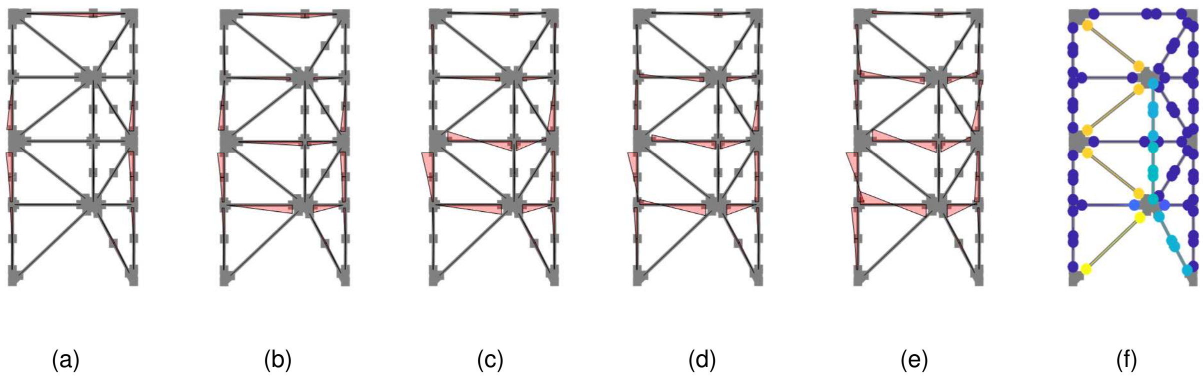

Figure 6.12. Case 2 – Response diagram at time of peak story shear.
(a) fully pinned beam link; (b) pinned beam-column connection; (c) alternating beam-column connection; (d) PR beam-column connection; (e) fixed beam-column connection; (f) demand-to-capacity ratio.

6.2.4 Case 3 – Column Base Fixity and Bending Orientation

As described in Chapter 1, the strongback portion of the frame tends to engage the fuses through a pivoting motion about its column base. The ability of the strongback to rotate about its base could be enhanced using a pin connection at the base of the strongback column. Alternatively, a column oriented in weak axis bending could provide similar axial capacity while limiting the bending moment able to develop at the column base; see Section 2.4.2.1. As such, Case 4 compared differences in seismic response due to variations in the column base fixity (i.e., pinned or fixed) and the column bending orientation (i.e., weak-axis or strong-axis oriented bending).

Plots of the envelope demands are shown in Figure C.6 through Figure C.10. The moment diagrams at the time of peak story shear are shown in Figure 6.12; other response diagrams are similar to Figure 6.9(d) and Figure 6.10(d) and are omitted. At the time of peak story shear, moment at the column base was largest for the fixed, strong-axis oriented columns, followed by the fixed, weak-axis oriented columns, and negligible for the pinned strong-axis oriented column.

Moment demands in the upper stories were similar for the pinned and fixed strong-axis oriented columns and were smaller for the weak-axis oriented columns.

In summary of Appendix C.2:

1. Axial-force demands in the elements are little impacted by the column base fixity or orientation.
2. Moment demands at the column base were most affected by the change in column base fixity from pinned to fixed. The base fixity has little effect on moment demands in upper stories.
3. The weak-axis column orientation reduced moments along the column height compared to the use of columns oriented in strong-axis bending. However, weak-axis oriented columns also have reduced moment capacity compared to columns oriented in strong-axis bending.

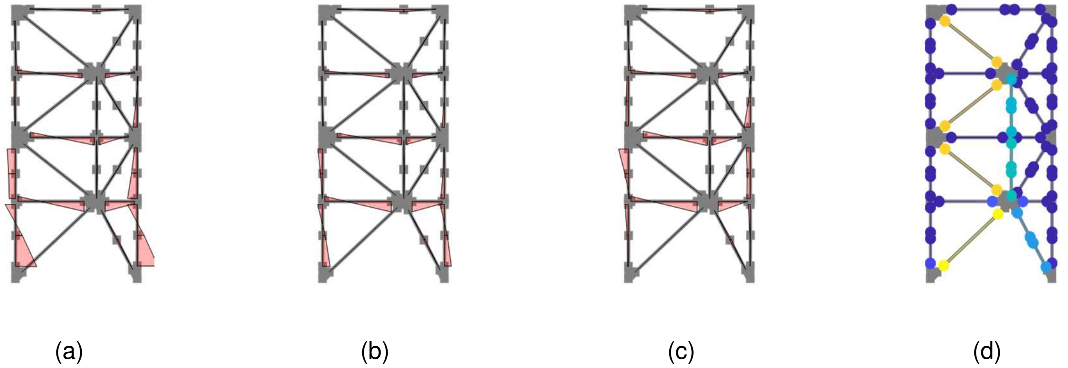

Figure 6.13. Case 3 – Response diagram at time of peak story shear.

(a) fixed column base with strong-axis oriented columns; (b) fixed column base with weak-axis oriented columns; (c) pinned column base with strong-axis oriented columns; (d) demand-to-capacity ratio

6.2.5 Case 4 – Beam Composite Action and Diaphragm Rigidity

Case 4 studied the impact of diaphragm rigidity and beam composite action on peak response. These parameters have a direct impact beam flexural and axial-force demands. Composite action was simulated by a wide-flange beam section with a concrete fiber slab modeled with a compression-only material. This section model assumed complete composite action between the slab and beam. Diaphragm rigidity was represented by a rigid elastic truss between beam nodes or by a compression-only concrete material truss representing the effective area of the concrete slab tributary to the benchmark frame.

Envelope comparisons of response quantities for each parameter are overlaid in Figure C.11 through Figure C.15. Moment and axial diagrams at the instance of peak story drift are shown in Figure 6.14. Composite action clearly resulted in asymmetric bending; see Figure 6.14(c). Axial forces were virtually zero for the rigid elastic diaphragm, asymmetrically reduced for the concrete diaphragm, and largest for the composite and non-composite bare beam.

In summary of Appendix C.3:

1. A rigid elastic diaphragm virtually eliminates axial forces in the beams.

2. A concrete truss diaphragm reduces compression demands on the beams and has little effect on the tension and flexural demands in the beams.
3. Explicit modeling of composite action asymmetrically affects the moment capacity and inelastic deformations of the beams. Composite action has little impact on other elements in the system.

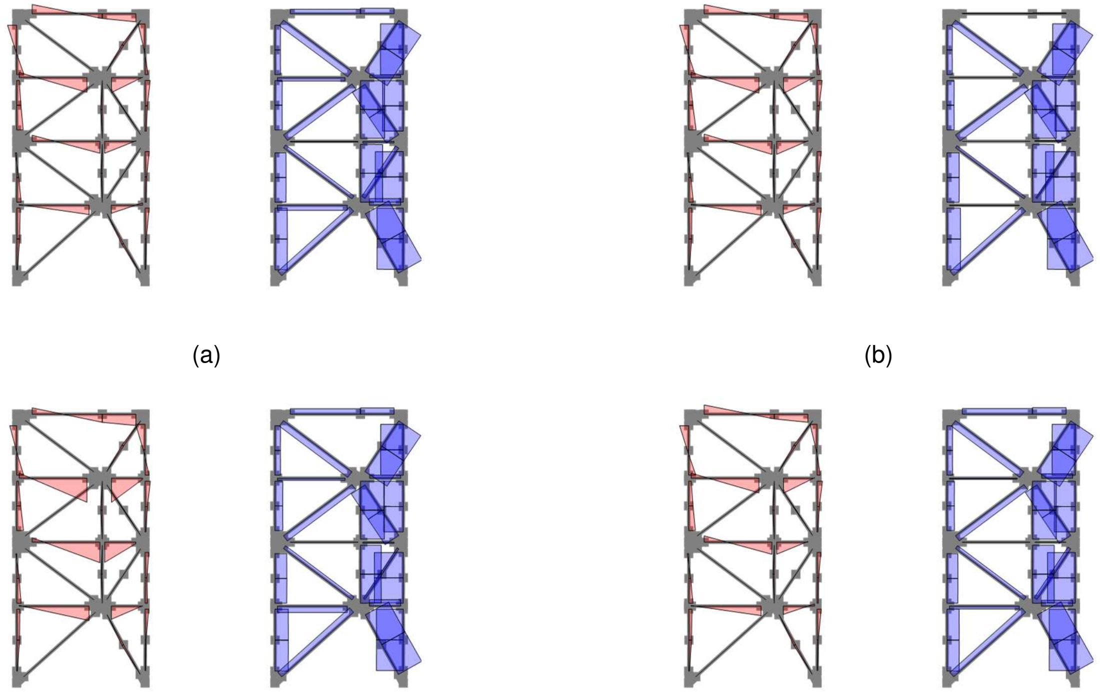
(a)

(b)

(c)

(d)

Figure 6.14. Case 4 – Axial and moment diagrams at time of peak story drift.
(a) bare, non-composite beam; (b) rigid elastic diaphragm; (c) composite beam; and (d) concrete diaphragm.

6.2.6 Case 5 – Strongback Brace and Tie End Conditions

Case 5 studied changes in response due to the strongback brace and tie end restraints. End conditions were specified as pinned or fixed. The impact of a continuous tie that was fixed at the second floor was also considered. Envelopes of the peak response quantities are shown in Figure C.16 through Figure C.20. In summary of Appendix C.4:

1. Strongback brace end rigidity has little impact on the benchmark system's response under gm44.
2. Though not explored herein, inelastic brace end conditions could also affect the strongback's response.

6.2.7 Comparison Case

Cases 2 through 5 examined the response of a strongback-braced frame subjected to different design alternatives. Some cases caused the strongback demand to increase with respect to the benchmark design while other cases caused the strongback demand to decrease. To illustrate the extremities of the simulated response, this section compares design alternatives that generally maximized demands in the strongback elements to design alternatives that generally minimized demands on the strongback elements under gm44. The following two cases were compared:

1. A maximization case corresponding to designs employing a fully pinned beam link, a fixed column base with the columns oriented in weak-axis bending, a rigid elastic diaphragm, and fixed strongback end conditions.
2. A minimization case corresponding to designs with fixed beam-column connections, a pinned column base with the columns oriented in strong-axis bending, a non-composite bare beam, and pinned strongback end conditions.

Results of this comparison are shown in Figure 6.15 through Figure 6.19. The compression demand in the fourth story strongback brace increased by 18% in the maximization case compared to the minimization case. This resulted in buckling in the fourth story strongback brace. Averaged over all the strongback braces, the maximization case resulted in an increase of 15% in compression demand; see Figure 6.16(a) and (b). The compression demand in the tie increased on average by 20%; see Figure 6.16 (c). Increases in strongback brace demands also resulted in increased axial-force demands on the strongback column; see Figure 6.18(c).

Though the DCF was larger in the fourth story for the maximization case, peak and residual drifts were smaller compared to the minimization case; see Figure 6.19(a), (b), and (c). In contrast, peak absolute accelerations and corresponding equivalent-lateral forces were larger for the maximization case; see Figure 6.19(d) and (e). This effect likely stems from the difference in periods for the maximization case versus the minimization case; see Table 6.1.

Table 6.1. Comparison Case: Elastic periods.

Parameter Description	T_1 $[s]$	T_2 $[s]$	T_3 $[s]$	T_4 $[s]$
Maximization of strongback demand	0.847	0.265	0.198	0.144
Minimization of strongback demand	0.834	0.269	0.160	0.118

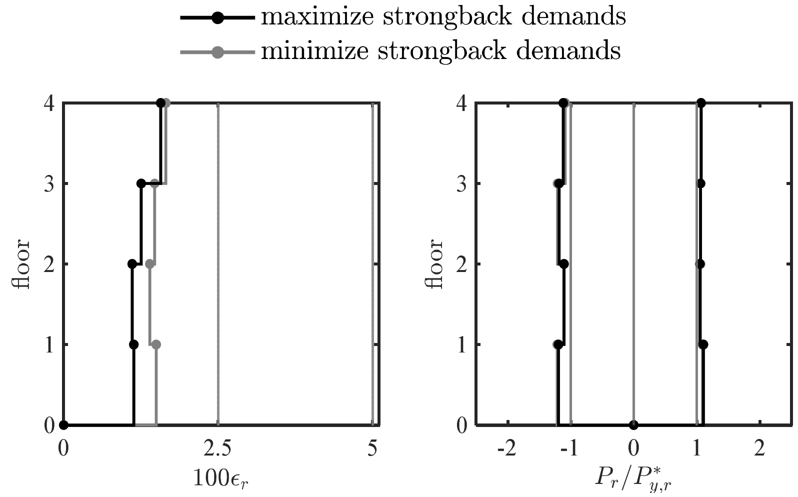

(a) (b)

Figure 6.15. Comparison case – Inelastic brace peak response envelopes. (a) strain demand, (b) axial demand-to-capacity ratio

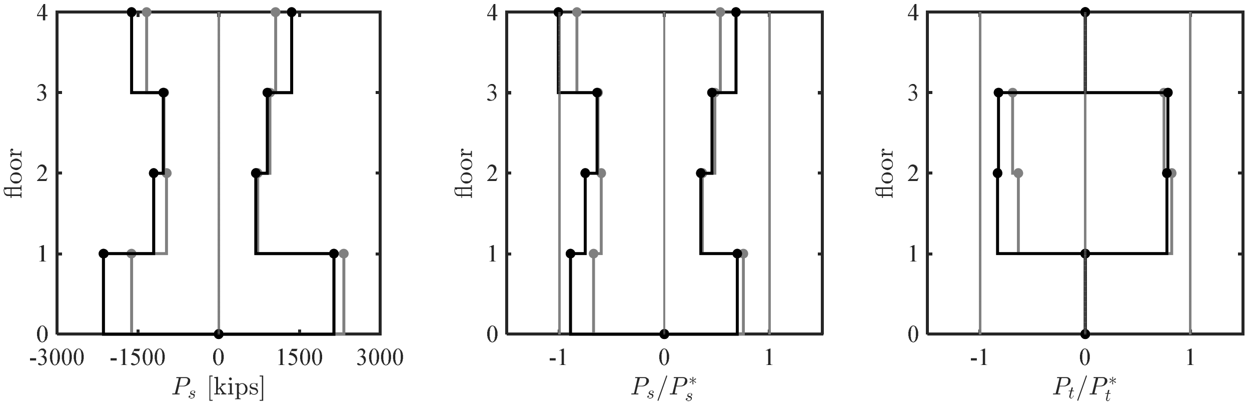

(a) (b) (c)

Figure 6.16. Comparison case – Strongback elements peak response envelopes. (a) axial-force demand; (b) and (c) axial demand-to-capacity ratio

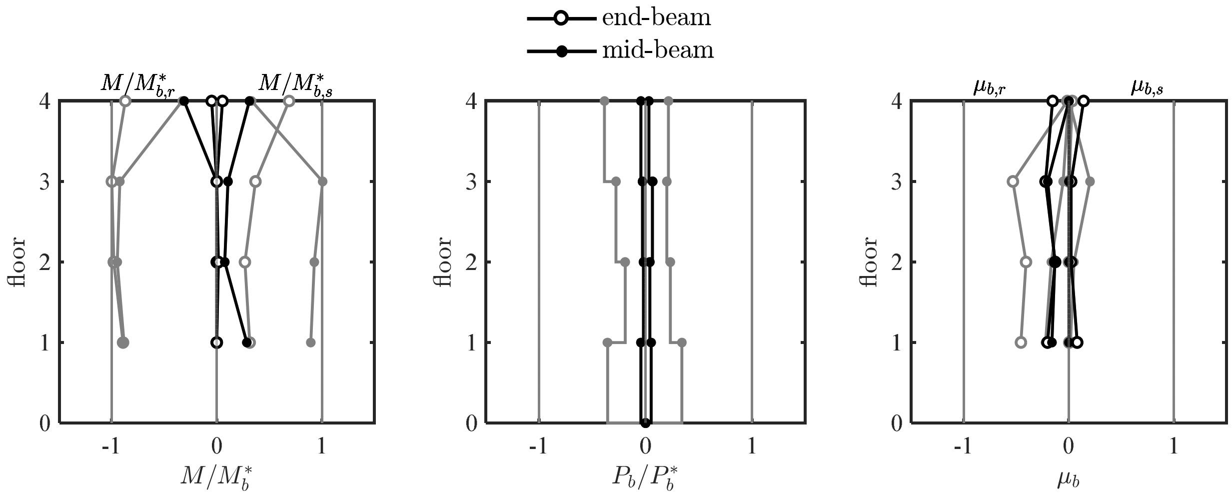

(a) (b) (c)

Figure 6.17. Comparison case – Beam peak response envelopes.
(a) moment demand; (b) axial-force demand; (c) deformation acceptability ratio

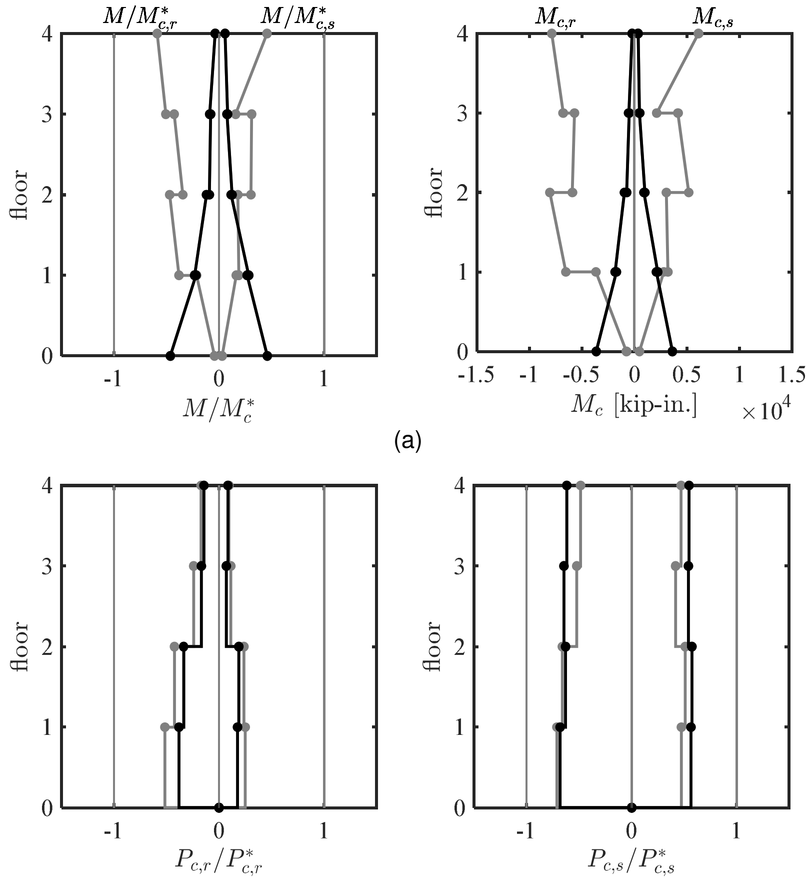

(b) (c)

Figure 6.18. Comparison case – Column peak response envelopes.
(a) moment demand; (b) and (c) axial-force demand. (a) axial-force demand; (b) and (c) axial demand-to-capacity ratio

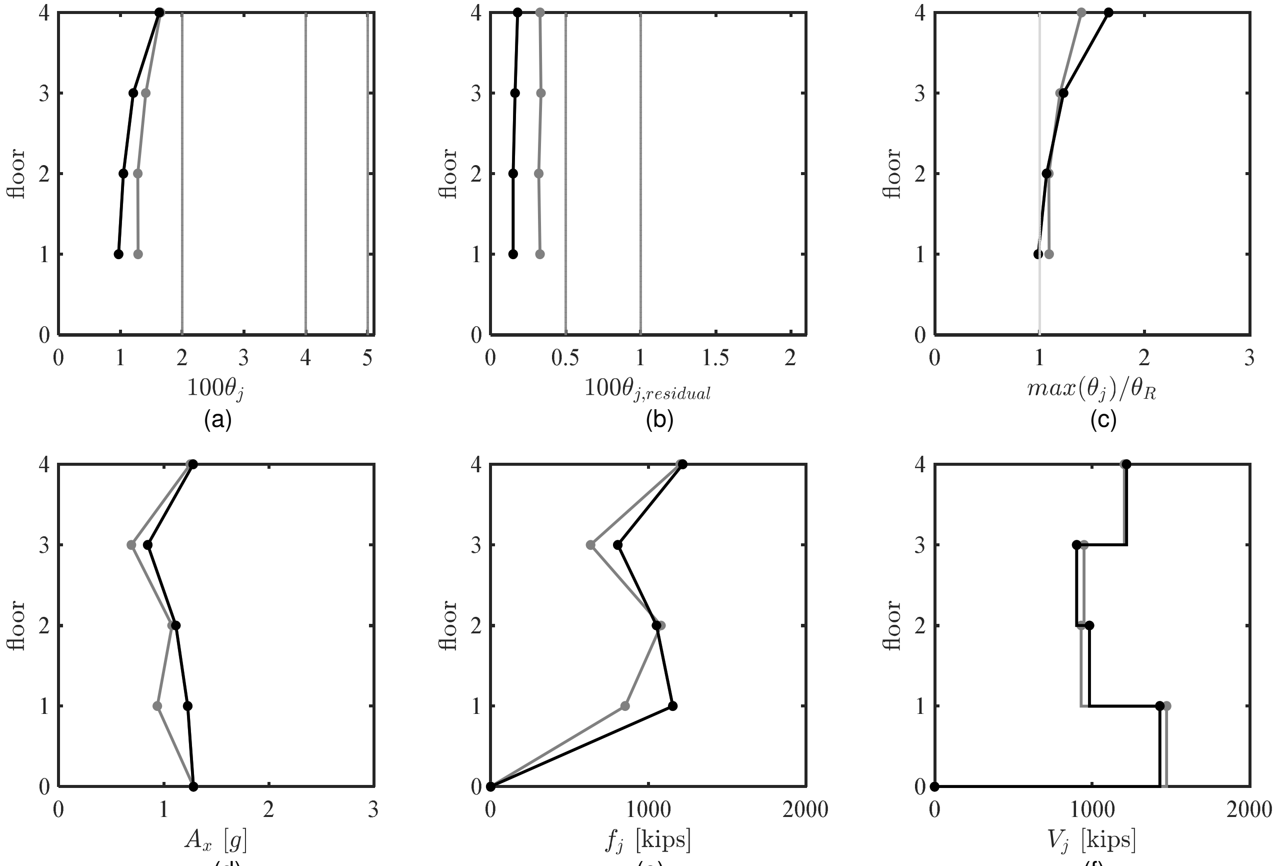

(a) (b) (c)

(d) (e) (f)

Figure 6.19. Comparison case – Global peak response envelopes.
(a) peak story drift ratio; (b) peak residual drift ratio; (c) drift concentration factor; (d) absolute acceleration; (e) estimated peak equivalent-lateral force distribution; (f) peak story shear

6.3 STATISTICAL COMPARISON OF CASES

Further investigation of a wider range of samples was needed to extend and verify the trends studied in Section 6.2. Ideally, mean values would show trends in the response and the coefficient of variation (COV) would reflect the sensitivity of the response to the characteristics of the ground motions. Responses insensitive to the characteristics of the ground excitation would exhibit uniform means and small COV.

However, the few cases when non-simulated failure modes were triggered at the MCE intensity level resulted in outliers. These outliers can significantly influence the mean and standard deviation response. As such, this section studied design alternatives in terms of the median and 85th percentile response, which are little influenced by extreme outliers like those caused by collapse or non-simulated limit state checks. In this sense, differences between the median 85th percentile are an indicator of the dispersion in the data.

6.3.1 Median and 85th Percentiles of Cases 2-5

The median and 85th percentile responses for the maximum story drift, $\max\theta_j$; maximum residual drift, $\max\theta_{j,residual}$; and normalized base shear, V_b/W, for Cases 2-5 are shown in Table 6.3 through Table 6.5. These statistical quantities were calculated with and without inclusion of the non-simulated failure modes. In these tables, cells showing "Inf" means that a non-simulated failure state was triggered at that percentile. For comparison, the mean and COV values are additionally shown alongside the median and 85th percentile values. The mean and COV were calculated without the inclusion of responses triggered by collapse or non-simulated failure modes.

The median response envelopes over several ground motions results in a smoother response profile compared to the envelopes from Section 6.2 under gm44; see plots of the median envelope response in Appendix D. Statistical evaluation of a response under multiple ground motions removes atypical behavior that may occur under a single ground motion. Note, however, that median response plots can attain peak values during the same or under different ground motions. As such, these values tend to result in a smoothed response envelope compared to envelopes of response quantities under a single ground motion.

Designs with fixed beam-column connections, fixed column bases, composite beams, and fixed strongback connections resulted in the smallest peak and residual drifts. However, the majority of these conditions resulted in non-simulated failure modes at the 85th percentile level. All non-simulated failure modes were triggered by excessive flexural deformation in the beam links.

Though similar, some observations were reversed from that of the case study described in Section 6.2. For example, in terms of both peak and residual story drift, the fully pinned beam link response exhibited the largest peak and residual drift response, though it also exhibited the smallest base shear response. The fully pinned beam link resulted in the smallest median strongback demand but the largest median inelastic brace axial strains. This trend was reversed with fixed beam-column connections. Generally, the benchmark frame exhibited neither the largest nor the smallest response for any of the global response quantities.

Table 6.2. Elastic periods of cases 2-5.

	Design alternative	T_1 [s]	T_2 [s]	T_3 [s]	T_4 [s]
	benchmark	0.840	0.267	0.157	0.125
Case 2	alternating beam-column connections	0.841	0.268	0.156	0.118
	fixed beam-column connections	0.833	0.267	0.156	0.118
	pinned beam-column connections	0.848	0.269	0.197	0.159
	fully pinned beam link	0.852	0.269	0.197	0.159
Case 3	fixed column base, x-axis bending	0.833	0.263	0.156	0.125
	fixed column base, y-axis bending	0.840	0.268	0.159	0.146
Case 4	bare beam	0.840	0.270	0.160	0.125
	rigid diaphragm	0.837	0.265	0.143	0.124
	composite beam	0.840	0.269	0.165	0.121
Case 5	fixed strongback brace connection	0.840	0.267	0.157	0.125
	continuous tie	0.838	0.267	0.157	0.125

Table 6.3. Statistical response of $\max(\theta_j)$.

	Design alternative	without non-simulated failure modes				with non-simulated failure modes			
		median	85th percentile	mean	COV	median	85th percentile	mean	COV
	benchmark	1.66	2.65	1.80	0.39	1.66	2.71	1.61	0.29
Case 2	alternating beam-column connections	1.67	2.72	1.79	0.39	1.67	Inf	1.54	0.25
	fixed beam-column connections	1.61	2.75	1.77	0.41	1.61	Inf	1.46	0.26
	pinned beam-column connections	1.70	2.67	1.84	0.39	1.70	2.67	1.71	0.31
	fully pinned beam link	1.70	2.64	1.90	0.40	1.70	2.64	1.90	0.40
Case 3	fixed column base, x-axis bending	1.64	2.75	1.80	0.40	1.64	2.75	1.71	0.35
	fixed column base, y-axis bending	1.68	2.73	1.80	0.39	1.68	2.73	1.71	0.34
Case 4	bare beam	1.67	2.60	1.79	0.39	1.67	2.60	1.60	0.28
	rigid diaphragm	1.68	2.73	1.80	0.39	1.68	2.73	1.61	0.29
	composite beam	1.61	2.64	1.81	0.41	1.61	Inf	1.39	0.22
Case 5	fixed strongback brace connection	1.65	2.73	1.80	0.40	1.65	Inf	1.54	0.25
	continuous tie	1.66	2.66	1.80	0.39	1.66	2.73	1.61	0.29

Table 6.4. Statistical response of $\max(\theta_{j,residual})$.

Design alternative		without non-simulated failure modes				with non-simulated failure modes			
		median	85th percentile	mean	COV	median	85th percentile	mean	COV
	benchmark	0.18	0.61	0.31	0.90	0.18	0.62	0.24	0.78
Case 2	alternating beam-column connections	0.21	0.58	0.31	0.94	0.22	Inf	0.21	0.75
	fixed beam-column connections	0.25	0.67	0.36	0.85	0.25	Inf	0.25	0.72
	pinned beam-column connections	0.23	0.57	0.32	0.86	0.23	0.65	0.29	0.84
	fully pinned beam link	0.35	0.69	0.41	0.69	0.35	0.69	0.41	0.69
Case 3	fixed column base, x-axis bending	0.17	0.61	0.29	0.96	0.17	0.61	0.27	0.97
	fixed column base, y-axis bending	0.16	0.57	0.29	0.93	0.16	0.57	0.27	0.94
Case 4	bare beam	0.18	0.59	0.31	0.88	0.18	0.59	0.24	0.80
	rigid diaphragm	0.19	0.58	0.30	0.89	0.19	0.59	0.23	0.76
	composite beam	0.21	0.63	0.33	0.90	0.24	Inf	0.18	0.74
Case 5	fixed strongback brace connection	0.22	0.59	0.33	0.85	0.24	Inf	0.24	0.73
	continuous tie	0.18	0.61	0.32	0.90	0.18	0.64	0.24	0.78

Table 6.5. Statistical response of peak V_b/W.

Design alternative		without non-simulated failure modes				with non-simulated failure modes			
		median	85th percentile	mean	COV	median	85th percentile	mean	COV
	benchmark	0.149	0.186	0.154	0.159	0.150	0.191	0.150	0.152
Case 2	alternating beam-column connections	0.149	0.184	0.153	0.161	0.150	Inf	0.148	0.153
	fixed beam-column connections	0.158	0.191	0.160	0.154	0.159	Inf	0.155	0.152
	pinned beam-column connections	0.145	0.179	0.148	0.163	0.145	0.183	0.146	0.160
	fully pinned beam link	0.140	0.175	0.143	0.168	0.140	0.175	0.143	0.168
Case 3	fixed column base, x-axis bending	0.158	0.193	0.161	0.164	0.158	0.194	0.159	0.164
	fixed column base, y-axis bending	0.153	0.188	0.155	0.157	0.153	0.189	0.154	0.154
Case 4	bare beam	0.150	0.185	0.153	0.152	0.150	0.187	0.151	0.153
	rigid diaphragm	0.152	0.182	0.155	0.171	0.153	0.192	0.151	0.156
	composite beam	0.152	0.185	0.156	0.150	0.164	Inf	0.149	0.146
Case 5	fixed strongback brace connection	0.150	0.187	0.155	0.168	0.151	Inf	0.150	0.156
	continuous tie	0.149	0.186	0.154	0.159	0.150	0.192	0.151	0.152

6.3.2 Location of Offset Intersection

The location of the brace-to-beam intersection due to an offset configuration was studied in terms of the recommendations for offset location made in Chapter 3. To isolate the impact of the design alternative from changes in period due to offset location, the inelastic brace size was varied to maintain similar stiffness for all offset locations. Inelastic brace area was back-calculated relative to the stiffness of the benchmark fame in each story. This back-calculation was conducted using Equation 3.1 assuming the strongback brace size remained the same. The resulting inelastic brace areas are shown in Table 6.6. This resulted in similar first-mode periods regardless of the offset location. The ratio, b/L, represents the ratio of the strongback truss width to the total bay width and is indicative of the amount of offset from the middle of the bay. Additional envelope plots can be found in Appendix C.5.

Envelopes of median response quantities for each offset geometry are shown in Figure 6.20 through Figure 6.24. Axial strain demands in the inelastic braces were significantly impacted by the offset location. Strain demands were largest for the inelastic braces in the centered scheme; see Figure 6.20(a). Strongback demands tended to be largest for the centered scheme and smallest for larger offsets; see Figure 6.21 and Figure C.22. Offset locations of 1/3, 1/4, and 1/5 the bay width resulted in similar strongback demands.

Beam deformations and axial-force demands tended to decrease with increasing offset; see Figure 6.22 and Figure C.23. These demands were similar for all offsets away from the centered scheme. Column moments tended to increase with increase offset, and were smallest for $\frac{b}{L} = \frac{1}{2}$ and $\frac{1}{3}$; see Figure 6.23(a) and Figure C.24. Inelastic column and strongback axial-force demands tended to respectively increase and decrease with increasing offset, reflecting larger and smaller axial demands in the corresponding braces; see Figure 6.23(b) and (c).

Median and 85th percentile global response quantities are tabulated in Table 6.7 through Table 6.9. The centered scheme triggered non-simulated failure modes at the 85th percentile response due to flexural deformations exceeding allowable limits in the beam links. The benchmark frame utilizing an offset of 1/3 the brace bay generally exhibited the smallest residual story drift ratios; see Figure 6.24(a) and (b). Larger drift concentration factors occurred in the lower stories with increasing offset; see Figure 6.24(c). Floor accelerations and estimated equivalent-lateral force distributions grew smaller with increasing offset; see Figure 6.24(d) and (e).

Demand-to-capacity ratios of the members are shown in Figure 6.25 and Figure 6.26 at the time of peak story drift and story shear. Depending on offset location, demands exhibited in these figures were variable. Like the benchmark design, plots at the time of peak story drift exhibited nonuniform engagement of the fuses. However, the distribution inelastic braces engagement differed depending on the offset location. Only the offset of 1/3 the bay width exhibited complete engagement of the inelastic braces at the time of peak story shear; see Figure 6.26.

In summary:

1. Generally, the observations observed in Chapter 3 can also be applied to the response of the four-story benchmark frame. Accelerations, inelastic demands, strongback axial-force demands, beam flexural and axial-force demands, and column axial-force demands tended

to decrease with increasing offset. Notably, column moment demands and inelastic column axial-force demands increased with increasing offset.

2. Median residual drift ratios were smallest for an offset located at $1/3$ the bay width. This is consistent with the recommendations made in Chapter 3 about the ideal offset location.
3. Inelastic demands were by far largest for the centered scheme. Beam link deformation demands for the centered scheme triggered non-simulated failure modes at the 85th percentile level.

Table 6.6. Offset case: Elastic periods.

Parameter Description	A_1 [in^2]	A_j [in^2]	T_1 $[s]$	T_2 $[s]$	T_3 $[s]$	T_4 $[s]$
$b/L = 1/2$	5.04	5.13	0.846	0.247	0.150	0.144
$b/L = 1/3$	8.00	8.00	0.839	0.267	0.157	0.125
$b/L = 1/4$	10.03	9.98	0.835	0.279	0.164	0.118
$b/L = 1/5$	11.45	11.37	0.831	0.285	0.169	0.122

Table 6.7. Offset case: statistical response of $\max(\theta_j)$.

Design alternative		without non-simulated failure modes				with non-simulated failure modes			
		median	85th percentile	mean	COV	median	85th percentile	mean	COV
Offset Case	$b/L = 1/2$	1.72	2.51	4.14	3.58	1.72	Inf	1.54	0.28
	$b/L = 1/3$	1.66	2.65	1.80	0.39	1.66	2.71	1.61	0.29
	$b/L = 1/4$	1.56	2.49	1.78	0.39	1.56	2.49	1.67	0.33
	$b/L = 1/5$	1.60	2.62	1.82	0.38	1.60	2.62	1.73	0.33

Table 6.8. Offset case: statistical response of $\max(\theta_{j,residual})$.

Design alternative		without non-simulated failure modes				with non-simulated failure modes			
		median	85th percentile	mean	COV	median	85th percentile	mean	COV
Offset Case	$b/L = 1/2$	0.28	0.69	2.73	5.50	0.32	Inf	0.28	0.81
	$b/L = 1/3$	0.18	0.61	0.31	0.90	0.18	0.62	0.24	0.78
	$b/L = 1/4$	0.23	0.59	0.32	0.76	0.23	0.63	0.29	0.71
	$b/L = 1/5$	0.26	0.58	0.34	0.81	0.26	0.58	0.30	0.72

Table 6.9. Offset case: statistical response of peak $\boldsymbol{V_b/W}$.

Design alternative		without non-simulated failure modes				with non-simulated failure modes			
		median	85th percentile	mean	COV	median	85th percentile	mean	COV
Offset Case	$b/L = 1/2$	0.166	0.199	0.184	0.671	0.170	Inf	0.165	0.196
	$b/L = 1/3$	0.149	0.186	0.154	0.159	0.150	0.191	0.150	0.152
	$b/L = 1/4$	0.144	0.171	0.147	0.134	0.144	0.171	0.145	0.120
	$b/L = 1/5$	0.144	0.166	0.147	0.134	0.144	0.167	0.145	0.117

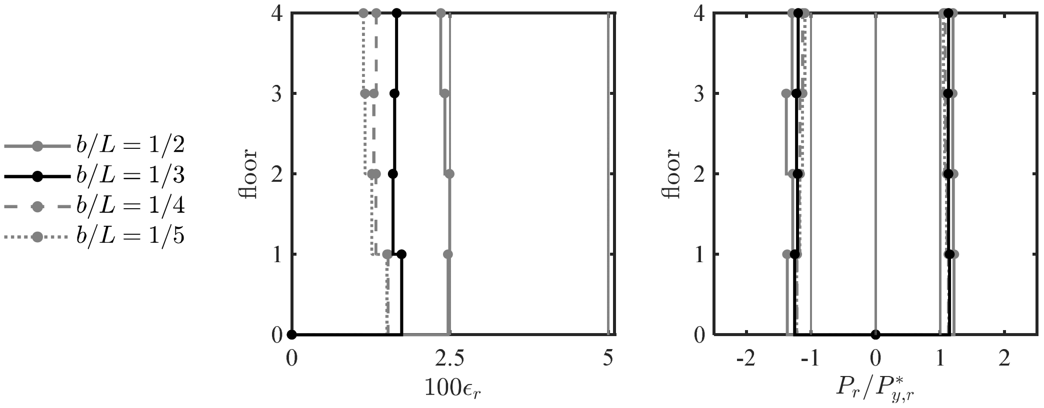

(a) (b)

Figure 6.20. Offset case median – Inelastic brace peak response envelopes.
(a) strain demand, (b) axial demand-to-capacity ratio

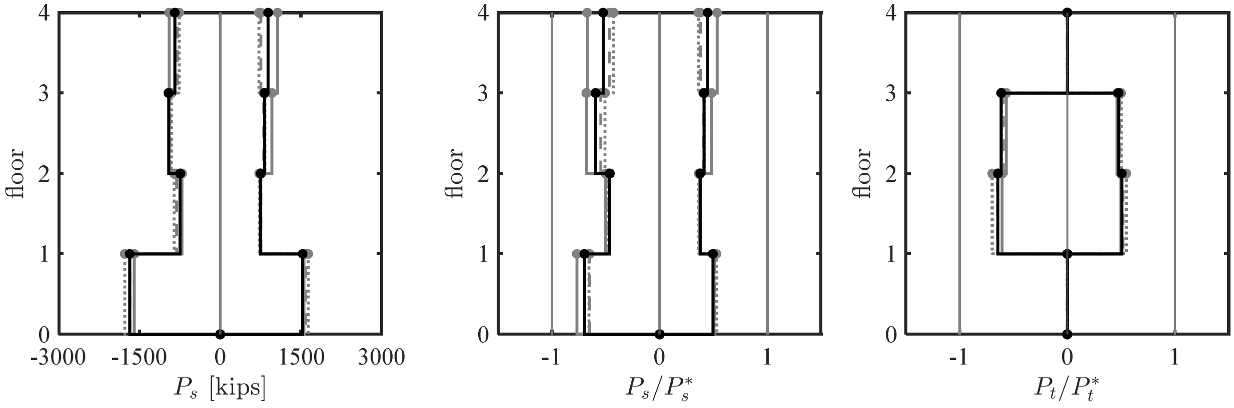

(a) (b) (c)

Figure 6.21. Offset case median – Strongback elements peak response envelopes.
(a) axial-force demand; (b) and (c) axial demand-to-capacity ratio

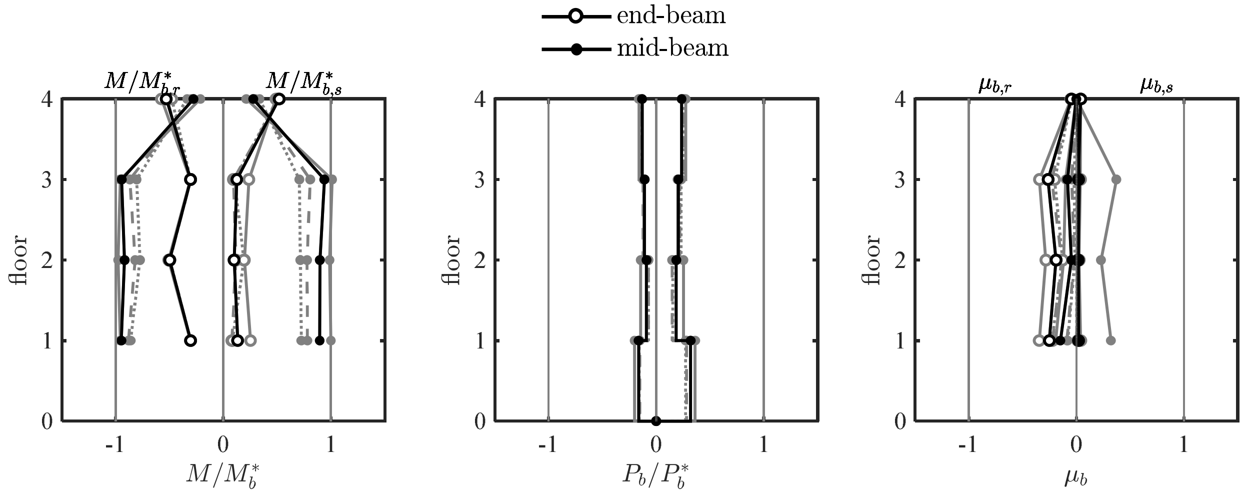

(a) (b) (c)

Figure 6.22. Offset case median – Beam peak response envelopes.
(a) moment demand; (b) axial-force demand; (c) deformation acceptability ratio

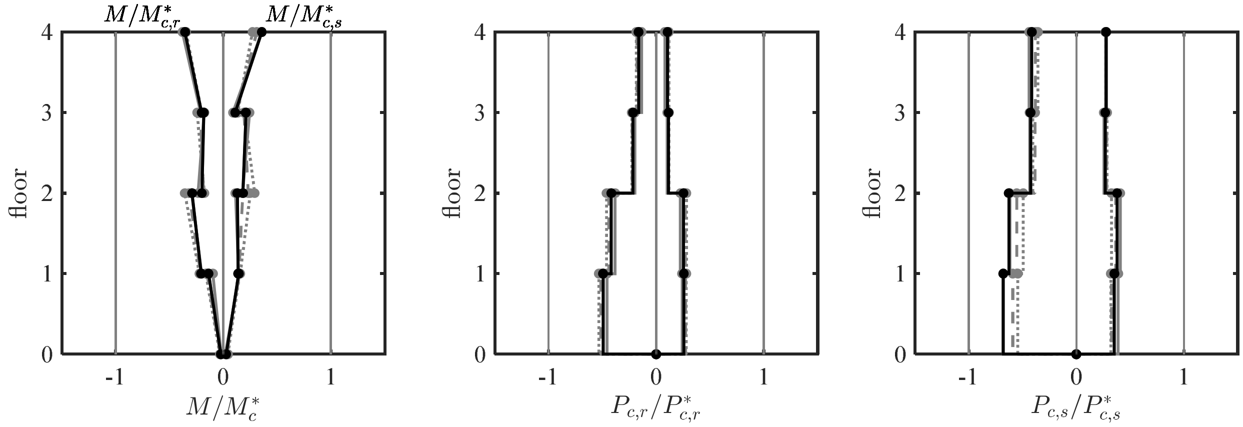

(a) (b) (c)

Figure 6.23. Offset case median – Column peak response envelopes.
(a) moment demand; (b) and (c) axial-force demand. (a) axial-force demand; (b) and (c) axial demand-to-capacity ratio

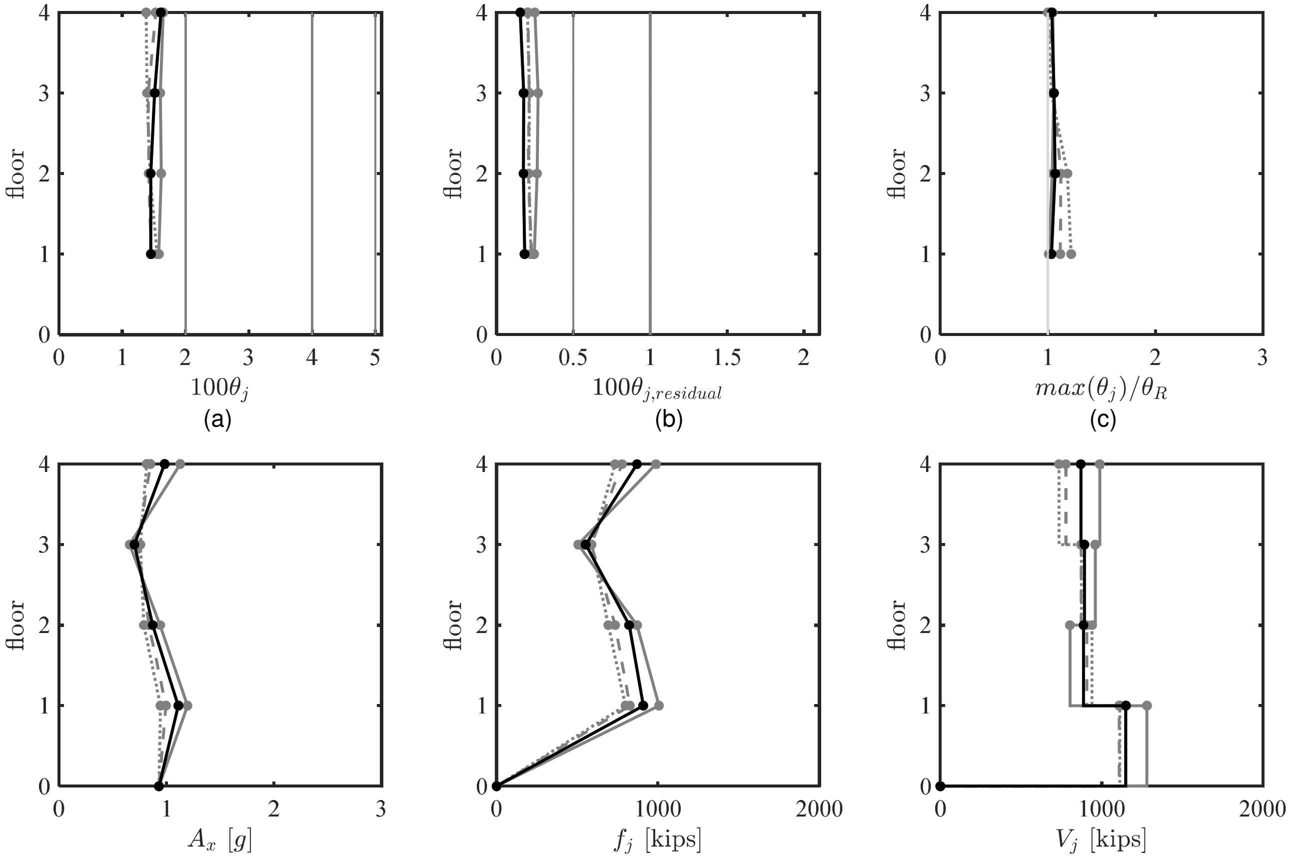

(a) (b) (c)

(d) (e) (f)

Figure 6.24. Offset case median – Global peak response envelopes.
(a) peak story drift ratio; (b) peak residual drift ratio; (c) drift concentration factor; (d) absolute acceleration; (e) estimated peak equivalent-lateral force distribution; (f) peak story shear

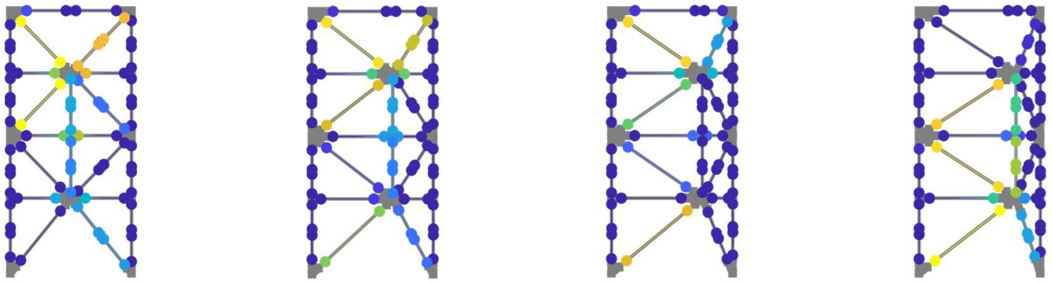

(a) (b) (c) (d)

Figure 6.25. Offset case – Response diagram at time of peak story drift ratio for gm44.
(a) $b/L = 1/2$; (b) $b/L = 1/3$; (c) $b/L = 1/4$; (d) $b/L = 1/5$

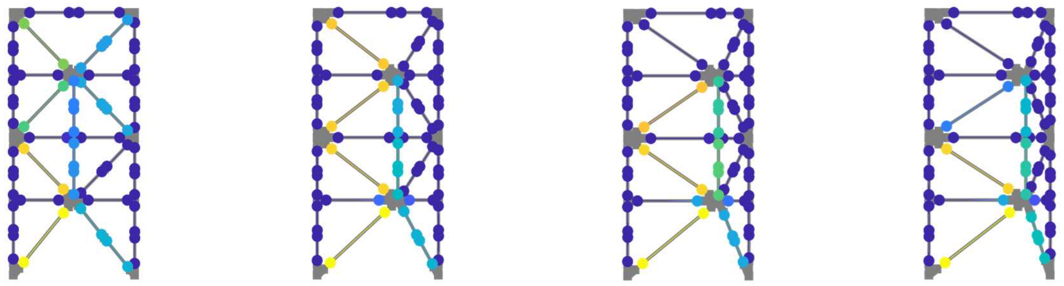

(a) (b) (c) (d)

Figure 6.26. Offset case – Response diagram at time of peak story shear for gm44.
(a) $b/L = 1/2$; (b) $b/L = 1/3$; (c) $b/L = 1/4$; (d) $b/L = 1/5$

6.3.3 BRBF and SBF Comparison

The benchmark strongback response was compared to that of the reference BRBF from Section 5.4.4.3 to give the observations of this chapter context with respect to a conventional system. To isolate the impact of BRB size with story level, two distributions of BRB sizes were investigated: [1] uniform BRB sizes in each story like that shown in Figure 5.14(a) and [2] distributed BRB sizes with uniform demand-to-capacity ratio under a first-mode equivalent-lateral force distribution like that shown in Figure 5.14(b). This resulted in somewhat longer periods where the uniform BRB size was utilized; see Table 6.10.

The median response envelopes for the benchmark SBF and reference BRBF including uniform and distributed BRB sizes are overlaid in Figure 6.27 through Figure 6.31. Both the distributed and uniform BRB sizes in the strongback benchmark design experienced similar median peak strains; see Figure 6.27(a). In contrast, strains in the BRBF system became progressively smaller with increasing story level. Relative to the BRBF utilizing distributed BRB sizes, uniform BRB sizes in the BRBF resulted in smaller strains in the upper story braces and increased strains in the lower story braces. Both the BRBF and SBF designs exhibited yielding of all four BRBs at the median level of response.

Median strongback axial-force demands were relatively independent of inelastic brace distribution; see Figure 6.28. Irrelevant of the inelastic brace size, the inelastic braces in the SBF systems exhibited uniform distributions of inelastic strains with building height.

Median moment and deformation demands in the beams were significantly smaller for the reference BRBF compared to the SBF; see Figure 6.29(a) and (c). Full yielding of the beam links was observed in the benchmark SBF; see Figure 6.29(a). Beam axial forces in the BRBFs were near zero at beams without brace-to-beam intersections; see Figure 6.29(b). Beam axial-force demands were similar in all stories of the SBF.

Median column moments were larger for the BRBF system than the SBF system; see Figure 6.30(a). This is because the BRBF utilizes bending in the columns as the mechanism to distribute demands vertically to adjacent stories. These demands were larger for the uniform BRB sizes than the distributed beam sizes. Though axial forces in the inelastic column and BRBF columns were similar, axial forces in the strongback column were significantly greater than that experienced by the BRBF columns; see Figure 6.30(b) and (c).

Median and 85th percentile demands are shown in Table 6.11 through Table 6.13. The SBF experienced much smaller drift levels compared to the BRBF; see Table 6.11. A similar trend was observed for the median residual drift; see Figure 6.31(b). This stems from the strongback's ability to average story drifts with building height. This trend was reflected in the difference in drift concentration factor between the two systems; see Figure 6.31(c).

Floor accelerations and story shears were significantly larger for the benchmark SBF than the reference BRBF and exhibited dissimilar height-wise profiles; see Figure 6.31 and Table 6.13. In the BRBF system, accelerations, and thus story shears, are limited by the strength of the bracing elements. This no longer holds true for the SBF system as the strongback has additional bracing elements that are designed to remain essentially elastic. Story shear profiles were relatively independent of bracing size. Demand-to-capacity ratio diagrams at the time of peak story shear emphasize the difference in demand distributions in the two systems; see Figure 6.32.

In summary:

- The reference BRBF exhibited non-uniform strain demands with building height. This was especially true for the BRBF utilizing uniform BRB sizes. In contrast, the SBF exhibited uniform inelastic brace strain demands independent of BRB distribution.
- Beam flexural and axial-force demands were larger for the SBF than the BRBF. As this is the mechanism of force re-distribution in the BRBF system, column moment demands were larger for the BRBF than the SBF. Axial forces in the strongback column were significantly larger than axial forces in the columns of the BRBF.
- Conventional BRBF systems with braces sized uniform to their first-mode demand-to-capacity ratios experience reduced concentrations of drift demands compared to systems using uniform brace sizes and non-uniform demand-to-capacity ratios. Note, however, that both BRB distributions in both BRBF systems exhibited drift concentration factors much larger than one.
- Accelerations and story shear demands tend to be larger for the SBF compared to the BRBF. Note that the height-wise acceleration and story shear profile is varies significantly between the two systems.

Table 6.10. SBF and BRBF comparison case: elastic periods

Parameter Description	T_1 $[s]$	T_2 $[s]$	T_3 $[s]$	T_4 $[s]$
SBF, uniform BRB size	0.839	0.267	0.157	0.125
SBF, distributed BRB size	0.848	0.275	0.162	0.125
BRBF, uniform BRB size	0.955	0.330	0.200	0.163
BRBF, distributed BRB size	0.944	0.351	0.220	0.163

Table 6.11. SBF and BRBF comparison case: statistical response of $\mathbf{max}(\boldsymbol{\theta}_{j})$.

Design alternative	without non-simulated failure modes				with non-simulated failure modes			
	median	85th percentile	mean	COV	median	85th percentile	mean	COV
SBF, uniform BRB size	1.66	2.65	1.80	0.39	1.66	2.71	1.61	0.29
SBF, distributed BRB size	1.79	2.54	1.89	0.39	1.79	2.54	1.72	0.29
BRBF, uniform BRB size	2.84	4.30	3.06	0.41	2.84	4.30	2.77	0.31
BRBF, distributed BRB size	2.40	3.35	2.48	0.44	2.40	3.35	2.39	0.40

Table 6.12. SBF and BRBF comparison case: statistical response of $\mathbf{max}(\boldsymbol{\theta}_{j,residual})$.

Design alternative	without non-simulated failure modes				with non-simulated failure modes			
	median	85th percentile	mean	COV	median	85th percentile	mean	COV
SBF, uniform BRB size	0.18	0.61	0.31	0.90	0.18	0.62	0.24	0.78
SBF, distributed BRB size	0.28	0.60	0.33	0.83	0.28	0.60	0.27	0.72
BRBF, uniform BRB size	0.36	0.65	0.41	0.57	0.37	0.84	0.40	0.58
BRBF, distributed BRB size	0.34	0.91	0.47	0.66	0.34	0.91	0.46	0.66

Table 6.13. SBF and BRBF comparison case: statistical response of peak $\boldsymbol{V_b/W}$.

Design alternative	without non-simulated failure modes				with non-simulated failure modes			
	median	85th percentile	mean	COV	median	85th percentile	mean	COV
SBF, uniform BRB size	0.15	0.19	0.15	0.16	0.15	0.19	0.15	0.15
SBF, distributed BRB size	0.15	0.19	0.16	0.18	0.15	0.20	0.16	0.18
BRBF, uniform BRB size	0.082	0.089	0.084	0.096	0.082	0.089	0.082	0.065
BRBF, distributed BRB size	0.095	0.105	0.096	0.093	0.095	0.105	0.095	0.077

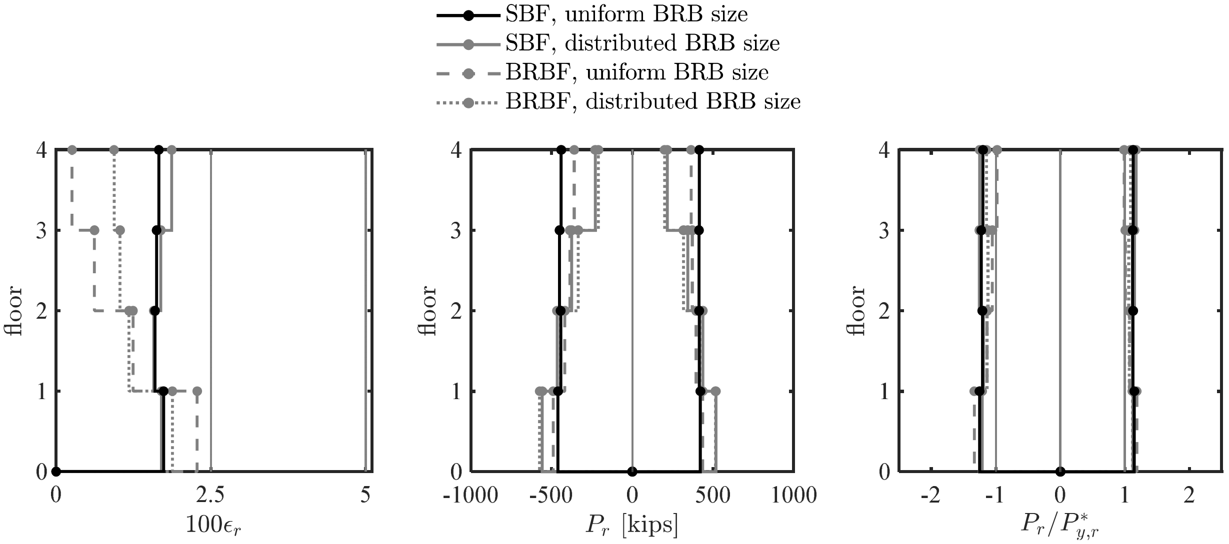

(a) (b) (c)

Figure 6.27. SBF and BRBF comparison, median – Inelastic brace peak response envelopes. (a) strain demand, (b) axial-force demand, and (c) axial demand-to-capacity ratio

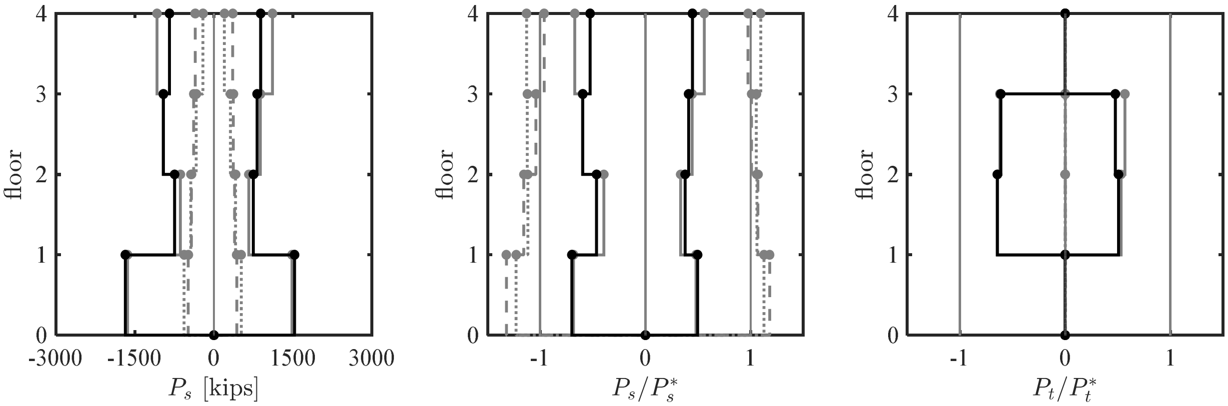

(a) (b) (c)

Figure 6.28. SBF and BRBF comparison, median – Strongback elements peak response envelopes. (a) axial-force demand; (b) and (c) axial demand-to-capacity ratio

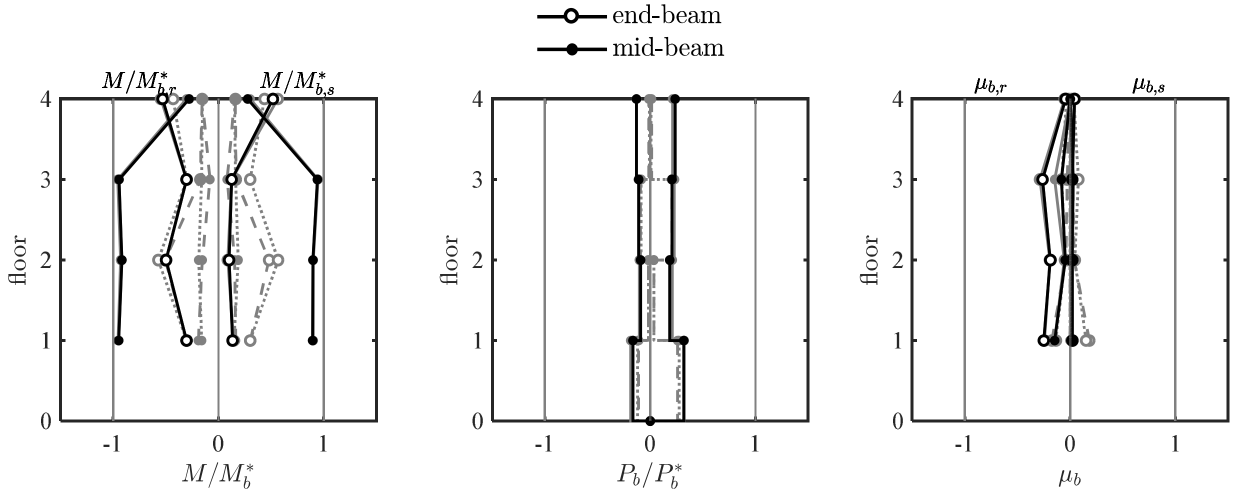

(a) (b) (c)

Figure 6.29. SBF and BRBF comparison, median – Beam peak response envelopes.
(a) moment demand; (b) axial-force demand; (c) deformation acceptability ratio

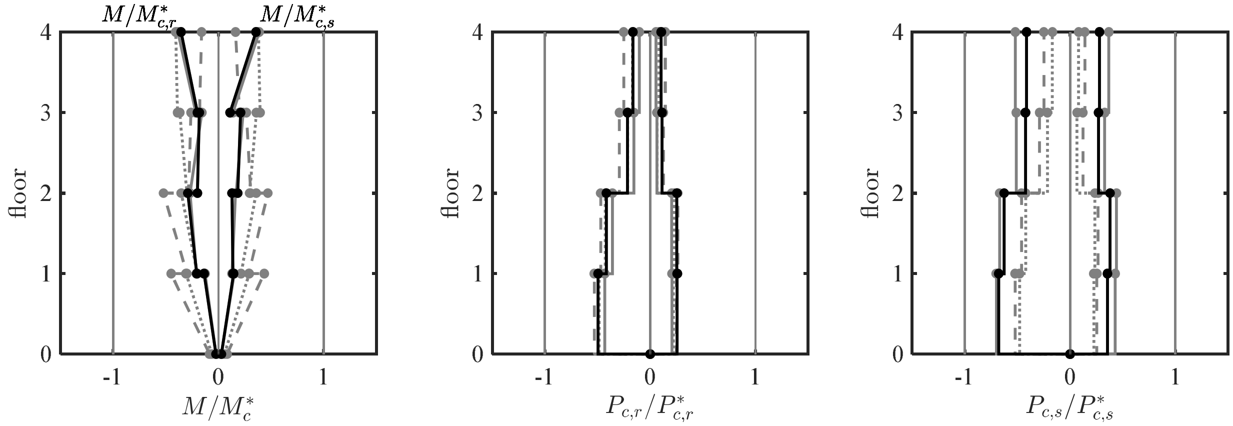

(a) (b) (c)

Figure 6.30. SBF and BRBF comparison, median – Column peak response envelopes.
(a) moment demand; (b) and (c) axial-force demand. (a) axial-force demand; (b) and (c) axial demand-to-capacity ratio

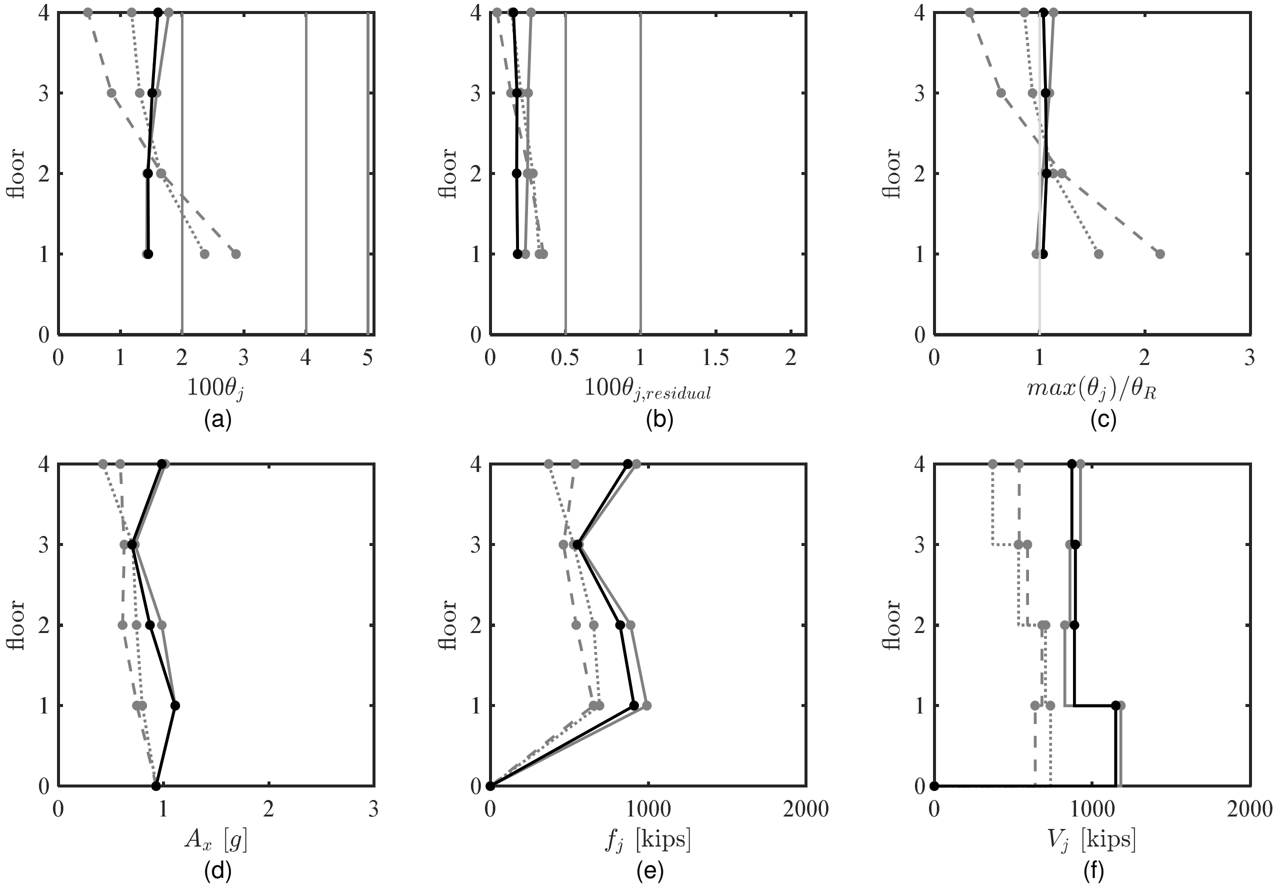

Figure 6.31. SBF and BRBF comparison, median – Global peak response envelopes.
(a) peak story drift ratio; (b) peak residual drift ratio; (c) drift concentration factor; (d) absolute acceleration; (e) estimated peak equivalent-lateral force distribution; (f) peak story shear

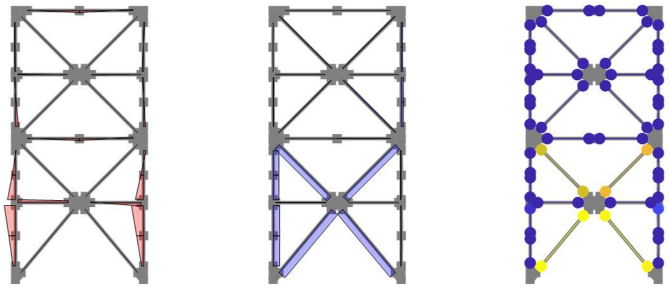

(a) BRBF

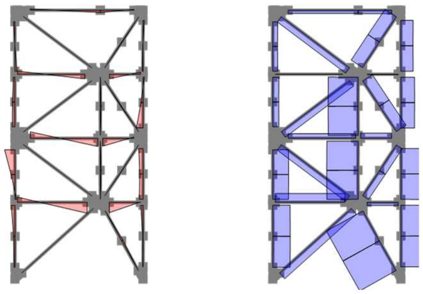

(a) SBF

Figure 6.32. SBF and BRBF comparison – Response diagram at time of peak story shear for gm44.

6.4 SUMMARY

In summary of this parametric study –

- The dynamic inelastic response was more sensitive to the characteristics of the ground motions than to design alternatives like connection condition, column base fixity, composite beam actions, etc. Those ground motions with larger spectral pseudo-accelerations at the higher-mode periods tended to have significant higher-mode effects. This primarily resulted in increased force demands on the strongback braces in the upper stories. The ground motion with the largest duration resulted in the largest peak and residual drift demands. Longer ground motions give the strongback opportunity to form a complete mechanism, potentially resulting in increased collapse potential.
- Non-simulated collapse modes were triggered by excessive deformations in the beam link at the 85th percentile level of response. This response was exacerbated in beams employing fixed end conditions. A fully pinned beam link results in substantially more deformation capacity of the beam link, but also results in increased peak and residual drifts compared to other types of beam-column connections. These demands were significantly smaller in a reference BRBF system. Proper detailing alternatives could provide more deformation capacity in this region.
- Axial-force demands in the strongback column can be significantly larger than that of the inelastic column. This stems from the larger axial forces that can develop in the strongback braces.
- The column base fixity impacts the flexural demands at the column base but has little impact on column flexural demands in the upper stories or on other elements in the system. A column oriented in weak-axis bending generally reduces moments in the system, but has less column flexural capacity than a system utilizing columns oriented in strong-axis bending.
- Inclusion of a rigid diaphragm results in negligible axial-force demands in the beams. Beam composite action asymmetrically affects beam flexural demands. The inclusion of composite action also resulted in the triggering of on-simulated collapse modes at the 85th percentile due to excessive deformations in the beam links. By equilibrium, beam bending moments can impact flexural demands in the columns if the beam-column connections are restrained.
- Brace end condition and tie continuity has little impact on the behavior of the system unless the beam-column connections are fixed. Though not a part of this study, the end condition of the inelastic braces could also affect behavior.
- The location of the offset can significantly affect force and deformation demands in the system. Careful choice of offset location or complete removal of the strongback to a different bay should be considered in a final design methodology.
- The distribution of inelastic brace size with building height has negligible impact on the strongback's dynamic response. As such, it is irrelevant for inelastic braces to be sized based on a first-mode demand-to-capacity ratio in an SBF system.
- Column moment demands were larger for the BRBF than the SBF as this is the mechanism of force re-distribution in the BRBF system.

Further investigation of a wider range of archetype designs is needed to extend any results from this chapter. The above observations depend on the design studied, in this case the four-story X-bracing strongback benchmark design. Larger or smaller differences in the response could result from the selection of a different benchmark frame, chosen design alternatives, or ground motion characteristics (e.g., some of these differences may become more apparent in designs with heavier beam sizes).

7 Characterizing the Behavior of Multi-Story Strongbacks

7.1 INTRODUCTION

Higher-mode effects have been identified as the cause of substantial force amplification in essentially elastic spine system like wall-type systems, rocking frames, etc. Since the essentially elastic nature of such systems is expected to be similar to that of the strongback, multi-story strongback systems can be expected to have similar higher-mode amplification and exhibit distinctly different behavior from conventional yielding system.

This hypothesis is supported by the findings of previous chapters. Story shear envelopes of a benchmark strongback-braced frame indicated a height-wise profile that was unlike that of a reference buckling-restrained braced frame; see Section 5.4.4.3. Parametric studies exploring the impact of ground motion characteristics on structural response found that ground motions with larger pseudo-accelerations at the higher-mode periods resulted in greater upper story shears and strongback-force demands; see Section 6.2.2. In structural dynamics, these results are consistent with observations that upper-story forces tend to be more affected by higher-mode contributions than lower-story forces (Chopra, 2011).

In this chapter, the fundamental behavior underlying the dynamic-force demands in multi-story strongbacks is studied in detail. This chapter studies the strongback's behavior in terms of: [i] static demands from plastic analysis, [ii] the strongback's lateral stiffness, [iii] compatibility between the inelastic and elastic portions of the strongback system, and [iv] dynamic higher-mode effects. Inelastic force re-distributions are studied analytically and governing parameters influencing dynamic behavior are identified.

7.2 PLASTIC ANALYSIS

An initial estimate for the strongback-force demands can be formulated by a rigid, plastic analysis of the structure at the "limit load" – the magnitude of lateral load needed to form a mechanism at incipient collapse. The plastic mechanism of a generalized strongback frame is shown in Figure 7.1. At incipient collapse, the frame can be assumed to deform in a rigid-plastic mechanism with a first-mode shape. This first-mode displaced shape is characterized by linear lateral displacements with story height; see Figure 7.1(b):

$$\theta = \frac{x_R}{H} = \frac{x_j}{\hat{h}_j} = \frac{\Delta_j}{h_j} \qquad \text{Equation 7.1}$$

$\theta =$ roof and story drift ratio; $j =$ story number. This linear shape assumes that the story drift ratio is uniform across all of the stories (i.e., $\theta_j = \theta$). Similar to the derivation in Section 3.4.1, geometric considerations under a virtual displacement field result in the following deformation relations on a story-by-story basis:

$$y_j = \theta b_j \qquad \text{Equation 7.2}$$

$$\theta_{b,j} = \frac{L}{l_j}\theta \qquad \text{Equation 7.3}$$

$$\delta_{r,j} = \frac{l}{r_j}\Delta_j + \frac{h_j}{r_j}y = \frac{h_j L}{r_j}\theta \qquad \text{Equation 7.4}$$

$y =$ vertical beam displacement; $\theta_b =$ beam link rotation angle; $\delta_{r,j} =$ inelastic brace axial deformation. For mathematical simplicity, each story j can be alternatively represented by vectors of the geometric terms in each story,

$$\boldsymbol{h} = \begin{Bmatrix} h_1 \\ \vdots \\ h_j \\ \vdots \\ h_{R-1} \\ h_R \end{Bmatrix}, \hat{\boldsymbol{h}} = \begin{Bmatrix} \hat{h}_1 \\ \vdots \\ \hat{h}_j \\ \vdots \\ \hat{h}_{R-1} \\ \hat{h}_R \end{Bmatrix} = \begin{Bmatrix} h_1 \\ \vdots \\ \Sigma_{i=1}^{j} h_i \\ \vdots \\ h_1 + \cdots + h_{R-1} \\ h_1 + \cdots + h_R = H \end{Bmatrix}, \qquad \text{Equation 7.5}$$

$$\boldsymbol{b} = \begin{Bmatrix} b \\ \vdots \\ b \\ \vdots \\ b \\ 0 \end{Bmatrix}, \boldsymbol{l} = \boldsymbol{L} - \boldsymbol{b} = \begin{Bmatrix} l \\ \vdots \\ l \\ \vdots \\ l \\ L \end{Bmatrix}, \boldsymbol{r} = \sqrt{l^2 + \boldsymbol{h}^2} = \begin{Bmatrix} r_1 \\ \vdots \\ r_j \\ \vdots \\ r_{R-1} \\ r_R \end{Bmatrix}, \boldsymbol{s} = \sqrt{b^2 + \boldsymbol{h}^2} = \begin{Bmatrix} s_1 \\ \vdots \\ s_j \\ \vdots \\ s_{R-1} \\ s_R \end{Bmatrix},$$

the element capacities in each story,

$$\boldsymbol{P}_r = \begin{Bmatrix} P^*_{r\,1} \\ \vdots \\ P^*_{r\,j} \\ \vdots \\ P^*_{r\,R-1} \\ P^*_{r\,R} \end{Bmatrix}, \boldsymbol{M}_b = \begin{Bmatrix} M^*_{b\,1} \\ \vdots \\ M^*_{b\,j} \\ \vdots \\ M^*_{b\,R-1} \\ M^*_{b\,R} \end{Bmatrix}, \boldsymbol{M}_r = \begin{Bmatrix} M^*_{r\,1} \\ \vdots \\ M^*_{r\,j} \\ \vdots \\ M^*_{r\,R-1} \\ M^*_{r\,R} \end{Bmatrix}, \qquad \text{Equation 7.6}$$

and the global displacements and deformations:

$$\boldsymbol{x} = \theta\hat{\boldsymbol{h}}, \boldsymbol{\delta}_r = \frac{\boldsymbol{h}L}{\boldsymbol{r}}\theta, \boldsymbol{\theta}_b = \frac{\theta L}{\boldsymbol{l}}, \boldsymbol{y} = \theta\boldsymbol{b} \qquad \text{Equation 7.7}$$

$1/(\cdot) =$ the reciprocal of each term in the associated vector; $R =$ total number of stories. In the case of roof beams like that in Figure 7.1(a), the inelastic width at the roof, l_R, becomes equal the bay width, L; see Equation 7.5. Where pinned rather than fixed connections have been detailed at possible plastic hinge locations, the expected capacity, $(\cdot)^*$, should be assumed to equal zero (i.e., $M^*_{r\,j} = 0$ or $M^*_{b\,j} = 0$ at the story location of the respective pin).

The applied gravity loads, $P_{g,j}$, and equivalent lateral loads, f_j, in each story can be expressed in vector format:

$$\boldsymbol{f} = \begin{Bmatrix} f_1 \\ \vdots \\ f_j \\ \vdots \\ f_{R-1} \\ f_R \end{Bmatrix}, \boldsymbol{P}_g = \begin{Bmatrix} P_{g_1} \\ \vdots \\ P_{g_j} \\ \vdots \\ P_{g_{R-1}} \\ P_{g_R} \end{Bmatrix} \qquad \text{Equation 7.8}$$

Use of this vector notation allows for an indexed representation of the variables on a story-by-story basis in terms of the vectors listed in Equation 7.5, Equation 7.6, and Equation 7.8. It also allows for a similar representation to that of the one-story strongback studied in Chapter 3.

The roof drift profile, $\boldsymbol{x}$, is a vector of virtual displacements under the kinematically acceptable plastic mechanism in Figure 7.1(b). External work can be interpreted as the dot product between the applied lateral-force distribution, $\boldsymbol{f}$, operating through the virtual displacement profile, $\boldsymbol{x}$. Internal work can be interpreted as the dot product of the internal forces undergoing virtual deformations; see Figure 7.1(c). By virtual work:

$$\lambda \boldsymbol{f}^T \boldsymbol{x} = \boldsymbol{P}_r^T \boldsymbol{\delta}_r + (\boldsymbol{M}_r + \boldsymbol{M}_b)^T \boldsymbol{\theta}_b + (M^*_{cr} + M^*_{cs})\theta \pm \boldsymbol{P}_g^T \boldsymbol{y}$$

Or in terms of the story drift ratio:

$$\lambda \boldsymbol{f}^T (\theta \widehat{\boldsymbol{h}}) = \boldsymbol{P}_r^T \left(\frac{\boldsymbol{h}L}{\boldsymbol{r}}\theta\right) + (\boldsymbol{M}_r + \boldsymbol{M}_b)^T \left(\frac{L}{\boldsymbol{l}}\theta\right) + (M^*_{cr} + M^*_{cs})\theta \pm \boldsymbol{P}_g^T(\boldsymbol{b}\theta) \qquad \text{Equation 7.9}$$

$\lambda =$ scalar amplification of applied lateral-force distribution, $\boldsymbol{f}$. The sign of the gravity loading, $\boldsymbol{P}_g$, depends on whether the direction of motion causes the beam to move upward or downward. If the beam moves upward, this contribution is additive. If the beam moves downward, this contribution is subtractive.

The left-hand side of Equation 7.9 represents the external work done by the applied equivalent-lateral forces. The right-hand side of Equation 7.9 represents the internal work done by the associated axial and flexural yielding of the inelastic braces, beam links, and column bases.

7.2.1 Limit Load

Scaling any lateral load distribution, $\boldsymbol{f}$, by the amplification ratio, λ, effectively amplifies that load distribution to the magnitude of loading required to form the plastic mechanism shown in Figure 7.1(c). Solving for λ:

$$\lambda = \left(\frac{1}{\boldsymbol{f}^T \widehat{\boldsymbol{h}}}\right)\left[\boldsymbol{P}_r^T \left(\frac{\boldsymbol{h}L}{\boldsymbol{r}}\right) + (\boldsymbol{M}_r + \boldsymbol{M}_b)^T \left(\frac{L}{\boldsymbol{l}}\right) + (M^*_{cr} + M^*_{cs}) \pm \boldsymbol{P}_g^T \boldsymbol{b}\right] \qquad \text{Equation 7.10}$$

Equation 7.10 can be re-written in summation format as:

$$\lambda = \frac{1}{\Sigma_{j=1}^{R} f_j \hat{h}_j}\left\{\sum_{j=1}^{R}\left[P_{r,j}^{*}\left(\frac{h_j L}{r_j}\right) + (M_{r,j}^{*} + M_{b,j}^{*})\frac{L}{l_j} \pm P_{g\,j} b_j\right] + (M_{cr}^{*} + M_{cs}^{*})\right\} \qquad \text{Equation 7.11}$$

By the upper bound theory of plastic analysis, the correct mechanism corresponds to the smallest amplification factor, λ. Other plastic mechanisms could also be considered to determine whether this mechanism gives the lowest value of the limit load.

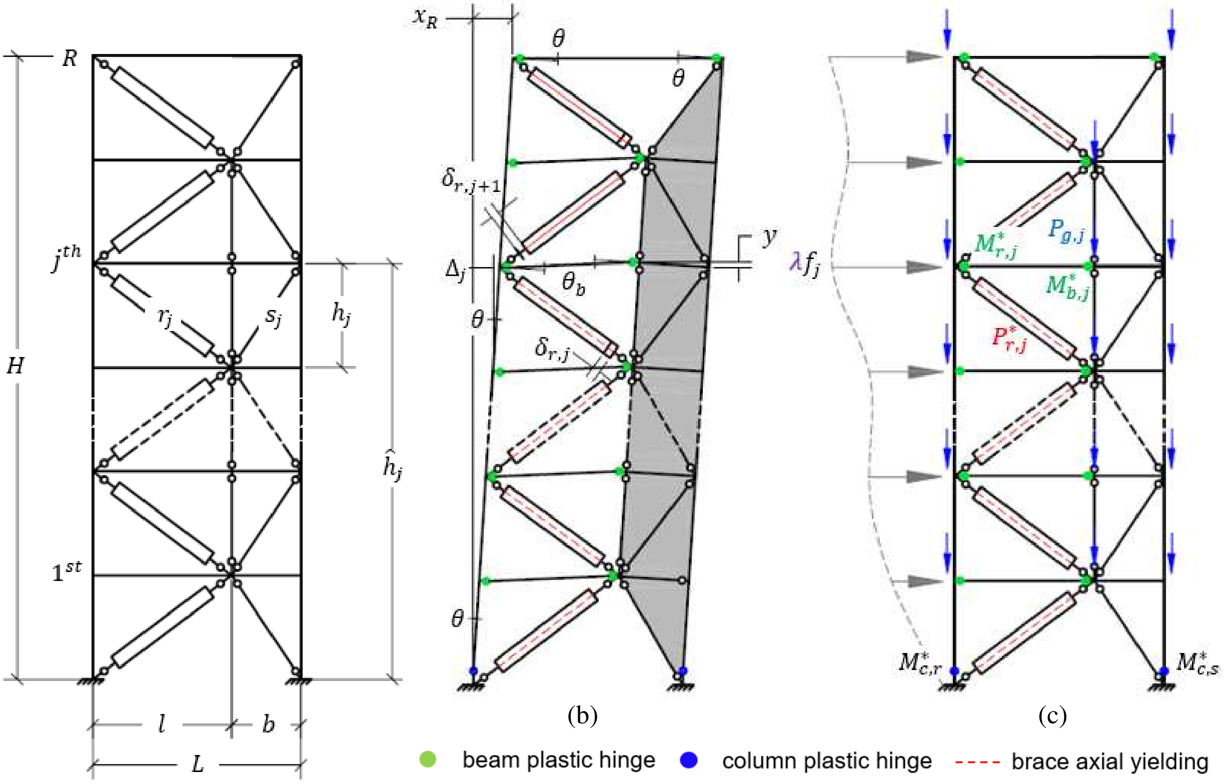

(a) (b) (c)

Figure 7.1. Kinematic mechanism example – (a) geometric labels; (b) plastic mechanism; (c) amplified lateral load

λf_j = amplified lateral force at j^{th} story
$M_{b,j}^{*}$ = j^{th} story flexural capacity near beam centerline
$M_{r,j}^{*}$ = j^{th} story flexural capacity at beam end
$P_{r,j}^{*}$ = j^{th} story inelastic brace axial capacity
$P_{g,j}$ = j^{th} story tributary gravity point load on beam
$M_{c,r}^{*}$ = j^{th} story flexural capacity of inelastic column base
$M_{c,s}^{*}$ = j^{th} story flexural capacity of strongback column base

7.2.2 Equilibrium

Equilibrium can be used to approximate the axial-force demands in the strongback elements. Neglecting column shears, essentially elastic brace demands, $P_{s,j}$, can be estimated considering the horizontal equilibrium at each story; see Figure 7.2:

$$V_j = P_{r,j}\frac{l}{r_j} + P_{s,j}\frac{b}{s_j} \qquad \text{Equation 7.12}$$

$V_j =$ the story shear calculated from the force distribution, $\boldsymbol{f}$. Solving for the strongback brace axial force:

$$P_{s,j} = \frac{s_j}{b}\left(V_j - P_{r,j}\frac{l}{r_j}\right) \qquad \text{Equation 7.13}$$

The strongback brace axial-force demand, $P_{s,j}$, can be interpreted as the diagonal component of the difference between the story shear demand generated from the applied lateral-force distribution, V_j, and the axial force in the opposite inelastic brace in the same story, $P_{r,j}$.

Demands in the vertical tie struts in each story, $P_{t,j}$, can be estimated considering vertical equilibrium between the vertical components of the axial load in the braces in the story above and the story below, the shear in the inelastic and strongback portions of the beam, $V_{r_j} = \frac{M_{r,j}+M_{b,j}}{l}$ and $V_{s_j} = \frac{M_{s,j}+M_{b,j}}{b}$, and tributary gravity loads; see Figure 7.3:

$$\begin{aligned} P_{t,j} &= P_{t,j-1} + \frac{b}{s_j}\left(P_{s,j-1} + P_{s,j}\right) - \frac{l}{r_j}\left(P_{s,j-1} + P_{s,j}\right) - P_{g,j-1} - V_{r,j-1} - V_{s,j-1} \\ &= P_{t,j+1} + P_{g,j} + V_{r,j} + V_{s,j} \end{aligned} \qquad \text{Equation 7.14}$$

At the limit load, forces and moments in the fuses are known and correspond to their plastic capacity, $(\cdot)^*$. The applied force distribution determines whether a brace is in compression or in tension. As such, axial-force demands in the strongback brace can be calculated per Equation 7.12 using the expected capacity of the opposite inelastic brace and the story shear demand amplified by λ. Once the axial forces in the strongback braces are known, the tie demands can be estimated through substitution of known quantities into the vertical equilibrium equations in Equation 7.14. For this estimation, the moment at the end of the strongback portion of the beam, $M_{b,s}$, can be neglected for straightforward determination of the strongback tie axial-force demands.

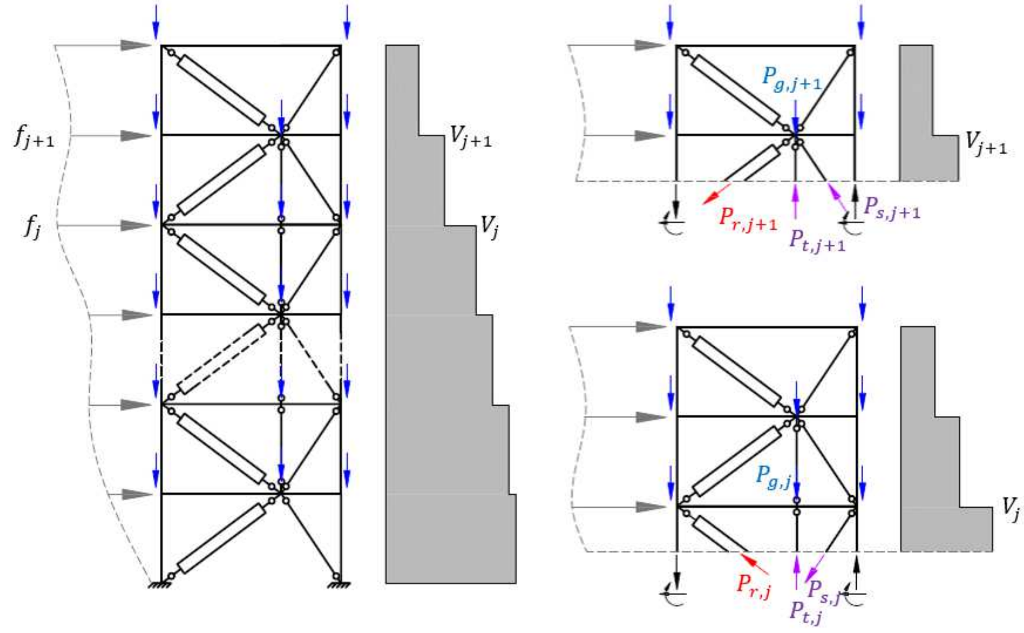

Figure 7.2. Horizontal equilibrium.

$P_{s,j} = j^{th}$ story strongback brace axial force

$\lambda V_j = j^{th}$ amplified story shear demand

$P_{t,j} = j^{th}$ story tie axial force

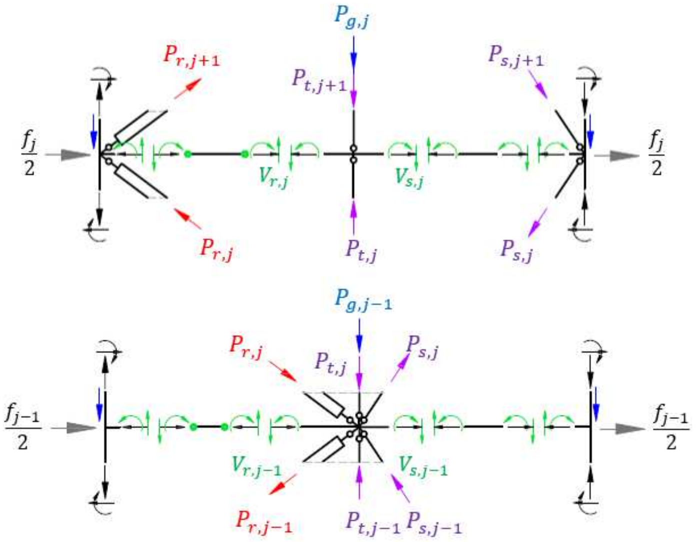

(b)

Figure 7.3. Vertical equilibrium.

$V_{r,j} = j^{th}$ story beam link shear force

$V_{s,j} = j^{th}$ story strongback beam shear force

7.3 LATERAL STIFFNESS

As observed in Section 5.4.4.1, the strongback is better able to maintain rigid body motion and a pivoting-like response with increasing flexural stiffness. This stiffness study focused on the stiffness contributions from the inelastic braces, strongback braces, and vertical tie. For simplicity, beams and columns have been excluded from this analytical derivation.

Consider a simplified story of a multi-story strongback like that shown in Figure 7.4(a). This story is similar to that of the one-story study conducted in Chapter 3, but includes a vertical component representing the additional contribution of the beam and tie to the stiffness of a story. No gravity loads are applied in this model. Beams and columns are considered to be axially inextensible.

By equilibrium, the story shear, V, can be estimated as the sum of the horizontal component of the braces in a story:

$$V = P_r \frac{l}{r} + P_s \frac{b}{s} \qquad \text{Equation 7.15}$$

This is the same as Equation 7.12 except the subscript, j, has been dropped for brevity. The net vertical force can be interpreted as an unbalanced force, P_{ub}, generated from the difference in the vertical components of the braces at the brace-to-beam intersection:

$$P_{ub} = P_r \frac{h}{r} - P_s \frac{h}{s} \qquad \text{Equation 7.16}$$

From the geometry of the frame under a lateral story drift, Δ, and vertical deflection, y, the inelastic brace elongates by δ_r and the strongback brace shortens by δ_s. These axial deformations can be written in terms of the story drift, Δ, and vertical displacement, y, as:

$$\begin{aligned} \delta_r &= \frac{l}{r}\Delta + \frac{h}{r}y \\ \delta_s &= \frac{b}{s}\Delta - \frac{h}{s}y \end{aligned} \qquad \text{Equation 7.17}$$

Axial forces can be written in terms of their elastic stiffness and axial deformation:

$$\begin{aligned} P_r &= k_r\delta_r = k_r\left(\frac{l}{r}\Delta + \frac{h}{r}y\right) \\ P_s &= k_s\delta_s = k_s\left(\frac{b}{s}\Delta - \frac{h}{s}y\right) \end{aligned} \qquad \text{Equation 7.18}$$

$k_s =$ strongback brace axial stiffness; $k_r =$ strongback brace axial stiffness. The vertical unbalanced load can be written similarly as:

$$P_{ub} = -k_v y \qquad \text{Equation 7.19}$$

k_v = effective vertical stiffness provided by tie and elements connected through the tie. To obtain an effective story tangent stiffness ($\widehat{K} = V/\Delta$), the equations for axial force in Equation 7.18 can be substituted into the equations of equilibrium in Equation 7.15 and Equation 7.16:

$$V = \left[k_r\left(\frac{l}{r}\right)^2 + k_s\left(\frac{b}{s}\right)^2\right]\Delta + \left(k_r\frac{lh}{r^2} - k_s\frac{bh}{s^2}\right)y$$

$$P_{ub} = -k_v y = \left(\frac{lh}{r^2}k_r - \frac{bh}{s^2}k_s\right)\Delta + \left[k_r\left(\frac{h}{r}\right)^2 + k_s\left(\frac{h}{s}\right)^2\right]\mathrm{y}$$

Equation 7.20

Solving for the story shear, V, in terms of the story drift, Δ, results in the following effective lateral stiffness:

$$\widehat{K} = \frac{V}{\Delta} = \left(\frac{l}{r}\right)^2 k_r + \left(\frac{b}{s}\right)^2 k_s - \frac{\left(\frac{lh}{r^2}k_r - \frac{bh}{s^2}k_s\right)^2}{k_v + \left(\frac{h}{r}\right)^2 k_r + \left(\frac{h}{s}\right)^2 k_s}$$

Equation 7.21

This equation can be written in condensed form as:

$$\widehat{K} = K_{br,xx} - \frac{K_{br,xy}^2}{k_v + K_{br,yy}}$$

Equation 7.22

$K_{br,xx} = \left(\frac{l}{r}\right)^2 k_r + \left(\frac{b}{s}\right)^2 k_s =$ lateral component of brace stiffness; $K_{br,yy} = \left(\frac{h}{r}\right)^2 k_r + \left(\frac{h}{s}\right)^2 k_s$ vertical component of brace stiffness; $K_{br,xy} = \frac{lh}{r^2}k_r - \frac{bh}{s^2}k_s =$ coupled component of brace stiffness.

Assuming perfectly plastic behavior, after yielding of the inelastic braces, $k_r = 0$, and $\widehat{K}$ reduces to:

$$\widehat{K} = \left(\frac{b}{s}\right)^2 k_s \left[1 - \frac{k_s}{k_v\left(\frac{s}{h}\right)^2 + k_s}\right]$$

Equation 7.23

If $k_v = 0$, the effective lateral stiffness of the story, $\widehat{K}$, after yielding of the inelastic braces becomes zero. Thus, the vertical component of the strongback stiffness is critical to maintaining lateral resistance after yielding in the inelastic braces. In a conventional system, this stiffness is provided by the surrounding beam-column elements that are neglected in this derivation. Note that some of this effect can be alleviated with inelastic brace strain hardening.

As the vertical stiffness, k_v, approaches infinity, Equation 7.21 reduces to:

$$\widehat{K} = K_{br,xx} = \left(\frac{l}{r}\right)^2 k_r + \left(\frac{b}{s}\right)^2 k_s$$

Equation 7.24

This is equivalent to the story stiffness of a shear building where the beam does not move vertically.

The vertical contribution term, k_v, can make it difficult to proportion strongback elements based on stiffness alone. The effective vertical stiffness includes the flexural stiffness of the floor beam along with all other stories linked to the story of interest through the vertical tie. Thus, this term represents the combined stiffness of the brace, beam, and tie from the other stories in the system.

To illustrate this point, this stiffness study was extended to an example two-story frame; see Figure 7.4(b). Neglecting the stiffness contributions of the beams and columns, the effective lateral stiffness of the braces for the two-story frame can be written as:

$$\widehat{K}_1 = K_{xx,1} - \frac{K_{xy,1}^2\left(K_{xy,2}^2 - K_{xx,2}\left(K_{yy,2} + k_v\right)\right)}{K_{yy,1}\left(K_{xy,2}^2 - K_{xx,2}K_{yy,2}\right) + k_v\left(K_{xx,2}\left(K_{yy,1} + K_{yy,2}\right) - K_{xy,2}^2\right)} \qquad \text{Equation 7.25}$$

k_v = effective beam and tie stiffness; the subscript $(\cdot)_{br}$ has been dropped for condensation of the equation. The subscripts, $(\cdot)_1$ and $(\cdot)_2$ represent contributions from the first and second level respectively, see Figure 7.4(b). The equation for effective lateral story stiffness becomes increasingly complex as the number of stories increases. When the vertical stiffness term, k_v, is zero, Equation 7.25 reduces to:

$$\widehat{K}_1 = K_{br,xx,1} - \frac{K_{br,xy,1}^2}{K_{br,yy,1}} \qquad \text{Equation 7.26}$$

Without the vertical tie tethering the stories together, the first story effective lateral stiffness decouples from the second story. The tie term, k_v, links the second story stiffness to the lateral stiffness of the first story. As such, the stiffness of one story is coupled with the stiffness of all the other stories, making it difficult to individually interpret stiffness on a story-by-story basis for SBF systems.

In the system where the strongback is embedded within the same bay as the inelastic braces, the inelastic and strongback brace response are coupled vertically as well as horizontally. The vertical coupling between these two portions of the system may be alleviated by separating the strongback from the inelastic brace bay.

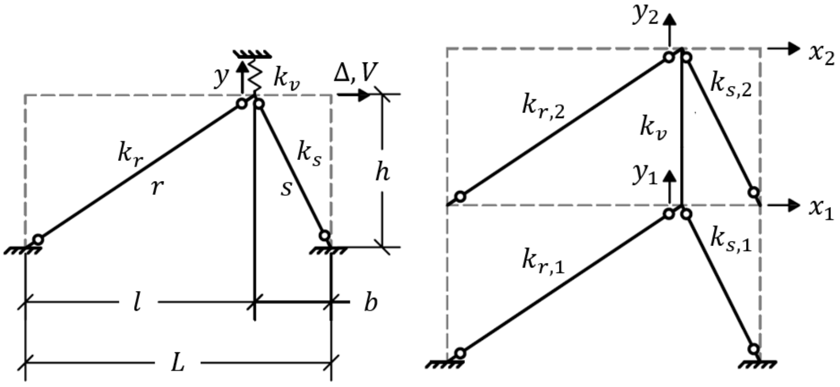

(a) (b)

Figure 7.4. Idealized frame for for stiffness study: (a) 1-story, (b) 2-story.

7.4 COMPATIBILITY

This section provides a simplified formulation of compatibility between the inelastic and strongback elements. This formulation illustrates the mechanism of interaction between the elastic and inelastic portions of the strongback system. Similar to the continuous column formulation proposed by Ji et al. (2009), this compatibility study was conducted using a simplified elastic model where the strongback is represented by a single continuous column and the inelastic brace bay can be characterized as a shear building. Deformation and force quantities for the separate inelastic and strongback portions of the system are defined in Figure 7.5 and Figure 7.6, respectively. The story height, h_j, cumulative story height, $\hat{h}_j$, and total building height, H, are defined in Figure 7.5.

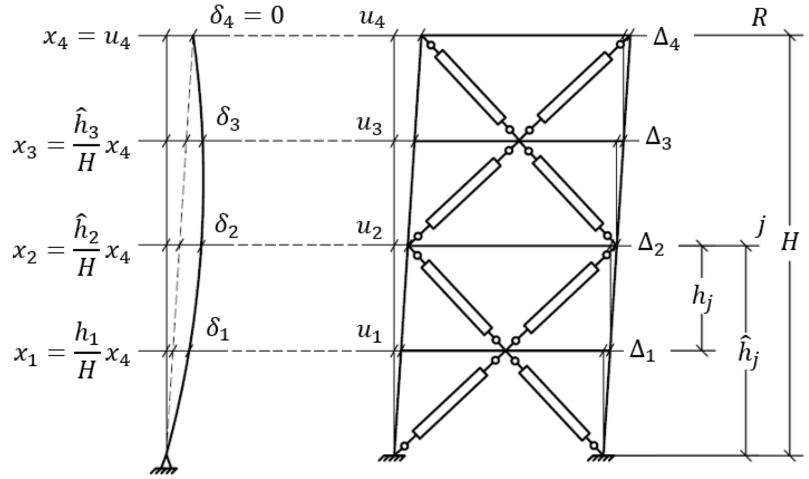

Figure 7.5. Deformation relations for compatibility formulation.

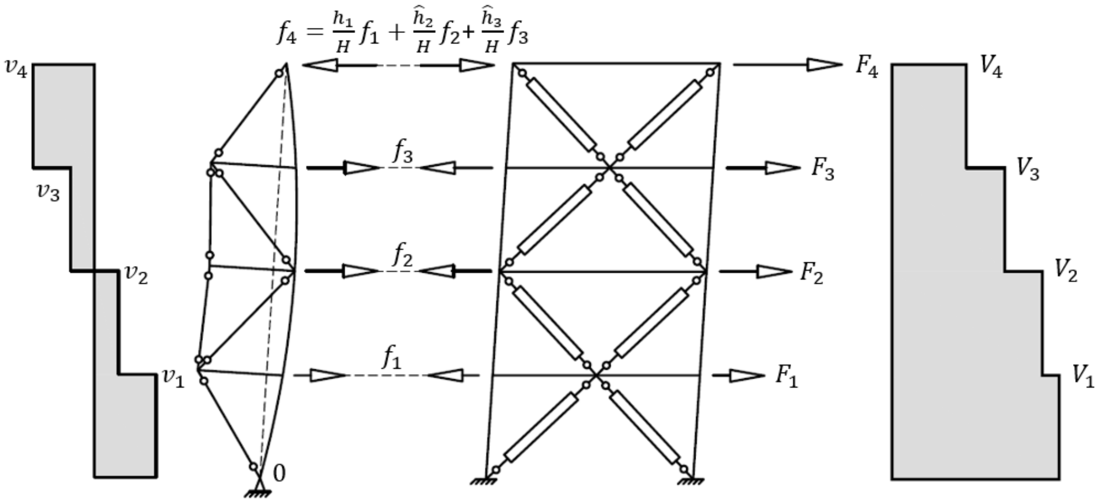

Figure 7.6. Free body diagram of force relations for compatibility formulation.

7.4.1 Inelastic Frame

The horizontal displacement at each story of the inelastic portion of the system (termed the inelastic frame), u_j, can be written as the sum of the story drift, Δ_j, and the displacement of the story below, u_{j-1}:

$$u_j = u_{j-1} + \Delta_j$$

The story drift of the inelastic portion can be written in terms of the inelastic frame's lateral stiffness, $\hat{k}_{r,j}$, and the difference in total story shear and shear taken by the strongback $(V_j - v_j)$:

$$\Delta_j = \frac{1}{\hat{k}_{r,j}} \left(V_j - v_j \right)$$

Equation 7.27

$V_j = \Sigma_{i=j}^{N} F_i =$ total story shear across the inelastic and strongback frames; $v_j = \Sigma_{i=j}^{N} f_i =$ story shear taken by the strongback frame.

7.4.2 Strongback

The story displacements in the strongback, u_j, can be divided into two contributions: [i] the contribution from the strongback's pivoting motion, x_j, and [ii] the relative bending exhibited by the strongback, δ_j:

$$u_j = x_j + \delta_j$$

Similar to that of the inelastic frame, relative bending of the strongback can be written in terms of the shear taken by the strongback, v_j, and the strongback's effective lateral stiffness, $\hat{k}_{s,j}$:

$$\delta_j = \frac{v_j}{\hat{k}_{s,j}}$$ Equation 7.28

Relative bending should consider both shear stiffness generated by the braces and bending stiffness generated by the force couple between the column and tie. A column representing the strongback with equivalent shear and bending stiffness could be used as means of estimating this effect (Chen et al., 2017).

The relative bending displacement is zero at the roof, $\delta_4 = 0$; see Figure 7.5. The pivoting displacement, x_j, can be related to the roof displacement, $x_4 = u_4$, by:

$$x_j = \frac{\hat{h}_j}{H} u_4$$

This assumes displacements due to the pivoting response are linear with cumulative story height.

7.4.3 Compatibility

Assuming the beams connecting the two portions of the system enforce compatibility, the story displacements in the inelastic frame and strongback are equal and yield the following compatibility relationship:

$$u_j = x_j + \delta_j = u_{j-1} + \Delta_j$$

From equilibrium, these can be written in terms of story shear as:

$$u_1 = \frac{h_1}{H} u_4 + \frac{v_1}{\hat{k}_{s,1}} = \frac{V_1 - v_1}{\hat{k}_{r,1}}$$
$$u_2 = \frac{\hat{h}_2}{H} u_4 + \frac{v_2}{\hat{k}_{s,2}} = u_1 + \frac{V_2 - v_2}{\hat{k}_{r,2}}$$
$$u_3 = \frac{\hat{h}_3}{H} u_4 + \frac{v_3}{\hat{k}_{s,2}} = u_2 + \frac{V_3 - v_3}{\hat{k}_{r,3}}$$
$$u_4 = x_4 = u_3 + \frac{V_4 - v_4}{\hat{k}_{r,4}}$$

Substituting u_4 into the first three equations for u_1, u_2, and u_3 and algebraically combining story shear terms gives the following system of equations:

$$v_1 \left[\frac{1}{\hat{k}_{s,1}} + \frac{1}{\hat{k}_{r,1}}\left(1 - \frac{h_1}{H}\right)\right] - \frac{h_1}{H}\left(\frac{v_2}{\hat{k}_{r,2}} + \frac{v_3}{\hat{k}_{r,3}} + \frac{v_4}{\hat{k}_{r,4}}\right) = \frac{V_1}{\hat{k}_{r,1}}\left(1 - \frac{h_1}{H}\right) - \frac{h_1}{H}\left(\frac{V_2}{\hat{k}_{r,2}} + \frac{V_3}{\hat{k}_{r,3}} + \frac{V_4}{\hat{k}_{r,4}}\right)$$

Equation 7.29

$$\frac{v_1}{\hat{k}_{r,1}}\left(1 - \frac{\hat{h}_2}{H}\right) + v_2 \left[\frac{1}{\hat{k}_{s,2}} + \frac{1}{\hat{k}_{r,2}}\left(1 - \frac{\hat{h}_2}{H}\right)\right] - \frac{\hat{h}_2}{H}\left(\frac{v_3}{\hat{k}_{r,3}} + \frac{v_4}{\hat{k}_{r,4}}\right) = \frac{V_1}{\hat{k}_{r,1}}\left(1 - \frac{\hat{h}_2}{H}\right) + \frac{V_2}{\hat{k}_{r,2}}\left(1 - \frac{\hat{h}_2}{H}\right) - \frac{\hat{h}_2}{H}\left(\frac{V_3}{\hat{k}_{r,3}} + \frac{V_4}{\hat{k}_{r,4}}\right)$$

$$\begin{aligned}&\frac{v_1}{\hat{k}_{r,1}}\left(1-\frac{\hat{h}_3}{H}\right)+\frac{v_2}{\hat{k}_{r,2}}\left(1-\frac{\hat{h}_3}{H}\right)+v_3\left[\frac{1}{\hat{k}_{s,3}}+\frac{1}{\hat{k}_{r,3}}\left(1-\frac{\hat{h}_3}{H}\right)\right]-\frac{\hat{h}_3}{H}\frac{v_4}{\hat{k}_{r,4}}\\&\quad=\frac{V_1}{\hat{k}_{r,1}}\left(1-\frac{\hat{h}_3}{H}\right)+\frac{V_2}{\hat{k}_{r,2}}\left(1-\frac{\hat{h}_3}{H}\right)+\frac{V_3}{\hat{k}_{r,3}}\left(1-\frac{\hat{h}_3}{H}\right)-\frac{\hat{h}_3}{H}\frac{V_4}{\hat{k}_{r,4}}\end{aligned}$$

If the base of the strongback is assumed to be pinned, moment equilibrium about the column base (point O in Figure 7.5) gives the following relationship between the roof level force and the other forces:

$$f_R = f_4 = -\left(\frac{\hat{h}_1}{H}f_1+\frac{\hat{h}_2}{H}f_2+\frac{\hat{h}_3}{H}f_3\right) = v_4 = -\left(\frac{h_1}{h_4}v_1+\frac{h_2}{h_4}v_2+\frac{h_3}{h_4}v_3\right) \qquad \text{Equation 7.30}$$

Using this relationship and given a lateral-force distribution, F_j, and associated story shear distribution, V_j, the demands on the strongback, v_j, can be found by solving the system of equations in Equation 7.29. Story drifts, and relative bending of the strongback can then be found by substituting these demands back into Equation 7.27 and Equation 7.28.

As an entire system, there is interaction between the inelastic frame – which primarily behaves in shear – and the strongback – which behaves in combined shear and bending. The magnitude of this interaction is sensitive to the relative stiffness of the strongback-to-the-inelastic frame, which changes as the structure yields.

Though this approach is unwieldly as a design method for similar reasons to the stiffness study conducted in Section 7.2, it does reveal a beam-like bending behavior in the strongback's response. Compatibility between the strongback and inelastic bay results in a sign reversal lateral-force distribution, f_j; see Equation 7.30. If this reversal occurs at the rood, this force reversal causes the strongback to behave as an upright, simply supported beam. As such, the strongback could even be modeled as a simply-supported beam of equivalent lateral stiffness.

7.5 DYNAMIC HIGHER-MODE RESPONSE

The distribution of lateral inertial forces – and associated story shear and force demands in force-controlled actions – is constantly changing with time due to the dynamic nature of the ground excitation. Figure 7.7 demonstrates the change in flexural demands in a column of a moment-resisting frame due to slight variations in the applied lateral-force distribution.

Moments in the column can be approximated using a plastic analysis considering the applied lateral load and the flexural strength of the fuses. However, if the distribution of the lateral load changes or is uncertain, the moments in the columns change even though the flexural strength of the fuses remains known and unchanged; see the force distributions and column moment demands at time instances t_1, t_2, and t_3 in Figure 7.7. Demands in force-controlled actions would be expected to vary from one-time instance to another as the inertial forces change with time. Slight changes in the relative flexural strengths of the fuses or lateral-force distribution could also result in another controlling mechanism (Kelly, 1974). Thus, the moment demands in the column are variable and uncertain.

The dynamic demands in the example column are similar to the force demands in a strongback truss. An iterative procedure, like the dynamic capacity design method outlined in Section 5.2, can statistically estimate the force demands in the strongback elements. However, nonlinear dynamic procedures are complicated and require a considerable amount of modeling expertise to properly implement. Such procedures also need a preliminary design to initiate the iterative design process. Information about a single response history can also be lost in aggregating the response from multiple ground motions into summary statistics.

A static analysis approach could be used to inform the design of force-controlled actions in strongback-braced frames by providing information on the fundamental dynamic response of the strongback without resorting to nonlinear dynamic analysis. As outlined in Section 7.2, strongback demands can be estimated from equilibrium between the story shear demands from the ground motion and the axial force exhibited by the inelastic brace in the same story. Compatibility between the strongback and the inelastic portions of the system can also be used to derive story shear demands; see Section 7.4.

However, these analysis methods depend on previous knowledge of the equivalent-lateral force distribution used to represent the inertial loads. Both the distribution of lateral forces and the corresponding force demands in the force-controlled actions are unknown. If an appropriate distribution of static lateral forces could be found, strongback-force demands could be estimated directly through equilibrium and compatibility using static analysis methods.

A reliable static analysis approach depends on finding a single or envelope of force distributions that appropriately bounds the force demands extracted from the nonlinear dynamic analyses. This section explores several different force distributions intended to estimate force demands on the strongback truss. Inertial force distributions were extracted from nonlinear dynamic analysis results using the four-story benchmark-strongback design from Chapter 5. Comparisons were made between force demands extracted from these analyses and the force demands estimated using several static force distributions. A perfectly plastic case study was used to illustrate the strongback's dynamic response. Based on these findings, the dynamic behavior of the strongback was characterized in terms of its higher-mode response.

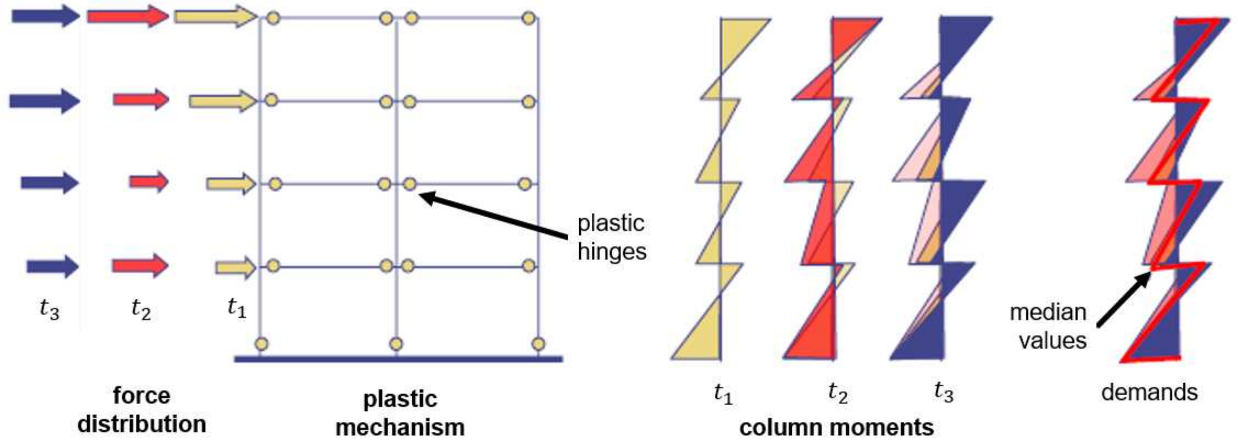

Figure 7.7. Effect of slight variation in force distribution (Mahin, 2017).

7.5.1 Traditional Force Distributions

Force demands in the strongback truss were calculated using a set of traditional force distributions. Extracted force demands were then compared to the nonlinear dynamic demands for the four-story benchmark strongback. Trial force distributions included:

1. an inverted triangular force distribution (ASCE-7-16, 2016),
2. a uniform force distribution (FEMA-356, 2000)
3. roof point load [similar to NBCC (2010)]
4. reverse triangular distribution, see Figure 7.8(4), to attempt to represent the "bending" response observed during the parametric study conducted in Chapter 6.

These force profiles and associated story shear distributions are shown in Figure 7.8(1)-(3). Force distributions were applied based on the floor mass and the amplification factor, λ, from Section 7.2.

Force demands were also estimated using a modified equivalent-lateral force (ELF) procedure. An elastic analysis subjected the benchmark strongback to ELF forces reduced by an R-factor calculated per ASCE-7-16 (2016). Forces in the strongback elements were multiplied by an overstrength factor of $\Omega_0 = \frac{3}{2}\frac{R}{2}$. This is equivalent to applying different R-factors to the inelastic and strongback portions of the system. The $\frac{3}{2}$ factor represents adjustment from the DBE-level to the MCE-level of response. This is similar to the Ω_0 design approach utilized by Lai and Mahin (2015); see Section 2.4.1.2.

Comparisons of strongback demands generated under each force distribution were compared to median and 85th percentile strongback demands extracted from nonlinear dynamic analyses of the benchmark-strongback design developed in Chapter 5. It is clear from the height-wise profiles of force demands that the trial force distributions grossly under-represent the demands extracted from the nonlinear dynamic analyses; see Figure 7.9. This is especially true of demands estimated in the upper stories.

Resulting axial-force demands on the strongback elements are tabulated in Table 7.1, Table 7.2 and Table 7.3. Force demands calculated using the inverted triangular distribution under-estimated force demands in the upper stories of the strongback. The uniform distribution resulted in larger estimates of the force-demands in the lower stories but critically under-estimated force demands in the upper stories. The point load distribution under-estimated force demands in every story. The reverse triangular distribution gave the best estimate of the force demands compared to the other trial force distributions, but still under-estimated the second- and third-story strongback brace demands by a significant margin.

The point load and ELF procedure provide the least appropriate estimates for the force demands in the strongback tie. Demands in the tie are activated by unbalanced demands between the vertical component of the axial force in the strongback and inelastic braces. The point load force distribution results in small unbalanced forces that do not adequately estimate the forces in the strongback tie. Similarly, the ELF analysis method is conducted in the elastic range where these unbalanced forces are small. Since force demands per the ELF procedure were calculated using an elastic analysis, this method was not able to directly capture inelastic behavior (e.g., force re-distributions due to yielding, strain hardening, etc.). Similar to the results reported by Lai and Mahin (2015), the ELF approach under-estimated force demands in the upper stories of the strongback truss.

Adaptive force distributions have been proposed by other researchers (FEMA-356, 2000) to better account for `inelastic response, including force distributions proportioned with respect to the deflected shape (Fajfar & Fischinger, 1988), load patterns based on mode shapes derived from secant stiffness at each load step (Eberhard & Sozen, 1993), and load patterns proportioned with respect to story shear resistance (Bracci et al., 1997). Such methods require nonlinear static analysis methods to determine the change in force distribution with every time step. However, comparisons between adaptive force distributions and constant vector force distributions (i.e., first mode, inverted triangular, etc.) found that such distributions resulted in small improvements and did not provide enough benefit to warrant their added complexity and computational effort (FEMA-440, 2005).

Table 7.1. Strongback demands from traditional equivalent-lateral force distributions.

Analysis Type	**Lateral Load Distribution**	**Axial-force demand**											
		$P_{s,1}$ [kips]		$P_{s,2}$ [kips]		$P_{s,3}$ [kips]		$P_{s,4}$ [kips]		$P_{t,2}$ [kips]		$P_{t,3}$ [kips]	
		min	max	min	max	min	max	min	Max	min	max	min	max
Dynamic	Median [1]	-1625	1614	-745	768	-956	859	-851	941	-1157	1176	-1141	1085
	85th percentile [1]	-2287	2342	-994	1002	-1411	1279	-1461	1474	-1713	1724	-1585	1719
ELF	Elastic with $\Omega_0 = \frac{3}{2}\frac{R}{2}$ [2]	-1698	1698	-942	942	-744	744	-228	228	-456	456	-432	432
Plastic	First mode [3]	-1198	1041	-842	678	-476	326	-214	55	-737	729	-617	609
	Uniform [3]	-1569	1414	-811	647	-287	137	-384	225	-1035	1029	-915	858
	Point load [4]	-724	565	-585	427	-583	434	-585	427	-114	103	-18	6
	Reverse triangular [6]	-2143	1991	-1179	1013	-283	130	-936	780	-1842	1839	-1722	1719

[1] at MCE; [2] $f_j = \Omega_0 \frac{w_j \hat{h}_j^k}{\Sigma_{j=1}^{R} w_j \hat{h}_j^k} V_b$; [3] $f_j = m_j \phi_{1,j}$; [4] $f_j = m_j$; [5] $\boldsymbol{f} = [0,0,0,1]^T$; [6] $\boldsymbol{f} = [m_1, 2m_2, m_3, 0]^T$

Table 7.2. Ratio of static demand to median dynamic response.

Analysis Type	Lateral Load Distribution	Demand Ratio											
		$P_{s,1}/P_{s,1}^{50\%}$		$P_{s,2}/P_{s,2}^{50\%}$		$P_{s,3}/P_{s,3}^{50\%}$		$P_{s,4}/P_{s,4}^{50\%}$		$P_{t,2}/P_{t,2}^{50\%}$		$P_{t,3}/P_{t,3}^{50\%}$	
		min	max	min	max	min	max	min	max	min	max	min	max
ELF	Elastic with $\Omega_0 = \frac{3}{2}\frac{R}{2}$	1.01	1.09	1.25	1.24	0.77	0.88	0.26	0.25	0.38	0.40	0.37	0.41
Plastic	First mode	0.71	0.67	1.12	0.89	0.49	0.39	0.25	0.06	0.61	0.64	0.53	0.57
	Uniform	0.93	0.91	1.08	0.85	0.30	0.16	0.44	0.24	0.86	0.91	0.79	0.81
	Point load	0.43	0.36	0.78	0.56	0.60	0.51	0.68	0.46	0.09	0.09	0.02	0.01
	Reverse triangular	1.27	1.28	1.57	1.33	0.29	0.15	1.08	0.84	1.53	1.62	1.48	1.62

Table 7.3. Ratio of static demand to 85th percentile dynamic response.

Analysis Type	Lateral Load Distribution	Demand Ratio											
		$P_{s,1}/P_{s,1}^{85\%}$		$P_{s,2}/P_{s,2}^{85\%}$		$P_{s,3}/P_{s,3}^{85\%}$		$P_{s,4}/P_{s,4}^{85\%}$		$P_{t,2}/P_{t,2}^{85\%}$		$P_{t,3}/P_{t,3}^{85\%}$	
		min	max	min	max	min	max	min	max	min	max	min	max
ELF	Elastic with $\Omega_0 = \frac{3}{2}\frac{R}{2}$	0.72	0.74	0.94	0.95	0.52	0.59	0.15	0.16	0.26	0.27	0.27	0.25
Plastic	First mode	0.51	0.46	0.84	0.68	0.33	0.26	0.15	0.04	0.42	0.43	0.38	0.36
	Uniform	0.67	0.62	0.81	0.65	0.20	0.11	0.26	0.15	0.59	0.61	0.57	0.51
	Point load	0.31	0.25	0.58	0.43	0.41	0.34	0.40	0.29	0.06	0.06	0.01	0.00
	Reverse triangular	0.91	0.87	1.18	1.02	0.20	0.10	0.63	0.53	1.05	1.09	1.07	1.01

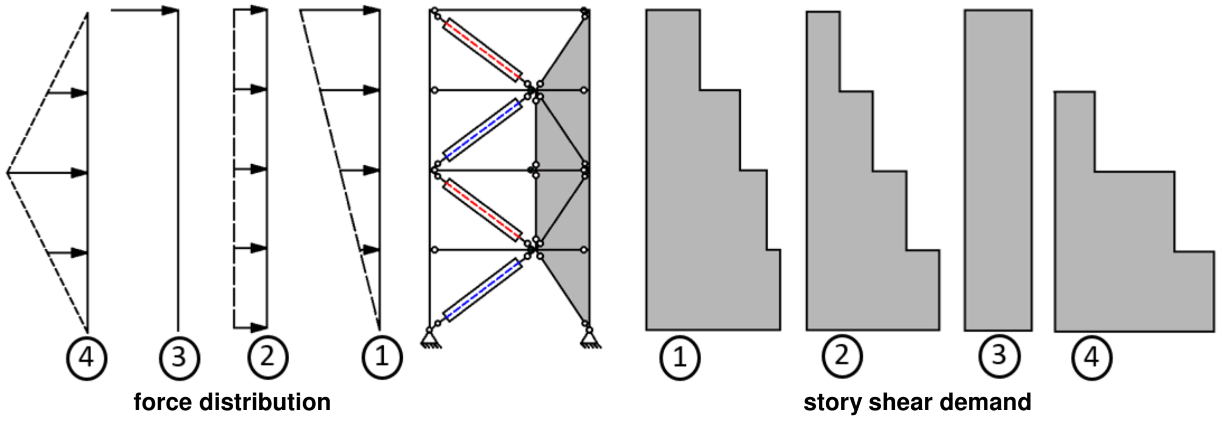

Figure 7.8. Possible force distributions.

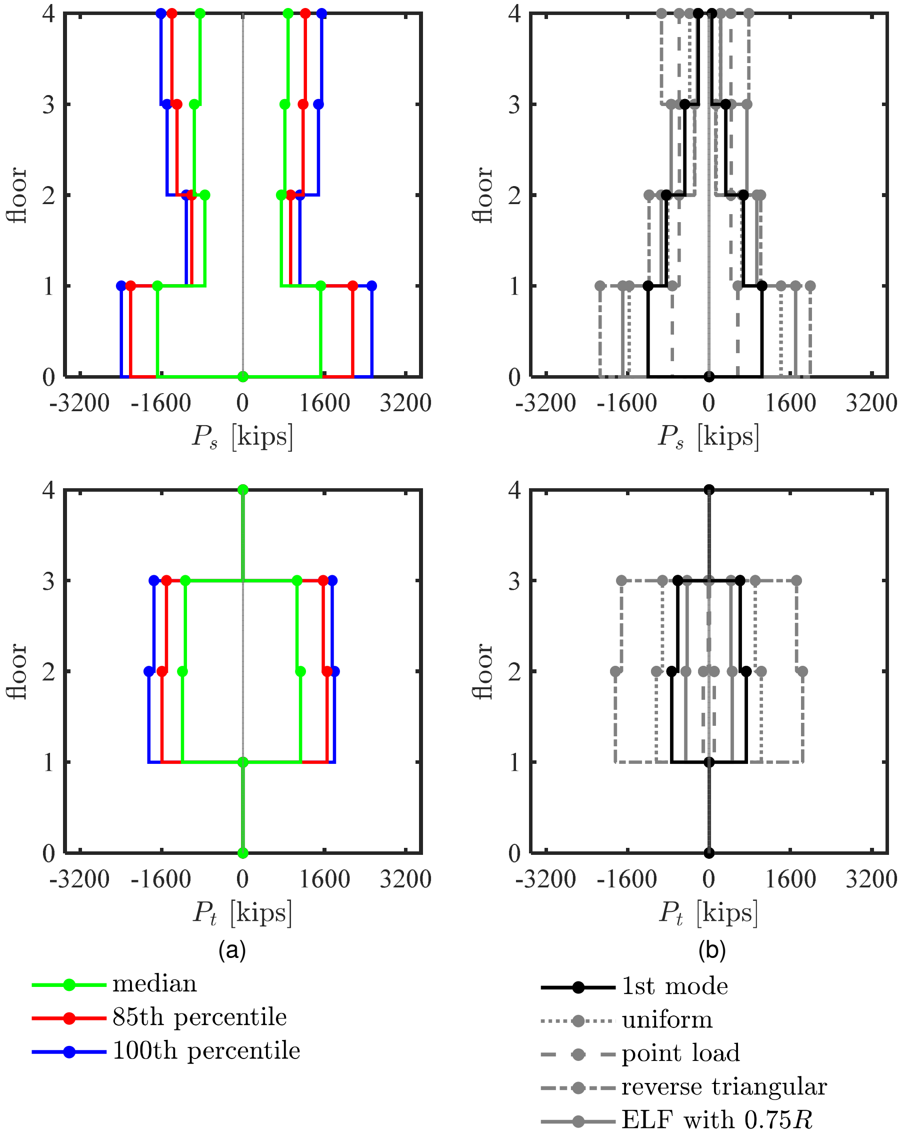

(a) (b)

Figure 7.9. Comparison of static demands to nonlinear dynamic output.

7.5.2 Peak Force Demands

The traditional lateral-force distributions tested in Section 7.5.1 under-estimated demands in the strongback elements, especially in the upper stories. As such, efforts were undertaken to extract equivalent-lateral force distributions from the nonlinear dynamic analyses. These force distributions were estimated based on the lateral story shear resistance of the elements in a story. Force distributions were extracted at the time of peak axial-force demand in the inelastic braces, strongback braces, and tie for each of the forty-four ground motions of the far-field record set.

The force distributions in Figure 7.10 through Figure 7.12 illustrate "snapshots" of force profiles extracted at instances of peak axial-force demand in a brace. The vertical axis in these plots corresponds to the brace of interest. If the label reads $\max(P_{(\cdot),j})$, the figure plots the peak tension brace force. If the label reads $\min(P_{(\cdot),j})$, the figure plots the peak compression brace force.

The median, 85th, and 100th percentile lines in these figures represent force profiles extracted for the ground motion representing the median, 85th, and 100th percentile of the peak axial force in a brace. The force distributions in these figures are not distorted and represent the force distribution exhibited by a single ground motion and time instance when the statistics of the brace force were expressed. This process was repeated in Figure 7.13 through Figure 7.21 for story shear force profile, story drift ratio profile, and inelastic brace axial force profile. Tabulated values for these peak demands and additional snapshots of the response distributions can be found in Appendix E.

Equivalent-lateral force distributions extracted at peak inelastic brace axial force are shown in Figure 7.10. These distributions follow an inverted triangular distribution with story height. The story shear profile tends to be either fully positive or fully negative, indicative of single sign inertial forces; see Figure 7.13. The inelastic braces develop peak axial-force demands when the story drift distribution is nearly uniform; see Figure 7.16. The lower-story inelastic braces experienced peak axial-force demands when all of the inelastic braces exhibited strain hardening after yielding. Upper-story inelastic braces exhibited peak axial-force demands under non-uniform distributions of inelastic brace yielding. These results suggest that the inelastic braces exhibit peak force demands under primarily first-mode contributions with slight higher-mode contributions.

Equivalent-lateral force distributions extracted at peak strongback brace and tie axial force are shown in Figure 7.11 and Figure 7.12. These force distributions exhibit distinct sign reversals, suggestive of higher-mode contributions. The story shear profiles exhibit similar sign reversals; see Figure 7.14 and Figure 7.15. The strongback braces and tie develop peak axial-force demands when the story drifts become non-uniform and the story displacements deviate from a linear profile; Figure 7.17 and Figure 7.18. The tie and lower-story strongback braces experienced peak axial-force demands when all of the inelastic braces exhibited strain hardening after yielding. Upper-story strongback braces exhibited peak axial-force demands under non-uniform distributions of inelastic brace yielding.

In summary, though the peak inelastic brace axial-force demands exhibit roughly first-mode demands, these results suggest that peak strongback-force demands exhibit dominant higher-mode effects. Upper story forces in the strongback truss are larger when the frame experiences non-uniform yielding and drift patterns compared to uniform yielding and drift patterns.

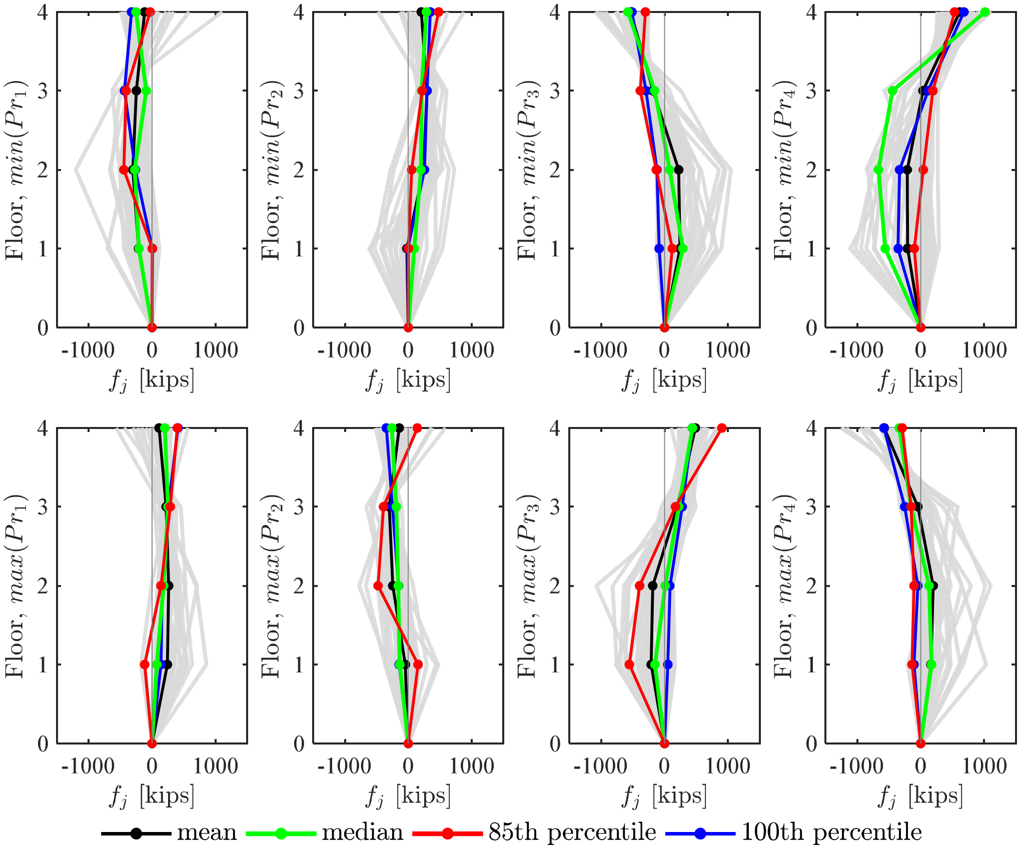

Figure 7.10. Equivalent-lateral force distribution at peak inelastic brace axial force.

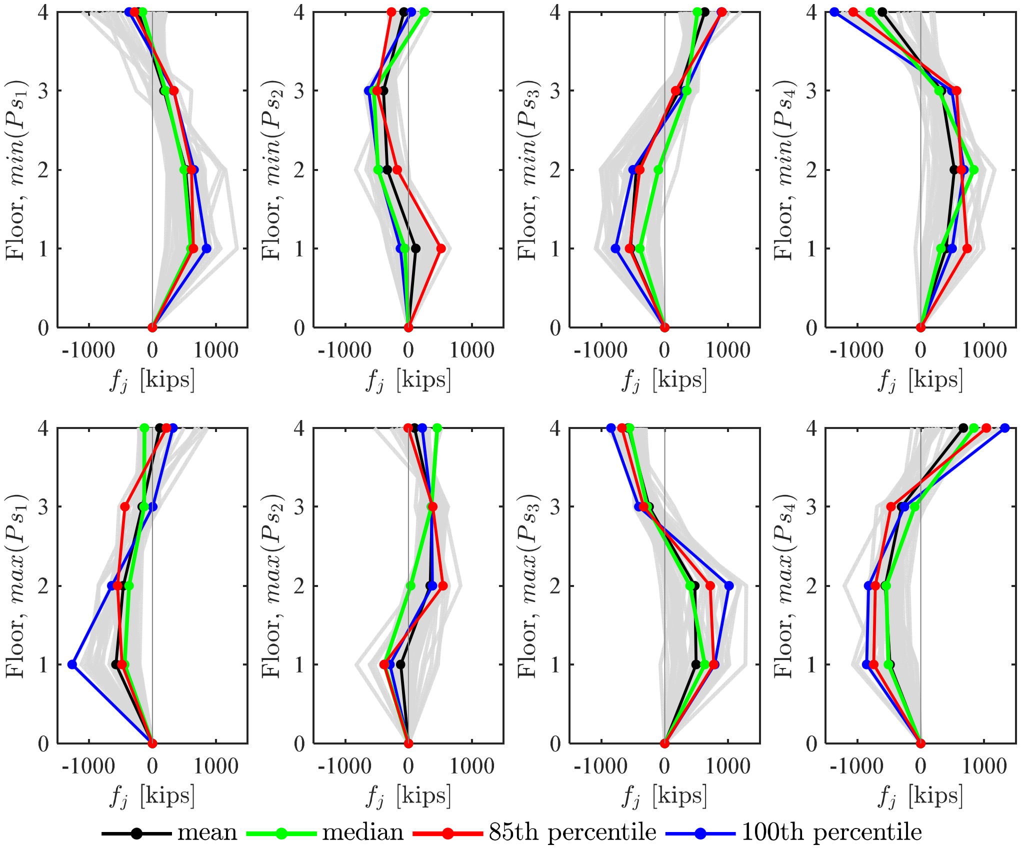

Figure 7.11. Equivalent-lateral force distribution at peak strongback brace axial force.

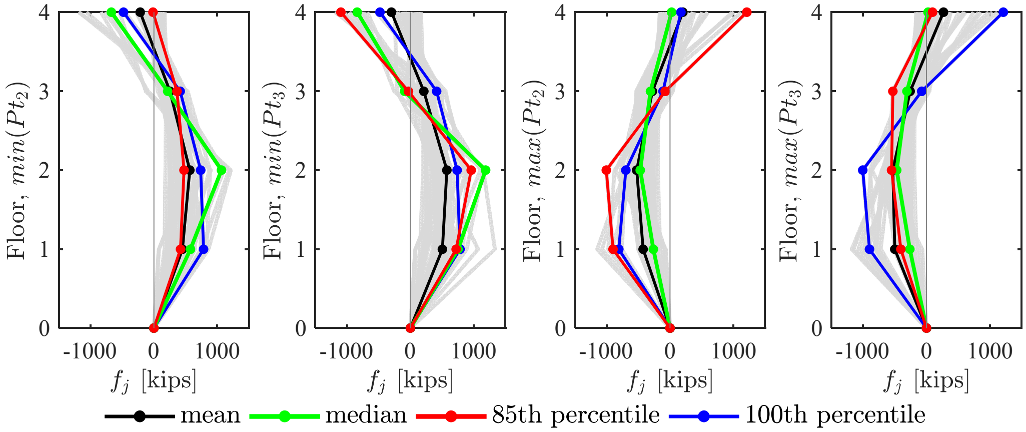

Figure 7.12. Equivalent-lateral force distribution at peak strongback tie axial force.

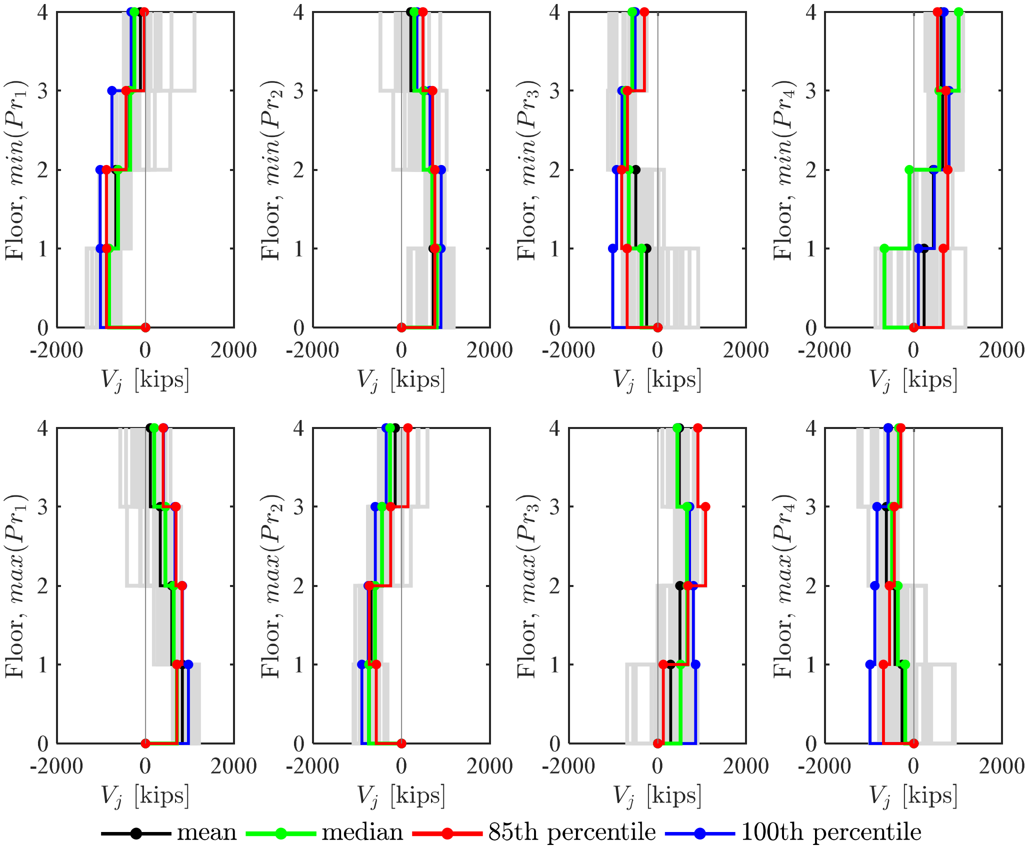

Figure 7.13. Story shear distribution at peak inelastic brace axial force.

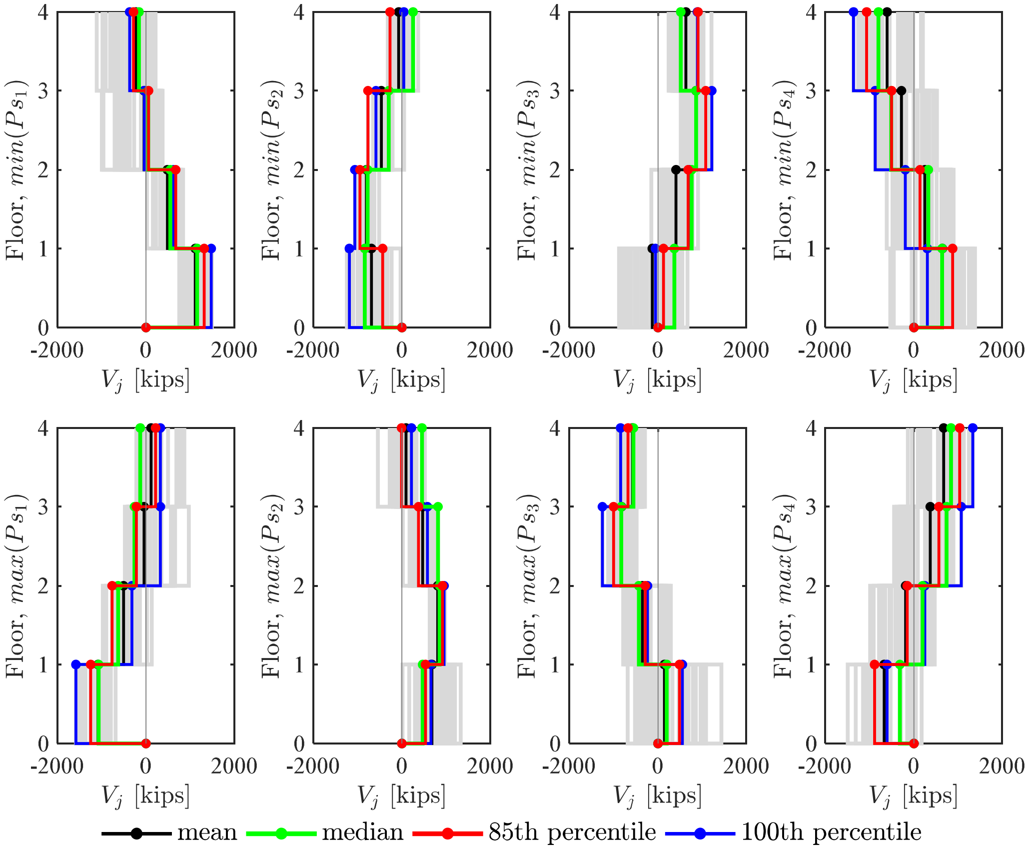

Figure 7.14. Story shear distribution at peak strongback brace axial force.

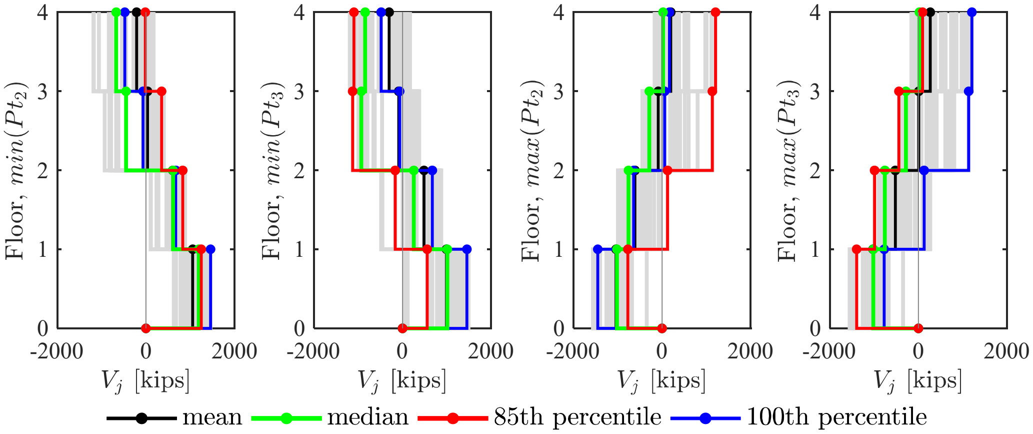

Figure 7.15. Story shear distribution at peak strongback tie axial force.

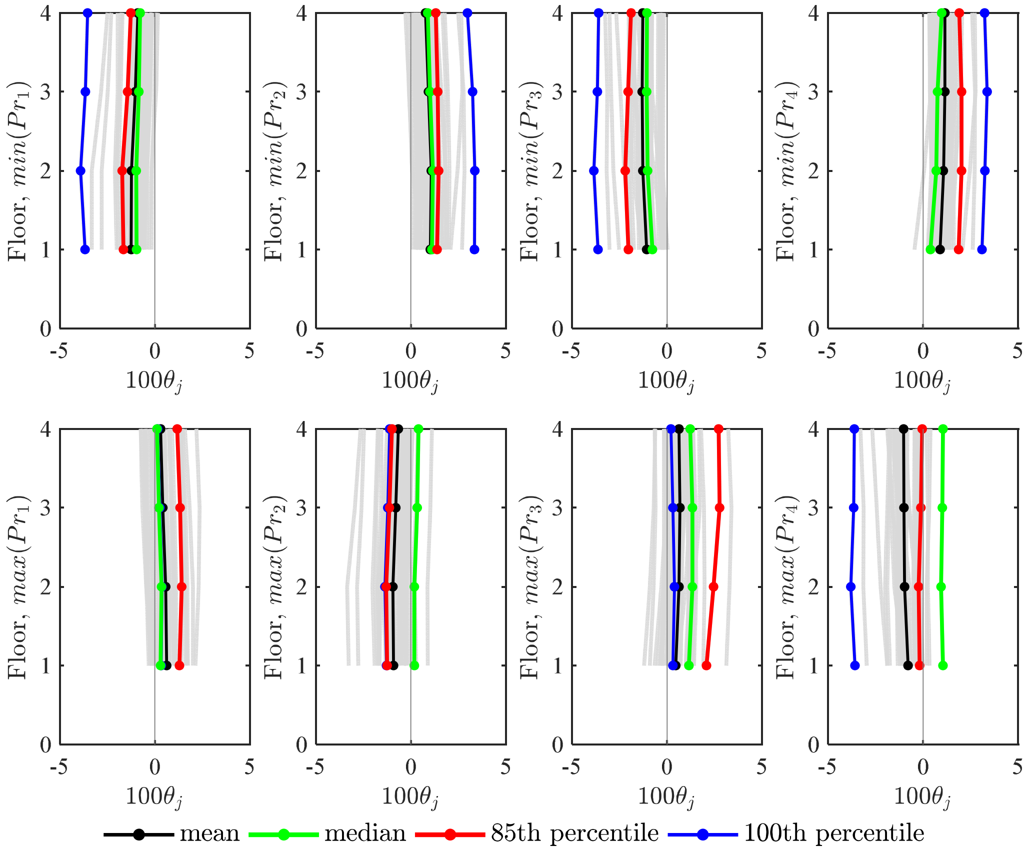

Figure 7.16. Story drift distribution at peak inelastic brace axial force.

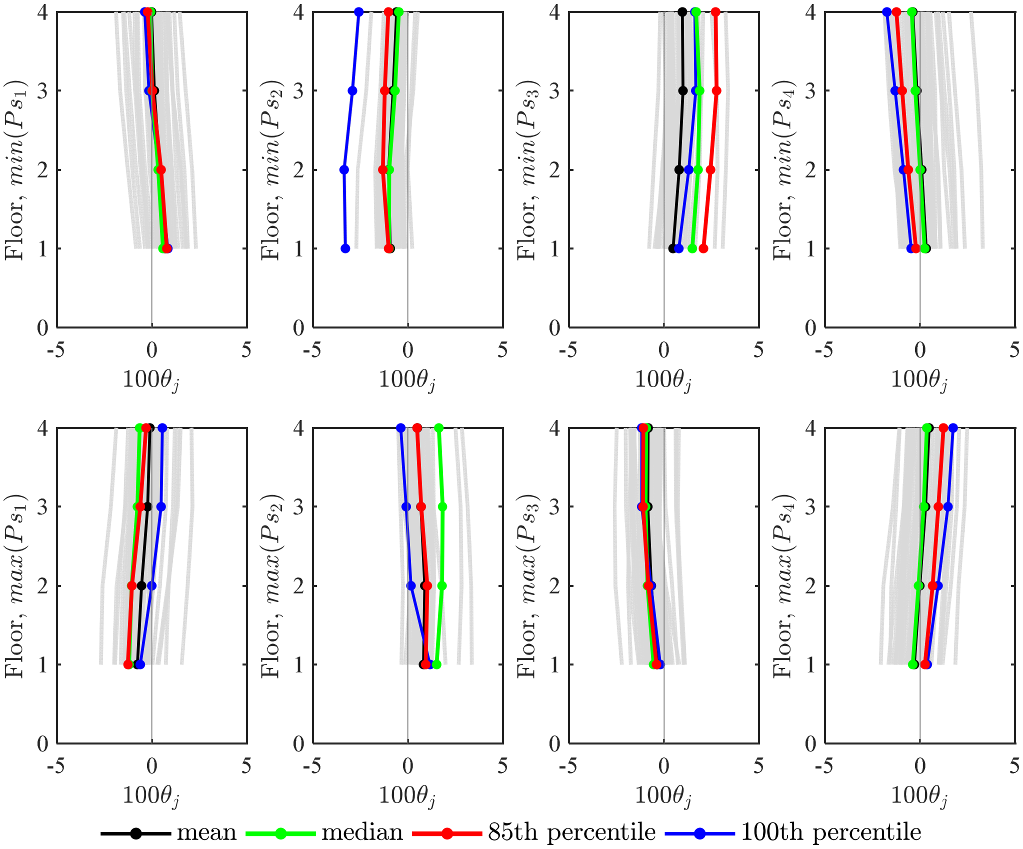

Figure 7.17. Story drift distribution at peak strongback brace axial force.

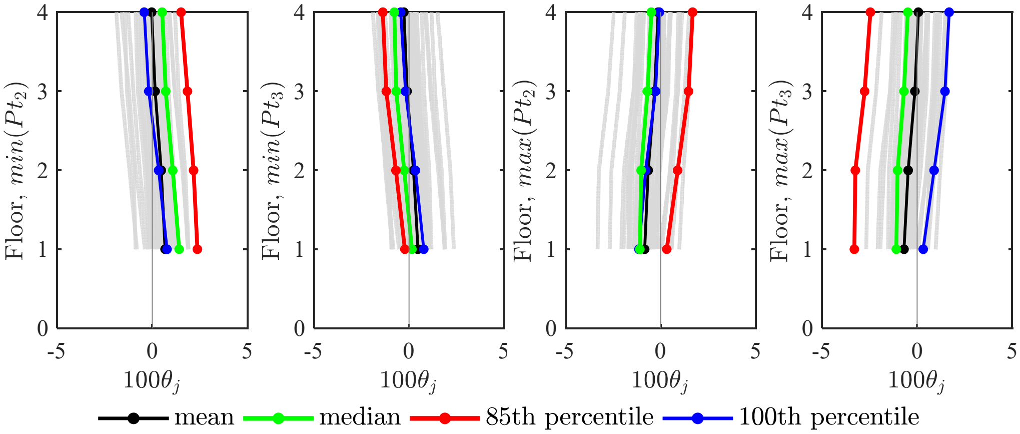

Figure 7.18. Story drift distribution at peak strongback tie axial force.

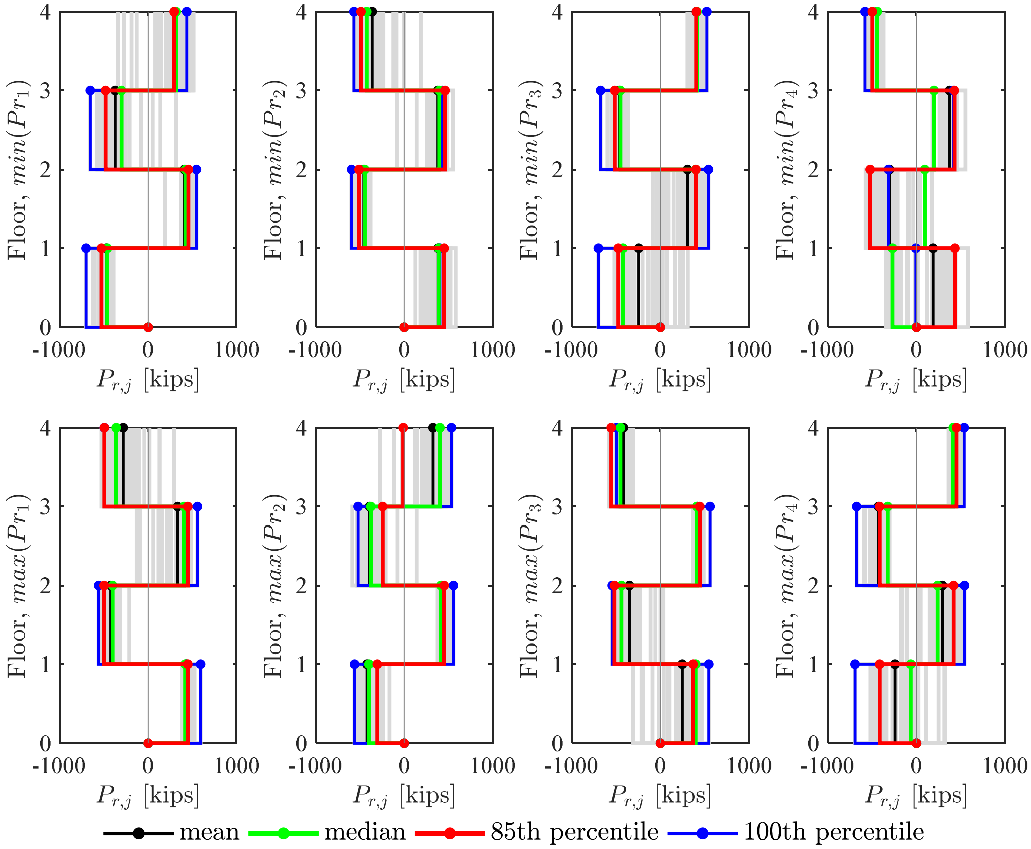

Figure 7.19. Inelastic brace axial force distribution at peak inealstic brace axial force.

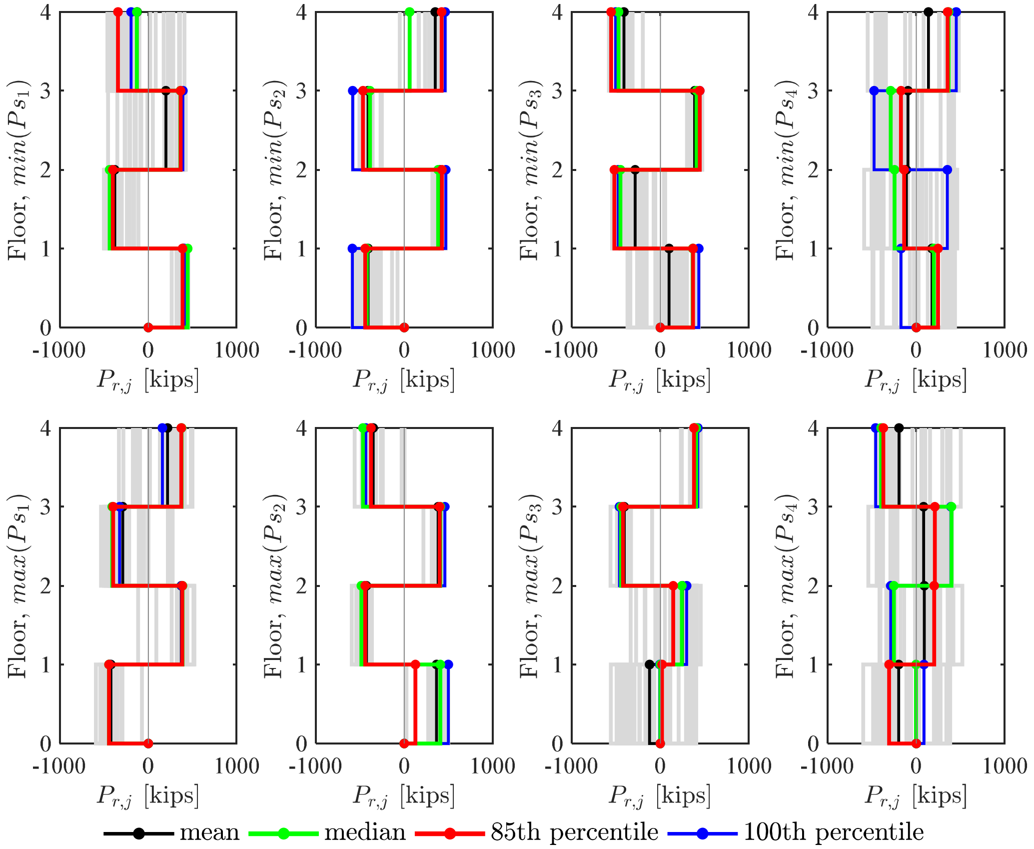

Figure 7.20. Inelastic brace axial force distribution at peak strongback brace axial force.

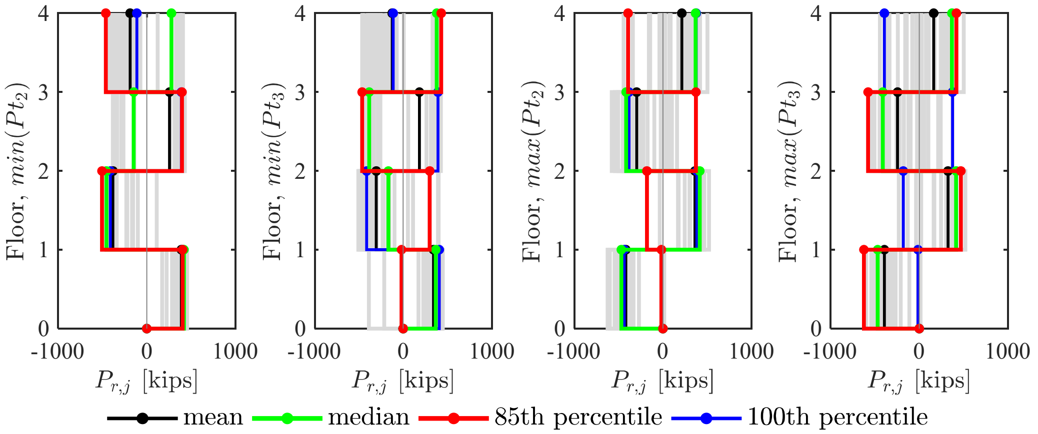

Figure 7.21. Inelastic brace axial force distribution at peak strongback tie axial force.

7.5.3 Perfectly Plastic Case Study

Results from 7.5.2 suggest that force demands in the strongback truss are indicative of higher-mode demands. To interpret this behavior, the strongback's dynamic response is presented in terms of a simple case study. This example is provided for illustrative purposes only.

The benchmark-strongback design was subjected to perfectly plastic pushover analyses in the first two modes using the structural analysis tool, FEDEUSlab (2013). The strongback braces and tie were modeled with an elastic material. Columns and beams were assumed to be inextensible with concentrated flexural hinges at their ends. Flexural-axial interaction was neglected. All braces were modeled as truss elements. Buckling-restrained braces were adjusted by the stiffness modifier, $Q = 1.4$, to account for connection and transition regions outside of the yielding length; see Section 4.4.2. Gravity loading was excluded from the numerical model. Mass was calculated from the design seismic weight per Section 4.5.5. In the first mode, the BRB axial strength was adjusted using the parameters, ω and β, from Table 4.5. In the second mode, the BRB axial strength used the expected yield strength.

The plastic pushover analysis results of the benchmark strongback model were compared to the results from a reference BRBF system. Figure 7.23 shows the first three modes calculated from an eigenvalue analysis of the structures. Figure 7.22 shows the propagation of plastic hinge formation from the pushover analysis in both the first and second modes. Pushover curves associated with the plastic hinge formation are shown in Figure 7.24.

In the first mode, the SBF and BRBF exhibit little lateral stiffness after yielding of the inelastic braces. The BRBF also exhibits little lateral strength after yielding of the fourth-story braces. However, the strongback exhibits significant stiffness and strength in the second and higher modes, even after yielding of the fuses. This response is a result of the elastic nature of the strongback truss. The first-mode base shear is limited by the yield capacity of the fuses. However, the strongback truss has significant capacity in higher-mode bending. In these second- and higher-modes the strongback truss remains elastic and continues to accumulate force demands after yielding of the fuses.

In summary, the BRBF exhibits little stiffness in the first and second mode as its story shear strength depends primarily on the inelastic strength of the braces. The SBF exhibits similar behavior in the first-mode but also exhibits significant bending capacity in the second- and higher-modes. If the strongback is expected to remain elastic under all modes of excitation, higher-mode force demands in the strongback truss are limited by the ground motion intensity rather than the strongback's bending capacity.

The amplification of higher modes has been observed in similar structures intended to remain elastic in shear, including concrete shear walls [e.g., Aoyama (1986), Ghosh and Markevicius (1990), Shahrooz and Moehle (1987), Eberhard and Sozen (1993), Panagiotou and Restrepo (2011), etc.] and rocking frames [e.g., Eatherton et al. (2014b), Wiebe and Christopoulos (2009), Roke et al. (2008) etc.]. It has been suggested that such behavior can be approximated by combining the modal responses using an appropriate modal combination rule and $R = 1$ for the higher modes (Eibl & Kreintzel, 1988). This is the method that has been adopted by Eurocode 8 (2004) for concrete shear walls.

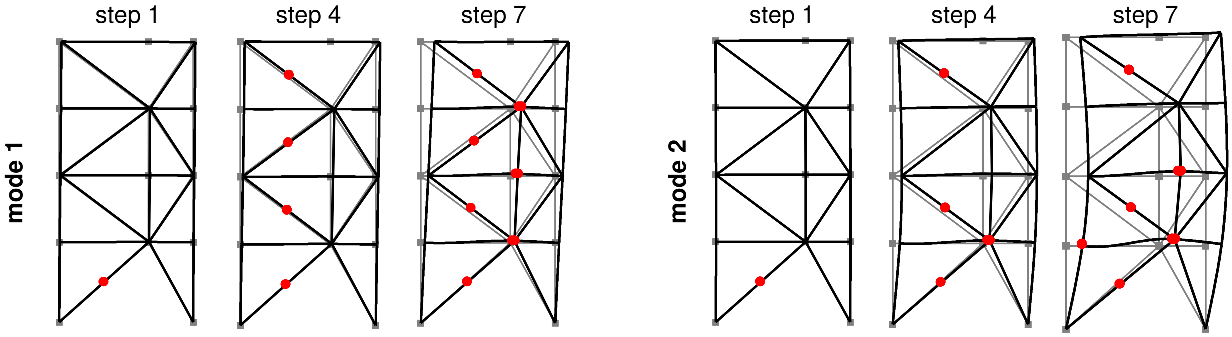

(a) SBF

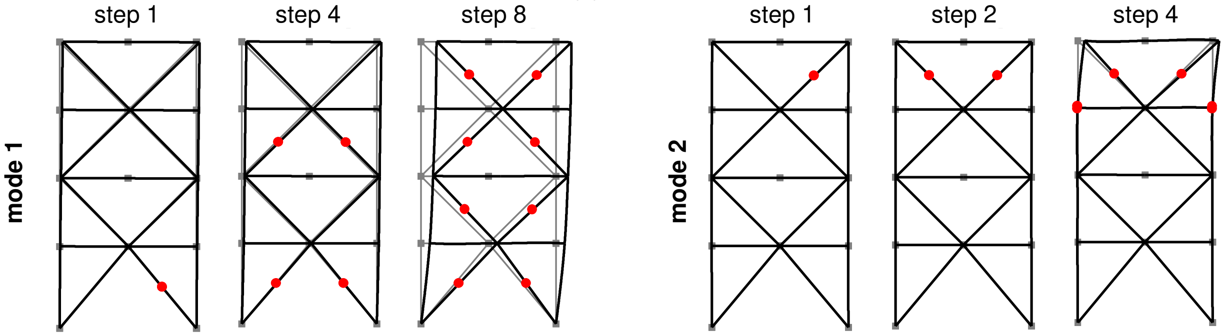

(a) BRBF

Figure 7.22. Propagation of plasticity.

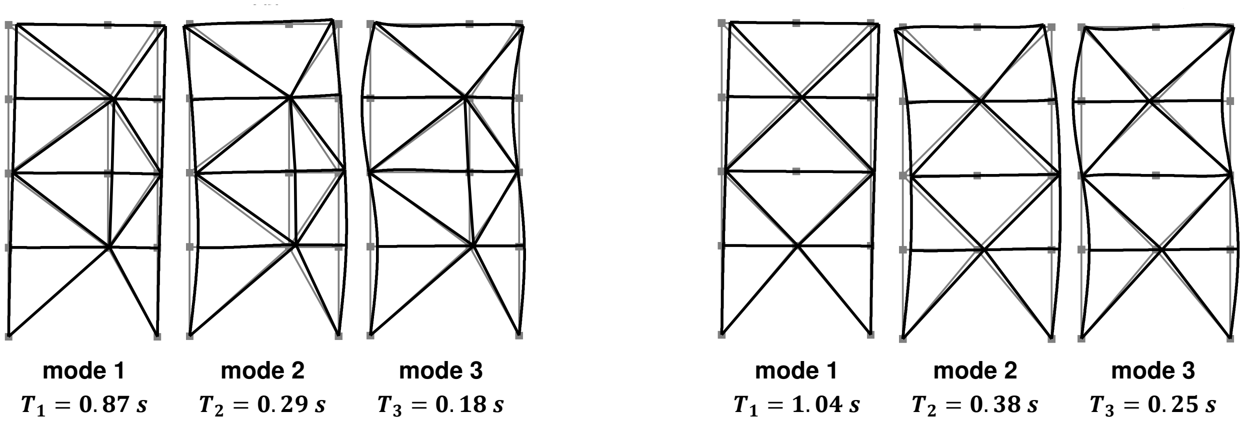

(a)

(b)

Figure 7.23. Modes for (a) SBF and (b) BRBF.

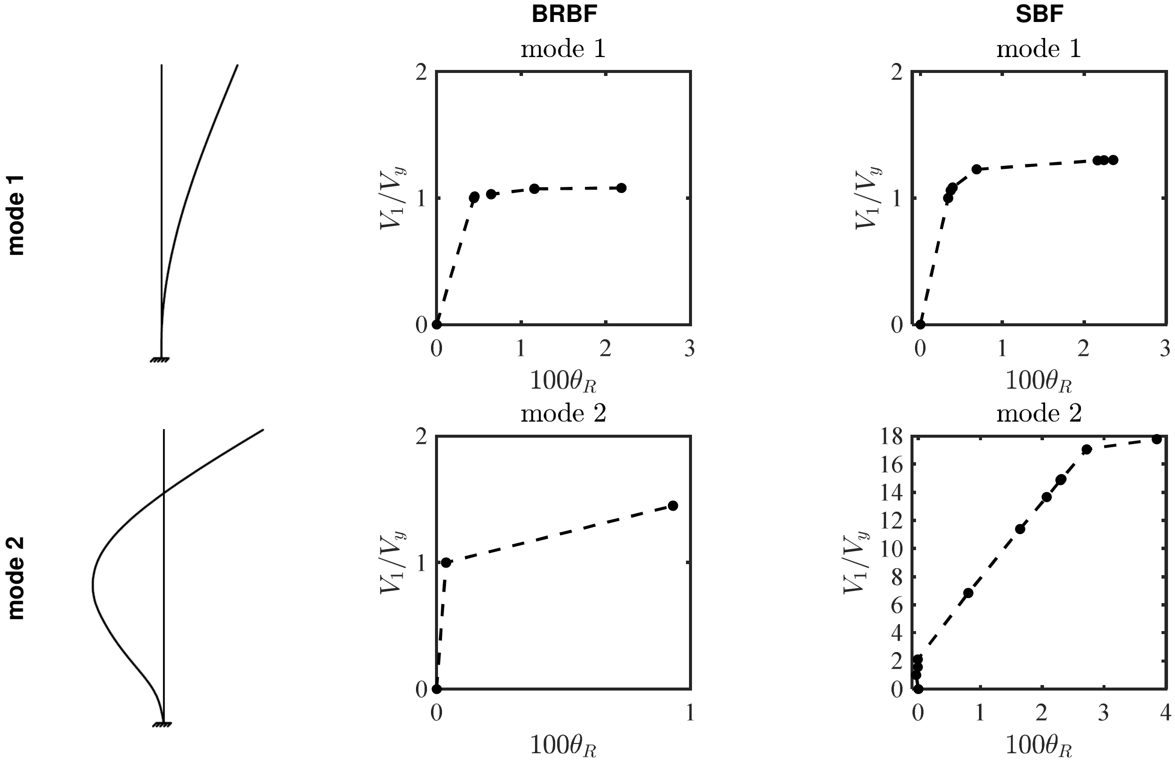

(a) (b) (c)

Figure 7.24. Lateral resistance-roof drift ratio pusover curves.
(a) mode shape of a uniform cantilever column, (b) pushover of BRBF, and (c) pushover of SBF.

7.5.4 Dynamic Behavior

Traditional force distributions that only account for a single-mode response are inadequate for estimating the force demands in the strongback truss. Though the strongback is intended to enforce a first-mode response, strongback demands are most critical when the system exhibits non-uniform yielding in the fuses or non-uniform drift distributions. The force demands extracted from nonlinear dynamic analysis were suggestive of higher-mode bending contributions. These higher-modes tend to be amplified due to the substantial bending strength of the strongback truss. This section explores the dynamic characteristics of the strongback system in terms of an equivalent-lateral force procedure using pseudo-accelerations derived from a response spectrum analysis.

7.5.4.1 Equivalent-lateral force Procedure

It is instructive to break-down the equations for equivalent static forces in terms of their derivation in structural dynamics. Equivalent static forces, $\boldsymbol{f}$, are external forces that, when applied to the structure, produce the same displacements and internal forces in the structure at the time of interest. In the elastic range, the distribution of these equivalent-lateral forces in mode n is:

$$\boldsymbol{f}_n = \boldsymbol{k}\boldsymbol{x}_n \qquad \text{Equation 7.31}$$

$\boldsymbol{k} = \omega_n^2 \boldsymbol{m}$ = elastic stiffness matrix in terms of natural modal frequency, ω_n, and mass matrix, $\boldsymbol{m}$. Using the equations from dynamics, the corresponding displacements in each mode can be written in terms of an equivalent single-degree-of-freedom oscillator:

$$\boldsymbol{x}_n = \Gamma_n \phi_n D_n \qquad \text{Equation 7.32}$$

$\Gamma_n = \frac{\Sigma_{j=1}^{R} m_j \phi_{n,j}}{\Sigma_{j=1}^{R} m_j \phi_{n,j}^2} = n^{th}$ mode participation factor assuming a diagonal mass matrix and a building symmetric in plan; $\phi_n = n^{th}$ natural mode of vibration; $D_n =$ displacement response of an equivalent single-degree-of-freedom oscillator. The variables, ω_n and ϕ_n, are the eigenvalues and eigenvectors computed from an eigenvalue analysis using the elastic stiffness and mass properties, $\boldsymbol{k}$ and $\boldsymbol{m}$.

Plugging Equation 7.32 into Equation 7.31, the equivalent-lateral forces become:

$$\boldsymbol{f}_n = \Gamma_n \boldsymbol{m} \phi_n A_n \qquad \text{Equation 7.33}$$

$A_n(t) = \omega_n^2 D_n(t) =$ pseudo-acceleration in the n^{th} mode. Demands can be determined for each mode at each time instant by static analysis of the structure subjected to $\boldsymbol{f}_n$. For a response spectrum analysis procedure, demands derived in each mode can be combined using an appropriate modal combination rule [e.g., square-root-of-the-sum-of-the-squares (SRSS), complete quadratic combination (CQC), etc.] and the spectral ordinates for the pseudo-acceleration response at period, T_n, and damping ratio, ζ_n.

For elastic systems, the initial elastic modes are orthogonal to one another and the equations of motion in each mode become decoupled. The n^{th} modal response then contains no contributions from the other modes, and the total response can be derived by the superposition of each modal response quantity.

For inelastic systems, modal orthogonality is no longer valid. The modes derived from elastic analysis become coupled as the structure yields, causing other elastic modes to contribute to the n^{th} modal response of interest. Assuming that the contribution of the coupled response using elastic modes is small for systems responding inelastically [i.e., the elastic modes are "weakly" coupled with inelastic response (Chopra, 2011)], approximations can be made by combining the inelastic response in the elastic modes and ignoring the coupled response. This can be circumvented by performing an eigenvalue analysis at every time step to obtain the inelastic modes at each time increment.

7.5.4.2 Modified Design Spectrum

The benchmark building was subjected to the FEMA-P695 far-field ground suite scaled to the fundamental period, T. Though appropriate for the fundamental mode, this scaling amplified the pseudo-accelerations at the higher-mode periods; see Figure 7.25. To account for higher-mode effects in design, a modified response spectrum, also shown in Figure 7.25, was created to match the FEMA-P695 design spectrum at the upper limit period, T, and to match the median far-field response spectra at the higher-mode periods. Spectral values for the modified design spectrum are shown in Table 7.4.

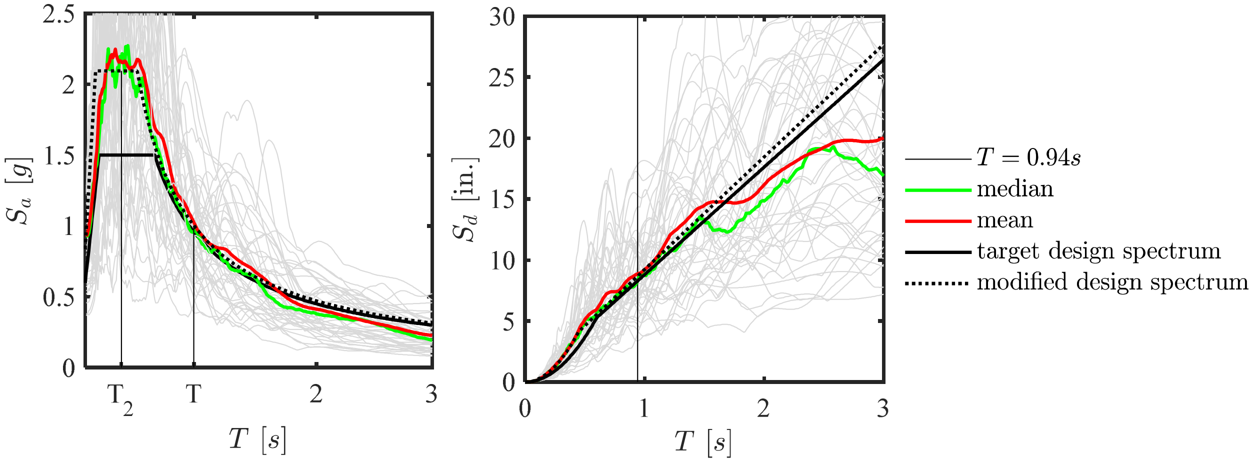

Figure 7.25. Modified response spectra for the FEMA-P695 far-field record set.

Table 7.4. Spectral values for modified spectrum.

Intensity	Pseudo-acceleration
S_S	2.09 g
S_1	0.63 g
S_{MS}	2.09 g
S_{M1}	0.94 g
S_{DS}	1.40 g
S_{D1}	0.63 g

7.5.4.3 Height-wise Variation of Higher-mode Response

Equivalent-lateral forces can be estimated for each mode using the modified design spectrum in Figure 7.25. Details for the calculation can be found in Table 7.5. The first-mode response was calculated per the plastic analysis method outlined in Section 7.2. The second and higher-mode force distributions were calculated assuming the system remained elastic and used the pseudo-acceleration ordinate of the elastic response spectrum (i.e., $R = 1$ in the second and higher modes).

In the first mode, the system's lateral capacity is dependent primarily on the lateral resistance of the inelastic braces and secondarily on flexural yielding in the beam links. Though eighty-five percent of the mass participates in the first mode, pseudo-accelerations are limited by the plastic capacity of the fuses in the first mode. Since the strongback system yields in the first mode, first-mode forces can be estimated through a reduction factor of $\frac{3}{2}\left(\frac{R}{\lambda}\right)$ to account for the system's inelastic response at the MCE-level of shaking; $R = 8$ is the response-modification factor for BRBFs per ASCE-7-16 (2016). The amplification factor, λ, is representative of the overstrength needed to yield all of the fuses in Equation 7.10.

The second mode has the next highest mass participation. Though only 13% of the mass participates in the second mode, pseudo-accelerations in the higher modes can be significant. Since the system remains essentially elastic in bending, force demands in the higher-modes are limited by the ground motion intensity and not by the fuse capacity. The higher-mode periods can be estimated from the constant acceleration range of an elastic response spectrum using $R = 1$.

Force distributions extracted from the nonlinear dynamic analyses in Section 7.5.2 were compared to the static lateral-force distributions estimated from Equation 7.33 using the elastic modes and pseudo-accelerations from the response spectrum; see Figure 7.26 through Figure 7.28. Pseudo-accelerations were reduced by $\frac{3}{2}\frac{8}{\lambda}$ in the first mode and $R = 1$ in the higher modes. The calculated first-mode force distribution aligns well with the peak inelastic brace axial force demands, while the second- and third-mode force distributions align well with the peak strongback force demands. This is true of both the median and 85th percentile level of response. The lack of perfect consistency is an indication of the complex dependence of the structural response on the earthquake excitation.

Figure 7.29 and Figure 7.30 break-down the total force distribution under gm44 into estimates of its modal contributions. Inelastic modes were estimated using an eigenvalue analysis at every time step. A time stepping procedure using the modal forces from the previous time step was used to estimate the modal forces at the current time step. The first mode dominates the response upon initial yielding of the inelastic braces, as shown by the orange color in Figure 7.29. The strongback participates little under this primarily first-mode distribution. However, the strongback elements become mode activated in second-mode bending, as exhibited by the green and light blue colors in Figure 7.30. At this time instant, the second-mode has the largest contribution to the total lateral force distribution.

Table 7.5. Equivalent static force distribution in each mode.

Mode	T_n [s]	$\frac{m_1^*}{m}$	Γ_n	Mode, ϕ_n				$\frac{1.5R}{\lambda}$	A_n[2] $[g]$	f [kips]			
				$\phi_{n,1}$	$\phi_{n,2}$	$\phi_{n,3}$	$\phi_{n,4}$			$f_{n,1}$	$f_{n,2}$	$f_{n,3}$	$f_{n,4}$
1	0.84	0.850	2.91	0.12	0.25	0.36	0.45	3.6[1]	1.12	106	214	310	380
2	0.27	0.129	1.14	0.39	0.34	0.06	-0.35	1	2.09	853	782	145	-795
3	0.16	0.016	0.40	0.37	-0.05	-0.36	0.27	1	2.09	295	-49	-338	219
4	0.13	0.000	0.01	0.05	-0.08	0.03	-0.02	1	2.09	1	-3	1	0

[1] per BRBF $R = 8$ in ASCE-7-16 and $\lambda = 3.3$ from plastic analysis in the first mode.

[2] MCE-level

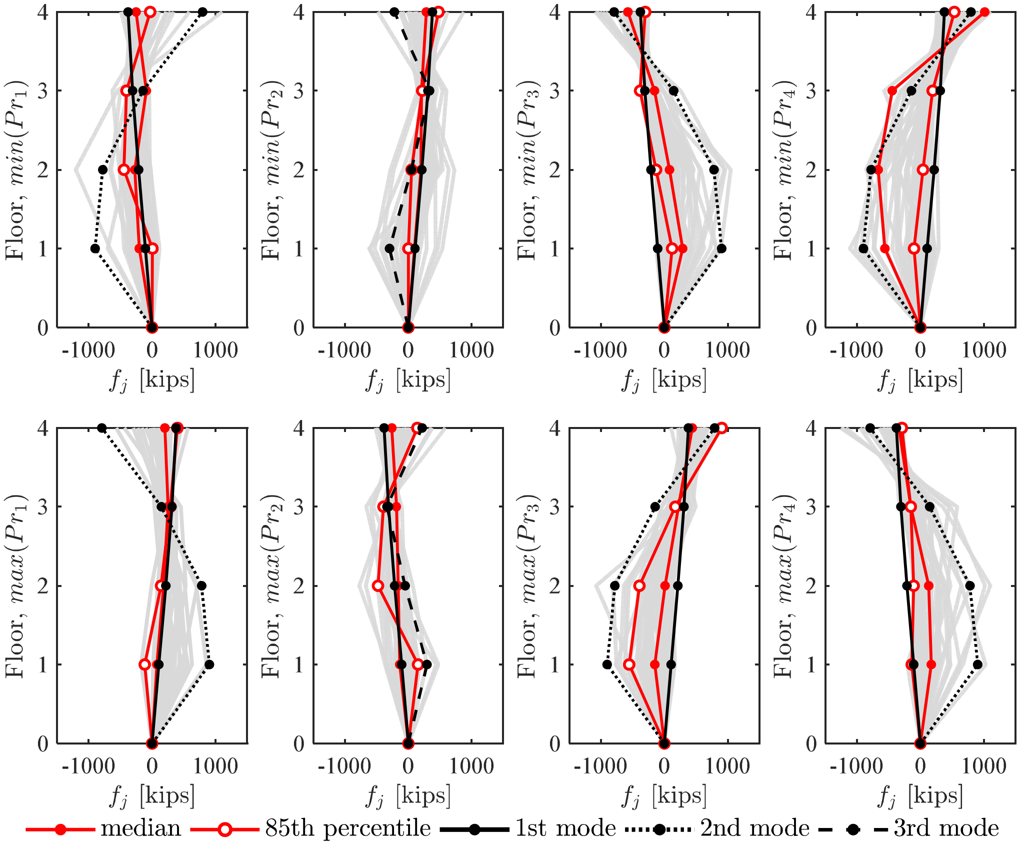

Figure 7.26. Modal comparison to force distribution at peak inelastic brace axial force.

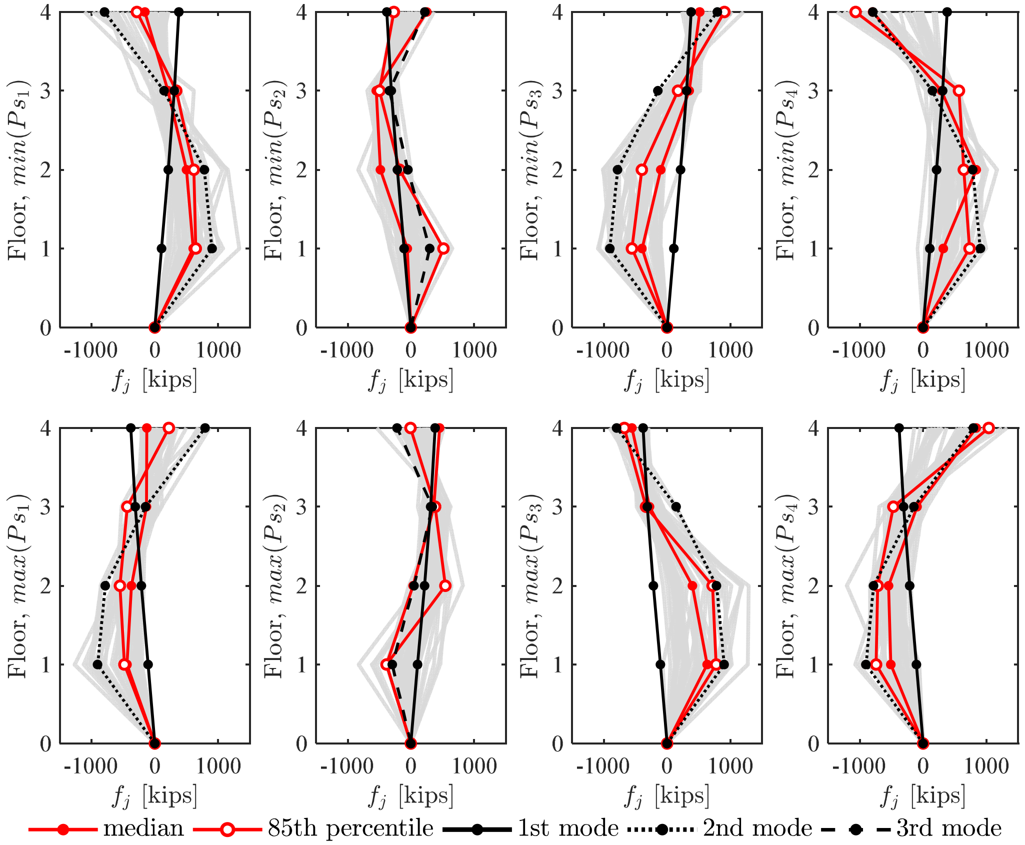

Figure 7.27. Modal comparison to force distribution at peak strongback brace axial force.

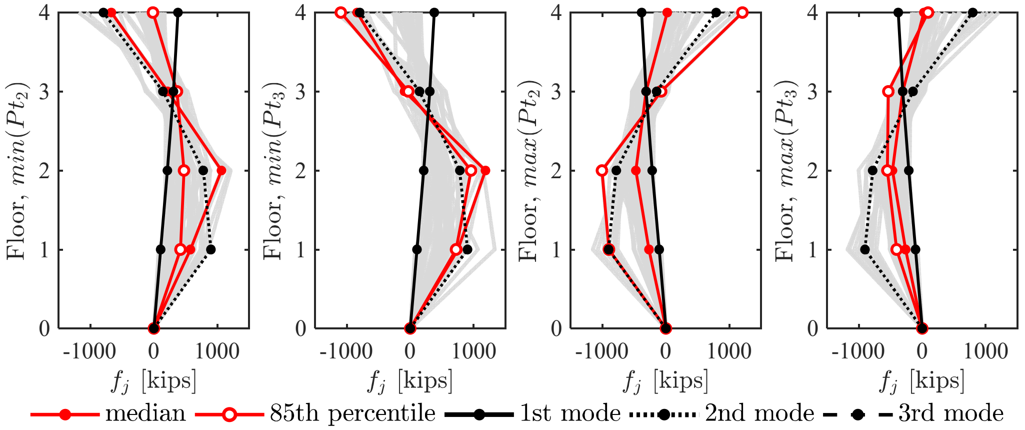

Figure 7.28. Modal comparison to force distribution at peak strongback tie axial force.

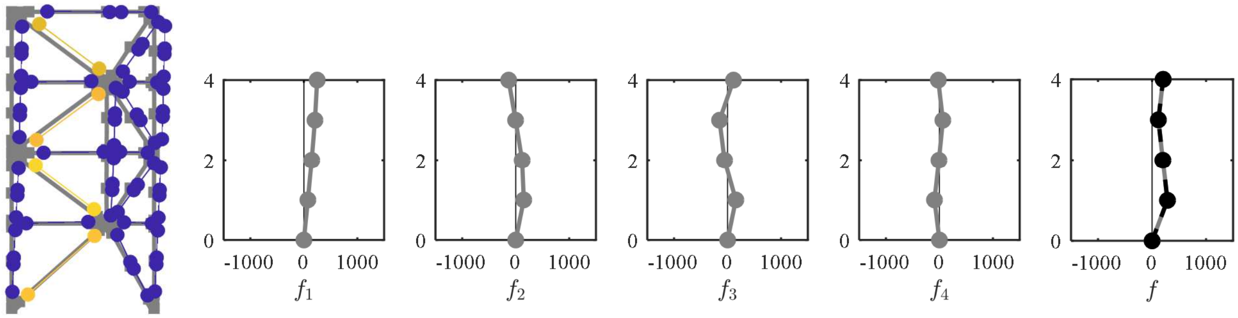

(a) (b) (c) (d) (e) (f)

Figure 7.29. Snapshot of first-mode response for gm44.
(a) schematic of demand-to-capacity ratios; (b)-(e) first, second, third, and fourth mode equivalent-lateral force distributions; (f) estimated total equivalent-lateral force distribution.

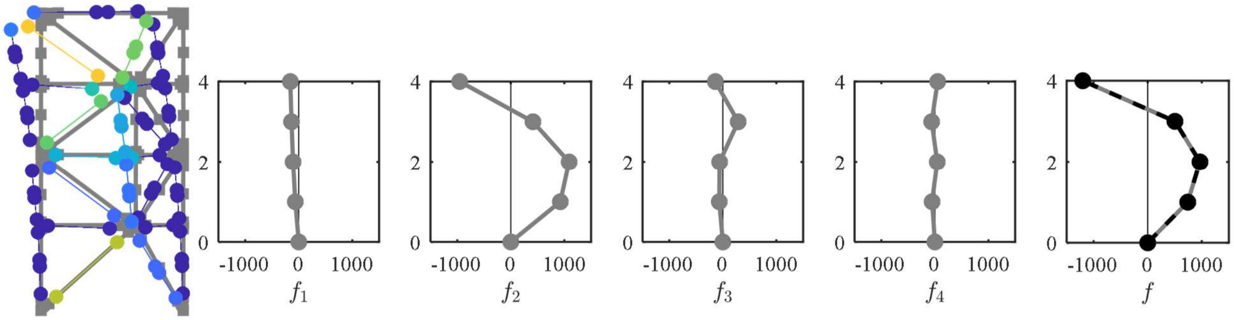

(a) (b) (c) (d) (e) (f)

Figure 7.30. Snapshot of second-mode response for gm44.
(a) schematic of demand-to-capacity ratios; (b)-(e) first, second, third, and fourth mode equivalent-lateral force distributions; (f) estimated total equivalent-lateral force distribution.

7.6 SUMMARY

The intent of this chapter was to better understand the basic mechanics of multi-story strongback-braced frames. In summary –

1. The force demands on the strongback braces can be derived through horizontal equilibrium and depend on the story shear demands generated from the ground motion and the axial force in the inelastic brace in the same story. Tie demands can be estimated by vertical equilibrium.
2. Equations estimating stiffness on a story-by-story basis like Equation 3.1 are valid only in the elastic range. Once the inelastic braces yield, the stiffness of the vertical tie needs to be

included in the lateral stiffness calculations. Coupling of the vertical and horizontal demands of the elastic and inelastic portions of an embedded strongback and coupling of every story through the tie can make design methods using stiffness metrics difficult and unwieldly for potential design methods.

3. Compatibility between a braced bay containing the fuses and a separated strongback truss revealed a load reversal effect resulting from moment equilibrium. The strongback's response is analogous to the "bending" response in a simply supported beam.
4. Though the strongback is intended to impose a uniform yielding and drift response, force demands in the strongback truss are primarily activated under non-uniform demand profiles, especially those associated with higher-mode reversal effects like the second-mode bending response.
5. If the strongback was infinitely stiff, strongback-braced frames would exhibit a solely first-mode response. However, higher-mode force demands need to be considered when optimizing the strongback to meet realistic strength and stiffness design criteria since the strongback is designed to remain elastic under all modes of excitation.
6. Though strongback-braced frames tend to exhibit near-uniform story drift profiles, the acceleration and story shear profiles show large higher-mode contributions. These higher modes are characterized by sign reversals in the height-wise force distribution and impact force demands in the upper stories.
7. A higher-mode bending response is amplified in strongback-braced frames due to the elastic nature of the strongback truss. Though forces in the first mode are limited by the fuse strength, forces in the second and higher modes are limited by the ground motion intensity. Strongback-braced frames exhibit significant strength in higher-mode bending. This higher-mode response is either elastic or associated with the formation of partial mechanisms.

An equivalent-lateral force procedure using pseudo-accelerations derived from an elastic response spectrum was able to approximate the force distributions extracted from nonlinear dynamic analyses. This procedure can be used to develop an analysis method to estimate higher-mode force demands for design.

8 Proposed Design Methods

8.1 INTRODUCTION

Capacity design is the traditional method for proportioning force-controlled actions in conventional yielding systems (Hollings, 1969; Park & Paulay, 1975). Deformation-controlled actions are specially detailed to enable them to deform well into the inelastic range without excessive loss of strength or failure. Per simplified capacity or plastic design, the remaining force-controlled actions are designed to remain essentially elastic under the forces delivered by the intended mechanism. This provides a hierarchy of strength to promote yielding in the ductile regions and protection of the force-controlled regions.

The elastic nature of the strongback truss ensures that yielding occurs primarily in the designated fuses. Demands and details in those inelastic regions can be determined by analysis methods typical of a conventional system [e.g., as required by ASCE/SEI 7-16 (2016)]. To remain elastic, strongback elements could then be designed for the force demands delivered by the fuses (including overstrength, strain hardening, etc.) per capacity design principles.

However, traditional capacity design alone is insufficient to bound the force demands in the strongback truss. Though deformation-controlled actions are well constrained by their respective fuse capacities, force-controlled actions in the strongback truss also depend on the inertial forces developed by the ground shaking. Traditional capacity design assumes that the strength of the fuses limits the forces that can develop under all modes of vibration. However, the strongback can exhibit significant strength and stiffness in higher mode bending. This “bending” strength can be significantly larger than the higher-mode inertial forces developed from an earthquake. Since the strongback is designed to remain elastic under all modes of vibration, inertial forces in the second and higher modes continue to accumulate after the fuses have yielded and as the ground shaking intensifies.

These seismic demands are dynamic and constantly changing with time. Though the displaced shape is dominated by a first-mode (uniform) response, the demands in the strongback elements are also subject to amplified higher-mode (bending) contributions. Thus, the required strength of the essentially elastic components is still bounded by capacity design principles but is additionally bounded by elastic or partially inelastic higher-mode bending effects. These demands can be significantly higher than those estimated solely from traditional capacity design principles. Higher-mode characterization of the strongback’s dynamic response was studied in detail in Chapter 7.

This chapter compares three analysis methods to estimate higher-mode demands on the strongback truss. The chapter introduces possible design methods for the sizing of the fuses. Quasi-static (traditional) capacity analysis methods for the design of the strongback elements are briefly discussed to provide justification of the other proposed methods. Modal analysis methods are divided into three categories: [i] nonlinear dynamic analysis methods, [ii] modal pushover analysis methods (MPA), and [iii] simplified modal enveloping methods (MEA). Simplified versions of the MPA and MEA methods are also evaluated. Possible approaches for the design the beams and columns of are also provided. Comparisons to nonlinear dynamic analysis results in this chapter were extracted from the nonlinear dynamic analysis of the benchmark strongback described in Chapter 5.

8.2 DESIGN OF THE FUSES

Table 1.1 outlined desirable deformation- and force-controlled actions for strongback-braced frames utilizing buckling-restrained braces. This section describes the analysis method used to design the fuses. Analysis methods for the design of the force-controlled actions in the strongback truss, beams, and columns are described in the following sections. It is recommended that the fuses be designed by either of the two following methods:

i. The fuses are designed for the forces developed at yield (i.e., the design base shear, V_b). These forces can be approximated using traditional earthquake forces reduced by a response modification (R) factor.

ii. The fuses are designed considering the force re-distributions that occur at the “limit load” upon formation of the first-mode plastic mechanism.

These methods of design are shown schematically in Figure 8.1. Method [i] is the conventional method for sizing the fuses [i.e., per equivalent-lateral force or response spectrum analysis procedures ASCE/SEI 7-16 (2016)]. Method [ii] assumes that the BRBs will all yield near-simultaneously because of the similar deformation demands imposed in every story by the strongback truss under rigid body rotation.

Each BRB experiences similar amounts of axial elongation and shortening at the plastic limit load. Method [ii] accounts for the ability of the strongback to engage all of the BRBs under similar levels of axial deformation under a first-mode displaced shape. Per method [ii], the BRBs are sized with respect to their expected deformation at the limit load. If every story has the same geometry, design forces for the BRBs per method [ii] are derived from the average of the design story shear forces.

To ensure adequate sizing of the BRBs, a minimum reduction of 0.8 times the design base shear is recommended herein. Comparison of peak response quantities in Section 6.3.3 using the distributed BRB sizes resulting from method [i] and the uniform BRB sizes resulting from method [ii] showed that there is little difference in dynamic response using either of the two methods to design the fuses when the minimum 0.8-reduction factor is utilized.

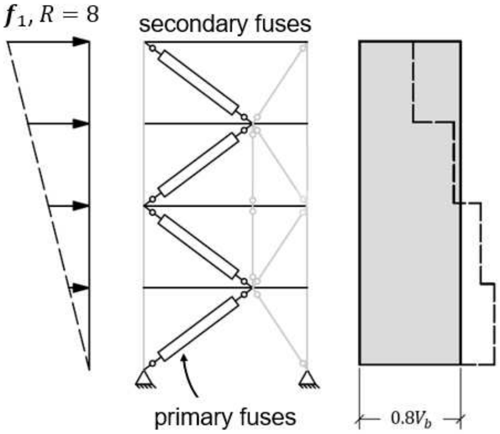

Figure 8.1. Schematic of analysis method for the fuses.

8.3 TRADITIONAL STATIC ANALYSIS

An equivalent-lateral force (ELF) method of elastic analysis is the simplest form of static analysis. Inelastic behavior is accounted for through a response-modification factor, R, and reduced code-level earthquake forces. Axial-force demands in the strongback can then be estimated considering the overstrength-factor, Ω_0, to approximate the forces developed upon yielding of all the fuses. However, as an elastic analysis method, the ELF procedure does not account for potential force re-distributions due to yielding, resulting in an under-representation of demands in actions governed by unbalanced forces like those in the tie. The ELF method with overstrength also does not explicitly incorporate the expected strength of the fuses or allowances for amplified demands arising from higher-mode effects.

A plastic analysis approach would be able to explicitly represent internal force re-distributions due to yielding. Such methods can be useful in understanding the effects of nonlinearity at the limit load but depend on the choice of lateral-force distribution. As such, slight variations in the distribution of lateral forces result in different demands in the force-controlled regions. Higher-mode effects may also result in some floors not yielding or yielding in opposite directions, resulting in an incomplete mechanism. The plastic analysis method typically results in a single critical mechanism, though other mechanisms could be nearly as critical. Slight variation in force distribution or element capacity could also change the intended mechanism.

Traditional capacity design raises similar issues to the plastic analysis approach. Per traditional capacity design, it is assumed that the capacity of the fuses limits the forces that can develop under all modes of vibration. Thus, it is possible to approximate demands in force-controlled regions by calculating the forces that can be developed in neighboring fuses on a story- or element-wise basis. However, traditional capacity design cannot account for the use of similar inelastic brace sizes in multiple stories, inelastic brace removal, or amplification of demands due to higher-mode effects. Unlike a traditional yielding system, inertial forces in strongback-braced frames are not limited by the capacity of the fuses but continue to accumulate as the ground shaking intensifies due to the elastic higher-mode bending response of the strongback truss. Traditional capacity design cannot account for these inertial force contributions, because force demands are estimated on an element-wise basis assuming that the inertial forces are limited by the capacity of the fuses

Traditional capacity or plastic design alone under-estimates the force demands in the strongback truss, especially in the upper stories. Demands extracted from nonlinear dynamic analysis of the benchmark four-story strongback were an order of magnitude greater than those estimated from a plastic analysis approach using traditional lateral-force distributions; see Section 7.5.1. Force demands estimated using these traditional approaches assume a first mode-only response and are inappropriate in both height-wise distribution and magnitude. Such methods do not adequately represent forces developed due to the strongback's elastic response under dynamic excitation.

8.4 DYNAMIC CAPACITY ANALYSIS

Dynamic capacity design was first introduced in Section 5.2 for the design of the benchmark strongback. As a nonlinear dynamic approach, dynamic capacity design explicitly accounts for the transient nature of strongback demands. Provided enough analyses are used to obtain results, dynamic capacity design can also account for aleatory variability in the material properties and ground motion characteristics and epistemic uncertainty in the design and modeling of the fuse and strongback elements.

The dynamic capacity procedure depends on nonlinear dynamic analysis of the system under multiple ground motion records. Demands in force-controlled regions are then based on statistical evaluation of the results [e.g., use of the procedure in Tall Building Initiative (PEER, 2017), ASCE 7-16 (2016), or ATC-114 (2017)]. As this approach is iterative, it requires several analyses and design phases; including a preliminary design stage, refinement with nonlinear-static (pushover) methods, and nonlinear dynamic analyses upon final or close to final design. Provided enough analyses are used to obtain results, dynamic capacity design can also account for aleatory variability in the material properties and ground motion characteristics and epistemic uncertainty in the design and modeling of the fuse and strongback elements.

Dynamic capacity design is not a design method appropriate for preliminary design. The nonlinear dynamic analyses needed for dynamic capacity design requires extensive data reduction, modeling expertise, and computational expense. Moreover, ground motion selection can have a considerable impact on the force estimates for the strongback truss. Ideally, ground motions would be selected for multiple periods to account for different ground motion characteristics near the first-mode and higher-mode periods.

8.5 MODAL PUSHOVER ANALYSIS

Modal response spectrum analysis can account for the elastic dynamic behavior of a structure subjected to multiple modes. The value of the total response is obtained by combining the peak modal responses with an appropriate modal combination rule [e.g., square root of the sum of the squares (SRSS), complete quadratic combination (CQC), etc.]. Such methods typically assume that the structure yields in every mode; i.e., the same R-factor can be applied to every mode. The following represents traditional elastic modal response spectrum analysis using the SRSS modal combination rule:

$$r = \sqrt{\left(\frac{r_{1,el}}{R}\right)^2 + \left(\frac{r_{2,el}}{R}\right)^2 + \cdots + \left(\frac{r_{n,el}}{R}\right)^2 + \cdots + \left(\frac{r_{J,el}}{R}\right)^2} \qquad \text{Equation 8.1}$$

$r =$ total response; $r_{1,el}$, $r_{2,el}$, $r_{n,el}$ = peak elastic response in the first, second, third, …, n^{th}, …, J^{th} modes. Since the strongback tends to reman elastic under higher-mode bending (i.e., $R = 1$ in the higher modes), Equation 8.1 can be revised to the following:

$$r = \sqrt{\left(\frac{r_{1,el}}{R}\right)^2 + r_{2,el}^2 + \cdots + r_{n,el}^2 + \cdots + r_{J,el}^2} \qquad \text{Equation 8.2}$$

Response spectrum analysis using different R-factors can be incorporated into conventional structural analysis software using a truncated response spectrum similar to that shown in Figure 2.12(c).

However, even with $R = 1$ in the higher modes, elastic modal response spectrum analysis cannot account for force re-distributions due to yielding and R is a substitute for the inelastic response. As described in Section 8.3, these force re-distributions can be captured by a plastic analysis method. These are typically captured assuming a first-mode only response:

$$r = r_{1,pl} \qquad \text{Equation 8.3}$$

$r_{1,pl}$ = response due to a full plastic mechanism in the first mode. Conventionally, this method is simplified using traditional capacity design methods to estimate force demands on a story- or element-wise basis. To incorporate higher-mode effects into the total response in Equation 8.4, the peak higher modes can be combined using a modal combination rule similar to Equation 8.2:

$$r = \sqrt{r_{1,pl}^2 + r_{2,inel}^2 + r_{3,el}^2 + \cdots + r_{n,el}^2 + \cdots + r_{J,el}^2} \qquad \text{Equation 8.4}$$

$r_{2,inel}$ = elastic or partially inelastic response due to the second mode; $r_{3,el}$ = elastic response due to the third mode. Equation 8.4 requires a pushover analysis in the second mode since the response is neither elastic nor fully plastic.

Though modal combination rules like the SRSS and CQC rule are not strictly valid for inelastic systems, if the elastic modes are assumed "weakly" coupled when the building deforms inelastically (i.e., the coupled terms are small), the coupling of the elastic modes can be ignored and an appropriate modal combination rule can still be applied to obtain total response quantities. This procedure of combining modal pushover analyses was developed by Chopra and Goel (2002; 2004) and termed Modal Pushover Analysis (MPA). This procedure has been adapted herein as an approximate method of incorporating force re-distributions due to yielding and of addressing the elastic higher-mode behavior of the strongback.

8.5.1 Superposition Modal Combination Rule

The MPA approach incorporates higher-mode demands in the strongback through a modal combination rule. Algebraic signs of the total response are lost during the modal combination calculation, and the combined response will not satisfy equilibrium. As such, total response quantities need to be combined from the peak response in each mode and cannot be derived from the modal combination of another response quantity.

Because the inelastic behavior of the strongback is primarily exhibited in the first mode, it can be assumed that the first mode plastic response is de-coupled from the second and higher modes. This can be interpreted as higher mode oscillations about the fundamental mode; see the results in Section 7.5.4.3. To model this phenomenon, an SRSS of the higher modes can be superimposed on the fundamental mode of the strongback by a superposition modal combination rule:

$$r = \left|r_{1,pl}\right| + \sqrt{r_{2,inel}^2 + r_{3,el}^2 + \cdots + r_{n,el}^2 + \cdots + r_{J,el}^2} \qquad \text{Equation 8.5}$$

This is the same modal combination rule as that proposed for rocking frames (Wiebe et al., 2015); see Section 2.3.6. This modal combination approach assumes the higher-mode periods are well separated. It is assumed that a partial mechanism response results in only “weak” coupling in the second and higher modes and is neglected in this study. Note, that since the first and second mode are inelastic, Equation 8.5 can result in double counting and a more appropriate modal combination rule may result in better estimates of the dynamic-force demands.

8.5.2 MPA Procedure

The MPA method is similar to the response spectrum analysis approach for elastic structures, but combines peak inelastic rather than elastic modal response quantities. Though analysis of fully elastic structures and complete plastic mechanisms is straightforward, potential partial mechanisms in the higher modes can make estimates of strongback demands challenging. It is not immediately clear which elements have yielded in a partial mechanism. Moreover, assuming the structure is elastic in a mode when it exhibits a partially inelastic response can be un-conservative and can result in smaller demands on the strongback truss than if the fuses had actually yielded in those modes; see Equation 7.13.

The final state of a partial mechanism requires incremental determination of the event-to-event change in stiffness upon yielding of each fuse. This makes a method utilizing pushover analyses appropriate for representing the partial mechanism behavior in the second and potentially higher modes. The steps for an MPA approach can be summarized as follows:

1. Designate deformation- and force-controlled actions.
2. Design deformation-controlled actions (e.g., axial force in the inelastic braces, flexural force in the beams, etc.) by traditional analysis methods, such as those provided in ASCE-7-16 (2016). Estimate the stiffness and capacity of the force-controlled actions (e.g., area and moment of inertia). See Section 5.4.1 for more details.

3. Determine the elastic natural frequencies, periods, and modes (ω_n, T_n, ϕ_n) by an eigenvalue analysis of the elastic structure. Determine the pseudo-acceleration for a single degree-of-freedom oscillator in each mode, $A_n(T_n, \zeta_n)$, by reading the elastic pseudo-acceleration ordinate from the elastic response spectrum. Estimate the modal participation factor in each mode by $\Gamma_n = \frac{\Sigma_{j=1}^{R} m_j \phi_{n,j}}{\Sigma_{j=1}^{R} m_j \phi_{n,j}^2}$.
4. Find the limit load of the system under a first mode equivalent static force distribution (e.g., $\lambda \boldsymbol{f}_1 = \lambda \boldsymbol{m} \phi_1$) using a perfectly plastic or appropriate nonlinear static analysis [e.g., ASCE-41-17 (2017)]; see Section 7.5.4. Compute the demands in the first mode, r_1, assuming the structure forms a full mechanism in the first mode.
5. Compute equivalent-lateral forces for the second and higher modes by $\boldsymbol{f}_n = \Gamma_n \boldsymbol{m} \phi_n A_n$ using the elastic modes, pseudo-accelerations, and modal participation factors calculated in [3]; see Section 7.5.4. Monotonically apply each modal force distribution until the modal base shear in the numerical model exceeds the base shear calculated from $\boldsymbol{f}_n$. Extract the force demands, r_n, from each pushover analysis in each higher mode, n.
6. Calculate the total response, r, by combining the first and higher-mode response quantities, r_1 and r_n, from [4] and [5] by an appropriate modal combination rule to account for at least the first and second-mode response and enough other higher modes to achieve 95% mass participation.

This method is comprised of two analyses: [i] an analysis for the deformation-controlled actions in step 2 and [ii] multiple sub-analyses for the force-controlled actions in steps 4 and 5; see Figure 8.2. The force-controlled sub-analyses are divided into a first mode fully plastic "pivoting" response in step 4 and higher-mode partially inelastic "bending" responses in step 5. The difference between steps 4 and 5 stems from different limitations on the force demands in the system. The forces in the pivoting response are limited by the capacity of the fuses while the forces under a bending response are limited by the ground motion intensity estimated from the elastic response spectrum.

Note that the application of modal combination rules to inelastic systems lacks a rigorous theoretical basis as the modes calculated from the elastic system become coupled when the system responds inelastically. As stated in Section, 7.5.4, approximations can be made by combining the inelastic response in the elastic modes by ignoring the coupled response if it is assumed that modes derived from the elastic system are weakly coupled when the system becomes inelastic (Chopra, 2011). It should be emphasized that this method is an estimation of the total response by combination of the peak inelastic modal responses. As such, results will not be exact.

This MPA process is shown schematically in Figure 8.2. Like the dynamic capacity approach, the MPA method still requires nonlinear material models for the fuses and post-processing of the results. Note that consideration of inelastic behavior may be performed by a plastic analysis in the first mode but does require pushover analyses to address potential partially inelastic behavior in the higher modes.

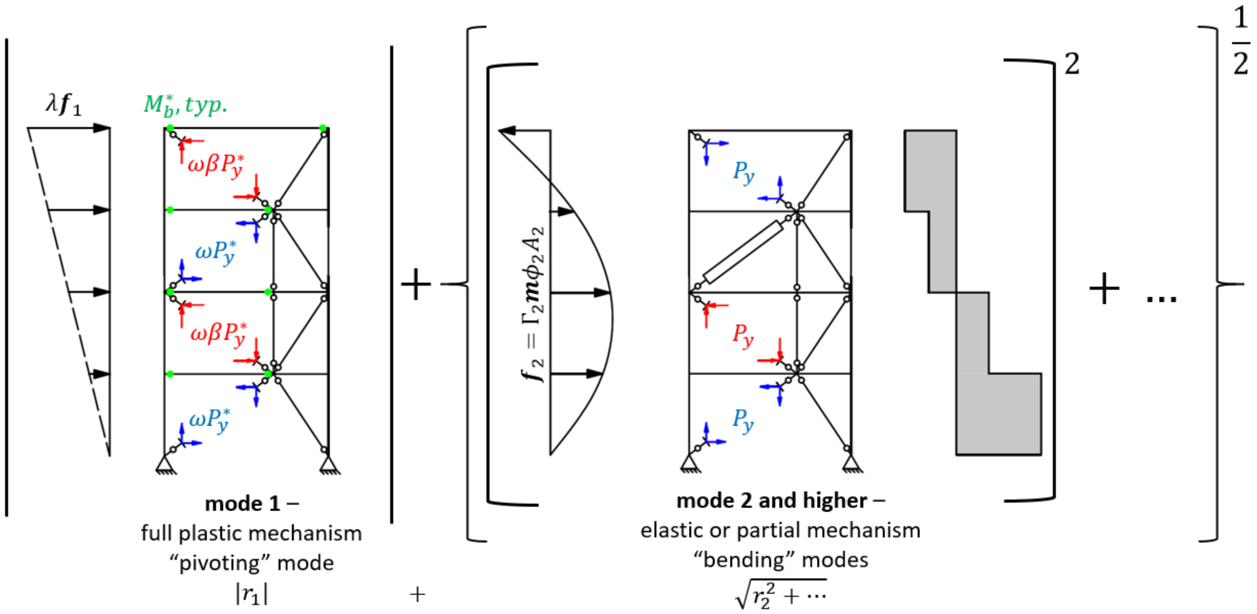

Figure 8.2. Schematic of Modal Pushover Analysis method.

8.5.3 MPA Case Study

To study the impact of material behavior on the MPA results, simulations of increasing simplicity were compared to the force demands extracted from nonlinear dynamic analysis of the benchmark numerical model. A description of the three types of models used for the MPA analyses can be found in Table 8.1. The standard square-root-of-the-sum-of-the-squares (SRSS) modal combination rule was additionally compared to the superposition modal combination rule presented in Equation 8.5.

The nonlinear pushover model (NP) was the most sophisticated of the models used in the MPA case study. Nonlinear material models, gravity loading, and mass were the same as that of the dynamic model. Elastic modes used for the pushover analyses were calculated based on an eigenvalue analysis of the elastic structure. This numerical model fostered direct comparison between the MPA outputs and the nonlinear dynamic outputs.

The second perfectly-plastic model (PP) introduced perfectly plastic material models for the yielding actions in the simulation. The use of perfectly plastic material allowed for direct calculation of the limit load per Equation 7.11 and interpolation of the higher-mode partial mechanism response between the sequential formation of plastic hinges; see dots representing the point of hinge formation in Figure 8.3. Note that a perfectly-plastic material assumption should not be applied to yielding actions experiencing strength degradation, like strongback-braced frames using buckling braces for the fuses.

Perfectly plastic material models have zero-stiffness upon yielding. To incorporate the adjusted brace strength of the BRBs in the first mode, perfectly plastic material models used the expected yield strength of the material including the adjustment parameters, ω and $\omega\beta$ from Table 4.5. Nominal yield strengths were used for the second and higher modes as these forces were expected to be near yield and away from the limit load. These material strengths are described schematically in Figure 8.2. Gravity loading and $P\Delta$ effects were neglected in this model and mass was calculated from the design seismic weight. Force-controlled actions were modeled as elastic in all of the modes.

The third model (EP) represents the simplest numerical model used in this case study. Like the PP model, demands from the first mode were calculated assuming a complete plastic mechanism response per Section 7.2. Analyses in the second and higher modes were linear elastic, and neglected potential yielding in the fuses due to partial mechanisms.

8.5.4 Comparison of MPA and Nonlinear Dynamic Results

Demands from each of the MPA models are compared to demands extracted from nonlinear dynamic analysis of the benchmark strongback in Table 8.2. The ratio of the MPA output to the median and 85th percentile output from the dynamic analyses are shown in Table 8.3 and Table 8.4, respectively. The distribution of static demands from the MPA models are shown side-by-side with the dynamic output in Figure 8.4.

The superposition modal combination rule generally gave better representations of the 85th percentile dynamic response compared to the SRSS modal combination rule. However, this modal combination did over-estimate demands in the first story strongback brace. Estimated demands using the NP model were closest to the dynamic output. The distribution of demands was well estimated by the NP model to within $\pm 1\%$ to $\pm 17\%$, except for the first story strongback brace demand which was over-estimated the 85th percentile response by 22 to 25%.

The NP model and the simplified PP model gave similar estimates for the strongback demands. The PP model estimated demands with more conservatism than the NP model but with less computational expense. For the benchmark case considered, elastic analyses could replace the third and fourth mode analyses as the fuses remained elastic under these modes; see Figure 8.3. Like the NP model, the PP model over-estimated demands in the first story strongback brace. Differences in the minimum and maximum demands in the strongback elements arise from differences in adjusted tension and compression strengths in the BRBs when the model was pushed to the "left" versus the "right".

The EP model was the least conservative of the MPA models. This model especially under-estimated demands in the upper story strongback braces and tie. This is because the deformation-controlled actions do not yield in the second mode of this simulation, resulting in inaccurate characterization of potential unbalanced forces in the second mode. Force re-distributions due to the partial mechanism behavior in the second mode are not represented in this model.

Table 8.1. Numerical models used in MPA case study.

Analysis Method	**Material Model for Deformation-Controlled Actions**	
	Mode 1	**Mode 2 and higher**
Modal Pushover (NP)	Same as dynamic model [Section 4.5]	Same as dynamic model [Section 4.5]
Modal Plastic (PP)	Perfectly plastic with expected yield strength	Perfectly plastic with nominal yield strength
Modal Elastic (EP)	Perfectly plastic with expected yield strength	Linear elastic

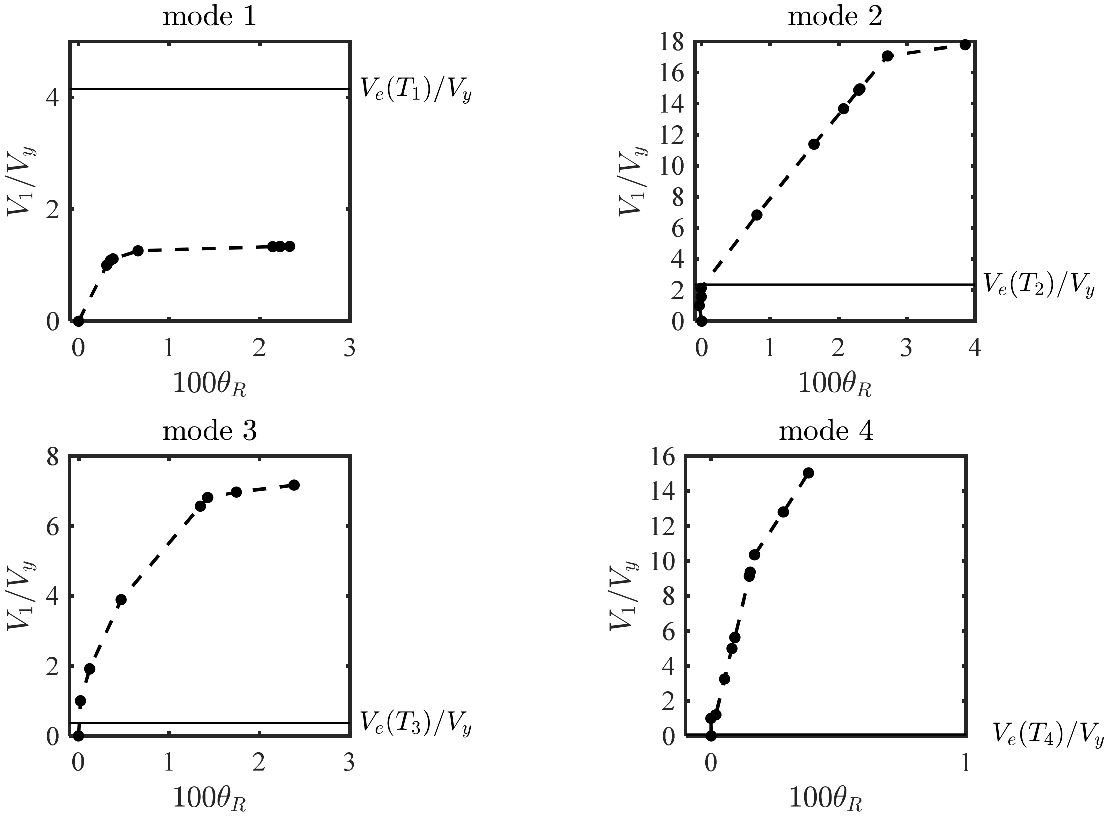

Figure 8.3. Example of interpolation usng PP model.

V_y = base shear at yield; V_e = elastic base shear calculated from the modal force distribution, f_n, in Equation 7.33 using elastic spectral pseudo-accelerations, $A_n(T_n)$, at the modal period, T_n.

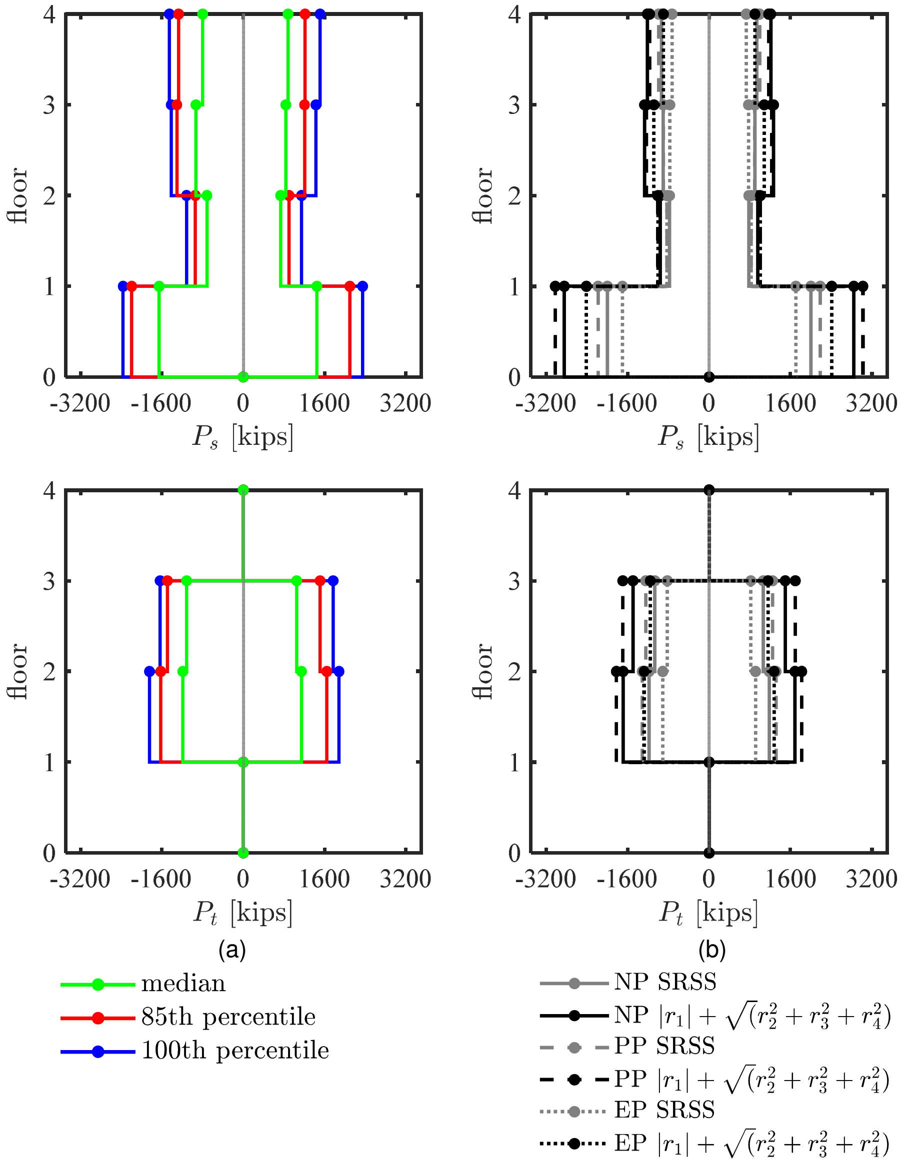

Figure 8.4. Comparison of static demands from MPA to nonlinear dynamic output.

Table 8.2. Static strongback demands using MPA.

Analysis Type	**Lateral Load Distribution**	**Axial-force demand**											
		$P_{s,1}$ [kips]		$P_{s,2}$ [kips]		$P_{s,3}$ [kips]		$P_{s,4}$ [kips]		$P_{t,2}$ [kips]		$P_{t,3}$ [kips]	
		min	max	min	max	min	max	min	max	min	max	min	max
Gravity	$(1.2 + 0.2S_{DS})D + 0.5L$	-81		3		-22		-6		-66		-23	
	$(0.9 - 0.2S_{DS})D$	-38		-1		-9		-5		-31		-13	
	$1.05D + 0.125L$	-57		-7		-14		-13		-44		-21	
Dynamic	Median [1]	-1625	1614	-745	768	-956	859	-851	941	-1157	1176	-1141	1085
	85th percentile [1]	-2287	2342	-994	1002	-1411	1279	-1461	1474	-1713	1724	-1585	1719
Modal Pushover, NP	r_1, 1st mode	-1346	1173	-759	632	-545	421	-341	181	-841	810	-630	607
	r_2, 2nd mode	-1468	1546	-37	51	-722	689	-853	859	-844	893	-839	887
	r_3, 3rd mode	-170	171	-200	198	-146	146	-219	219	-15	17	-16	17
	r_4, 4th mode	0	0	-1	1	-1	1	0	0	0	1	0	1
	$\sqrt{r_1^2 + r_2^2 + r_3^2 + r_4^2}$	2057		787		916		949		1226		1088	
	$\|r_1\| + \sqrt{r_2^2 + r_3^2 + r_4^2}$	2852		965		1282		1227		1734		1517	
Modal Plastic Pushover, PP	r_1, 1st mode	-1204	1057	-802	659	-470	345	-198	50	-728	708	-607	-607
	r_2, 2nd mode	-1815	1815	-103	103	-753	753	-952	952	-1095	1095	-1088	-1088
	r_3, 3rd mode	-133	133	-173	173	-109	109	-196	196	-22	22	-22	-22
	r_4, 4th mode	-12	12	-45	45	-47	47	-12	12	-16	16	-16	-16
	$\sqrt{r_1^2 + r_2^2 + r_3^2 + r_4^2}$	2182		828		895		992		1315		1246	
	$\|r_1\| + \sqrt{r_2^2 + r_3^2 + r_4^2}$	3024		1009		1232		1170		1822		1696	
Modal Elastic Pushover, EP	r_1, 1st mode	-1204	1057	-802	659	-470	345	-198	50	-728	708	-607	-607
	r_2, 2nd mode	-1200	1200	-96	96	-603	603	-673	673	-550	550	-550	-550
	r_3, 3rd mode	-133	133	-173	173	-109	109	-196	196	-22	22	-22	-22
	r_4, 4th mode	-12	12	-45	45	-47	47	-12	12	-16	16	-16	-16
	$\sqrt{r_1^2 + r_2^2 + r_3^2 + r_4^2}$	1705		828		773		729		912		820	
	$\|r_1\| + \sqrt{r_2^2 + r_3^2 + r_4^2}$	2411		1005		1084		899		1278		1158	

Table 8.3. Ratio of static demand using MPA to median dynamic response.

Analysis Type	**Lateral Load Distribution**	**Axial-force demand Ratio**											
		$P_{s,1}/P_{s,1}^{50\%}$		$P_{s,2}/P_{s,2}^{50\%}$		$P_{s,3}/P_{s,3}^{50\%}$		$P_{s,4}/P_{s,4}^{50\%}$		$P_{t,2}/P_{t,2}^{50\%}$		$P_{t,3}/P_{t,3}^{50\%}$	
		min	max	min	max	min	max	min	max	min	max	min	max
NP	$\sqrt{r_1^2+r_2^2+r_3^2+r_4^2}$	1.22	1.32	1.05	1.03	0.94	1.08	1.10	1.02	1.02	1.08	0.94	1.02
	$\lvert r_1\rvert+\sqrt{r_2^2+r_3^2+r_4^2}$	1.70	1.83	1.28	1.27	1.32	1.52	1.42	1.32	1.44	1.53	1.31	1.43
PP	$\sqrt{r_1^2+r_2^2+r_3^2+r_4^2}$	1.30	1.40	1.10	1.09	0.92	1.06	1.15	1.07	1.09	1.16	1.07	1.17
	$\lvert r_1\rvert+\sqrt{r_2^2+r_3^2+r_4^2}$	1.80	1.94	1.34	1.33	1.27	1.46	1.35	1.26	1.52	1.61	1.46	1.59
EP	$\sqrt{r_1^2+r_2^2+r_3^2+r_4^2}$	1.01	1.10	1.10	1.09	0.80	0.91	0.84	0.79	0.76	0.81	0.71	0.77
	$\lvert r_1\rvert+\sqrt{r_2^2+r_3^2+r_4^2}$	1.43	1.55	1.34	1.32	1.12	1.28	1.04	0.97	1.06	1.13	1.00	1.09

Table 8.4. Ratio of static demand using MPA to 85th percentile dynamic response.

Analysis Type	**Lateral Load Distribution**	**Axial-force demand Ratio**											
		$P_{s,1}/P_{s,1}^{85\%}$		$P_{s,2}/P_{s,2}^{85\%}$		$P_{s,3}/P_{s,3}^{85\%}$		$P_{s,4}/P_{s,4}^{85\%}$		$P_{t,2}/P_{t,2}^{85\%}$		$P_{t,3}/P_{t,3}^{85\%}$	
		min	max	min	max	min	max	min	max	min	max	min	max
NP	$\sqrt{r_1^2+r_2^2+r_3^2+r_4^2}$	0.88	0.90	0.79	0.79	0.64	0.72	0.64	0.65	0.70	0.73	0.68	0.64
	$\lvert r_1\rvert+\sqrt{r_2^2+r_3^2+r_4^2}$	1.22	1.25	0.96	0.97	0.90	1.01	0.83	0.84	0.99	1.03	0.94	0.89
PP	$\sqrt{r_1^2+r_2^2+r_3^2+r_4^2}$	0.93	0.95	0.83	0.83	0.63	0.71	0.67	0.68	0.75	0.78	0.78	0.73
	$\lvert r_1\rvert+\sqrt{r_2^2+r_3^2+r_4^2}$	1.29	1.32	1.01	1.01	0.86	0.97	0.79	0.80	1.04	1.08	1.06	1.00
EP	$\sqrt{r_1^2+r_2^2+r_3^2+r_4^2}$	0.73	0.75	0.83	0.83	0.54	0.61	0.49	0.50	0.52	0.54	0.51	0.48
	$\lvert r_1\rvert+\sqrt{r_2^2+r_3^2+r_4^2}$	1.03	1.06	1.00	1.01	0.76	0.86	0.61	0.62	0.73	0.76	0.72	0.68

8.6 MODAL ENVELOPE ANALYSIS

A simplified modal static method was developed based on the higher-mode framework outlined for the MPA method in Section 8.5. Recalling the equation of horizontal equilibrium calculated in Section 7.2, the strongback brace demand in a story, $P_{s,j}$, can be estimated by:

$$P_{s,j} = \frac{s_j}{b}\left(V_j - P_{r,j}\frac{l}{r_j}\right) \qquad \text{Equation 8.6}$$

V_j = story shear demand; $P_{r,j}$ = axial force in the adjacent inelastic brace. The upper bound of the strongback brace axial force, $P_{s,j}$, occurs with one of the three following scenarios takes place:

1. The story shear is zero ($V_j = 0$) such that $P_{s,j} = -\frac{s_j}{b}\frac{l}{r_j}P_{r,j}$.
2. The axial force in the inelastic brace is zero ($P_{r,j} = 0$) such that $P_{s,j} = \frac{s_j}{b}V_j$.
3. The story shear and inelastic brace axial force act in the same direction such that $P_{s,j} = -\frac{s_j}{b}\left(V_j + P_{r,j}\frac{l}{r_j}\right)$.

These scenarios are generally supported by observations extracted from nonlinear dynamic analysis of the benchmark strongback. The zero-story shear in scenario [1] is justified by Figure 7.15. The story shear envelopes in this plot exhibit near-zero story shear in some of the stories when the corresponding strongback demand is at a peak. The axial force in the inelastic braces in scenario [2] is justified by Figure 7.20 and Figure 7.21. Inelastic brace forces can be near zero at the time of peak strongback demands. This scenario would also occur upon BRB rupture. Scenario [3] is unlikely and was not observed to be a primary characteristic of the forty-four ground motions analyzed for the benchmark strongback. Scenarios [1] and [2] are then left as probable upper bounds to the strongback brace force.

If it is assumed that the strongback is designed for the entirety of the dominant higher-mode response and has little participation in the first mode other than through yielding in the fuses, then an upper estimate for the strongback brace demands can be estimated from the following envelope:

$$\phi P^*_{s,j} \geq P_{s,j} = \max\left[\frac{s_j}{b}\left(\frac{l}{r_j}P^*_{r,j}\right), \frac{s_j}{b}V_{2,j}\right] \qquad \text{Equation 8.7}$$

$V_{2,j}$ = story shear developed by a second-mode force distribution at the second-mode period, T_2; $P^*_{r,j}$ = adjusted strength of the inelastic braces. This approximation assumes that the fuses do not contribute lateral resistance in the second mode. As such, the strongback is designed for the entirety of the second-mode response.

This procedure, termed the Modal Envelope Analysis (MEA) method, separates force demands in the strongback truss into two parts: [i] the forces developed from the diagonal component of the axial force in the adjacent inelastic brace in the same story and [ii] an elastic higher-mode "bending" response that does not include the fuses. In some cases, the third mode may also contribute significantly to demands in the strongback elements. This contribution will depend on the mass participation of the third mode and on whether the second-mode period is in the constant acceleration range or on the descending branch of the constant velocity range of the elastic response spectrum. For the case when there the third mode should also be included, Equation 8.7 becomes:

$$\phi P^*_{s,j} \geq P_{s,j} = \max\left[\frac{s_j}{b}\left(\frac{l}{r_j}P^*_{r,j}\right), \sqrt{\left(\frac{s_j}{b}V_{2,j}\right)^2 + \left(\frac{s_j}{b}V_{3,j}\right)^2}\right] \qquad \text{Equation 8.8}$$

Strongback forces are then calculated from an envelope including the demands from the second- and third-mode story shear distributions.

8.6.1 MEA Procedure

Every analysis in the MEA procedure is elastic, thereby eliminating the partial mechanism analyses requirements in the MPA procedure. Strongback demands are estimated by enveloping the demands delivered by the fuses under a first mode pivoting response and elastic analysis in the higher modes involving only the essentially elastic actions. The MEA procedure modifies steps [4-6] from the MPA procedure as follows:

4. Calculate the force demands delivered to the strongback elements under a first mode distribution considering the full plastic mechanism, r_1.
5. Compute the equivalent-lateral forces for the second-mode period by $\boldsymbol{f}_2 = \Gamma_2 \boldsymbol{m} \phi_2 A_2$ using the second-mode pseudo-acceleration and modal participation factor from an eigenvalue analysis of the full elastic structure (see [3] in the MPA procedure). Create a separate analysis of the strongback frame with the inelastic braces removed and pins designated for the locations of expected beam flexural hinging. Add a roller at the roof level for stability and compute the second-mode demands, r_2, using the separate model.
6. Repeat step [5] for additional modes as needed to achieve 95% mass participation. Combine the additional modes with the demands from [5] using an appropriate modal combination rule (e.g., SRSS or CQC).
7. Calculate the total response, r, by enveloping the first and higher-mode response quantities, $r = \max(|r_1|, |r_n|)$, from [4] and [5,6].

This method is shown schematically in Figure 8.5. Analysis 1 for the deformation-controlled actions is similar to the MPA method in Figure 8.2.

Though this method removes the need for nonlinear material models in the simulations, it requires two numerical models: [i] an eigenvalue analysis of the full structure to calculate the necessary modes and to perform a first mode plastic analysis and [ii] a higher-mode analysis of the strongback-only model. To simplify this process further, the following section introduces a simplified higher-mode force distribution to estimate the first mode plastic analysis step and to account for the higher-mode bending without resorting to a supplemental eigenvalue analysis of the full model.

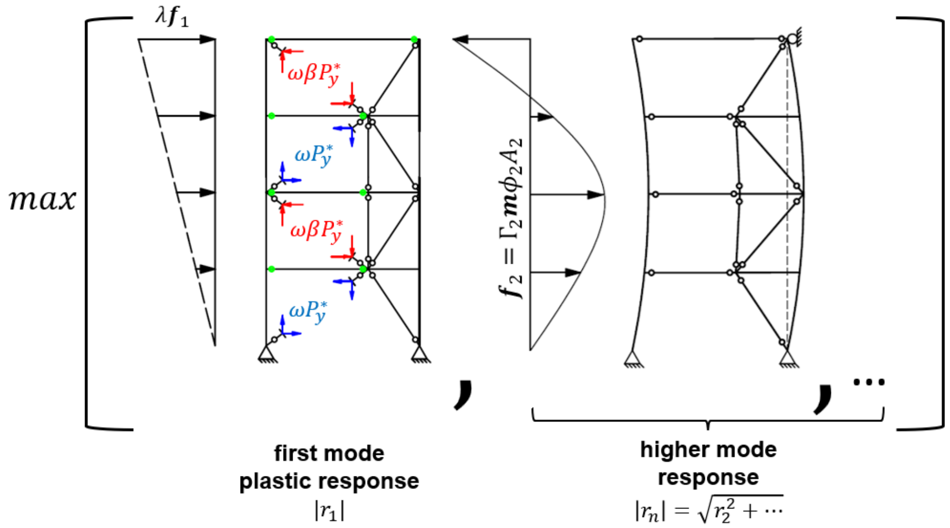

Figure 8.5. Schematic of Modal Envelope Analysis method.

8.6.2 Simplified Higher-mode Distribution

Elastic modes become coupled as the system behaves inelastically, and inelastic modes change with time with changes in stiffness. Thus, though justified for the MPA procedure, use of elastic modes and inelastic behavior is approximate and relies on assumptions of "weak" coupling. In light of these less than rigorous assumptions, this section presents a simplified applied force distribution that does not rely on eigenvalue analysis.

The higher-mode sign reversal was deemed critical to estimating higher-mode bending effects. Based on this premise, force reversal rather than elastic mode shape was emphasized for the simplified force distribution. This section focuses on force reversals representing the second-mode response. Similar simplifications can be made for other higher-mode shapes.

This simplification begins by using the ELF method in ASCE-7-16 (2016) to approximate a first-mode shape. Herein, the ELF procedure representing a first-mode force distribution will be termed ELF$_1$. Force distributions per ELF$_1$ can be written as:

$$f_{j,1} = \frac{w_j \hat{h}_j^k}{\Sigma_{j=1}^{R} w_j \hat{h}_j^k} V_{b,1} \qquad \text{Equation 8.9}$$

f_j = force at level j; $V_{b,1}$ = design base shear; R = roof level. The subscript $(\cdot)_1$ indicates a first mode response. The first mode shape, $\phi_{j,1}$, can be extracted from Equation 8.9 to vary linearly ($k = 1$) with cumulative height, $\hat{h}_j$:

$$\phi_{j,1} = \frac{w_j \hat{h}_j}{\Sigma_{j=1}^{R} w_j \hat{h}_j} \qquad \text{Equation 8.10}$$

w_j = lumped floor seismic weight as a proxy for mass. The effective weight, w_1^*, in the first mode can be estimated using the first mode shape in Equation 8.10 normalized its magnitude at the roof ($\hat{\phi}_{j,1} = \frac{\phi_{j,1}}{\phi_{R,1}}$):

$$w_1^* = \Sigma_{j=1}^{R} w_j \hat{\phi}_{j,1}^2 \qquad \text{Equation 8.11}$$

This is an estimate of the seismic weight participating in the first mode assuming a symmetric building with the mass lumped at every floor level. Mass participation in the second mode, w_2^*, can be estimated from the difference between the total seismic weight, W, and w_1^*:

$$w_2^* = W - w_1^* \qquad \text{Equation 8.12}$$

w_2^* = estimated seismic weight acting in the second mode. This formulation assumes that all of the remaining seismic weight in the higher-modes acts in the second mode. Alternatively, mass participation can be calculated per an eigenvalue analysis. The second-mode base shear, $V_{b,2}$, can be estimated as:

$$V_{b,2} = w_2^* A_2 \qquad \text{Equation 8.13}$$

$A_2(T_2)$ = pseudo-acceleration at the second-mode period, $T_2 = T_1/3$, in units of g. The higher-mode periods for a shear building can be estimated from the first mode period and are shown in Table 8.5. Usually this pseudo-acceleration would fall in the constant acceleration range of the elastic design spectrum and can be estimated as $A_2 = S_{MS}$ or S_{DS} depending on whether the strongback is expected to remain elastic at the MCE- or DE-level.

A simplified second-mode shape, ψ, can be generated based on a reversal of a uniform load distribution over N stories. The second-mode reversed shape, ψ_2, for a four-story building is shown in Figure 8.6 and written in vector format below:

$$\psi_2 = \{1, 1, 0, -1\}^T \qquad \text{Equation 8.14}$$

Note that the forces cancel at the third-floor level because of the sign reversal. The base shear from the reversed shape, ψ_2, needs to be amplified to equal the second-mode base shear, $V_{b,2}$. Assuming the strongback behaves like a simply supported beam (see Section 7.4), the base shear from ψ_2 can be calculated by taking moment equilibrium about the roof of the strongback; point 0 in Figure 8.6. The base shear, $v_{1,2}$, resulting from ψ_2 can be written in terms of seismic floor weight, w_j, frame height, H, and cumulative height, $\hat{h}_j$, as:

$$v_{b,2} = \Sigma_{j=1}^{R} \left(w_j \, \psi_{j,2} \frac{H - \hat{h}_j}{H} \right) \qquad \text{Equation 8.15}$$

The final reversed force distribution, $f_{j,2}$, can then be scaled to the base shear from Equation 8.13:

$$f_{j,2} = w_j \psi_{j,2} \frac{V_{b,2}}{v_{b,2}} = \frac{w_j \psi_{j,2}}{\Sigma_{j=1}^{R} \left(w_j \, \psi_{j,2} \frac{H - \hat{h}_j}{H} \right)} V_{b,2} \qquad \text{Equation 8.16}$$

This equation has been formulated similar to Equation 8.9 to mimic the traditional ELF$_1$ force distribution from ASCE-7-16. Herein, it is termed the ELF$_2$ procedure. Note that this formulation assumes a residual reaction force at the roof level takes the place of the roof level load; see $R_{R,j}$ in Figure 8.6:

$$R_{R,2} = V_{b,2} - \Sigma_{j=1}^{R} f_{j,2} \qquad \text{Equation 8.17}$$

Story shears can be calculated using this reaction force to satisfy equilibrium. Conceptually, this reaction force is a representation of the simply supported beam analogy for the strongback derived in Section 7.4. This force reversal assumes that all the higher modes are represented by the second-mode representation, ψ_2. It is envisioned that the participating mass in the third and higher modes would require nested variations of this derivation.

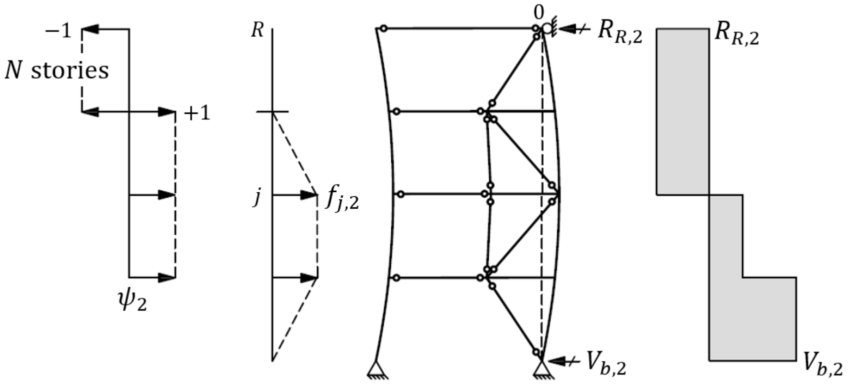

Figure 8.6. Simplified higher-mode distribution for ELF2 procedure.

8.6.3 Points of Load Reversal

The number of stories, N, participating in the sign reversal for ψ_2 can be estimated from the mode shape of a cantilever beam with uniform mass and stiffness; see Figure 8.7. A uniform cantilever column has elastic vibrational modes:

$$\phi_n(\hat{h}) = C_1[\cosh \beta_n \hat{h} - \cos \beta_n \hat{h} - \frac{\cosh \beta_n H + \cos \beta_n H}{\sinh \beta_n H + \sin \beta_n H}(\sinh \beta_n \hat{h} - \sin \beta_n \hat{h}) \qquad \text{Equation 8.18}$$

$C_1 =$ arbitrary constant. The parameter, $\beta_n H$, can be solved numerically for each mode ($\beta_n H =$ 1.8751, 4.6941, 7.8548, 10.996) (Chopra, 2011). The roots of Equation 8.18 for the first four modes can be found in Table 8.5. The heights found in this table estimate the point of load reversal for the first four modes. The number of stories participating in the reversal, N, can be estimated by interpolating between the closest floor levels and the point of load reversal, $\hat{h}/H$; see Figure 8.7.

For the four-story benchmark building, this reversal occurs approximately three-quarters up the height of the building, corresponding to a load reversal at the third story; see Figure 8.6. As the strongback gets taller and other modes besides the second become more dominant, multiple load reversal effects other than the second-mode reversal may also need to be considered. Though not studied for the four-story benchmark strongback, potential load profiles estimating the third and fourth modes are shown for completeness.

Table 8.5. Estimate of point of load reversal with building height.

			Location of reversal, $\hat{h}/H$ [2]			
Mode	T_1/T_n [1]	$\beta_n H$ [2]	**1**	**2**	**3**	**4**
Mode 1	1	1.8751	0			
Mode 2	3	4.6941	0	0.78		
Mode 3	5	7.8548	0	0.50	0.87	
Mode 4	7	10.996	0	0.36	0.64	0.85

[1] Estimated from a uniform shear building.

[2] Estimated from a uniform cantilever beam.

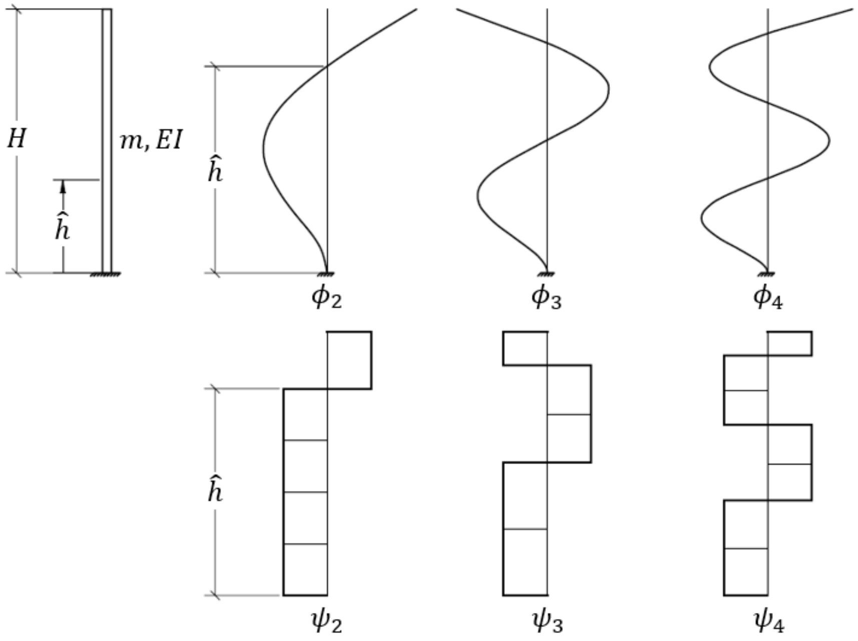

Figure 8.7. Schematic of load reversal profiles.

8.6.4 SMEA Procedure

The Simplified Modal Envelope Analysis (SMEA) method uses the load reversal formulated in Section 8.6.2 and approximates demands delivered by the fuses using an overstrength factor, $\Omega_0 = \frac{3}{2}\frac{R}{2}$, as a proxy for the amplification factor, λ, from Equation 7.10. This overstrength factor was calibrated to the nonlinear dynamic results of the benchmark strongback and is not reflective of the overstrength factors for conventional systems in ASCE 7-16; see Section 7.5.1. This procedure simplifies steps [3-7] of the MEA method to the following:

3. Estimate the second-mode period from the fundamental period, $T_2 = T_1/3$. Determine the second-mode pseudo-acceleration, $A_2(T_2)$, by reading the pseudo-acceleration ordinate

from the elastic response spectrum. Alternatively, $A_2(T_2) = S_{MS}$ or S_{DS} depending on whether the strongback is expected to remain elastic at the MCE- or DE-level.

4. Calculate the demands, r_1, delivered by the forces using the ELF$_1$ procedure with $k = 1$. Use $\Omega_0 = \frac{3}{2}\frac{R}{2}$ to estimate forces in the strongback truss.
5. Compute the reversed force distribution using Equation 8.16 and the pseudo-acceleration from [3]. Remove all fuse actions by removing the inelastic braces and specifying pins at the locations of expected beam flexural hinging. Add a roller at the roof level for stability and compute the bending response, r_2, using the separate model. Alternatively, fuses can be given an appropriately small material stiffness (e.g., $0.1E$). If a roller at the roof is not used for stability, the ELF_2 distribution needs to include a force reversal at the upper levels, N.
6. Calculate the total response, r, by enveloping force demands from [4] and [5]; $r = \max(|r_1|, |r_2|)$.

The SMEA method estimates demands delivered by the fuses through $\Omega_0 = \frac{3}{2}\frac{R}{2}$ and provides a simple means of estimating higher-mode bending effects. More research is needed to evaluate appropriate values for Ω_0 and to extend this work to taller strongback systems with dominant third or fourth modes.

Note that step [4] is intended to approximate demands delivered by the fuses. However, this step uses an elastic analysis that cannot capture force re-distributions due to yielding and does not incorporate the adjusted strength of the fuses; e.g., inclusion of ω and β for the BRBs. Moreover, if the strongback was separated from the inelastic brace bay, this step would result in minimal strongback demands. As such, step [4] would ideally be replaced with a plastic analysis or pushover analysis after preliminary design.

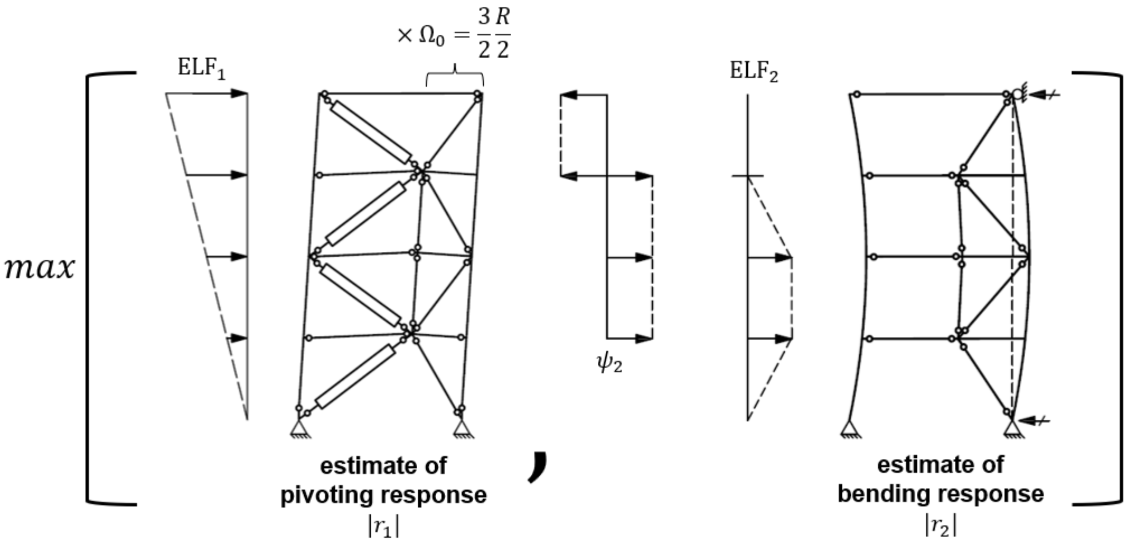

Figure 8.8. Schematic of Simplified Modal Envelope Analysis method.

8.7 COMPARISON OF PROPOSED DESIGN METHODS

To validate the proposed analysis methods, estimates of strongback demands using the MPA, MEA, and SMEA procedures were compared to the output from nonlinear dynamic analysis of the four-story benchmark strongback. To emphasize the difference between a single-mode and multi-mode method of analysis, comparisons were also made using a first mode-only plastic analysis and the ELF_1 procedure using $\Omega_0 = \frac{3}{2}\frac{R}{2}$. Force demands in the strongback from each of the analyses are tabulated in Table 8.6. The ratio between the static-to-median and -85th percentile dynamic response for each analysis is shown in Table 8.7 and Table 8.8. The distribution of estimations alongside the dynamic demand output is shown in Figure 8.9.

When compared to the results from the nonlinear dynamic analyses, the modal procedures provide superior estimates of strongback demands compared to that of the traditional first mode-only distributions. The MPA results are tabulated in terms of the NP and PP models using the superposition modal combination rule. The MPA procedure gives the closest estimate to the nonlinear dynamic response for all elements other than the first-story strongback brace, which was over-estimated by 28 to 44%. The MPA method explicitly includes the inelastic response of the first four dominant translational modes.

The MEA and SMEA enveloping procedures provide better estimates for the demands in the first-story strongback brace than the MPA methods but over-estimate demands in the tie by 37 to 50% compared to the 85th percentile response. Note that the MEA procedure calculates the modes from the original model and applies these modes separately to a model where the fuses are removed. The SMEA procedure utilizes the simplified force reversal calculated per Equation 8.16.

To justify use of the elastic modes in the MEA methods, comparisons were also made to force distributions estimated from the mode shapes extracted from a strongback-only model with the fuses removed and a roller at the roof. These modes are termed transient modes as they account for the low post-yield stiffness of the fuses by removing their contribution to the eigenvalue calculations. The first mode of the transient modes corresponds to the desired bending response. Calculation of a transient first mode using the strongback-only model over-estimated strongback demands in the fourth story strongback brace and tie by a significant margin.

The SMEA procedure using the simplified force-reversal distribution gave similar estimates to the MEA procedure. The MEA procedure additionally compared estimates using the second mode and an SRSS of the second-to-fourth translational modes. Use of more than the second mode in the MEA procedure did little to improve estimates of the strongback demands. Demands estimated from a plastic analysis using a first mode force distribution and the ELF_1 method with $\Omega_0 = \frac{3}{2}\frac{R}{2}$ served as an appropriate lower bound for the SMEA method. This lower bound controlled the demands in the second-story strongback brace. Note that a more appropriate estimate of tie demands could be obtained by assuming a notional value of force in the fuses instead of complete inelastic element removal.

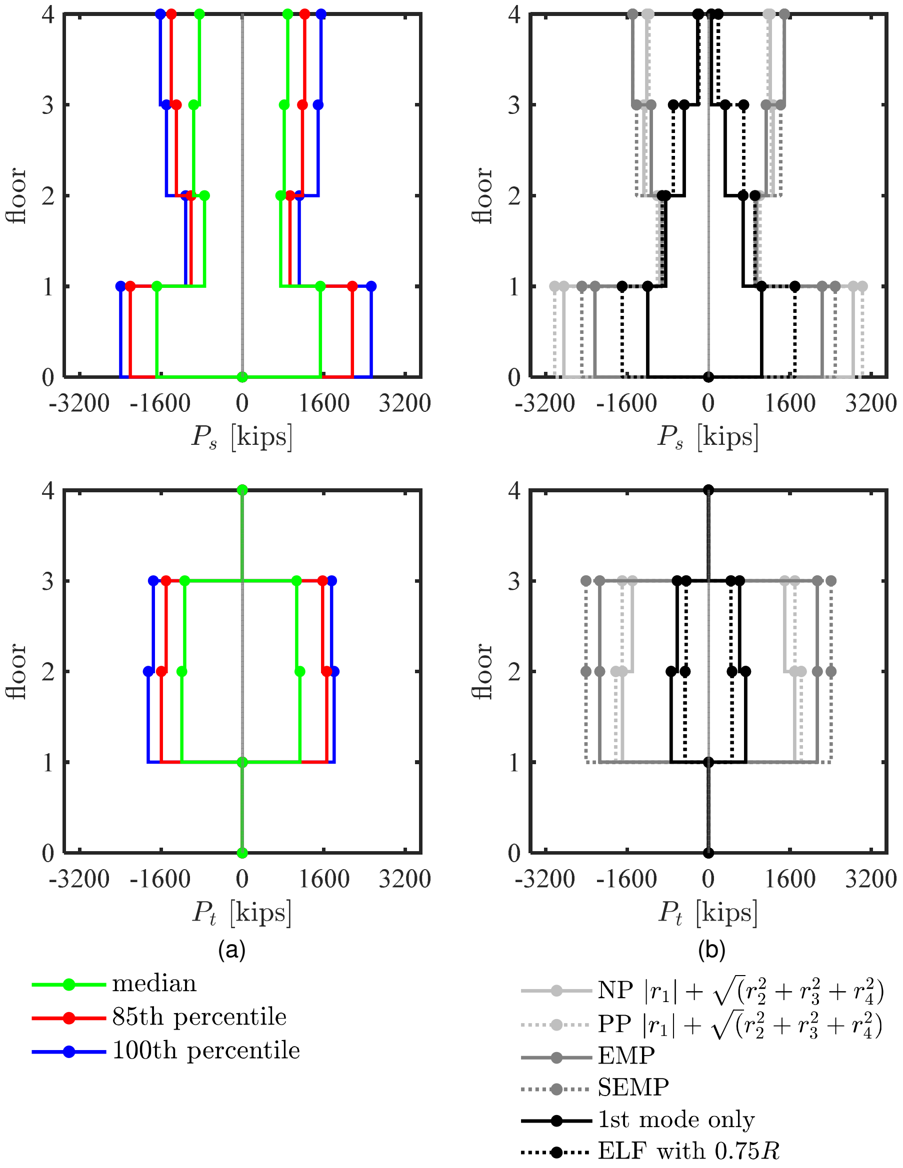

(a) (b)

Figure 8.9. Comparison of static demands from proposed methods to nonlinear dynamic output.

Table 8.6. Static strongback demands.

Analysis Type	Lateral Load Distribution	Axial-force demand											
		$P_{s,1}$ [kips]		$P_{s,2}$ [kips]		$P_{s,3}$ [kips]		$P_{s,4}$ [kips]		$P_{t,2}$ [kips]		$P_{t,3}$ [kips]	
		min	max	min	max	min	max	min	max	min	max	min	max
Gravity	$(1.2 + 0.2S_{DS})D + 0.5L$	-81		3		-22		-6		-66		-23	
	$(0.9 - 0.2S_{DS})D$	-38		-1		-9		-5		-31		-13	
	$1.05D + 0.125L$	-57		-7		-14		-13		-44		-21	
Dynamic	Median [1]	-1625	1614	-745	768	-956	859	-851	941	-1157	1176	-1141	1085
	85th percentile [1]	-2287	2342	-994	1002	-1411	1279	-1461	1474	-1713	1724	-1585	1719
NP	$\lvert r_1\rvert + \sqrt{r_2^2 + r_3^2 + r_4^2}$	2852		965		1282		1227		1734		1517	
PP	$\lvert r_1\rvert + \sqrt{r_2^2 + r_3^2 + r_4^2}$	3024		1009		1232		1170		1822		1696	
Plastic	1st mode	-1198	1041	-842	678	-476	326	-214	55	-737	729	-617	609
ELF_1	Elastic with $\Omega_0 = \frac{3}{2}\frac{R}{2}$	-1698	1698	-912	912	-685	685	-192	192	-462	462	-438	438
Elastic [1]	2nd mode	-2224	2224	-229	229	-1109	1109	-1457	1457	-2135	2135	-2135	2135
	3rd mode	-159	159	-293	293	-197	197	-313	313	-105	105	-105	105
	4th mode	-13	13	-72	72	-76	76	-18	18	-49	49	-49	49
	Transient 1st mode	-2593	2593	-776	776	-1084	1084	-2417	2417	-2912	2912	-2912	2912
	Simplified reversal	-2489	2489	-299	299	-1418	1418	-1492	1492	-2407	2407	-2407	2407
Envelope	MEA of 2nd mode	-2224	2224	-842	678	-1109	1109	-1457	1457	-2135	2135	-2135	2135
	MEA of higher modes [2]	-2230	2230	-842	678	-1129	1129	-1485	1485	-2138	2138	-2138	2138
	SMEA with ELF_2	-2489	2489	-912	912	-1418	1418	-1492	1492	-2407	2407	-2407	2407

[1] analysis does not include contributions from fuses or gravity

[2] uses SRSS modal combination of second through fourth translational modes

Table 8.7. Ratio of static strongback demands to median dynamic response.

Analysis Type	Lateral Load Distribution	Axial-force demand											
		$P_{s,1}/P_{s,1}^{50\%}$		$P_{s,2}/P_{s,2}^{50\%}$		$P_{s,3}/P_{s,3}^{50\%}$		$P_{s,4}/P_{s,4}^{50\%}$		$P_{t,2}/P_{t,2}^{50\%}$		$P_{t,3}/P_{t,3}^{50\%}$	
		min	max	min	max	min	max	min	max	min	max	min	max
NP	$\lvert r_1 \rvert + \sqrt{r_2^2 + r_3^2 + r_4^2}$	1.70	1.83	1.28	1.27	1.32	1.52	1.42	1.32	1.44	1.53	1.31	1.43
PP	$\lvert r_1 \rvert + \sqrt{r_2^2 + r_3^2 + r_4^2}$	1.80	1.94	1.34	1.33	1.27	1.46	1.35	1.26	1.52	1.61	1.46	1.59
Plastic	1st mode	0.71	0.67	1.12	0.89	0.49	0.39	0.25	0.06	0.61	0.64	0.53	0.57
ELF$_1$	Elastic with $\Omega_0 = \frac{3}{2}\frac{R}{2}$	1.01	1.09	1.21	1.20	0.71	0.81	0.22	0.21	0.38	0.41	0.38	0.41
Envelope	MEA of 2nd mode	1.32	1.43	1.12	0.89	1.14	1.31	1.69	1.57	1.78	1.89	1.84	2.01
	MEA of higher modes	1.33	1.43	1.12	0.89	1.16	1.34	1.72	1.60	1.78	1.89	1.84	2.01
	SMEA with ELF$_2$	1.48	1.60	1.21	1.20	1.46	1.68	1.73	1.61	2.00	2.13	2.07	2.26

Table 8.8. Ratio of static strongback demands to 85th percentile dynamic response.

Analysis Type	Lateral Load Distribution	Axial-force demand											
		$P_{s,1}/P_{s,1}^{85\%}$		$P_{s,2}/P_{s,2}^{85\%}$		$P_{s,3}/P_{s,3}^{85\%}$		$P_{s,4}/P_{s,4}^{85\%}$		$P_{t,2}/P_{t,2}^{85\%}$		$P_{t,3}/P_{t,3}^{85\%}$	
		min	max	min	max	min	max	min	max	min	max	min	max
NP	$\lvert r_1 \rvert + \sqrt{r_2^2 + r_3^2 + r_4^2}$	1.22	1.25	0.96	0.97	0.90	1.01	0.83	0.84	0.99	1.03	0.94	0.89
PP	$\lvert r_1 \rvert + \sqrt{r_2^2 + r_3^2 + r_4^2}$	1.29	1.32	1.01	1.01	0.86	0.97	0.79	0.80	1.04	1.08	1.06	1.00
Plastic	1st mode	0.51	0.46	0.84	0.68	0.33	0.26	0.15	0.04	0.42	0.43	0.38	0.36
ELF$_1$	Elastic with $\Omega_0 = \frac{3}{2}\frac{R}{2}$	0.72	0.74	0.91	0.92	0.48	0.54	0.13	0.13	0.26	0.27	0.27	0.26
Envelope	MEA of 2nd mode	0.95	0.97	0.84	0.68	0.78	0.88	0.99	1.00	1.22	1.27	1.33	1.26
	MEA of higher modes	0.95	0.98	0.84	0.68	0.79	0.89	1.01	1.02	1.22	1.27	1.33	1.26
	SMEA with ELF$_2$	1.06	1.09	0.91	0.92	0.99	1.12	1.01	1.02	1.37	1.43	1.50	1.42

8.8 BEAM AND COLUMN DESIGN

This section describes approaches for the design of the beams and columns in strongback-braced frames. Axial forces in the columns extracted from each of the proposed analysis methods were compared to that from the nonlinear dynamic analysis of the benchmark strongback. Recommendations of minimal column flexural strength for flexural-axial interaction checks of the columns are also provided.

8.8.1 Beam Design

Beams are considered deformation-controlled in flexure and force-controlled under axial compression and shear. Flexural strength is determined per traditional analysis, such as those provided in ASCE-7-16 (2016). Moment strength of the beam is determined from flexural demands generated from gravity loading as if the braces in the story above and below were not present.

Shear developed from beam plastic hinging should be accounted for in designing for the shear strength of the beam. This could be considered based on capacity design assuming flexural plastic hinging at the beam link ends. Beam links should conform to the classification and deformation limits associated with links in eccentrically braced frames (EBFs); see Section 2.2.2. Provided the beams are long enough, they can be assumed to conform to flexural links with a strain hardening adjustment factor of 1.0.

Axial-force demands are checked based on demands extracted by any one of the proposed analysis methods; see Sections 8.4 through 8.6. If these axial-force demands are significant, axial-flexural interaction of the beam should be considered.

8.8.2 Column Design

Columns are deformation-controlled in flexure and force-controlled under axial compression. Both moments and axial loads can be calculated per any one of the proposed analysis methods accounting for higher-mode bending in Sections 8.4 through 8.6.

Columns can be designed considering accumulated gravity loading, P_{g,c_j}; the vertical component of the adjoining braces, C_j^*, T_j^*, or $P_{s,j}$; and the shear developed from plastic hinging in the beam links, $V_{r,j}$ or $V_{s,j}$; see Figure 8.10. Note that the 0.88 reduction factor allowed for the design of columns in EBFs three stories and greater is not applicable for the design of strongback-braced frames as all inelastic braces and beam links can yield at the same time due to the presence of the strongback; see Section 2.2.2.

Axial-force demands are well-constrained for the design of the inelastic column. However, these demands are less well constrained in the strongback column due to uncertainty in determining the forces in the strongback braces and the randomness of the ground motion. To account for uncertainty in the ground motion intensity, it is recommended that that axial forces in the strongback truss include an adjustment factor of at least 1.1 for calculating column axial-force demands. Further analysis is needed to justify the value of this adjustment factor.

Comparisons of the demands extracted from the analysis and the modal pushover and enveloping procedures for the strongback column are shown in Table 8.6. Though axial-force demands are well estimated by the proposed analysis methods, the models used for the PP modal pushover analysis and MEA and SMEA enveloping methods under-estimated in-plane flexural moments developed in the strongback column. These models assumed pins at all beam-column connections while the nonlinear dynamic model used partially-restrained springs at those locations. Note that at the 85th percentile, column flexural demands were 18 and 44% of the column's expected plastic flexural capacity at the first and fourth story respectively.

Column compression forces should be checked based on the lower-bound limit states of flexural, flexural-torsional, and torsional buckling. To account for the high axial-force demands that can develop in the strongback column, columns should also consider a minimum flexural capacity; see Figure 8.11. Herein, it is recommended that columns be designed including interaction between the calculated axial forces and bending moments of 20% of the column's expected plastic moment strength (CSA-S16-14, 2014). Alternatively, flexural demands can be extracted directly from the analysis; see Figure 8.11. Further analysis is needed to justify the magnitude of the additional bending moment.

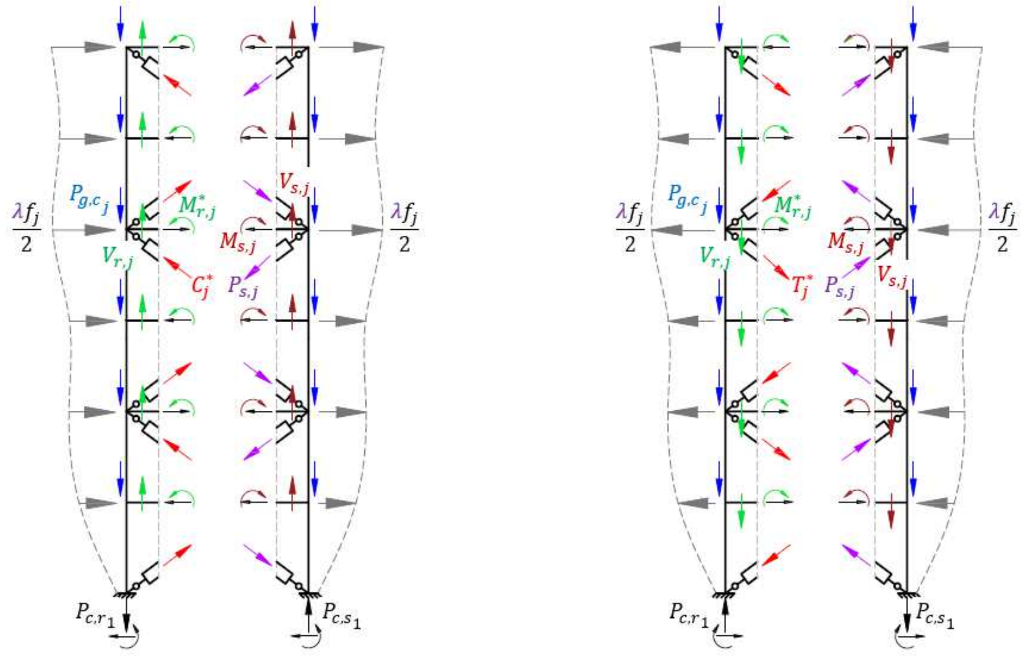

(a) (b)

Figure 8.10. Column free body diagram – (a) positive loading, (b) negative loading.
Note: directions of internal forces may change depending on assumed distribution of lateral loading.

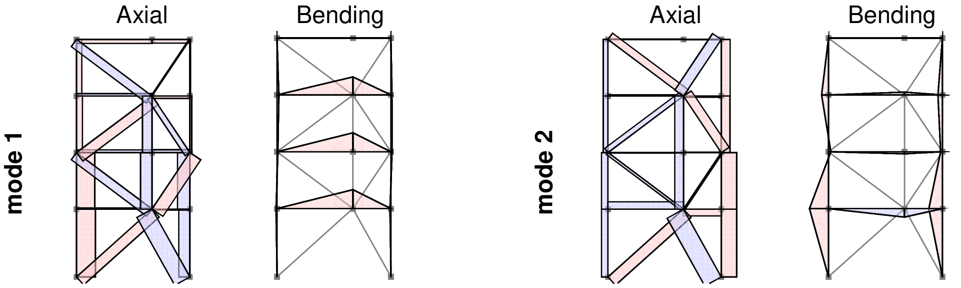

Figure 8.11. Axial and moment diagrams extracted from pushover analyses in first and second mode.

Table 8.9. Static strongback column demands.

Analysis Type	Lateral Load Distribution	Force Demand											
		$P_{cs,1}$ [kips]		$P_{cs,2}$ [kips]		$P_{cs,3}$ [kips]		$P_{cs,4}$ [kips]		$M_{cs,1}$ [1] [k-in.]	$M_{cs,2}$ [1] [k-in.]	$M_{cs,3}$ [1] [k-in.]	$M_{cs,4}$ [1] [k-in.]
		min	max	min	max	min	max	min	max				
Gravity	$(1.2 + 0.2S_{DS})D + 0.5L$	-140		-115		-70		-45		-	-	-	-
	$(0.9 - 0.2S_{DS})D$	-72		-57		-36		-22		-	-	-	-
	$1.05D + 0.125L$	-131		-99		-64		-32		-	-	-	-
Dynamic	Median	-1486	1262	-1504	1290	-763	764	-811	720	2467	2359	3120	4775
	85th percentile	-2095	1736	-2175	1826	-1235	1199	-1262	1272	3128	3035	4392	5933
Modal Pushover, NP	r_1, 1st mode	-386	506	-460	637	-234	385	-112	238	-	-	-	-
	r_2, 2nd mode	-1380	1318	-1363	1300	-712	709	-721	720	-	-	-	-
	r_3, 3rd mode	-106	106	-105	105	-184	183	-185	184	-	-	-	-
	r_4, 4th mode	0	0	0	0	0	0	0	0	-	-	-	-
	$\sqrt{r_1^2 + r_2^2 + r_3^2 + r_4^2}$	1474		1508		830		781		2957	2928	3956	6549
	$\lvert r_1 \rvert + \sqrt{r_2^2 + r_3^2 + r_4^2}$	1885		2003		1120		982		4179	4100	5072	8363
Modal Plastic Pushover, PP	r_1, 1st mode	-534	672	-614	753	-122	245	-42	165	-	-	-	-
	r_2, 2nd mode	-1520	1520	-1506	1506	-789	789	-792	792	-	-	-	-
	r_3, 3rd mode	-72	72	-72	72	-162	162	-163	163	-	-	-	-
	r_4, 4th mode	-8	8	-8	8	-10	10	-10	10	-	-	-	-
	$\sqrt{r_1^2 + r_2^2 + r_3^2 + r_4^2}$	1663		1685		842		825		2292	2292	1009	967
	$\lvert r_1 \rvert + \sqrt{r_2^2 + r_3^2 + r_4^2}$	2194		2260		1051		974		2935	2935	1352	1341
Plastic	1st mode	-534	672	-614	753	-122	245	-42	165	779	853	853	535
ELF	Elastic with $0.75R$	-1530	1530	-1548	1548	-168	168	-186	186	1200	1200	198	198
Envelope	2nd mode	-1945	1945	-1945	1945	-1212	1212	-1212	1212	2500	2500	2188	704
	Simplified reversal	-2173	2173	-2173	2173	-1241	1241	-1241	1241	2656	1241	1241	340

[1] maximum moment along column length.

8.9 SUMMARY AND CONCLUSIONS

Two methods were proposed to size the fuses in strongback-braced frames:

1. Sizing by traditional demand-to-capacity ratios at yield due to first-mode demands.
2. Sizing for potential force re-distributions at the limit load using plastic analysis.

Higher-mode effects are amplified by the presence of the strongback. As such, traditional capacity design assuming a first-mode shape is inadequate for estimating demands in the strongback elements. This chapter proposed three methods of analysis to estimate demands in the strongback truss:

1. Dynamic capacity analysis
2. Modal pushover analysis (MPA)
3. Modal envelope analysis (MEA)

The MPA method combines individual pushover analyses in each mode. First-mode demands can be estimated from a plastic analysis using the complete mechanism. Pushover analyses can be used to account for potential partial mechanism response in the second and higher modes. Elastic analyses can be used to estimate the response in those modes that remain elastic. A superposition modal combination rule was found to well-estimate forces extracted from nonlinear dynamic analysis. Use of a simple, perfectly plastic material model introduced an appropriate level of conservatism at reduced computational cost. Such perfectly plastic analyses, however, are limited to elements with stable, full hysteretic behavior and cannot be applied to strongback-braced frames utilizing buckling braces as fuses.

A simple enveloping analysis approach was proposed for preliminary strongback design. The enveloping method broke apart the strongback's response into a "pivoting" first mode response and a "bending" strongback-only higher-mode response. This eliminated the need for analyses involving partial mechanisms in the higher modes. A simplified force distribution was derived to represent higher-mode force reversal effects without the need for eigenvalue analysis. As formulated herein, the enveloping method is intended to provide immediate information for design. Note that the point of force reversal for this method was derived based on assumptions of uniform mass and stiffness. As such, this method may not be suitable for structures exhibiting large vertical stiffness or mass irregularities.

The methods herein utilized spectral ordinates of an MCE-level response spectrum. Any one of the proposed methods could be adjusted using spectral ordinates from a DE-level response spectrum. This gives the engineer the flexibility to choose a desired performance level provided ductile details are utilized where the strongback is expected to buckle or yield at other levels of ground shaking.

The proposed analysis methods require both experimental and numerical studies to evaluate their robustness and ensure their validity. For example, the benchmark strongback used to rationalize the proposed methods used a strongback embedded in the same bay as the inelastic braces and the same BRB size in every story. Observations about modal response may be more salient when the strongback bay is separated from the inelastic brace bay. These analysis methods did not address the non-simulated collapse modes triggered by deformation limits in the beam link during the nonlinear dynamic analyses conducted in Chapter 5. Further verification of the proposed methods using other ground motion characteristics, bracing configurations, bracing type, building heights, story heights, etc. is needed to more fully evaluate the proposed analysis methods. Supplemental detailing, stiffness, and compatibility requirements are also needed to ensure appropriate inelastic response.

9 Summary and Conclusions

9.1 SUMMARY

The strongback is intended to mitigate story mechanisms, re-distribute inelastic demands vertically, and efficiently mobilize the fuses across every story. Though strongback-braced frames have shown promise in both research and in practice, prior studies have found it difficult to proportion the elastic members in the strongback truss and have recognized that the strongback can induce significant deformation demands in the fuses. As such, this study characterized the dynamic response and seismic performance of the strongback system and developed simple and robust analysis methods for estimating force demands in the strongback truss.

A summary of the studies conducted as part of this research is provided below:

- An analytical study investigated the force, stiffness, and plastic deformation parameters that influence the behavior of a one-story strongback with an offset bracing scheme. Based on several design objectives, the offset geometry was optimized to maximize elastic lateral stiffness and minimize plastic deformations.
- A buckling-restrained brace material model was calibrated to eight component BRB tests and one quasi-static experimental test of a strongback system. A BRB simulation using the calibrated material model was subjected to the qualification loading protocol from AISC-341-16 (2016) to derive adjustment factors, ω and β, for design.
- The number of integration points and the number of sub-elements needed to characterize brace curvature and fiber strains for low-cycle fatigue were studied in detail. The numerical perturbation used to initialize buckling in the strongback braces and tie were calibrated to the elastic and inelastic buckling equations in AISC-360-16 (2016) per Equation 4.6.
- A four-story benchmark strongback was designed per dynamic capacity design using nonlinear dynamic analyses supplemented with the acceptance criteria from FEMA-P695 (2009). The strongback truss was designed for less than 10% probability of inelastic response in any one of the strongback elements. Strongback-braced frames designs were evaluated based on an acceptable 10% collapse probability at the MCE-level of shaking. Adequate collapse performance was also verified through incremental dynamic analysis.
- The benchmark-strongback design was utilized to parametrically study the sensitivity of strongback brace frame's response to various design alternatives, including beam releases,

column base fixity, columns orientation, beam composite and diaphragm action, and brace end conditions. The response of embedded strongback configurations with varying offset and BRB sizes were also compared to the response of conventional BRBFs. These parameters were studied in terms of the median and 85th percentile response.

- Multi-story strongback-braced frames were analytically characterized in terms of plastic analysis, stiffness, compatibility, and dynamic higher-mode behavior. Several analysis methods were proposed to estimate the force demands that develop due to higher mode “bending” effects for the design of the strongback truss.

9.2 CONCLUSIONS

Significant conclusions are summarized below -

- The addition of a strongback can induce significant deformation demands in the fuses that are larger than that of a typical yielding system. An embedded strongback configuration without an offset results in BRB axial deformations and beam link flexural deformation that are about twice that of a conventional BRBF. As such, appropriate details are needed to ensure that the fuses have enough deformation capacity to ensure adequate ductile behavior. Offsetting the brace-to-beam intersection from the centerline of the braced bay can reduce inelastic deformations provided the frame is designed with sufficient lateral stiffness. Optimal offsets of the brace-to-beam intersection between the range of 1/3 to 1/4 the bay width provided a balance between adequate lateral stiffness and reduced deformation demands on the fuses. Brace axial deformations can also be reduced by moving the strongback to a separate bay. This separated configuration, however, does not result in reduced deformation demands in the beam links.
- Strains in the fibers of distributed plasticity elements in a buckling brace non-objectively depend on the number of integration points used in the element. As such, parameters defining the low-cycle fatigue material model used in this study need to be re-calibrated to experimental results for choices of numerical modeling parameters, like the number of brace sub-elements, number of integration points per sub-element, etc. different than those used for the calibration studies conducted herein.
- The inelastic and associated strain-hardening behavior of buckling-restrained braces depends on the loading history. As such, it is important that BRB material models be able adapt to changes in loading and appropriately reflect experimental data. Herein, a procedure was developed to consistently relate experimental data and design factors to potential dynamic loading. Provided the material model is history dependent, this method of calibration can also account for changes in the loading history. Note that calibrated models reported herein could be further refined with a larger experimental database of BRBs with different core cross-sections, connections, manufacturers, etc.
- Ground motion characteristics were found to have a greater impact on peak response over the other design alternatives parametrically considered herein; see Section 6.4. Ground motions with long durations or large pseudo-accelerations at the higher-mode periods significantly

affect the strongback's dynamic response. As such, site location and the expected ground motion characteristics should be carefully considered.

- The addition of a strongback results in an averaged drift profile compared to that of a conventional buckling-restrained braced frame. Though this results in smaller peak story drifts, it also results in decreased drifts in some stories and increased drifts in other stories. Due to the elastic nature of the strongback, accelerations also exhibit a different height-wise profile and tend to be larger than that of buckling-restrained braced frames. Though the collapse performance of strongback-braced frames is expected to be better than that of conventional braced frames, it is unclear how the strongback compares to conventional systems in terms of the performance of drift-sensitive and acceleration-sensitive components.
- Incremental dynamic analysis of the benchmark strongback triggered non-simulated failure modes associated with the deformation capacity of the beam links. The rotational capacity of the beam links was the primary factor limiting the collapse performance of the four-story benchmark strongback considered herein. Non-simulated deformation demands triggered in the beam links and observed failure modes in this region during an experimental study illustrate the critical nature of inelastic demands induced in this region. Supplemental studies with fully pinned beam links and separated strongback configurations resulted in near-zero collapse probability. Details with enough deformation capacity should be considered to ensure adequate ductility of the beam links.
- The strongback is better able to maintain a near-uniform drift profile with increasing lateral stiffness relative to that of the fuses. Though an infinitely stiff strongback would exhibit a first mode-only response, the prohibitive cost and unrealistic nature of such a structural assembly necessitates optimization of the strongback elements. This unavoidable flexibility in the strongback truss introduces higher-mode demands. Since the strongback has significant higher-mode bending capacity compared to than that of a typical yielding system, the higher-mode force demands depend on the intensity of ground shaking rather than the yield strength of the fuses.
- If the strongback elements are intended to remain essentially elastic under all modes of excitation, the strongback elements must be designed to resist elastic or partially inelastic higher-mode demands. These demands stem from the non-zero mass participation in the second and potentially higher modes and an elastic or partially inelastic strongback bending response. The presence of these higher-mode demands is supported by their amplification in similar essentially elastic spine systems, such as concrete shear walls and rocking frames. Note that some yielding allowed at intermediate levels of shaking could still result in adequate performance and limit the large force demands that can develop due to these higher-mode effects.
- Since higher modes contribute to force demands in the strongback elements, traditional capacity or plastic design alone are insufficient to bound the demands in the strongback truss. Capacity design assumes that the capacities of the fuses limit the forces that can develop during an earthquake. However, since the strongback truss is dually designed to remain essentially elastic and resist lateral loads, it continues to accumulate demands in the second and higher modes after the fuses have yielded and as the ground shaking intensifies. As such, any analysis

method used to design the elements in the strongback should estimate the force demands from this higher-mode bending response.

9.3 PROPOSED ANALYSIS METHODS

The essentially elastic nature of the strongback truss ensures yielding occurs primarily in the designated fuses. The strength of the fuses is generally controlled by the first-mode response. Demands and details in those inelastic regions are well defined by the capacity of the fuses. As such, design of the fuses can be determined by traditional design methods typical of a conventional system [e.g., as required by ASCE/SEI 7-16 (2016)].

Demands in the essentially elastic actions a less well-defined. Though the displaced shape is dominated by a first mode (inverted triangular) response, the demands in the strongback elements are maximized under higher-mode (bending) contributions. Thus, the required strength of the essentially elastic components is still bounded by capacity design principles but is additionally bounded by elastic or partially inelastic higher-mode effects. These force demands can be significantly larger than those estimated from methods that assume a first mode-only response. Two static analysis methods incorporating higher-mode demands were proposed: [i] modal pushover analysis and [ii] modal envelope analysis. Both of these methods included simplifications to make them more accessible for preliminary design. A summary of the methods is provided below:

1. A modal pushover analysis procedure that combined the pushover responses in each mode was found to closely match the results extracted from nonlinear dynamic analysis. A simplified analysis procedure utilizing a perfectly plastic material response was able to estimate force demands in the strongback truss at reduced computational cost. Perfectly plastic material assumptions are not appropriate in strongback-braced frames utilizing buckling braces for the fuses. A modal combination rule similar to that of rocking frames was suggested to account for coupling of inelastic modes.
2. It is critical that any proposed design methods recognize both the stochastic nature of the ground excitation and the yielding response of the fuses. As such, an enveloping analysis procedure was proposed to bound the demands on the strongback elements. This procedure assumes the strongback is designed for the entirety of the higher-mode demands. As a lower bound, strongback elements are also designed for the first-mode demands delivered by the fuses. It was found that this analysis procedure closely matched the distribution of peak demands in the strongback braces, but over-estimated demands in the tie.
3. A simplified enveloping procedure was proposed that enveloped strongback demands from a “pivoting” and “bending” response. This approximated first mode demands utilizing a different R-factor for the inelastic and strongback portions of the system. A reversed force distribution was proposed to mimic higher-mode bending in the strongback. The force distribution was derived to imitate the equivalent-lateral force procedure from ASCE-7-16 (2016). The simplified enveloping approach resulted in similar estimates of demands to the other proposed methods, but more research is needed to determine the limitations of this method.

Herein, the strongback is kept elastic under the average MCE-level of excitation. Any of the above methods can be modified to meet performance objectives at the DE-level provided that ductile details are used for the design of the strongback elements.

9.4 FUTURE WORK

This study is a step towards a comprehensive design method for strongback-braced frames. The following work is needed to supplement the design procedures proposed herein:

1. The proposed analysis methods should be verified against other bracing configurations, types of bracing (e.g., buckling braces, re-centering braces, etc.), and building height other than the four-story embedded strongback investigated herein. Minimum stiffness and compatibility requirements are additionally needed to ensure adequate stiffness of the strongback truss. Finalized design guidelines should explicitly evaluate the limitations of the proposed design methods and include recommendations for drift limits, detailing requirements, etc.
2. In this study strongback was kept essentially elastic under MCE-level excitation, and as such, ordinary details could be used in the strongback truss. Some inelastic behavior could be allowed in the strongback if the designed details are adequately ductile. For example, designing the strongback to remain essentially elastic at the DE-level may be a more economical performance objective and still result in acceptable collapse performance.
3. The design of the columns is based on the estimated axial forces expected to develop in the strongback braces. As such, the proposed design methods could result in substantial strongback brace sizes that could overload the columns, connections, and tie under some instances of more severe levels of shaking. Evaluation of the 1.1 multiplier recommended herein to adjust strength demands in the columns is needed to ensure that the strongback braces and/or tie exhibit inelastic behavior before buckling is triggered in the columns. This would provide confidence that a desirable hierarchy of failure modes is achieved for cases where the expected intensity of the ground motion is exceeded.
4. An embedded strongback within the same bay as the inelastic braces complicates the system's global response by coupling the inelastic actions in the yielding portions of the system with that of the strongback and results in significant plastic deformation demands on the fuses. Future work should further study the advantages of separating the strongback from the inelastic brace bay.
5. As the building height and frame slenderness increases, flexural deformation and higher-mode effects will become more significant. Extension to taller frames is essential in validating the design methods proposed in this study. Note that multi-modal strongbacks (i.e., strongback designed to impose a second or third rather than first mode response) may become more viable for taller systems. Introducing controlled inelastic behavior in the tie and separating the strongback to a separate bay may become necessary for economic design of taller strongbacks.
6. The inherent vertical redundancy of the strongback system has been used to justify a redundancy factor, $\rho = 1$ (Panian et al., 2015). It is unclear at the time of this research how

this redundancy factor would impact the collapse performance of strongback-braced frames compared to other systems. Though the strongback could conceivably bridge across stiffness and mass and irregularities (e.g., due to inelastic brace removal or uncertainty in the loading conditions), such configurations and loading conditions were not explored during this study.

7. This study focused on utilizing buckling-restrained braces for the inelastic braces. The strongback could also be added to other conventional system. For example, strongbacks could be added to moment-resisting frames to alleviate restrictions on strong-column-weak-beam capacity design. A deep column or shear wall could be more efficient than a strongback truss for certain frame heights. The addition of a strongback could also aid bridging over story irregularities in existing buildings.
8. Detailed collapse assessment utilizing the methodology in FEMA-P695 or more sophisticated collapse assessment procedures are needed to verify the performance of strongback-braced frames designed under the proposed methods and to justify the use of R, C_d, and Ω_0 factors.
9. The elastic nature of the strongback results in distinctly different dynamic response than that of a typical steel system. Strongback and similar spine-like systems are not currently addressed in current design provisions. A cohesive narrative for all elastic spine systems, including strongback-braced frames, rocking systems, wall-like systems, etc. is needed to characterize their dynamic behavior and produce simple guidelines for their implementation in practice.

Though this study used the FEMA-P695 methodology to design a working strongback, this methodology is prone to a number of limitations that may not be suitable in validating the performance of the strongback system. Limitations included the following:

1. As observed in Section 6.2.2, duration of shaking may be an important parameter in the strongback's dynamic response. Large magnitude earthquakes can be associated with deep subduction zone events and would affect the related seismic performance. The performance evaluated herein was performed only for the far-field ground motion suite from FEMA-P695. Ground motion characteristics associated with subduction and near-field events should also be considered.
2. Scaling the normalized far-field record set from FEMA-P695 near the upper limit period of the building resulted in amplified spectral accelerations at the higher-mode periods. To account for this in design, a modified response spectrum was proposed that corrected the design response spectrum to include the higher-mode periods. This allowed for continued use of the FEMA-P695 methodology. However, period-dependent ground motion selection would more appropriately represent the first-mode and higher-mode effects. The use of conditional mean spectra, for example, conditioned on the fundamental and higher-mode periods could more realistically emulate the spectral shape at the fundamental and higher-mode periods and circumvent use of the spectral shape factor from FEMA-P695.

By mitigating story mechanisms, the strongback's performance is expected to be better than that of a conventional braced frame. However, enhanced design, alternative analysis methods, configurations, details, and proportioning strategies have been discussed – but not investigated –

that would reduce or delay the onset of damage that would require post-earthquake repair. For example:

1. Different brace strengths or the use of BRBs that use low yield strength steel can result in structures that are stiffer but not stronger, thus limiting peak drifts and accelerations.
2. Residual displacements in a strongback system are reduced but not eliminated. Self-centering braces can be used in conjunction with the strongback system to reduce residual drifts, resulting in decreased repair time and cost after an earthquake.
3. A conventional column to baseplate connection at the base of a strongback and at the beam links provides adequate safety, but may also suffer damage (local buckling, local fractures) that will require repair and result in loss of occupancy. Other details (an RBS or pin type connection) may eliminate damage requiring repair.

It is not clear at the time of this study whether larger drifts in a few stories result in increased repair time and repair cost compared to distributed damage across all stories. Developing a performance-based design philosophy for the strongback systems would enhance its ability to satisfy serviceability requirements for minor, frequent earthquakes and avoid collapse or life-threatening damage during major, rare earthquakes. This could include return on investment type calculations using FEMA-P-58.

REFERENCES

Abramson, M., Audet, C., Chrissis, J., & Walston, J. (2009). Mesh adaptive direct search algorithms for mixed variable optimization. *Optimization Letters*, 3(1), 35–47.

AISC-341-16. (2016). *Seismic Provisions for Structural Steel Buildings.* Chicago, IL: AISC/ANSI Standard 341, American Institute of Steel Construction.

AISC-360-16. (2016). *Specification for Structural Steel Buildings.* Chicago, IL: AISC/ANSI Standard 360, American Institute of Steel Construction.

Aoyama, H. (1986). Earthquake Resistant Design of Reinforced Concrete Frame Buildings with Flexural Walls. *2nd US-Japan Workshop on Improvement of Building Seismic Design and Construction Practice*, (pp. 101–129). San Francisco, CA.

Ariyaratana, C., & Fahnestock, L. (2011). Evaluation of buckling-restrained braced frame seismic performance considering reserve strength. *Engineering Structures*, 77-89.

Arteta, C. A., & Abrahamson, N. (2017). Methodology based on conditional scenario spectra to estimate engineering demand parameter risk. *16th World Conference on Earthquake Engineering.* Santiago, Chile: 16WCEE.

ASCE-41-17. (2017). *Seismic Evaluation and Retrofit of Existing Buildings.* Reston, VA: ASCE/SEI Standard, American Society of Civil Engineers.

ASCE-7-16. (2016). *Minimum Design Loads for Buildings and Other Structures.* Reston, VA: ASCE/SEI Standard, American Society of Civil Engineers.

ATC-114. (2017). *Recommended Modeling Parameters and Acceptance Criteria for Nonlinear Analysis in Support of Seismic Evaluation, Retrofit, and Design.* Redwood City, CA: Applied Technology Council, Rept. No. NIST GCR 17-917-45.

Atlayan, O., & Charney, F. (2014). Hybrid buckling-restrained braced frames. *J. Constr. Steel Research*, 95-105.

Baker, J. (2005). *Vector-Valued Ground Motion Intensity Measures for Probabilistic Seismic Demand Analysis.* Stanford University, Stanford, California: Department of Civil and Environmental Engineering.

Baker, J. (2014). Efficient analytical fragility function fitting using dynamic structural analysis. *Earthquake Spectra*, Technical Note.

Baker, J., & Cornell, C. (2006). Spectral shape, epsilon and record selection. *Earthquake Engng. Struct. Dyn.*, 34(10): 1993-1217.

Ballio, G., & Castiglioni, C. (1995). A Unified Approach for the Design of Steel Structures under Low and/or High Cycle Fatigue. *J. Constr. Steel Research, 34*, 75-101.

Black, C., Makris, N., & Aiken, I. (2002). *Component testing, stability analysis and characterization of buckling-restrained Unbonded Braces.* University of California, Berkeley, CA: Pacific Earthquake Engineering Research Center.

Bondy, K. B. (2003). Moment Redistribution—Principles and Practice Using ACI 318-02. *PTI Journal, Post-Tensioning Institute*, 1(1): 3-21.

Bouc, R. (1971). Modèl mathématique d'hysteresis. *Acustica*, 24:16-25.

Bracci, J. M., Kunnath, S. K., & Reinhorn, A. M. (1997). Simplified Seismic Performance and Retrofit Evaluation of Reinforced Concrete Structures. *J. Struct. Eng*, 123(1): 3-10.

Bradley, C., Fahnestock, L., Hines, E., & Sizemore, J. (2017). Full-scale cyclic testing of low-ductility concentrically-braced frames. *J. Struct. Eng.*, 143(6): 04017029.

Bruneau, M., Uang, C., & Sabelli, R. (2011). *Ductile Design of Steel Structures, 2nd Ed.* New York, NY: McGraw-Hill Companies, Inc.

Charney, F. (2008). Unintended Consequences of Modeling Damping in Structures. *J. Struct. Eng.*, 134(4): 581-592.

Chen, C. H., & Mahin, S. (2012). *Performance-based seismic design of concentrically braced steel frame buildings.* University of California, Berkeley, CA: Pacific Earthquake Engineering Research Center.

Chen, X., Takeuchi, T., & Matsui, R. (2017). Simplified design procedure for controlled spine frames with energy dissipating members. *J. Const. Steel Research, 114*, 135: 242:252.

Chen, X., Takeuchi, T., & Matsui, R. (2018). Seismic Performance and Evaluation of Controlled Spine Frames Applied in High-rise Buildings. *Earthquake Spectra*, preprint.

Chopra, A. K. (2011). *Dynamics of Structures - Theory and Applications to Earthquake Engineering, 4th ed.* Upper Saddle River, New Jersey: Prentice Hall.

Chopra, A. K., & Goel, R. K. (2002). A Modal Pushover Analysis Procedure for Estimating Seismic Demands for Buildings. *Earthquake Engng. Struct. Dyn.*, 31: 561–582.

Chopra, A. K., & Goel, R. K. (2004). Modal Pushover Analysis Procedure to Estimate Seismic Demands for Unsymmetric-Plan Buildings. *Earthquake Engng. Struct. Dyn.*, 33: 903-927.

Chopra, A. K., & McKenna, F. (2016a). Modeling viscous damping in nonlinear response history analysis of buildings for earthquake excitation. *Earthquake Engng. Struct. Dyn.*, 45:193–211.

Chopra, A. K., & McKenna, F. (2016b). Response to John Hall's Discussion (EQE-16-0008) to Chopra and McKenna's paper, ‘Modeling viscous damping in nonlinear response history analysis of buildings for earthquake excitation’. *Earthquake Engng. Struct. Dyn.*, 45: 2235-2238.

Christopoulos, C., Tremblay, R., Kim, H., & Lacerte, M. (2008). Self-Centering Energy Dissipative Bracing System for the Seismic Resistance of Structures: Development and Validation. *J. Struct. Eng.*, 134(1): 96-107.

Clark, P., Kasai, K., Aiken, I., & Kimura, I. (2000). Evaluation of design methodologies for structures incorporating steel unbonded braces for energy dissipation. *Proceedings of the 12th World Conference on Earthquake Engineering.* Upper Hut, New Zealand.

Clough, R., & Huckelbridge, A. (1977). *Preliminary experimental study of seismic uplift of a steel frame.* Berkeley, CA: Earthquake Engineering Research Center, University of California.

Cohn, M. Z. (1965). Rotational Compatibility in the Limit Design of Reinforced Concrete Continuous Beams. *Flexural Mechanics of Reinforced Concrete, SP-12, American Concrete Institute/American Society of Civil Engineers*, 359-382.

Coleman, J., & Spacone, E. (2001). Localization Issues in Force-Based Frame Elements. *J. Struct. Eng.*, 127(11): 1257-1265.

CSA-S16-14. (2014). *Design of steel structures.* Ontario, Canada: Canadian Standards Association.

de Souza, R. M. (2000). *Force-based finite element for large displacement inelastic analysis of frames.* Berkeley, CA: University of California.

Djojo, G. S., Clifton, G. C., & Henry, R. S. (2014). Rocking steel shear walls with energy dissipation devices. *Proc., New Zealand Society for Earthquake. Engineering Conf.* Wellington, New Zealand: NZSEE.

Eatherton, M. R., & Hajjar, J. F. (2010). *Large-Scale cyclic and hybrid simulation testing and development of a controlled-rocking steel building system with replaceable fuses.* Urbana, IL: Newmark Structural Engineering Laboratory Report Series, Univ. of Illinois.

Eatherton, M., & Hajjar, J. (2014). Hybrid simulation testing of a self-centering rocking steel braced frame system. *Earthquake Engng. Struct. Dyn.*, 43:1725–1742.

Eatherton, M., Ma, X., Krawinkler, H., Deierlein, G. G., & Hajjar, J. (2014a). Quasi-static cyclic behavior of controlled rocking steel frames. *J. Struct. Eng.*, 140(11): 04014083.

Eatherton, M., Ma, X., Krawinkler, H., Mar, D., Billington, S., Hajjar, J., & Deierlein, G. (2014b). Design Concepts for Controlled Rocking of Self-Centering Steel-Braced Frames. *J. Struct. Eng.*, 140(11): 04014082.

Eberhard, M., & Sozen, M. (1993). Behavior-based Method to Determine Design Shear in Earthquake-Resistant Walls. *J. Struct. Eng.*, 119(2): 619-640.

Eibl, J., & Kreintzel, E. (1988). Seismic Shear Forces in RC Cantilever Shear Walls. *Proceedings, 9th World Conference on Earthquake Engineering.* Tokyo-Kyoto, Japan.

Engelhardt, M. D., & Popov, E. P. (1989). On design of eccentrically braced frames. *Earthquake Spectra*, 5(3): 495-511.

Eurocode-8. (2004). *Design of structures for earthquake resistance, part 1, general rules, seismic actions and rules for buildings.* Brussels, Belgium: Comité Européen de Normalisation.

Fahnestock, L. A., Ricles, J. M., & Sause, R. (2007). Experimental evaluation of a large-scale buckling-restrained braced frame. *J. Struct. Eng.*, 133(9), 1205-1214.

Fajfar, P., & Fischinger, M. (1988). N2—A Method for Non-Linear Seismic Analysis of Regular Structures. *Proceedings of the Ninth World Conference on Earthquake Engineering.* Tokyo-Kyoto, Japan.

Fell, B. V., Kanvinde, A. M., Deierlein, G. G., & Myers, A. T. (2009). Experimental investigation of inelastic cyclic buckling and fracture of steel braces. *J. Struct. Eng.*, 135(1): 19-32 .

FEMA-356. (2000). *Prestandard and Commentary for the Seismic Rehabilitation of Buildings.* Reston, VA: Prepared by the American Society of Civil Engineers for the Federal Emergency Management Agency.

FEMA-440. (2005). *Improvement of Nonlinear Static Seismic Analysis Procedures.* Redwood City, CA: Applied Technology Council (ATC-55 Project).

FEMA-P695. (2009). *Quantification of Building Seismic Performance Factors.* Redwood City, CA: Applied Technology Council.

Filippou, F. (2013). *FEDEASLab - Finite Elements in Design, Evaluation and Analysis of Structures.* Retrieved from URL http://www.ce.berkeley.edu/˜filippou/Courses/FEDEASLab.htm

Filippou, F. C., Popov, E. P., & Bertero, V. V. (1983). *Effects of bond deterioration on hysteretic behavior of reinforced concrete joints.* Univ. of California, Berkeley, CA: Earthquake Engineering Research Center.

Foutch, D. A., Goel, S. C., & Roeder, C. W. (1987). Seismic Testing of Full-Scale Steel Building - Part I. *J. Struct. Eng., 113*(11), 2111-2129.

Fujimoto, M., Aoyagi, T., Ukai, K., Wada, A., & Saito, K. (1972). Structural Characteristics of Eccentric K-Braced Frames. *Trans. AIJ*, 195: 39-49.

Ghosh, S., & Markevicius, V. (1990). Design of Earthquake Resistant Shearwalls to Prevent Shear Failure. *Proceedings, 4th US National Conference on Earthquake Engineering* (pp. 2: 905-913). Oakland, CA: Earthquake Engineering Research Institute.

Goggins, J., & Salawdeh, S. (2013). Validation of nonlinear time history analysis models for single-storey concentrically braced frames using full-scale shake table tests. *Earthquake Eng. Struct. Dyn.*, 42(8) 1151-1170.

Grigorian, C., & Grigorian, M. (2016). Performance Control and Efficient Design of Rocking-Wall Moment Frames. *J. Struct. Eng.*, 142(2): 04015139.

Hall, D. H. (1981). Proposed Steel Column Strength Criteria. *Journal of the Structural Division*, 107(4): 649-670.

Hall, J. F. (2006). Problems encountered from the use (or misuse) of Rayleigh damping. *Earthquake Engng. Struct. Dyn.*, 35, 525–545.

Haselton Baker Risk Group, L. (2018). SP3 Webinar 5: SP3 Building-specific risk assessment and resilient design for buckling-restrained braced frames.

Hines, E., Appel, M., & Cheever, P. (2009). Collapse performance of low-ductility chevron braced steel frames in moderate seismic regions. *Engineering Journal, 3rd Quarter*, 149-180.

Hjelmstad, K., & Popov, E. (1984). Characteristics of Eccentrically Braced Framse. *J. Struc. Eng., 110*(2), 340-353.

Hollings, J. P. (1969). Reinforced Concrete Seismic Design . *Bulletin of New Zealand Society for Earthquake Engineering*, 2(3): 217-250.

Hsiao, P. C., Lehman, D. E., & and Roeder, C. W. (2012). Improved analytical model for special concentrically braced frames. *J. Constr. Steel Res.*, 73(3), 80–84.

Hsiao, P., Lehman, D., & Roeder, C. (2013). A model to simulate special concentrically braced frames beyond brace fracture. *Earthquake Engng. Struct. Dyn., 42*, 183-200.

Huang, Y., & Mahin, S. A. (2010). *Simulating the inelastic seismic behavior of steel braced frames including the effects of low-cycle fatigue.* Berkeley, CA: Pacific Earthquake Engineering Research Center, Univ. of California.

Ibarra, L. F. (2005). Hysteretic models that incorporate strength and stiffness deterioration. *Earthquake Eng. Struct. Dyn.*, 34(12): 1489-1511.

Ikeda, K., & Mahin, S. A. (1986). Cyclic response of steel braces. *J. Struct. Eng.*, 112(2), 342–361.

Ikeda, K., Mahin, S., & Dermitzakis, S. (1984). *Phenomenological modeling of steel braces under cyclic loading.* Berkeley, CA: Earthquake Engineering Research Center, University of California.

Imanpour, A., & Tremblay, R. (2017). Analysis Methods for the Design of Special Concentrically Braced Frames with Three or More Tiers for In-Plane Seismic Demand. *J. Struct. Eng.*, 143(4): 04016213.

Imanpour, A., Auger, K., & Tremblay, R. (2016a). Seismic design and performance of multi-tiered steel braced frames including the contribution from gravity columns under in-plane seismic demand. *Advances in Engineering Software*, 101: 106-122.

Imanpour, A., Tremblay, R., Davaran, A., Stoakes, C., & Fahnestock, A. (2016b). Seismic Performance Assessment of Multitiered Steel Concentrically Braced Frames Designed in Accordance with the 2010 AISC Seismic Provisions. *J. Struct. Eng.*, 142(12): 04016135.

Ji, X., Kato, M., Wang, T., Hitaka, T., & Nakashima, M. (2009). Effect of gravity columns on mitigation of drift concentration for braced frames. *J. Constr. Steel Res., 65*(12), 2148-2156.

Kanvinde, A. M., & Deierlein, G. G. (2007). A cyclic void growth model to assess ductile fracture in structural steels due to ultra low cycle fatigue. *J. Structural Engineering Mechanics*, 133(6): 701-712.

Karamanci, E., & Lignos, D. (2014). Computational Approach for Collapse Assessment of Concetrically Braced Frames in Seismic Regions. *J. Struct. Eng., 140*(Computational Simulation in Structural Engineering).

Kasai, K., & Popov, E. (1986). Cyclic Web Buckling Control for Shear Link Beams. *J. Struct. Eng.*, 112(2) 505-523.

Kelly, D. J., Bonneville, D. R., & Bartoletti, S. J. (2000). 1994 Northridge earthquake: damage to a four-story steel braced frame building and its subsequent upgrade. *12th World Conference on Earthquake Engineering.* Upper Hutt, New Zealand: New Zealand Society for Earthquake Engineering.

Kelly, T. E. (1974). *Some Seismic Design Aspects of Multistorey Concrete Frames.* Christchurch, New Zealand: University of Canterbury.

Kelly, T. E. (2009). Tentative Seismic Design Guidelines for Rocking Structures. *Bulletin of the New Zealand Society for Earthquake Engineering*, 42(4): 239-274.

Kersting, R. A., Fahnestock, L. A., & Lopez, W. A. (2015). *Seismic Design of Steel Buckling Restrained Braced Frames.* Gaithersburg, MD: Applied Technology Council, NEHRP Seismic Design Technical Brief No. 11.

Khatib, I. (1988). *Seismic behavior of concentrically braced frames.* University of California, Berkeley, CA: Rept. No. UCB/EERC-88/01, Earthquake Engineering Research Center.

Kiggins, S., & Uang, C. M. (2006). Reducing residual drift of buckling-restrained braced frames as a dual system. *Engineering Structures*, 28: 1525-1532.

Kostic, S., & Filippou, F. (2012). Section Discretization of Fiber Beam-Column Elements for Cyclic Inelastic Response. *J. Struct. Eng.*, 138(5): 592-601.

Lai, J., & Mahin, S. (2013). *Experimental and Analytical Studies on the Seismic Behavior of Conventional and Hybrid Braced Frames.* University of California, Berkeley, CA: Pacific Earthquake Engineering Research Center.

Lai, J., & Mahin, S. (2015). Strong-back System: A Way to Reduce Damage Concentration in Steel Braced Frames. *J. Struc. Eng.*, 141(9): 04014223.

Lee, K., & Bruneau, M. (2005). Energy dissipation of compression members in concentrically braced frames: Review of experimental data. *J. Struct. Eng.*, 131(4): 552-559.

Lee, S., & Goel, S. (1987). *Seismic behavior of hollow and concrete filled square tubular bracing members.* Department of Civil Engineering, University of Michigan. Ann Arbor, MI: Research Report UMCE 87-11, Department of Civil Engineering, University of Michigan.

Lignos, D., & Krawinkler, H. (2011). Deterioration modeling of steel components in support of collapse prediction of steel moment frames under earthquake loading. *J. Struct. Eng.*, 137(11): 1291-1302.

Liu, J., & Astaneh-Asl, A. (2000). Cyclic testing of simple connections including effects of slab. *J. Struct. Eng.*, 126(1), 32–39.

Lopez, W. A., & Sabelli, R. (2004). *Seismic Design of Buckling-Restrained Braced Frames.* Lafayette, CA: Structural Steel Education Council Technical Information and Product Service.

Ma, X., Krawinkler, H., & Deierlein, G. G. (2011). *Seismic design and behavior of self-centering braced frame with controlled rocking and energy dissipating fuses.* Stanford, CA.: The John A. Blume Earthquake Engineering Center, Stanford Univ.

MacRae, G., Kimura, Y., & Roeder, C. (2004). Effect of Column Stiffness on Braced Frame Seismic Behavior. *ASCE, J. Struct. Eng., 130:3*(381), 381-391.

Mahin, S. (2017). CE 227 Lecture Notes.

Manson, S. S. (1965). Fatigue: A complex subject—some simple. *Exp. Mech.*, 5(4), 193–226.

Mar, D. (2010). Design examples using mode shaping spines for frame and wall buildings. *9th U.S. National and 10th Canadian Conference on Earthquake Engineering.* Earthquake Engineering Research Institute, Oakland, CA.

Martini, K., Amin, N., Lee, P., & Bonowitz, D. (1990). The Potential Role of Non-Linear Analysis in the Seismic Design of Steel Structures. *Proceedings of th e4th U.S. National Conference on Earthquake Engineering* (pp. 67–76). EERI.

MATLAB. (2017b). Version 9.3.0.713579. Natick, MA: The Mathworks Inc.

McKenna, F. (1997). *Object oriented finite element programming frameworks for analysis, algorithms, and parallel computing.* University of California, Berkeley, CA: Dept. of Civil and Environmental Engineering.

Merritt, S., Uang, C., & Benzoni, G. (2003a). *Subassemblage Testing of CoreBrace Buckling Restrained Braces.* La Jolla, CA: University of California, San Diego.

Merritt, S., Uang, C., & Benzoni, G. (2003b). *Subassemblage Testing of Star Seismic Buckling-Restrained Braces.* La Jolla, CA: Department of Structural Engineering, University of California, San Diego.

Merritt, S., Uang, C., & Benzoni, G. (2003c). *Uniaxial Testing of Associated Bracing Buckling Restrained Braces.* La Jolla, CA: University of California, San Diego.

Merzouq, S. (2006). *Le dual-BRB, une alternative pour un comportement sismique ameliore.* Polytechnique de Montreal: Department of Civil, Geological, and Mining Engineering.

Merzouq, S., & Tremblay, R. (2006). Seismic Design of Dual Concentrically Braced Steel Frames for Stable Seismic Performance for Multi-Story Buildings. *Proceedings of the 8th U.S. National Conference on Earthquake Engineering.* San Francisco, CA.

Miller, D., Fahnestock, L., & Eatherton, M. (2012). Development and experimental validation of a nickel–titanium shape memory alloy self-centering buckling-restrained brace. *Engineering Structures*, 40: 228-298.

Miner, M. (1945). Cumulative damage in fatigue. *J. Applied Mech.*, 12:159−164.

Moehle, J. (2014). *Seismic Design of Reinforced Concrete Buildings.* New York, NY: McGraw Hill Education.

Nakamura, H., Maeda, Y., Sasaki, T., Wada, A., Takeuchi, T., Nakata, Y., & Iwata, M. (2000). *Fatigue Properties of Practical-Scale Unbonded Braces.* Tokyo, Japan: Nippon Steel Technical Report.

NBCC. (2010). *The National Building Code of Canada.* Ottawa, Canada: Canadian Commission on Building and Fire Codes, National Research Council.

Neuenhofer, A., & Filippou, F. C. (1997). Evaluation of nonlinear frame finite-element models. *J. Struct. Eng.*, 123(7): 958-966.

NZS3101. (2006). *Concrete Design Standard, NZS3101:2006, Part 1 and Commentary on the Concrete Design Standard.* Wellington, New Zealand: Standards Association of New Zealand.

Osteraas, J., Hunt, J., & Luth, G. (2017). Performance Based Seismic Design of the Gigafactory in Tesla Time. *SEAOC Convention.* San Diego, CA.

Panagiotou, M., & Restrepo, J. (2011). Displacement-Based Method of Analysis for Regular Reinforced-Concrete Wall Buildings: Application to a Full-Scale 7-Story Building Slice Tested at UC–San Diego. *J. Struct. Eng.*, 137(6): 677-690.

Panian, L., Bucci, N., & Janhunen, B. (2015). BRBM Frames: an improved approach to seismic-resistant design using buckling-restrainted braces. *Second ATC & SEI Conference on Improving the Seismic Performance of Existing Buildings and Other Structures.*

Park, R., & Paulay, T. (1975). *Reinforced Concrete Structures.* New York, NY: John Wiley & Sons, Inc.

PEER. (2017). *Tall Building Initiative: Guidelines for Performance-Based Seismic Design of Tall Buildings, Version 2.0.* University of California, Berkeley, CA: Pacific Earthquake Engineering Research Center.

Petrini, L., Claudio, M., Priestley, N., & Calvi, M. (2008). Experimental Verification of Viscous Damping Modeling for Inealstic Time History Analyzes. *J. of Earthquake Eng.*, 125-145.

Pollino, M., Derek Slovenec, S., Qu, B., & Mosqueda, a. G. (2017). Seismic Rehabilitation of Concentrically Braced Frames Using Stiff Rocking Cores. *ASCE, J. Struct. Eng., 143*(9).

Popov, E. P., Ricles, J. M., & Kasai, K. (1992). Methodology for Optimum EBF Link Design. *Earthquake Engineering, Tenth World Conference* (pp. 3983-3988). EERI.

Qu, B., Sanchez-Zamora, F., & Pollino, M. (2015). Transforming Seismic Performance of Deficient Steel Concentrically Braced Frames through Implementation of Rocking Cores. *J. Struct. Eng.*, 141(5): -1--1.

Qu, Z., Wada, A., Motoyui, S., Sakata, H., & Kishiki, S. (2012). Pin-supported walls for enhancing the seismic performance of building structures. *Earthquake Engng Struct. Dyn.*, 41:2075–2091.

Rai, D., & Goel, S. (2003). Seismic evaluation and upgrade of chevron braced frames. *J. Constr. Steel Res., 59*(8), 971-994.

Ricles, J. M., & Popov, E. P. (1989). Composite Action in Eccentrically Braced Frames. *J. Struct. Eng.*, 115(8): 2046-2065.

Roeder, C. W., & Popov, E. P. (1978). Eccentrically Braced Steel Frames for Earthquakes. *J. of the Structural Division*, 104: 2130-2145.

Roke, D., Sause, R., Ricles, J., & Gonner, N. (2008). Design concepts for damage-free seismic-resistant self-centering steel concentrically-braced frames. *Proceedings of the 14th World Conference on Earthquake Engineering.* Beijing, China: WCEE.

Roke, D., Sause, R., Ricles, J., Seo, C-Y, & Lee, K.-S. (2006). Self-centering seismic-resistant steel concentrically-braced frames. *Proc., 8th National Conf. on Earthquake Eng.* San Francisco, CA.

Roke, D., Sause, R., Ricles, J., & Gonner, N. (2009). Damage-free seismic-resistant self-centering steel concentrically braced frames. *Proceedings of the 6th International Conference on Behaviour of Steel Structures in Seismic Areas (STESSA 2009).* Philadelphia, PA.

Rossi, P. (2007). A design procedure for tied braced frames. *Earthquake Engng Struct. Dyn.*, 36:2227–2248.

Rutenberg, A. (2013). Seismic shear forces on RC walls: review and bibliography. *Bulletin of Earthquake Engineering*, 11(5):1726–1751.

Sabelli, R. (2001). *Research on improving the design and analysis of earthquake-resistant steel braced frames.* Oakland, CA: NEHRP Fellowship Rept. No. PF2000-9, Earthqake Engineering Research Institute.

Salawdeh, S., & Goggins, J. (2013). Numerical Simulation for Steel Brace Members Incorporating a Fatigue Model. *Engineering Structures*, 46: 332-349.

Sause, R., Ricles, J., Roke, D., Chancellor, N., & Gonner, N. (2010). Seismic performance of a self-centering rocking concentrically-braced frame. *Proceedings of the 9th US and 10th Canadian Conference on Earthquake Engineering.* Toronto, ON.

Scott, M. (2011). *Numerical Integration Options for the Force-Based Beam-Column Element in OpenSees.* Retrieved from OpenSeesWiki: http://opensees.berkeley.edu/wiki/index.php/Force-Based_Beam-Column_Element

Scott, M., & Fenves, G. (2006). Plastic Hinge Integration Methods for Force-Based Beam-Column Elements. *J. Struct. Eng.*, 132(2): 244-252.

SEAOC. (2008). *Reinforced concrete structures.* Redwood City, CA: Seismology Committee, Structural Engineers Association of California.

Sen, A. D., Roeder, C. W., Berman, J. W., Lehman, D. E., Li, C.-H., Wu, A.-C., & Tsai, a. K.-C. (2016). Experimental Investigation of Chevron Concentrically Braced Frames with Yielding Beams. *J. Struct. Eng.*, 142(12): 04016123 .

Shaback, B., & Brown, T. (2001). *Behavior of square HSS braces with end connections under reserved cyclic axial loading.* Calgary, Canada: Department of Civil Engineering, University of Calgary.

Shahrooz, B., & Moehle, J. (1987). *Experimental Study of Seismic Response of R.C. Setback Buildings.* Berkeley, CA: University of California.

Simpson, B., & Mahin, S. (2018a). Experimental and Numerical Evaluation of Older Chevron Concentrically Braced Frames with Hollow and Concrete-Filled Braces. *J. Struct. Eng.*, 144(3): 04018007.

Simpson, B., & Mahin, S. (2018b). Experimental and Numerical Investigation of Strongback Braced Frame System to Mitigate Weak Story Behavior. *ASCE, J. Struct. Eng.*, 144(2).

Simpson, B., Mahin, S., & Lai, J. (2017). *Experimental Investigation of the Behavior of Vintage and Retrofit Concentrically Braced Steel Frames under Cyclic Loading.* University of California, Berkeley, CA: Pacific Earthquake Engineering Research Center.

Sizemore, J. G., Fahnestock, L. A., Hines, E. M., & Bradley, C. R. (2017). Parametric study of low-ductility concentrically braced frames under cyclic static loading. *J. Struct. Eng.*, 143(6): 04017032 .

Slovenec, D., Sarebanha, A., Pollino, M., Mosqueda, G., & Qu, B. (2017). Hybrid Testing of the Stiff Rocking Core Seismic Rehabilitation Technique. *J. Struct. Eng.*, 143(9): 04017083.

SNZ. (2004). *Structural design actions—Part 5: Earthquake actions—New Zealand.* Wellington, New Zealand: Standards New Zealand.

Spacone, E., Filippou, F. C., & Taucer, F. F. (1996). Fiber beam-column model for nonlinear analysis of R/C frames, part I: Formulation. *Earthquake Eng. Struct. Dyn.*, 25(7): 711-725.

Steele, T., & Wiebe, L. (2016). Dynamic and equivalent static procedures for capacity design of controlled rocking steel braced frames. *Earthquake Engng Struct. Dyn.*, 2349–2369.

Stoakes, C. D., & Fahnestock, L. A. (2011). Cyclic flexural testing of concentrically braced frame beam-column connections. *J. Struct. Eng.*, 137(7): 739-747.

Sullivan, T., Priestley, M., & Calvi, G. (2008). Estimating the Higher-Mode Response of Ductile Structures. *J. Earthquake Engng.*, 12(3): 456-472.

Takeuchi, T., Chen, X., & Matsui, R. (2015). Seismic performance of controlled spine frames with energy-dissipating members. *J. Constr. Steel Research*, 114: 51–65.

Terzic, V., & Mahin, S. (2017). Using PBEE to Assess and Improve Performance of Different Structural Systems for Low-Rise Steel Buildings. *Int. J. of Safety and Security Eng.*, 7(4): 532-544.

Tirca, L., & Chen, L. (2014). Numerical Simulation of Inelastic Cyclic Response of HSS Braces Upon Fracture. *Advanced Steel Construction, 10*(4), 442-462.

Tremblay, R. (2003). Achieving a stable inelastic seismic response for multi-story concentrically braced frames. *AISC J. Struct. Eng., 40*(2), 111-129.

Tremblay, R., & Poncet, L. (2007). Improving the Seismic Stability of Concentrically Braced Steel Frames. *Engineering Journal, AISC*, 44(2): 103-116.

Tremblay, R., & Tirca, L. (2003). Behavior and Design of Multistory Zipper Concentrically Braced Steel Frames for the Mitigation of Soft Story Response. *Proceedings of 4th International Conference on Behavior of Steel Structures in Seismic Areas (STESSA)*, (pp. 471-477). Naples, Italy.

Tremblay, R., Archambault, M.-H., & Filiatrault, A. (2003). Seismic response of concentrically braced steel frames made with rectangular hollow bracing members. *J. Struct. Eng.*, 129(12):1626–1636.

Tremblay, R., Bruneau, M., Nakashima, M., Prion, H., Filiatrault, A., & DeVall, R. (1996). Seismic design of steel buildings: lessons from the 1995 Hyogo-ken Nanbu earthquake. *Can. J. Civ. Eng.*, 23: 727-756.

Tremblay, R., Chen, L., & Tirca, L. (2014). Enhancing the Seismic Prerformance of Multi-storey Buildings with a Modular Tied Braced Frame System with Added Energy Dissipating Devices. *International J. High-Rise Buildings*, 3(1): 21-33.

Tremblay, R., Poirier, L., Bouaanani, N., Leclerc, M., Rene, V., Fronteddu, L., & Rivest, S. (2008). Innovative viscously damped rocking braced steel frames. *14th World Conf. on Earthquake Engineering.* Beijing, China.

Tremblay, R., Timler, N., Bruneau, M., & and Filiatrault, A. (1995). Performance of steel structures during the 1994 Northridge earthquake. *Can. J. of Civ. Eng.*, 22: 338-360.

Tsai, K., Wu, A., Wei, C., Lin, P., Chuang, M., & Yu, Y. (2014). Welded end-slot connection and debonding layers for buckling-restrained braces. *Earthquake Engng. Struct. Dyn., 43(12)*, 1785-1807.

Uang, C. M., & Bertero, V. V. (1986). *Earthquake Simulation Tests and Associated Studies of a 0.3-Scale Model of a Six-Story Concentrically Braced Steel Structure.* Berkeley, CA: Earthquake Engineering Research Center.

Uriz, P., & Mahin, S. (2008). *Toward earthquake resistant design of concentrically braced steel frame structures.* University of California, Berkeley, CA: Rept. No. PEER-2008/08, Pacific Earthquake Engineering Research Center.

Vamvatsikos, D., & Cornell, C. A. (2002). Incremental Dynamic Analysis. *Earthquake Engng. Struct. Dyn., 31*(3), 491-514.

Watanabe, A., Hitomi, Y., Saeki, E., Wada, A., & Fujimoto, M. (1988). Properties of brace encased in buckling-restraining concrete and steel tube. *Proceedings of the 9th World Conference on Earthquake Engineering.* Tokyo-Kyoto, Japan.

Whittaker, A., Uang, C., & Bertero, V. (1990). *An Experimental Study of the Behavior of Dual Steel Systems.* Berkeley, CA: Earthquake Engineering Research Center.

Wiebe, L., & Christopoulos, C. (2009). Mitigation of higher mode effects in base-rocking systems by using multiple rocking sections. *J. Earthquake Eng.*, 13(S1), 83–108.

Wiebe, L., & Christopoulos, C. (2015a). A cantilever beam analogy for quantifying higher mode effects in multistorey buildings. *Earthquake Engng. Struct. Dyn.*, 44:1697–1716.

Wiebe, L., & Christopoulos, C. (2015b). Performance-Based Seismic Design of Controlled Rocking Steel Braced Frames. II: Design of Capacity-Protected Elements. *J. Struct. Eng.*, 141(9): 04014227.

Wiebe, L., Christopoulos, C., & Pampanin, S. (2007). Seismic response of self-centering base-rocking steel structures. *Proceedings of the 9th Canadian Conference on Earthquake Engineering.* Ottawa, ON.

Wiebe, L., Christopoulos, C., Tremblay, R., & Leclerc, M. (2013a). Mechanisms to limit higher mode effects in a controlled rocking steel frame. 1: Concept, modelling, and low-amplitude shake table testing. *Earthquake Engng. Struct. Dyn.*, 42:1053–1068.

Wiebe, L., Christopoulos, C., Tremblay, R., & Leclerc, M. (2013b). Mechanisms to limit higher mode effects in a controlled rocking steel frame. 2: Large-amplitude shake table testing. *Earthquake Engng. Struct. Dyn.*, 42:1069–1086.

Wiebe, L., Sidwell, G., & Gledhill, S. (2015). *Design guide for controlled rocking steel braced frames.* Manukau City, New Zealand: Steel Construction New Zealand.

Yang, C. S., Leon, R. T., & DesRoches, R. (2008). Design and Behavior of Zipper Braced Frames. *Engineering Structures*, 30(4): 1092-1100.

Yang, T. Y., Moehle, J. P., & Stojadinovic, B. (2009). *Performance Evaluation of Innovative Steel Braced Frames.* University of California, Berkeley, CA: Pacific Earthquake Engineering Research Center .

Yim, C., Chopra, A., & Penzien, J. (1980). *Rocking Response of Rigid Blocks to Earthquakes.* University of California, Berkeley, CA: Earthquake Engineering Research Center.

Yoo, J. H., Roeder, C. W., & Lehman, D. E. (2008). Analytical Performance Simulation of Special Concentrically Braced Frames. *J. Struct. Eng.*, 134(6): 881-889.

Zayas, V. A., Popov, E. P., & and Mahin, S. A. (1980). *Cyclic inelastic buckling of tubular steel braces.* Berkeley, CA: Earthquake Engineergin Research Center.

Zsarnoczay, A. (2013). *Experimental and Numerical Investigation of Buckling Restrained Braced Frames for Eurocode Conform Design Procedure Development.* Budapest, Hungary: Department of Structural Engineering, Budapest University of Technology and Economics.

Appendix A Gravity Loading

This appendix describes the gravity loading used for the archetype building in Chapter 4.

A.1 GRAVITY LOADING

Superimposed Dead						
	3.25" LWC (3000psi)	39	psf			
	W2 2" 18 gage deck	2.7	psf	PLN-24 3" 16 gage deck	4.2	psf
		42	psf			
Typical Floor		**Gravity**			**Seismic weight**	
	Floor finish	1	psf		1	psf
	Fire proofing	1	psf		1	psf
	Mechanical / plumbing / electrical	4	psf		4	psf
	Ceiling	4	psf		4	psf
	Partitions	-	psf		10	psf
	Miscellaneous	3	psf		3	psf
		13	psf		23	psf
	Slab on deck	41.7	psf			
	Estimated steel framing	10	psf			
Live Load	Offices	50	psf			
	Partitions	15	psf			
		65	psf			
	Corridors	100	psf			

Roof		**Gravity**		**Seismic weight**	
	Built-up roof	6	psf	6	psf
	Fire proofing	1	psf	1	psf
	Insulation	2	psf	2	psf
	Mechanical / plumbing / electrical	4	psf	4	psf
	Ceiling	4	psf	4	psf
	Partitions	-	psf	5	psf
	Miscellaneous	3	psf	3	psf
		20	psf	25	psf
	Slab on deck	42	psf		
	Estimated steel framing	8	psf		
Live Load	Ordinary flat roof	20	psf		

Penthouse		**Gravity**		**Seismic weight**	
	Superimposed dead	13	psf	13	psf
	Partitions	-	psf	10	psf
	Equipment	-	psf	33	psf
		13	psf	56	psf
	Slab on deck	42	psf		
	Estimated steel framing	10	psf		
Live Load	Equipment	100	psf		

Penthouse roof		**Gravity**		**Seismic weight**	
	Built-up roof	6	psf	6	psf
	Fire proofing	1	psf	1	psf
	Insulation	2	psf	2	psf
	Mechanical / plumbing / electrical	4	psf	4	psf
	Ceiling	-	psf	-	psf
	Partitions	-	psf	-	psf
	Miscellaneous	3	psf	3	psf
		16	psf	16	psf
	Deck	4.2	psf		
	Estimated steel framing	8	psf		
Live Load	Ordinary flat roof	20	psf		

Exterior Wall		**Gravity**		**Seismic weight**	
	Cladding	8	psf	8	psf
	Metal studs	2	psf	2	psf
	Insulation	2	psf	2	psf
	5/8-in. gypsum board	3	psf	3	psf
	Miscellaneous	5	psf	5	psf
		20	psf	20	psf

Appendix B Additional BRBF and SBF Envelope Plots

This appendix provides additional plots of the benchmark strongback response at the DE, MCE, and $1.3 \times MCE$-level from Chapter 5.

B.1 DE INTENSITY LEVEL

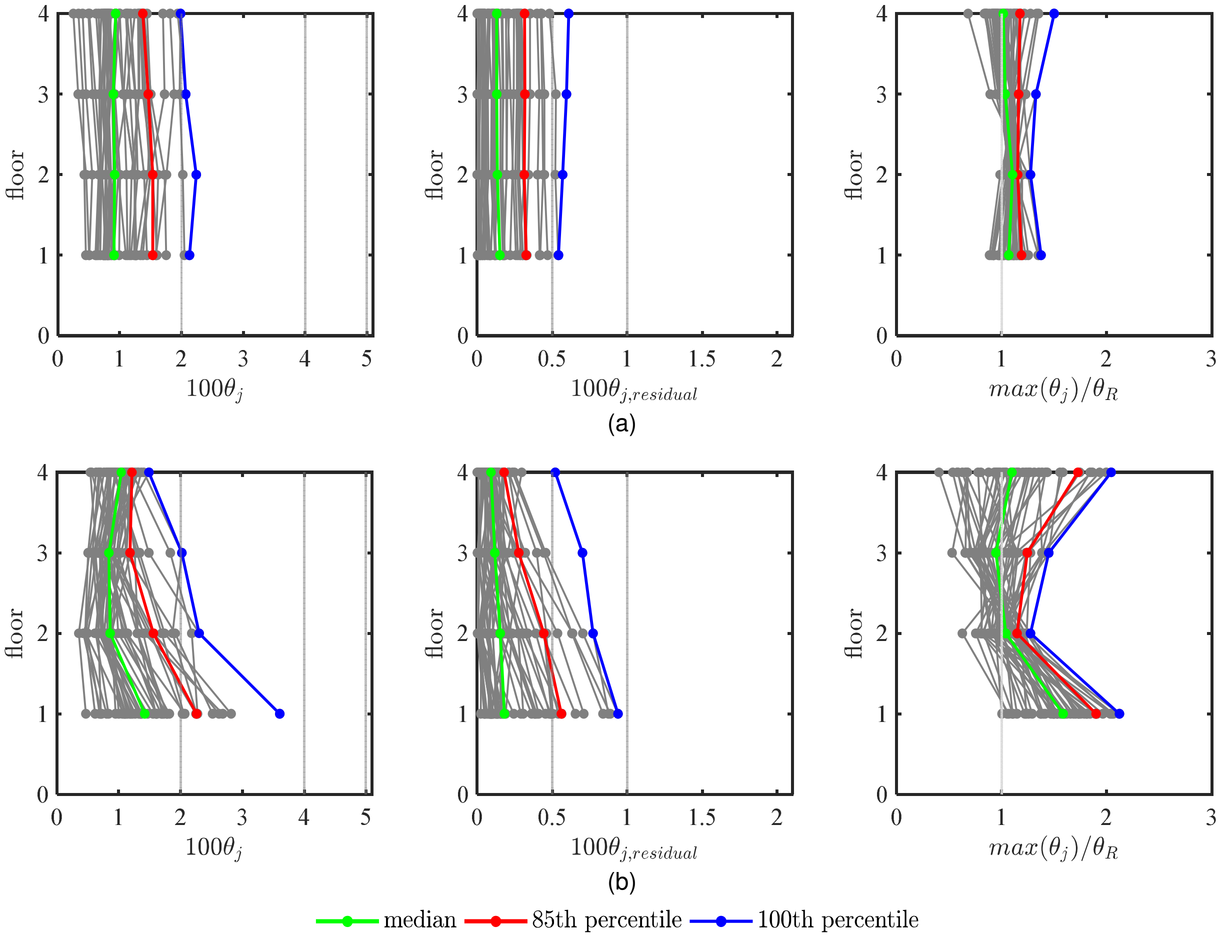

(a)

(b)

Figure B.1. Peak drift response at DE: (a) SBF, (b) BRBF

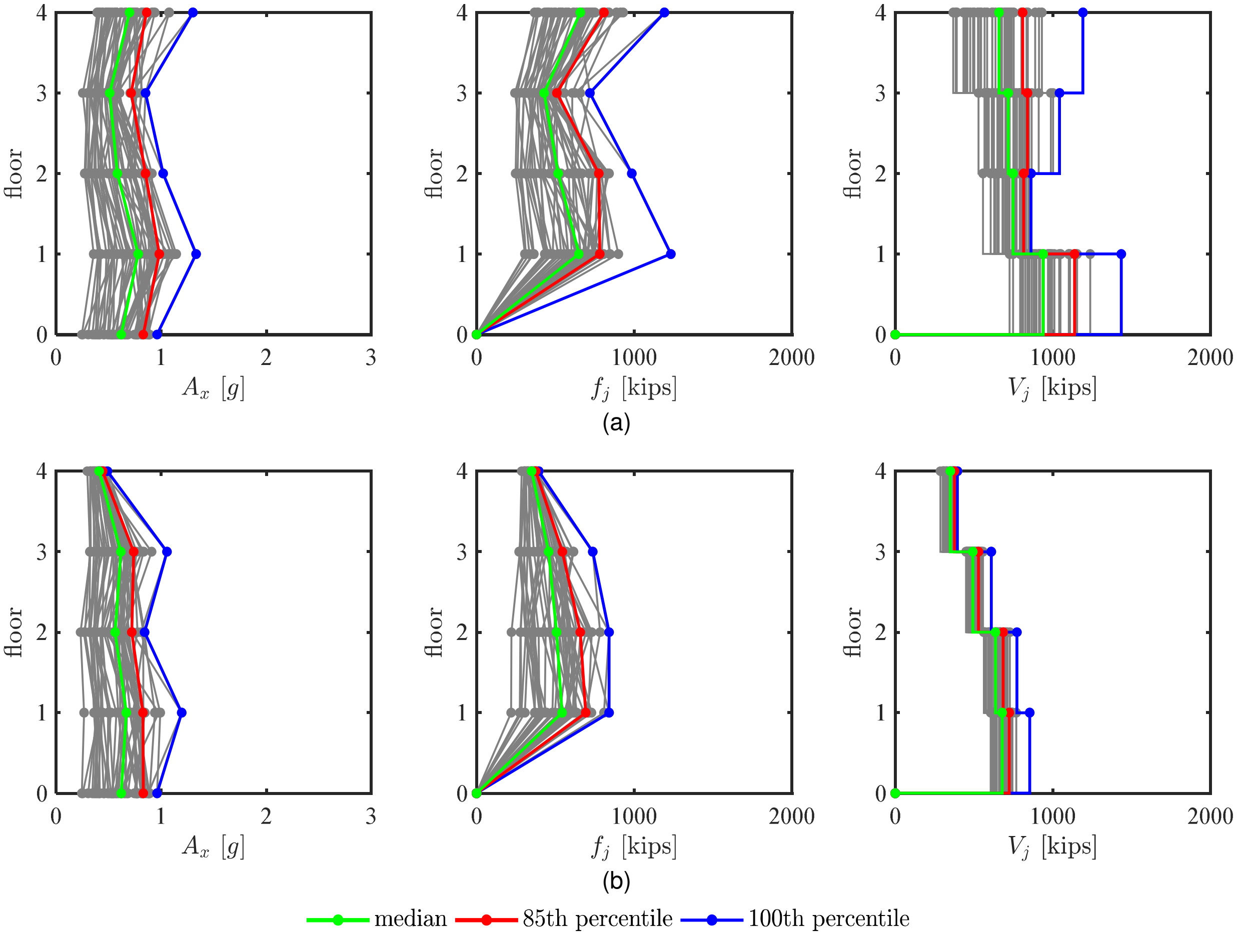

(a)

(b)

Figure B.2. Peak acceleration, A_x, estimated equivalent-lateral force distribution, f_j, and story shear, V_j, response at DE: (a) SBF, (b) BRBF

B.2 MCE INTENSITY LEVEL

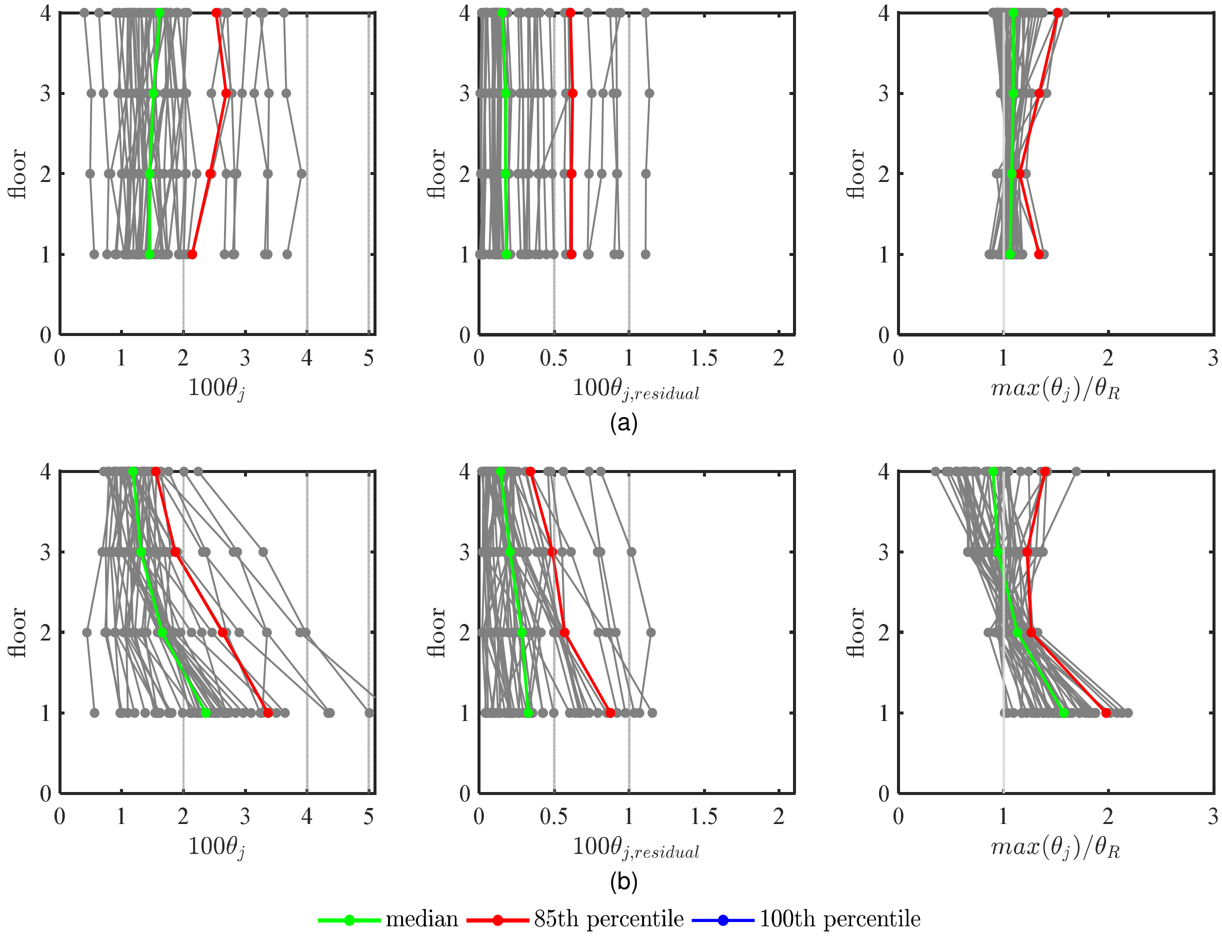

Figure B.3. Peak drift response at MCE: (a) SBF, (b) BRBF

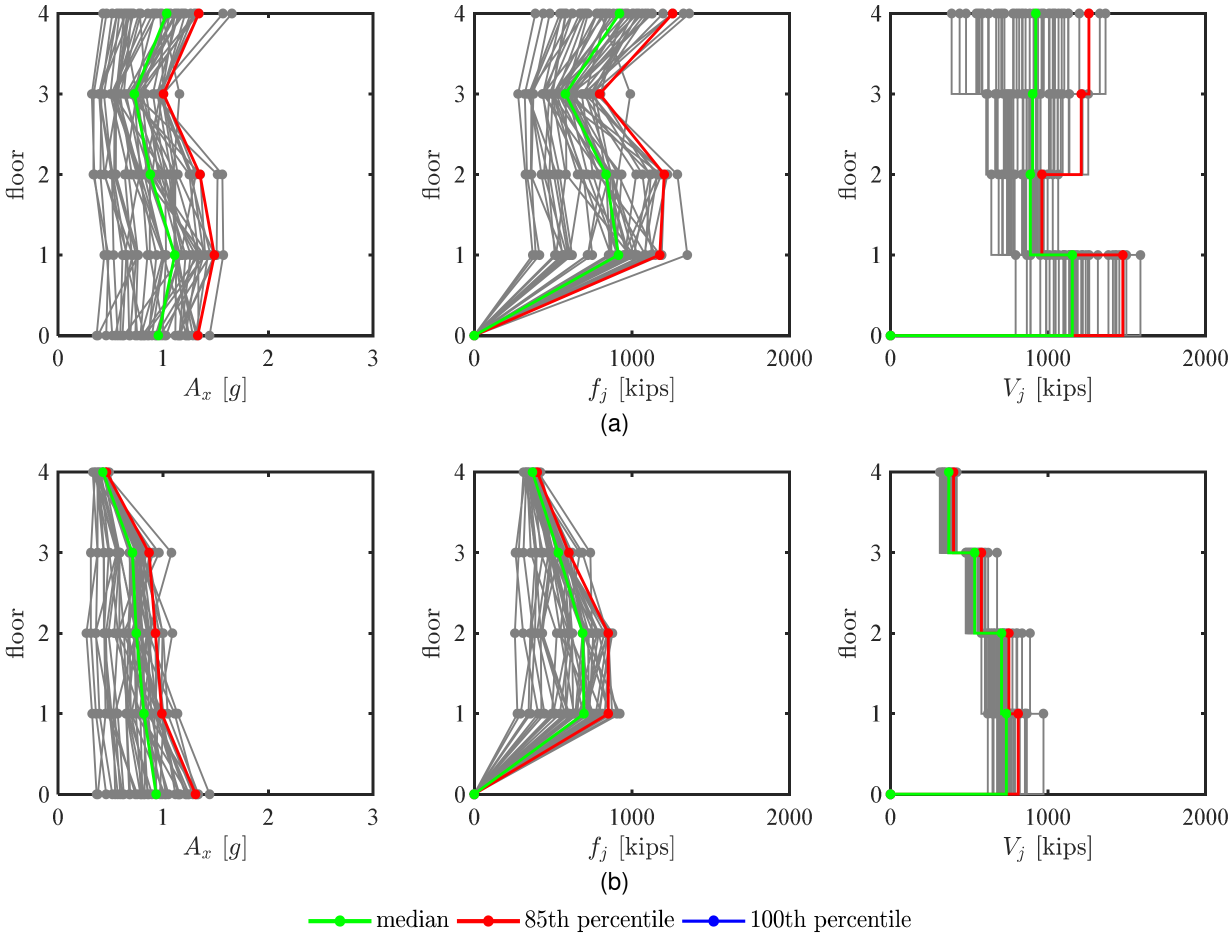

(a)

(b)

Figure B.4. Peak acceleration, A_x, estimated equivalent-lateral force distribution, f_j, and story shear, V_j, response at MCE: (a) SBF, (b) BRBF

Appendix C Additional Envelope Results from the Parametric Study

This appendix describes the results of the parametric study conducted in Chapter 6 in more detail.

C.1 CASE 2 – BEAM END CONNECTIONS

The axial strain envelope for the inelastic braces was largest for the fully fixed beam-column connection and smallest for the fully pinned beam link; see Figure C.1(a). Peak axial force in the inelastic braces were negligibly different for all the beam end conditions; see Figure C.2(b). Though the trend was imperfect, the pinned end conditions resulted in larger compression demands in the first and fourth stories while the fixed end conditions resulted in reduced demands at those locations; see Figure C.2.

End moments in the strongback portion of the beam tended to be smaller than moments in the beam link, indicating near rigid global rotation of the strongback truss; see Figure C.3(a). For all cases, moment demands at the ends of the roof beam are smaller than the moment demands in lower stories. Different end conditions caused little variation in beam axial-force demands; see Figure C.3(b). Deformation demands in the beam link were largest for the fixed beam-column condition and smallest for the other connection types; see Figure C.3(c).

Column moment demands were affected by the beam end conditions; see Figure C.4(a). Where the beam-column connection is fixed or a PR connection, the moment demands generated in the beams are transferred to the column through equilibrium. This effect is more apparent in the inelastic column where the end of the beam link reaches its full plastic moment. The pinned end condition and fully pinned beam still results in moment in the columns, but this moment is solely due to the bending nature of the frame rather than the development of plastic hinges in the beam links. Differences in axial force in the inelastic column resulted from additional shear developed in the beam links due to plastic hinging at its ends; see Figure C.4(b). This beam shear had negligible impact on the axial-force demands in the strongback column; Figure C.4(c).

The fully pinned beam link resulted in the lowest peak drift ratio; see Figure C.5(a). This was followed closely by the pinned beam-column connections, alternating beam-column connections, PR beam-column connections, and fixed beam-column connections. The largest DCF occurred in the fourth story for all beam-column connections, though the trend was in reverse to that of the peak drift ratio; see Figure C.5(c).

The general shape of the acceleration profile remained similar between all end conditions; see Figure C.5(d). Generally, story shear demands were largest for the fixed beam end condition, followed by the PR end condition, the alternating end condition, the pinned end condition, and the fully pinned beam link; see Figure C.5(f).

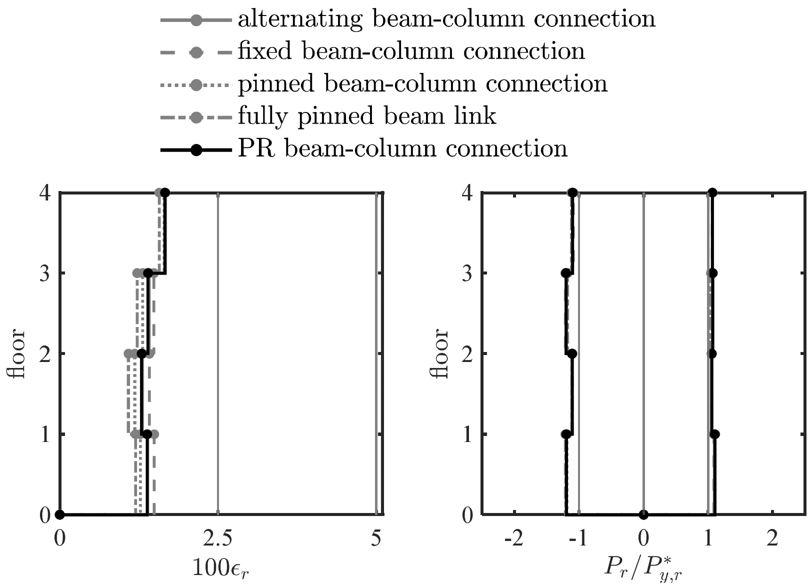

(a) (b)

Figure C.1. Case 2 – Inelastic brace peak response envelopes.
(a) strain demand, (b) axial demand-to-capacity ratio

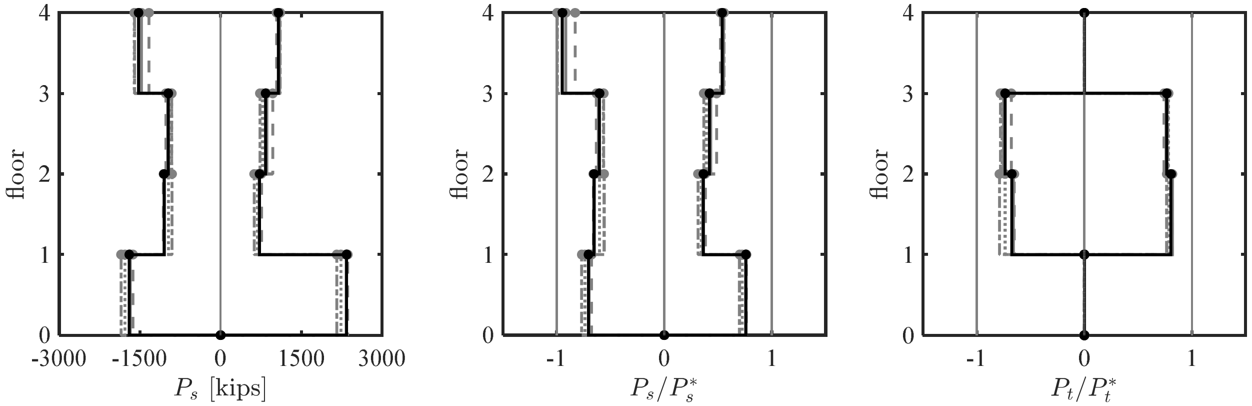

(a) (b) (c)

Figure C.2. Case 2 – Strongback elements peak response envelopes.
(a) axial-force demand; (b) and (c) axial demand-to-capacity ratio

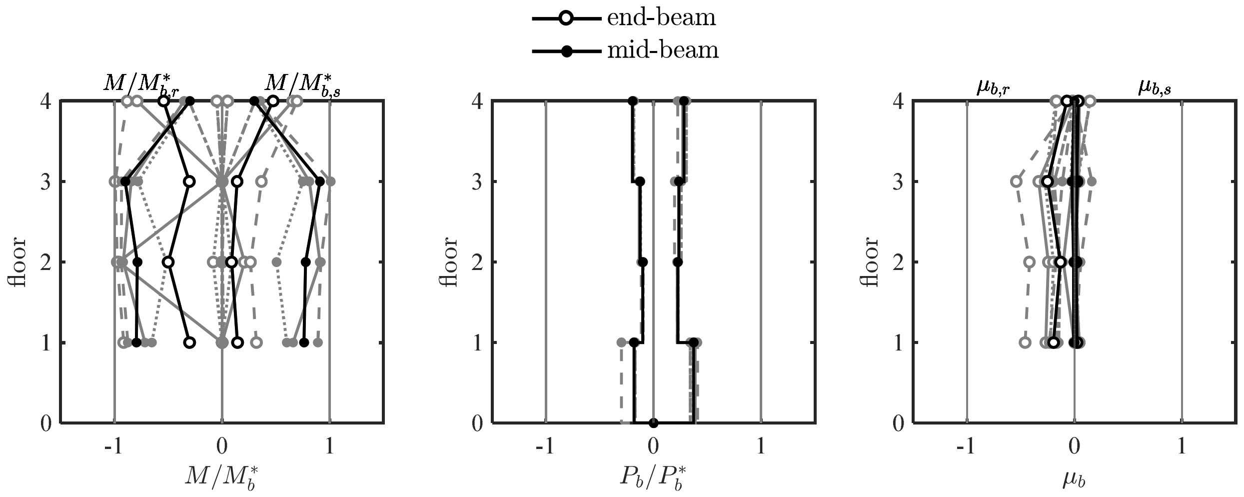

(a) (b) (c)

Figure C.3. Case 2 – Beam peak response envelopes.
(a) moment demand; (b) axial-force demand; (c) deformation acceptability ratio

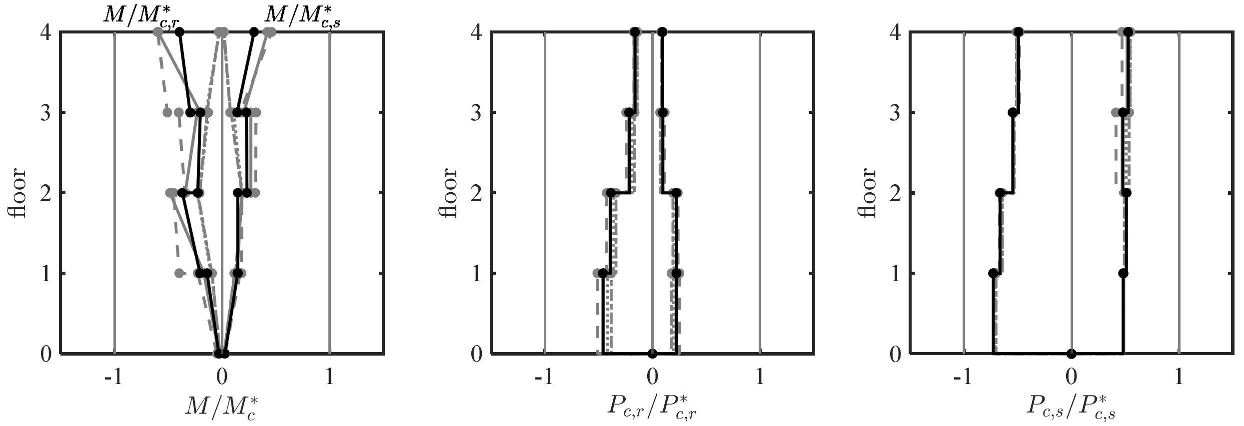

(a) (b) (c)

Figure C.4. Case 2 – Column peak response envelopes.
(a) moment demand; (b) and (c) axial-force demand. (a) axial-force demand; (b) and (c) axial demand-to-capacity ratio

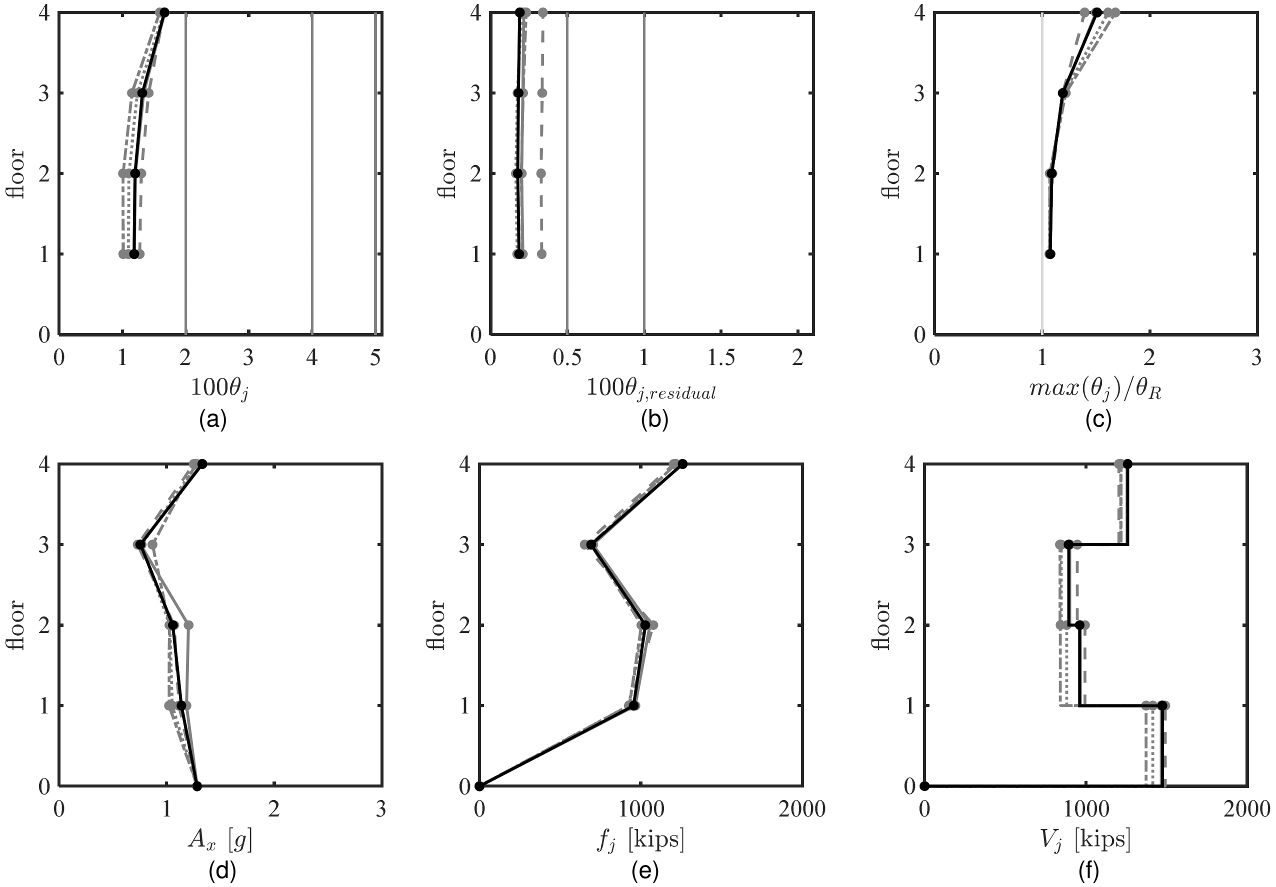

(a) (b) (c)

(d) (e) (f)

Figure C.5. Case 2 – Global peak response envelopes.
(a) peak story drift ratio; (b) peak residual drift ratio; (c) drift concentration factor; (d) absolute acceleration; (e) estimated peak equivalent-lateral force distribution; (f) peak story shear

C.2 CASE 3 – COLUMN BASE FIXITY AND BENDING ORIENTATION

Axial-force demands in the inelastic braces, strongback tie, beam, and columns were relatively unaffected by the change in column base fixity; see Figure C.6, Figure C.7(c), Figure C.8(b), and Figure C.9(c) and (d). Tensile axial-force demands were largest in the first-story for the pinned column base and largest in the second-story for the fixed column base; see Figure C.7(a) and (b). Beam deformation demands were little affected by column fixity and orientation; see Figure C.8(c).

The moment demands in the roof beam and height-wise moment distributions in the columns were most impacted by the change in column fixity and bending orientation. A column oriented in weak axis bending reduced the flexural demands at bean ends of the roof level beam; see Figure C.8(a). Though the weak-axis oriented column has less moment capacity, column moments over the story height tended to be reduced with the utilization of a weak-axis column; see Figure C.9(a). The difference between the pinned and fixed column base were most apparent at the base of the columns. Differences between the fixed and pinned column base condition with strong-axis oriented columns were negligible in the upper stories. Global response parameters were little affected by the change in base fixity; see Figure C.10.

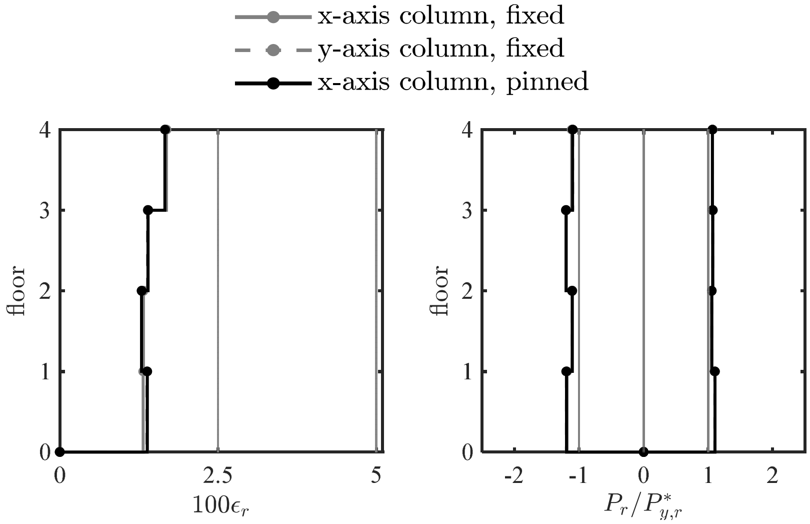

(a) (b)

Figure C.6. Case 3 – Inelastic brace peak response envelopes.
(a) strain demand, (b) axial demand-to-capacity ratio

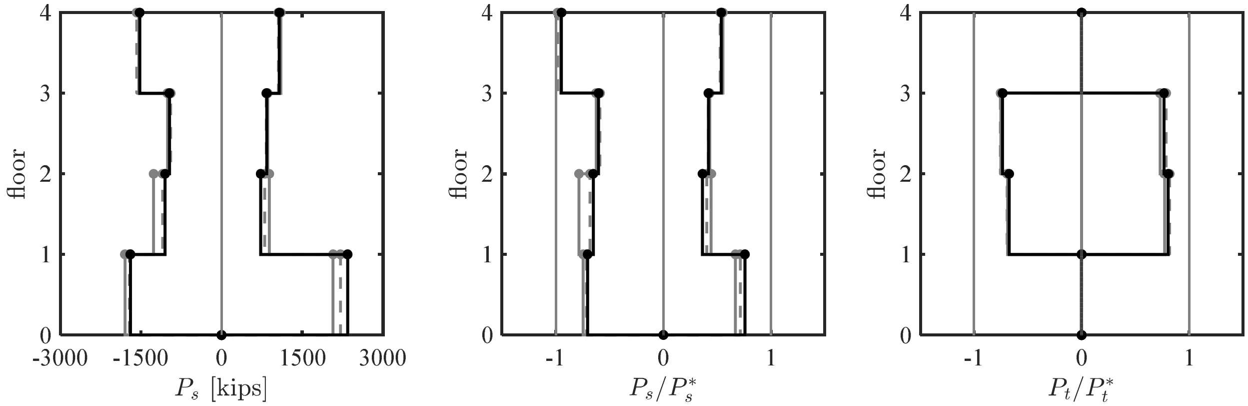

(a) (b) (c)

Figure C.7. Case 3 – Strongback elements peak response envelopes.
(a) axial-force demand; (b) and (c) axial demand-to-capacity ratio

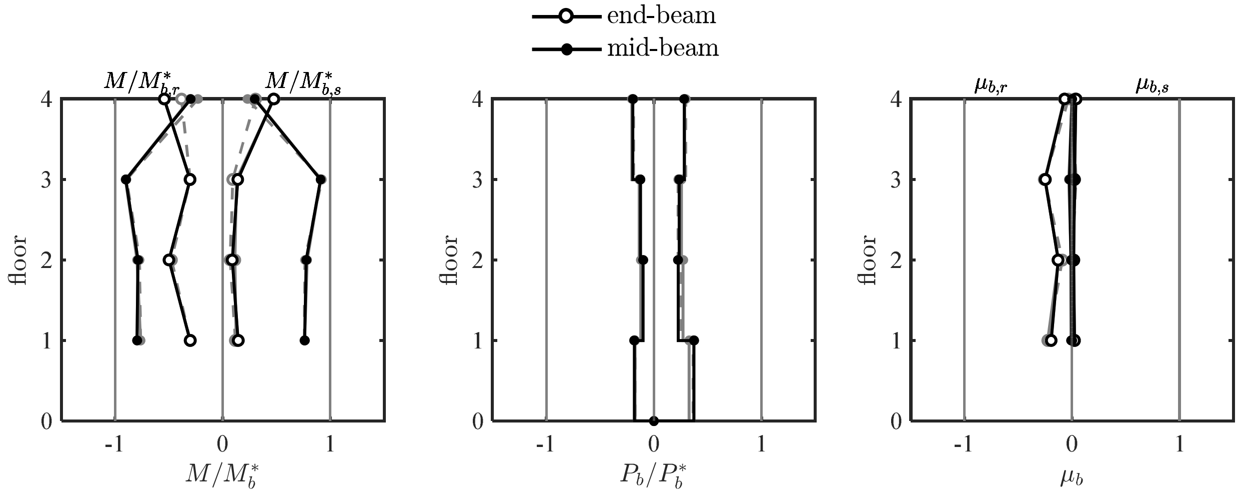

(a) (b) (c)

Figure C.8. Case 3 – Beam peak response envelopes.
(a) moment demand; (b) axial-force demand; (c) deformation acceptability ratio

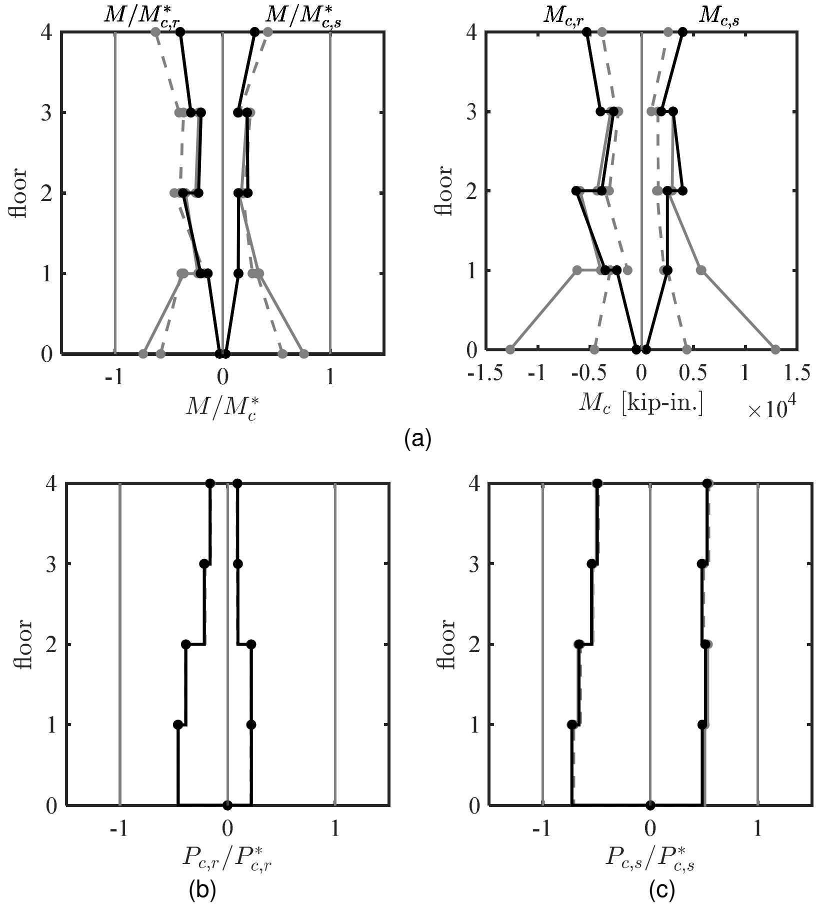

(a)

(b) (c)

Figure C.9. Case 3 – Column peak response envelopes.
(a) moment demand; (b) and (c) axial-force demand. (a) axial-force demand; (b) and (c) axial demand-to-capacity ratio

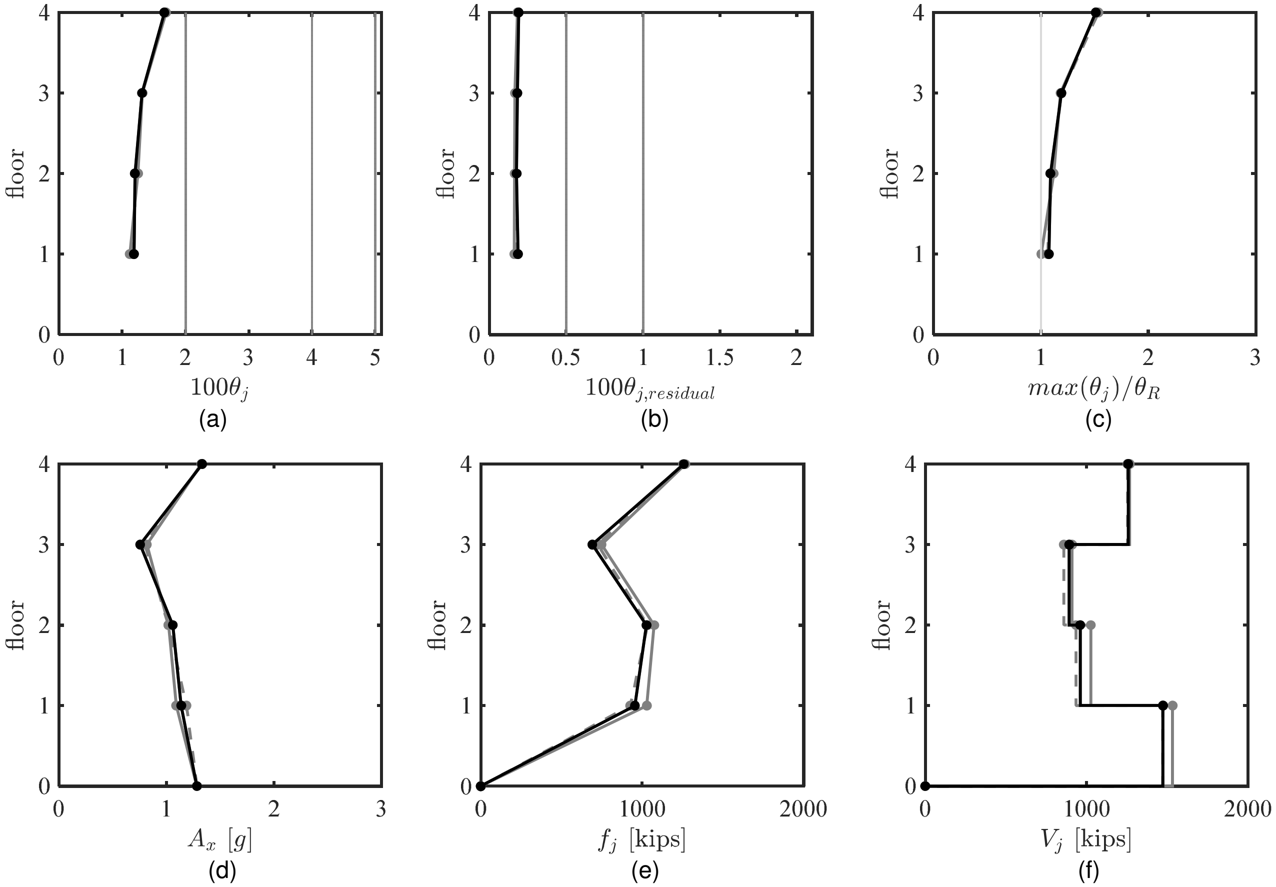

Figure C.10. Case 3 – Global peak response envelopes.
(a) peak story drift ratio; (b) peak residual drift ratio; (c) drift concentration factor; (d) absolute acceleration; (e) estimated peak equivalent-lateral force distribution; (f) peak story shear

C.3 CASE 4 – BEAM COMPOSITE ACTION AND DIAPHRAGM RIGIDITY

Axial-force demands in the fuses, tie, and inelastic column were similar for all the parameters studied in case 4; see Figure C.11, Figure C.12(c), and Figure C.14(b). The strongback braces were impacted by the rigidity of the beam, but little impacted by the inclusion of composite beam action; see Figure C.13(a) and (b). This increased demand had some impact on the strongback column axial-force demand; see Figure C.14(c).

Diaphragm modeling and composite action primarily affected axial and flexural demands in the beams. Composite action asymmetrically increased the moment capacity of the beams, but had little impact on the beam axial-force demands; see Figure C.13(a). In contrast, the type of diaphragm had little impact on beam moments but decreased beam axial-force demands; see Figure C.13(b). Fiber element models derive axial force from axial strains due to elongation and shortening observed at the fiber section level. As such, any axial constraint along the beam length results in near-zero axial force in the beam elements. A concrete truss diaphragm reduced beam compression demands and had little effect on the beam tension demand. Deformation demands were by far largest with the composite fiber section; see Figure C.13(c).

Composite action and diaphragm rigidity had little impact on the drift response; see Figure C.15(a) through (c). Acceleration demands and estimated equivalent-lateral force distributions were largest for the rigid diaphragm; see Figure C.15(d) and (e).

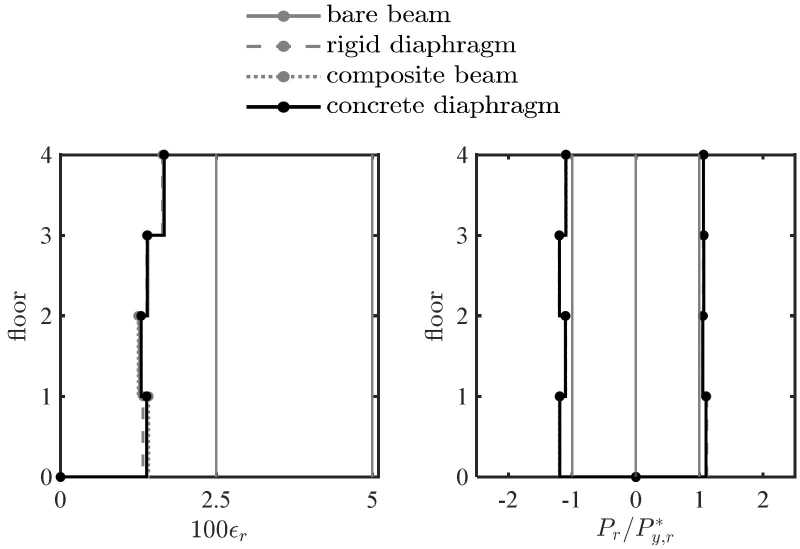

(a) (b)

Figure C.11. Case 4 – Inelastic brace peak response envelopes.
(a) strain demand, (b) axial demand-to-capacity ratio

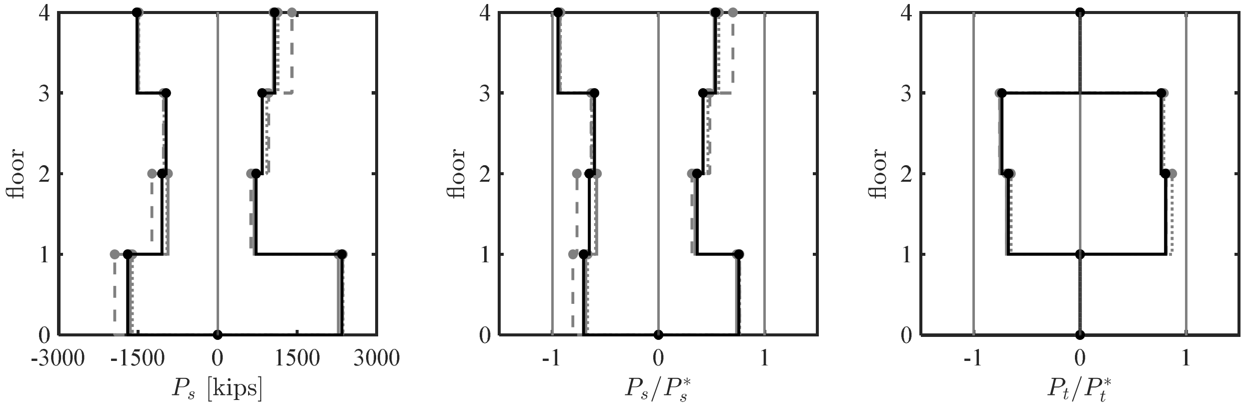

(a) (b) (c)

Figure C.12. Case 4 – Strongback elements peak response envelopes.
(a) axial-force demand; (b) and (c) axial demand-to-capacity ratio

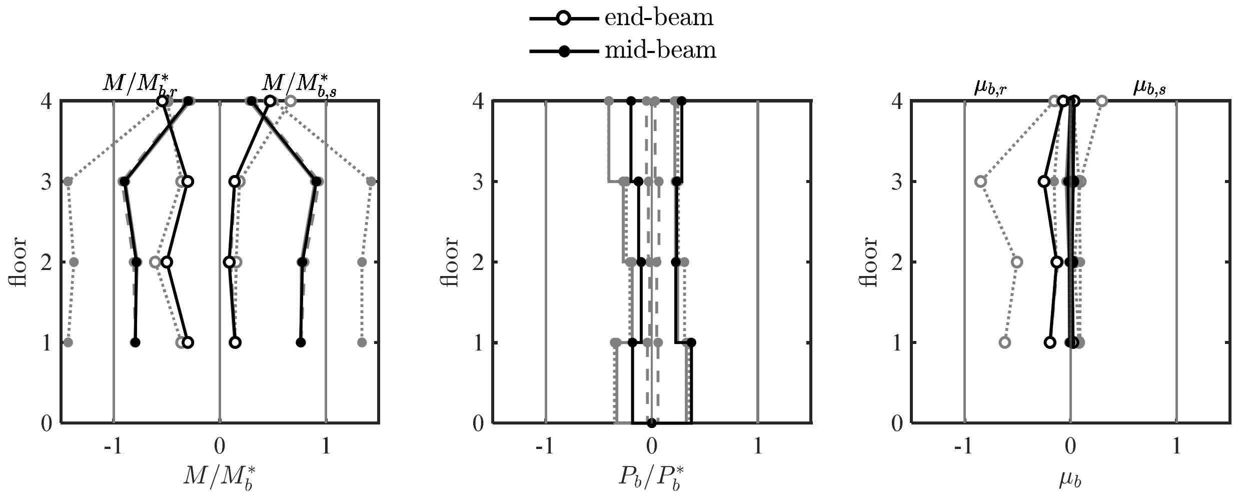

(a) (b) (c)

Figure C.13. Case 4 – Beam peak response envelopes.
(a) moment demand; (b) axial-force demand; (c) deformation acceptability ratio

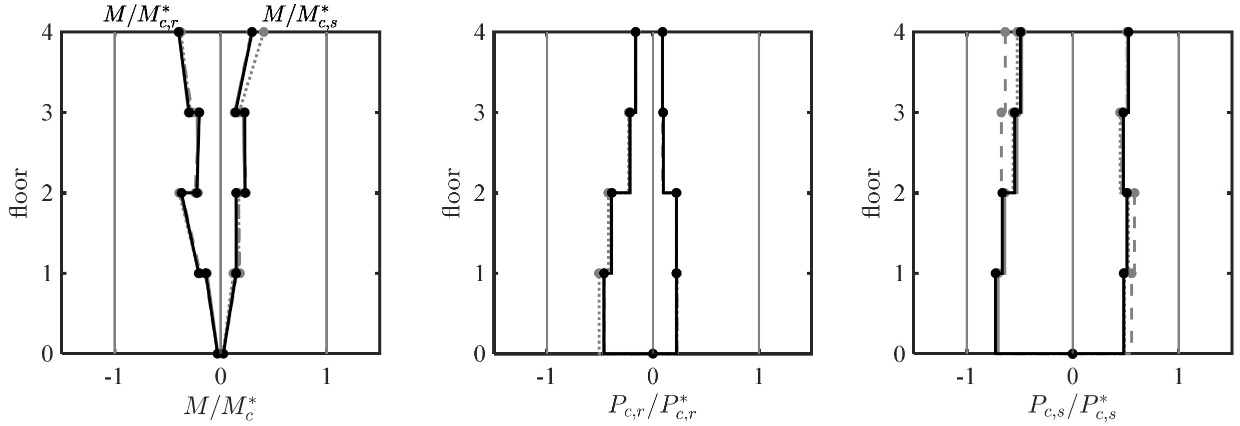

(a) (b) (c)

Figure C.14. Case 4 – Column peak response envelopes.
(a) moment demand; (b) and (c) axial-force demand. (a) axial-force demand; (b) and (c) axial demand-to-capacity ratio

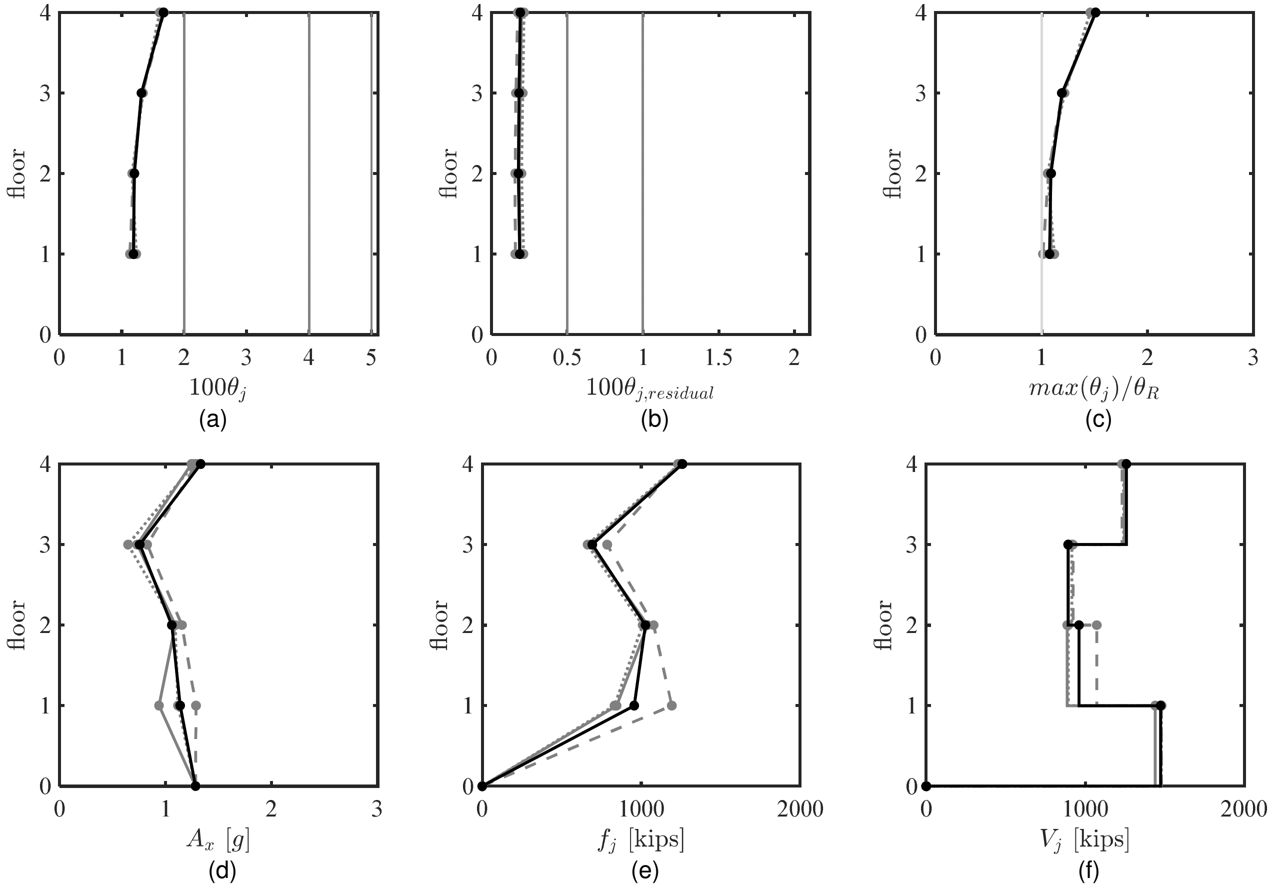

Figure C.15. Case 4 – Global peak response envelopes.
(a) peak story drift ratio; (b) peak residual drift ratio; (c) drift concentration factor; (d) absolute acceleration; (e) estimated peak equivalent-lateral force distribution; (f) peak story shear

C.4 CASE 5 – STRONGBACK BRACE AND TIE END CONDITION

Other than the beam moments, strongback brace end condition had little impact on any of the response quantities. Less bending moment was observed in the strongback portion of the beams if the beam ends were fixed, as it was instead distributed through equilibrium to the strongback tie and braces; see Figure C.18(a).

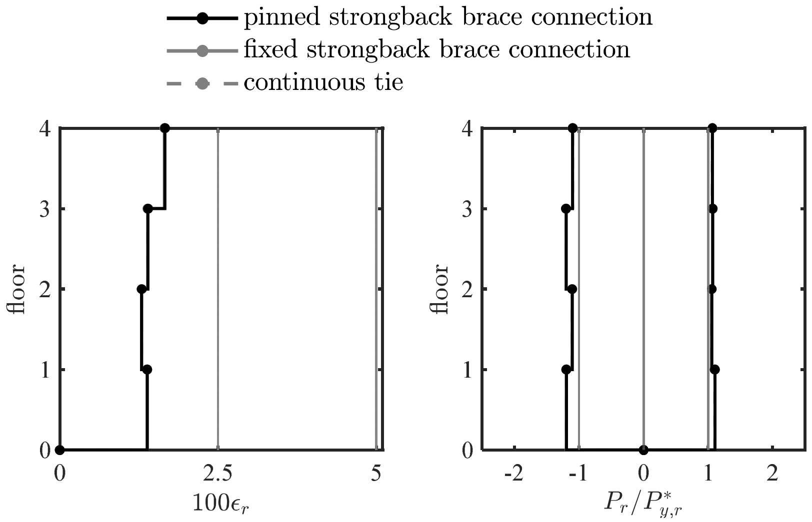

(a) (b)

Figure C.16. Case 5 – Inelastic brace peak response envelopes.
(a) strain demand, (b) axial demand-to-capacity ratio

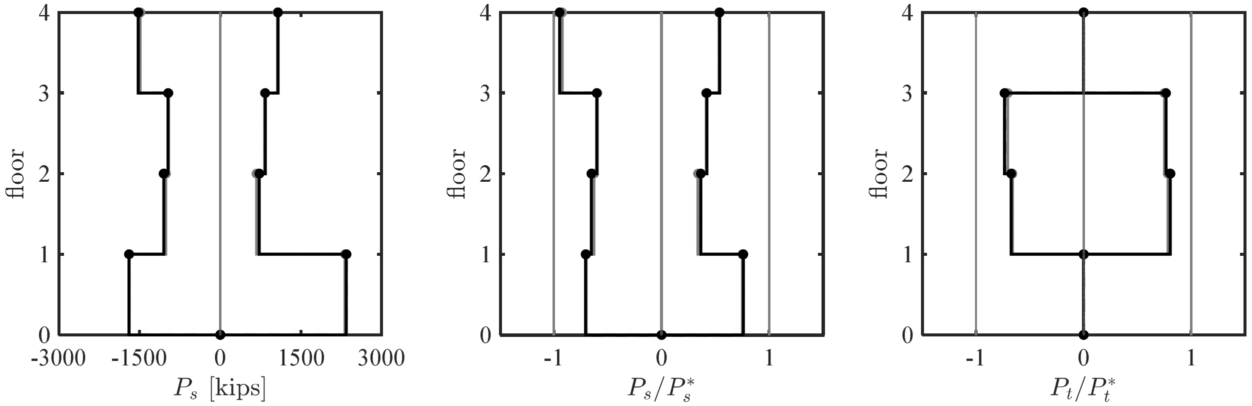

(a) (b) (c)

Figure C.17. Case 5 – Strongback elements peak response envelopes.
(a) axial-force demand; (b) and (c) axial demand-to-capacity ratio

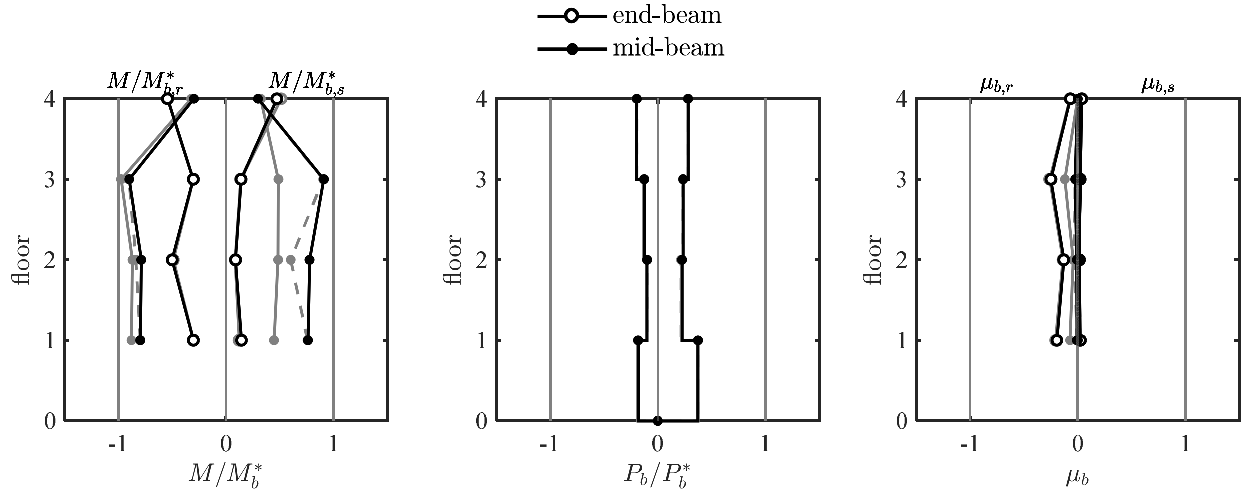

(a) (b) (c)

Figure C.18. Case 5 – Beam peak response envelopes.
(a) moment demand; (b) axial-force demand; (c) deformation acceptability ratio

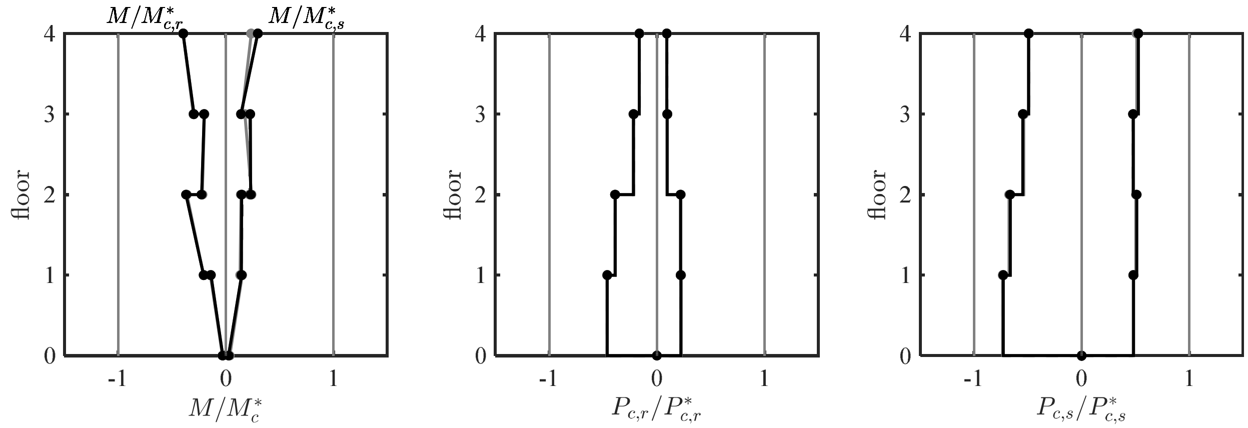

(a) (b) (c)

Figure C.19. Case 5 – Column peak response envelopes.
(a) moment demand; (b) and (c) axial-force demand. (a) axial-force demand; (b) and (c) axial demand-to-capacity ratio

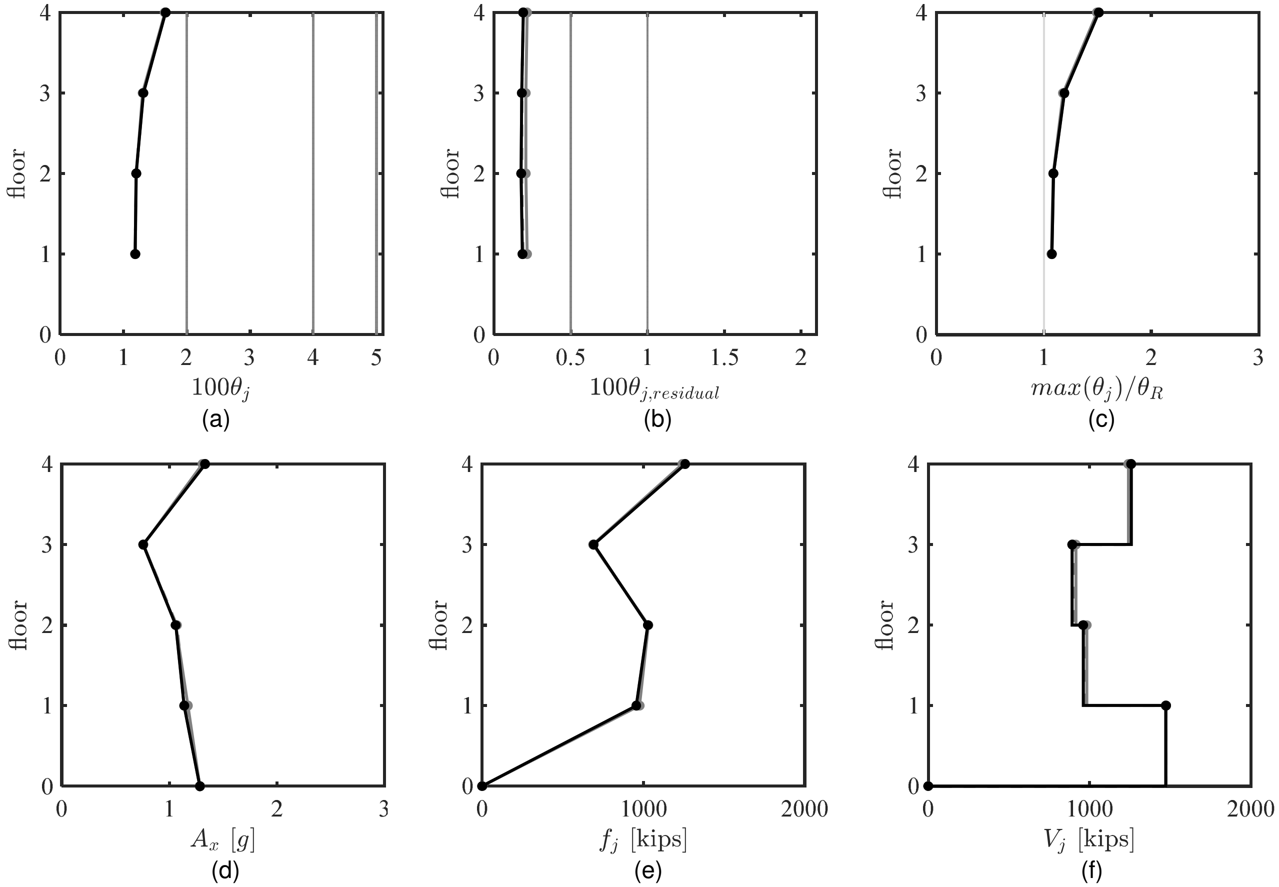

Figure C.20. Case 5 – Global peak response envelopes.
(a) peak story drift ratio; (b) peak residual drift ratio; (c) drift concentration factor; (d) absolute acceleration; (e) estimated peak equivalent-lateral force distribution; (f) peak story shear

C.5 OFFSET CASE – LOCATION OF BRACE-TO-BEAM INTERSECTION

A description of these results can be found in Section 6.3.2.

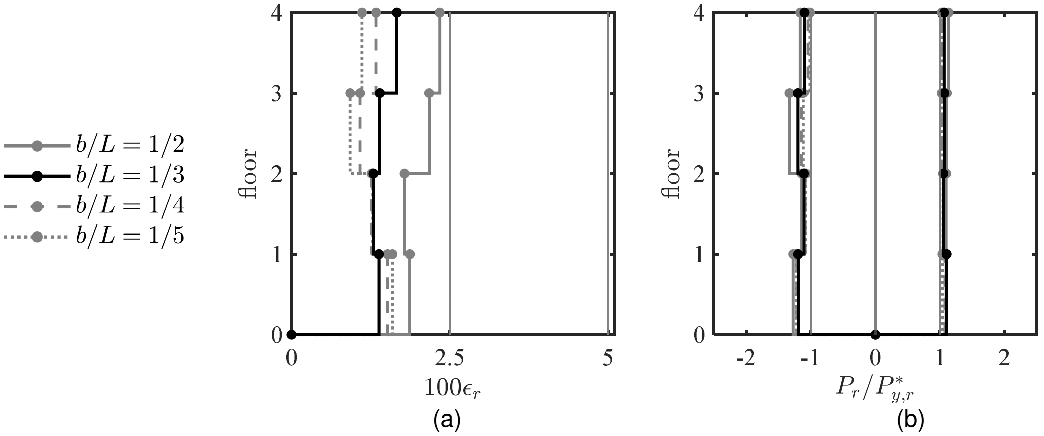

Figure C.21. Offset case – Inelastic brace peak response envelopes.
(a) strain demand, (b) axial demand-to-capacity ratio

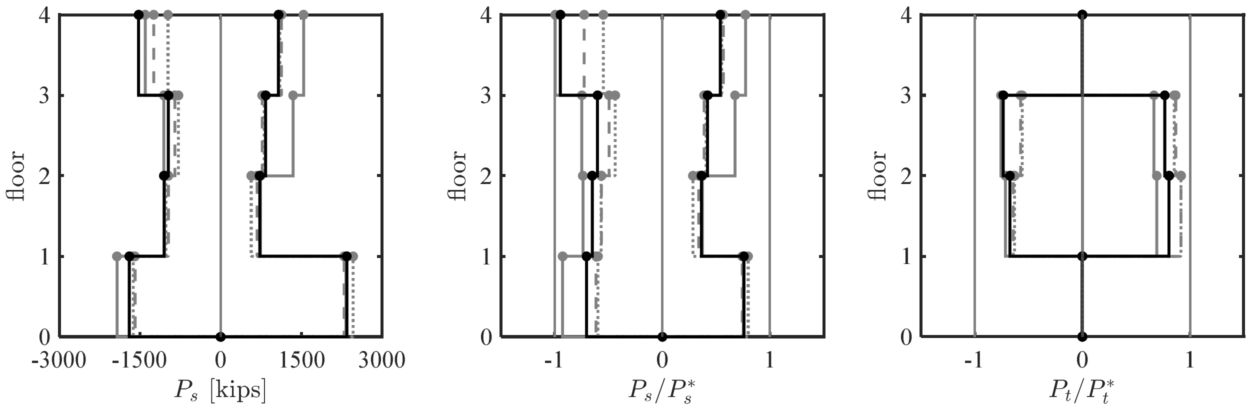

(a) (b) (c)

Figure C.22. Offset case – Strongback elements peak response envelopes.
(a) axial-force demand; (b) and (c) axial demand-to-capacity ratio

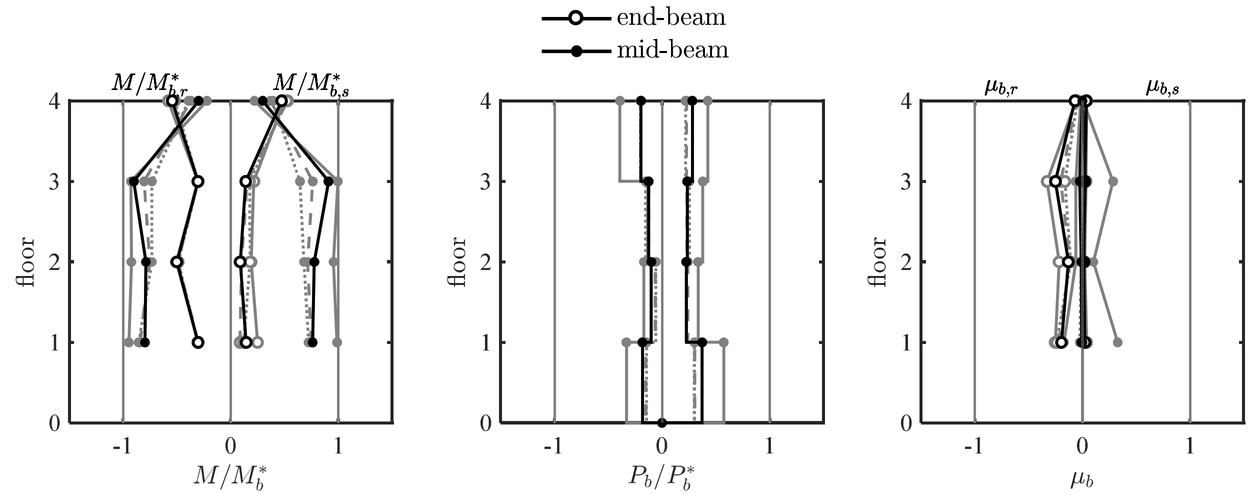

(a) (b) (c)

Figure C.23. Offset case – Beam peak response envelopes.
(a) moment demand; (b) axial-force demand; (c) deformation acceptability ratio

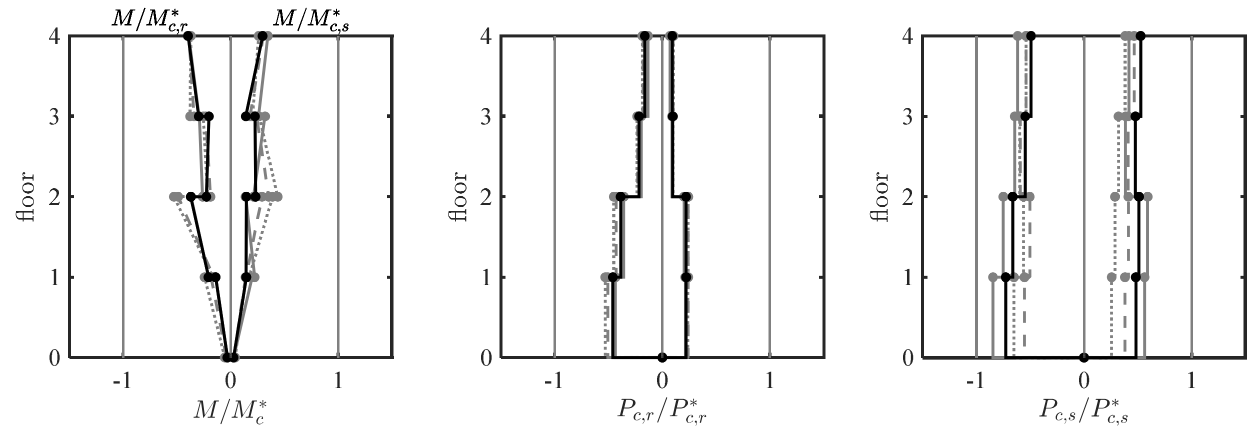

(a) (b) (c)

Figure C.24. Offset case – Column peak response envelopes.

(a) moment demand; (b) and (c) axial-force demand. (a) axial-force demand; (b) and (c) axial demand-to-capacity ratio

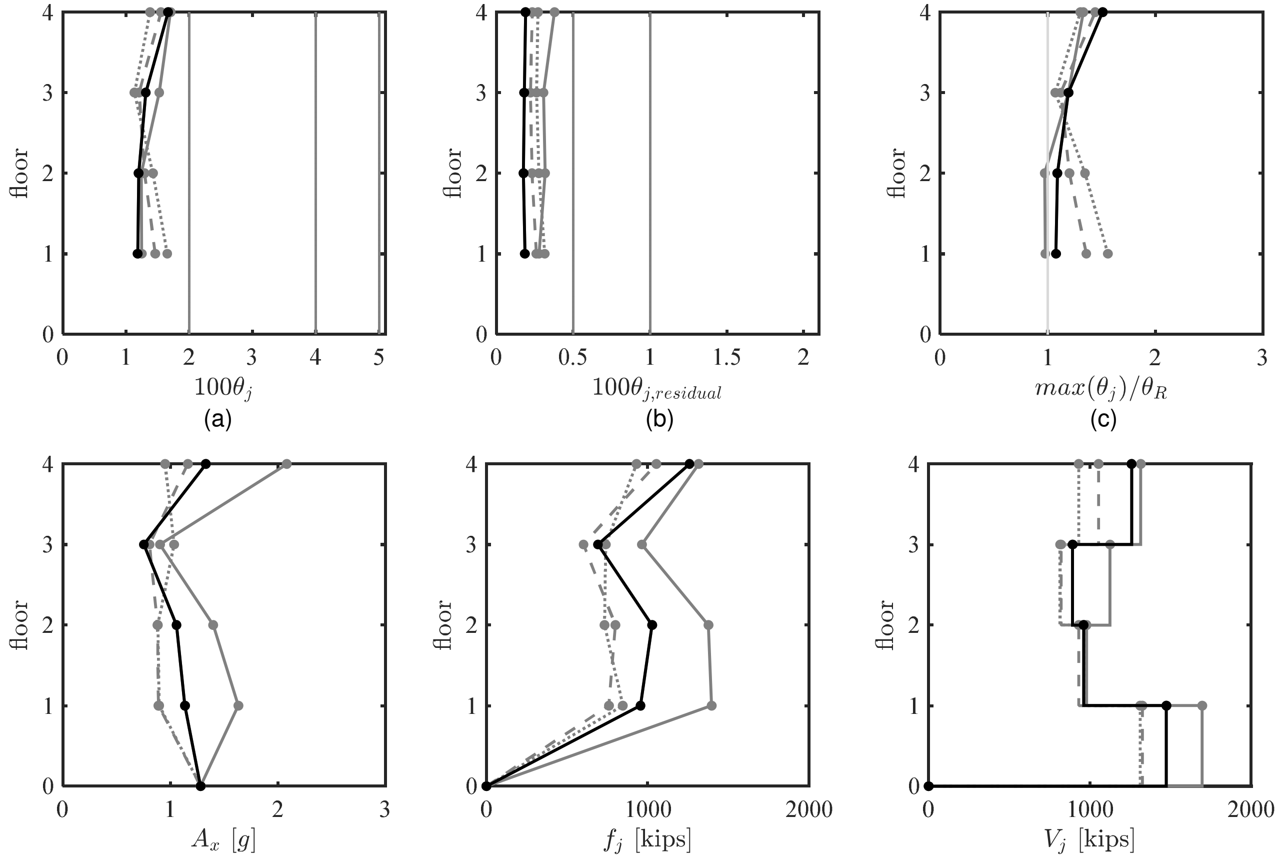

(a) (b) (c)

(d) (e) (f)

Figure C.25. Offset case – Global peak response envelopes.

(a) peak story drift ratio; (b) peak residual drift ratio; (c) drift concentration factor; (d) absolute acceleration; (e) estimated peak equivalent-lateral force distribution; (f) peak story shear

Appendix D Median Envelope Results from the Parametric Study

This appendix provides additional plots of the median envelopes described in the parametric study conducted in Chapter 6.

D.1 CASE 2 – MEDIAN BEAM END CONNECTIONS

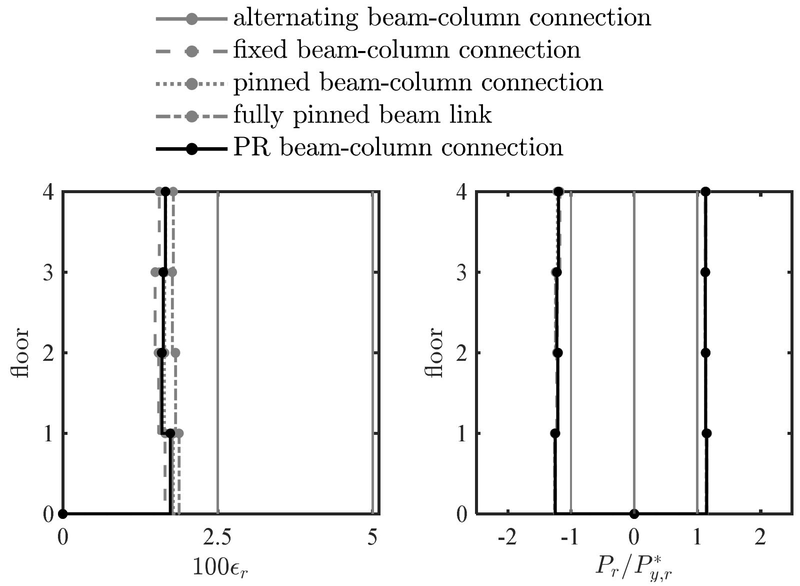

(a) (b)

Figure D.1. Case 2 median – Inelastic brace peak response envelopes.
(a) strain demand, (b) axial demand-to-capacity ratio

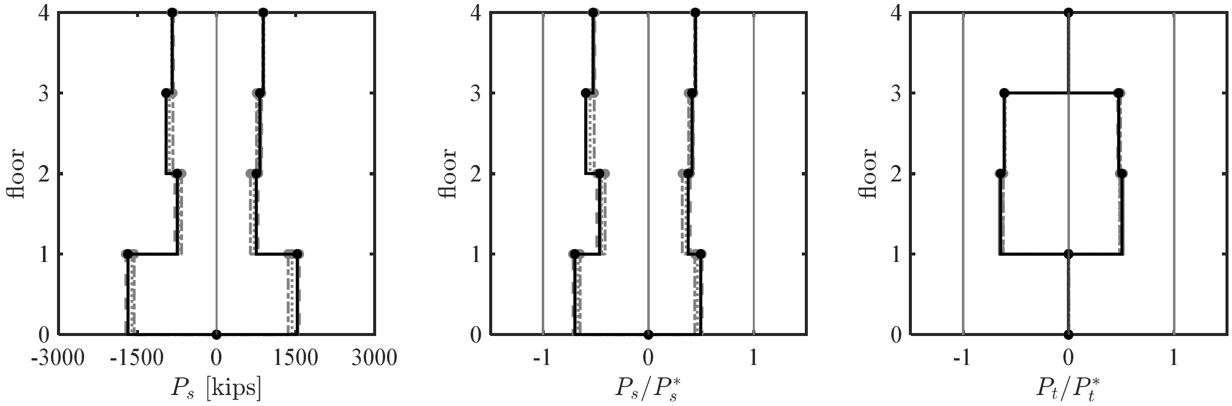

(a) (b) (c)

Figure D.2. Case 2 median – Strongback elements peak response envelopes.
(a) axial-force demand; (b) and (c) axial demand-to-capacity ratio

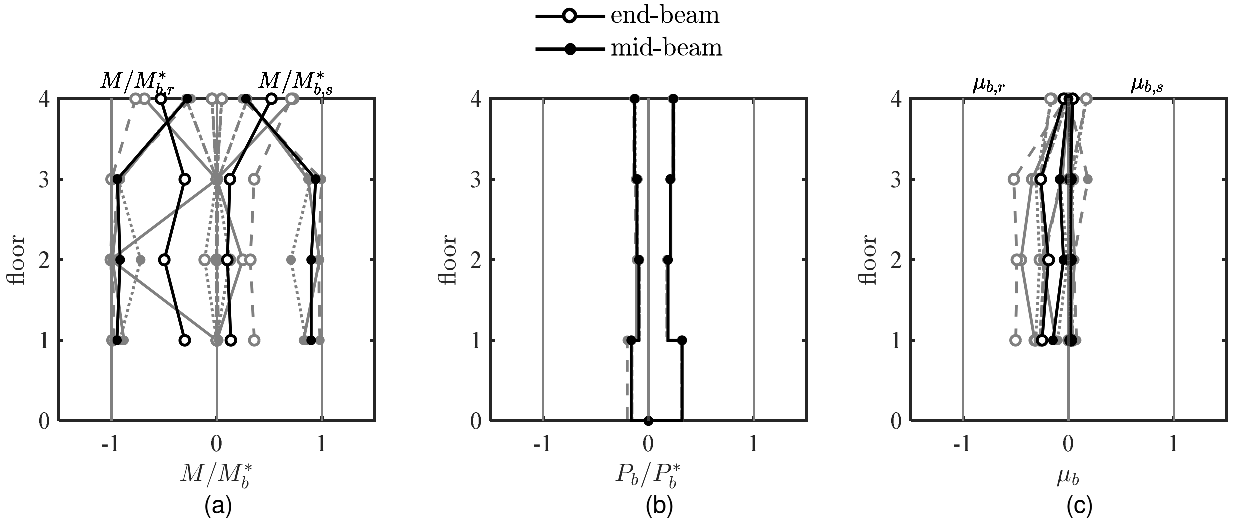

(a) (b) (c)

Figure D.3. Case 2 median – Beam peak response envelopes.
(a) moment demand; (b) axial-force demand; (c) deformation acceptability ratio

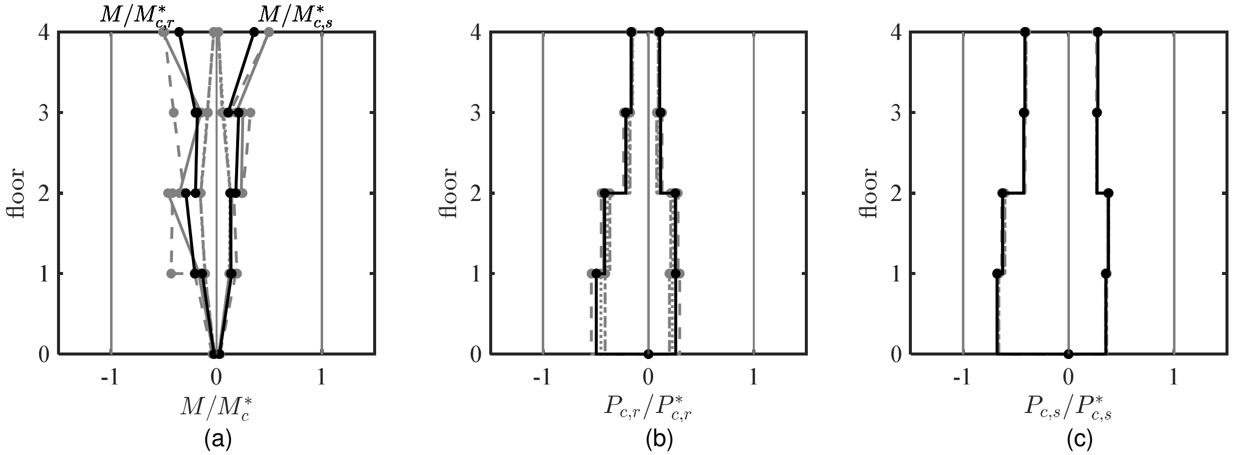

(a) (b) (c)

Figure D.4. Case 2 median – Column peak response envelopes.
(a) moment demand; (b) and (c) axial-force demand. (a) axial-force demand; (b) and (c) axial demand-to-capacity ratio

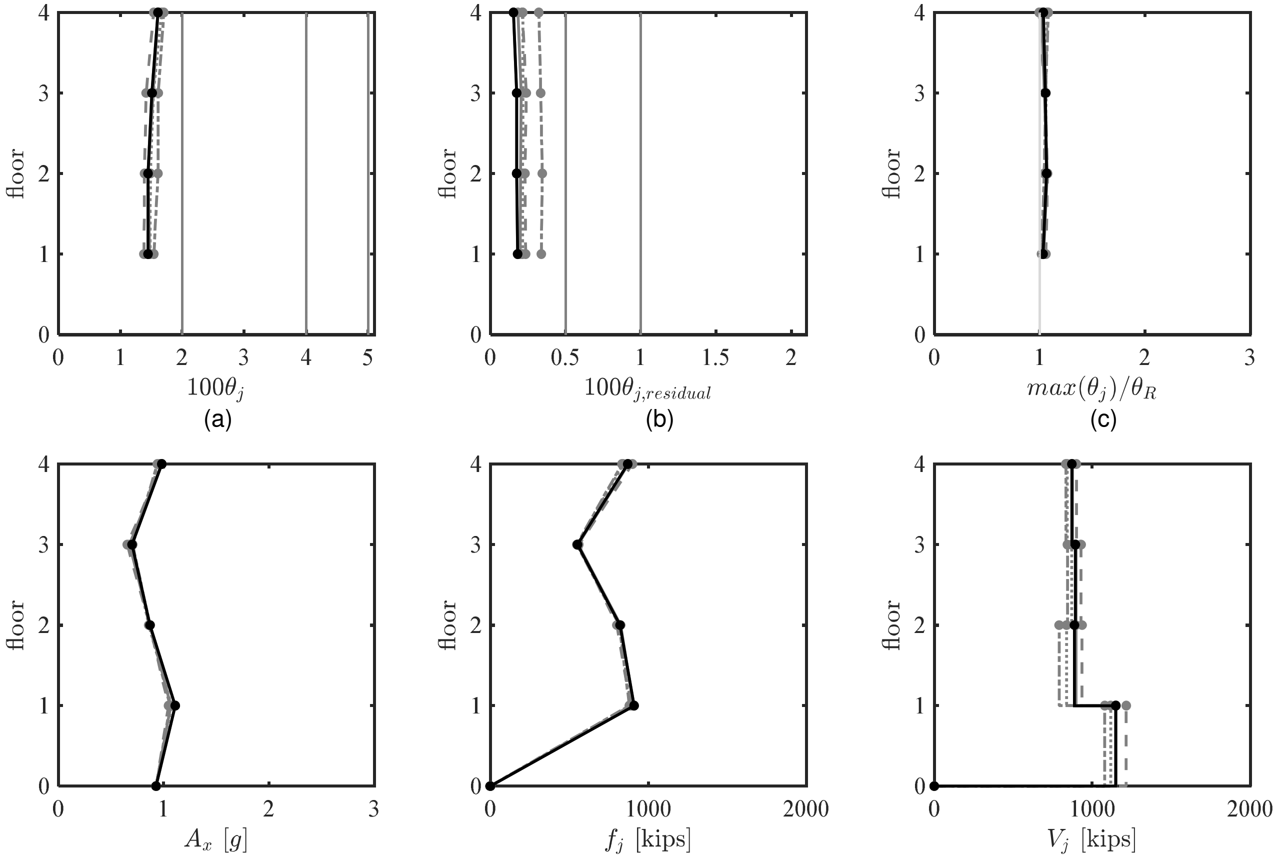

(a) (b) (c)

(d) (e) (f)

Figure D.5. Case 2 median – Global peak response envelopes.
(a) peak story drift ratio; (b) peak residual drift ratio; (c) drift concentration factor; (d) absolute acceleration; (e) estimated peak equivalent-lateral force distribution; (f) peak story shear

D.2 CASE 3 – MEDIAN COLUMN BASE FIXITY AND BENDING ORIENTATION

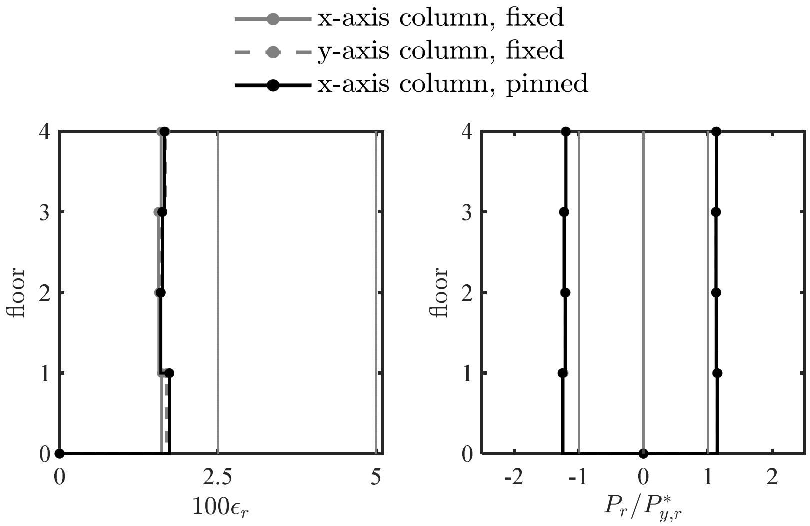

(a) (b)

Figure D.6. Case 3 median – Inelastic brace peak response envelopes.
(a) strain demand, (b) axial demand-to-capacity ratio

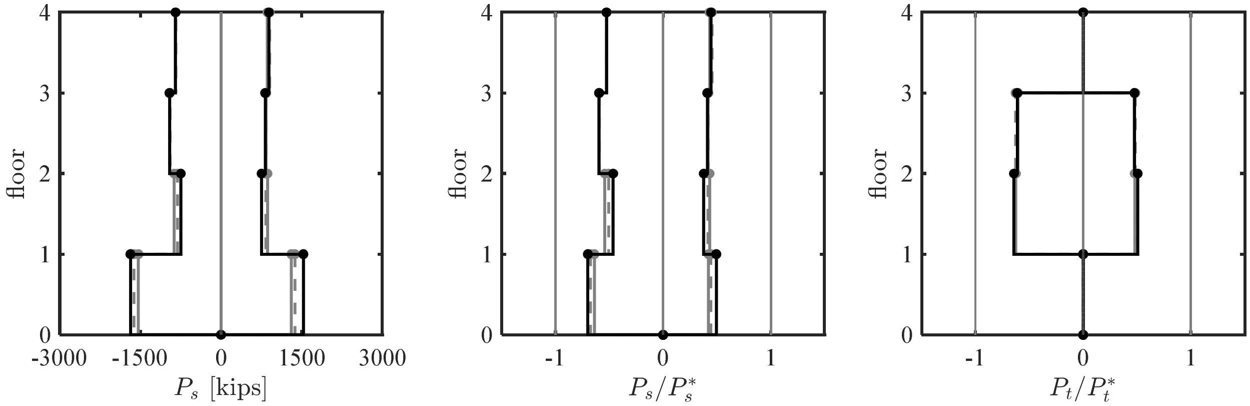

(a) (b) (c)

Figure D.7. Case 3 median – Strongback elements peak response envelopes.
(a) axial-force demand; (b) and (c) axial demand-to-capacity ratio

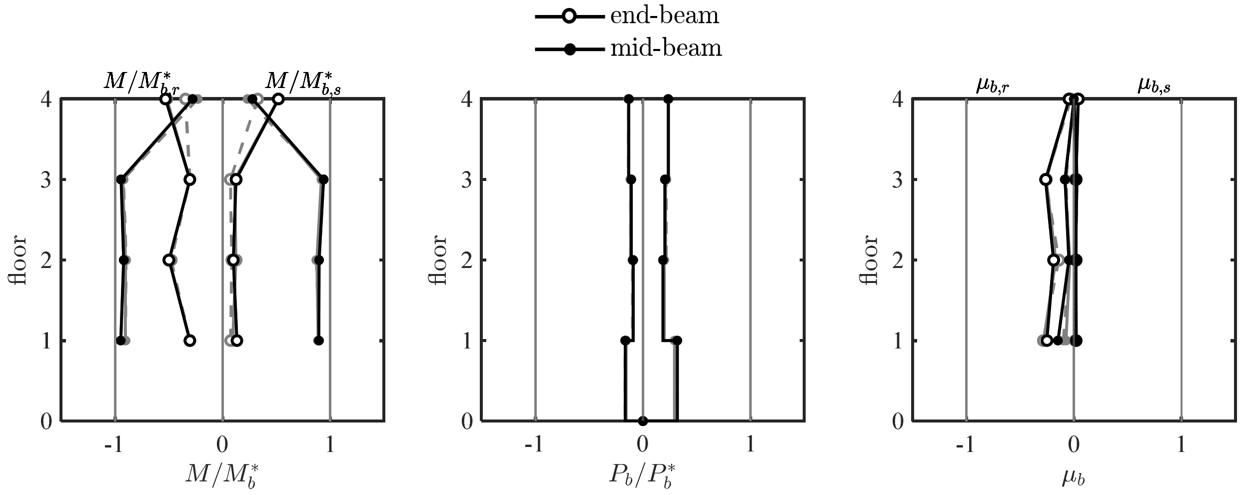

(a) (b) (c)

Figure D.8. Case 3 median – Beam peak response envelopes.
(a) moment demand; (b) axial-force demand; (c) deformation acceptability ratio

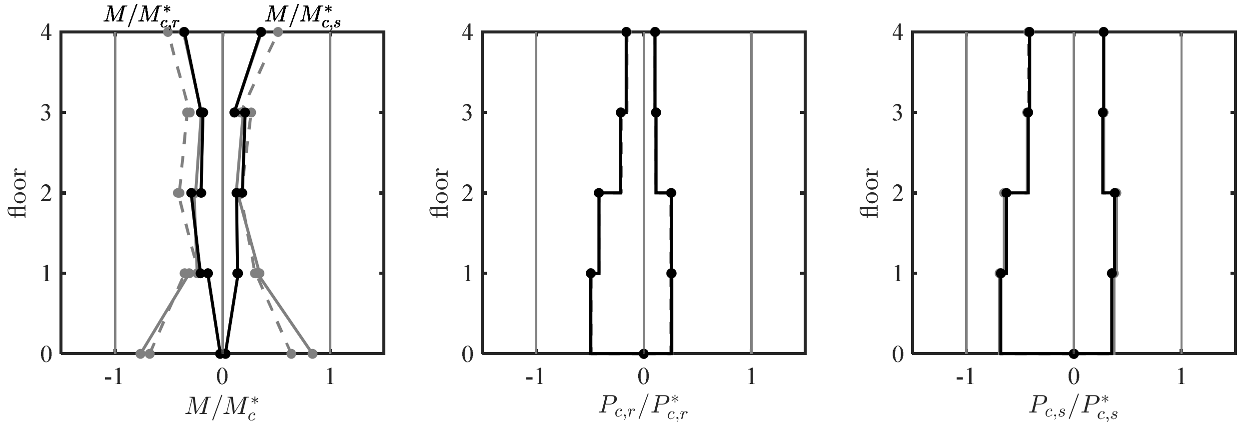

(a) (b) (c)

Figure D.9. Case 3 median – Column peak response envelopes.
(a) moment demand; (b) and (c) axial-force demand. (a) axial-force demand; (b) and (c) axial demand-to-capacity ratio

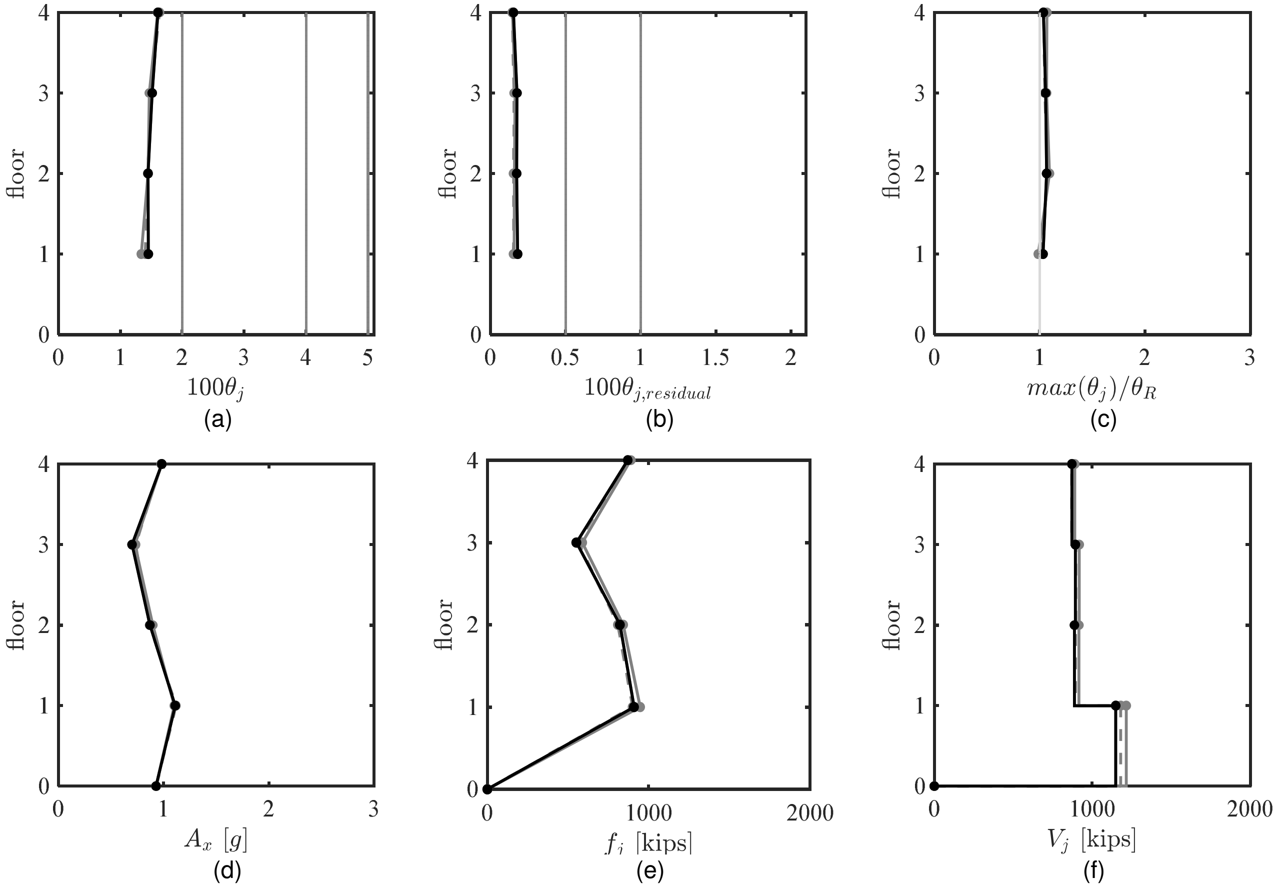

Figure D.10. Case 3 median – Global peak response envelopes.
(a) peak story drift ratio; (b) peak residual drift ratio; (c) drift concentration factor; (d) absolute acceleration; (e) estimated peak equivalent-lateral force distribution; (f) peak story shear

D.3 CASE 4 – MEDIAN BEAM COMPOSITE ACTION AND DIAPHRAGM RIGIDITY

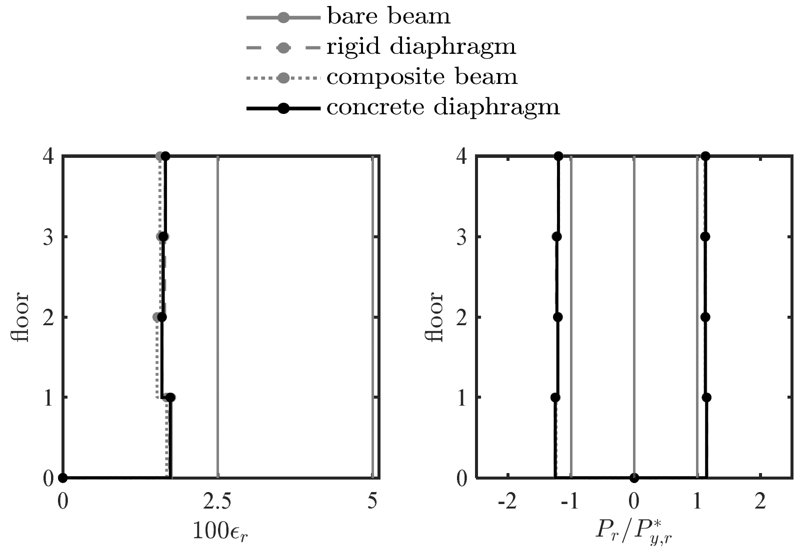

(a) (b)

Figure D.11. Case 4 median – Inelastic brace peak response envelopes.
(a) strain demand, (b) axial demand-to-capacity ratio

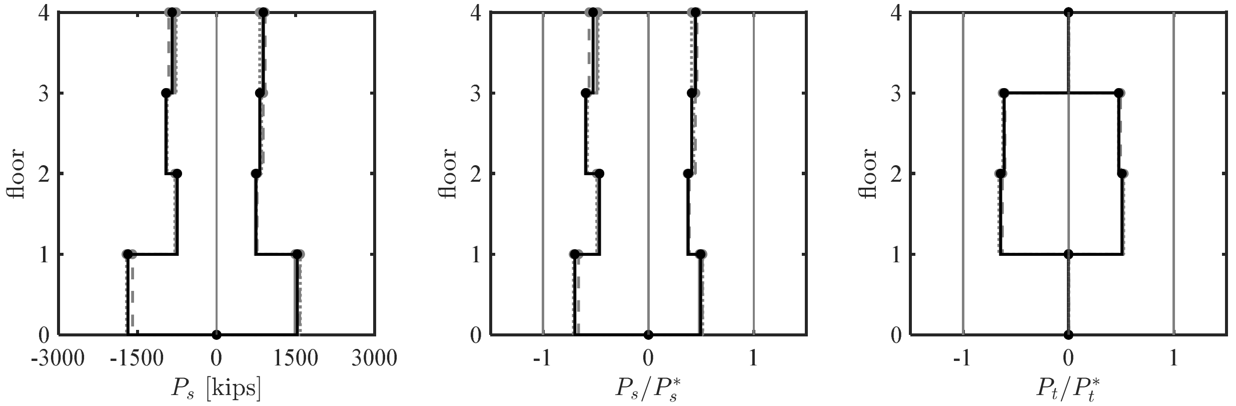

(a) (b) (c)

Figure D.12. Case 4 median – Strongback elements peak response envelopes.
(a) axial-force demand; (b) and (c) axial demand-to-capacity ratio

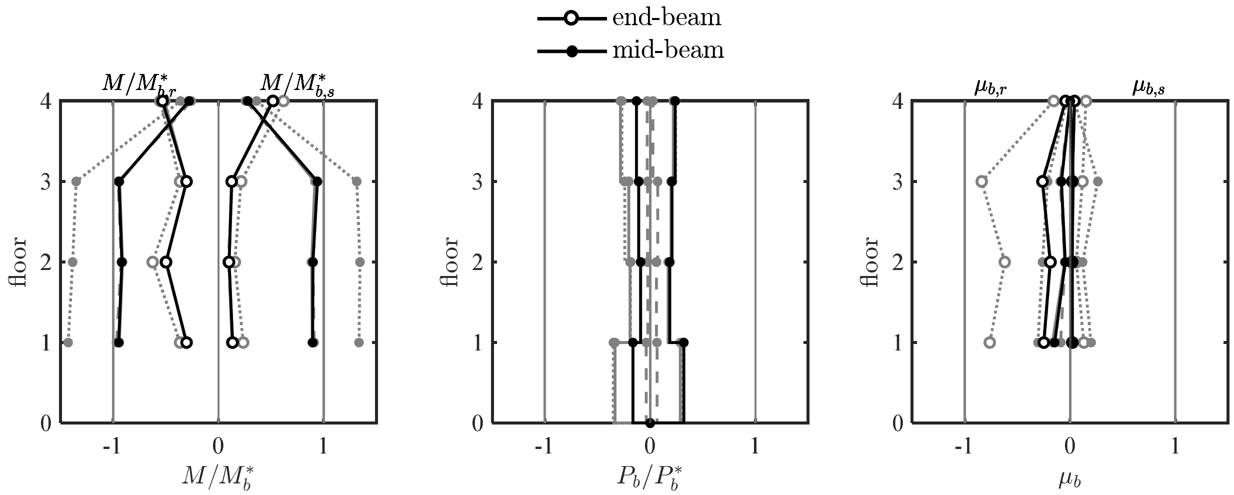

(a) (b) (c)

Figure D.13. Case 4 median – Beam peak response envelopes.
(a) moment demand; (b) axial-force demand; (c) deformation acceptability ratio

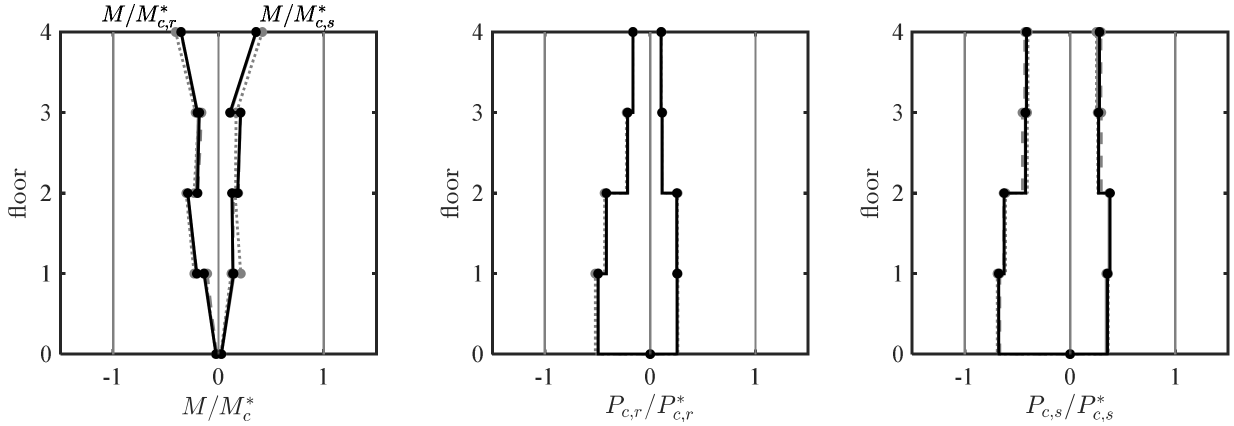

(a) (b) (c)

Figure D.14. Case 4 median – Column peak response envelopes.
(a) moment demand; (b) and (c) axial-force demand. (a) axial-force demand; (b) and (c) axial demand-to-capacity ratio

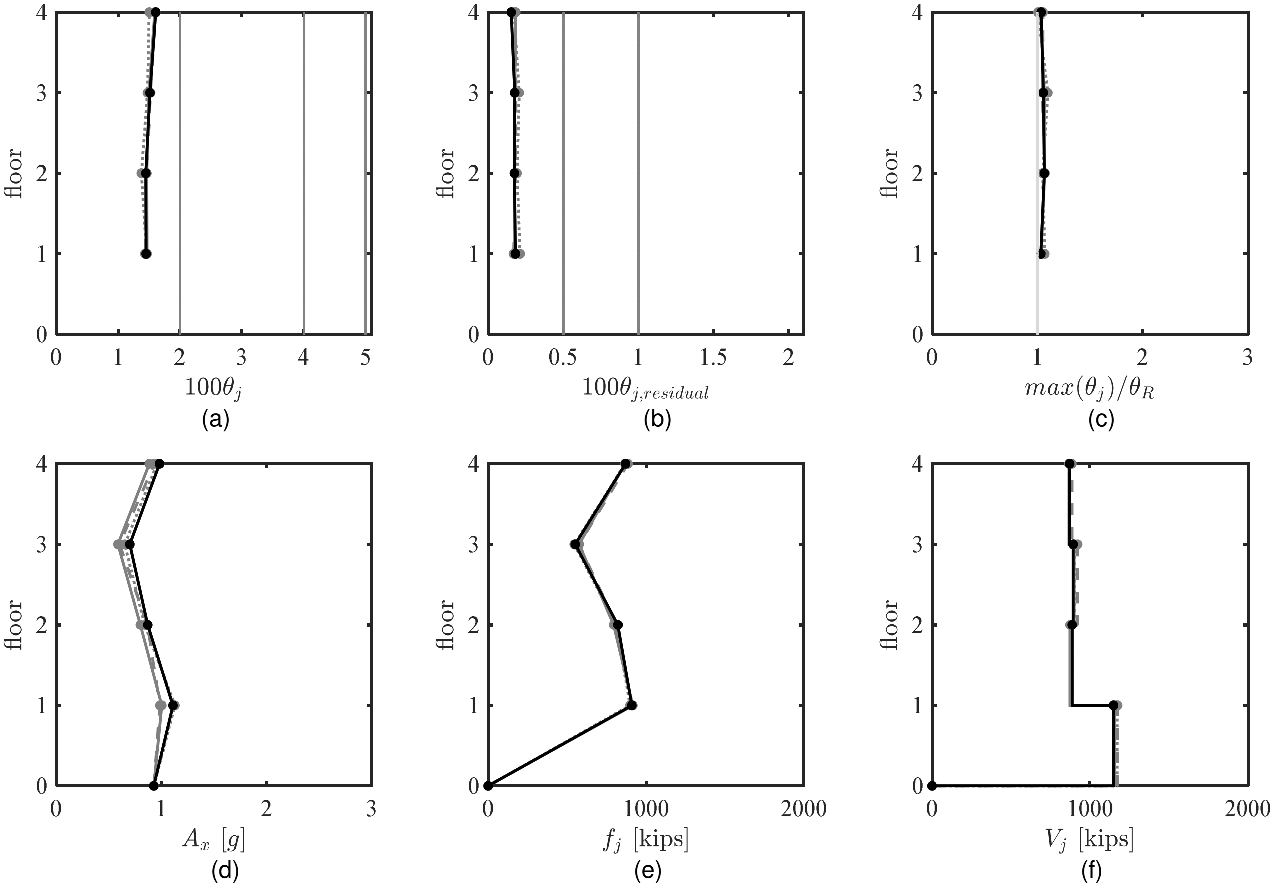

Figure D.15. Case 4 median – Global peak response envelopes.

(a) peak story drift ratio; (b) peak residual drift ratio; (c) drift concentration factor; (d) absolute acceleration; (e) estimated peak equivalent-lateral force distribution; (f) peak story shear

D.4 CASE 5 – MEDIAN STRONGBACK BRACE AND TIE END CONDITION

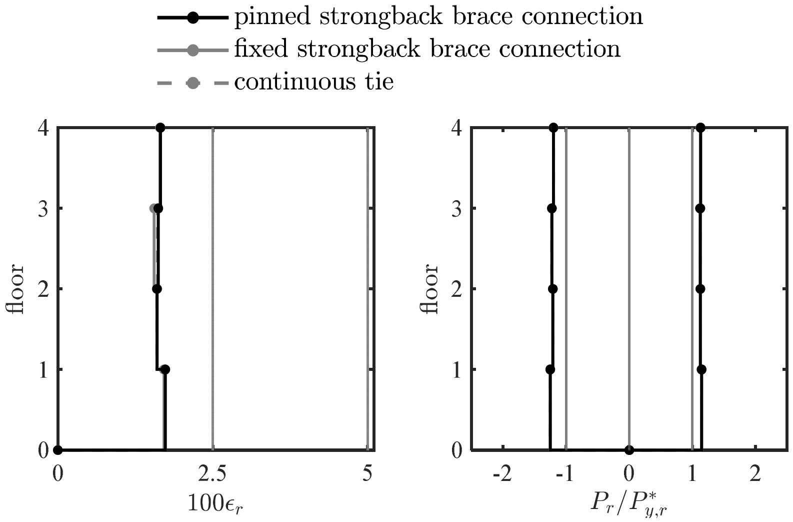

(a) (b)

Figure D.16. Case 5 median – Inelastic brace peak response envelopes.
(a) strain demand, (b) axial demand-to-capacity ratio

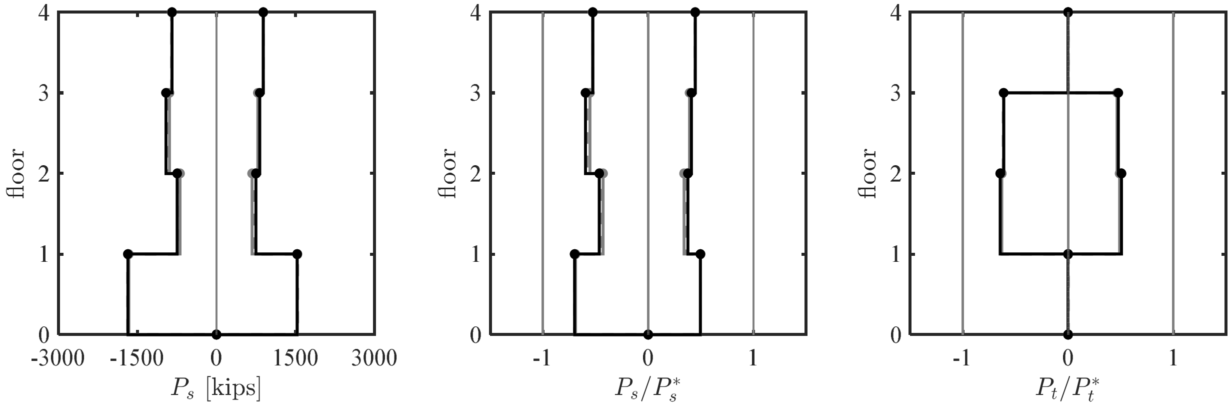

(a) (b) (c)

Figure D.17. Case 5 median – Strongback elements peak response envelopes.
(a) axial-force demand; (b) and (c) axial demand-to-capacity ratio

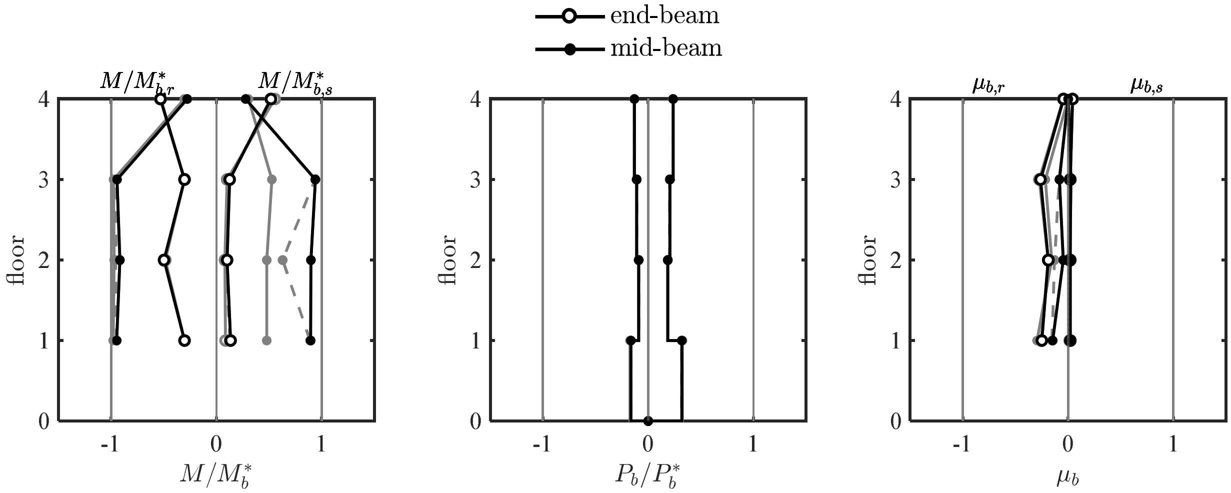

(a) (b) (c)

Figure D.18. Case 5 median – Beam peak response envelopes.
(a) moment demand; (b) axial-force demand; (c) deformation acceptability ratio

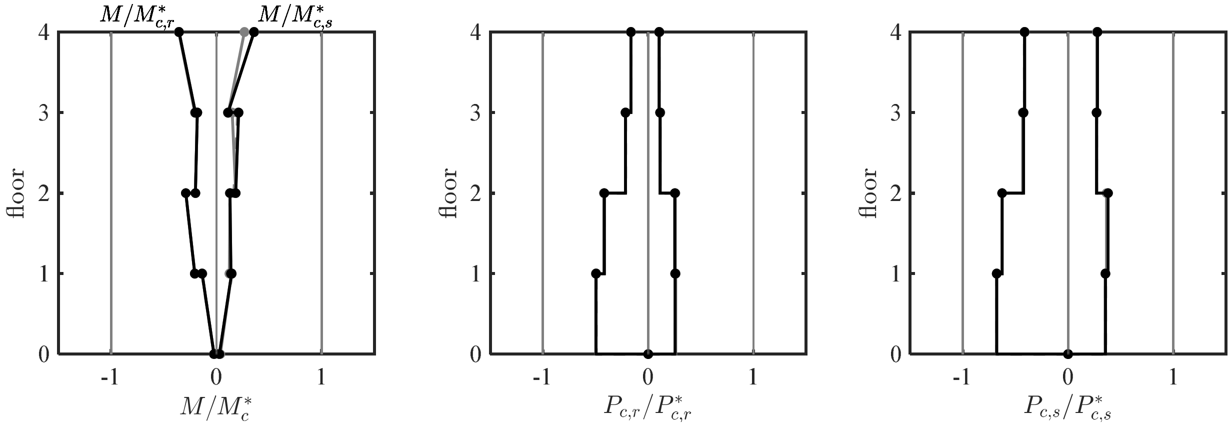

(a) (b) (c)

Figure D.19. Case 5 median – Column peak response envelopes.
(a) moment demand; (b) and (c) axial-force demand. (a) axial-force demand; (b) and (c) axial demand-to-capacity ratio

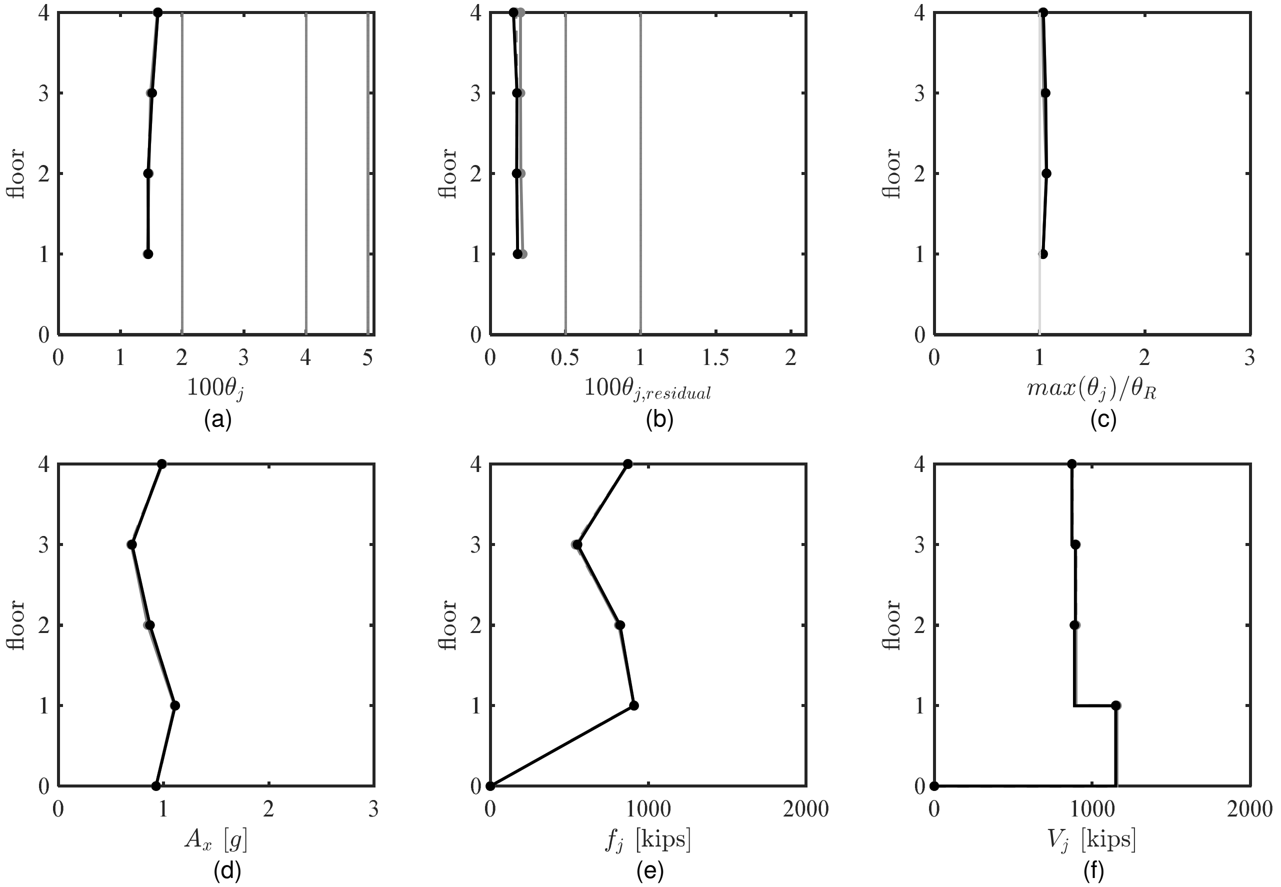

(a) (b) (c)

(d) (e) (f)

Figure D.20. Case 5 median – Global peak response envelopes.
(a) peak story drift ratio; (b) peak residual drift ratio; (c) drift concentration factor; (d) absolute acceleration; (e) estimated peak equivalent-lateral force distribution; (f) peak story shear

Appendix E Peak Response Plots

This appendix gives additional calculations of plots of the height-wise distribution of demands at the time of peak inelastic brace, strongback brace, and tie axial force from Chapter 7.

E.1 PEAK RESPONSE

Table E.1. Median of peak response.

Peak Response	**gm no.**	**Axial-force demand [kips]**									
		$P_{r,1}$	$P_{r,2}$	$P_{r,3}$	$P_{r,4}$	$P_{s,1}$	$P_{s,2}$	$P_{s,3}$	$P_{s,4}$	$P_{t,2}$	$P_{t,3}$
$\boldsymbol{min(P_{r1})}$	30	-461	422	-301	314	991	-445	210	87	539	402
$\boldsymbol{min(P_{r2})}$	4	391	-447	396	-425	-1051	530	-347	-184	-670	-503
$\boldsymbol{min(P_{r3})}$	4	-423	399	-451	414	128	-535	661	-347	-83	-197
$\boldsymbol{min(P_{r4})}$	5	-269	95	198	-443	910	-108	-755	1051	782	934
$\boldsymbol{max(P_{r1})}$	29	421	-401	406	-359	-828	492	-224	-166	-540	-469
$\boldsymbol{max(P_{r2})}$	28	-398	415	-378	403	857	-433	266	142	537	454
$\boldsymbol{max(P_{r3})}$	36	401	-438	413	-449	-493	532	-619	40	-226	-96
$\boldsymbol{max(P_{r4})}$	21	-63	239	-324	415	300	-265	409	12	227	175
$\boldsymbol{min(P_{s1})}$	9	447	-439	363	-129	-1687	308	385	-465	-1096	-1034
$\boldsymbol{min(P_{s2})}$	36	-425	383	-388	59	1083	-752	-7	572	949	842
$\boldsymbol{min(P_{s3})}$	15	368	-449	410	-471	-243	664	-966	91	-46	155
$\boldsymbol{min(P_{s4})}$	29	199	-245	-285	366	-997	217	485	-854	-735	-717
$\boldsymbol{max(P_{s1})}$	31	-444	387	-408	375	1519	-499	-86	379	1085	963
$\boldsymbol{max(P_{s2})}$	15	408	-486	409	-467	-383	751	-894	-15	-192	9
$\boldsymbol{max(P_{s3})}$	2	2	244	-443	407	-381	-375	821	-340	-257	-354
$\boldsymbol{max(P_{s4})}$	33	-3	-253	399	-398	624	-29	-716	887	756	799
$\boldsymbol{min(P_{t2})}$	1	-35	-1	-6	-6	-57	-7	-14	-13	-44	-21
$\boldsymbol{min(P_{t3})}$	24	418	-457	-147	276	-1811	391	545	-859	-1197	-1033
$\boldsymbol{max(P_{t2})}$	23	368	-168	-385	377	-1492	198	1055	-851	-1121	-1135
$\boldsymbol{max(P_{t3})}$	1	-35	-1	-6	-6	-57	-7	-14	-13	-44	-21

Table E.2. 85th percentile of peak response.

Peak Response	**gm no.**	**Axial-force demand [kips]**									
		$P_{r,1}$	$P_{r,2}$	$P_{r,3}$	$P_{r,4}$	$P_{s,1}$	$P_{s,2}$	$P_{s,3}$	$P_{s,4}$	$P_{t,2}$	$P_{t,3}$
$\boldsymbol{min(P_{r1})}$	8	-527	455	-481	293	1019	-843	158	448	875	784
$\boldsymbol{min(P_{r2})}$	26	452	-512	461	-489	-892	551	-610	27	-433	-237
$\boldsymbol{min(P_{r3})}$	8	-475	402	-514	408	730	-806	529	191	595	438
$\boldsymbol{min(P_{r4})}$	1	435	-523	429	-500	-743	568	-716	72	-315	-107
$\boldsymbol{max(P_{r1})}$	24	451	-497	450	-495	-798	690	-606	-104	-492	-314
$\boldsymbol{max(P_{r2})}$	33	-305	451	-244	-10	721	-597	131	322	536	409
$\boldsymbol{max(P_{r3})}$	2	372	-518	445	-557	250	459	-1276	657	603	806
$\boldsymbol{max(P_{r4})}$	26	-416	420	-417	452	779	-351	199	113	437	438
$\boldsymbol{min(P_{s1})}$	6	386	-401	365	-342	-2104	545	390	-966	-1692	-1604
$\boldsymbol{min(P_{s2})}$	24	-443	426	-466	423	252	-994	714	195	374	245
$\boldsymbol{min(P_{s3})}$	2	372	-518	445	-557	250	459	-1276	657	603	806
$\boldsymbol{min(P_{s4})}$	39	247	-137	-171	356	-1383	85	656	-1258	-1088	-1170
$\boldsymbol{max(P_{s1})}$	5	-443	386	-398	374	1881	-726	-163	951	1595	1483
$\boldsymbol{max(P_{s2})}$	43	126	-442	399	-377	-935	893	-153	-589	-1068	-932
$\boldsymbol{max(P_{s3})}$	39	21	146	-422	381	-939	-274	1134	-582	-749	-843
$\boldsymbol{max(P_{s4})}$	26	-305	202	211	-373	1322	-16	-720	1173	939	1064
$\boldsymbol{min(P_{t2})}$	1	-35	-1	-6	-6	-57	-7	-14	-13	-44	-21
$\boldsymbol{min(P_{t3})}$	28	405	-506	397	-464	-1965	687	-126	-835	-1523	-1312
$\boldsymbol{max(P_{t2})}$	13	-20	299	-465	429	-1149	123	1283	-1230	-1358	-1447
$\boldsymbol{max(P_{t3})}$	1	-35	-1	-6	-6	-57	-7	-14	-13	-44	-21

Table E.3. 100th percentile of peak response.

Peak Response	**gm no.**	**Axial-force demand [kips]**									
		$P_{r,1}$	$P_{r,2}$	$P_{r,3}$	$P_{r,4}$	$P_{s,1}$	$P_{s,2}$	$P_{s,3}$	$P_{s,4}$	$P_{t,2}$	$P_{t,3}$
$\boldsymbol{min(P_{r1})}$	10	-701	545	-654	438	1062	-957	501	195	757	588
$\boldsymbol{min(P_{r2})}$	21	403	-596	431	-567	-1259	700	-588	-357	-844	-622
$\boldsymbol{min(P_{r3})}$	10	-698	545	-676	524	1046	-806	547	-16	614	442
$\boldsymbol{min(P_{r4})}$	21	-8	-318	417	-580	-269	359	-851	212	-141	73
$\boldsymbol{max(P_{r1})}$	10	593	-560	559	-494	-1102	621	-404	-42	-610	-469
$\boldsymbol{max(P_{r2})}$	10	-561	557	-523	533	999	-519	349	155	540	510
$\boldsymbol{max(P_{r3})}$	10	548	-546	561	-497	-948	602	-491	16	-497	-354
$\boldsymbol{max(P_{r4})}$	10	-695	544	-675	538	993	-728	588	-110	505	333
$\boldsymbol{min(P_{s1})}$	5	407	-416	392	-193	-2391	430	580	-934	-1759	-1685
$\boldsymbol{min(P_{s2})}$	42	-588	469	-584	463	1573	-1116	296	894	1469	1305
$\boldsymbol{min(P_{s3})}$	24	434	-476	447	-505	728	569	-1492	734	913	1093
$\boldsymbol{min(P_{s4})}$	25	-172	352	-476	451	-858	171	892	-1613	-1313	-1422
$\boldsymbol{max(P_{s1})}$	25	-441	378	-324	159	2532	-11	-989	756	1682	1691
$\boldsymbol{max(P_{s2})}$	25	497	-448	459	-436	-516	1120	-348	-241	-680	-567
$\boldsymbol{max(P_{s3})}$	13	-5	300	-463	427	-1116	-10	1486	-825	-1211	-1292
$\boldsymbol{max(P_{s4})}$	43	87	-287	392	-460	1342	8	-1319	1546	1535	1698
$\boldsymbol{min(P_{t2})}$	1	-35	-1	-6	-6	-57	-7	-14	-13	-44	-21
$\boldsymbol{min(P_{t3})}$	5	406	-413	391	-114	-2360	529	626	-1014	-1849	-1751
$\boldsymbol{max(P_{t2})}$	5	406	-413	391	-114	-2360	529	626	-1014	-1849	-1751
$\boldsymbol{max(P_{t3})}$	1	-35	-1	-6	-6	-57	-7	-14	-13	-44	-21

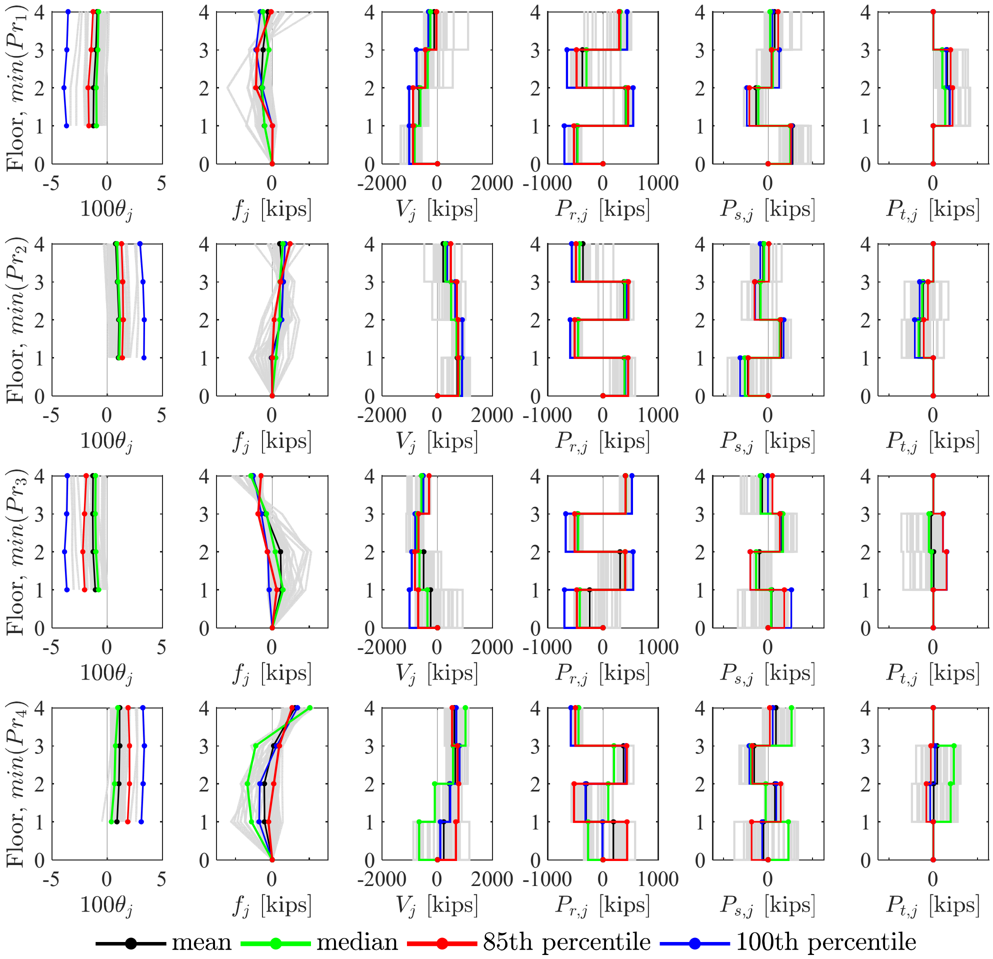

Figure E.1. Snapshot at minimization of inelastic brace demands.

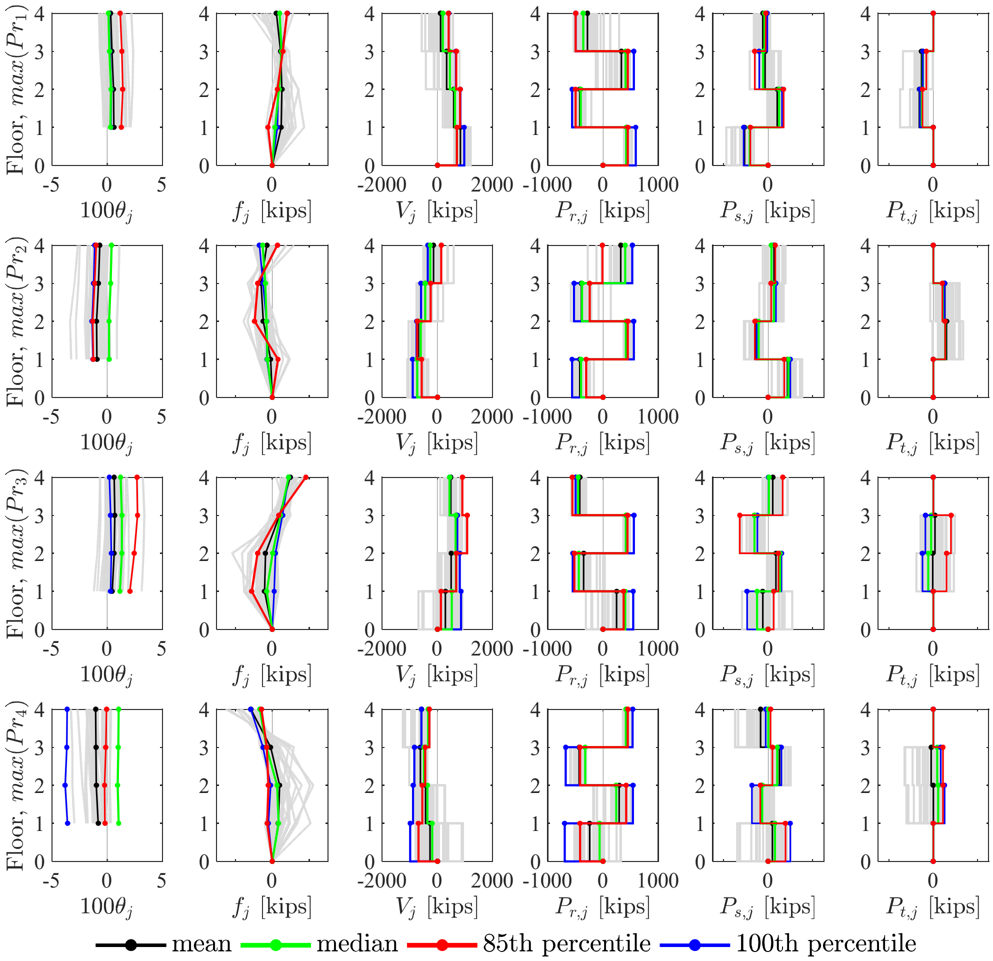

Figure E.2. Snapshot at maximization of inelastic brace demands.

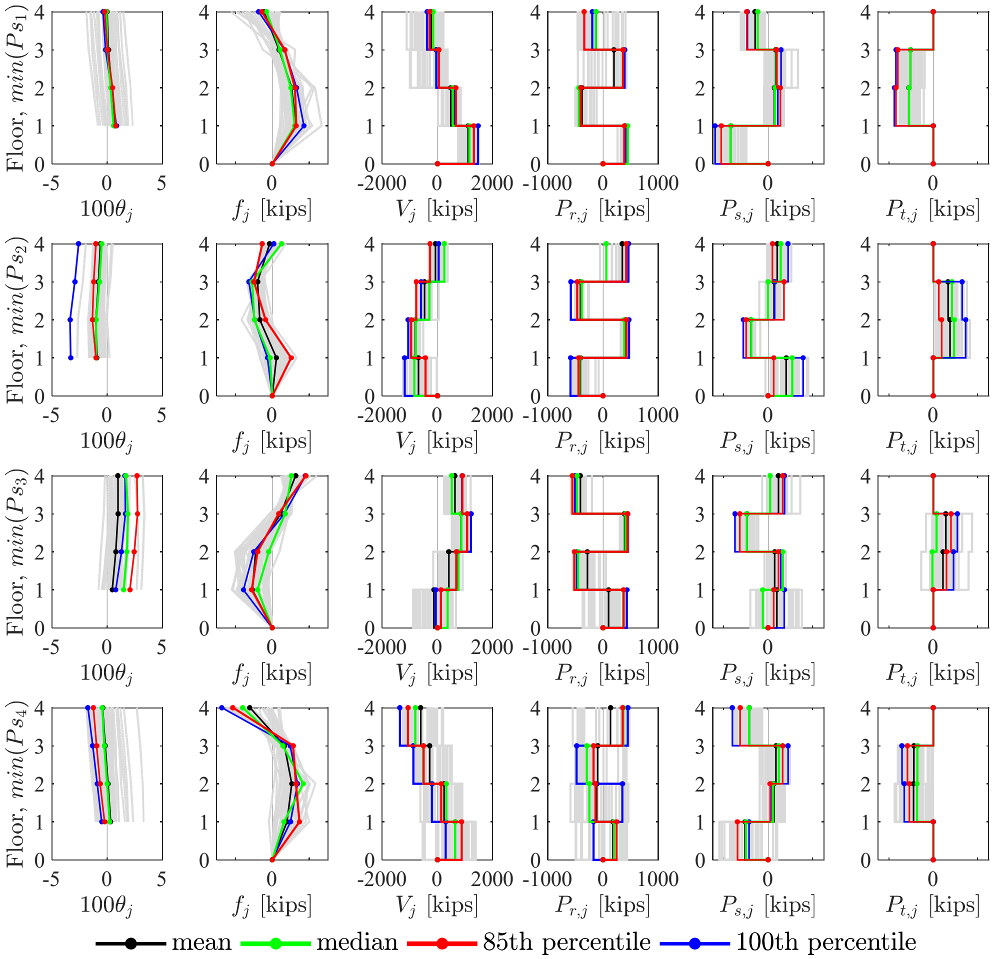

Figure E.3. Snapshot at minimization of strongback brace demands.

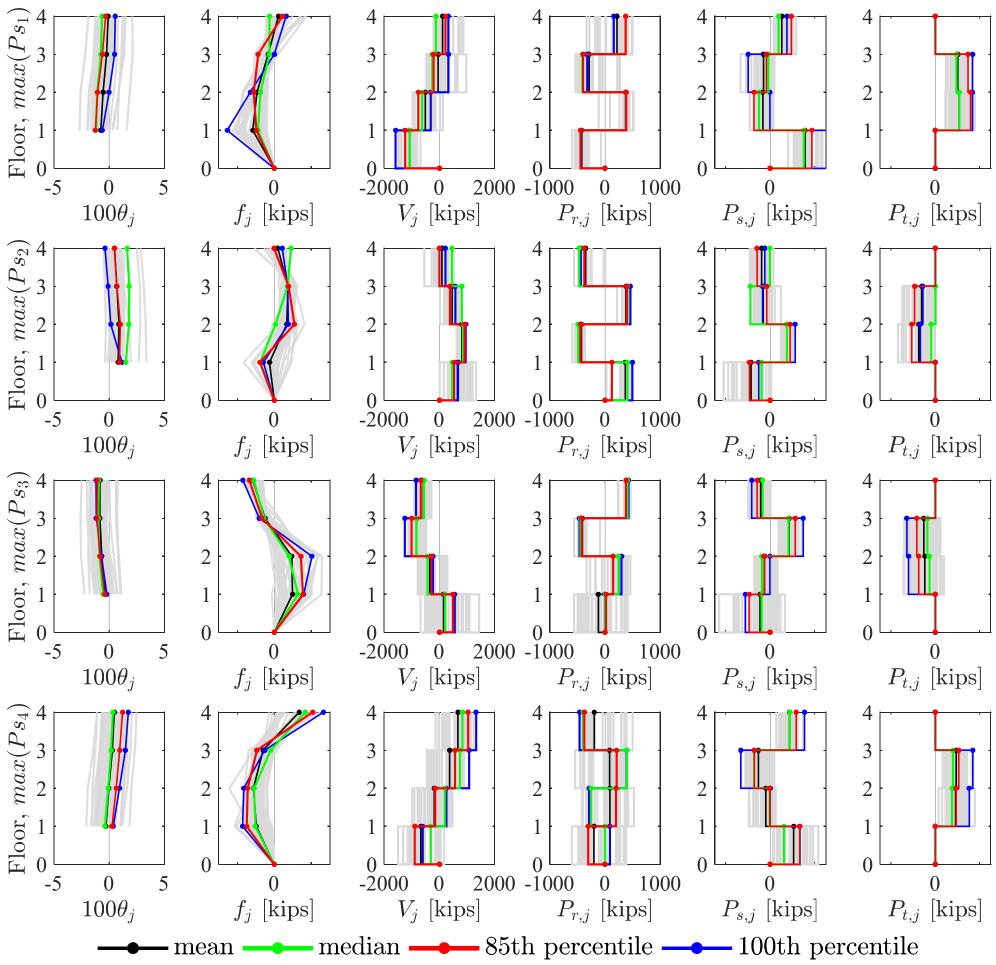

Figure E.4. Snapshot at maximization of strongback brace demands.

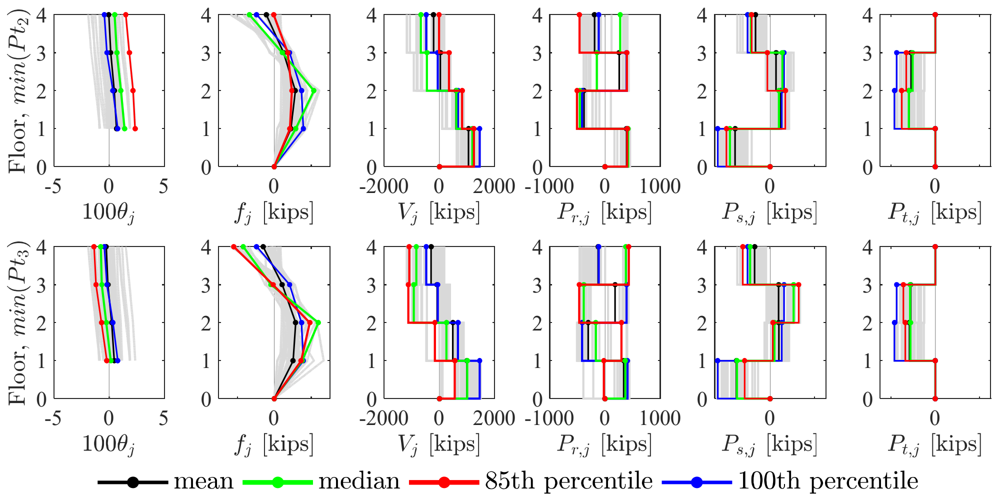

Figure E.5. Snapshot at minimization of tie demands.

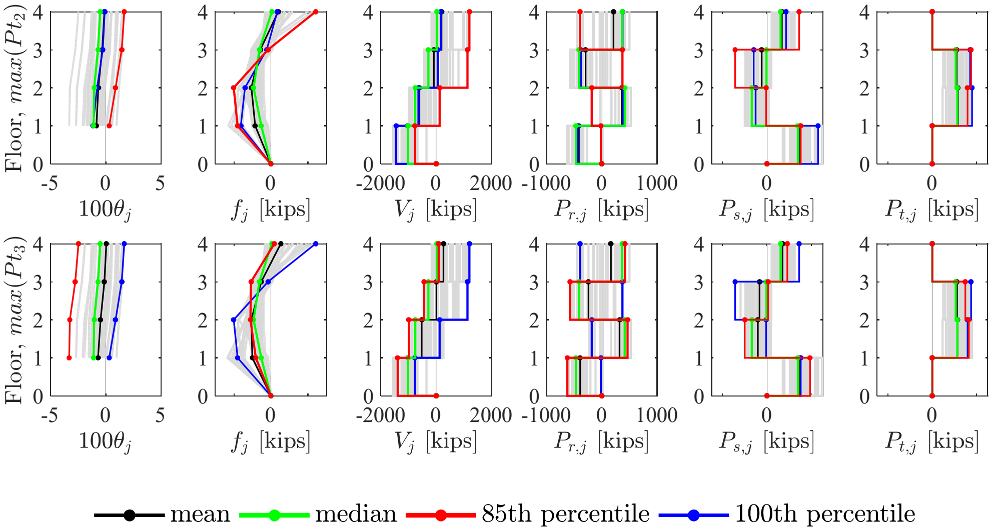

Figure E.6. Snapshot at maximization of tie demands.